

# REPORT DOCUMENTATION PAGE

Public reporting burden for this collection of information is estimated to average 1 hour per response, including the time for reviewing instructions, searching the collection of information. Send comments regarding this burden estimate or any other aspect of this collection of information, including suggestions for reducing the burden, to the Office of Management and Budget, Paperwork Reduction Project and Reports, 1215 Jefferson Davis Highway, Suite 1204, Arlington, VA 22202-4302, and to the Office of Management and Budget, Paperwork

AFRL-SR-BL-TR-98-

*0253*

Reviewing  
Information

<b>1. AGENCY USE ONLY (Leave blank)</b>			<b>2. REPORT DATE</b> March 1998	<b>3. REPORT</b> Final Technical Report 15 Jul 97 - 14 Dec 97
<b>4. TITLE AND SUBTITLE</b> (U) (HBCU/MI) WORKSHOP ON INTELLIGENT NDE SCIENCES FOR AGING AND FUTURISTIC AIRCRAFTS			<b>5. FUNDING NUMBERS</b> F49620-97-1-0470  62228D 4276/AS	
<b>6. AUTHOR(S)</b> ROBERTO A OSEGUEDA, CARLOS FERREGUT, SOHEIL NAZARIAN AND ROY ARROWOOD				
<b>7. PERFORMING ORGANIZATION NAME(S) AND ADDRESS(ES)</b> FAST CENTER FOR STRUCTURAL INTEGRITY OF AEROSPACE SYSTEMS THE UNIVERSITY OF TEXAS AT EL PASO EL PASO TX 79968			<b>8. PERFORMING ORGANIZATION REPORT NUMBER</b>  <i>NA</i>	
<b>9. SPONSORING/MONITORING AGENCY NAME(S) AND ADDRESS(ES)</b> Air Force Office of Scientific Research Aerospace & Materials Sciences Directorate 110 Duncan Avenue, Suite B-115 Bolling AFB DC 20332-8050			<b>10. SPONSORING/MONITORING AGENCY REPORT NUMBER</b>  <i>NA</i>	
<b>11. SUPPLEMENTARY NOTES</b>     <i>NA</i>				
<b>12a. DISTRIBUTION AVAILABILITY STATEMENT</b> APPROVED FOR PUBLIC RELEASE DISTRIBUTION IS UNLIMITED			<b>12b. DISTRIBUTION CODE</b>	
<b>13. ABSTRACT (Maximum 200 words)</b> <p>This volume contains the papers of the workshop on Intelligent NDE Sciences for Aging and Futuristic Aircraft held at the University of Texas at El Paso on September 30 - October 2, 1997. The workshop was organized to assess the state-of-the-art in the emerging field and to provide a forum to discuss and identify key basic and applied research issues that are critical to the development of intelligent NDE systems for aircraft.</p> <p>NDE is the interdisciplinary field of study which is concerned with the development of analysis techniques and measurement technologies for the quantitative characterization of materials and structures by noninvasive means. Intelligent NDE sciences can be defined as the branch of NDE related to the interpretation of data and the decision making process. Intelligent NDE sciences are also associated with the search for models, analytical tools, and the inference process to allow computer interpretation and decision making regarding the integrity of structures. It is also the science of smart machines that can learn, teach, advise, decide and recommend.</p> <p>The workshop brought together more than sixty representatives of the aircraft NDE and structural integrity community from industry, academia and government to discuss major aspects of intelligent NDE sciences. The 24 technical papers that composed the program covered a range of topics in smart processing of signals and images, intelligent interpretation, smart NDE systems and corrosion issues.</p>				
<b>14. SUBJECT TERMS</b>    <i>19980331 058</i>			<b>15. NUMBER OF PAGES</b> 5	
<b>17. SECURITY CLASSIFICATION OF REPORT</b> UNCLASSIFIED			<b>18. SECURITY CLASSIFICATION OF THIS PAGE</b> UNCLASSIFIED	
<b>19. SECURITY CLASSIFICATION OF ABSTRACT</b> UNCLASSIFIED			<b>20. LIMITATION OF ABSTRACT</b> UNCLASSIFIED	

---

---

---

# **Proceedings**

## **INTELLIGENT NDE SCIENCES FOR AGING AND FUTURISTIC AIRCRAFT**

---



Edited by: C. Ferregut, R. Osegueda, A. Nuñez

**Workshop on Intelligent Nondestructive Evaluation Sciences for Aging  
and Futuristic Aircraft**

**FINAL REPORT**

**by**

**Roberto A. Osegueda  
Carlos Ferregut  
Soheil Nazarian  
and  
Roy Arrowood**

**FAST Center for Structural Integrity  
of Aerospace Systems  
The University of Texas at El Paso  
El Paso, Texas 79968**

**Submitted to**

**U. S. Air Force Office of Scientific Research  
Attention: Dr. Spencer Wu  
Popcorn Grants Program**

**March, 1998**

## **Introduction**

Non-destructive Evaluation is the interdisciplinary field of study concerned with the development of analysis techniques and measurement technologies for the quantitative characterization of materials and structures by noninvasive means. Intelligent NDE Sciences can be defined as the branch of NDE related to the interpretation of data and the decision making process. Intelligent NDE sciences are also associated with the search for models, analytical tools, and the inference processes to allow computer interpretation and decision making regarding the integrity of a structure. It is also the science of smart machine that can learn, teach, advice, decide and recommend.

In the Fall of 1997 the Fast Center for Structural Integrity of Aerospace Systems at the University of Texas at El Paso (UTEP) organized, and held a Workshop on Intelligent NDE Sciences for Aging and Futuristic Aircraft. The workshop took place during September 30 – October 2 at UTEP’s campus. The objective of the workshop was to assess the state-of-the-art in the field of Intelligent NDE Sciences, and to provide a forum to discuss and identify key basic and applied research issues that are critical to the development of intelligent NDE systems for aircraft. The workshop also promoted exchanges and cross-fertilization among many disciplines. Presentations were made by, invited and selected, distinguished speakers. The workshop’s secondary objective was to provide directional support to the research activities conducted at the FAST Center for Structural Integrity of Aerospace Systems.

The workshop was organized by a committee of faculty members from UTEP, with the help of an advisory committee of distinguished researchers from academia and government. UTEP’s organizing committee was formed with: Dr. Roy Arrowood, Dr. Carlos Ferregut, Dr. Soheil Nazarian and Dr. Roberto Osegueda, all of them members of UTEP’s FAST Center. Members of the advisory committee included Dr. Yoseph Bar-Cohen (JPL/Caltech), Dr. Dale Chimenti (Iowa State University), Dr. Robert Green (Johns Hopkins University), Dr. Thomas Paez (Sandia National Laboratories) and Dr. Spencer Wu (Air Force Office of Scientific Research). Several potential speakers were

identified by the members of these committees. The advisory committee also revised the list of topics that made the program of the workshop.

### **Pre-Workshop Activities**

During Spring and Summer 1997, the UTEP organizing committee and the advisory committee decided on the final format for the workshop, identify potential speakers and compile a mailing list for the distribution of two brochures, one calling for papers and another one containing the final program.

The FAST Center prepared a brochure announcing the workshop and calling for papers. These brochure was mass mailed to about 1200 institutions. A copy of the brochure is attached to this report. At the same time thirteen distinguished researchers were contacted and invited to participate in the workshop. The following individuals accepted the invitation from the FAST Center:

Dr. Jan Achenbach, Northwestern University  
Dr. Yoseph Bar-Cohen, JPL/Caltech  
Dr. Dale Chimenti, Iowa State University  
Dr. Robert Green, Johns Hopkins University  
Dr. Ajit Mal, University of California at Los Angeles  
Dr. Thomas Paez, Sandia National Laboratories  
Dr. Mel Siegel, Carnegie Mellon University  
Dr. Wolfgang Sachse, Cornell University  
Dr. D.O. Thompson, Iowa State University  
Dr. G. Tomlinson, The University of Sheffield  
Dr. Satish Udupa, Iowa State University  
Dr. R.P. Wei, Lehigh University  
Dr. W.P. Winfree, NASA Langley Research Center

In addition to the thirteen invited speakers, thirteen more papers were selected from the response to our call for proposals. All papers were organized into the following five sessions,

Session I – Intelligent Interpretation and Smart Processing of Signals and Images (PART A)

Session II – Smart NDE Systems

Session III - Aircraft Corrosion

Session IV - Intelligent Interpretation and Smart Processing of Signals and Images (PART B)

Session V – Trends and Areas to focus Intelligent NDE Research and Development

The workshop program and registration mailed to speakers and other workshop attendees is attached to this report. The program and the papers abstracts were also posted on the FAST Center web page.

To facilitate the editing of the proceedings of the workshop, the organizers prepared a set of instructions for the authors to help them in the preparation of their manuscript. A sample of the instruction's booklet is also attached.

### **Workshop Attendance**

The workshop brought together 66 representatives of the aircraft NDE and structural integrity community from industry, academia and government. During the opening session Col. Jan Cerveny and Dr. C.I. Chang brief the audience on issues related to the FAST Centers Program and the Aging Aircraft Program. A round table discussion was held at the end of the second day of the workshop. Most of the 26 sessions of the workshop were videotaped for the future use of the students and researchers of the FAST Center.

### **Workshop Proceedings**

During the months of October and November, the wokshop speakers submitted their manuscripts, and some of them also included their written answers to questions asked during their presentations. The manuscripts and the discussions have been edited and put together into a Proceedings volume entitled: "Intelligent NDE Sciences for Aging and

Futuristic Aircraft", the editors of the proceedings are: Carlos Ferregut, Roberto Osegueda and Alina Nunez. The proceeding were printed by UTEP's print shop and were assigned an ISBN: 87404-279-8. Two hundred and fifty copies of the proceedings were printed.

### **Final Comments**

The Workshop on Intelligent NDE Sciences for Aging and Futuristic Aircraft was the first of its kind in this rapidly growing field. Several papers, in which artificial intelligence methodologies, pattern recognition, genetic programming, wavelets, and other modern modeling techniques are applied to the NDE process, were given. The issues of inspection automation, corrosion modeling and optimal sensor location generated extensive discussions among researchers with different knowledge and experience. Therefore, the main objective of the workshop was met.

Researchers and students at UTEP's FAST Center benefited from the contacts made and from the informal discussions they had with colleagues from other institutions during and after the workshop. This discussions have help the researchers at UTEP's FAST Center to refocus the direction of some activities in their projects, and have created the opportunity to increase the number of collaborations with other institutions. We therefore believe that the secondary objective of the workshop was also met.

September 30 - October 2, 1997

---

---

## Proceedings

Approved for public release,  
distribution unlimited.

U.S. AIR FORCE  
OFFICE OF SCIENTIFIC  
RESEARCH (AFSC)

Approved for public release,  
distribution unlimited.  
Release per AFM 190-12  
is permitted.

RECEIVED

MAR - 9 1998

SPONSORED PROJECTS

### Workshop on:

# INTELLIGENT NDE SCIENCES FOR AGING AND FUTURISTIC AIRCRAFT

---



Edited by: C. Ferregut, R. Osegueda, A. Nuñez

Organized by: FAST Center for Structural Integrity of Aerospace Systems,  
The University of Texas at El Paso

Sponsored by: U.S. Air Force Office of Scientific Research

Approved for public release,  
distribution unlimited

**ISBN: 87404-279-8**

**Copyright**

**Not to be reprinted without written authority**

**The Organizing Committee is not responsible for the statements made or for the opinions expressed  
in this Proceedings.**

**Design: Blanca Carrasco  
Geronimo Garcia**

---

**FAST Center for Structural Integrity of Aerospace Systems  
500 West University, El Paso, TX 79907  
Telephone: (915) 747-7891 Fax: (915) 747- 5921 E-mail: fast@utep.edu**

**Published under the auspicious of Texas Western Press  
Printed at The University of Texas at El Paso Print Shop**

## **ORGANIZING COMMITTEE at UTEP**

- Dr. Roberto Osegueda
- Dr. Carlos Ferregut
- Dr. Roy Arrowood
- Dr. Soheil Nazarian

## **ADVISORY COMMITTEE**

- Dr. Yoseph Bar-Cohen, JPL/Caltech
- Dr. Dale Chimenti, Iowa State University
- Dr. Robert Green, Johns Hopkins University
- Dr. Thomas Paez, Sandia National Laboratories
- Dr. Spencer Wu, Air Force Office of Scientific Research

# Preface

This volume contains the papers of the workshop on Intelligent NDE Sciences for Aging and Futuristic Aircraft held at the University of Texas at El Paso on September 30 - October 2, 1997. The workshop was organized to assess the state-of-the-art in this emerging field and to provide a forum to discuss and identify key basic and applied research issues that are critical to the development of intelligent NDE systems for aircraft.

NDE is the interdisciplinary field of study which is concerned with the development of analysis techniques and measurement technologies for the quantitative characterization of materials and structures by noninvasive means. Intelligent NDE sciences can be defined as the branch of NDE related to the interpretation of data and the decision making process. Intelligent NDE sciences are also associated with the search for models, analytical tools, and the inference process to allow computer interpretation and decision making regarding the integrity of structures. It is also the science of smart machines that can learn, teach, advice, decide and recommend.

The workshop brought together more than sixty representatives of the aircraft NDE and structural integrity community from industry, academia and government to discuss major aspects of intelligent NDE sciences. The 24 technical papers that comprised the program covered a range of topics in smart processing of signals and images, intelligent interpretation, smart NDE systems and corrosion issues.

Because of the valuable information provided during the discussions of the papers, a written version of questions and answers has been included after some of the papers. The papers and the discussions should make this volume a valuable reference on recent developments in intelligent NDE sciences as applied to aircraft and other structural systems. It is our hope that the material in this volume will help to further advance the state of science and practice of this rapidly growing subject.

On behalf of the Organizing Committee of the Workshop, we would like to thank the USA AFOSR for promoting and sponsoring this workshop. We would also like to thank all the students associated with UTEP's FAST Center for their help in organizing the workshop.

C.M. Ferregut  
R.A. Osegueda  
A. Nuñez

Editors

El Paso, Texas... October 1997.

# Table of Contents

A Real Time, High Resolution Ultrasound Imaging System for Aging Aircraft Inspection. M. E. Lasser, G. Harrison .....	1
Synergistic Diagnostics of Aircraft Materials and Structures. X.Lu, E. Govekar, W. Sachse and I. Grabec .....	11
Improved Nondestructive Damage Detection via Combining Individual Detection Theories. N. Stubbs and S. Choi .....	23
Damage Detection Methods Based on Wavelet Analyses of Sensor Signals X.Deng, Q.Wang, C.A. Rogers, V. Giurgiutiu and M.A. Sutton .....	37
Remote and Automated Inspection: Status and Prospects M. Siegel .....	47
Computational Geometry and Artificial Neural Networks: A Hybrid Approach to Optimal Sensor Placement for Aerospace NDE R. Osegueda, C. Ferregut, M.J. George, J.M. Gutierrez, V. Kreinovich .....	59
Evaluation of Lattice/Skin Composite Structures with Shearography A. K. Maji .....	73
Quantitative Detection and Characterization of Corrosion in Aircraft X. Han, L.D. Favro and R.L. Thomas .....	83
Autonomous Rapid Inspection of Aerospace Structures Y. Bar-Cohen .....	93

Enhanced Remote Visual Inspection of Aircraft Skin M. Siegel, P. Gunatilake .....	101
Aging of Airframe Aluminum Alloys: From Pitting to Cracking R. P. Wei .....	113
Some New Approaches to Understanding and Characterizing Exfoliation Corrosion in Aircraft Aluminum Alloy Sheet Metal. L.E. Murr, M. Posada, R.M. Arrowood, D. Little .....	123
Electrochemical In-Situ Sensors for Detecting Corrosion on Aging Aircraft G.D. Davis, C.M. Dacres, M.B. Shook, B.S. Wenner .....	141
Superconducting Quantum Interference Devices for Nondestructive Testing. J.R. Claycomb, N. Tralshawala, H.M Cho, M. Boyd, J.H, Miller Jr. ....	155
Hidden Corrosion Modeled as Surface Roughness Detected Using Guided Plate Waves D. Chimenti, O. I. Lobkis ..	167
The Application of Neural Networks to Defect Sizing M. Takadoya, T. Ogi, J.D Achenbach .....	179
Innovative Approaches to the Analysis of NDE Data S. S. Udupa, L. Udupa .....	193
Neural Networks for Damage Identification T. L. Paez and S. E. Klenke .....	205

Recent Advances in NDE Technologies for Aircraft Inspection W. P. Winfree .....	217
Model-based Fault Detection Using Lamb Waves. C. Wolters, S. A. Billings, S. G. Pierce, K. Worden, G. Tomlinson.....	229
Preliminary Evaluation of NDE Technologies for the Detection and Characterization of High Cycle Fatigue Damage. G. Light .....	245
Real Time Characterization of Isotropic Plates Using Lamb Waves E. Rodriguez, H. Pardo, S. Nazarian, J.H. Pierluissi, .....	257
Emerging Technologies for NDE of Aging Aircraft Structures R. E. Green, Jr. ....	267
Inversion of Ultrasonic Data Using Genetic Algorithms for Application in Composite Material Characterization. K. Balasubramaniam .....	279
Keyword Index .....	291
Author Index .....	292

# **A real time, high resolution ultrasound imaging system for aging aircraft inspection**

Dr. Marvin Lasser  
Imperium, Inc.  
Rockville, Maryland 20850

Dr. George Harrison  
University of Maryland Medical School  
Baltimore, Maryland

## **ABSTRACT**

A novel NDE system with an ultrasound sensitive multi-element array has been demonstrated and is currently in product development. The tool is capable of imaging internal defects (e.g. voids, delamination, corrosion) and provide *real-time, depth sensitive* C-scan information. The system uses a patented sensor array of ultrasound sensitive elements (128 x 128) that generates images in real time. This low cost, portable tool requires no mechanical scanning to acquire C-scan images and can be used for inspection of subsurface corrosion and composite flaws. The system installation could be similar to traditional C-Scan systems by immersing targets or through water squirter methods. However, since the system requires no mechanical scanning, it can be implemented as a handheld probe, not requiring targets to be submerged in a fluid at all. The probe can be used for spot inspection by an operator, or integrated into manufacturing processes for immediate production control over large areas. The application of the system for composites will enable characterization both *while they are forming*, as well as for field testing of in-service materials. The system operates at thirty frames a second allowing rapid movement over larger areas. This work is supported in part by the Navy SBIR program.

## **KEYWORDS:**

NDE, Imaging, Real-Time, Ultrasound, Corrosion, Composites, On-line, Manufacturing

We are reporting on the capability of our novel ultrasonic imaging camera system to rapidly characterize various materials. The ultrasound system is capable of imaging entire areas of internal targets at TV frame rates. This contrasts to conventional C-scan type systems which generate images only by moving a point by point sensor. The result is a tool which can provide real-time, large area imagery of subsurface faults.

It is important to perform characterizations of materials rapidly. More specifically, it would be highly desirable to:

1. Evaluate large areas of metals and composite materials quickly
2. Give immediate, user friendly imagery to an operator

The insertion of NDE technologies into material development with the ability to provide immediate production control feedback, and in-field structural health monitoring becomes more readily achievable. The basis for the technology is a patented ultrasound sensitive integrated circuit which reads out two-dimensional ultrasound data into a standard TV output, enabling ultrasound C-scanning in real time.

Although ultrasonic C-scanning was originally developed for inspection of homogeneous materials, the method has been now been applied to inspection for detection of corrosion, delaminations, porosity and inclusions, and to monitor the initiation and progression of damage resulting from applied mechanical loads and other environmental factors. The ultrasound imager builds on that capability by allowing these inspections to be made much more rapidly. The sort of problems encountered that we intend to monitor include real time imaging of:

1. Corrosion
2. Orientation of fibers
3. Fiber matrix/interface conditions
4. State of cure
5. Interlaminar cracks
6. Volume fraction

### **NEED FOR IMPROVED C-SCANNING TECHNOLOGY**

For the assessment of small imperfections, high resolution systems are required. Furthermore, measurements need to be made over large areas such as of an aircraft body. This requires considerable time to conduct these measurements and also places a severe burden on human inspectors to evaluate what they observe without being overcome by boredom and a lack of concentration. Automated systems are needed to assist the inspectors in the performance of their tasks. In order to establish improved screening and detection, a system which provides detailed visualization of a 3-D volume of materials is needed. This technology bridges the large gap between taking point by point scans of the materials of interest and evaluations that can be done quickly during the manufacturing process or after field use.

### **APPLICATIONS**

The installation of a real time C-scanning tool can be for any usage of C-scanning technology today, only thousands of times faster, and more easily implemented. Overall application benefits of such a tool include:

1. Better determination of economic impacts of aging systems
2. Easier implementation through low weight, portable probe

3. Better process control
4. Quicker in-situ inspection
5. Less defective products produced
6. Less operator intervention

Specific applications that we have addressed are as follows:

1. Real time corrosion imaging of pipes, aircraft, ships, storage tanks
2. On-line, large area aerospace composite production process control
3. Real-time, in-service composite aircraft inspection
4. Real-time automotive composite manufacturing inspection
5. Real-Time semiconductor package inspection

The implementation of the system for corrosion detection on aircraft using a hand held probe generating 'slices' inside targets in Figure 1.

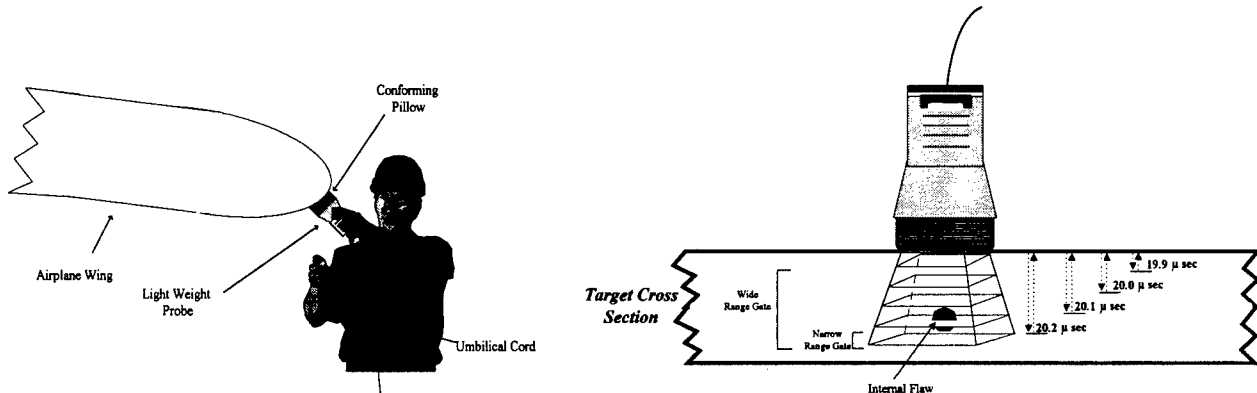


Figure 1: Real-time Ultrasound Imaging Implementation Using

As the operator moves along the target under study, he or she would get immediate subsurface imagery as well as quantitative data. One user interface is shown in Figure 2, where the signal processed RS170 image of corrosion is shown on the right hand side (colorized, edge enhanced, etc.), and the left display shows the quantitative A-scan at the intersection of the crosshairs on the image (e.g. for detailed depth information). As the

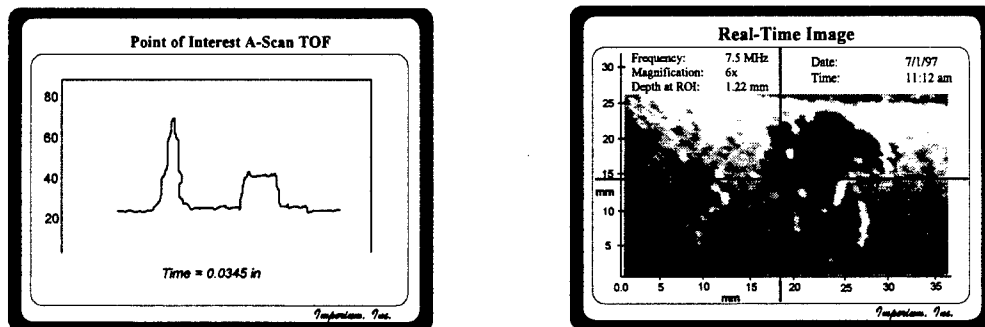


Figure 2: User Interface Screen

probe is moved, both the image and the A-scan would reflect the current position. Alternatively, the probe could be mounted on a track which scans along the surface of the aircraft skin and cover an entire area, with high resolution, in minimal time (10 to 15 minutes) and stored on video for later evaluation of areas of interest.

## SYSTEM DESCRIPTION

The system is best described as a 'camcorder for sound'. Similar to a conventional camcorder which is based on CCD technology sensitive to light, Imperium has developed a novel 2D read out IC sensitive to ultrasound, not light. The technique can be used in either reflection (pulse-echo) or transmission. The transmitter is *separate* from the novel IC receiver. The system is broadband, working over a wide range of frequencies.

A large area, uniform ultrasound beam insonifies the desired target. In the reflection mode, the beam strikes the target and returns back towards the sensor. An acoustic lens is used to collect the resulting beam and focus the information onto the IC array.

The pattern formed strikes the ultrasound sensitive pixel elements (128 x 128) of the array. The voltage generated at each pixel is transferred to a silicon CMOS multiplexer which is designed to read out the individual voltages sequentially, producing a TV like image.

Signal processing provides 'range gating' by controlling the acquisition time of the array to occur when the ultrasound pulse generated by the source transducer returns from a predetermined depth within the target (e.g. 5 mm in depth). Each of the thirty frames per second can be programmed to return from a different depth, providing 3D information (e.g. 3 mm to 8 mm, with 1 mm increments). Alternatively, at a single depth, the frames could be integrated to provide enhanced signal to noise. The RS170 TV signal is then frame grabbed and coupled to a standard machine vision system which performs acceptance/rejection criteria, image enhancement, false color, image annotation, etc.

The separation of the receive and transmission functions is not intended to imply that they are to be physically separated from each other. However, the separation into the receive and transmission modes does point out the flexibility inherent in the design of the imager.

Our transducer array was made by bonding a piezoelectric array to a focal plane array multiplexer. An array we are evaluating is approximately 1 cm on a side (128 elements with 85 micron center to center spacing). If 85 micron resolution is desired, it could be achieved but with 1 cm area coverage. In this case, the target area covered is equal to the area of the array. However, if the required resolution is 1 mm, then by setting the lens position, an area coverage of 128 mm of the target will be achieved. Since the camera operates at 30 frames a second or higher, reasonably large areas would be covered in times much less than required by a point by point scan. Similarly, if higher resolution is required, magnification of the image will result in better resolution, but sacrifice area coverage. The objective is a 'zoom in' or 'zoom out' as the operator desires as shown in

Figure 3. The ultimate resolution will be limited by the wavelength of the ultrasound employed.

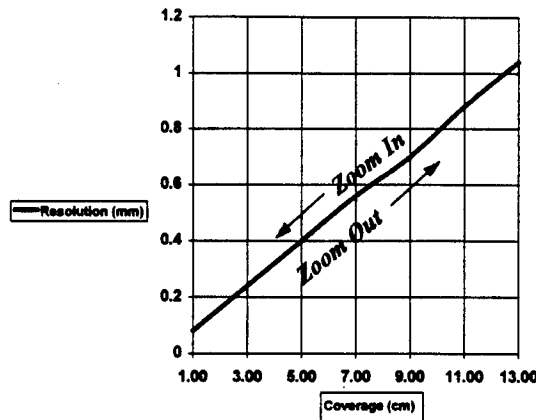


Figure 3: Adjustable 'Zoom' Selection

All other approaches to ultrasonic imaging have used focused pulses, whereas our preferred approach requires spatially uniform insonation of the plane of interest. Uniform insonation is a research specialty of Dr. George Harrison and of the University of Maryland who have been teamed with Imperium Inc. in some of the efforts. He has the only published calculations and experimental realizations of such insonation fields. One highly uniform field is shown in Figure 4. For the improved spatial resolution, special transducers operating at center frequencies of 375 KHz, 1 MHz, 2.5 MHz, 5 MHz and 15 MHz were used for imaging. The size and shape of the source transducer was determined from field propagation simulations.

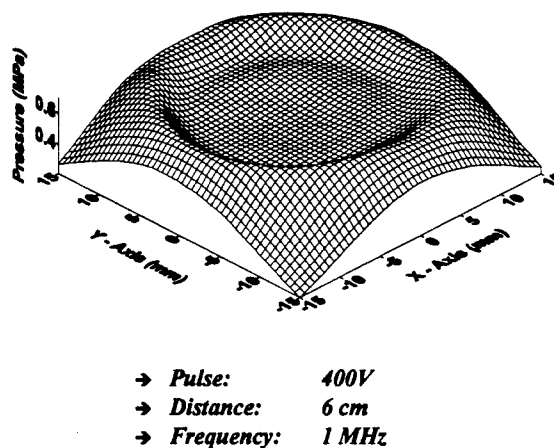


Figure 4: A Highly Uniform Pulse Used For Real-Time Imaging

The influence of advanced signal processing and pattern recognition algorithms, and an enhanced hardware for ultrasonic non-destructive testing capabilities has been

phenomenal. The recent systems store more data and analyze and image with good efficiency and hence make the whole system automatic and more reliable. Our TV formatted image is immediately adaptable to well developed commercial machine vision systems which perform immediate:

1. Frame grabbing of frames with particular features of interest
2. Conversion of shades of gray to color to bring out features not otherwise detectable, especially at higher frame rates
3. Intensity plots of image features rather than relying on image intensity to detect features
4. Dynamic range modification over different regions to enhance contrast beyond what is observed with uniform gain conditions
5. Edge enhancement
6. Image subtraction to not only look for changes, but also to remove fixed pattern noise
7. Image addition for improvement of signal to noise

### **REAL TIME IMAGES**

Once real time images were obtained, a number of features of these images could be investigated.

A relatively small target, a 7 mm diameter metal washer was imaged. The width of the metal ring is approximately 2 mm. In order to obtain images for inclusion in this report, single frames of the video images were frame grabbed and then stored to disk. Figure 5 shows a framed grabbed image of the washer held by a clamp. By moving the washer to a position closer to the focal plane of the lens and refocusing the image plane at the plane of the array, the image size increased. The enlarged image is shown in Figure 6. This is of course standard practice when operating in the visible and infrared regions of the spectrum. Mechanical C-scanning can provide the same information but at a much slower rate. It is the speed at which the images can be generated that makes this system unique. The Images in Figure 5 and Figure 6 below were taken at both 30 frames /second and at 50 frames/second. The real time feature greatly simplifies the focusing adjustment, allowing the operator to adjust the focus and then to readjust the focus if a different magnification is chosen.

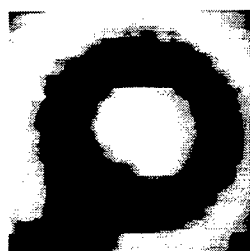


Figure 5: Without Zoom



Figure 6: With Zoom

Close examination of Figures 5 and 6 shows that the images are made up of a set of small squares or pixels. The smallest squares are generated by the actual pixel separation in the focal plane array. In this array the pixels are 85 microns apart. Knowing the pixel size one can determine the image size by counting the number of pixels across the image.

As a first approximation it is typical to invoke the Rayleigh criterion:

$$\theta_{\min} = 1.22\lambda / D$$

where  $\theta_{\min}$  is minimum angular separation of two points in the target,  $\lambda$  is the wavelength of the ultrasound signal, and  $D$  is the diameter of the lens. In fact, the resolution of a scanning system with high enough sensitivity and dynamic range can resolve the depth of the saddle point between the two point images and thereby improve on the achievable resolution.

Figure 7 is an image of an airplane rivet where a crack can clearly be seen emanating straight up. Figure 8 is an aluminum plate with spots of corrosion.



Figure 7: Aircraft Rivet with Crack Pointing Up



Figure 8: Corroded Aluminum Plate

It is important to point out that images of targets moving across the field of view, either by panning the camera or by moving the target, appear more detectable. The motion of details within the image catch the observer's eye and are readily tracked across the image plane.

## CONCLUSIONS

A new generation of ultrasound NDT imaging equipment based on microelectronic techniques has been demonstrated. This system substitutes microelectronic processing for mechanical scanning and is therefore not only much faster than existing equipment, but inherently a lower cost system. Imperium is actively looking for technologically advancing organizations currently involved in nondestructive testing to determine the application specific product specifications that will meet the needs of the NDT industry.

## **REFERENCES**

1. X. Zhang, G.H. Harrison, and E.K. Balcer-Kubiczek, Exposimetry of unfocused pulsed ultrasound. *IEEE Trans. UFFC* 41:80-83, 1994.
2. G.H. Harrison and E.K. Balcer-Kubiczek, Uniform Pulsed Fields for Ultrasonic Bioeffect Experimentation. *Ultrasonics*, 29:264-267, 1991.

## DISCUSSION

### A Real Time, High Resolution, Ultrasound Imaging System for Aging Aircraft Inspection.

Speaker: Lasser

How does one use your "ultrasonic camera" to visualize sub-surface material inhomogeneities? —Wolfgang Sachse

*By 'range gating' plane images. This technique generates image slices as a function of depth.*

Given that you have a short pulse, i.e., broad band, how do you avoid problems with chromatic aberration? —Mel Siegel

*The dispersion of the lens that we use is low enough that chromatic aberration is not observable.*

How do you "zoom" the lens? —Mel Siegel

*Zooming is done by adjusting (moving) the object and image distances as is conventionally done with any camera system.*

Does camera obtain data at top of image at same time as at bottom of image? —L. D. Favro

*We illuminate the target with a short period large area uniform ultrasound beam. This generates a latent (voltage) area image on the array. This 'frozen' area image, at a pre-selected depth, is then read out in a few milliseconds.*

You are scanning the A-scan signal at a rate of 1/30 second. This is clearly inadequate. How are you able to overcome the problem of poor sampling rates? —Satish Udupa

*We are reading out a sequence of C-scan frozen plane images. Each plane (see question 4) is then read out in 1/30 second. Each plane contains 128 x 128 elements. In order to get the equivalent of an A-scan requires a series of planes. In one second, we get (128 x 128) x 30 elements. This is a much higher sampling rate than obtained previously.*



# SYNERGISTIC DIAGNOSTICS OF AIRCRAFT MATERIALS AND STRUCTURES

X. Lu<sup>1</sup>, E. Govekar<sup>2</sup>, W. Sachse<sup>1</sup> and I. Grabec<sup>2</sup>

<sup>1</sup> Department of Theoretical and Applied Mechanics  
Cornell University, Ithaca, New York - 14853-1503 USA

<sup>2</sup> Faculty of Mechanical Engineering  
University of Ljubljana, 1000 Ljubljana SLOVENIA

## Abstract

We describe in this paper the first steps towards the development of a new and innovative integrated approach for monitoring the structural integrity of aging aircraft materials and structural components. We call this approach *synergistic diagnostics* because it is based on the union of *sensing, processing, modeling* and *forecasting* of the condition of a structure with respect to its performance. While the principal goal of any structural monitoring procedure involves the automatic detection and early identification of potentially dangerous conditions which threaten the integrity of a structure, the long-range goal may, in fact, also include forecasting of the performance and lifetime of the structure and specifying the permissible environments under which the structure may be operated safely. *Synergistic diagnostics* touches on the fields of measurement science, signal processing, materials failure, chaotic dynamics, adaptive systems and neural networks.

The examples presented in this paper utilize an *automatic modeler* that resembles the operation of a neural-like network. We show how such a system can be trained using measured crack growth data of aircraft Al-alloys undergoing mixed-mode fatigue loading. Once trained, the system requires only data that is measured during the initial portion of a fatigue test of a specimen to forecast its subsequent crack growth and predict its lifetime. We also demonstrate the utility of this modeling approach with pre-existing data obtained from a material property data base.

## INTRODUCTION

Living beings are remarkable in their ability to use their senses and to learn from their experiences in order to predict the future performance of a system. Such beings are an example of a synergistic measurement system which possesses capability for *sensing, processing, modeling* and *forecasting*.[1] For example, a synergistic *ultrasonic* measurement system is one which is based on the union of sensing and processing of active (UT) or passive (AE) ultrasonic signals, and the subsequent modeling, forecasting and possibly even controlling the condition of a system or a machine with respect to its performance. In the future, such ultrasonic systems will likely be used in non-destructive testing, materials characterization, structural integrity monitoring and process control applications. The development of synergistic measurement systems is described in a recent monograph.[1]

In this paper, we explore the use of a synergistic system which relies on data measured during the initial portion of a fatigue-loaded, thin-plate, pre-cracked Al-alloy specimen to forecast its subsequent crack growth and lifetime. Portions of this paper are taken from Ref. [2] Here, *sensing* refers to the measurement of crack length data on a specimen which can subsequently be used to predict the fatigue performance of the specimen. *Processing* refers to the amplification, filtering and modification of signals to enhance their information content and to recover missing information. In electronic measurement systems which may be used to monitor the growth of a crack, this operation refers to the evaluation of signals from the crack region and relating these to the growth of a crack. *Modeling* refers to a concise description of the fatigue-fracture phenomenon which will permit predicting as well as forecasting missing information. *Forecasting* refers to the prediction of the future evolution of a crack in a specimen or structure, that is, its growth rate and the specimen lifetime from past measurements of the growing crack.

## APPROACH

Central to a synergistic measurement system is a neural-like, adaptive signal processing procedure which permits modeling the non-linear relationships between measured signals or information and the condition and specifically, the fatigue properties of a specimen. The procedure which we utilize here, relies on a statistical treatment of measured data to generate an empirical modeler of the natural law describing the phenomena. Such an *automatic modeler*[3] is based on a self-organized, optimal preservation of empirical information that utilizes the principle of maximum entropy of information and an optimal, associative estimation of missing information resembling a non-parametric regression. The approach corresponds, in part, to a neural network based on a set of radial basis functions or a 3-layer perceptron.[1]

We denote the initial  $s$ -components of the measured crack growth rate data as  $S = (x_1, x_2, \dots, x_s)$ . These may be functions of crack length or other controlling parameters, such as stress intensity factors or energy release rate. The subsequent crack growth rate data are written as  $P = (x_{s+1}, x_{s+2}, \dots, x_{s+P})$ . Thus, the concatenated signal description of the crack growth rate of a specimen undergoing fatigue is expressed by the data vector

$$X = S \oplus P = (x_1, x_2, \dots, x_s, x_{s+1}, \dots, x_{s+P}) \quad (1)$$

To learn from examples, one collects the data vectors  $X_1, X_2, \dots, X_N$  during a series of training measurements. These data vectors form the basis of the *memory* of the modeler. The formation of this memory corresponds to an *adaptation* of the system. For processes in which there is a continuous set of measured data, as, for example, continuous acoustic emission or electrical impedance data from the growing crack, one represents the data by a fixed, finite set of representative *prototype data* vectors which are selected by a self-organization procedure.[1] Once the memory has been developed, an optimal estimation of the material property characteristics  $\hat{P}_O(S)$  from the measured sensor data is obtained via *multi-dimensional, non-parametric regression*. This is the *analysis* mode of the modeler. Specifically,

$$\hat{P}_O(S) = \int P \cdot f(P|S) dP \implies \sum_{n=1}^N C_n P_n \quad (2)$$

where the *measure of similarity* is expressed by the coefficients

$$C_n = \frac{g(S - S_n)}{\sum_{n=1}^N g(S - S_n)} \quad (3)$$

Here,  $g$  represents the Gaussian functions which are formed from the data measured during learning,  $S_n$ , and during an subsequent, actual experiment,  $S$ .

Our goal here, is to train the automatic modeler to model the fatigue crack phenomenon so that it can subsequently be used to predict the crack growth and hence the lifetime of a specimen. Specifically, we shall demonstrate the utility of this approach for predicting crack growth in aircraft Al-alloys loaded under tension and torsion mixed-mode fatigue loading.

When there is only one or a small number of cracks in a specimen, fatigue damage is usually described in terms of the length of the dominant crack and its growth rate as a function of fatigue cycle count. One of the standard procedures for determining crack size and monitoring its growth is the use of direct optical measurements. Such a determination relies on a calibrated measuring microscope. However, an alternative procedure for sizing cracks is desirable – one which would permit the monitoring of cracks remotely and in an actual structural component while it is in-service.

In the past, a number of crack sizing measurement techniques have been proposed and demonstrated. These include techniques based on eddy current, electrical resistance, and several based on ultrasonics. The use of crack tip diffracted signals in active ultrasonic measurements to determine the position of the crack tip has been described elsewhere.[6, 7] The advantages of AE measurements as the basis of a continuous, on-line structural monitoring system are often cited. Just as a living being is able to use its sense of hearing to quickly identify sources of sound, we have explored whether it is possible to use AE data as input to a synergistic measurement system. In particular, we have explored the use of AE data to provide information about crack growth which could be used as input data to the modeler.[2] Unfortunately, it was found that such data often do not reliably correlate with the precise characteristics of the crack. And since good prediction of actual crack growth rate is obtained only when the input data used to make the prediction closely resembles that which already resides in the memory, it is for this reason that AE data may not be suitable for forecasting subsequent crack growth.[2] The results presented in this paper all relied on direct optical measurements to determine the crack size.

## MEASUREMENTS AND MEASUREMENT RESULTS

It is recognized that the pressurization of an aircraft fuselage results in both tensile and transverse (out-of-plane tearing) stresses on a crack near a lap joint.[4] Crack tip tensile stresses arise from the hoop stress in the fuselage skin while the out-of-plane tearing stresses arise from the internal pressure in the fuselage. To study the fatigue crack growth under both tensile and transverse shear stresses, Zehnder and Viz [4] tested double-edge notched (DEN) specimens of 2024-T3 Al-alloys such as that shown in Fig. 1(a) under constant amplitude cyclic tensile and torsional loadings using the mechanical testing system shown in Fig. 1(b). The work presented here will include fatigue studies

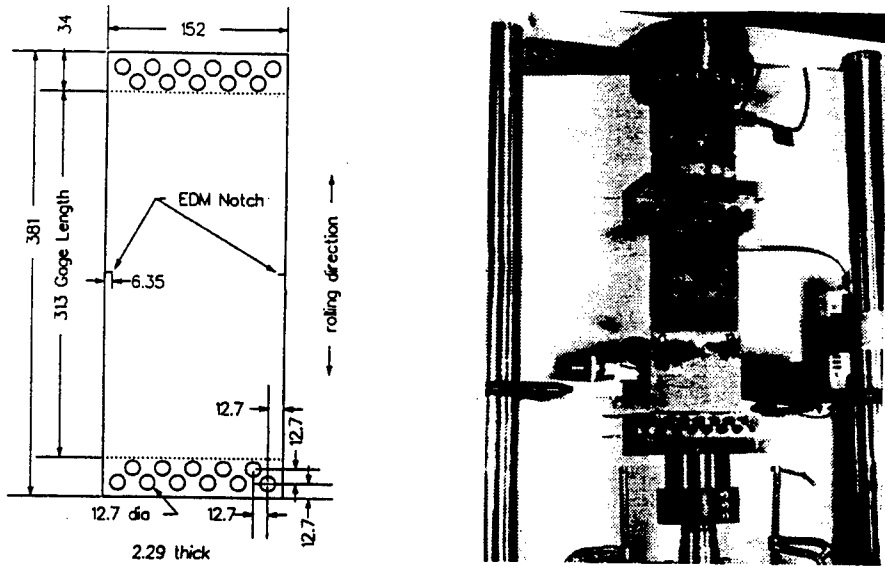


**Figure 1:** (a) Tension/torsion specimen geometry; (b) Mechanical testing configuration (from Ref. 3)

as these as well as 7076-T6 Al-alloy and Ti6Al4V. Measurements were also made on single-edge notched specimens (SEN) of 2024-T3 and 7076-T6 Al-alloys.

The direct optical measurements which were used to measure and monitor a growing crack relied on a traveling microscope which was capable of resolving the position of the crack tip to within about 0.001 in (25  $\mu\text{m}$ ). In this study the growth of the crack was measured approximately every 0.020 in. (0.5 mm) and the fatigue cycle count noted.

## FATIGUE MODELING BASED ON MEASURED CRACK LENGTH

A critical question is whether a synergistic system can be adapted and subsequently used to predict fatigue crack growth. For this, we require precise crack growth data while a specimen is undergoing fatigue. Two kinds of specimens were fatigue tested. In the double-edge-notched (DEN) specimens, as that shown in Fig. 1(a), the crack growth from one of the notches was used to predict the growth of the crack emanating from the other notch. In the single-edge notch specimens, the crack growth prediction was based on the data collected from other specimens.

### Crack Growth in Double-Edge-Notched Specimens

Fatigue crack growth measurements were carried out on double-edge-notched 2.29 mm-thick sheets of 2024-T3, 7076-T6 Al-alloys and Ti6Al4V. The specimens and conditions under which they were tested are listed in Table 1. A compilation of the optically-measured crack growth data collected is shown in Fig. 2. The two crack growth curves shown for each specimen correspond to each of the two cracks in the double-edge notch sample.

The crack-length data for one of the cracks on the double-edge-notch sample was used to develop the memory of the modeler. The formation of this memory corresponds to *adaptation* of the system.

Table 1: Single-edge-notched specimens tested and test parameters (**P**: axial load; **T**: applied torque; **f**: test frequency).

Test Number	Material	$P_{\min} - P_{\max}$ [kN]	$T_{\min} - T_{\max}$ [N·m]	$f$ [Hz]
1	2024-T3 Al	1.34 - 13.35	6.72 - 67.2	0.3
2	2024-T3 Al	29.59 - 42.28	90.44 - 106.4	0.4-1.0
3	2024-T3 Al	8.9 - 17.8	22.4 - 44.8	0.1
4	7075-T6 Al	8.9 - 17.8	22.4 - 44.8	0.5
5	Ti6Al4V	8.9 - 17.8	22.4 - 44.8	0.5

To test the system's capability for predicting expected crack growth, only the first five initial crack length data values were used as input to the modeler from which all the remaining evolution of the crack growth was predicted. The results for four experiments are shown in Figs. 3(a)-(d).

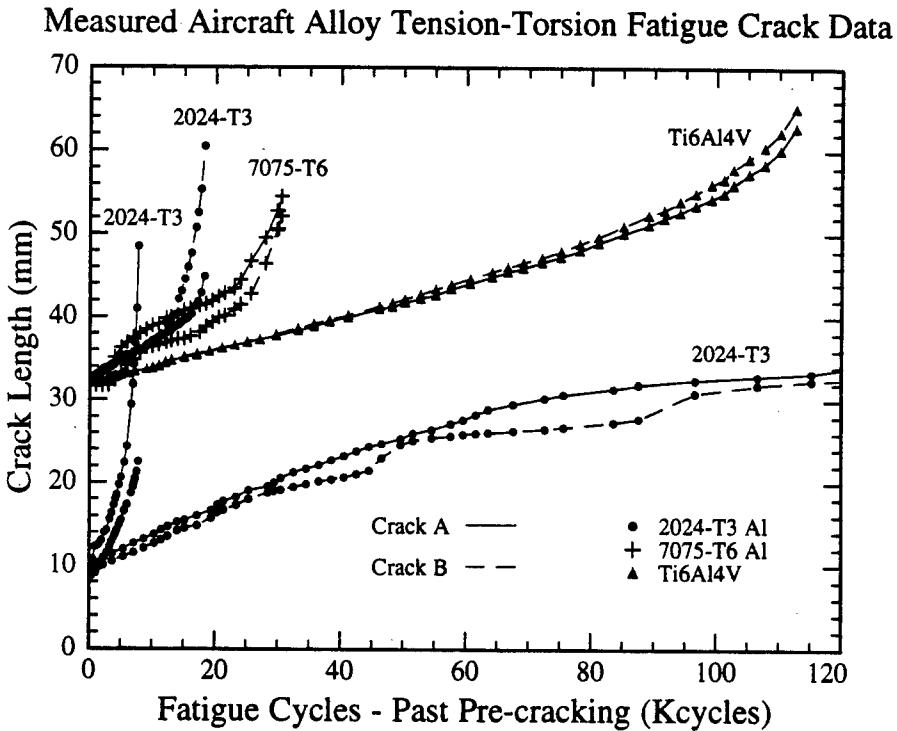
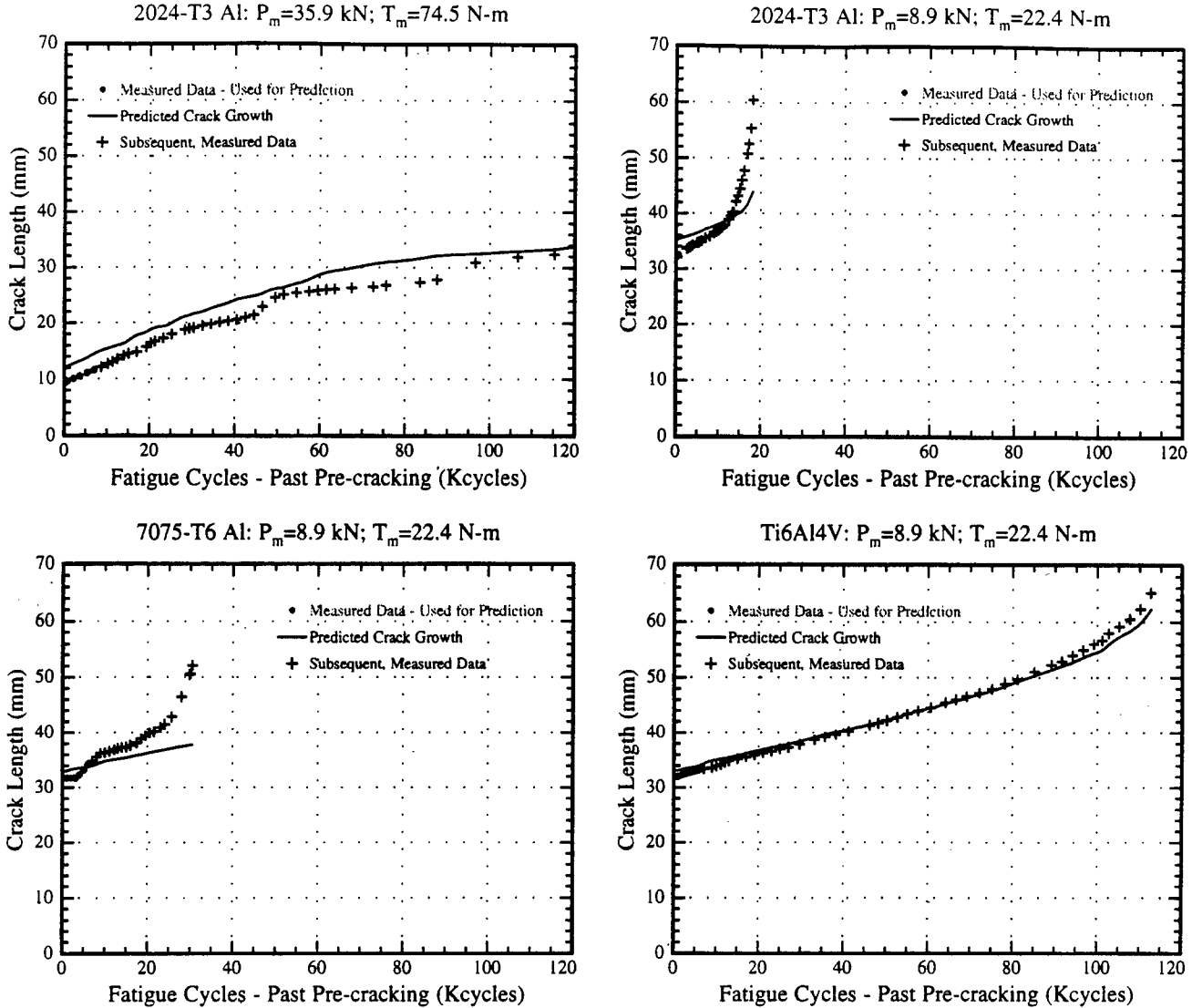


Figure 2: Tension/torsion fatigue crack growth data used to develop the *memory*

These results demonstrate that the crack growth can be predicted given several initial crack length data. But our results also have shown that reliable prediction of the crack length appears to be only possible when the measured data, which is input, reasonably closely corresponds to data already in the memory. The result of the 2024-T3 Al-alloy specimen which is shown in Fig. 3(a) exhibits good agreement between the predicted and the subsequently measured crack growth curve. In this particular test, the specimen was subjected to a combined large average axial load and large torsional load. This combination results in an increased plastic zone around the crack tip



**Figure 3:** Predicted fatigue crack growth behavior (based on five initial points). (a)-(b) 2024-T3 Al-alloy; (c) 7075-T6 Al-alloy; (d) Ti6Al4V alloy.

and increased crack surface roughness, resulting in increased crack closure which has been found to lead to a reduction in crack growth rate.[5] Also, as Fig. 2 shows, the growth of both cracks in the DEN specimen is very similar as would be expected if the crack growth is symmetric. In this case, the predictive capability of the *automatic modeler* based on only the first few points in a crack-growth curve seems to be quite good. In contrast, when growth of the cracks is not symmetric which appears to be the case when the torsional load is small, the crack growth is more rapid,[5] as Fig. 3(b) illustrates. When the measured crack growth differs from the data in the memory, a prediction based on only the first few points may lead to large errors, particularly when the memory of the system is sparse. It appears that under such conditions the modeler cannot properly predict the crack growth. It may need to be trained with additional data that will improve its capabilities.

## Crack Growth in Single-Edge-Notched Specimens

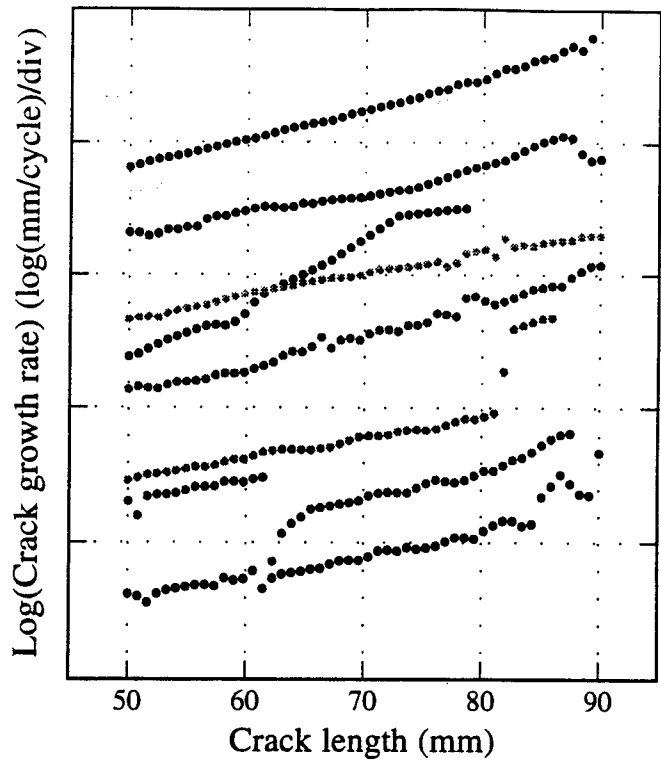
Since the cracks in such specimens may influence each other, we also completed a series of fatigue crack growth measurements on specimens with single-edge notches. These were cut from 2.29 mm-thick sheets of 2024-T3 and 7076-T6 Al-alloys. As before, the crack growth data was collected on specimens undergoing tension-tension, torsion-torsion fatigue but over a broader range of maximum and minimum applied loads and torques than before. A list of the specimens and conditions under which they were tested is in Table 2.

Table 2: Single-edge-notched specimens tested and test parameters ( $P$ : axial load;  $T$ : applied torque;  $f$ : test frequency). The notch length data indicated by  $\dagger$  is the notch plus pre-crack length. Specimens #6 and #7 were used as ‘unknown’ test specimens.

Test Number	Material	Initial Crack Length [mm]	$P_{\min} - P_{\max}$ [kN]	$T_{\min} - T_{\max}$ [N·m]	$f$ [Hz]
1	2024-T3 Al	0.010	8.896 - 31.14	5.649 - 13.56	0.4
2	2024-T3 Al	0.040	8.896 - 17.79	0.0 - 0.0	0.4
3	2024-T3 Al	0.040	8.896 - 17.79	5.649 - 16.95	0.4
4	2024-T3 Al	0.020	8.896 - 26.69	5.649 - 13.56	0.4
5	2024-T3 Al	0.030	13.34 - 22.24	3.389 - 5.649	0.4
6	2024-T3 Al	0.050	8.896 - 17.79	3.389 - 5.649	0.4
7	7075-T6 Al	0.046	8.896 - 17.79	3.389 - 5.649	0.4
8	7075-T6 Al	0.016	8.896 - 17.79	3.389 - 5.649	0.4
9	7075-T6 Al	0.029 $\dagger$	13.34 - 26.69	5.423 - 9.038	0.4
	7075-T6 Al	0.062 $\dagger$	8.896 - 17.79	3.389 - 5.649	0.4
	7075-T6 Al	0.062 $\dagger$	13.34 - 22.24	5.423 - 7.683	0.4
10	7075-T6 Al	0.037	13.34 - 22.24	5.423 - 7.683	0.4

The optically measured crack growth rate data as a function of crack length obtained on these specimens is shown in Fig. 4. This data constitutes the *memory* of the modeler. As before, once the memory of the modeler has been developed, it can be used to recover missing information in the data vectors (i. e. Eq. (2)) which are presented to it. Here we wish to recover components of the missing property descriptors,  $P$ , which correspond to predicting the expected crack growth rate. Only the first ten, initial crack length data values were input to the modeler from which the remaining evolution of the crack growth was predicted. We show in Figs. 5(a)-(b) the results of two blind experiments.

These results confirm others which show that reliable prediction of the crack growth appears to be only possible when the input data reasonably closely corresponds to data already in the memory. The result of the 7075-T6 Al-alloy specimen which is shown in Fig. 5(a) exhibits good agreement between the predicted and the subsequently measured crack growth curve. It happens that the first ten points of the measured data used for prediction as well as the subsequent, measured data closely resemble one of the curves in the memory which was generated under similar loading conditions but had a different initial crack length. In that case, the predictive capability of the automatic modeler based on only the first few points in a crack-growth curve seems to be quite good.



**Figure 4:** Crack growth data on 2024-T3 and 7075-T6 fatigued Al-alloy specimens which was used to develop the modeler *memory*.

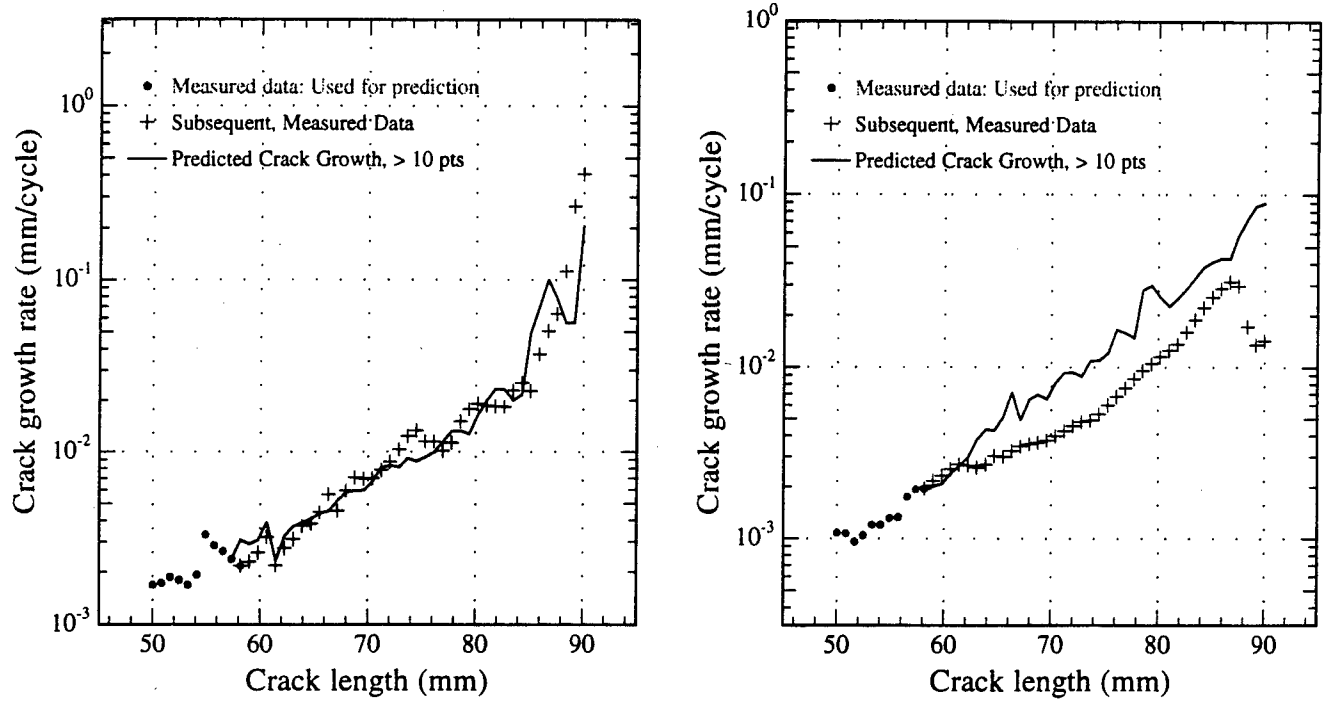


**Figure 5:** Modeler prediction of crack growth data in fatigue-loaded Al-alloy specimens. (a) 7075-T6 showing excellent prediction; (b) 2024-T3 showing poor prediction.

In contrast, the crack growth data for the 2024-T3 Al-alloy specimen differs significantly from each of the curves comprising the memory because the test shown in Fig. 5(b) was carried out under loading conditions which differed significantly from those used to produce the memory. It appears that under these loading conditions the modeler cannot properly predict the crack growth. It may need to be trained with additional data, such as loading information, that also controls the crack growth, in order to improve its predictive capabilities. Exactly which data or parameters are the controlling factors in such crack growth and thus need to also be input to the modeler is not yet known and this is currently still under investigation.

### Predictor-Corrector Modeler

In all the foregoing examples in which the modeler was used to predict the future crack growth, the modeler operated as a *long-term predictor*. That is, a small number of crack growth data values were used to predict all of the expected, future values. An alternative may be a *moving window predictor* in which a small number of data values are used to predict one or only a small number of expected future data values. Subsequent crack growth is predicted sequentially by moving the window of predicted crack growth rate data step-by-step ahead. None of these procedures continues to improve the memory of the modeler.

The *predictor-corrector* on the other hand, uses previously-measured crack growth data to predict the crack growth expected for only a small number of steps ahead. The predicted value is subsequently corrected by the actual, measured value. This leads quite naturally to the *one-step ahead predictor-corrector* in which the modeler uses the measured crack growth data at  $\{k - 4, k - 3, k - 2, k - 1 \text{ and } k\}$  to predict the crack growth just one step ahead, at  $\{k + 1\}$ .

The performance of these different operating modes of the modeler is compared using the data previously shown in Fig. 5(b). This is shown in Fig. 6 in which the operating modes of the modeler are used with either five or ten points initial points. And the performance of each of the operating modes is shown. It is seen that nearly all of the enhanced prediction approaches result in little improved performance of the modeler. But the prediction obtained by the predictor-corrector modeler with five initial points, approaches the actual, subsequent, measured data as the crack length increases.

### Crack Prediction from a Material Property Data Base

For the past several years a round-robin fatigue crack growth rate test program was carried out using "as received" as well as "artificially corroded" C/KC-135 fuselage and upper wing skin materials.[8] The test program investigated four materials, fatigue tested in tension-tension at two levels of humidity and two loading frequencies. The goal was to obtain data which would provide a basis for calculating the crack growth parameters of corroded and non-corroded typical airframe materials.

We have obtained access to this fatigue crack growth data base and have used the data of four experiments to develop the memory of the modeler. This is shown in Fig. 7(a). Here  $K_{\max}$  denotes the maximum stress intensity factor,  $R$  is the *min/max* load ratio and  $q$  is an empirical

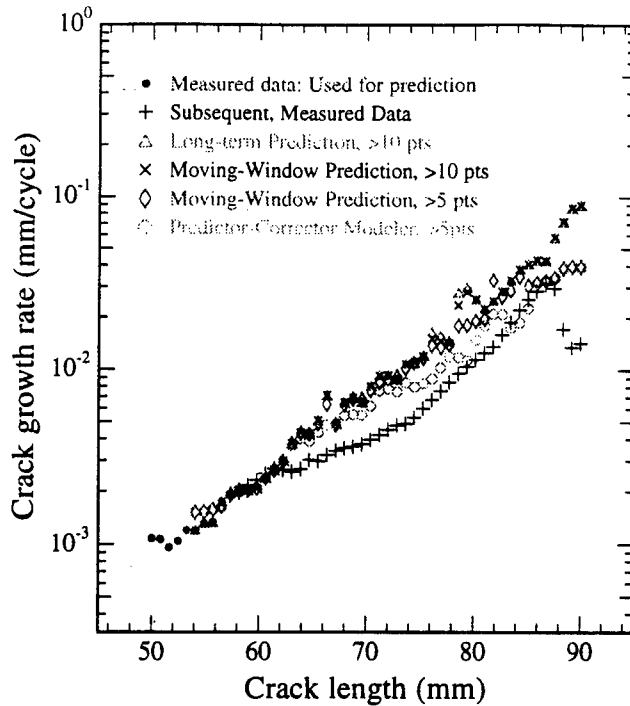


**Figure 6:** Performance enhancement of the modeler to predict fatigue crack growth in a 2024-T3 Al-alloy specimen which was not residing in the memory of the modeler. Tension-tension: 2-4 kips; torsion-torsion: 30-50 lbs-in. 12.42 Kcycles to failure.

constant. The first five crack growth data points of another experiment (same material, same testing parameters) was then input to the modeler to forecast the subsequent predicted crack growth curve. This is shown in Fig. 7(b). The subsequent, actual measured crack growth data is also shown in the figure. The agreement between the prediction and that actually measured is excellent. The crack growth rate was correctly predicted.

In another repeat test, the fatigue crack growth data of specimens loaded in a corrosive environment, greater than 85% relative humidity was used. These results are shown in Figs. 8(a) and (b). While the data comprising the memory of the modeler shows considerably more variation, it is still able to adequately predict the crack growth rate for another test sample.

## CONCLUSIONS

We have described in this paper a *multi-dimensional, non-parametric regression* approach, or *automatic modeler* and its use to predict fatigue crack growth in Al-alloys under certain conditions. The approach has been demonstrated with measured data as well as existing data contained in a corrosion-fatigue material property data base. In the measurements reported here, the crack growth measurements used to generate the *memory* of the modeler were obtained using direct optical measurements. It was found that the prediction performance of the modeler is good if the measured input data closely resembles one of the previous data sets residing in the *memory*. An enhanced predictive performance can be obtained from the modeler if a *predictor-corrector* algorithm is used.

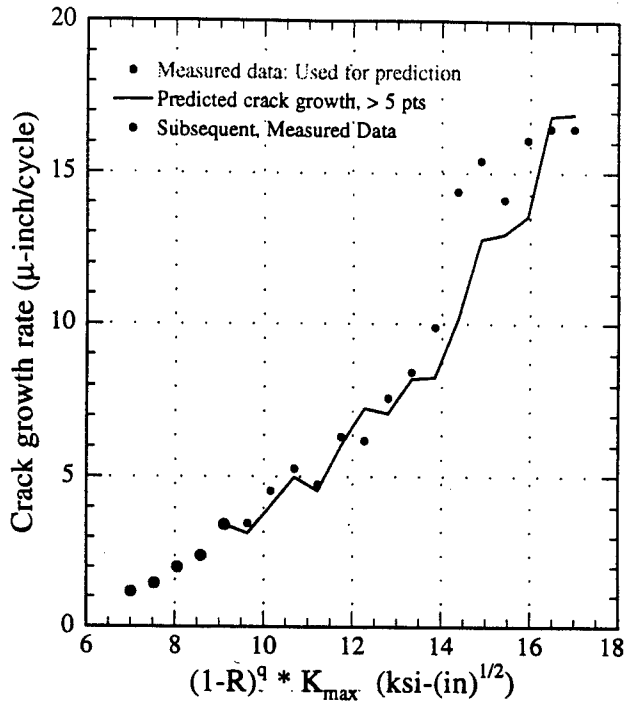
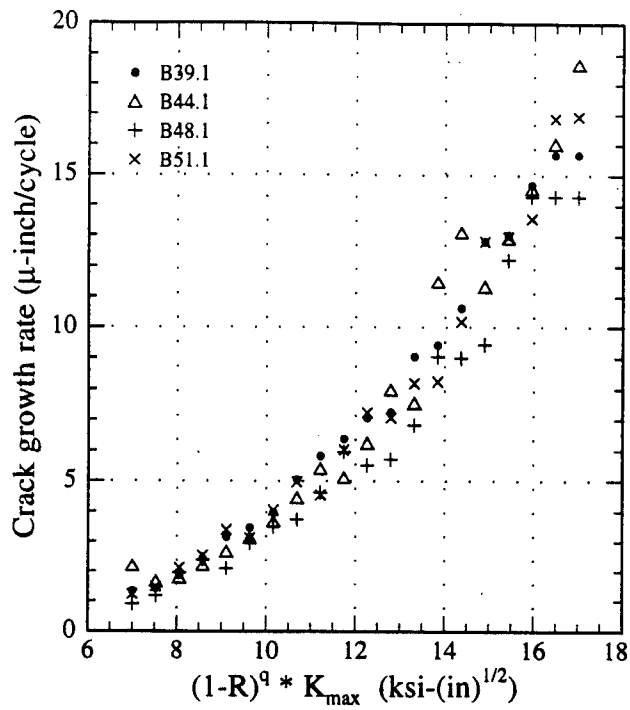


**Figure 7:** 2024-T3 Fatigue data base: As-received; tested at 15% relative humidity; 10 Hz testing frequency. (a) Development of the modeler memory; (b) Prediction of crack growth on a specimen not included in the memory.

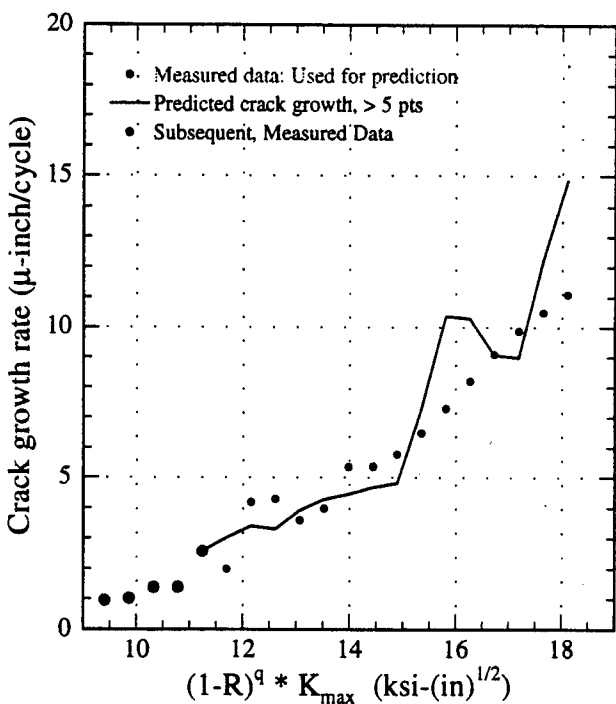
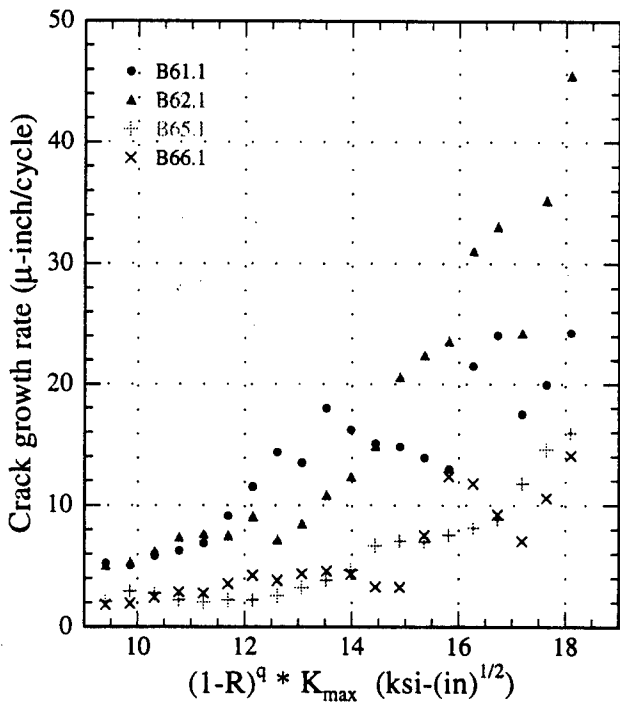


**Figure 8:** 2024-T3 Fatigue data base: As-received; tested at >85% relative humidity; 10 Hz testing frequency. (a) Development of the modeler memory; (b) Prediction of crack growth on a specimen not included in the memory.

## ACKNOWLEDGMENTS

This work was supported by the Air Force Office of Scientific Research under Contract #F49620-95-1-0383. We appreciate the use of the mechanical testing machine in Prof Zehnder's lab. The fatigue data of the double-edge notch specimens was collected by G. Manthei. We thank J. Luzar of Boeing's Product Support Division for making the corrosion fatigue crack data base available to us. Use of the facilities of the Materials Science Center at Cornell University which is funded by the National Science Foundation is also acknowledged.

## REFERENCES

1. I. Grabec and W. Sachse, *Synergetics of Measurement, Prediction and Control*, Springer-Verlag, Heidelberg (1997).
2. X. Lu, W. Sachse, E. Govekar and I. Grabec, "Predictive measurement using AE: Fracture and lifetime of Al-alloys", Materials Science Center Report #8238, Cornell University, Ithaca, NY (August 1997). To appear: *Nondestructive Characterization of Materials*, C. O. Ruud and R. E. Green, Eds., Plenum Press, New York (1997).
3. I. Grabec and W. Sachse, "Automatic modeling of physical phenomena: Application to ultrasonic data", *J. Appl. Phys.*, **69**(1), 6233-6244 (1991).
4. M. J. Viz and A. T. Zehnder, "Fatigue crack growth in 2024-T3 Aluminum under tensile and transverse shear stresses", in *FAA/NASA International Symposium on Advanced Structural Integrity Methods for Airframe Durability and Damage Tolerance*, NASA Conference Publication 3274, Part 2, C. E. Harris, Ed., NASA, Washington, D. C. (September 1994), pp. 891-909.
5. M. J. Viz, A. T. Zehnder and J.-D. Bamford, "Fatigue fracture of thin plates under tensile and transverse shear stresses", in *Fracture Mechanics: 26th Volume*, ASTM STP 1256, W. G. Reuter, J. H. Underwood and J. C. Newman, Jr., eds., American Society for Testing and Materials, Philadelphia (1995), pp. 631-651.
6. W. Sachse and S. Golan, "The scattering of elastic pulses and the non-destructive evaluation of materials", in *Elastic Waves and Non-destructive Testing of Materials*, AMD-Vol. 29, Y. H. Pao, ed., American Society of Mechanical Engineers, New York (1978), pp. 11-31.
7. X. Lu and W. Sachse, "Self-calibrating active ultrasonic technique for crack tip location" MSC Report #8239, Materials Science Center, Cornell University, Ithaca, NY (August 1997).
8. J. Luzar, *Integrated C/KC-135 Corrosion Program Round Robin Testing*, Report for AF Contract F34601-90-C-1336, Boeing Product Support Division, Wichita, KS (May 1996).

# **Improved Nondestructive Damage Detection via Combining Individual Detection Theories**

N. Stubbs and S. Choi

Department of Civil Engineering, Texas A&M University, College Station, Texas 77843

## **ABSTRACT**

The possibility of improving the performance of damage detection via combining the predictions of more than one damage theory is explored in this paper. The theories, which are utilized here to demonstrate the approach, incorporate changes in the strain energy distribution of an element and the flexibility distribution at a point in the structure. The basic elements of the approaches are summarized in the generic sense that various types of measurement sets (e.g., displacements, strains, curvatures, etc.) may be applied. The performance of each methodology is evaluated using the data generated in a space structure. Both static and dynamic measurements are utilized to increase the number of damage prediction sets. Three logical rules for combining the theories are proposed and the performances of these rules are compared with the performance of the individual theories.

**Keywords:** nondestructive damage detection, combination of theories, flexibility, strain energy, weighted general mean, performance evaluation

## **1. INTRODUCTION**

To date, researchers have invested considerable effort to identify and size damage in mechanical systems. As a result, many non-destructive damage detection (NDD) theories have been proposed and developed on various grounds<sup>1</sup>. These theories are based on different assumptions and measures. The performance of these theories may be evaluated using such indicators as the percentage of correctly predicted locations, the percentage of false positives, and the percentage of false negatives. Here, a false positive means that damage is reported where there is no damage, and a false negative means that damage is not reported when damage is indeed present. So far, however, it is observed that no non-destructive damage theory has been shown to be correct in all situations. Each and every one of these theories has its limitations as well as advantages when applied to practical problems. These limitations may result in an increase in the relative number of predictions of false positive and false negative damage locations.

As a possible remedy to this situation, this paper explores the possibility of combining the predictions of more than one damage localization theory to improve the performance of the predictions. The motivation for this approach is as follows: the greater the number of independent theories that are utilized in a given prediction, the greater the number of underlying physical principles that may be included in the exercise, and, therefore, the prediction of the consensus (or combination) of theories might be more representative of reality.

---

Further author information -

N.S.(correspondence): Email: n-stubbs@tamu.edu; Telephone: 409-845-2449; Fax:409-845-6156

S.C.: Email: schoi@tamu.edu; Telephone: 409-845-0368; Fax:409-845-6156

Two recently proposed damage theories<sup>2</sup> are selected for this purpose. One theory utilizes the changes in the flexibility at a point in the structure; the other theory utilizes the changes in the strain energy of an element of the structure. Both static and dynamic measurements are utilized to double the number of damage prediction sets. The basic elements of the two theories are summarized and the performance of each methodology is evaluated using the data generated in a space structure. The damage in the example structure is simulated by reducing the elastic modulus of an element by some known amount. Three ways of combining the prediction sets are proposed. These combinations, which utilize the weighted general mean (WGM) concept<sup>3</sup>, represent the extremes of fuzzy union and fuzzy intersection. The performances of these rules are compared with the damage detection performance of the individual theories.

## 2. NONDESTRUCTIVE DAMAGE DETECTION THEORIES

Damage in a structure may be detected by utilizing certain measures which reflect the physical state of the structure. These measures may be dynamic or static displacements, strains, curvatures, or others. The following two theories - a theory developed on the basis of the flexibility at a point in a structure, and a theory developed on the basis of the strain energy of an element of the structure - are described here. Note that the term, generalized displacement, which will appear in following two theories may be interpreted either a static or dynamic displacement, strain, or curvature.

### 2.1. Flexibility Index

The governing differential equation for an arbitrary structure may be written as follows:

$$\mathbb{L} w(q_1, q_2, \dots, q_n) = CQ(q_1, q_2, \dots, q_n) \quad (1)$$

where  $\mathbb{L}$  is a differential operator;  $w$  is a generalized displacement;  $C$  is a flexibility coefficient;  $q_1, q_2, \dots, q_n$  is a set of generalized coordinates; and  $Q$  is a generalized force. Eq (1) can be rewritten for a point  $j$  and  $i = 1, 2, \dots, N$  sets of measurements (e.g., mode shapes for dynamic measurements and load cases for static measurements) as follows:

$$\mathbb{L} w_i(q_1^j, q_2^j, \dots, q_n^j) = CQ_i(q_1^j, q_2^j, \dots, q_n^j) \quad (2)$$

Similarly for a damaged structure:

$$\mathbb{L} w_i^*(q_1^j, q_2^j, \dots, q_n^j) = C^*Q_i(q_1^j, q_2^j, \dots, q_n^j) \quad (3)$$

where the superscript asterisks represent the parameters for the damaged structure. Since  $Q_i$  is invariant with respect to the undamaged and damaged structures, a damage index,  $\beta'_{ij}$ , may be formulated using Eq (2) and (3) as follows:

$$\beta'_{ij} = \frac{C^*}{C} = \frac{\mathbb{L} w_i^*}{\mathbb{L} w_i} \quad (4)$$

To avoid the problem of division by zero, which may arise at a node of a mode in dynamic measures or a support in static measure, we shift the domain of interest in the problem by adding unity to the denominator and numerator of Eq (4):

$$\beta_{ij} = (\mathbb{L} w_i^* + 1) / (\mathbb{L} w_i + 1) \quad (5)$$

For N sets of measurements, the following expression will be a convenient form of damage index:

$$\beta_j = \left( \sum_{i=1}^N w_i + 1 \right) / \left( \sum_{i=1}^N w_i + 1 \right) \quad (6)$$

Note that the indices represented by Eqs (4) to (6) are "point" indices. Note also that, in case of the three dimensional truss problem, as shown in Figure 1, the point may be taken as the center point of each member. The damage index,  $\beta_{ij}$ , for  $j^{\text{th}}$  member in  $i^{\text{th}}$  measurement set can be, therefore, defined by associating the extension of the  $i^{\text{th}}$  member with the center point,  $w_i(L/2)$ , as depicted in Figure 1.

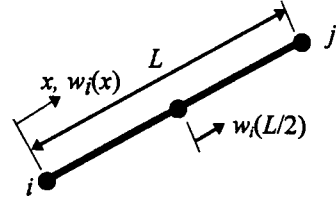


Figure 1. Schematic of Typical Truss Member

## 2.2. Energy Index

The strain energy for a structure may be written in terms of a generalized displacement vector,  $W$ , as follows:

$$U = \frac{1}{2} W^T K W \quad (7)$$

where  $U$  is the strain energy and  $K$  is a generalized stiffness matrix. Fraction of the strain energy for element  $j$  and the  $i^{\text{th}}$  set of deformation measurements in a structure is given by:

$$F_{ij} = \frac{U_{ij}}{U_i} = \frac{W_i^T K_j W_i}{W_i^T K W_i} \quad (8)$$

where  $U_i$  represents the strain energy for  $i^{\text{th}}$  set of measurements and  $U_{ij}$  represents the strain energy stored in  $j^{\text{th}}$  element for the  $i^{\text{th}}$  set of measurements. Similarly for damaged structure,

$$F_{ij}^* = \frac{U_{ij}^*}{U_i^*} = \frac{W_i^{*T} K_j^* W_i^*}{W_i^{*T} K^* W_i^*} \quad (9)$$

The contribution of the  $j^{\text{th}}$  element to the generalized stiffness matrix,  $K_j$ , in Eq (9) and (10) can be written as follows:

$$K_j = k_j D_j \quad (10)$$

and

$$K_j^* = k_j^* D_j \quad (11)$$

where  $k_j$  is a parameter representing the material stiffness properties of the  $j^{\text{th}}$  member of the structure, and  $D_j$  involves only geometric quantities (and possibly terms containing Poisson's ratio). The fraction of strain energy for the undamaged and damaged structures are related by<sup>4</sup>:

$$F_{ij}^* = F_{ij} + dF_{ij} \approx F_{ij} \left(1 - dk_j/k_j\right) \quad (12)$$

Substituting Eqs (9), (10), (11), and (12) into Eq (13) and solving for damage index,  $\beta'_{ij}$ , gives:

$$\beta'_{ij} = \frac{k_j}{k_j^*} = \frac{1}{2} \left( f_{ij}^*/f_{ij} + 1 \right) \quad (13)$$

$$\text{where } f_{ij} = \frac{W_i^T D_j W_i}{U_i} \text{ and } f_{ij}^* = \frac{W_i^{*T} D_j W_i^*}{U_i^*} \quad (14)$$

Shifting the domain to avoid dividing by zero yields the modified damage index:

$$\beta_{ij} = \frac{1}{2} \left[ (f_{ij}^* + 1) / (f_{ij} + 1) + 1 \right] \quad (15)$$

When N sets of measurements are used, the results obtained for each set may be superposed as follows:

$$\beta_j = \frac{1}{2} \left[ \left( \sum_{i=1}^N f_{ij}^* + 1 \right) / \left( \sum_{i=1}^N f_{ij} + 1 \right) + 1 \right] \quad (16)$$

Note that the damage index for the energy method is associated with an element.

### 3. DAMAGE LOCALIZATION

Damage in a structure can be localized by utilizing the results from classification analysis<sup>5</sup>. The classification rule used here utilizes hypothesis testing. The alternate ( $H_1$ ) and null ( $H_0$ ) hypotheses are defined as follows:

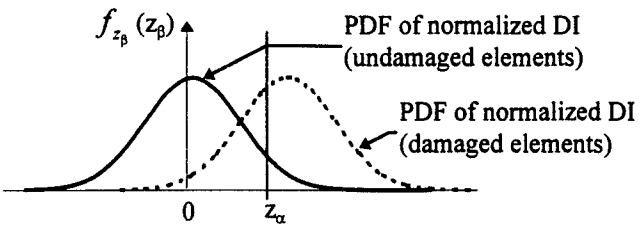
$H_0$  : Element or location j of the structure is not damaged

$H_1$  : Element or location j of the structure is damaged

To perform the testing, the damage indices, which are shown in Eqs (5), (6), (15), and (16), are to be normalized using the following Eq (17):

$$z_{ij} = \frac{\beta_{ij} - \mu_\beta}{\sigma_\beta} \quad (17)$$

where  $z_{ij}$  is the normalized damage index for j<sup>th</sup> location (element) for the i<sup>th</sup> measurement set, while  $\mu_\beta$  and  $\sigma_\beta$  represent the mean and the standard deviation of  $\beta_{ij}$ 's. The probability density function (PDF) of normalized damage indices for both damaged and undamaged locations (elements) are depicted in Figure 2. In Figure 2,  $z_\alpha$  is the threshold value, and  $\alpha$  is the level of significance of the test. Thus, the test may be restated as follows:



- i) choose  $H_0$  if  $z_{ij} < z_\alpha$ , or
- ii) choose  $H_1$  if  $z_{ij} \geq z_\alpha$

Note that typical values of  $\alpha$  used by the authors are  $z_{0.01} = 2.326$  and  $z_{0.025} = 1.96$

Figure 2. PDF's of Normalized Damage Index

#### 4. EVALUATION OF PERFORMANCE OF NDD THEORIES

To evaluate the performance of the theories, appropriate performance criteria must first be provided. Since the percentage of correctly predicted locations is a complement of the percentage of false negatives, two criteria, the percentage of false positives and the percentage of false negatives, are selected in this paper. The performance indices for the percentage of false positives,  $I_p$ , and for the percentage of false negatives,  $I_n$ , can be calculated as follows:

$$\begin{aligned} I_p &= 100 - (\text{percentage of false positives}), \text{ and} \\ I_n &= 100 - (\text{percentage of false negatives}) \end{aligned} \quad (18)$$

Then, the overall performance index,  $I_{all}$ , may be obtained by weight-averaging these indices as follows:

$$I_{all} = \left( \sum_{i=1}^n W_i I_i \right) / \sum_{i=1}^n W_i \quad (19)$$

where  $W_i$  is the relative weight assigned to each index. Note that  $W_i$  is assigned in accordance with the relative importance of each performance criterion. Since the false negatives are more critical than the false positives, the false negatives are weighted three times greater than the level for the false positives.

#### 5. COMBINATION OF NDD ALGORITHMS

For each and every location or element in the structure,  $n$  predictions of damage can be obtained by applying as many NDD theories and measurement sets. In the two NDD algorithms discussed in this paper, the normalized damage index,  $z_j$ , may be regarded as indicators for each location or element. The concept of WGM can be utilized as a logical means for combining the damage indicators. For example, if we have  $n$  damage indicators for the  $j^{\text{th}}$  location (element), a probability measure of damage at that location for each theory may be given by:

$$P_{z_j} = P(x \leq z_j) = \Phi(z_j) \quad (20)$$

where  $\Phi(z_j)$  is the normal cumulative distribution function. We propose that any  $n$  predictions may be combined using the following weighted generalized mean connective:

$$\hat{P}_{z_j} = \left( \sum_{k=1}^n w_k (P_{z_j})_k^\gamma \right)^{1/\gamma} \quad (21)$$

where  $\gamma$  is a parameter which identifies the type of mean (e.g., arithmetic, harmonic, geometric, etc.). Note that as  $\gamma$  approaches  $+\infty$ ,  $\hat{P}_{z_j}$  approaches the maximum value of the  $P_{z_j}$ 's (i.e., it is effectively assigning a probability measure to a fuzzy union). Conversely, as  $\gamma$  approaches  $-\infty$ ,  $\hat{P}_{z_j}$  approaches the minimum value of the  $P_{z_j}$ 's (i.e., it is effectively assigning a probability measure to a fuzzy intersection). Therefore, by varying  $\gamma$ , we can create a full range of logical filters. For the purpose of this paper, we utilize the following three filters :

- i)  $\hat{P}_{z_j} = \max_{k=1}^n (P_{z_j})_k$  (i.e.,  $\gamma \rightarrow +\infty$ ),
- ii)  $\hat{P}_{z_j} = \min_{k=1}^n (P_{z_j})_k$  (i.e.,  $\gamma \rightarrow -\infty$ ), and
- iii)  $\hat{P}_{z_j} = \text{mean}_{k=1}^n (P_{z_j})_k$  (i.e.,  $\gamma = 1$ )

These three filters represent the extremes and the middle of the WGM function given by Eq (21).

## 6. NUMERICAL EXAMPLE

The relative performance of the two preceding NDD theories (i.e., the flexibility and energy approaches) and the three combination rules for the theories are evaluated here using a numerical example of space structure.

### 6.1. Description of Example Structure

The schematic of the example structure, a typical hexagonal truss, the boundary conditions, and the simulated locations of damage are shown in Figure 3. The structure is 190.25 inches long and consists of twelve evenly spaced bays. It is modeled using 300 elements and 91 nodes. The damages are simulated by reducing the elastic modulus of corresponding elements. The structure is subjected to three damage scenarios. The damage locations and magnitudes for each scenario are summarized as follows:

- Damage case 1 : reduce the stiffness of element 87 by 10 %.
- Damage case 2 : reduce the stiffness of element 63 by 5 % and element 200 by 3 %.
- Damage case 3 : reduce the stiffness of element 81 by 1 %, element 128 by 8 %  
, and element 187 by 23 %

To obtain the static set of data, the structure is subjected to five static loading cases. The location, direction, and magnitude of the static load for each load case are described as follows:

- Load case 1 : 200 lb at node 1615 in z-direction
- Load case 2 : 200 lb at node 1165 in x-direction
- Load case 3 : 200 lb at node 1315 in y-direction
- Load case 4 : 200 lb at node 1320 in x-direction
- Load case 5 : 200 lb at node 1470 in y-direction

Note that the damaged elements and the locations of the static loads are shown in Figure 3.

### 6.2. Damage Localization Results

Static and free vibration analyses are performed using the commercial FORTRAN code (ABAQUS)<sup>6</sup>. Since, to the naked eye, the corresponding mode shapes for undamaged and damaged structures are indistinguishable,

only the mode shapes for the undamaged structure are shown in Figure 4. Figures 5 to 7 show the damage localization results of the flexibility and energy method individually and three combination rules using all 5 modes or load cases. Note that a 95% confidence level is used for the significance test. The comparative performance of the individual theories and the combinations are summarized in Table 1 through 3.

## 7. DISCUSSION

The overall indices used here to evaluate the performance of a theory of damage localization include the percentage of false positives and the percentage of false negatives. The percentage of correctly predicted locations is not considered because it is a complement of the percentage of false negatives. The performance of two basic theories using static and dynamic displacements are briefly summarized in Tables 1 through 3. From the Tables, the flexibility method tends to out-perform the energy method when single mode or load case as well as all five modes or load cases are used. It is also observed that the performance of each theory is better when static displacements are used. When three logical filters are included in the comparison, the following observations are made. With respect to the number of false positives, the minimum and average probability filters have the effect of reducing the number of false positives. This effect is visualized in Figures 5 through 7. With respect to the number of false negatives, the maximum probability filter reduces the number of false negatives at the expense of predicting additional false positives.

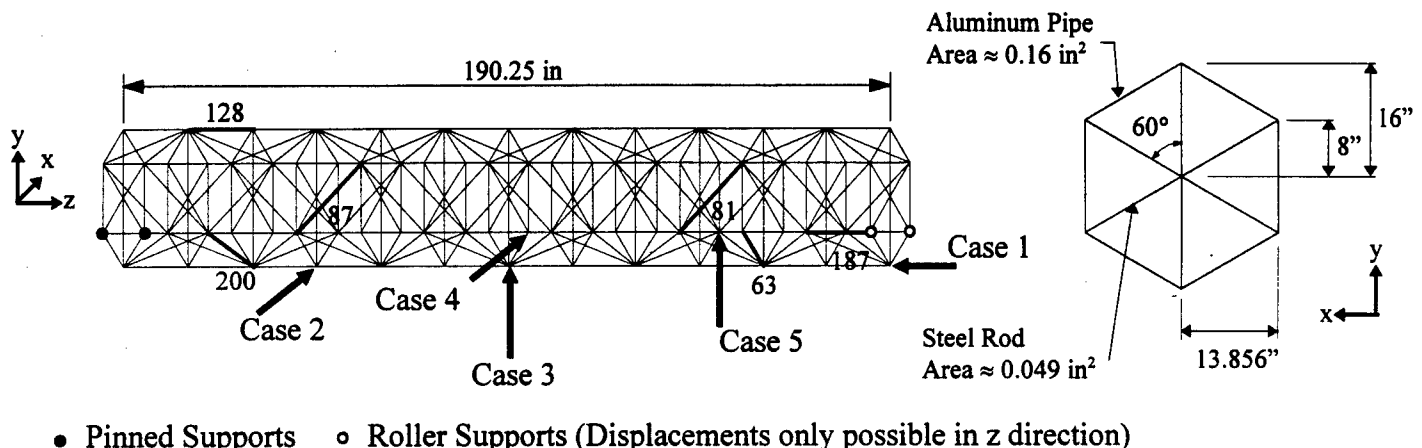


Figure 3. Schematic of the Example Structure

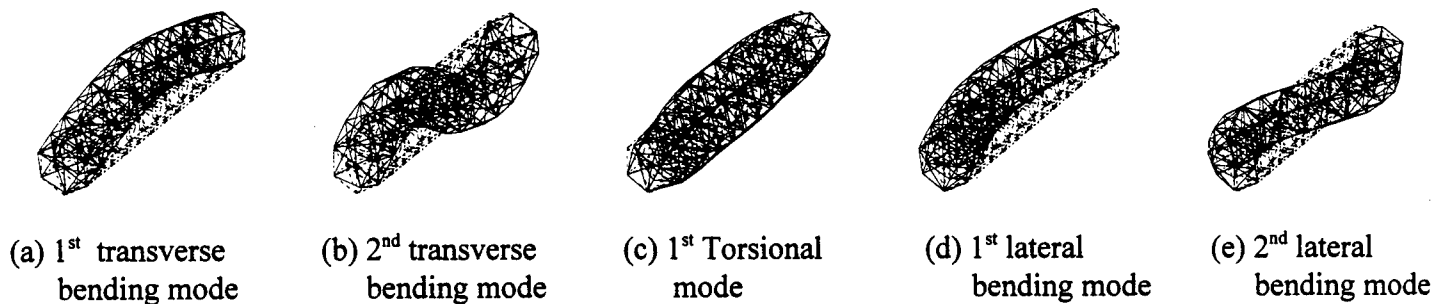


Figure 4. Mode Shapes of the Structure

## 8. SUMMARY AND CONCLUSION

This paper explored the possibility of the performance improvement via combining multiple damage predictions. The localization performance of a damage theory was evaluated using the percentage of false positive predictions and the percentage of false negative predictions. Two prominent damage theories were considered. One theory utilizes the changes in the flexibility at a point in the structure; the other theory utilizes the changes in the strain energy of an element of the structure. Both static and dynamic measurements were utilized to yield four damage prediction sets. Three ways of combining the four prediction sets were considered. These combinations, which were based on the generalized mean concept, represented the extremes of fuzzy union (maximum probability filter), fuzzy intersection (minimum probability filter), and an arithmetic mean connective (average probability filter). The performances of the combination rules were examined via a numerical example utilizing a space structure. Three major findings can be reported here. First, the minimum probability filter reduces the number of false positives at the expense of increasing the number of false negatives. Second, the maximum probability filter reduces the number of false negatives at the expense of increasing the number of false positives. Thus, these two filters form two extremes, but the maximum probability filter yields better performance in almost all cases because it minimizes the percentage of false negatives. Finally, the average probability filter reduces the number of false positives (as in the case of the minimum probability filter), but slightly decreases the number of false negatives (when compared to the minimum probability filter). Thus, on the basis of these results, it can be concluded that the combination of damage detection theories can, in fact, improve the overall performance of damage detection.

## ACKNOWLEDGMENTS

Funding for this effort was sponsored by the Air Force Office of Scientific Research, Air Force Materiel Command, USAF, under grant number F49620-95-1-0518, (FAST Center for Structural Integrity of Aerospace Systems). The U.S. Government is authorized to reproduce and distribute reprints for Governmental purposes notwithstanding any copyright notation thereon.

## REFERENCES

1. Farrar, C. and Jauregui, D., *Damage Detection Algorithms Applied to Experimental and Numerical Modal Data from the I-40 Bridge*, Los Alamos National Lab., Los Alamos, 1996.
2. Choi, S. and Stubbs, N. "Nondestructive Damage Detection Algorithms for 2D Plates", *Smart Structures and Materials 1997: Smart Systems for Bridges, Structures, and Highways, SPIE Proceedings*, ed N. Stubbs, vol. 3043, pp. 193-204, SPIE, 1997.
3. Klir, G. J. and Folger, T. A. *Fuzzy Sets, Uncertainty, and Information*, Prentice Hall, Englewood Cliffs, 1988.
4. Stubbs, N. and Garcia, G. "Application of Pattern Recognition to Damage Localization", *Micro Computers in Civil Engineering*, Vol. 11, pp. 395-409, 1996.
5. Gibson, J. D. and Melsa, J. L. *Introduction to Nonparametric Detection with Applications*, Academic Press, New York, 1975.
6. *ABAQUS Version 5.4 User Manual*, Hibbit, Karlsson & Sorensen, Inc., Pawtucket, 1994.

Table 1. Performance Comparison for Damage Scenario 1

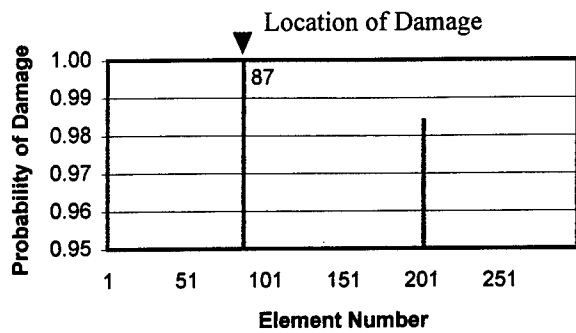
	No. of False Positive		Performance Index		No. of False Negative		Performance Index		Overall Index		
	Energy	Flex.	Energy	Flex.	Energy	Flex.	Energy	Flex.	Energy	Flex.	
Dynamic	Mode 1	3	2	99.0	99.3	0	0	100.0	100.0	99.8	99.8
	Mode 2	13	10	95.7	96.7	0	0	100.0	100.0	98.9	99.2
	Mode 3	3	5	99.0	98.3	0	0	100.0	100.0	99.8	99.6
	Mode 4	5	4	98.3	98.7	0	0	100.0	100.0	99.6	99.7
	Mode 5	19	13	93.6	95.7	1	0	0.0	100.0	23.4	98.9
	5 Modes	1	2	99.7	99.3	0	0	100.0	100.0	99.9	99.8
Static	Load Case 1	7	1	97.7	99.7	0	0	100.0	100.0	99.4	99.9
	Load Case 2	8	0	97.3	100.0	0	0	100.0	100.0	99.3	100.0
	Load Case 3	1	2	99.7	99.3	0	0	100.0	100.0	99.9	99.8
	Load Case 4	4	1	98.7	99.7	0	0	100.0	100.0	99.7	99.9
	Load Case 5	5	2	98.3	99.3	0	0	100.0	100.0	99.6	99.8
	5 Load Cases	0	0	100.0	100.0	0	0	100.0	100.0	100.0	100.0
Minimum Filter		0		100.0		0		100.0		100.0	
Average Filter		0		100.0		0		100.0		100.0	
Maximum Filter		3		99.0		0		100.0		99.8	

Table 2. Performance Comparison for Damage Scenario 2

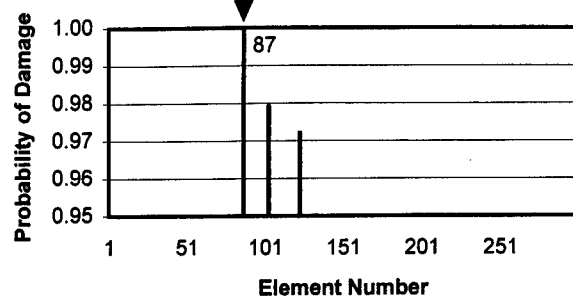
	No. of False Positive		Performance Index		No. of False Negative		Performance Index		Overall Index		
	Energy	Flex.	Energy	Flex.	Energy	Flex.	Energy	Flex.	Energy	Flex.	
Dynamic	Mode 1	4	13	98.7	95.6	1	0	50.0	100.0	62.2	98.9
	Mode 2	1	3	99.7	99.0	1	0	50.0	100.0	62.4	99.8
	Mode 3	2	6	99.3	98.0	1	1	50.0	50.0	62.3	62.0
	Mode 4	8	11	97.3	96.3	1	1	50.0	50.0	61.8	61.6
	Mode 5	18	23	94.0	92.3	2	1	0.0	50.0	23.5	60.6
	5 Modes	0	2	100.0	99.3	1	0	50.0	100.0	62.5	99.8
Static	Load Case 1	0	0	100.0	100.0	1	0	50.0	100.0	62.5	100.0
	Load Case 2	0	2	100.0	99.3	1	1	50.0	50.0	62.5	62.3
	Load Case 3	1	0	99.7	100.0	1	0	50.0	100.0	62.4	100.0
	Load Case 4	0	0	100.0	100.0	1	1	50.0	50.0	62.5	62.5
	Load Case 5	5	12	98.3	96.0	2	0	0.0	100.0	24.6	99.0
	5 Load Cases	0	0	100.0	100.0	1	0	50.0	100.0	62.5	100.0
Minimum Filter		0		100.0		1		50.0		62.5	
Average Filter		0		100.0		1		50.0		62.5	
Maximum Filter		2		99.3		0		100.0		99.8	

Table 3. Performance Comparison for Damage Scenario 3

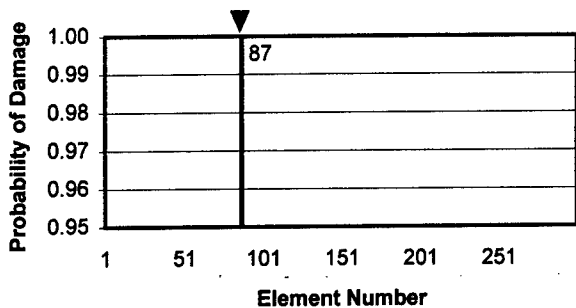
	No. of False Positive		Performance Index		No. of False Negative		Performance Index		Overall Index		
	Energy	Flex.	Energy	Flex.	Energy	Flex.	Energy	Flex.	Energy	Flex.	
Dynamic	Mode 1	2	2	99.3	99.3	2	2	33.3	33.3	49.8	49.8
	Mode 2	7	21	97.6	92.9	2	2	33.3	33.3	49.4	48.2
	Mode 3	0	7	100.0	97.6	2	2	33.3	33.3	50.0	49.4
	Mode 4	16	5	94.6	98.3	2	2	33.3	33.3	48.6	49.6
	Mode 5	0	2	100.0	99.3	2	1	33.3	66.7	50.0	74.9
	5 Modes	0	1	100.0	99.7	1	1	66.7	66.7	75.0	75.0
Static	Load Case 1	4	0	98.7	100.0	2	1	33.3	66.7	49.7	75.0
	Load Case 2	11	5	96.3	98.3	2	2	33.3	33.3	49.1	49.6
	Load Case 3	2	2	99.3	99.3	1	1	66.7	66.7	74.9	74.9
	Load Case 4	8	2	97.3	99.3	2	2	33.3	33.3	49.3	49.8
	Load Case 5	1	3	99.7	99.0	1	1	66.7	66.7	75.0	74.8
	5 Load Cases	1	0	99.7	100.0	1	1	66.7	66.7	75.0	75.0
Minimum Filter		0		100.0		1		66.7		75.0	
Average Filter		0		100.0		1		66.7		75.0	
Maximum Filter		2		99.3		1		66.7		74.9	



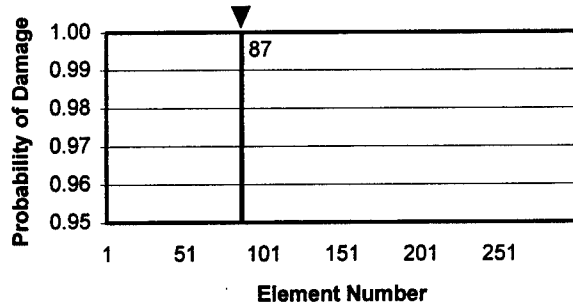
(a) Strain Energy (Dynamic) : 5 Modes



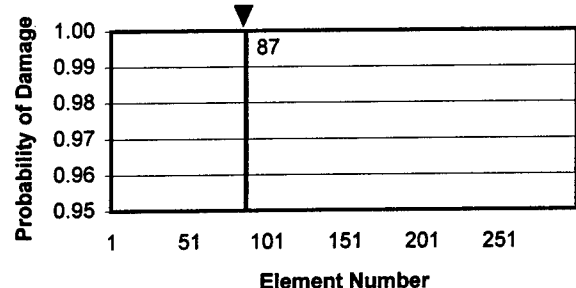
(b) Flexibility (Dynamic) : 5 Modes



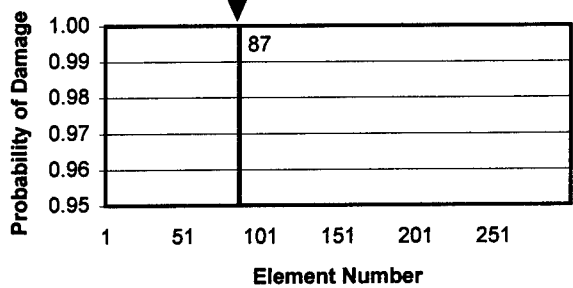
(c) Strain Energy (Static) : 5 Load Cases



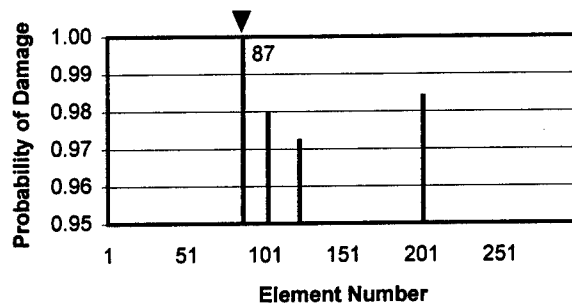
(d) Flexibility (Static) : 5 Load Cases



(e) Minimum Probability Filter

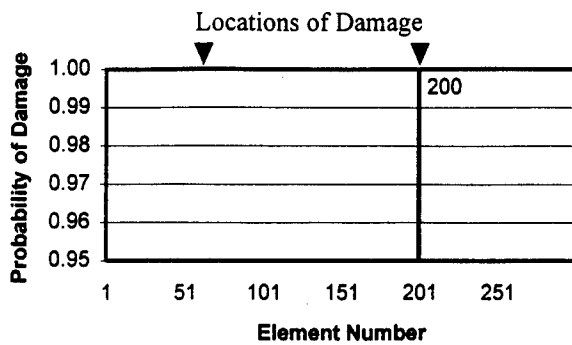


(f) Average Probability Filter

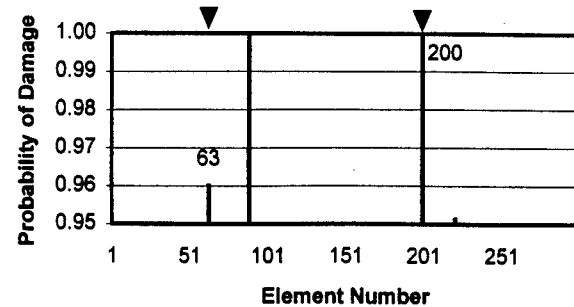


(g) Maximum Probability Filter

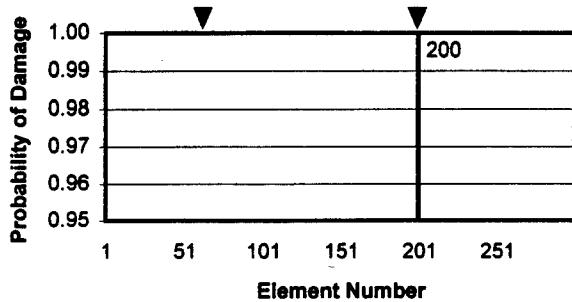
Figure 5: Damage Localization Results for Damage Case 1



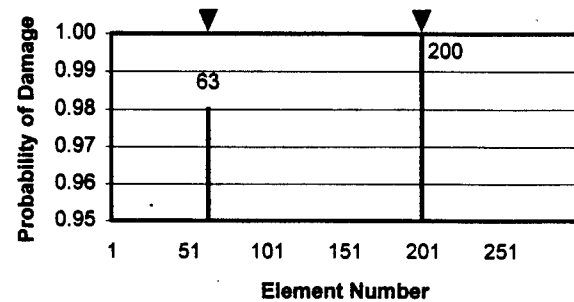
(a) Strain Energy (Dynamic) : 5 Modes



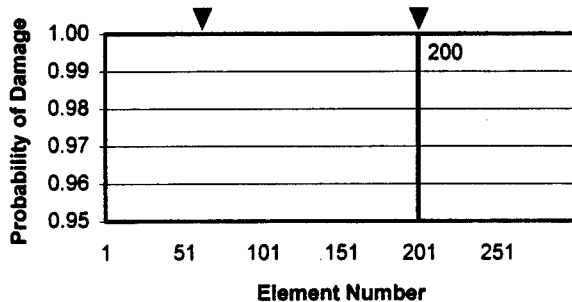
(b) Flexibility (Dynamic) : 5 Modes



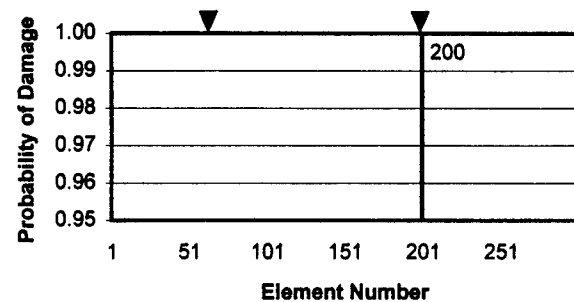
(c) Strain Energy (Static) : 5 Load Cases



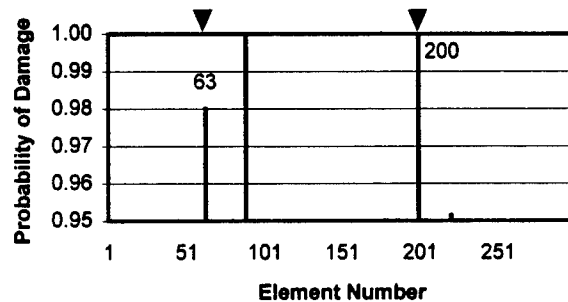
(d) Flexibility (Static) : 5 Load Cases



(e) Minimum Probability Filter

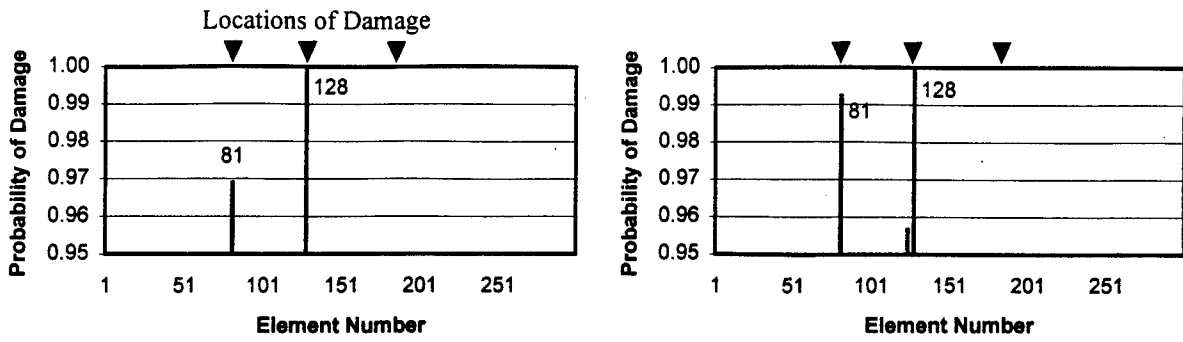


(f) Average Probability Filter



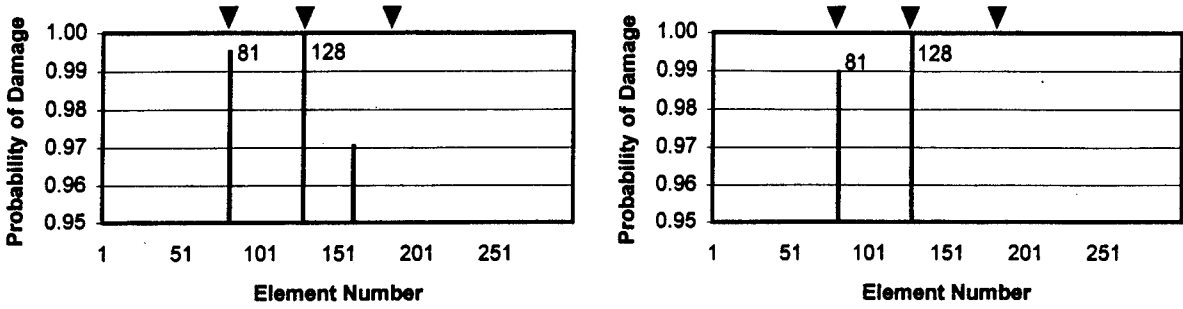
(g) Maximum Probability Filter

Figure 6: Damage Localization Results for Damage Case 2



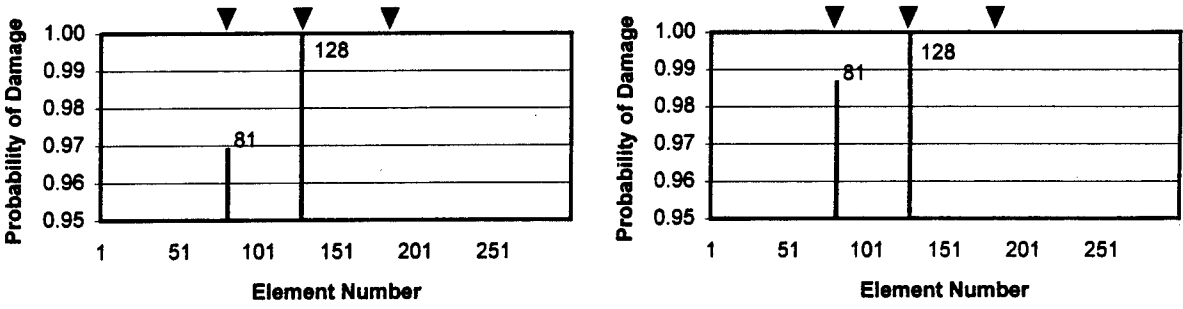
(a) Strain Energy (Dynamic) : 5 Modes

(b) Flexibility (Dynamic) : 5 Modes



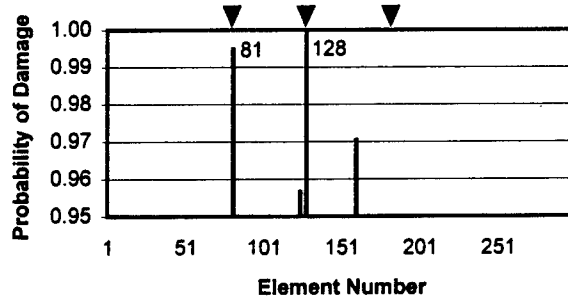
(c) Strain Energy (Static) : 5 Load Cases

(d) Flexibility (Static) : 5 Load Cases



(e) Minimum Probability Filter

(f) Average Probability Filter



(g) Maximum Probability Filter

Figure 7: Damage Localization Results for Damage Case 3

## **DISCUSSION**

### **Improved Nondestructive Damage Detection via Combining Individual Detection Theories**

Speaker: Choi

There are two ways in which two theories can be "different": (1) one can be right and one wrong (or both wrong), so method should tell which; (2) both can be right, but address different aspects of the problem, so method should tell how to best combine them. Does your method address (1) or (2) or both? —Mel Siegel

*We assume that both theories are correct but address different aspects of the problem.*



# **Damage detection methods based on wavelet analyses of sensor signals**

X. Deng\*, Q. Wang, C. A. Rogers, V. Giurgiutiu, and M. A. Sutton

Center for Mechanics of Materials and NDE, Department of Mechanical Engineering,  
University of South Carolina, Columbia, SC 29208

## **ABSTRACT**

In this paper we discuss our recent effort in applying the wavelet transform to structural damage detection studies. Our effort is directed at monitoring the structural health of helicopter rotor blades (which may suffer from several types of crack-like damage) by analyzing NDE signals obtained from rotor-blade structures with the wavelet transform. The results presented here are limited to wavelet transforms of simulated, spatially distributed deformation signals. The results show that perturbations in the spatial signals induced by crack-like damage contain inherent features that can be enhanced and detected by the wavelet transforms of the signals. Work is also in progress in developing wavelet-based damage detection methods using wave propagation signals.

**Keywords:** damage detection, health monitoring, wavelet transform, rotor blades.

## **1. INTRODUCTION**

The objective of a damage-detection and health-monitoring system in structural applications is to detect structural damage in a structure before it seriously affects the performance and integrity of the structure. A particular application that is of interest to us is the detection of crack-like damage in helicopter rotor blades.

Because rotor blades provide the necessary flight driving force for a rotorcraft, their structural integrity is of critical concern. However, depending on the type of construction, a rotor blade may suffer from several types of crack-like damage. If not detected early, rotor-blade damage could lead to excessive helicopter vibration and even catastrophic failure. Furthermore, an early detection of rotor-blade damage can also keep the maintenance cost down—the repair cost for a blade is usually a small fraction of its replacement cost.

Recently we have been working with the South Carolina Army National Guard to develop damage detection methods for helicopter rotor blades. Our goal is to seek methods that can quickly and automatically provide structural damage information using sensor signals obtained from rotor blades, without relying on heavy structural-analysis or optimization computations. To this end, it appears that a particularly promising class of methods may be developed based on the wavelet

---

\* E-mail address: deng@enr.sc.edu

transform theory. The wavelet transform provides a desirable signal-processing tool for extracting embedded features in a signal and for detecting local perturbations in a signal.

A recent literature survey by us reveals that the wavelet transform has been applied to structural vibration signals to detect localized damage in gears<sup>1-3</sup>. However, it is not clear how to use the wavelet transform to analyze vibration signals to extract damage information for general structures without relying on extensive structural-analysis or optimization computations.

Our current effort is directed towards the detection of crack-like damage by applying the wavelet transform to spatially distributed signals and wave-propagation signals. While work is in progress with wavelet analysis of wave signals, preliminary results have been obtained for wavelet analysis of spatial signals. These results are based on numerically simulated displacement signals for cracked plates and beams, and are used to demonstrate that crack-like damage induces spatial perturbations whose features can be enhanced and detected by the wavelet transform.

## 2. WAVELET ANALYSIS

Wavelet analysis is related to but also distinct from Fourier analysis. In Fourier analysis, a signal is analyzed for its frequency composition. In a non-windowed Fourier transform, the whole history of the signal is used and the frequency composition obtained is averaged over the whole history. The disadvantage is that there is no time resolution in the frequency composition. In a windowed Fourier transform, only the part of the signal history that fits into a window centered at a time of interest is used and the frequency composition obtained is averaged over the width of the window. This moving window gives the frequency composition a better time resolution, at the price of losing some frequency resolution.

In wavelet analysis, on the other hand, a signal is decomposed into basis functions called wavelets. Unlike sine and cosine functions, wavelets are functions with compact support, in the sense that they decay to zero outside a certain interval (called support). As such, a position can be assigned to every wavelet to denote its region of support. Besides their positions, wavelets also come with various scales. At a fine scale, the wavelets are very narrow, and at a coarse scale, the wavelets are stretched out. It is the position and scale of the wavelets that allow desirable combinations of time and frequency resolutions of a signal. In the text below, we give a brief (and not necessarily rigorous) mathematical description of the wavelet transform. More formal descriptions can be found in relevant references, such as those<sup>4-7</sup> cited in this paper.

Let  $f(t)$  be a signal of interest in the domain  $(-\infty, +\infty)$ . Let  $\psi(t)$  be a complex-valued function localized in both time and frequency domains. We call  $\psi(t)$  a mother wavelet and generate wavelets from  $\psi(t)$  by operations of translation and dilation, as follows

$$\psi_{a,b}(t) = |a|^{-1/2} \psi\left(\frac{t-b}{a}\right) \quad (1)$$

where  $a$  is called the dilation parameter and  $b$  the translation parameter. The mother wavelet must satisfy the admissibility condition below

$$\int_{-\infty}^{+\infty} |\psi^*(\omega)|^2 \frac{d\omega}{\omega^2} < \infty \quad (2)$$

where  $\psi^*(\omega)$  is the Fourier transform of  $\psi(t)$ . The wavelet transform of  $f(t)$  is then defined by

$$c_{a,b} = \int_{-\infty}^{+\infty} f(t) \overline{\psi}_{a,b}(t) dt \quad (3)$$

where the over-bar denotes the complex conjugate of a function. The wavelet transform  $c_{a,b}$  is also called the wavelet coefficient for the wavelet  $\psi_{a,b}$ . If necessary, the original signal  $f(t)$  can be reconstructed by the inverse wavelet transform

$$f(t) = \int_{-\infty}^{+\infty} \int_{-\infty}^{+\infty} c_{a,b} \psi_{a,b} \frac{dadb}{a^2} \quad (4)$$

Although wavelets are usually used to analyze signals in the time domain, spatially distributed signals can also be represented with wavelets. Without loss of generality, we consider a spatial signal  $f(x)$  defined on  $[0,1]$ , where  $x$  refers to a spatial coordinate. For example, this signal can be a displacement or strain measurement over a region of interest for a structure under static or dynamic loading. Note that this region of interest (assuming it is one-dimensional for the purpose of this paper) can always be normalized to occupy  $[0, 1]$ . By choosing orthogonal wavelets that are localized in  $[0, 1]$ , the signal can be decomposed into the following wavelet series,

$$f(x) = c_0 + \sum_{j=0}^{\infty} \sum_{k=0}^{2^j-1} c_{j,k} \Psi_{j,k}(x) \quad (5)$$

where  $c_0$  is the average value of  $f(x)$  over  $[0,1]$ , and  $\psi_{j,k}$  is generated from

$$\psi_{j,k}(x) = 2^{j/2} \psi(2^j x - k) \quad (6)$$

In this paper, we will analyze spatial signals with the Haar wavelets<sup>8</sup>, which are the simplest orthonormal wavelets, where the mother Haar wavelet is defined by  $\psi(x) = 1$  if  $0 \leq x < 1/2$ ,  $\psi(x) = -1$  if  $1/2 \leq x < 1$ , and  $\psi(x) = 0$  otherwise. The coefficients for the wavelets in Eq. (5) can be written as

$$c_{j,k} = \int_0^1 f(x) \psi_{j,k}(x) dx \quad (7)$$

### 3. DAMAGE DETECTION

An advantage of the wavelet decomposition in Eq. (5) is that finer details of a signal can be represented by finer scale wavelets. Because of this *multi-resolution property* of the wavelet decomposition, local perturbations in a signal can be detected by fine-scale wavelets (those with relatively large  $j$  values in Eq. (5)) positioned (given by the  $k$  values in Eq. (5)) at the locations of the perturbations. In other words, one can determine the perturbation sites in a signal by examining the variations of the wavelet coefficients with their position. In principle, this idea forms the basis for detecting damage with spatially distributed signals.

In the following, we will present simulation results based on displacement signals computed by the finite element method along line segments near crack-like damage. The results indicate that the wavelet transform can enhance the signals and reveal the crack-tip locations, and that it may be used for structural damage detection provided the signals contain local perturbations caused by the presence of damage (e.g. cracks) over the region where the signals are collected. Such signals may be obtained from surface or internal measurements of displacement, strain, or other quantities whose values can be disturbed by the presence of damage.

The procedure for this damage detection method is as follows. First, collect spatially distributed signals over an area of interest. Second, perform the wavelet transform to the signal to obtain wavelet coefficients for *fine-scaled* wavelets (e.g. wavelets of scales  $j=8$  or higher). The reason why fine-scale wavelets must be used is that only wavelets of sufficient levels will be able to detect local variations in a signal. Third, for each level of wavelets, plot the value of the wavelet coefficients in the region spanned by the corresponding wavelets. Fourth, examine the distributions of the wavelet coefficients at each level. A sudden change (e.g. a spike) in the distribution of the wavelet coefficients signifies a strong local perturbation in the signal in the region spanned by the corresponding wavelet. If a detected perturbation is not caused by a known source (such as a known geometric or material discontinuity), then it will be attributed to the presence of damage at or near the site of the perturbation.

In the first example, we consider a large plate containing a through-thickness central crack under remote uniform-tension loading, as shown in Fig. 1(a). The finite element method is used to calculate the displacement response of the plate, and the displacement distribution along some line segments (see Fig. 1(b)) near the crack is collected. Figure 2 shows the displacement component variations with the  $y$ -coordinate along a vertical line segment, where the crack-tip location is indicated by a dip in the  $u_x$  displacement component at  $y=0$ . However, the crack-tip location is not evident from the variation of the  $u_y$  component. Now both of the displacement component variations are processed with the wavelet transform. In Fig. 3, the magnitude of the wavelet coefficients is plotted against the position of the wavelets along the  $y$ -axis for wavelets of scales 6 and 10. It is clear from Fig. 3 that the wavelet transform is able to enhance the signals and provide strong indicators for the crack tip location.

In the second example, a cantilever beam is considered (see Fig. 4). The beam contains a transverse edge crack at the mid-span and is loaded by a point force at the free end. The beam response is solved by the finite element method under plane strain conditions. The resulting displacement response along the bottom surface of the beam is shown in Fig. 4. The displacement response is then processed with the wavelet transform, and the results for wavelets of scales 9 and 10 are given in Figs. 5 (a) and (b). The crack location is identified as marked by the arrows.

Finally, the cantilever beam in the previous example is modified to contain a subsurface crack near the bottom surface of the beam, as shown in Fig. 6, where the displacement response of the beam along the bottom surface is also given. Figure 7 then shows the result of the wavelet transform at scale 10. Both tips of the subsurface crack are identified, as indicated by the arrows.

#### **4. CONCLUSION**

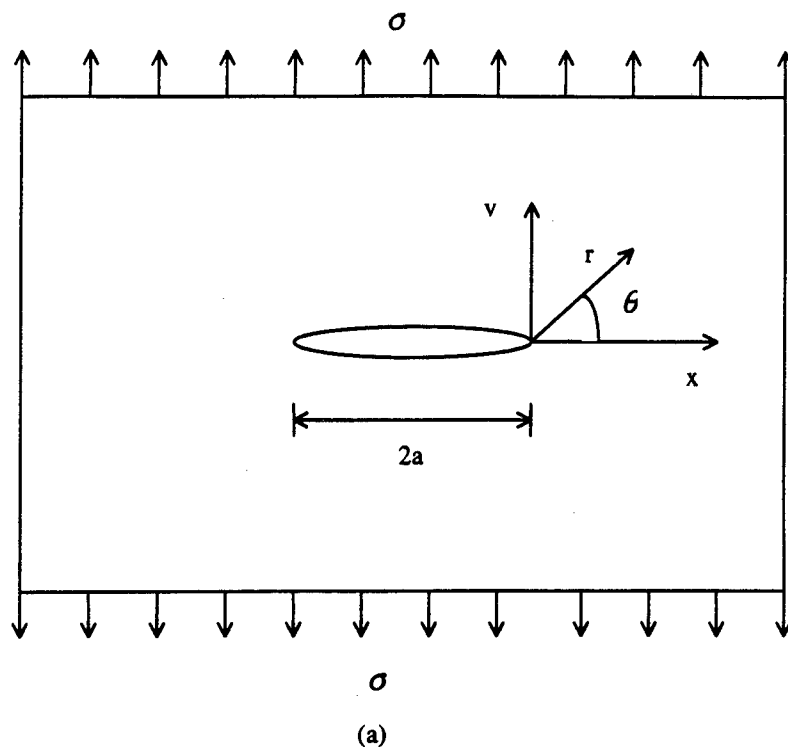
This paper presented preliminary results of a recent study of wavelet-based damage detection methods that may be applicable to rotorcraft blade structures. In particular, the wavelet transform has been applied to simulated displacement signals from plate and beam structures containing crack-like damage. The results show that perturbations in a spatially distributed signal caused by crack-like damage contain inherent features that can be enhanced and detected by the wavelet transform. Further research is needed in order to demonstrate the practicality of damage detection methods based on wavelet analyses of sensor signals without relying on intensive structural analysis and optimization computations.

#### **ACKNOWLEDGMENTS**

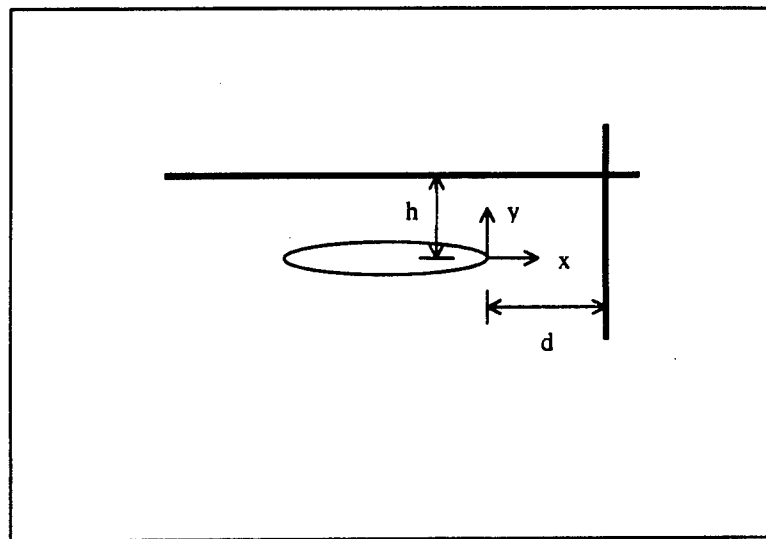
The authors acknowledge the support and cooperation of the South Carolina Army National Guard (project coordinator: Lemuel Grand). This study was supported in part by an NSF/EPSCoR grant through Cooperative Agreement No. EPS-9630167 and by a grant from the South Carolina Space Grant Consortium.

#### **REFERENCES**

1. Staszewski, W. J. and Tomlinson, G. R. "Application of the wavelet transform to fault detection in a spur gear," *Mechanical Systems and Signal Processing*, Vol. 8, No. 3, pp. 289-307, 1994.
2. Wang, W. J. and McFadden, P. D. "application of wavelets to gearbox vibration signals for fault detection," *Journal of Sound and Vibration*, Vol.192, pp. 927-939, 1996.
3. Wang, W. J. and McFadden, P. D. "Application of orthogonal wavelets to early gear damage detection," *Mechanical Systems and Signal Processing*, Vol. 9, pp. 497-508, 1996.
4. Daubechies, I. "Orthonormal bases of compactly supported wavelets," *Comm. Pure and Applied Maths*, Vol. XLI, pp. 909-996, 1988.
5. Mallat, S. "A theory for multi-resolution signal decomposition: the wavelet representation," *IEEE Trans. Pattern Anal. And Machine Intell.*, Vol. 11, pp. 674-693, 1989.
6. Daubechies, I. "The wavelet transform, time-frequency localization and signal analysis," *IEEE Trans. On Information Theory*, Vol. 36, pp. 961-1005, 1990.
7. Chui, C. K. *An Introduction to Wavelets*. Academic Press, San Diego, 1992.
8. Haar, A. "Zur Theorie der Orthogonalem Funktionensysteme," *Math. Ann.*, Vol. 69, pp. 331-371, 1910.



(a)



(b)

Fig. 1 (a) A large plate with a center crack under remote uniform tension loading; (b) vertical and horizontal line segments along which the displacement response will be obtained and used in wavelet analysis.

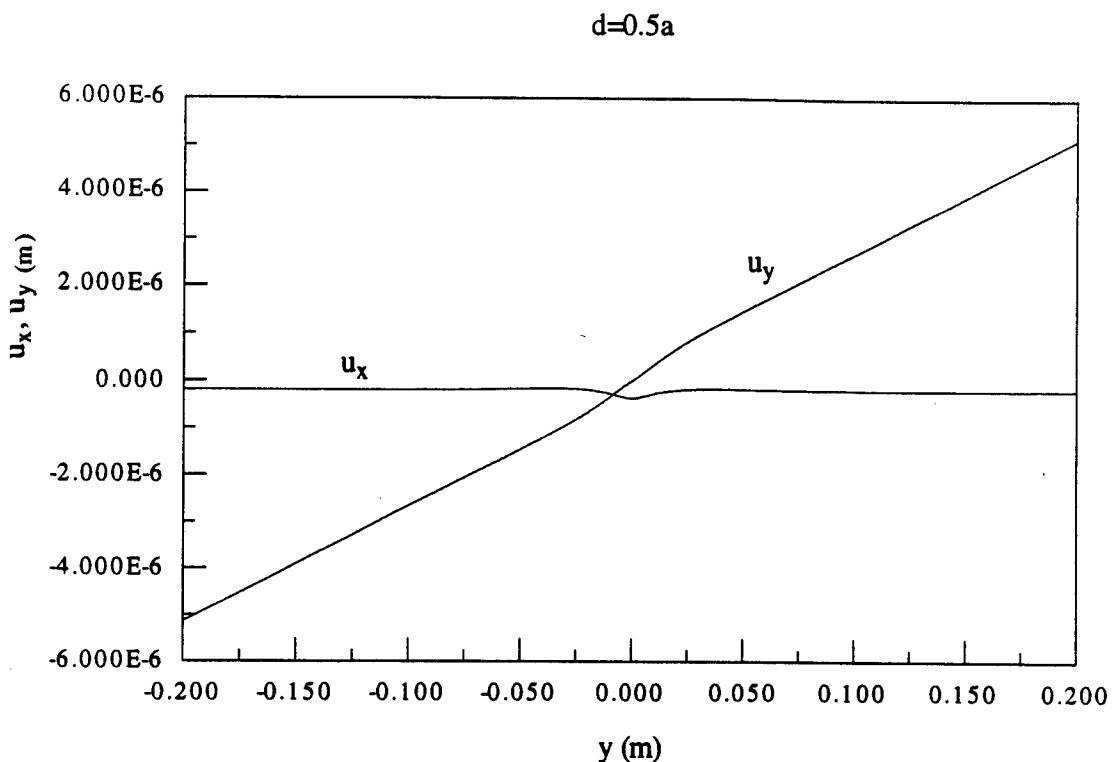


Fig. 2 Elastic displacement response along the vertical line segment in Fig. 1(b), with  $d=0.5a$  and  $a=40$  mm, and for a unit-thickness steel plate subject to  $\sigma = 5$  MPa.

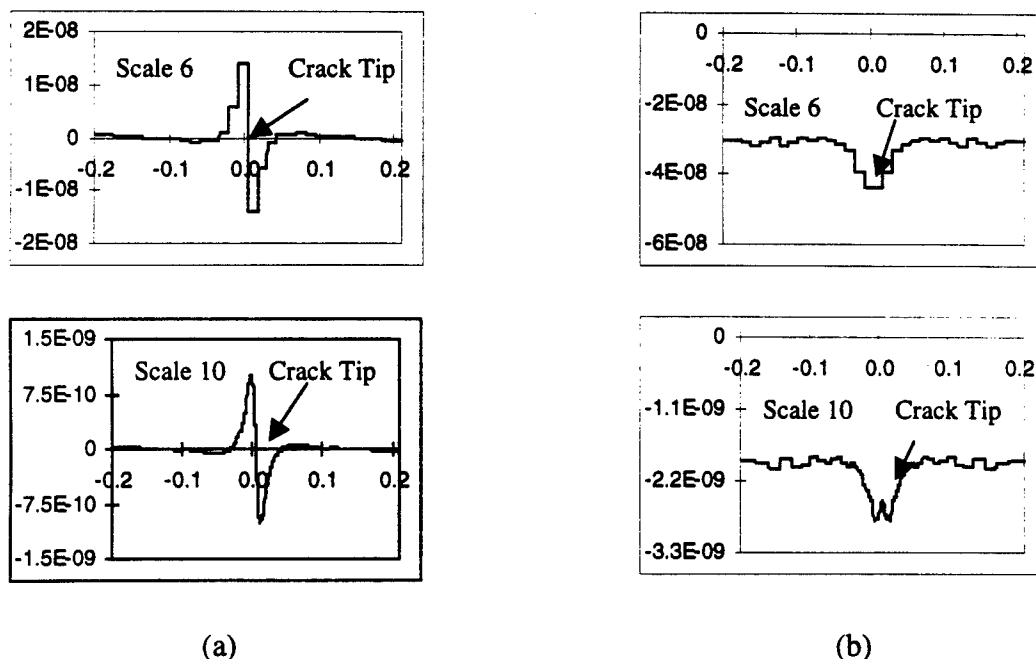


Fig. 3 Wavelet transforms of (a)  $u_x$  and (b)  $u_y$  in Fig. 2 at scales 6 and 10.

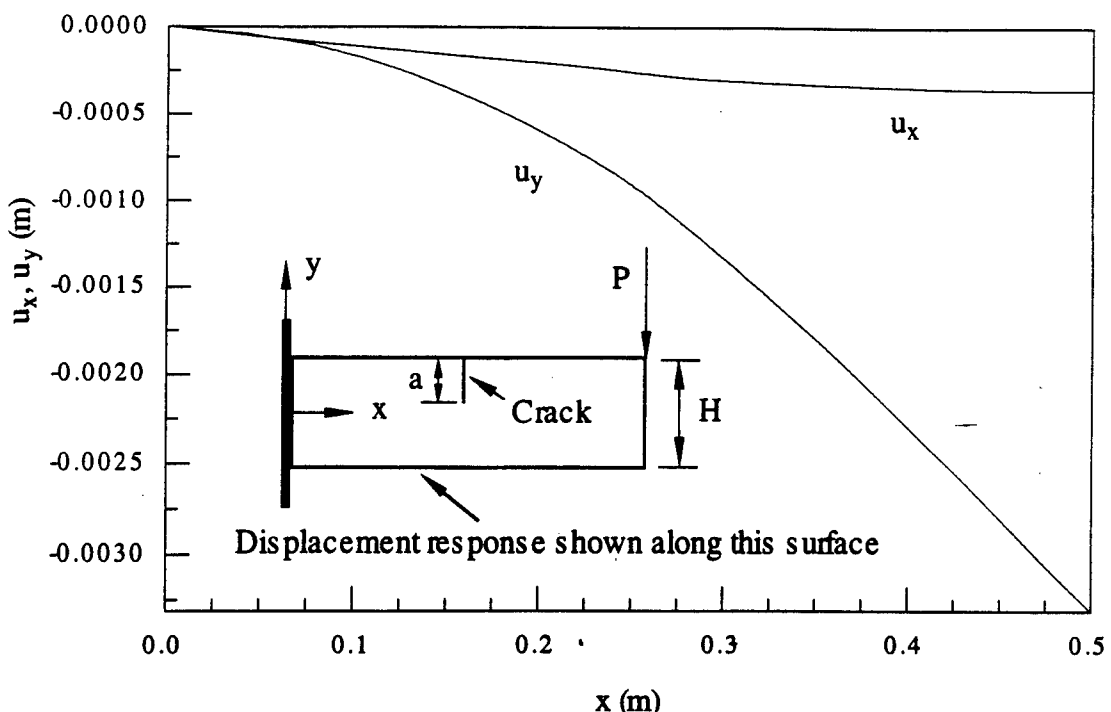


Fig. 4 Elastic displacement response of a cantilever beam with a transverse crack at mid-span and under a static load at the free end, where beam length=0.5 m, width=75 mm,  $a/H=1/3$ ,  $H=75$  mm, and  $P=878$  kN, with conventional steel properties.

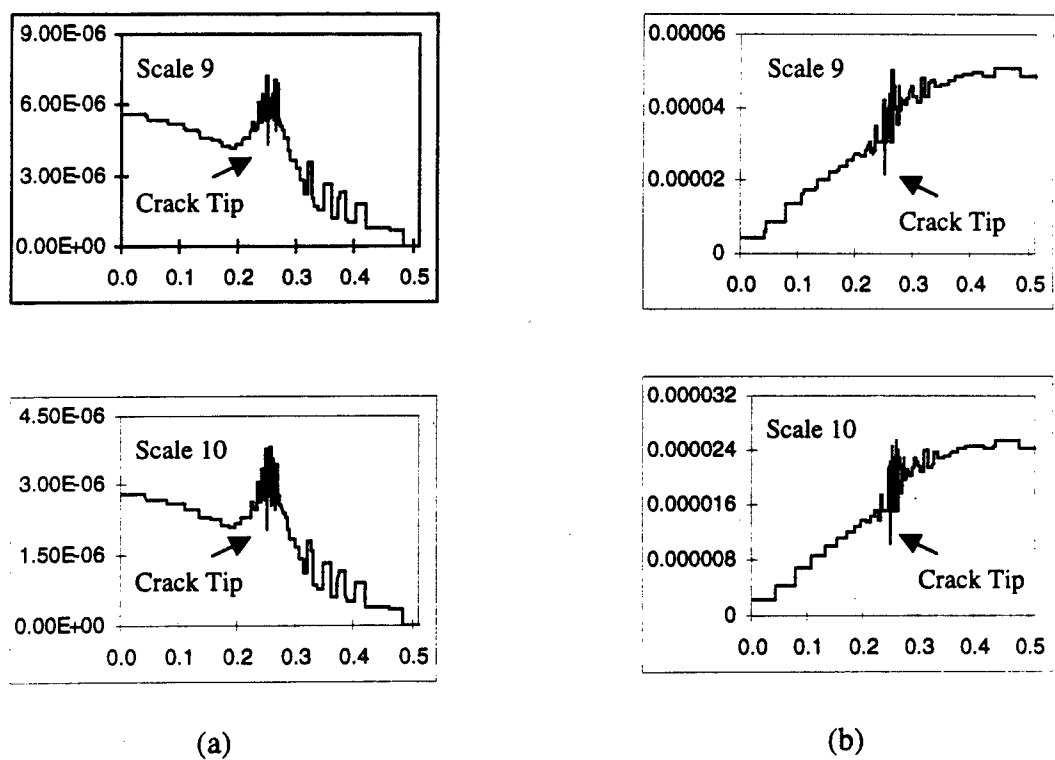


Fig. 5 Wavelet transforms of (a)  $u_x$  and (b)  $u_y$  in Fig. 4 at scales 9 and 10.

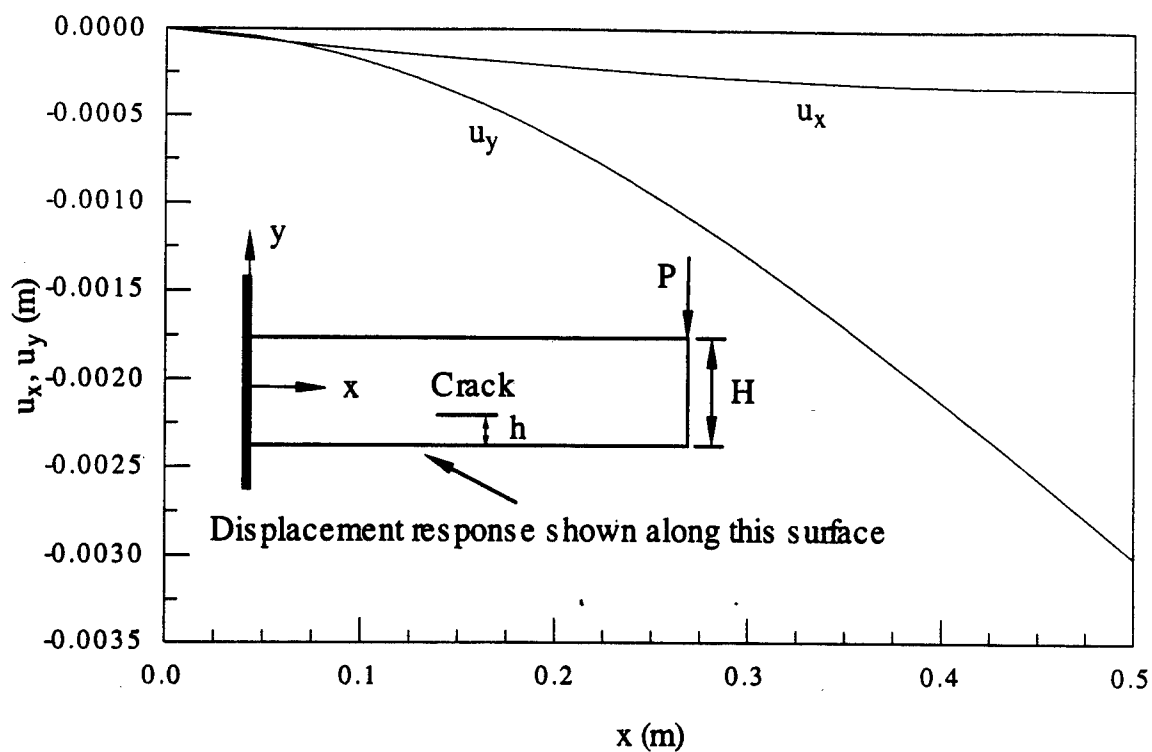


Fig. 6 Elastic displacement response of a cantilever beam with a longitudinal sub-surface crack at mid-span and under a static load at the free end, where beam length=0.5 m, width=75 mm, crack length=50 mm,  $h/H=1/4$ ,  $H=75$  mm, and  $P=878$  kN, with conventional steel properties.

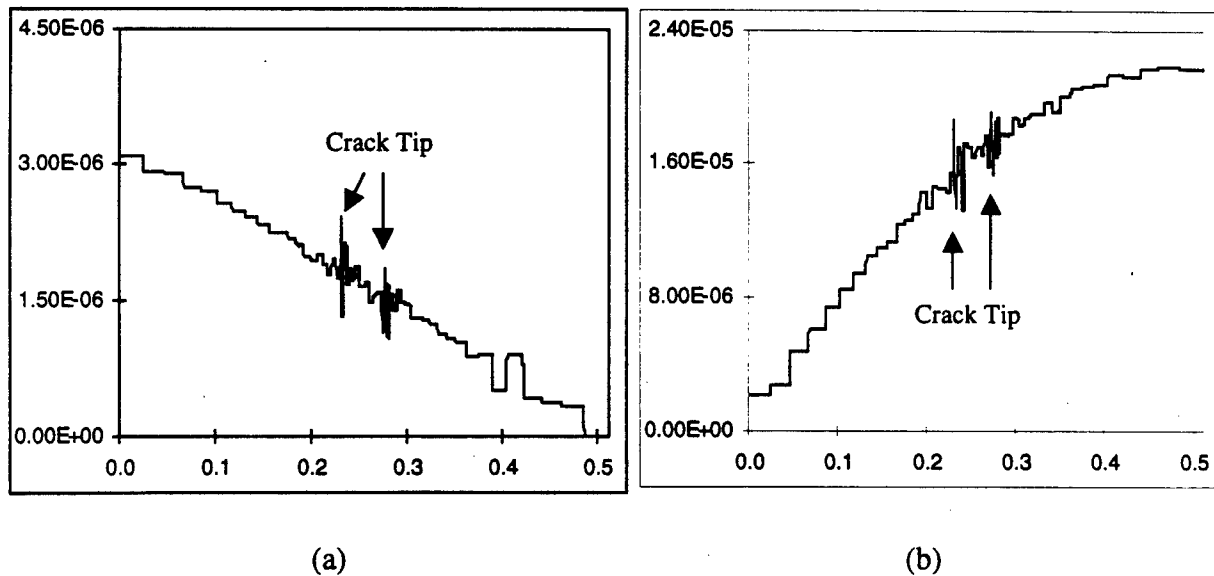


Fig. 7 Wavelet transforms of (a)  $u_x$  and (b)  $u_y$  in Fig. 6 at scale 10.



# Remote and automated inspection: status and prospects\*

Mel Siegel

The Robotics Institute -- School of Computer Science -- Carnegie Mellon University  
Pittsburgh, Pennsylvania 15213-3891

## ABSTRACT

Remotely or automatically operated vehicles (mobile "robots") for deploying visual and NDI inspection equipment are critically reviewed. After a brief introduction, reasons for using robots for aircraft skin inspection are reviewed. General design scenarios for robotic systems are then reviewed. Actual designs for five substantial US efforts are then described and illustrated, and the performance of these designs is discussed. Some smaller US and overseas efforts are mentioned briefly. The closing section discusses the lessons of efforts to date and suggests a course of action for the future.

**KEYWORDS:** automated robot visual NDI inspection ANDI CIMP MACS ROSTAM AutoCrawler

## 1. INTRODUCTION

Since 1989 at least five experimental "robots" for remote (and to some extent automated) inspection of aircraft have been built in the US. Three were built at universities (one at Wichita State<sup>1,2</sup> and two at Carnegie Mellon (CMU)),<sup>6,8</sup> one at a NASA facility (JPL),<sup>11</sup> and one privately (AutoCrawler LLC).<sup>14</sup> These efforts have been supported by the FAA,<sup>1,2,6</sup> the Air Force,<sup>11</sup> the State of Pennsylvania,<sup>8</sup> Boeing,<sup>1</sup> private entrepreneurs,<sup>8,14</sup> and, in kind if not in cash, by US Airways<sup>6,8</sup> and Northwest Airlines.<sup>8</sup> Outside the US, the Singapore Air Force is currently supporting a substantial local effort for robotic underwing inspection of F-5 aircraft,<sup>15</sup> and there are persistent rumors of one or more ongoing efforts, particularly in Japan, that are not being reported in the open literature. In addition, several university and commercial groups have designed and built robots for specific or generic "wall climbing" applications and mentioned aircraft inspection as possible future uses of their devices.

In the aggregate, the five US prototypes have demonstrated all of the technical capabilities needed to implement a robotically assisted inspection system: measurement (NDI sensors, and cameras for remote visual inspection), manipulation (actuators that can place, guide, and scan the sensors), mobility (a vehicular platform that can negotiate the aircraft surface), and monitoring (signal acquisition, data processing, and information display). However no one has demonstrated all these "4M-s" at once. Probably only one of the robots (the second of the two developed at CMU) has actually delivered to an aircraft inspector in the field anything that could with a straight face be called useful inspection data.

This paper focuses, more sharply in hindsight than was possible in foresight, on why building an aircraft inspection robot that actually delivers useful data has proven so difficult. In the course of reviewing the rationale for robotic deployment of NDI equipment for aircraft inspection and describing the major research efforts to date, it elucidates how universal issues in teleoperation and automation are manifest specifically in the aircraft inspection environment. In describing the five major and several minor efforts, CMU's contributions of necessity emphasized, as they are best known to the author personally, and also most thoroughly documented in print; however it is my goal to be as comprehensive as openly available knowledge permits. The paper concludes by outlining a path to a comprehensive, economical, and culturally acceptable system for remote automation-assisted deployment of NDI and enhanced visual inspection equipment.

---

\* This is an updated version of my paper of the same title presented at the First Joint DoD/FAA/NASA Conference on Aging Aircraft, 1997 July 08-10, Ogden UT.

## **2. WHY USE ROBOTS FOR AIRCRAFT INSPECTION?**

Numerous hypothesized advantages of computer controlled mobile remote deployment platforms (for short, "robots") for aircraft inspection instruments and remote cameras for visual inspection have been expounded at length elsewhere, so here I will mention, briefly, only the arguments my personal experience has led me to believe are most realistic and realizable. The key arguments relate to *thoroughness*, *correctness*, and *recordability*. Some early arguments that I and others offered, particularly those relating to allegedly increased bodily safety of the inspectors and other advantages of "getting the man off the airplane," I have come to think are less important as the likely deployment scenario (primarily during heavy maintenance) and the personalities of the inspectors (they enjoy being on the airplanes) have been clarified by probing discussions and actual field experience.

### **2.1. THOROUGHNESS**

The robot will cover the programmed inspection path or area completely, with a uniformly high level of concentration, and it will remember the result faultlessly.

### **2.2. CORRECTNESS**

The robot will deploy the correctly set up inspection instrument using exactly the programmed deployment protocol.

### **2.3. RECORDABILITY**

The robot will faultlessly see and remember the outcome of every observation. Thus the correct data will always be available for interpretation (by computer software or by human experts), the location on the airplane where the data were obtained will always be known exactly (enabling advanced "C-scan" image-accumulation-and-display whatever the sensor), and precise trend analysis over arbitrary time periods will be possible (enabling better understanding of the development and evolution of problems, and allowing the operator and the regulatory authorities to choose statistically appropriate inspection intervals).\*

## **3. DESIGN SCENARIOS FOR ROBOTS FOR AIRCRAFT INSPECTION**

### **3.1. THREE BASIC DESIGNS**

Imagining systems that could bring the advantages of robots and automation technology to the field of aircraft inspection, especially skin inspection, leads to three scenarios to which I attach the pictorial labels "*car wash*," "*cherry picker*," and "*skin crawler*."

The *car wash* scenario imagines a central facility dedicated to inspection: aircraft are flown in specifically for inspection "with a fine tooth comb." In this scenario inspection can be carried out without interference from operations, maintenance, or anything else. Under these ideal circumstances, the technically most excellent job can probably be accomplished by a *gantry robot* arrangement, like a huge automatic car wash, from which extremely precise deployment of a variety of inspection devices can be carried out unhurriedly and thoroughly. The conflict that this scenario presents for economical operation in the civilian sector (and perhaps for mission readiness in the military sector) probably makes it impractical despite its technical superiority over all alternatives.

The *cherry picker*, in contrast to the car wash, imagines bringing the inspection apparatus to the airplane rather than the reverse. In this scenario a vehicle-mounted cherry picker, of the sort used for a variety of operations in typical maintenance and inspection hangars, is used to deploy inspection devices in much the same manner as in the car wash scenario: in both, mobility and manipulation use separate mechanisms and operate at substantially different scales. In the big picture, the *cherry picker* is much less disruptive of normal operations than is the *car wash*. However discussions with responsible individuals in the civilian sector uncover substantial objections to this method. Objections are primarily on two

---

\* It will of course not escape the estute reader that the legal departments of commercial airlines may not regard recordability and recording as desirable features; in the military aviation sector, however, they are usually regarded positively.

grounds, first the fear that an automatically or teleoperated cherry picker will collide with and damage the aircraft under inspection, and second the complaint that the floor space around an airplane undergoing heavy maintenance and inspection is too busy and too cluttered to tolerate the routine intrusion of a cherry picker. I don't yet know whether the same objections exist, or exist as strongly, in the military sector.

Given the substantial operational and economic objections to the car wash and the cherry picker, we are left with only the *skin crawler*: a small self-mobile device that adheres to the aircraft skin and maneuvers under some mix of teleoperation and autonomous control to carry out a sequence of inspections at a sequence of locations. In this scenario the line between mobility and manipulation may be fuzzy, as some actuators may be used both to move the vehicle and to scan the sensors. From the operational perspective a small skin crawler, particularly one without a tethering umbilicus, is ideal: an inspector affixes it, at shoulder height, to the airplane at any convenient ground location, it crawls wherever it needs to go and does whatever it needs to do, then it returns to the original or another ground accessible place where the inspector removes it. Everyone likes this idea. The problem is that building a crawler that will be practical in the aircraft inspection environment is easier said than done!

### **3.2. WHY SKIN CRAWLERS ARE HARD, AND THE CONSEQUENCES**

It is not easy to make a skin crawler because a crawler needs to adhere to the airplane, and the only practical way to make it both adherent and mobile is to use suction cups. Although passive suction cups are a possibility, operational and safety considerations demand active suction cups, i.e., suction cups that depend on a vacuum supply. Elementary analysis shows that the power required to obtain the necessary vacuum pumping speeds for a reasonable operating time exceeds what is available from any practical on-board energy storage system. So the only alternative is an umbilicus carrying a vacuum hose or, better, an air hose that can generate vacuum on board via venturi-effect "ejectors". The problem is that the umbilicus gets in the way of the easy mobility contemplated in the previous paragraph. Even worse, managing the umbilicus becomes a frustrating, expensive, often simply intractable problem: the umbilicus literally becomes the tail that wags the dog.

As a consequence I can say with reasonable confidence that no group anywhere in the world has succeeded in building a generally mobile skin crawling robot for aircraft inspection that has actually delivered useful inspection data: all the effort has gone into the mobility, leaving no time or resources for developing a useful inspection capability. The efforts that I know about, which I believe are all that have occurred, are summarized in Section 4.

### **3.3. AN INTERIM WAY OUT**

In particular, recognizing the difficulty of the general mobility-with-umbilicus problem, yet wanting desperately to demonstrate the value of remote inspection technology (in part as a rationale for continuing to work on the mobility problem), my group recently built a robot of limited mobility, restricted to the crown of a DC-9 or 737 (or larger) aircraft, minimizing the mobility problem so we could concentrate on the inspection problem. The project and results, yielding a robot called CIMP, the Crown Inspection Mobile Robot, are reported in Section 4.5.

## **4. A ZOO LOAD OF CRAWLERS**

### **4.1. ROSTAM I THROUGH IV: WICHITA STATE UNIVERSITY**

Benham Bahr and his students at Wichita State University, Wichita KS may have been the first to describe a family of robots specifically conceived to carry NDI sensors and video cameras for aircraft skin inspection. With FAA support (Prof. Bahr spent several summers at the FAA Technical Center in Atlantic City coordinating aspects of the Aging Aircraft Research program), they built the series of wall climbing robots ROSTAM I through IV. Aircraft inspection was addressed as first among many possible applications for a generic suction-cup-based crawler.

The series is notable for a design that uses one very large diameter suction cup on its “belly” and a smaller suction cup on each “leg” (or “arm”). ROSTAM III<sup>2</sup> is shown on a section of aircraft material (apparently wing) in Fig. 1. Many theoretical aspects of the ROSTAM series design (suction cups,<sup>3</sup> safety issues,<sup>2</sup> sensory guidance)<sup>4</sup> and their hypothetical inspection capability (automated crack monitoring using a vision system)<sup>5</sup> have been reported

in the technical conference and scholarly archival literature; however it does not appear that any verifiably practically useful inspection data were ever delivered in field tests of any of the series.

In support of the ANDI program at CMU (Section 4.2), Prof. Bahr also conducted analyses of the requirements and optimal designs of suction cups for aircraft inspection crawlers.

#### 4.2. ANDI: CARNEGIE MELLON UNIVERSITY

The FAA Aging Aircraft Research program sponsored the design, construction, and testing of the Automated NonDestructive Inspector (ANDI) at Carnegie Mellon University, Pittsburgh PA, in a joint project of the Carnegie Mellon Research Institute (CMRI), the university’s applied research arm, and my lab, the Intelligent Sensors, Measurement, and Control Lab, in the Robotics Institute of the School of Computer Science. ANDI’s design was dictated by the FAA’s state of mind and by the state of NDI technology around 1990, when the project was defined and begun. The state of mind at the time, still dominated by the Aloha incident of 1988, was that large scale eddy current “fishing expeditions” are a desirable way to head off future Alohas, and that large scale instrumented inspection could be made palatable to commercial airline operators if there were an economically acceptable automated device to deploy the sensors. The state of technology for eddy current sensors at the time was mainly manually manipulated point probes and complex impedance plane displays of their signals. These circumstances led to a design that maneuvers most gracefully along long fore-aft lines of rivets, maintaining precision alignment with them so that an eddy current pencil probe scanned parallel to the line of motion would follow the desired scanning path with little or no need for additional closed loop path control.<sup>7</sup>

The design developed for this scenario is drawn in Fig. 2; below the drawing is a photograph of the near-final ANDI on a DC-9 nose section at the Aging Aircraft Nondestructive Testing Center (AANC, Sandia National Laboratories, Albuquerque NM). This design, a form of what is known in the robotics literature as a “beam walker,” achieves mobility by suitable motions of the bridges (arms) relative to the spine as the suction cup groups on the spine and the bridges are alternately affixed and released. The eddy current probe is scanned by one of the bridges moving along the spine while the spine’s suction cups are affixed to the aircraft skin. ANDI is equipped with four cameras for navigation and alignment: one each fore and aft to align the spine with the rivet line, one adjacent to the eddy current probe to verify location and alignment, and one high mounted with a wide angle field of view for navigation, obstacle avoidance, and proprioception (“self awareness”). In contrast to CIMP, the second CMU aircraft inspection robot (Section 4.5), whose capability is focused on enhanced remote visual inspection, ANDI’s cameras were not intended to have sufficient resolution to be useful for visual inspection per se.

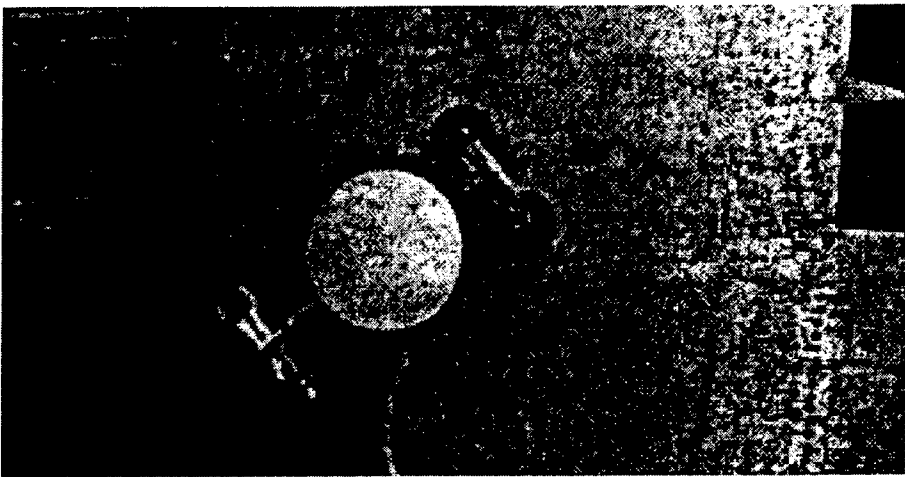


Fig. 1: ROSTAM III on a section of aircraft material.

Despite essential successes in mobility (getting where it needed to be), automatic alignment (using a machine vision rivet line finding algorithm), manipulation (moving the eddy current probe smoothly along the desired path), and measurement (collecting and delivering eddy current sensor data to the ground), as well as the articulation of a comprehensive system architecture for integrating robotics and automation into aircraft maintenance and inspection, unforeseeable changes in the context for ANDI led to its early marginalization.

First among these factors was a de facto return to the model that visual inspection should be the lion's share of skin inspection, with eddy current and other NDI technologies being used for backup, confirmation, and a relatively small number of directed inspections for specific flaws at specific problematic locations. A robot designed for large area eddy current inspection along rivet lines would have a hard time being economically competitive in an environment that views eddy current as a confirming technology for suspected visual flaws and as a survey technology only for a few specific fuselage locations, e.g., locations known from structural models or past experience to present specific cracking or corrosion patterns.

Simply stated, at least in the civilian sector, there is no economic interest in a robot that does the 10% of inspections that are instrumented; to make an impact with the commercial airline operators, a robotic inspection system will have to do the visual inspections that account for 90% of the inspection effort.

Another development that weighs substantially against the viability of ANDI is the recent advance in sensors and display systems for C-scan rendering of eddy current data. We now have linear and area arrays (or their equivalent in, e.g., MOI), and inspectors now expect to see false-color images rather than oscilloscope traces, making ANDI's mechanical optimization for point probes somewhat pointless.

#### **4.3. AUTO CRAWLER: AUTO CRAWLER LLC**

Henry R. Seemann's Seattle WA based company AutoCrawler LLC, with support from Boeing, has developed a tank-like multi-suction-cup-tracked vehicle, AutoCrawler, with a clever valving arrangement that applies vacuum only to those suction cups that are actually in contact with the surface (Fig. 3). AutoCrawler is a behemoth of a mobile platform, capable of carrying enormous loads at very high speeds thanks to its powerful air motors and high capacity vacuum ejectors. On the other hand, it demands an enormous air compressor, and it makes a hell of a racket. Although suction cups of optimized material and shape have been custom designed and manufactured for the application, aluminum surface scuffing is still very evident in the AutoCrawler's wake. Boeing's experimental area array eddy current sensor and the PRI Magneto-Optic Imager have been carried by AutoCrawler on a 737 fuselage section with known defects, and images from the Boeing sensor have been exhibited in AutoCrawler's sales literature. Based on our experience (Section 4.2) with ANDI's eddy current sensor's tendency to "chatter" if not scanned

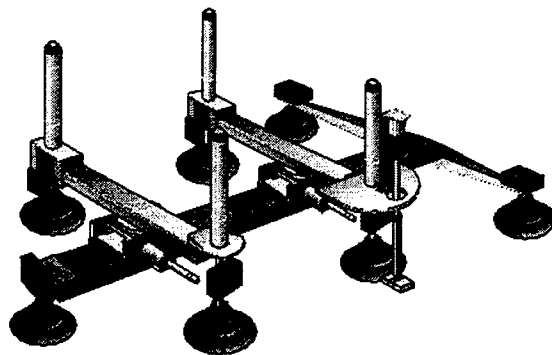


Fig. 2: (above) ANDI as a design drawing, and (below) photographed on the nose section of a DC-9. In the drawing, the eddy current sensor is seen on the near end of the far bridge (arm). In the photo the small black box (on an outrigger on the far side) contains one of the two alignment cameras (see text for camera arrangement).

with a sufficiently firm but light touch, it seems likely that a point sensor deployed by AutoCrawler would suffer from this problem in spades; however, as the described demonstrations confirm, AutoCrawler's mechanics are well suited to area-type sensors, as they do not require precise placement and scanning. The AutoCrawler has not been reported in the technical conference or archival scholarly literature; however some early work toward a window washing robot, in which project Mr. Seemann participated, is reported in the trade magazine *Robotics Engineering*.<sup>17</sup>

Mr. Seemann reports in a personal communication that he is currently investigating an Air Force NDI application on a contract routed through the University of Dayton Research Institute.<sup>16</sup>

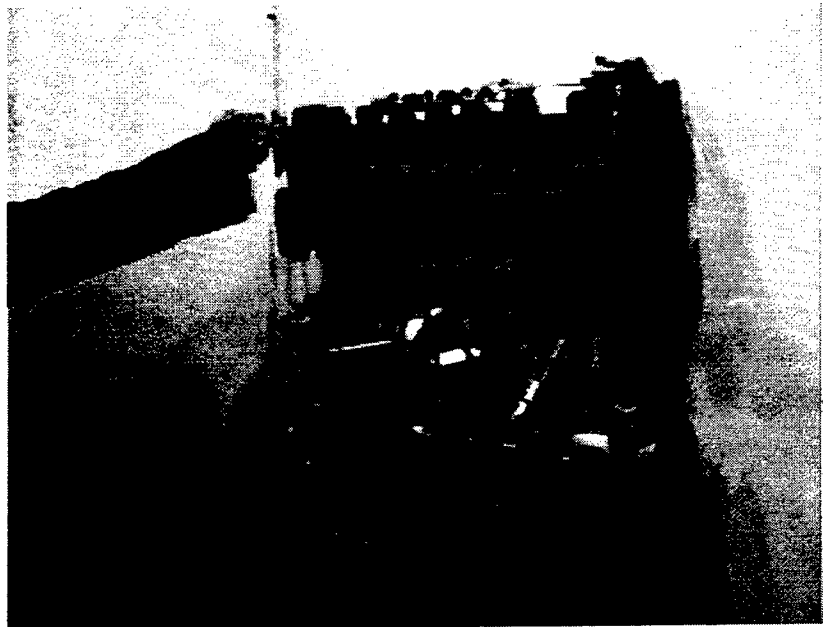


Fig. 3: AutoCrawler on the side of an airplane. The hand is about to install, on the "periscope" at the center of the AutoCrawler, a retroreflector that is part of the laser tracking system used for locating the robot absolutely relative to the hangar floor.

#### 4.4. MACS I THROUGH III: NASA JPL

The Air Force Robotics and Automation Center of Excellence (RACE)<sup>13</sup> at Kelly Air Force Base, San Antonio TX, funded a group led by Paul Backes at NASA's JPL, Pasadena CA, to develop a series of mobile platforms, Multifunction Automated Crawling System (MACS) I through III. Leveraging NASA's efforts in developing miniature planetary rovers, telerobotic devices, and NDE technology, the MACS team has applied the years of experience and cutting-edge innovative ideas of its members, with their state-of-the-art expertise in robotics (Backes), NDI (Bar-Cohen), mechanical design (Joffe), and ultrasonic motors (Lih), supported by NASA's highly trained technicians' unique hands-on skills in fabrication, electronics, and assembly (Barlow, Proniewicz), to developing this family of small, light weight, high carrying capacity ratio mobile platforms that use suction cups for attachment and ultrasonic motors for motion.

The MACS family walking paradigm of alternate attachment and detachment of half the suction cups<sup>12</sup> is essentially the same as ANDI's (Section 4.2). The group reports that in the future a descendant of the MACS I through III series with increased on-board intelligence, tetherless operation, operation over the internet, and integration of multiple sensor payloads might be able to carry NDI sensors, e.g., new miniature cameras, tap testers, eddy current sensors, ultrasonic sensors, etc., on an aircraft surface.<sup>11</sup> Fig. 4 shows MACS in the lab and on a C5 airplane. Inasmuch as Kelly Air Force Base is being shut down as part of the Base Realignment and Closing (BRAC) program, RACE's civilian leader Scott Petroski has

taken a new assignment, and RACE is now slated for shutdown rather than relocation, the future of the MACS program seems uncertain.

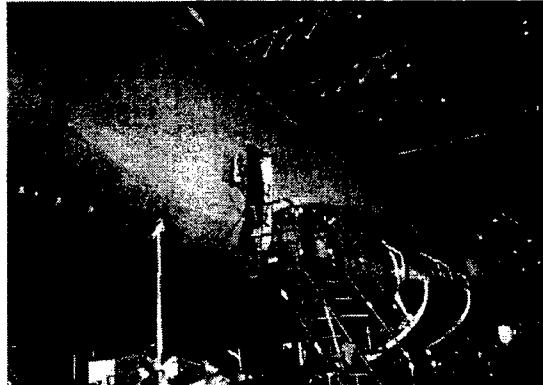
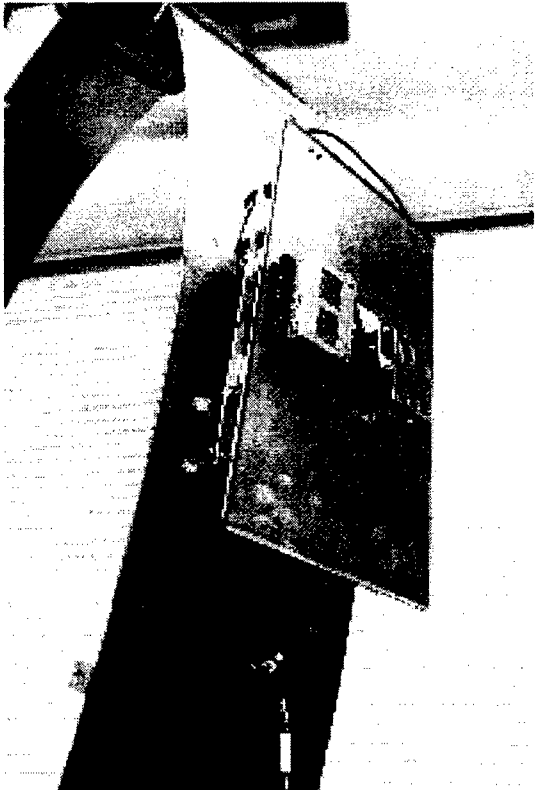


Fig. 4: MACS on a piece of sheet metal in the lab (left) and on a C5 airplane (above, at shoulder height, slightly to the left of the doorway).

#### 4.5. CIMP: CARNEGIE MELLON UNIVERSITY

CIMP, built in my laboratory (see Section 4.2) with support from the Ben Franklin Technology Center of Western Pennsylvania and my lab's spin-off company Aircraft Diagnostics Corporation, is an aircraft inspection robot that is explicitly *not* a "wall crawler." Chastised by the two lessons of ANDI (*if you spend all your time working on the robot's mobility you'll never get any inspection data and if you can't do visual inspection nobody will be interested in your robot*), we set out to demonstrate that a robot could generate data, first and foremost video data whose quality inspectors would gladly accept for routine visual inspection, and to deliver the data to an "inspector's workstation" off the airplane. To allow us to concentrate on inspection data and not inspection equipment transportation, we designed an interim robot whose mobility is limited to the fuselage crown: CIMP, the Crown Inspection Mobile Platform.

Because CIMP works with gravity instead of against it, it does not need a tether. It was designed for the curvature of a DC-9, and for window-line to window-line on mobility on that aircraft type; however it turned out to be more convenient to test the prototype on a 747, on which it ran with no difficulty despite having the "wrong" curvature.

Because its power requirements are tiny compared to a robot that has to adhere to the fuselage in arbitrary orientations, CIMP does not need an umbilicus. It runs for several hours on its internal batteries; exactly how long depends on the variable demands of mobility, manipulation, illumination, etc. Control signals are transmitted to CIMP wirelessly using off-the-shelf model airplane transmitter technology. Video data are returned wirelessly using micropower radiofrequency channels; in the prototype these are off-the-shelf 2.4 GHz cable eliminators sold in the consumer market to connect a home VCR and TV set without

dragging a wire under the rug. In a commercial version of CIMP somewhat more sophisticated (and costly) channel options would be appropriate to avoid signal degradation due to multipath effects.



Fig. 5: CIMP on a 747 in a heavy maintenance bay at Northwest Airlines Minneapolis headquarters. The inspector, observed by a CMU staffer, is performing an eddy current check of a visual anomaly detected using the remote vision system shown in Fig. 7. Future models would incorporate remotely operated eddy current sensing.

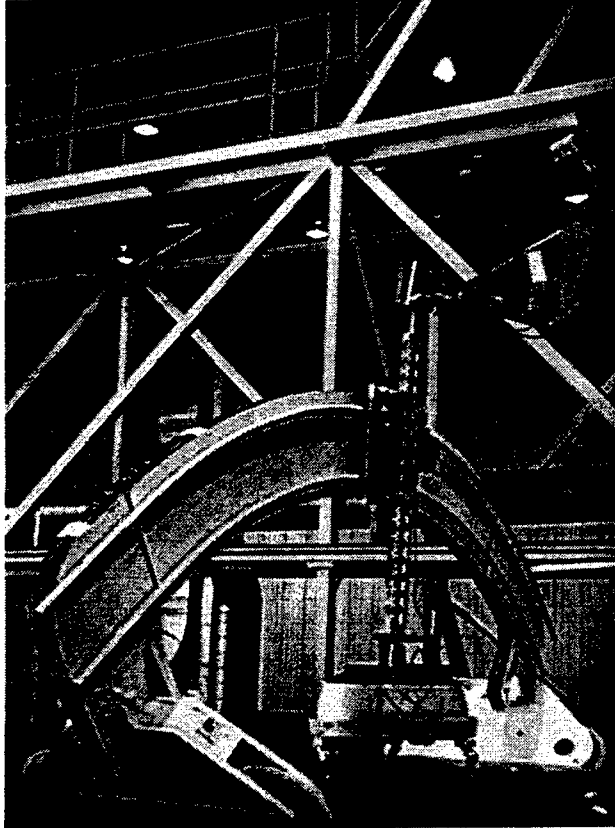


Fig. 6: CIMP showing mobility (differentially driven wheels), sensor pod mounted off circumference-scanning carriage, and wide angle cameras for navigation and proprioception or "self-awareness" (upper right). The vertical stalk and the sensor pod rotate to change the camera viewing azimuth. Curvature was designed for window-line to window-line access on a DC9.

Watching how visual inspectors work, we concluded that they use binocular disparity (the small differences between left and right eye perspectives) in several important ways. First, binocular disparity is the primary origin of stereopsis, the human perception of depth via the fusion of slightly different left and right eye images; depth perception is important for perceiving the difference between dents and lighting anomalies, bulges and depressions, etc. Second, aircraft inspectors routinely use dynamic lighting and grazing angles of observation to discern subtle textural anomalies even on essentially flat surfaces; these they apparently discriminate via the strong binocular disparity that originates in specular (vs. diffuse) reflection features. Thus we decided to provide CIMP with a 3D-stereoscopic video system that gives the inspectors remote *binocular* inspection capability.

Fig. 5 shows a distant shot of CIMP on a 747 at Northwest Airlines heavy maintenance facility in Minneapolis MN. Fig. 6 shows a comprehensive view of CIMP, and Fig. 7 shows a close-up of the sensor pod, which contains the 3D-stereoscopic cameras and remotely controlled dynamic lighting, and

potentially a variety of other sensors, e.g., eddy current probes. Fig. 8 shows a Northwest Airlines inspector at the workstation, operating the remote controller and observing the 3D-stereoscopic imagery.

Fig. 8 shows several examples of the imagery returned by the inspection cameras; these pictures have been through several stages of subsampling prior to recording, 8mm taping, digitizing, and MPEG-type data compression, so their quality is not indicative of what the inspector sees live; the live view actually gives each eye an independent NTSC/VGA resolution signal stream with very high perceived quality.

CIMP has been successfully operated on a 747 at Northwest (as shown in the accompanying figures) and on a DC-9 at US Airlines. Working aircraft inspectors have been uniformly enthusiastic about the quality and utility of the imagery that the CIMP remote 3D-stereoscopic video system delivers. However many are skeptical about the economic benefits that might reasonably be expected from robotic deployment of inspection equipment. Some also question whether the introduction of robotic deployment equipment would enhance their job satisfaction; despite our best intentions to make the inspector's job easier, safer, etc., by "getting the man off the airplane," sometimes we find that the man likes his job because he likes being on the airplane.

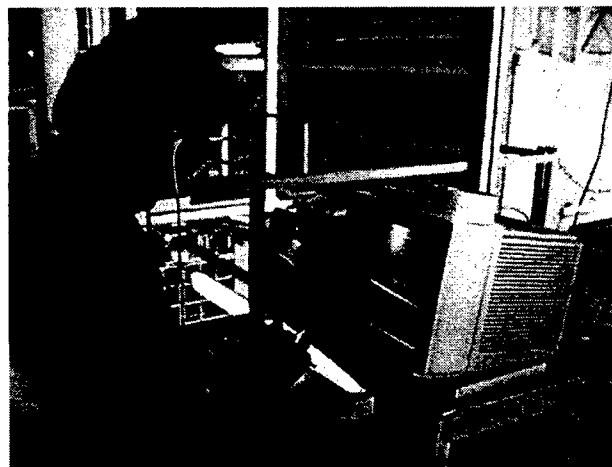
Somewhat to our surprise, the inspectors have been enthusiastic about the idea of using computer image enhancement and automated image understanding for flaw detection. We have made significant progress in these areas, reported in references.<sup>8, 9, 10</sup>

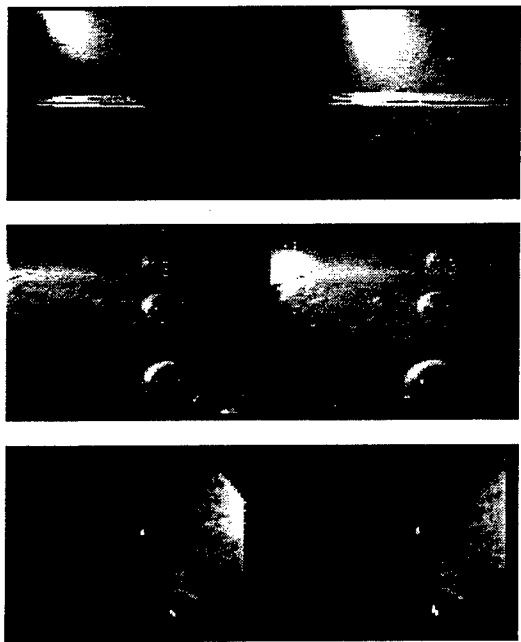


Fig. 6: Sensor pod, showing 3D-stereoscopic camera (white box with black endcap left of and below center) and remotely movable low angle illuminator.

Inspector can remotely swing this illuminator in a 300 degree arc centered on the forward viewing direction of the camera, reproducing the way he typically uses his flashlight to pick up highlights. The flood illuminator is not visible in this view.

Fig. 7: Inspector at the prototype workstation. Small monitor at left shows one eye's view. Large monitor in front of inspector shows left and right eye views 3D-stereoscopically when viewed through the goggles seen. Inspector is driving robot, controlling lighting, cameras, etc, via the model radio controller joysticks, switches, and control knobs.





**Fig. 8:** Three left and right eye 3D-stereoscopic views from the 4.5x 3D-stereoscopic camera in the sensor pod. Top is a lap joint, middle is a row of buttonhead rivets, bottom is a sheet metal sample from a “defect library.” Note, in addition to the perspective differences between the two views (which stimulates depth perception), the distinct differences in specular reflections (which we believe stimulates texture recognition).

#### 4.6. OTHER “WALL CLIMBING” ROBOTS

The Wichita State, Carnegie Mellon, Autocrawler, and JPL robots described above are all specifically targeted at aircraft skin inspection applications. Many other “wall climbing” systems developers mention aircraft inspection as possible applications for robots developed for other applications, or robots developed with an unfocused approach to wall climbing as a generic set of applications. Several of these, and a survey of them, are described briefly in this section.

##### 4.6.1. ROBIN: VANDERBILT UNIVERSITY

Robert T. Pack et al in the Electrical Engineering Department at Vanderbilt University describe ROBIN, their ROBotic INspector.<sup>18</sup> It is essentially two rods connected by a hinge, with suction cups at the two free ends, and pneumatic actuators for walking, similar to earlier “walking-elbow” designs for space station maintenance robots,<sup>19</sup> etc. Echoing the underlying theme of the present paper, the ROBIN’s inventors say “it is intended to carry cameras and other sensors onto man-made structures such as bridges, buildings, aircraft and ships for inspection ... cameras on its back and other contact sensors, like eddy current probes on its feet, but current development focuses on improving the climbing vehicle itself.”

##### 4.6.2. TEXAS RESEARCH INSTITUTE / AUSTIN

Texas Research Institute / Austin, operator of the Nondestructive Testing Information Analysis Center (NTIAC), reports that among the products it has developed in sponsored R&D efforts for government and commercial applications there is a “rubber-to-metal debond robotic inspection system”<sup>20</sup> that sounds like it might be of interest in the aircraft skin inspection world. However at the time of this writing no further information was available.

##### 4.6.3. SURVEY: MCGILL UNIVERSITY

A tabular “Survey of Climbing Robots,” with annotated photos of some of the included robots, is available on the WWW at McGill University.<sup>21</sup> Note that many of these use magnets to attach to the surfaces of, e.g., steel liquid storage tanks, making them generally uninteresting for aircraft inspection.

## 5. LESSONS, CONCLUSIONS, AND THE FUTURE

After the Aloha "incident" of 1988 several research groups embarked confidently on paths toward mobile robotic platforms and computer-based automatic control systems for deployment of NDI and visual inspection equipment on aircraft surfaces. The ambitious plans included agile vehicles, sophisticated deployment of sophisticated sensors, a high level of intelligent, sensible autonomy in task and path planning, navigation, and inspection, elegant and functional human-computer interfaces, hierarchical data and information displays matched to the needs of inspectors, supervisors, and management, totally automated networked integration of inspection with maintenance, engineering, operations, and management databases, and the emergence of a safer and more economical inspection and maintenance system based on massive analysis of massive quantities of data that would permit just-in-time, but never earlier than necessary, predictive response to developing repair requirements. At the time of this writing, in mid-1997, there is still no working system that comes anywhere near these early expectations; there is not yet even a demonstration of a robot that is both agile (able to go 'anywhere' on the aircraft's skin) and functional (able to deliver data that inspectors want). Furthermore there is a sense of diminished confidence that there will be any such system any time soon.

On the positive side, in fact all four key modules needed by a useful robotic inspection system -- measurement, manipulation, mobility, and monitoring -- have been separately demonstrated. It has been hard to tie the modules together in a fully functional system in large part because the generic hard problems that must be faced in designing and building an aircraft skin mobility module -- adhering to arbitrarily curved and oriented surface regions, moving gracefully over lapjoints and buttonhead rivets, managing a safety tether and an energy-lifeline umbilicus -- have disproportionately diverted attention from the other three key modules.

However the diversion has actually paid off: we now have multiple examples of mobile platforms matched to various operational scenarios: ANDI for precision deployment of traditional point probe sensor types, AutoCrawler for manhandling large area survey instruments, and MACS for the anticipated next generation of light weight sensors, among others.

In my lab we set out with CIMP to demonstrate a complete system via the expedient of temporarily sidestepping the general mobility problem: we built only a simple (though wireless!) platform whose mobility is restricted to the fuselage crown. Thus we were able to concentrate the extremely limited resources that were available to us for this project on demonstrating the single most important capability of a robotic inspection system: its ability to deliver useful inspection data to the ground. We succeeded in delivering inspection-quality visual data to an inspector who was remotely driving the robot from a rudimentary but acceptable workstation. The mobility and manipulation components were comprehensive enough that the inspector could scan along a useful path, stop at a possible flaw, and inspect more closely by varying the camera's viewing angle and the character of the illumination (flood or spot), and the direction of spot illumination. In the lab, we have also made substantial progress toward useful image enhancement and automated image understanding algorithms for visually detectable flaws.

These successes are, at least to me, clear demonstrations that we are ready to respond to a well defined real-world application demand with a technically and economically justified system.

## 6. ACKNOWLEDGEMENTS

The cooperation of the commercial airline operators, especially US Airways and Northwest Airlines, has been essential to this work. The administrative support of Russell Jones and Roy Weatherbee of US Airways and Jeff Register of Northwest has been invaluable. The inspectors in both their organizations have been extremely hospitable and open, and remarkably tolerant of our incessant silly questions and wild ideas. The ANDI project was supported by the FAA Aging Aircraft Research program. The CIMP project was supported by the Ben Franklin Technology Center of Western Pennsylvania and Aircraft Diagnostics Corporation. The staff of the ANDI project at CMRI included Bill Kaufman, Chris Alberts, Chris Carroll, the late Court Wolfe, and many others; Alan Guisewite and graduate student Ian Davis

helped on the Robotics Institute side. The staff of the CIMP project at the Robotics Institute included Gregg Podnar, Alan Guisewite, and graduate students Priyan Gunatilake and Huadong Wu.

## 7. REFERENCES

1. Bahr, B., "Automated Inspection for Aging Aircraft", International Workshop on Inspection and Evaluation of Aging Aircraft, May 18-21, 1992, Albuquerque, NM, sponsored by the Federal Aviation Administration, hosted by Sandia National Laboratories.
2. Bahr, B., F. Wu, "Design and safety analysis of a portable climbing robot", International Journal of Robotics and Automation, v. 9 #4, 1994, pp 160-166.
3. Bahr, B., Y. Li, M. Najafi, "Design and Suction Cup Analysis of a Climbing Robot", Journal of Computers and Electrical Engineering, v. 22 #3 (1996), pp 193-209.
4. Bahr, B., T. J. Huang, K. F. Ehmann, "Sensory Guidance for Seam Tracking Robot", Journal of Robotics Systems, v. 11 #1 (1994), pp 67-76.
5. Bahr, B., S. Motavalli, "Automated Crack Monitoring System Using Vision System", Second IE Research Conference, Los Angeles, May 26-27, 1993.
6. Siegel, M. W., W. M. Kaufman, C. J. Alberts, "Mobile robots for difficult measurements in difficult environments: Application to aging aircraft inspection", Robotics and Autonomous Systems 11 (1993) 187-194 (Elsevier).
7. Wolfe, C., M. W. Siegel, C. J. Alberts, "Robot with Cruciform Geometry", Patent US5429009, July 4, 1995.
8. Gunatilake, P., M. W. Siegel, A. G. Jordan, G. W. Podnar, "Image Enhancement and Understanding for Remote Visual Inspection of Aircraft Surfaces", SPIE Conference on Nondestructive Evaluation Techniques for Aging Infrastructure and Manufacturing, 3-5 December 1996, Scottsdale, Arizona, session on NDE of Aging Aircraft, Airports, and Aerospace Hardware.
9. Gunatilake, P., M. W. Siegel, A. G. Jordan, G. W. Podnar,, "Image understanding algorithms for remote visual inspection of aircraft surfaces", Proceedings of the SPIE Conference on Machine Vision Applications in Industrial Inspection V, San Jose, February 1997, SPIE v. 3029, pp 2-13.
10. Siegel, M. W., P. Gunatilake, "Remote Inspection Technologies of Aircraft Skin Inspection", Proceedings of the 1997 IEEE Workshop on Emergent Technologies and Virtual Systems for Instrumentation and Measurement, Niagara Falls, CANADA, pp 79-78.
11. Backes, P. G., Jet Propulsion Laboratory (JPL), California Institute of Technology, Pasadena, CA 91109. Personal communication. See <http://robotics.jpl.nasa.gov/tasks/macs/homepage.html>.
12. Backes, P. G., Y. Bar-Cohen, B. Joffe, "The Multifunction Automated Crawling System (MACS)", Proceedings of the 1997 IEEE International Conference on Robotics and Automation, Albuquerque NM, April 1997, pp 335-340.
13. See <http://www.kellyafb.org/links/orgs/race/race.htm>.
14. Seemann, H. R., AutoCrawler Corporation, Seattle, WA. Personal communication and corporate sales literature, videos, etc. Mr. Seemann, CEO and President of AutoCrawler Inc., can be found at 206-367-8163, FAX 206-440-8893, email H579@aol.com.
15. Lim, S. Y., Gintic Institute of Manufacturing Technology, Nanyang Technological University, Singapore 638075. Personal communication. See <http://www.gintic.ntu.ac.sg:8000>.
16. University of Dayton Research Institute, <http://www.udri.udayton.edu/general.htm>.
17. I. R. Technologies, "Product feature: the Skywasher", Robotics Engineering Magazine, December 1986.
18. Pack, R. T., J. L. Christopher, Jr., K. Kawamura, "A Rubbertuator-Based Structure-Climbing Inspection Robot", Proceedings of the 1997 IEEE International Conference on Robotics and Automation, Albuquerque, New Mexico, April 1997, pp 1869-1874.
19. Brown, Jr., H. B., M. B. Friedman, T. Kanade, "Development of a 5-DOF Walking Robot for Space Station Application: Overview", Proceedings of the International Conference on Systems Engineering, IEEE, Pittsburgh PA, August 1990.
20. Texas Research Institute / Austin, <http://www.texasresearchintl.com/express/austin/avindx3x.html>.
21. "Survey of Climbing Robots", [http://www.cim.mcgill.ca/~arlweb/ACROBAT/climbing\\_rob.html](http://www.cim.mcgill.ca/~arlweb/ACROBAT/climbing_rob.html).

# **Computational geometry and artificial neural networks: a hybrid approach to optimal sensor placement for aerospace NDE**

Roberto Osegueda, Carlos Ferregut, Mary J. George,  
Jose M. Gutierrez, and Vladik Kreinovich<sup>1</sup>

FAST Center for Structural Integrity of Aerospace Systems  
University of Texas at El Paso  
El Paso, TX 79968, USA

## **ABSTRACT**

The ideal design of an airplane should include built-in sensors that are pre-blended in the perfect aerodynamic shape. Each built-in sensor is expensive to blend in and requires continuous maintenance and data processing, so we would like to use as few sensors as possible. The ideal formulation of the corresponding optimization problem is, e.g., to minimize the average detection error for fault locations. However, there are two obstacles to this ideal formulation:

- First, this ideal formulation requires that we know the probabilities of different fault locations etc., and there are usually not enough statistics to determine these probabilities.
- Second, even for a known distribution, finding the best locations is a very difficult computational problem.

To solve these problems, *geometric symmetries* are used; these symmetries enable to choose several possible sets of sensor locations; the best location is then found by using a *neural network* to test all these (few) selected locations.

**Keywords:** Non-destructive evaluation, aerospace structures, aging aircraft, futuristic aircraft, neural networks, symmetry groups, geometry.

## **1. Introduction**

### **1.1. Checking structural integrity of aerospace systems is very important**

Structural integrity is extremely important for airplanes, because in flight, the airframe is subjected to such stressful conditions that even a relatively small crack can be disastrous.

This problem becomes more and more important as the aircraft fleet ages.

At present, most airplanes do not have built-in sensors for structural integrity, and even those that have do not have a sufficient number of them, so additional sensors must be placed to test the structural integrity of an airframe.

---

<sup>1</sup>E-mail addresses: osegueda@utep.edu, ferregut@utep.edu, mjgeorge@utep.edu, jgutierrez@utep.edu, and vladik@cs.utep.edu.

## **1.2. It is important to test structural integrity in-flight**

Each integrity violation (crack etc.) starts with a small disturbance that is only detectable in stressful in-flight conditions. Therefore, to detect these violations as early as possible, we should complement on-earth testing by in-flight measurements. Hence, we need *sensors* for in-flight tests.

## **1.3. The problem of sensor placement**

Where should we place sensors for in-flight tests?

Most *existing* airplanes do not have built-in sensors for testing structural integrity (or at least do not have a sufficient number of these sensors), so, to test these airplanes, we must place these sensors *outside* the airframe. Sensors attached outside the airframe interfere with the airplane's well-designed aerodynamics; therefore, we should use as few sensors as possible.

This limitation leads to the following problem:

*GIVEN:* the number of sensors that we can locate on a certain surface of an airframe,

*FIND:* the optimal placements of these sensors, i.e., locations that allow us to detect the locations of the faults with the best possible accuracy.

For *future* aircraft, we have a similar problem of sensor placement. The ideal design of a future airplane should include built-in sensors that are pre-blended in the perfect aerodynamic shape. Each built-in sensor is expensive to blend in and requires continuous maintenance and data processing, so again, we would like to use as few sensors as possible.

## **1.4. The problem of optimal sensor placement is difficult, because it requires optimization under uncertainty**

In both cases, the *ideal* formulation of the corresponding optimization problem is to minimize, e.g., the average detection error for fault locations.

However, this ideal formulation requires that we *know* the *probabilities* of different fault locations and the probabilities of different aircraft exploitation regimes. In reality, we do not know these probabilities:

- for a *new* aircraft, we do not have this statistics; and
- for the *aging* aircraft, the statistics gathered from its earlier usage may not be applicable to its current state.

Therefore, instead of a well-defined optimization problem, we face a not so well defined problem of *optimization under uncertainty*.

Since the problem is not well defined, we cannot simply use standard numerical optimization techniques.

## **1.5. To solve the optimal sensor placement problem, we will use intelligent techniques**

Since we cannot use *standard* numerical methods, we will use *intelligent* techniques:

### **1.5.1. First step: Geometric techniques**

The problem of choosing an optimal sensor placement is formulated in *geometric* terms: we need to select *points* (sensor placements) on a *surface* of the given structure.

To solve this problem, we use the experience of solving similar geometric problems of optimization under uncertainty in image processing and image extrapolation<sup>1-3</sup>. Namely, astronomic image processing faces the problem of selecting the best family of images for use in extrapolation. It turns out that for every optimality criterion that satisfies the natural symmetry conditions (crudely speaking, that the relative quality of two image reconstructions should not change if we simply shift or rotate two images), the extrapolation shapes that are optimal with respect to this criterion can be described as orbits of the corresponding Lie transformation groups, which leads to exactly the shapes used in astronomy (such as spirals, planes, spheres, etc).

In this paper, we show that, since the basic surface shapes are symmetric, a similar symmetry-based approach can be applied to the problem of optimal sensor placement. For the simplest surfaces, this general approach describes several geometric patterns that every sensor placement, which is optimal with respect to reasonable (symmetric) optimality criterion, must follow.

Some of our results were announced in<sup>4-5</sup>.

### **1.5.2. Second step: Neural networks**

After we have selected several possible sensor locations, we then use neural networks:

- first, to *confirm* that these placement patterns indeed lead to better fault location, and
- second, to *select* a pattern that leads to the best results for each particular problem.

## **1.6. The results: in brief**

As a result of this analysis, we get several possible optimal sensor placements.

A similar problem of optimal placement of NDE sensors is also important for *space* structures.

## **2. Preliminary analysis: we need the optimal sensor placement**

### **2.1. It is desirable to find the optimal sensor placements**

The quality of NDE essentially depends on the placement of the sensors: e.g., if all the sensors are concentrated in one area, and few are located in the remainder of the structure, then possible cracks and other faults in the under-covered area may go dangerously unnoticed. Therefore, it is important to choose a good sensor placement.

Currently, the choice of sensor placements is mainly made either *ad hoc*, or, at best, by testing a few possible placements and choosing the one that performs the best on a few benchmark examples. There are two drawbacks in this approach:

- In this approach, only a few possible placements are analyzed, so it is quite possible that we miss really good placements.
- Even when the placement that is good “on average” is indeed present among the tested placements, the very fact that we only test these placements on a few examples leads to the possibility that we will choose different placements, that work well for the tested examples, but that are, on average, much worse than the rejected placement.

In other words, often, the normal engineering *good enough* approach does not work for our problem.

It is, therefore, desirable to find the *optimal (best)* sensor placements.

## 2.2. “Optimal” in what sense?

2.2.1. Since we do not know the exact optimality criterion, we will try to describe sensor placements that are the best relative to all possible reasonable optimality criteria

If we knew the exact probabilities of different exploitation regimes and of different faults, then we could formulate the exact optimality criterion and look for the sensor placement that is optimal relative to this criterion. In reality, however, as we have already mentioned in the Introduction, we do not know the exact optimality criterion.

Since we do not know *the exact criterion*, the natural idea is to do the following:

- consider *all possible* optimality criteria that are reasonable for this problem;
- describe all the placements that are optimal relative to each of these criteria;
- and finally, depending on the exact situation, choose the best placement among the “possibly best” ones.

In this manner, we still face the problem of choosing between several possible placements (and we may still make a wrong choice), but we are, at least, guaranteed that we do not initially miss the best placement.

## 2.2.2. This general program sounds ambitious and computationally intractable, but it is actually doable

Even when we know the optimality criterion, finding the optimal sensor placement is extremely computationally difficult and time-consuming. According to the above program, we intend to describe sensor placements that are optimal relative to *all* possible reasonable optimality criteria. Since there are many such criteria, it may seem, at first glance, that we need to repeat the (already time-consuming) computations so many times that the resulting required computation time will make this problem computationally intractable.

Fortunately, we will see that this problem is quite doable: namely, it is possible to describe all possibly optimal placements without actually solving all possible optimization problems, but using *geometric* arguments instead.

Before we start describing and using these arguments, we must describe in precise terms what we mean by a “reasonable” optimality criterion.

## 2.2.3. Optimality criteria can be arbitrarily complicated

Traditionally, the quality of different alternatives is described by a *numerical* optimality criterion, in which the quality of each alternative  $a$  from the set  $A$  of all possible alternatives is characterized by a real number  $J(a)$ , and we choose the alternative  $a$  for which this value  $J(a)$  is the smallest possible (i.e.,  $J(a) \rightarrow \min$ ). For example, for the problem of placing the given number  $n$  of sensors,  $A$  is the set of all possible placements of these sensors, and  $J(a)$  is, e.g., equal to the mean square average detection error of fault location based on the data from these sensors.

Such numerical criteria are useful and often sufficient, but in many cases, we end up with *several* alternatives with the same smallest possible value of the average error  $J(a)$ . In this case, it makes sense to select, among them, an alternative  $a$  for which, e.g., the *worst-case* error  $J'(a)$  is the smallest possible. This very natural idea leads to a non-numerical optimality criterion, according to which *two* different functions  $J(a)$  and  $J'(a)$  are given, and an alternative  $a$  is considered to be *better* than an alternative  $b$  if either  $J(a) < J(b)$ , or  $J(a) = J(b)$  and  $J'(a) < J'(b)$ .

This more complicated criterion can also result in several “best” alternatives, in which case we will be able, simultaneously, to optimize a third characteristic, etc. As a result, we can have arbitrarily complicated non-numerical optimality criteria. Since we want to describe placements that are optimal with respect to *all* possible reasonable criteria, we have to consider all these criteria.

How can we describe them?

#### **2.2.4. A general description of an optimality criterion**

In general, when we say that an optimality criterion is given, this means that for every two alternatives  $a$  and  $b$  from the set  $A$  of all alternatives, one of the following four possibilities holds: either  $a$  is better than  $b$  according to this criterion (we will denote it by  $a < b$ ), or  $b$  is better than  $a$  ( $b < a$ ), or  $a$  and  $b$  are of the same quality (we will denote it by  $a \sim b$ ), or, according to the given criterion, the alternatives  $a$  and  $b$  are incompatible (we will denote this case by  $a \parallel b$ ).

So, we can describe the optimality criterion as a pair of relations  $(<, \sim)$ .

These two relations must satisfy natural consistency conditions, e.g., if  $a$  is better than  $b$  and  $b$  is better than  $c$ , then  $a$  should be better than  $c$ , etc. A pair that satisfies these natural consistency conditions is called a *pre-ordering* relation. In these terms, an optimality criterion is a *pre-ordering relation* on the set of all alternatives.

There is also one additional requirement that we have used before, when we talked about the necessity for complicated optimality criteria: that there should be *exactly one* optimal alternative. Indeed, if there are several alternatives that are equally good according to some criterion, it means that we still need to choose between them; thus, the current optimality criterion is not final. We are interested in *final* criteria, i.e., in pre-ordering relations in which there exists exactly one best alternative.

Now, that we have a general definition of an optimality criterion, we must describe all sensor placements that are optimal relative to these criteria. For this description, as we have mentioned, we will use the geometric techniques.

### **3. Geometric techniques**

#### **3.1. Geometric transformations: a seeming complication**

The idea of using symmetries first appeared not as a method for *solving* the problem, but rather as an additional unexpected complication that made its solution even harder. Namely, we started with simplified toy examples, and tried to use an optimization method to find the optimal placements for these toy problems. Since we were solving an extremely simplified problem, we expected that the optimization algorithm would soon give us a single optimal sensor placement. Instead, for each problem, different applications of the numerical algorithm, applications that started with different randomly chosen initial sensor placements, resulted in drastically different optimal sensor placements.

When we plotted these seemingly different solutions, we saw a simple explanation for this non-uniqueness: these “different” solutions turned out to be approximately one and the same solution, but differently rotated and/or shifted. How can we explain this behavior?

### 3.2. Symmetries of aerospace shapes explain the observed complication

There is a simple geometric explanation for the above-described behavior. This explanation is based on the fact that most surfaces that form an airframe can be described, within a good accuracy, in simple geometric terms.

#### 3.2.1. Basic geometric shapes of aerospace structures and their symmetries

Let us first describe the geometric shapes of basic aerospace structures:

- The airplane cabin can be described as a *cylinder*.
- The surface of the wings can be approximately described as a *plane* (same, for the tail).
- Finally, the plane’s “nose” can be approximately described as either a part of the *sphere* (to be more precise, a half-sphere), or as a piece of a *cone*.

Each of these geometric shapes has certain geometric *symmetries*, i.e., geometric transformations that leave this shape invariant:

- a *cylinder* is invariant with respect to shifts along its axis and rotations around this axis;
- a *plane* is invariant with respect to shifts in the plane, rotations in this plane, and dilations (similarities);
- a *sphere* is invariant with respect to arbitrary rotations around its center;
- finally, a *cone* is invariant with respect to rotations around its axis and dilations centered at its vertex.

#### 3.2.2. For perfectly symmetric shapes, optimal placement is non-unique

Let us first consider the idealized situation in which the shape is *precisely* symmetric (e.g., a perfect sphere, that is invariant with respect to arbitrary rotation  $T$  around its center). Let  $P = \{p_1, \dots, p_n\}$  be a sensor placement for which the optimality criterion (e.g., the average fault location error) is the smallest possible, and let  $T$  be one of the symmetries. Since the shape is invariant with respect to this symmetry, locations  $T(p_1), \dots, T(p_n)$  also belong to this same shape. Since natural optimality criteria are also invariant with respect to these geometric symmetries, the quality of the rotated placement  $T(P) = \{T(p_1), \dots, T(p_n)\}$  is equal to the quality of the original placement and therefore, the rotated placement is also optimal.

Thus, if  $P$  is an optimal placement, then for every symmetry  $T$  of the geometric shape, the placement  $T(P)$  is also optimal. This explains non-uniqueness of optimal sensor placement for *perfectly symmetric* shapes.

#### 3.2.3. For approximately symmetric shapes, optimal placement is also non-unique

Since optimal placement is non-unique for *perfectly symmetric* shapes, it is natural to expect that a similar complication occurs for the shapes that are *close* to the perfectly symmetric shapes (e.g., for a slightly deformed sphere).

### 3.2.4. Optimal sensor placement is non-unique even when for geometric shapes that are only locally symmetric

As we have mentioned earlier in this section, the actual shapes of aerospace structures are indeed close to perfectly symmetric ones, but they are only *locally* close to the perfectly symmetric shapes:

- For example, the shape of a cabin is close to a cylinder. An (infinite) cylinder is invariant with respect to rotations *and* shifts; however, the shape of a cabin is only a *piece* of this infinite cylinder.
- Similarly, a *wing* is only a piece of a plane, a *nose* is only a piece of a sphere or of a cone, etc.

In other words, the actual shapes are not themselves symmetric, they are only locally close to the symmetric shapes. However, for sensors testing structural integrity, local is all we need: the very need for numerous sensors comes from the fact that the effects of each newly appearing small structural fault are so small that they can be only detected by a sufficiently close sensor. So, the interaction of a fault and of a nearby sensor on, e.g., a small piece of a spherical surface depends only on the *local* properties of this surface and practically does not depend on whether this surface is the whole sphere or a piece of it.

Thus, if a surface locally coincides with the symmetric one, the local quality of each sensor placement on this surface coincides with the local quality of their placement on the perfectly symmetric shape, and therefore, the *optimal* placement on the actual surface locally coincides with the optimal sensor placement on the ideal symmetric surface.

Since the optimal placement on an ideal surface is non-unique, the placement on its piece is also non-unique.

### 3.3. Due to non-uniqueness, we have not a single optimal sensor placement, but a family of different optimal sensor placements

We have shown, both experimentally and theoretically, that, due to symmetry of the basic shapes of airframes, optimal sensor placements are non-unique: for every optimal placement  $P$  and for every symmetry  $T$ , the placement  $T(P)$  is also optimal. Therefore, we cannot find a *unique* optimal sensor placement. Instead, we must look for a *family* of optimal sensor placements (that correspond to different symmetries  $T$ ).

### 3.4. So far, symmetries only made our problem more complicated, but symmetries can also help

So far, symmetries only made the optimal sensor placement problem more complicated. However, in general, symmetries are known to help in solving numerical problems.

For example, if we know that a solution  $f(x, y, z)$  of a partial differential equation is invariant with respect to arbitrary rotations around 0, this means that the value of the desired function  $f(x, y, z)$  depend only on a single parameter: distance  $r = \sqrt{x^2 + y^2 + z^2}$  from 0. Therefore, instead of a *partial* differential equation that describes a function of three variables, we have a much easier-to-solve *regular* differential equation that describes an unknown function  $f(r)$  of only one variable.

We will show that a similar simplification happens for the sensor placement problem.

### 3.5. Two-step approach

We start with a 2-dimensional geometric shape, and we want to find a finite number of points on this shape, i.e., in geometric terms, a 0-dimensional shape. Since moving directly from a 2D to 0D sets is complicated, we will do this transition in two, hopefully easier, steps – from 2D to 1D and then from 1D to 0D:

- On the first step, we will find a 1D curve or curves along which the optimal sensor placement will occur.
- Then, on the second step, we will find the optimal sensor placements on the chosen curves.

Let us first describe the first step.

#### 3.6. First step: finding the optimal curve or curves on which sensors will be placed

Let us start with re-formulating our problem in precise mathematical terms.

##### 3.6.1. What is given

We are given a geometric surface  $\alpha$  that has several symmetries.

We can easily describe the set  $G$  of all these symmetries, i.e., in precise terms, the set of all geometric transformations (rotations, shifts, and dilations) that leave this surface invariant. Thus, we can assume that this set  $G$  is given as well.

##### 3.6.2. An important comment about transformation groups

The set of transformations is very important because it is a particular case of a concept that plays a central role in modern theoretical physics: the concept of a *transformation group*.

Namely, it is easy to see that if transformations  $g$  and  $g'$  belong to this set  $G$  (i.e., leave the surface  $\alpha$  invariant), then their composition  $g \circ g'$  and the inverse transformation  $g^{-1}$  also leave the same surface invariant. A set of transformations that satisfies this property is called a *transformation group*.

##### 3.6.3. The objective of the first step: from informal description to precise formulation

The goal of the first step is to find either a single curve or a family of curves that are optimal in some reasonable sense.

To describe this goal formally, we must explain which families of curves we will consider and what we mean by “optimal”. Let us start with *families*.

In general, a *curve* can be described as a mapping that traces this curve, i.e., in more formal terms, a mapping  $\vec{r}$  that maps real numbers  $t$  into points  $\vec{r}(t)$  in 3D space. Correspondingly, a *family* of curves can be described as a family of such mappings characterized by one or several parameters  $C_1, \dots, C_p$ , i.e., in more precise terms, as a mapping that maps tuples  $(C_1, \dots, C_p, t)$  of real numbers into points  $\vec{r}(C_1, \dots, C_p, t)$  of a 3D space. If we fix some values of  $p$  parameters  $C_1, \dots, C_p$ , we get a curve from this family. (For example, the formula  $\vec{r}(t) = (t, C_1 \cdot t + C_2)$  describes the family of all straight lines in a plane except for the lines that are parallel to the  $y$  axis.)

How many parameters do we need in a sensor placement problem? In the simplest possible case of 1-parametric family ( $p = 1$ ), the set of all points from all curves from this family already spans a 2D surface. Thus, we do not need more than one parameter to describe the lines of optimal sensor

placements. So, in the following text, we will consider either single curves, or 1-parametric families of curves.

Now that we formalized the notion of a family, we must describe what “optimal” means. Here, the set of alternatives is the set of all curves (or of all 1-parametric families of curves) on the surface  $\alpha$ . As before, the optimality criterion is a pre-ordering relation on this set for which there exists exactly one optimal curve (or family of curves).

We also want the optimality criterion to be *natural*, which means, in particular, that the relative quality of different placement curves should not change if we apply any transformation  $g$  that leaves the original surface  $\alpha$  invariant. In precise terms, we require that the pre-ordering relation  $\langle <, \sim \rangle$  that describes our optimality criterion satisfy the following two conditions:

- if  $a > b$  and  $g \in G$ , then  $g(a) > g(b)$ ;
- if  $a \sim b$  and  $g \in G$ , then  $g(a) \sim g(b)$ .

A pre-ordering relation that satisfies these two conditions is called *invariant* with respect to the transformation group  $G$ .

So, we get the following precise formulation of the problem that correspond to the first step:

*GIVEN*: a surface  $\alpha$  that is invariant with respect to a group  $G$  of geometric transformations.

*WE KNOW*: that on the set of all 1-parametric families of curves on a surface  $\alpha$ , a pre-ordering relation is given that is invariant with respect to the transformation group  $G$ , and for which exactly one family is optimal.

*FIND*: the optimal 1-parametric family.

### 3.6.4. General solution to this problem

The problem, as formulated above, is a particular case of a *general problem* of finding optimal families of sets as formulated in the papers<sup>1–3</sup>. In these papers, we have actually solved this general problem by describing the *general solution* to it.

To formulate this general solution, we need to introduce two notions: of a *subgroup* and of an *orbit*.

- A *subgroup*  $G_0$  of a transformation group  $G$  is a subset  $G_0 \subseteq G$  that is itself a transformation group.

For example, the set of all rotations around the  $x$ -axis is a subgroup of the group of all rotations.

- To describe an *orbit* of a transformation group  $G$ , we must fix a point  $\vec{r}$ . If we apply all transformation from  $G$  to this point  $\vec{r}$ , then the resulting set  $\{g(\vec{r}) | g \in G\}$  is exactly the orbit.

For example, for the group  $G$  of all rotations around the  $x$ -axis, depending on the choice of the point  $\vec{r}$ , we get either a point (if  $\vec{r}$  is on this axis), or a circle circling around the axis.

In these terms, the above-mentioned solution is as follows: *Every set from the optimal family consists of one or several orbits of subgroups of the original transformation group.*

Thus, to apply this general solution to our problem, we must, for all the geometric shapes enumerated above:

- find all subgroups  $G_0$  of the corresponding transformation groups  $G$ ; and then
- find all orbits of these subgroups.

This is a (somewhat tedious but) doable task. The results are as follows:

### 3.6.5. The results of Step 1: Optimal curves for sensor placement

- For a *cylinder*, possibly optimal curves (i.e., orbits of subgroups) are:
  - *straight lines* parallel to the cylinder's axis;
  - *circles* orthogonal to the cylinder's axis; and
  - *cylindric spirals*.

These spirals can be easily described in cylindric coordinates  $(z, \rho, \varphi)$ , in which  $z$  is a coordinate along the cylinder's axis,  $\rho$  is a distance from this axis, and  $\varphi$  is an angle from some fixed direction orthogonal to the  $z$ -axis. In these coordinates, a spiral takes the form  $\rho = \text{const}$  and  $\varphi = k \cdot z$ , for some constant  $k$ .

Cylindric spirals are *generic* orbits; straight lines and circles can be viewed as their *degenerate* cases.

- For a *plane*, possibly optimal curves (i.e., orbits of subgroups) are:
  - *straight lines*;
  - *circles*;
  - *logarithmic spirals*, i.e., curves describe by the equation  $\rho = C \cdot \exp(k \cdot \varphi)$  in polar coordinates.

Here, logarithmic spiral is a generic shape.

- For a *sphere*, possibly optimal curves (i.e., orbits of subgroups) are *circles*.
- For a *cone*, possibly optimal curves (i.e., orbits of subgroups) are:
  - *straight line rays* going from the vertex of the cone;
  - *circles* that are orthogonal to the cone's axis; and
  - *conic spirals*.

In cylindrical coordinates  $(z, \rho, \varphi)$ , in which the cone is described by the equation  $\rho = C \cdot z$ , a conic spiral is described by the formula  $\varphi = k \cdot z$  for some constant  $k$ .

Conic spirals are the generic type of orbits.

Therefore, depending on the shape, sensors should be placed along one or several of these curves.

### 3.6.6. Important comments

1. If the optimal sensor placement is not along a single curve, but along *several* curves, then the same ideas of transformation groups can be used to choose appropriate families (as orbits of *discrete* subgroups). Let us give a few examples:

- If we have several straight lines on the cylinder, these straight lines must be *equidistant* in the sense that the angular distance between every two neighboring lines is the same.
- If we have several circles around the cylinder, then these circles should be equidistant.
- If we have several straight lines on a plane, then these straight lines should be:
  - either parallel and equidistant,
  - or parallel at distances that form a geometric progression, or
  - pass through the same point and form equidistant angles.
- If we have several circles on a plane, then these circles must be:
  - either parallel, equal, and equidistant,
  - or concentric, with their radii forming a geometric progression, etc.

2. In *space structures*, we face yet another shape: a paraboloid ( $y = z = c \cdot x^2$ ). This structure is invariant with respect to rotations and *re-scalings*  $x' = \lambda x$ ,  $y' = \lambda^2 y$ ,  $z' = \lambda^2 z$ . For this group, we can also describe the resulting orbits as spirals ( $\rho = C \cdot \exp(k \cdot \varphi)$  in cylindric coordinates).

### 3.7. Second step: finding the actual sensor placements (main idea)

The problem that corresponds to the second step, i.e., the problem of selecting a 0D subset from a 1D curve can be formulated and solve in a similar manner as the problem that we solved at the first step.

- We started with a surface  $\alpha$  with a transformation group  $G$ .
- On the first step, optimal curves for sensor placements from orbits of subgroups  $G_0$  of this group  $G$ .
- Similarly, on the second step, optimal sensor placements form orbits of subgroups  $G_1$  of the corresponding groups  $G_0$ .

From the mathematical viewpoint, the main difference between these two steps is that on the second step, we start already with a 1D transformation group  $G_0$  and thus, its subgroups  $G_1$  are *discrete*. Thus, we face the problem of describing all orbits of discrete subgroups of the above groups.

Due to lack of space, we are not able to enumerate all possible orbits of this type here, but we will briefly enumerate the ones that correspond to generic curves: on a cylinder, we get equidistant points on a cylindric curve; on a plane and on a cone, we get points on the corresponding spiral whose distances from the center of this spiral form a geometric progression.

In all these families, there are still a few parameters whose choice depends on what exactly our goal is. The specific values of these parameters are determined by a neural network.

#### 4. Neural networks: in brief

Ideally, we should test different sensor placements on different fault locations using the precise model an aerospace structure. However, such a precise model is very computationally intensive, so this direct way is intractable. Instead, we train a neural network to describe the structure, and then test different sensor placements by using this easier-to-compute neural model.

#### Acknowledgments

This research was supported by the Future Aerospace Science and Technology Program (FAST) Center for Structural Integrity of Aerospace Systems, effort sponsored by the Air Force Office of Scientific Research, Air Force Materiel Command, USAF, under grant number F49620-95-1-0518. The U.S. Government is authorized to reproduce and distribute reprints for Governmental purposes notwithstanding any copyright notation thereon.

The views and conclusions contained herein are those of the authors and should not be interpreted as necessarily representing the official policies or endorsements, either expressed or implied, of the Air Force Office of Scientific Research or the U.S. Government.

V. Kreinovich was also partly supported by NASA under cooperative agreement NCCW-0089, and by NSF grants No. DUE-9750858 and No. EEC-9322370.

#### References

1. A. Finkelstein, O. Kosheleva, and V. Kreinovich, "Astrogeometry, error estimation, and other applications of set-valued analysis", *ACM SIGNUM Newsletter* 31(4): 3-25, 1996.
2. A. Finkelstein, O. Kosheleva, and V. Kreinovich, "Astrogeometry: towards mathematical foundations", *International Journal of Theoretical Physics* 36(4): 1009-1020, 1997.
3. A. Finkelstein, O. Kosheleva, and V. Kreinovich, "Astrogeometry: geometry explains shapes of celestial bodies", *Geombinatorics* 6(4): 125-139, 1997.
4. R. Osegueda, C. Ferregut, M. J. George, J. M. Gutierrez, and V. Kreinovich, "Non-Equilibrium Thermodynamics Explains Semiotic Shapes: Applications to Astronomy and to Non-Destructive Testing of Aerospace Systems", *Proceedings of the International Conference on Intelligent Systems and Semiotics (ISAS'97)*, National Institute of Standards and Technology Publ., Gaithersburg, MD, 1997.
5. R. Osegueda, C. Ferregut, M. J. George, J. M. Gutierrez, and V. Kreinovich, "Maximum Entropy Approach to Optimal Sensor Placement for Aerospace Non-Destructive Testing", *The Seventeenth International Workshop on Maximum Entropy and Bayesian Methods*, August 3-7, 1997, Boise, Idaho, Abstracts (available at <http://cme.idbsu.edu/conf>); full text will appear in G. Erickson (ed.), *Maximum Entropy and Bayesian Methods 1997*, Kluwer, Dordrecht, 1997.

## DISCUSSION

### Computational Geometry and Artificial Neural Networks: A Hybrid Approach to Sensor Placement

Speaker: Kreinovich

Are you aware of any successful efforts on online NDE sensor during flight? Several published efforts I have come across have raised more questions than solutions. —Krishnan Balasubramaniam

*You are absolutely right, in-flight NDE for planes is still in a very experimental stage. In-flight NDE is, however, successfully used in space exploration, where, e.g.:*

*For a space station, it is impossible to ground it, so all testing has to be done in flight, and for a Space Shuttle, it is extremely important to test it in-flight before landing.*

*In-flight NDE for planes has its potential advantages, and the main reason why in-flight NDE is not actively used for planes is that planes are not designed for in-flight NDE. As I mentioned in the talk, if we simply add sensors to existing planes, we create lots of problems with aerodynamics, maintenance, collecting information, etc. One of the goals of our present research is to promote the design of new planes with built-in in-flight NDE sensors and systems.*

Which are the criteria used for the sensor placement? —M. Castro-Colin

*For different situations, different criteria are most appropriate:*

*In some situations, the main objective is to timely detect a fault; as soon as the fault is detected, we can, e.g., ground the plane and thoroughly test it on the ground.*

*For such situations, it is natural to choose the sensor placement for which the probability of detecting a fault (of a certain given size) is the largest possible.*

*In other situations, it is desirable not only to detect a fault, but also to estimate its size and location, so that we will be able to determine its potential consequences and, if necessary, make appropriate corrections in the flight control.*

*For such situations, it is more appropriate to choose the sensor locations for which, e.g., the least square error of determining fault parameters is the smallest possible.*

*In view of the potential multitude of different optimality criteria, in our research project, we did not fix a single criterion, but instead, tried to consider all possible (engineering meaningful) optimality criteria. As a result, we have a two-stage description of the optimal sensor locations:*

*On the first stage, we describe all possible sensor locations that are optimal relative to some criteria. The collection of these locations does not depend on the choice of the criterion, and it is formulated in geometric terms.*

*On the second stage, we use the exact criterion to choose, among all possibly optimal sensor locations (i.e., locations that can be optimal for different criteria), the sensor location that is the best with respect to this particular criterion.*

*For the second stage, we have so far used only the two particular criteria explained above, but our methodology can be easily applied to other possible criteria as well.*



# **Evaluation of lattice/skin composite structures with Shearography**

Arup K. Maji

University of New Mexico  
Albuquerque, NM 87131

## **ABSTRACT**

Graphite-epoxy composites consisting of a skin and an attached stiffening grid has now been flight tested and is under consideration for a number of space structures applications. The predominant failure mode in these composites stem from the disbonding of the skin from the rib system. Electronic shearography was used as a full-field, non-invasive means of detecting such disbonds.

Two applications of shearography are discussed in this paper, i) to study the propagation of a preexisting crack under flexural loading, and ii) to study the detectability of such disbonds in a closed cylinder structure. Finite element analyses involving fracture mechanics and quantifying the strain field corresponding to applied loading were used to interpret the shearography results. The analysis also allows the evaluation of various methods of stressing such structures for the purpose of conducting shearography inspection.

**Keywords :** Composite, Shearography, Nondestructive, Lattice, Fracture, Graphite, Epoxy.

## 1. INTRODUCTION

### 1.1 Shearography

Advances in laser interferometry and image processing hardware has made shearography<sup>1</sup> an attractive tools for the measurement of surface phenomena. The setup for shearography involves an object lighted by an extended laser beam, and an imaging system used to capture its image (Figure 1). Currently, imaging and data processing is implemented with the aid of electronic technology. Images are stored with a CCD (charge coupled device) camera, which is operated by a personal computer and an image analysis system. Digital image processing technology has now been integrated with shearography for the detection of disbonds in aerospace structures<sup>2,3</sup>. The video camera takes only 1/60 seconds to acquire an image, therefore, vibration isolation and ambient light are not problems encountered with the ES technique.

An image of the object containing numerous speckles is first acquired by the image analysis system and stored in computer memory. These speckles are caused by the interference of the laser beam with the object's surface; therefore no specimen preparation is necessary. The specimen is thereafter deformed by loading while the ccd camera continues to acquire images. The image processing system continuously subtracts the initial image stored in memory, and displays the image resulting from the subtraction on the video screen. This produces a fringe pattern on the video screen. The fringes increase in number with increasing deformation. Testing and inspection can therefore be carried out in real time. The image at a point on the image plane is caused by the interference of the speckle patterns arising from two points on the object plane, and vice-versa. This is done by an image shearing device, in our case a birefringent crystal<sup>3</sup> that separates two orthogonally polarized components of the laser light going to the image plane. The technique therefore uses the interference of coherent laser beams to detect displacement derivatives or strains. Also, because the fringe pattern designates strains, rather than displacements, the setup is not as sensitive to rigid body motions as other interferometry techniques.

### 1.2 Lattice-skin Structure

The development of structural components with high strength and stiffness, which are also lightweight and economical have always been important to the aerospace industry. In the late 1960s and the early 1970s, McDonnell Douglas pioneered the design and manufacture of an aluminum structure comprising of a skin, stiffened by a system of grids or lattice<sup>4</sup>. A simple triangular system of stiffening elements at 60° orientations provided an overall isotropic behavior; hence the name 'isogrid' (Figure 2). Structural design methods developed in the 70s led to the extensive use of aluminum alloy isogrids as the payload shroud and the interstage of the Titan and Delta spacecrafts. The successes and the excitements in the space program in the 1970s, coupled with the global energy crises instigated the exploration of composite materials for manufacturing the next generation of isogrid structures<sup>5</sup>. Reddy et al.<sup>6</sup> compared the isogrid with other lattice reinforcement schemes (orthogrid and generalized orthogrid), under various loading combinations, and concluded that the isogrid was the most attractive due to its damage tolerant characteristics. Advanced space applications of isogrids are currently being pursued for solar array panels, satellites (Mightysat), payload shroud (flown in 1996), etc. A significant portion of these developments are being pursued by the structural composites section of the Air Force laboratories in Albuquerque, NM.

### **1.3 Research Objectives**

The rib/skin interface in isogrids is a matrix dominated interface which consequently forms a weak link in the isogrid structure. Disbonds can develop during manufacture, or due to in-service loads. Two issues addressed in this paper are :

- i) Under what load would an existing interface crack propagate, i.e., how much weaker is that interface compared to a good interface<sup>6</sup>? and
  - ii) Can such interface cracks be detected from outside of a cylindrical isogrid structure<sup>7</sup>?
- The details of these two issues have been presented elsewhere<sup>6,7</sup>, and the application of shearography towards these two problems is discussed here.

## **2. IDENTIFYING CRACK PROPAGATION**

### **2.1 Fracture Mechanics Analysis**

According to linear elastic fracture mechanics, a crack is expected to propagate when  $G$ , the Energy release rate due to the applied loading reaches a critical value  $G_c$ , which is an experimentally determined material property.  $G$  is used rather than the stress intensity factors because it is better defined in the context of fracture at bimaterial interfaces. The finite element method (FEM) was used to numerically calculate  $G$  for the interface cracks. A commercially available finite element software, 'IDEAS' was used because of its ability to incorporate orthotropic material model and its post-processing capabilities. The T-beams tested in our laboratory (discussed later) were modeled next using a 2-dimensional mesh with a different thickness for the rib and the skin sections (Figure 3). Orthotropic material properties were used, different for the rib (web) and the skin (flange)<sup>6</sup>. Four noded rectangular 'thin shell' elements were used to generate the initial mesh. Crack surfaces (1/2" and 1" long) were introduced by separating the nodes on the two sides at the appropriate locations.

### **2.2 Testing Precracked Beams**

Specimens 2" in span were cut out of a 18" square isogrid panel made of IM7 graphite fiber and 977-2 epoxy preprints and tows. Diamond cutting blade was used to cut rib-skin specimens and to insert the 1/2" and 1" cracks at the rib/skin interfaces. The T-beams with and without the preinserted cracks were tested in three point bending. The loading fixture was mounted on an optical table to facilitate examination with electronic shearography. Based on the LEFM energy release rate criteria (crack propagates when  $G = G_c$ ), the failure loads for the 1/2" and 1" crack specimens were calculated to be 106 lbs. and 32 lbs. respectively, which agrees reasonable well with the test data Figure 4.

### **2.3 Use of Shearography**

The initial plan to use shearography during these tests was to see when the cracks propagate, and how much, at different loading stages. It turned out that there was no slow crack growth, and the crack propagation occurred in an unstable manner at the peak load. Up to that point the shearography fringe patterns showed a strain concentration at the crack tip (Figure 5), but no evidence of ductility or slow crack growth. All the specimens tested failed at the rib-skin connection, and from the tip of the artificial notches as expected. Not observing crack propagation motivated the use of linear elastic fracture mechanics to capture the loss of strength at a disbonded rib/skin interface. It also justified the use of the original crack length in our estimate of  $G$  in the finite element analyses.

### 3. DETECTABILITY OF THE DISBONDS

The manufacture and design of cylindrical composite isogrids are also being pursued by the structural composites section of the Air Force laboratories in Albuquerque (Figure 6). The cylinders were made by a five axis filament winding machine. These specimens were also made of IM7 graphite fiber and 977-2 epoxy prepgres and tows.

The rib-skin interface of such structures are prone to failure both due to stress concentrations and due to microstructural anomalies. There are distinct resin rich zones (bands) where there are no fibers at or near the interface which is prone to cracking. Such zones provide a weak shear plane which leads to crack initiation and consequent premature buckling of the ribs. This occurs due to excessive compaction of the ribs during cure, from the use of rubber molds with high coefficient of thermal expansion. The objective of this experiment was to see if shearography could be used to differentiate between an intact rib and a disbanded one.

#### 3.1 Finite Element Analyses

The same finite element package 'I-deas' was used. A two dimensional analysis was performed with linear beam elements to model the ribs (dark lines) and three-noded triangular shell elements to model the skin sections. The rib length between the nodes was 3.6", as in the actual structure. The accuracy of the FEM mesh was verified against theoretical values.

Post-processing capabilities were used to generate contour plots of  $dw/dx$  (rotation about the y- axis), since the shearography fringes are sensitive to the same quantity. These contour plots are FEM predictions of shearography fringe pattern. The ribs were 0.05" thick and 0.5" high, and the skin was 0.02" thick, as in the isogrids tested.

Figure 7a shows the FEM mesh generated; dark lines showing the ribs. An unit load in the Z direction was applied close to the horizontal rib, at the point encircled. The fringe pattern expected from shearography is also predicted in this Figure. Note that the fringe pattern (Figure 7a) is qualitatively similar to the experimentally observed fringe pattern (Figure 7b).

The rib below the fringe pattern is then separated from the skin by detaching it at the four intermediate nodes. The FEM and experimental fringe pattern now changes to that in Figure 8a and 8b. Note that the fringe pattern continues into the adjacent triangle, since the deformation field is significant in the adjacent triangle. Also, it takes an order of magnitude less force to create each fringe line, compared with the previous case (intact rib).

#### 3.2 Adjustments to Shearography

Two problems were encountered for global nondestructive inspection :

- i) Inspecting a large area was difficult with our set-up due to the speckle size being too small to be resolved by our system (11 microns pixel resolution). This could be overcome with a better camera system or with a more powerful laser (to decrease aperture and hence increase speckle size). The area inspected was reduced to a 6"x 6" square.
- ii) The panel was very reflective and the variation in amplitude due to the speckles was smeared by the light directly reflected. Adjusting the illumination angle helped alleviate the problem. The reflective component can be further reduced by placing a polarizer in front of the birefringent crystal and the ccd camera. The speckle intensity field is randomly polarized, whereas the reflected component is polarized. Therefore, adjusting the polarizer makes it possible to reduce the detrimental effect of the reflective component.

#### **4. CONCLUSIONS**

Shearography showed the strain concentration at the tip of rib/skin cracks. It demonstrated that the crack propagation is sudden at the peak load, and not accompanied by any slow crack growth. The use of electronic shearography (ES) to locate partially disbonded ribs in lattice/skin structures was successful. ES shows promise for rapid in-service inspection of such composite structures. The fringe patterns observed during our inspection agreed with those predicted from finite element analyses. Such analyses can also help design the ES inspection set-up with proper sensitivity.

#### **5. ACKNOWLEDGMENT**

Dr. Maji's interactions with the Air Force Phillips Laboratory in Albuquerque was facilitated by an AFOSR grant under the university resident research professor program, and the technical support of many laboratory staff members.

#### **6. REFERENCES**

1. Hung Y. Y. (1982) "Shearography: A New Optical Method for Strain Measurement and Nondestructive Testing", *Optical Engineering*, V 21, No. 3, pp. 391-395.
2. Hung Y. Y. (1989) "Shearography : A Novel and Practical Approach for Nondestructive Inspection", *J. of Nondestructive Evaluation*, V 8, No. 2, pp. 55-67.
3. Newman J., "Shearographic Inspection of Aircraft Structure", *Materials Evaluation*, V49, No.9, 1991, pp. 1106-1109.
4. NASA report no. CR124075, prepared by McDonnell Douglas Co., 1973.
5. Rhodes M. and Mikulas M.M., "Composite Lattice Structures", NASA Technical Memorandum, TM X-72771, 1975.
6. Reddy A.D., Rao V.R. and Rehfield L.W., "Continuous Filament Wound Composite Concepts for Aircraft Fuselage Structures", *J. Aircraft*, V22, No. 3, 1985, pp. 249-255.
7. Maji, Fosness, Satpathi, Pemble and Donnelly, "Evaluation of Rib/skin Fracture in Composite Isogrid", *J. of Engineering Mechanics, ASCE.*, Jan., 1997, pp. 83-90.
8. Maji A. K. and Satpathi D., "Electronic Shearography for Detecting Disbonds in Lattice/Skin Structures", *J. of Research in NDE*, V9, No. 1, 1997, pp. 1-11.

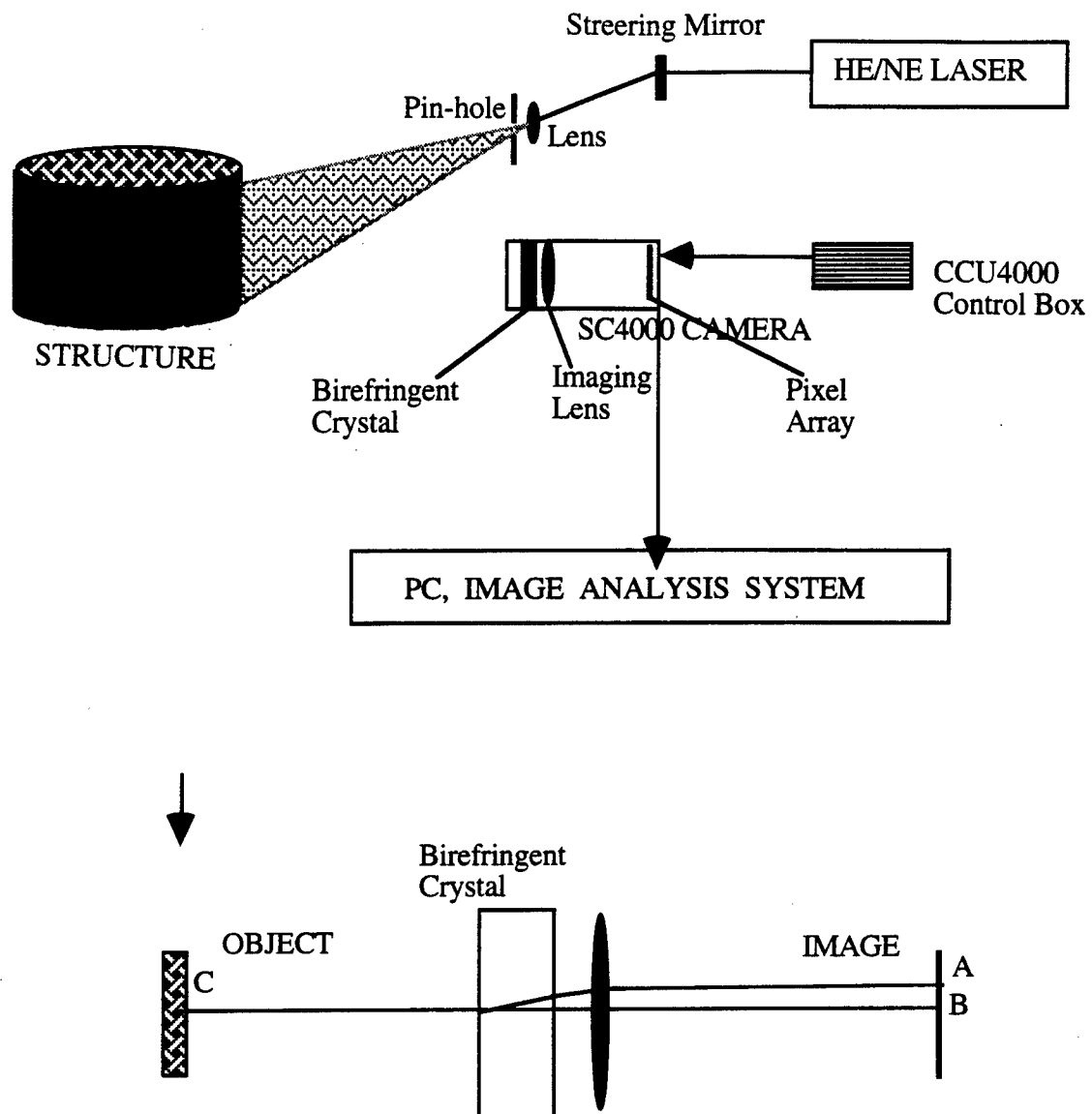


Figure 1. Electronic Shearography Set-up

Isogrid Panel

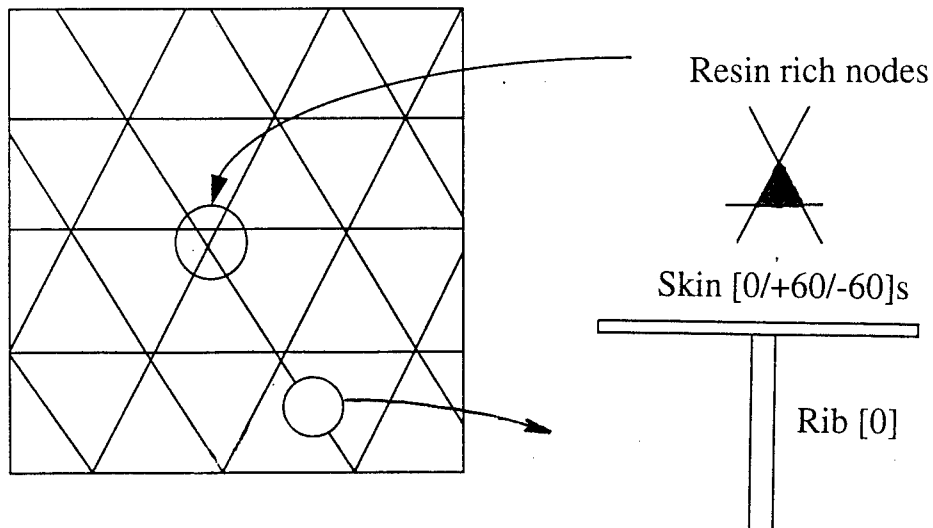


Figure 2. Isogrid Structure

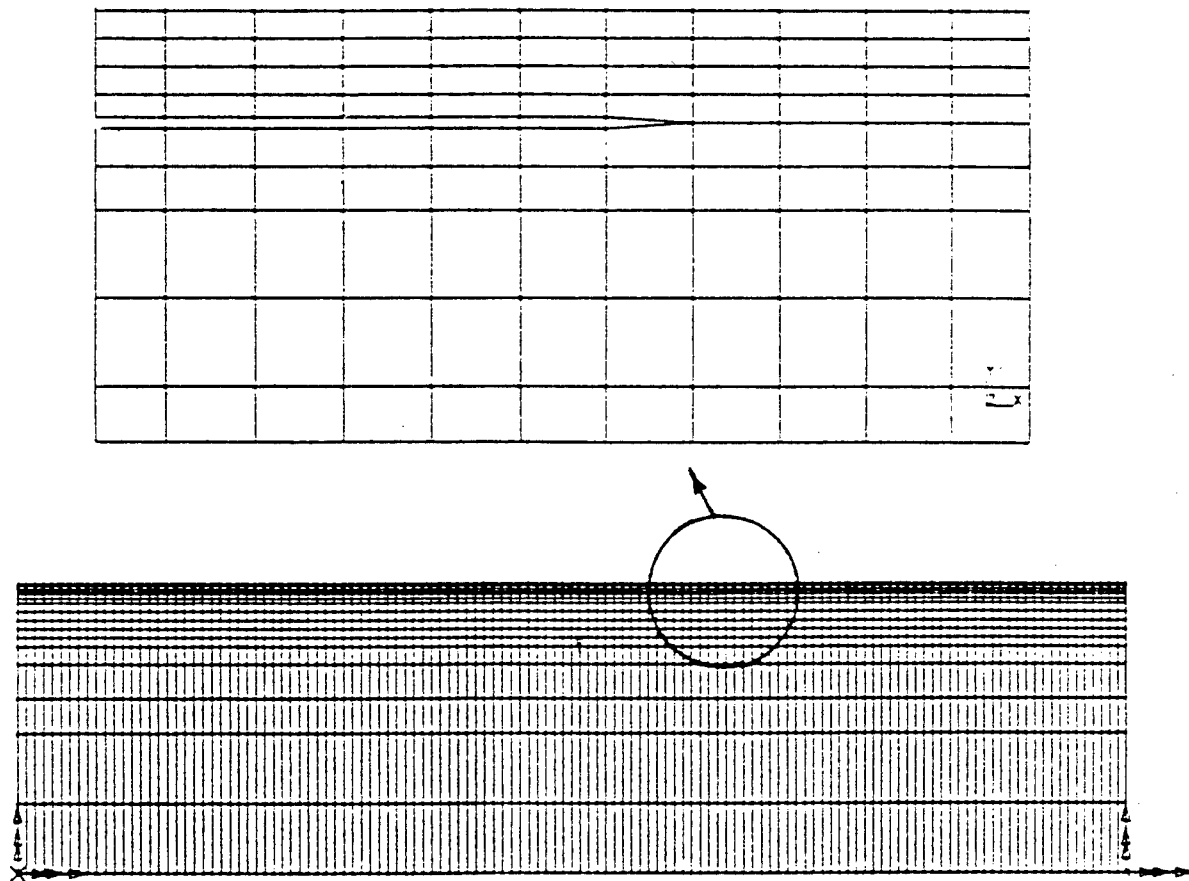


Figure 3. Finite Element Mesh to Analyze Cracked T-Beam

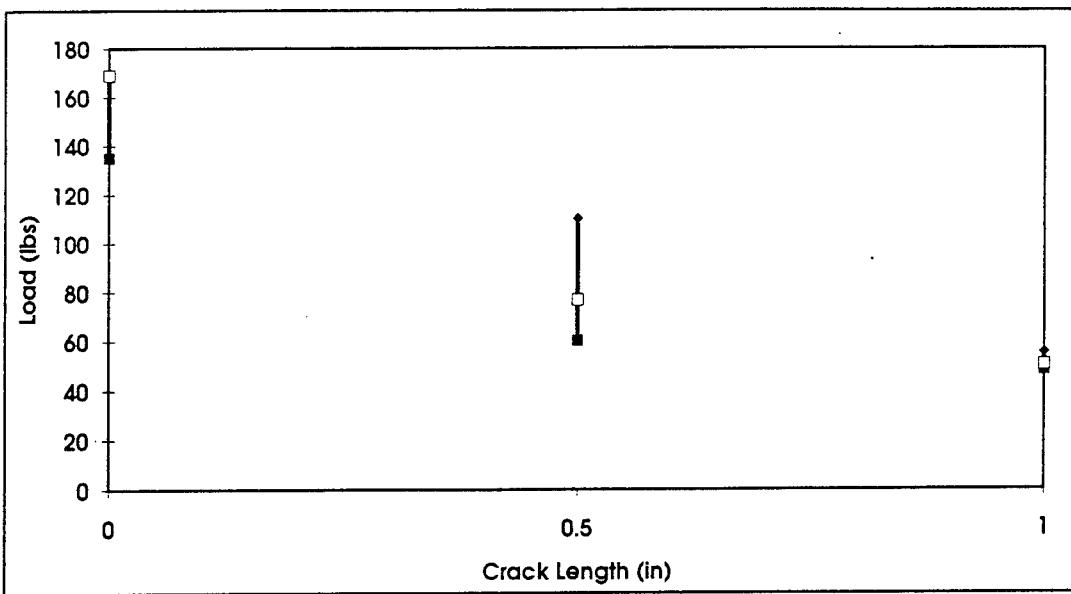


Figure 4. Failure Load vs. Crack Length



Figure 5. Fringe Concentration at the Tip of 1/2" and 1" Cracks

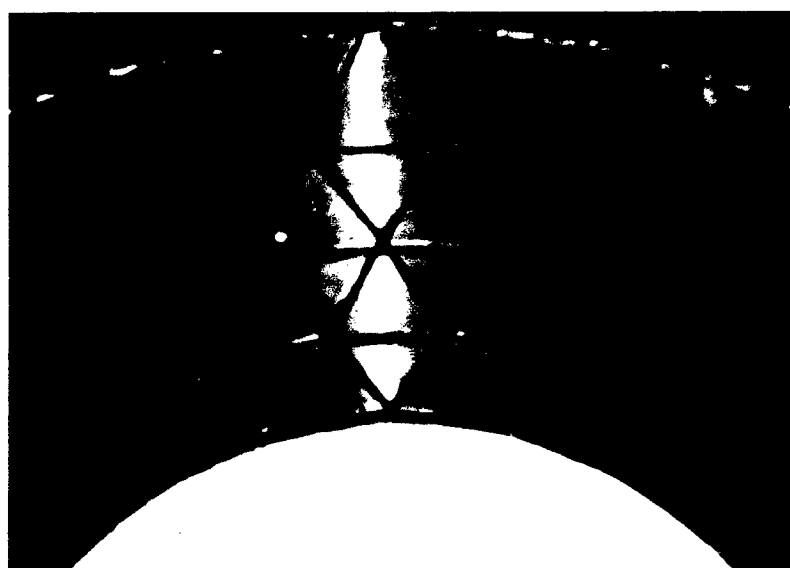


Figure 6. Isogrid Cylinder

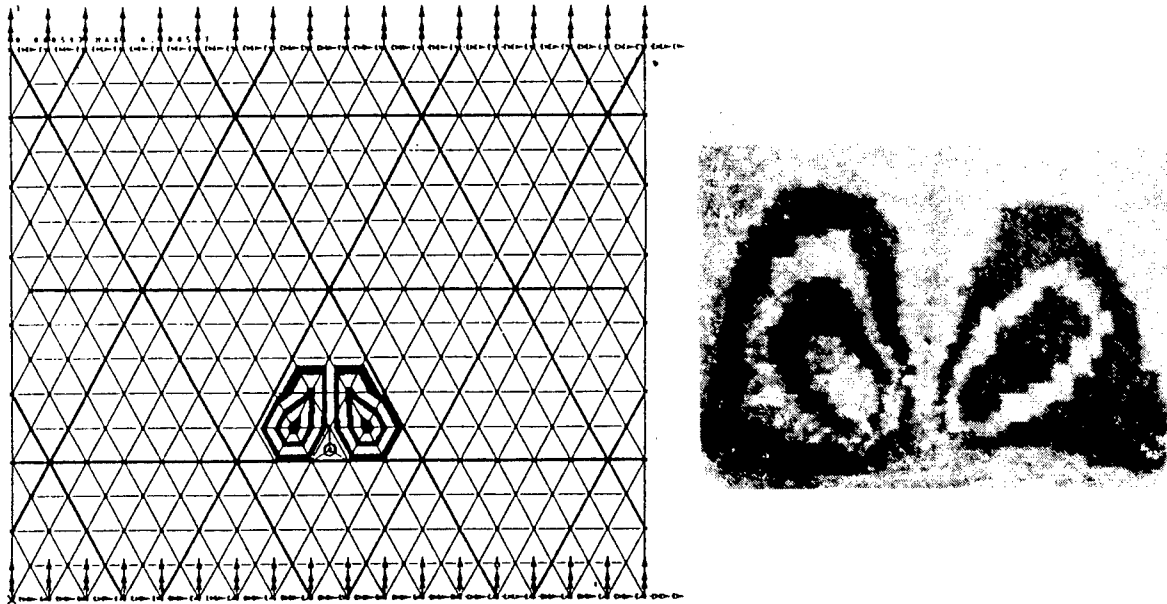


Figure 7a,b. FEM and Shearography Fringe Pattern (Intact Rib)

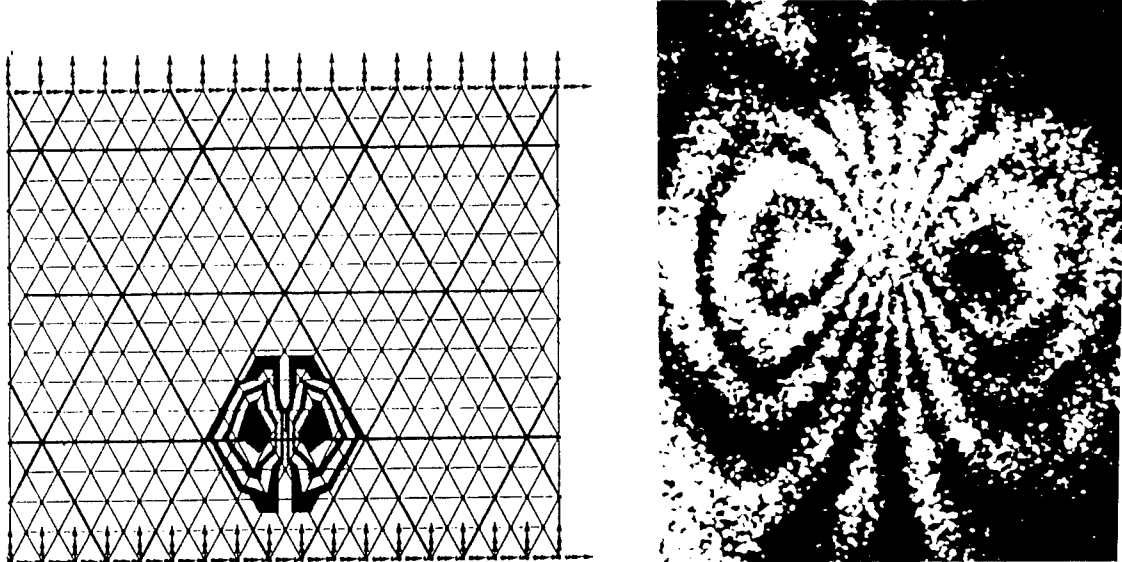


Figure 8a,b. FEM and Shearography Fringe Pattern (Broken Rib)

## DISCUSSION

### Evaluation of Lattice/Skin Composite Structures with Shearography

Speaker: Maji

The type of loading that would be best for a given structure appears to be difficult to determine a priori, your FEM models should be a good way to do this. —Ajit Mal

*Yes, one can decide if mechanical or thermal deformation is best and the required magnitude based on FEM analyses.*

Work has been done on dynamic shearography. Are you familiar with the work of Krishnaswamy? —J. D. Achenbach

*Not specifically. I have seen a lot of work on low frequency dynamic stressing and shearography. I have seen Krishnaswami's work on dynamic ESPI and phase modulated shearography.*

# **Quantitative detection and characterization of corrosion in aircraft**

Xiaoyan Han, L.D. Favro, and R.L. Thomas

Department of Physics and Institute for Manufacturing Research

Wayne State University, Detroit, MI 48202, USA

(313) 577-2970/FAX: (313) 577-7743 bob@thermal.physics.wayne.edu

## **ABSTRACT**

We describe an infrared thermal wave technique for imaging and making corrosion thinning measurements on aircraft skins. The technique uses pulsed surface heating and fast, synchronous IR imaging of the surface temperature contrast to form wide-area images of subsurface structures on time scales on the order of two or three seconds. Structures revealed include rear-surface skin corrosion, disbonded doublers, etc. Quantitative corrosion thinning measurements with a sensitivity on the order of one percent are described. Results from recent laboratory experiments and hangar tests are presented.

**Keywords:** corrosion, aircraft, thermal wave, infrared, imaging

## **1. INTRODUCTION**

Thermal wave imaging is a nondestructive evaluation (NDE) technique which is capable of measuring aircraft skin corrosion thinning. This technique uses pulses of heat in a fashion which is similar to pulsed ultrasonics for echo-ranging. A short pulse of heat is applied uniformly over a wide area (typically a square foot or more) of the surface, usually by means of high-power photographic flashlamps. This pulse propagates into the material as a plane wave, which, when it encounters any sharp change in thermal properties, is partially reflected back to the surface where it affects the time dependence of the surface temperature. The delay time involved in the propagation of the pulse down to the defect and back to the surface is a quadratic function of the depth of the defect. This behavior differs from that of ultrasonic pulses, for which the delay time is linear in the depth of the defect. This difference results from the different form of the elastic wave equation and the heat equation. While both equations have second order spatial derivatives, the elastic equation also has second order time derivatives, but the thermal diffusion equation is first order in time. The result is that, while both equations have wave-like solutions, the solution of the heat equation for a single Fourier component of the applied heat pulse is critically damped - i.e., it has equal real and imaginary parts to its propagation vector, such that it has been reduced by a factor of more than 500 in a propagation distance of one thermal wavelength. Also, the velocities of different Fourier components are proportional to the square root of their frequencies, so that a pulse is extremely dispersive. The combined effect of these two features is to produce the observed quadratic time/distance relationship. In addition, the dispersion causes the original, few millisecond wide pulse to become dramatically broadened, so that for the typical aircraft fuselage skin, the returning pulse has a width of several tens of milliseconds.

A practical version of such a thermal wave imaging instrument for use in inspecting aircraft uses pulse heating of the aircraft by means of two linear photographic flashlamps which are enclosed in a metal shroud which traps and funnels the light uniformly onto the surface during the 5 msec duration of the pulse. An infrared (IR) focal plane array camera, aimed and focused at the surface through an opening in the rear of the hand-held shroud, monitors the rapid cooling of that surface following the pulse. Regions of the skin which have been thinned because of hidden corrosion cool less rapidly than the surrounding uncorroded skin, because the returning thermal wave pulse slows down the cooling. The thermal wave system acquires images in a series of time gates after the flash. With appropriate selection of the gate time(s) for monitoring the cooling, thinner areas show up as distinct lighter features in the resulting thermal wave images. The entire image acquisition process is carried out under the control of a Windows™ program in a portable computer. Our system has the electronics and computer mounted on a two-wheeled cart, and the imaging head (shroud/lamps/camera) remotely located and connected to the cart by a long (50-ft) umbilical cable. Figure 1 shows a photograph of this system in use for imaging disbonded doubler structures in a B747 at a commercial airline maintenance facility. The white area on the 747 is a layer of aircraft wax prior to buffing. This layer is used to minimize reflections, and is simply wiped off after the inspection.

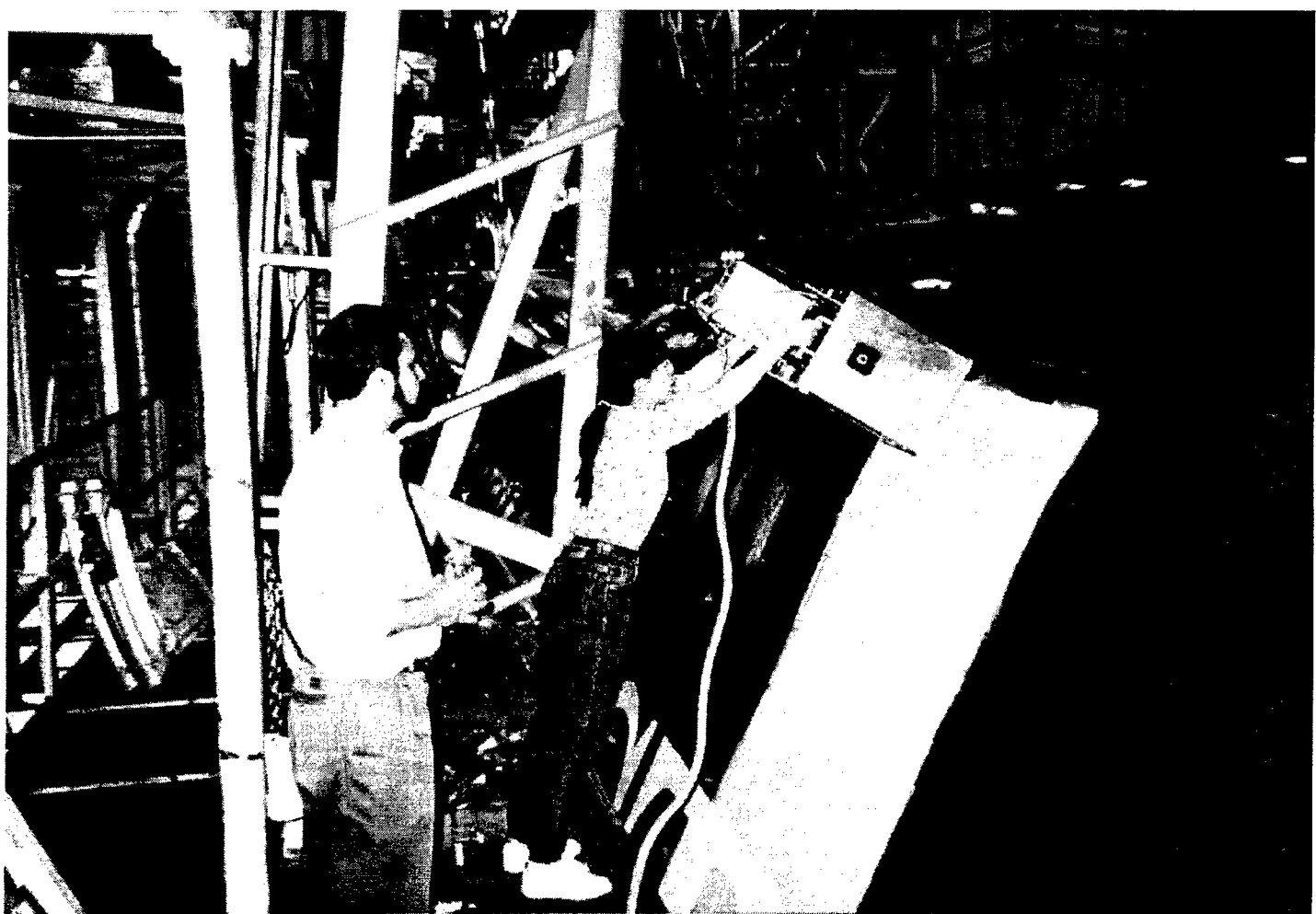


Fig. 1 Photograph of the thermal wave imaging system in use in a commercial airline maintenance facility.

## 2. DETECTION OF HIDDEN CORROSION

The thermal wave imaging system described above has the capability for rapid detection of hidden corrosion on aircraft. We have tested this capability using the AANC B737 testbed aircraft. An example thermal wave image from this testing is shown in Fig. 2. There is extensive corrosion showing as lighter, irregularly shaped regions in this image. The lighter regular stripe-like areas are areas where the tear strap/doublers have disbonded, and it is evident that all of the doublers in this region are disbonded. The corroded areas can be distinguished from the disbonded, but uncorroded areas by means of the thermal wave corrosion analysis technique which will be described in the following section. To show the contrast between corroded and/or disbonded areas, in Fig. 3 we show another area from the same aircraft, but one which displays neither corrosion nor disbonding.

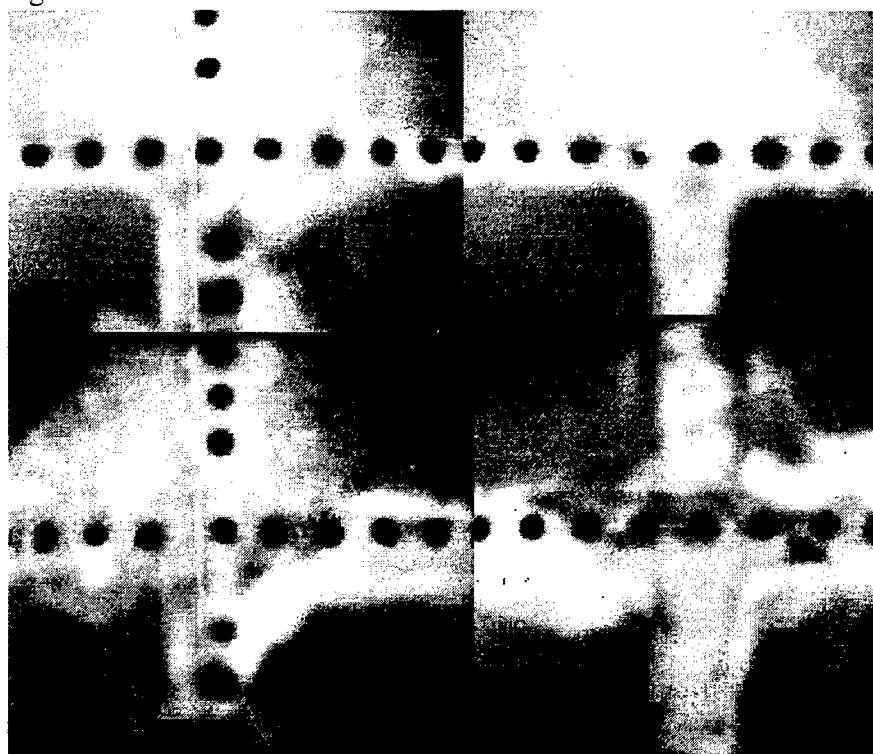


Fig. 2 A montage of thermal wave images of a region of fuselage skin from the B737 testbed aircraft in the AANC hangar. The dark circles are fasteners and are spaced approximately one inch apart. The irregular lighter areas are corrosion.

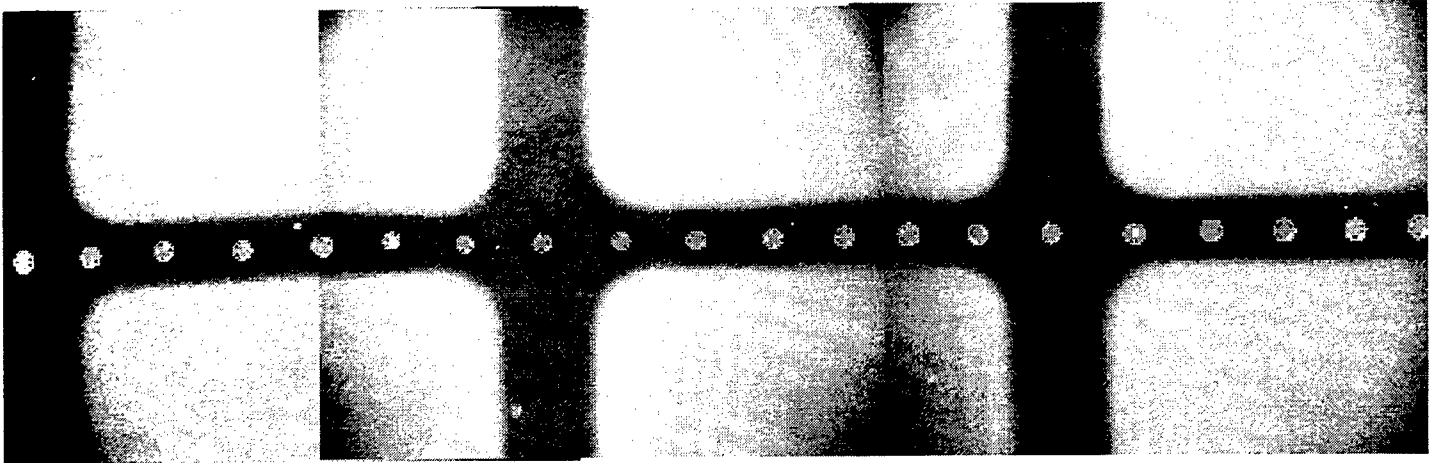


Fig. 3 A montage of thermal wave images of a region of uncorroded fuselage skin from the B737 testbed aircraft in the AANC hangar. The dark horizontal and vertical bands are well-bonded tear strap doubler structures.

Figure 4 shows thermal wave images of intergranular corrosion extending outward from the countersinks of KC-135 steel fasteners in aluminum wingskin. The corrosion shows up as diffuse lighter areas extending out from the circular shape of the rivet head. The rivet head itself shows as a bright thermal wave feature, because of the fact that the steel has much lower thermal conductivity than the surrounding aluminum. In obtaining these images, the IR optics were changed so as to obtain greater magnification than was used to image the large areas of fuselage shown in Figs. 2 and 3. These images are part of a set of 80 fasteners in KC-135 and B-52 wingskin

coupons, which were used for a round-robin "blind" test of NDE technologies during the past year. The results of that testing showed that the thermal wave inspection found nearly ninety percent of the corroded fasteners without a single "false call." The corrosion was artificially produced under controlled conditions, and the coupons were sectioned after the round-robin testing to verify the presence of corrosion and determine its severity. However, such corrosion is known to be a problem in both KC-135 and B-52 wing skins and occurs naturally in those aircraft. It also can be a problem in commercial aircraft, as is illustrated in Fig. 5, which shows naturally occurring intergranular corrosion in the upper wingskin of the AANC B737 testbed, in the vicinity of a set of steel fasteners.

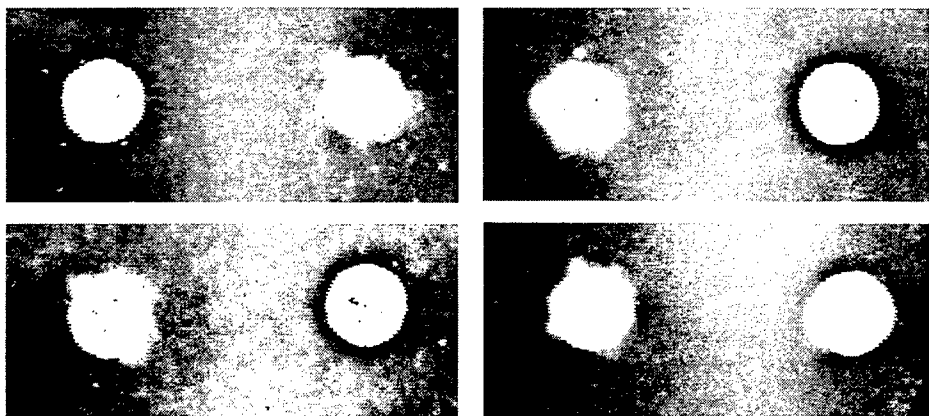


Fig. 4 Thermal wave images of several wingfasteners in a section of KC-135 wingskin. All but three of these fasteners exhibit intergranular corrosion, extending out from the countersink of the fastener. This corrosion is beneath the surface, and cannot be detected visually. These fasteners show up as light on a darker background because they are steel and have a much lower thermal conductivity than the aluminum skin in which they are countersunk.

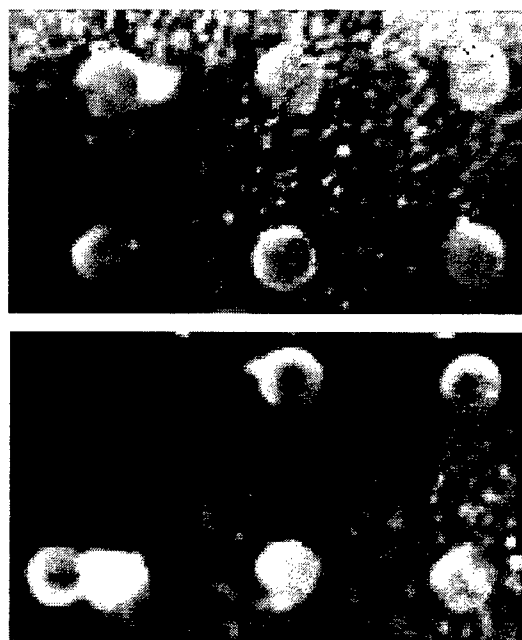


Fig. 5 Thermal wave images of several wingfasteners in a section of wingskin on the B737 testbed aircraft at AANC. Several of these fasteners exhibit the same kind of intergranular corrosion as seen on the KC-135 skin shown above in Fig. 4. This corrosion occurred naturally, and in two cases is considerably more severe than the artificially produced corrosion in the KC-135 sample of Fig. 4.

### 3. QUANTIFICATION OF CORROSION

In Fig. 6, we show a thermal wave image in the form of a 3-D perspective plot, showing five intentionally corroded regions on the rear surface of a 40-mil aluminum skin. The percentages of material loss shown in the figure were determined through the use of a corrosion analysis computer algorithm<sup>1,2</sup> which is available immediately following the acquisition of the data, which takes just two seconds after the flash heating of the skin. This algorithm uses the uncorroded skin in the vicinity of the corrosion as a calibration reference, and therefore does not require a prior knowledge of the absolute thickness of the skin nor a prior knowledge of the particular alloy used for the skin. If absolute skin thickness measurement is desired, a separate calibration plate can be placed in the field of view of the thermal wave imager. We have generated a number of such corrosion regions on skins with both 40-mil and 71-mil thicknesses, and have compared the results of our thermal wave corrosion analysis algorithm against direct micrometer measurements. The results of our comparison are shown as a graph in Fig. 7, and the agreement is excellent. The mildest region of corrosion was less than 1% material loss, showing that the sensitivity of the technique is much better than that typically required for aircraft inspection.

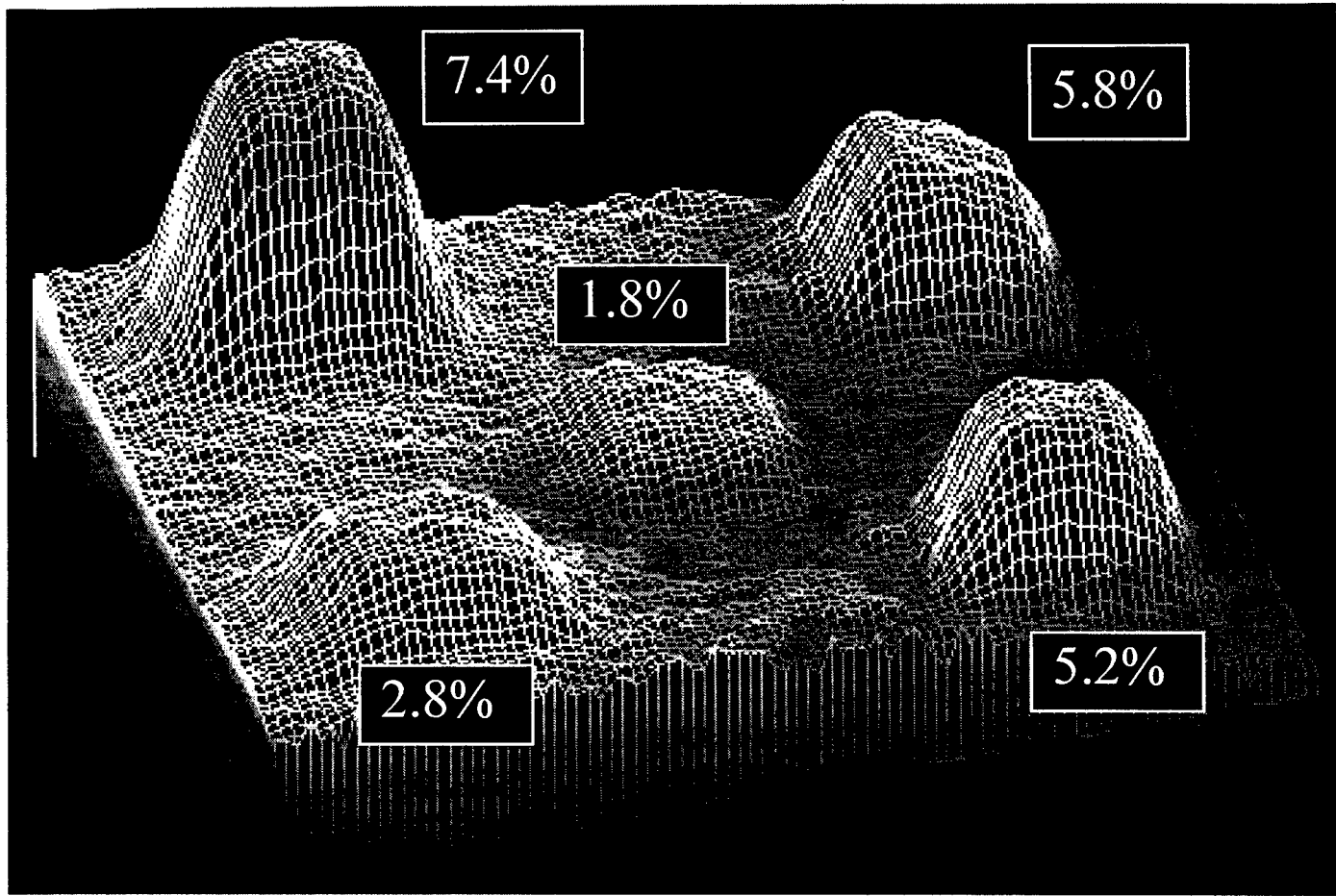


Fig. 6 Thermal wave image in the form of a 3-D perspective plot, showing five intentionally corroded regions on the rear surface of a 40-mil aluminum skin. The percentages of material loss shown in the figure were determined through the use of a corrosion analysis computer algorithm which is available immediately following the acquisition of the data, which takes just two seconds after the flash heating of the skin.

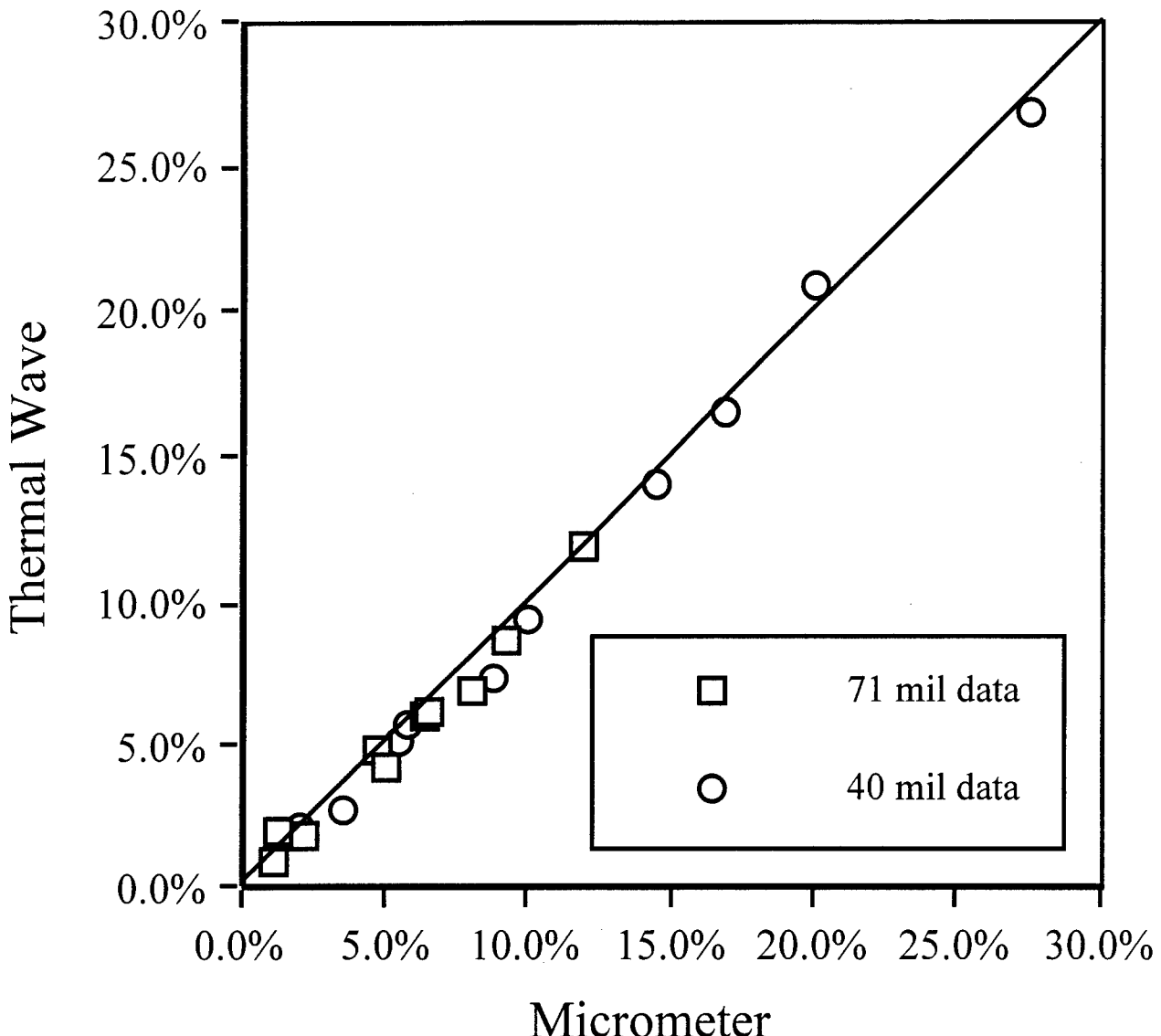


Fig. 7 Comparison between thermal wave measurements of material corrosion loss and direct micrometer measurements for twenty regions of intentional corrosion on four skins (two which are 40-mil thickness, and two which are 71-mil thickness), showing the accuracy and sensitivity of the thermal wave corrosion analysis.

In Fig. 8 we show a thermal wave image from a region of lap splice on the B737 testbed at AANC. This image shows naturally occurring corrosion, both on the single skin and within the lapslice region. The number (20%) which appears in Fig. 8 is the result of applying the quantitative corrosion thinning algorithm to the bright region indicated by the arrow. Following our measurement, one of the AANC staff members utilized a standard eddy current corrosion thinning measurement instrument and indicated that the corrosion was indeed approximately 20%.

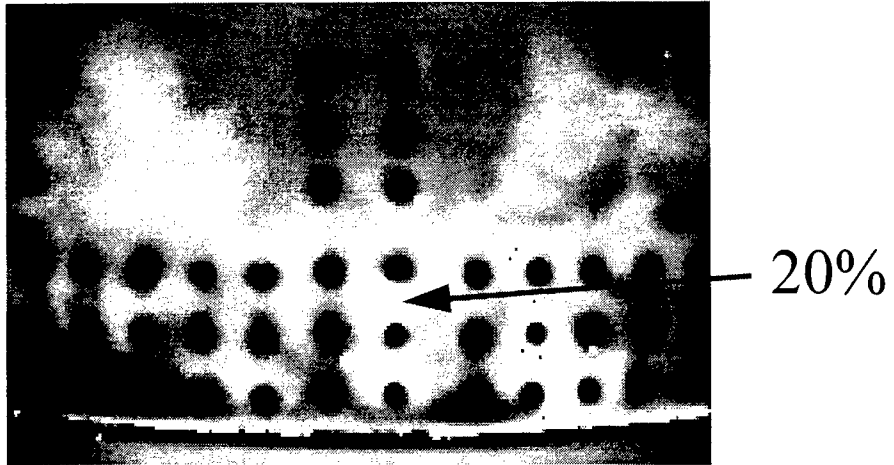


Fig. 8 Thermal wave image of a region of corroded lapssplice on the B737 testbed aircraft in the FAA's Aging Aircraft NDI Validation Center (AANC). The estimate (20%) is obtained from the thermal wave imaging corrosion analysis algorithm..

#### 4. ACKNOWLEDGMENTS

This material is based upon work performed by the FAA-Center for Aviation Systems Reliability, operated at Iowa State University and supported by the Federal Aviation Administration Technical Center in Atlantic City, New Jersey, under grant number 95-G-025, and by AFOSR under Grant No. F49620-96-1-0166.

#### 5. REFERENCES

1. Xiaoyan Han, L.D. Favro, T. Ahmed, Zhong Ouyang, Li Wang, Xun Wang, Feng Zhang, P.K. Kuo and R.L. Thomas, "Quantitative Thermal Wave Imaging of Corrosion on Aircraft," Review of Progress in Quantitative NDE, Vol. 16, edited by D.O. Thompson and D. Chimenti, Plenum New York, pp. 353-356 (1997).
2. Xiaoyan Han, L.D. Favro, P.K. Kuo and R.L. Thomas, "Early-Time Pulse-Echo Thermal Wave Imaging," Rev. Prog. in Quant. Nondestr. Eval., Ed. D.O. Thompson and D.E. Chimenti, Vol. 15, pp. 519-524 Plenum Press, New York, (1996).



# AUTONOMOUS RAPID INSPECTION OF AEROSPACE STRUCTURES

Yoseph Bar-Cohen

JPL, California Institute of Technology, 4800 Oak Grove Dr. (125-224)  
Pasadena, CA 91109, yosi@jpl.nasa.gov

## ABSTRACT

Effective assurance of the integrity and performance of aging aircraft structures, particularly those that are made of composite materials, requires rapid inspection of large areas. Removal from the aircraft for NDE at an inspection facility is not economical and preferably the inspection should be performed at the field setting. Detection and characterization of defects are labor intensive, time consuming and when the process is manual the results are subjected to human error. These limitations of the standard NDE methods created a need for portable, user friendly inspection systems that can rapidly and automatically scan large areas of complex structures and locate all the detrimental material conditions. Addressing this need has been an evolutionary process that followed the technology trend, and unique devices were developed to perform field inspection. Such a development required integration of expertise in multidisciplinary areas that include NDE, telerobotics, neural networks, materials science, imbedded computing and automated control. Various portable inspection systems have emerged and the trend is toward fully automatic systems that autonomously inspect aircraft.

## KEYWORD

NDE, Autonomous inspection, Crawlers, MACS, MAUS, Aging aircraft inspection, remote operation, intelligent inspection.

## INTRODUCTION

The current use of aging aircraft significantly longer than their design life has added a great degree of urgency to the ongoing need for low-cost, rapid, simple-to-operate, reliable and efficient NDE methods for detection and characterization of flaws. The issue of aging aircraft is of concern to the users and operators of both the military and commercial aircraft. The 1988 failure of the Boeing aircraft operated by Aloha Airlines heightened the level of attention to the issue of aging commercial aircraft from manufacturers, users and the Federal Aviation Administration (FAA). In many cases, the problem of field inspection is complex due to the limitation of current technology and the need to disassemble aircraft structures for NDE in lab conditions.

Labor intensive inspection in field conditions demands great attention to details by inspection personnel and is subject to human errors and limited in reliability. The interpretation of the data depends critically on the inspectors' experience, competence, attentiveness and meticulous dedication. For instance, rivet crack inspection with eddy current detectors is known to be a mundane and painstaking task, which can lead to a significant decrease in the inspector attention during a long inspection session. On the other hand, disassembly of structures and inspection in laboratory conditions is costly and not practical in many cases. These inspection limitations are hampering the growth in usage of composite structures for construction of aircraft since these structures are sensitive to impact damage that can occur at any point and any time over large areas. To overcome the limitations of standard NDE methods, reliable field inspection systems are being developed for rapid NDE of large and complex-shape structures. For military aircraft, an additional constraint needs to be

accounted and it is requirement to operate also at harsh, hostile and remote conditions (extreme temperature, battlefield, remote expertise, etc.) with minimum human interference.

In recent years, to address the need for rapid inspection in field conditions, various types of portable scanners were developed using such NDE methods as visual, eddy currents, ultrasonics, shearography, and thermography. The emphasis of this manuscript is on ultrasonic NDE scanners, their evolution the expected direction of development and the role that intelligent NDE can play.

## RAPID INSPECTION SCANNERS

For more than four decades, ultrasonics has been one of the leading NDE methods. The development of scanners made the biggest impact on the wide use of this method since scanners allowed producing detailed images of the flaws size and location. Further, the process of recording the data became consistent and allowed the application of simple reception/rejection criteria for the simplification of the inspection standards. For a long time, the automated inspection capability (also known as C-scan) was available only for lab conditions and field inspection was performed manually. The emergence of microprocessors enabled to make such systems capable to perform contour following of structures and to operate concurrently with the details of the CAD drawing. Full aircraft structures, such as the wing of the Harrier, are now tested routinely by such systems in lab conditions (see Figure 1).

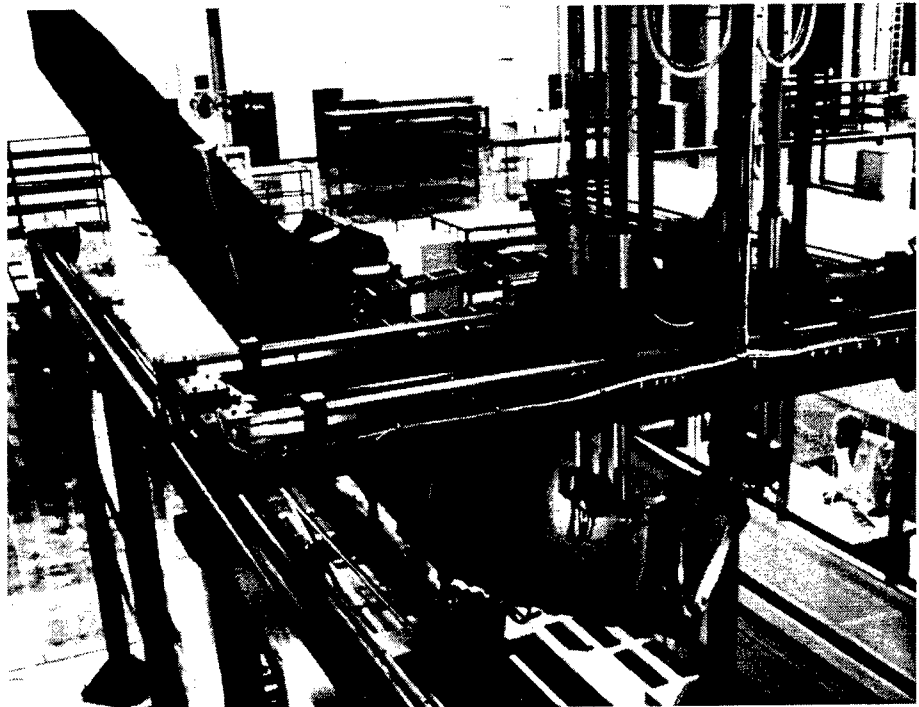


Figure 1: MDC large scanner testing a full wing of an aircraft.

With the evolution of personal computers and microelectronics, it became possible to produce portable C-scanners that can operate in the field [1]. The original portable scanners were relatively heavy and consisted of a simple bridge with mobile set of boxes that were carried to the field and performed scanning, data acquisition, imaging and storage. To support the formation of the C-scan images, encoding methods were developed to provide probe location information while operating on aircraft structures directly in the field. Such position encoding methods include the use of acoustic waves, as is ISIS that was developed by General Dynamics under a contract from the Air Force (see Figure 2), optical scales, and various other encoding techniques. Due to the inaccuracy of the acoustic encoding technique it was phased out and most of the current portable scanners rely on the use of optical encoders. To inspect vertical surfaces or testing the bottom surface of aircraft wings, strapping techniques and vacuum cups were employed (e.g., QMI's portable scanner, see

Figure 3) securing the attachment of the C-scan bridge. Since aircraft structures have a complex geometry, the use of flat portable C-scan bridges is encountered with difficulties associated with the gap that is formed between the straight bridge and the curved surface of the aircraft. The PANDA Scanner (made by Tektrend) addressed this issue by employing a flexible arm that flexes its curvature to conform to the surface contour and ensures contact between the transducer that test surface. The introduction of portable c-scan bridges enabled the automation of ultrasonic field inspection and significantly improved the reliability of such field tests. However, such scanners provide an effective inspection capability only over the area that is covered by the scanner bridge. Covering a large area of an aircraft requires performing multiple scans where the operator moves the scanner from one location to another to form scan-tiles until the full structure is covered.

1. ULTRASONIC INSTRUMENTS
2. CONTROL/POWER ELECTRONICS
3. PRINTER/PLOTTER
4. KEYBOARD
5. DISPLAY TERMINAL
6. POSITION RECEIVER ASSEMBLY
7. ULTRASONIC PROBE
8. SHIPPING ENCLOSURE
9. MOBILE CART

Figure 2: ISIS

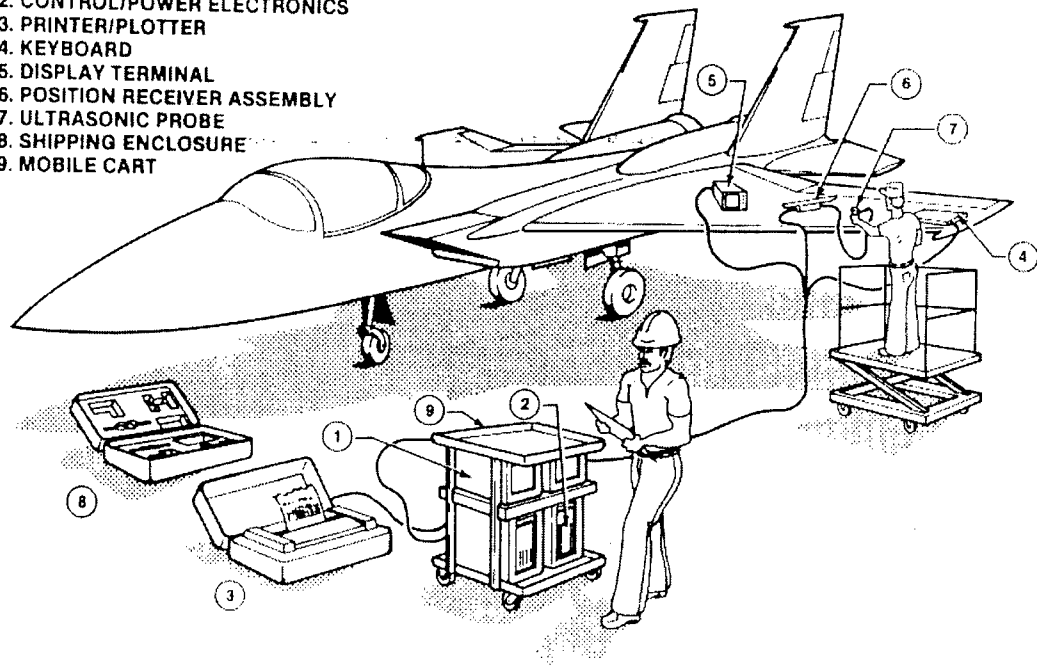
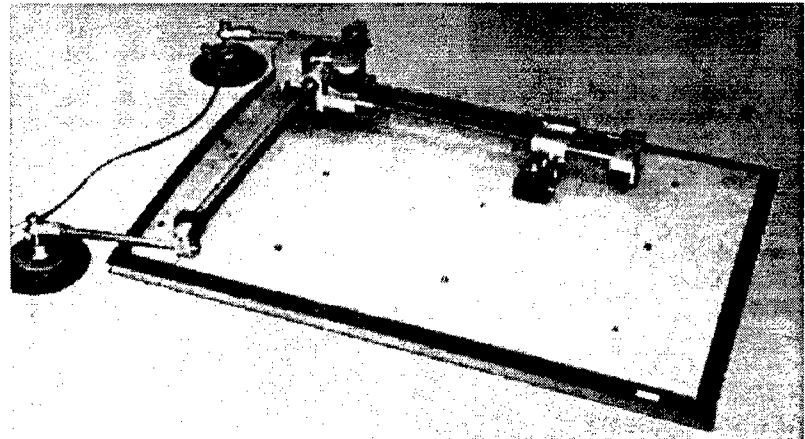


Figure 3: QMI scanner using a portable bridge and two suction cups to secure the bridge position during scan.



## INSPECTION CRAWLERS

Automated devices that can be attached to an aircraft skin and travel on it while scanning and inspecting it can greatly expedite the rate of inspection and minimize human interference in this task that requires minimal skill. Increasingly crawling devices are being reported as a solution to the need for mobile unconstrained scanners. The use of suction cups has become a leading form of controlled adherence to aircraft surfaces and

several successful devices were reported in the last several years. The Automated Non Destructive Inspector and the Autocrawler are some of the more known mobile portable scanners [1-2]. In recognition of the need to have a compact, more maneuverable crawler, JPL recently developed a small, highly dexterous crawler with a payload to weight ratio of about 10:1. This Multifunction Automated Crawling System (MACS) was designed to perform complex scanning tasks [3]. MACS employs ultrasonic motors for mobility and suction cups for surface adherence. MACS has two legs for linear motion and a rotation element for turning, thus allowing to perform any simultaneous combination of motion from linear to rotation around the central axis. In Figure 4, MACS is shown crawling vertically on the surface of an Air Force C-5 aircraft. A schematic view of the steps that are involved with mobilizing MACS and the position of the various suction cups and legs are shown in Figure 5.

Applications of MACS include inspection of composite and metallic structures for detection of cracks, corrosion, impact damage, unbonds, delaminations, fire damage, porosity and other flaws, paint thickness measurement. Also, MACS can be used to identify dents and individual fasteners. The development of MACS was benefited from the ongoing JPL development of miniature planetary rovers, telerobotic technology and NDE techniques.

Figure 4: MACS crawling on the C-5 aircraft [patent pending].

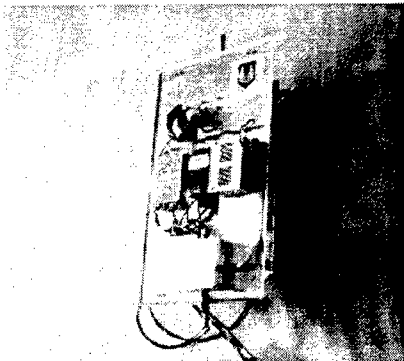
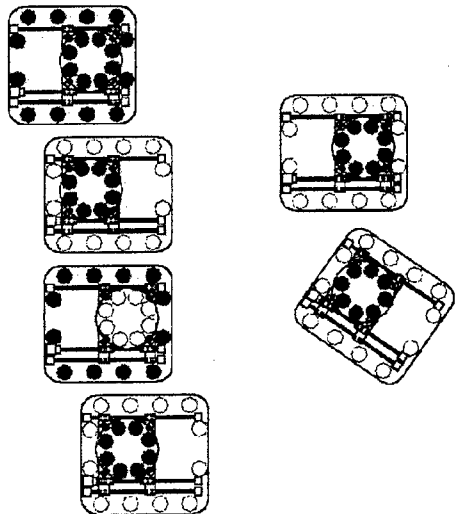


Figure 5: MACS crawler mobility control. Solid circles represent activated suction cups and hollow circles represent resting cups. Forward travel is shown on the left and a simultaneous travel/rotation is shown on the right.



## AUTONOMOUS CRAWLERS USING INTELLIGENT NDE

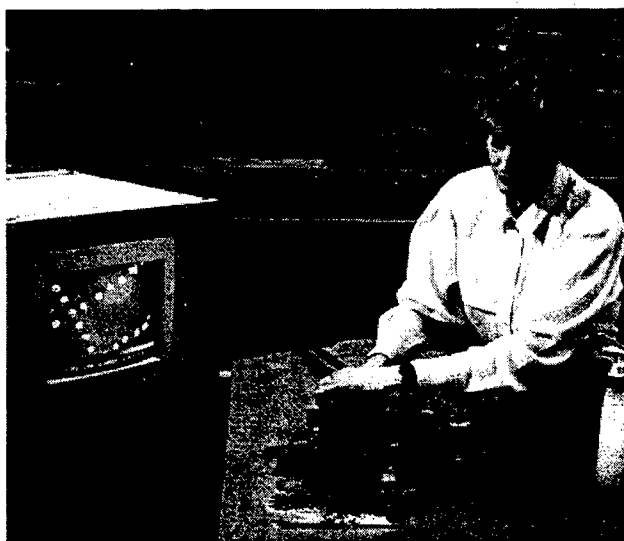
Autonomy of NDE crawlers is a key technology for the automation of such devices for field scanning of complex aerospace structures. An autonomous crawler can be monitored remotely by centrally located experts that are equipped with know-how, database, analytical tools, CAD drawing, and accept/reject criteria. Such a capability will allow rapid response to inspection needs, particularly in cases of crisis where there is a need to

rapidly examine a full flight of a particular aircraft model all over the world. An autonomous crawler can be operated during aircraft idle time allowing to reduce the need to ground aircraft for inspection. A combination of visual, eddy current and ultrasonic payload (methods that offer portable sensors) are expected to be the leading NDE methods that are used on an autonomous crawler.

The technology that can enable such capabilities has been in development at JPL for the exploration of Mars, where the Mars Pathfinder already enjoyed some of its benefits. Miniature robotic technologies with on-board intelligence are being developed for future missions where the rovers will examine, select and collect samples from Mars while avoiding obstacles during operation in an unknown terrain. Since communication between Earth and Mars takes about 12 minutes each way, the need for autonomous operation rather than remote control is critical to the success of the missions. The JPL's crawler MACS is currently using umbilical cord for power, communication/control and to provide air pressure for the ejection and activation of the vacuum cups. Future efforts will involve increased autonomous operation and a complete wireless portability. Potential future development includes a miniature on-board vacuum pump, power and computing capability. Further, intelligent NDE techniques can be used to allow detection and characterization of flaws and material properties determination [4]. Crawlers can employ local Global Positioning Systems (GPS) to determine the absolute coordinate without the need for a complex, expensive and heavy encoder. Further, such GPS systems will allow relating the location of the crawler on the aircraft to the detailed drawing and assist in the data interpretation and flaw location and identification.

The use of such crawlers as MACS to serve as a shuttle crawler to carry the probe head of the McDonnell Douglas' MAUS unit (which is highly supported by the Air Force) can provide a powerful inspection tool. MAUS is a device that uses a hand-held scanner to move a series of probes horizontally while an operator moves the scanner vertically. Employing a crawler as the MACS for forward and backward mobility will enable one to autonomously inspect vertical surfaces and bottom of aircraft structures. To protect elements of the aircraft that rise above the surface from accidental damage, a virtual vision system will be used with collision avoidance software. To enhance the inspection capability of the combined systems, a neural network data interpretation can be used. MACS can be controlled remotely via the use of Internet allowing multiple users to control it using password and thus limiting the access to the control capability.

FIGURE 6: A view of the MAUS portable scanner in operation. The scanner is a hand-held unit.



## **ACKNOWLEDGEMENT**

The development of MACS was done under a Jet Propulsion Laboratory, California Institute of Technology, contract with the Air Force Material Command, Kelly Air Force Base.

## **REFERENCES**

1. P. Backes and Y. Bar-Cohen, "Miniaturization Technologies for Aircraft Inspection," JPL Report D-13876, (July 1996).
2. V. Bahr, "Wall-Climbing Robot in Non-Structural Environment," Transaction Robotics Research, Robotics International, Society of Manufacturing Engineering, Vol. 2 (1992), pp. 1-24.
3. Y. Bar-Cohen, B. Joffe and P. Backes "Multifunction Automated Crawling System (MACS)", Disclosure of New Technology, Item No. 9460, Docket 19847, November 29, 1995. (Patent Pending, CIT 2432, Submitted on August 1, 1996).
4. C. A. Vazquez and Y. Bar-Cohen, "Application of Artificial Intelligence to NDE," Report No. K4870, (MDC, Long Beach, CA. April 1990) pp. 1-32.

## DISCUSSION

### Autonomous Rapid Inspection of Aerospace Structures

Speaker: Bar-Cohen

What are the new scientific/technical issues involving the autonomous rapid inspection of aging aircraft (vs. autonomous control of spacecraft in the areas of sensing, actuation, processing and control)? —Spencer Wu

*The development of autonomous robotic mobile platforms, for rapid NDE of aging aircraft structures, requires addressing the following scientific/technical issues:*

*Model forward and backward kinematics for inspection/scanning on or inside an aircraft structure*

*Autonomous mobility on complex geometry typical to aircraft structures (fuselage, wing, etc.) and internal components (engine, etc.).*

*Artificial vision to support the operation on aircraft using landmarks and position monitoring and collision avoidance.*

*Effective NDE science base and smart data interpretation – using real-time model-based calculation to predict the remaining life of the structure.*

*Also, effective early detection of corrosion and crack initiation for sites.*

*MEMS and miniature NDE technology for miniature robotic inspectors.*

*Sensor modeling to predict their response, assuring robust operation and determining the probability of detection.*

*Using neural networks, genetic algorithms and pattern recognition analysis.*



# Enhanced remote visual inspection of aircraft skin\*

Mel Siegel<sup>a</sup>, Priyan Gunatilake<sup>b</sup>

<sup>a</sup>The Robotics Institute, School of Computer Science

<sup>b</sup>Department of Electrical and Computer Engineering  
Carnegie Mellon University, Pittsburgh PA 15213 USA

## ABSTRACT

Visual inspection is the most widely used method in commercial aircraft surface inspection. We have developed a prototype remote visual inspection system, designed to facilitate testing the feasibility and advantages of remote visual inspection of aircraft surfaces. We describe experiments with image understanding algorithms to aid remote visual inspection by enhancing and recognizing surface cracks and corrosion from live imagery. Also described are the supporting mobile robot platform that delivers the imagery, and the inspection console through which the inspector accesses it. We discuss initial results of the image understanding algorithms and speculate on their future use in aircraft surface inspection.

**KEYWORDS:** enhanced remote robotic visual inspection stereoscopic multiresolution ANDI CIMP

## 1. INTRODUCTION

Visual inspection of aircraft is the most widely used method employed for ensuring the structural integrity of an aircraft skin and its substructure. For example, a typical heavy inspection carried out on a commercial aircraft after every 12,000 flying hours, is about 90% visual and 10% non-destructive inspection (NDI).<sup>1</sup> Visual inspection involves putting a human inspector on the body of the aircraft to visually examine its surface for defects such as cracks, corrosion, damaged rivets, lightning strikes, etc. This practice raises safety issues for the inspector, is time consuming, and suffers at times from being ineffective due to inspector fatigue or boredom.<sup>2</sup>

An attractive alternative to the current inspection practice is remote visual inspection. In remote visual inspection, the inspector examines, at an inspection console, high-quality imagery of the inspection surface that is captured and delivered to the console by a remote mobile robot on the body of the aircraft. The robot may be teleoperated via low level controls, it may navigate autonomously under computer control, or typically something in between with high level commands issued by the inspector and low level details decided and executed by the computer. This method, while inherently safe (since the inspector is on the ground), allows for direct human observation of the remote aircraft surface. It also provides for computer processing of the delivered imagery for image processing, enhancing and understanding. Image processing involves adjusting contrast or range of the imagery dynamically, for improved visualization. Image enhancement amplifies high spatial frequencies of the imagery to highlight features suggestive of surface defects which are typically of high frequency nature.<sup>3</sup> Image understanding via characterization and recognition of surface defects, allows for automated defect detection and classification of the surface imagery. With the aid of these facilities, an inspector can safely, quickly and accurately perform the necessary visual inspection from the inspection console.

In Section 2 of this paper, we describe a prototype mobile robot called the Crown Inspection Mobile Platform (CIMP) designed to test and demonstrate the hypothesized feasibility and advantages of the remote visual inspection of an aircraft surface. Also included in section 2 is a brief description of the predecessor to CIMP, the Automated NonDestructive Inspection (ANDI) robot.<sup>4,5</sup> Section 3 discusses the inspection console that displays the remote imagery and a graphical user interface (GUI) that provides the inspector

\* This is an updated version of the paper "Image Understanding Algorithms for Remote Visual Inspection of Aircraft Surfaces", Priyan Gunatilake, M.W. Siegel, A.J.Jordan, and G. Podnar, Proceedings of SPIE "Machine Vision Applications in Industrial Inspection V", A. Ravishankar Rao and Ning Chang, Chairs/Editors, 10-11 February 1997, San Jose, CA, SPIE Vol. 3029.

with access to image processing, enhancing and understanding algorithms. Section 4 contains a brief discussion of image understanding for surface defect detection and a description of two common aircraft surface defects. Section 5 describes a surface crack detection algorithm. Section 6 describes a surface corrosion detection algorithm. Section 7 describes an approach to subsurface corrosion detection. Section 8 provides a summary discussion and thoughts about future work, and Section 9 draws some conclusions.

## 2. CIMP

The first aircraft-capable mobile robot developed at CMU was ANDI (the Automated NonDestructive Inspector of aging aircraft). ANDI successfully demonstrated mobility, manipulation and navigational capabilities on an aircraft surface. However, due to the ANDI project emphasis on mobility and navigational issues, the delivery of high quality visual imagery useful for remote visual inspection was not addressed at length. After the initial demonstrations of ANDI, the first author launched another research effort with the twin objectives of designing a high quality remote imaging system that delivers useful inspection data and developing an inspection console consisting of a graphical user interface (GUI) and a library of image enhancement and understanding algorithms, through which an inspector could access, enhance and recognize surface defects from the live imagery. [See the Acknowledgments section for additional historical details.]

CIMP was developed as a part of this second research effort. CIMP is a wireless remote-controlled mobile vehicle that carries a sensor package designed to deliver high quality, live imagery of the aircraft crown on which it travels. The sensor package of CIMP contains a stereoscopic pair of inspection cameras, a dynamic lighting array consisting of two fixed flood lights and a rotatable directional light source, and a stereoscopic pair of proprioceptive navigational cameras. The inspection cameras were developed in our laboratory, and are constructed in a geometrically correct imaging configuration that provides 3.5x magnified, natural, easy to view, high quality stereoscopic imagery of the aircraft surface.<sup>6,7</sup> The navigational and proprioceptive cameras provide a wide-angle stereoscopic view of CIMP with respect to the aircraft body that is used by the inspector to control and navigate CIMP. Left and right frames of the inspection or navigational camera pairs are interleaved at 120 Hz on a monitor in the inspection console, and viewed stereoscopically through active eyewear. Figures 1 and 2 show the ANDI and CIMP robots.

## 3. INSPECTION CONSOLE

The inspection console, through the display of stereoscopic imagery delivered by the inspection cameras and the proprioceptive navigational cameras, provides for remote visual inspection of aircraft surface and remote control and navigation of CIMP on the aircraft body. The current inspection console consists of two primary displays and their supporting equipment and a radio transmitter (of the type used to control model vehicles) that controls forward and backward motion, left right steering, camera position and orientation, and lighting selection and orientation. The first display is a monitor that provides live, flicker-free, full spatial and temporal resolution per eye, stereoscopic imagery of either the

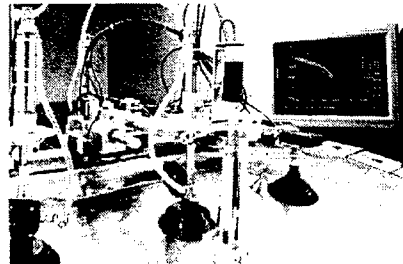


Fig 1. Automated NonDestructive Inspection (ANDI) robot

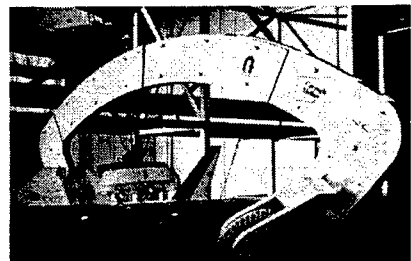


Fig 2. Crown Inspection Mobile Platform (CIMP) robot



Fig 3a. remote live video station

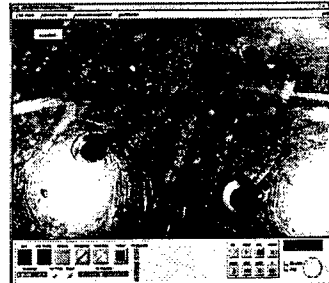


Fig 3b. Intelligent Inspection Window (IIW)

inspection or navigational camera pair. The second is a Silicon Graphics Indy workstation with a GUI that we call the Intelligent Inspection Window (IIW). The IIW performs a variety of tasks: it displays live monoscopic or still stereoscopic imagery; it acts as the operational interface and output display unit to the image enhancement and understanding algorithms that are tied to the menus and buttons of the IIW; and in the future, it will contain facilities for creating, editing, storing and retrieving multimedia records of surface defects. Figure 3a displays the live video station. Figure 3b displays the IIW.

#### **4. IMAGE UNDERSTANDING AND SURFACE DEFECTS - BACKGROUND**

The goal of an image understanding algorithm is to recognize and classify certain surface flaws from the live imagery. The recognition capability of this algorithm is achieved by correlating features of the live imagery with prior or learned knowledge of the surface flaw type. A high correlation of a feature in the live imagery with a flaw type will result in the feature being classified as a flaw of the correlated type. However, developing a successful image understanding algorithm remains a non-trivial challenge due to its dependency on factors such as normal and defect feature characterization, imaging resolution and environment factors such as illumination.

One scenario for application of image understanding algorithms in remote visual inspection is screening large volumes of image data. The image understanding algorithm can conservatively label all plausible defects, so that the inspector separates a larger fraction of actual defects from normal features in a smaller volume of raw data. Another scenario is the interactive use of these algorithms by inspectors to obtain a second opinion about a particular suspicious flaw. The latter possibility is most attractive when the real-time inspector is relatively inexperienced, in general or with respect to a specific problem, compared to the inspector or inspectors whose expertise has been incorporated (explicitly or implicitly) in the algorithm; in this case the computer fulfills a training role in addition to its direct inspection role.

We have developed prototype algorithms that detect surface cracks, surface corrosion, and subsurface corrosion evidenced by surface pillowowing; the pillowowing detection algorithm uses an auxiliary laser spot projector to facilitate precise height mapping of the inspected surface.

##### **4.1. SURFACE CRACKS**

Pressurization and de-pressurization of the aircraft during each flight cycle causes its body to expand and contract in a manner similar to inflating and deflating of a balloon. This expansion and contraction induces stress fatigue at rivets (which hold the aircraft surface skin to its frame), resulting in the growth of cracks outward from the rivets. The growth of a surface crack is essentially exponential in nature. There are many reliable models<sup>8</sup> which predict crack growth quite accurately as a function of the number of pressurization and depressurization cycles. The goal of visual inspection is to detect cracks that are above a minimum threshold length. This threshold length provides a safety margin that allows a crack to be missed in two or three consecutive inspections before it is big enough to endanger the structure of the aircraft.

One of the main methods inspectors use to find cracks is to observe the reflection of directional lighting incident on a rivet location, using a flashlight held at a low angle to the surface.<sup>9</sup> Absence of reflecting light from an edge (line on the surface) emanating from the rivet suggests the possibility of a crack; on the other hand, reflection of light indicates a scratch, which if small is harmless. Therefore the task for an inspector is to first detect edges emanating outwards from the rivets and then to discriminate the cracks from scratches and other edges from that edge pool. Since there may be hundreds of thousands of rivets on the aircraft body, inspection for cracks is a demanding and tiring task for the inspector.

#### 4.2. SURFACE CORROSION

Corrosion is common due to the frequent exposure of the aircraft body to environments such as aircraft operating fluids, liquids spilled in the galleys, lavatory liquids, moisture of sea air, etc. Corrosion can appear as subsurface or surface corrosion. Surface corrosion is recognized by the appearance of corrosion texture. Subsurface corrosion is recognized by the bulging of the affected surface region, called "pillowing". Since corrosion results in a loss of structural material of the affected area, early detection is crucial. Corrosion is also known to induce cracking.

#### 5. SURFACE CRACK DETECTION ALGORITHM

The crack detection algorithm that we have developed is modeled closely on the widely practiced test for detection of cracks using directional lighting. We simulate the directional lighting produced by the inspectors flashlight with a remotely controlled rotatable directional light source on CIMP. The inspector can remotely rotate the light source around a rivet location and examine the resulting live monoscopic or stereoscopic imagery of the rivet and its neighborhood for cracks. In addition, the inspector can run the crack detection algorithm on these images for detection or verification of cracks in the live imagery. The stereoscopic imagery can also be recorded (at slightly reduced resolution) on a standard VHS recorder for future examination or computer processing.

Figure 4a shows a section of an aircraft surface containing two natural cracks and several scratches appearing in the neighborhood of a rivet hole. The first crack emanating from the rivet hole is 1/2 inch in length while the second crack which is partly masked by the scratch beside it is 1/3 inch long. The output of the surface crack detection algorithm is shown in Figure 4b. Edges that are marked in black indicate suspected cracks. Edges marked in grey indicate edges that the algorithm detects but classifies as "non-cracks". The algorithm detects the two known cracks which are marked in black in the output image. It also correctly classifies the edges of the rivet hole and scratches as "non-crack" edges. The other edges that are marked in black are false alarms for cracks. Figure 5 displays a block diagram of the crack detection algorithm.

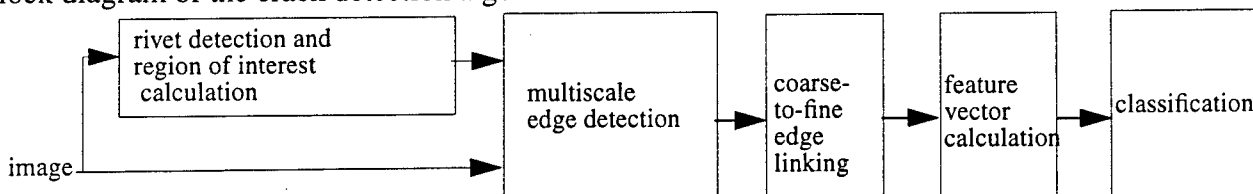


Figure 5. Block diagram of the surface crack detection algorithm

##### 5.1. RIVET DETECTION AND REGION OF INTEREST CALCULATION

The first step of our crack detection algorithm is to find rivet locations in the image. Since cracks appear in the neighborhood of rivets, finding rivet locations enables the algorithm to focus on areas that are most likely to contain cracks. The neighborhood surrounding the rivet that is examined for cracks is defined as the Region of Interest (ROI). The algorithm defines for each detected rivet, a ROI. By focussing on ROIs, the algorithm avoids unnecessary processing of features outside the ROIs; they are not likely to be cracks. Rivets are identified by detecting the circular arc edges made by their heads. Rivet detection and ROI determination consists of the following steps.



Fig 4a. Metal surface with two cracks and several other crack-like features.

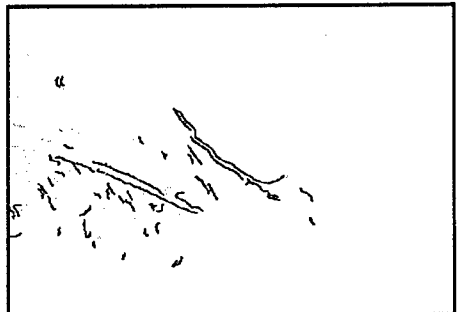


Fig 4b. Output of crack detection algorithm; cracks in black; non-cracks in gray.

1. Smooth with a gaussian filter. Convolve with the x- and y- partial derivatives. Calculate the *gradient magnitude image*.
2. Calculate the histogram of the gradient magnitude image. Define a *high threshold* above which lie a specified fraction of the pixels. Mark the pixels above the high threshold as *edge points*. Link the edge points to create *edges*.
3. Define a *low threshold* below which lie a specified fraction of the pixels. Grow edges with adjacent pixels below the low threshold. Discard edges that contain fewer than 10 pixels.
4. Fit a circular arc to each edge. Discard edges whose fit error is worse than a minimum value. The remaining edges are *rivet head edges*.
5. Merge nearby rivet head edges into *rivets*. Define the *ROI* as a fixed-size box whose center is the rivet centroid.

Figure 6a displays a section of an aircraft surface with three simulated cracks appearing as dark lines from the two rivets. This image is processed by the crack detection algorithm. Figure 6b displays the two ROIs found by the algorithm

## 5.2. MULTISCALE EDGE DETECTION

An ROI in the live image contains a large number of edges, most of which are caused by rivet edges, scratches, dirt marks, lap joints of metal repair plates on the surface and occasionally real cracks. Therefore, we need an analysis framework which lends itself to the discrimination of the small fraction of cracks which are edges of interest to us from those edges that are not of interest.

A crack is typically very small compared to other objects present on the aircraft surface such as rivets, scratches, etc. This motivated us to select a multiscale edge detection framework for the detection and analysis of edges in the ROIs. Multiscale edge detection is defined as detection of edges at multiple scales or equivalently multiple resolutions. Here, scale implies the size of the neighborhood in which intensity changes are detected for edge determination. In multiscale edge detection, edges belonging to small objects appear at low scales or high resolutions while edges of large objects appear at higher scales or coarser resolutions. Therefore, performing multiscale edge detection and analysis on the detected edges in the ROIs will allow us to characterize each edge by assigning a relative size corresponding to the object that created the edge. This is an important feature useful in the discrimination of cracks from non-cracks due to the relatively small size of a typical crack in comparison to other objects appearing on the aircraft surface.

Multiscale edge detection is a two step process where the ROI is first decomposed into different resolutions, usually by successive smoothing, followed by edge detection at each resolution. We have selected wavelet based filters for the projection of the ROI to different resolutions and estimations of intensity variation in them for multiscale edge determination. Wavelets are basis functions with good spatial and frequency localization that is controlled by a scaling parameter attached to the wavelets. Hence, they are a natural choice for multiresolution analysis due to the ease of defining the resolution of interest through the use of the scaling parameter of the wavelet.

We have chosen the cubic spline and its derivative the quadratic spline, described by Mallat,<sup>10</sup> as our scaling and wavelet functions. The frequency responses of these functions are shown in Figure 7. Note that scaling and wavelet functions are low pass and high pass in nature. The wavelet transform of a ROI at scale  $s$  is equal to the convolution of the ROI with a filter derived from the wavelet of scale  $s$ . Since the wavelet we chose is the derivative of a smoothing function, the wavelet transform is equivalent to first smoothing the ROI to a scale  $s$  by a smoothing filter, and then taking its first derivative. This is identical to the sequence of operations undertaken in classical edge detection. Note that the edge points of the ROI at a particular scale corresponds to the extrema of the wavelet transform of that scale. By varying the scaling parameter of the wavelet by successive factors of two (dyadic scale), we generate edges of the ROI at multiple scales. To summarize, listed below are steps taken to generate multiscale edges within each ROI.



Fig 6a. Metal surface with three synthetic cracks and other crack like features

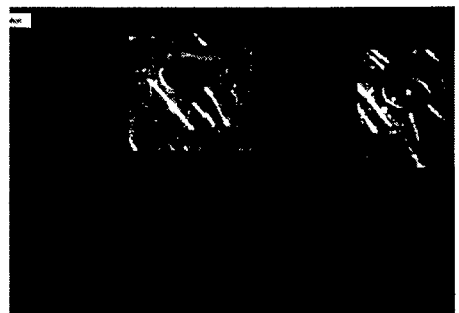


Fig 6b. ROIs found in Fig 6a.

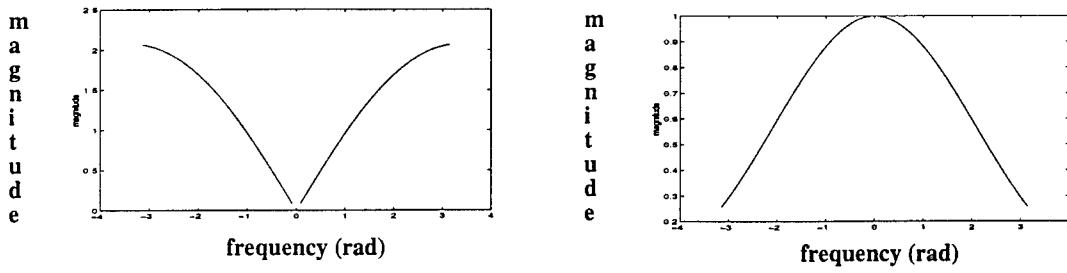


Fig 7. Frequency response of the wavelet and scaling functions

1. Filter each ROI with the dyadic scale filter bank shown in Figure 8a.
2. Calculate the magnitude  $M_i$  and angle  $A_i$  images for each scale of the wavelet transform images  $W_x$  and  $W_y$  using

$$M_i = \sqrt{W_{xi}^2 + W_{yi}^2} \quad A_i = \text{atan}(W_{yi}/W_{xi}) \quad \text{for } i=0,1,2$$

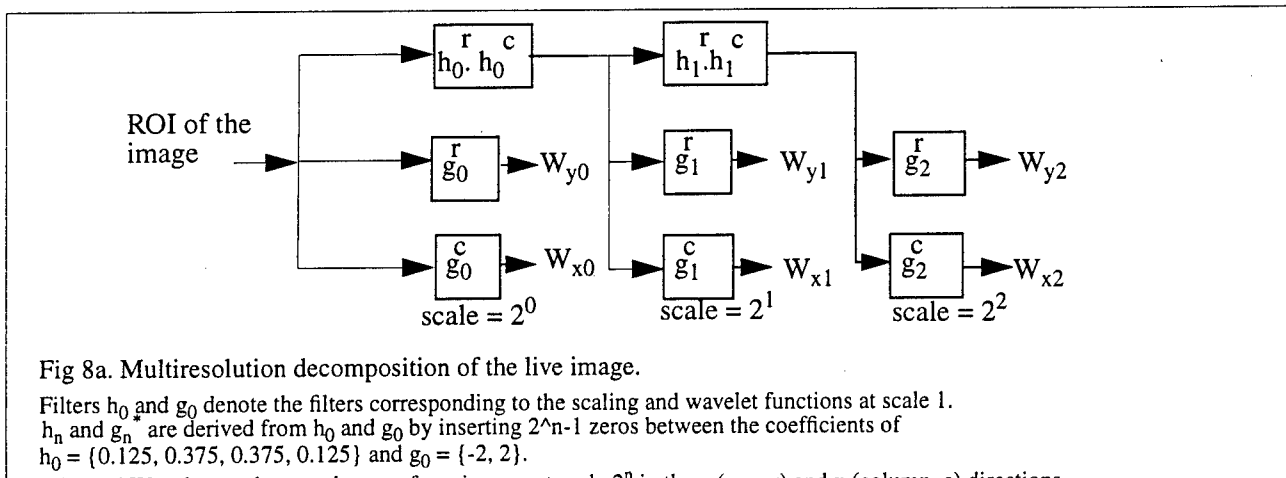
3. Threshold each magnitude image using a threshold calculated from its histogram. Mark pixels above the threshold as *edge points*.
4. Link edge points if their corresponding angles differ by less than a threshold angle. This produces edges that are smoothly varying in direction, and thus characteristic of natural edges such as cracks

This process generates a list of edges in each ROI at each scale. Figure 9 displays the edges in Figure 6b..

### 5.3. COARSE-TO-FINE EDGE LINKING

Multiscale edge detection described in the previous section generates edges, at several scales, for each ROI in the image. It is clear in Figure 9 that edges of the same object are present in more than one scale. For example, parts of the rivet head edges appear in all three scales while the simulated cracks shown in Figure 6a appear only at the first two scales. The next step of this process is to assign to each edge a feature value that will provide information about the size of the object that produced the edge. This size information is useful in the discrimination of edges of cracks from edges of non-cracks appearing in each ROI.

We model an edge belonging to an object appearing at multiple scales, as the propagation of that edge along scale (or resolution) space. We define propagation depth as the number of scales in which the edge appears. We then assign a propagation depth value to each edge at scale 1. The propagation depth captures the size information of the object revealed by multiscale edges. For example, edges of objects that are small will have a lower propagation depth than edges of objects that are large. This explains why edges corresponding to the simulated cracks (actually black fibers of approximately  $10 \mu\text{m}$  diameter), appear only in two scales, whereas edges of the rivets and scratches appear in all three scales in Figure 9.



We use a coarse-to-fine edge linking process to find the propagation depth of all edges appearing at scale 1. The coarse-to-fine edge linking process attempts to trace an edge from a coarse resolution (high scale) to a fine resolution (low scale). We define active pixels as those pixels that belong to the edge of reference. Given below are the steps of the coarse-to-fine edge linking process.

1. Assign to each edge, in each scale (scale = 1, 2, 4), a feature vector with the following components:
    - a. Centroid of the active pixels
    - b. Average wavelet magnitude of the active pixels
    - c. Number of active pixels that constitute the edge
  2. For each edge  $E$  in scale 4, define a window centered on its centroid in scale 2. Find all unlinked edges  $\{e\}$  in scale 2 that are within the window. Find the edge  $e_i$  of  $\{e\}$  that produces the minimum weighted square difference between itself and  $E$ . Link  $E$  to  $e_i$ .
  3. Do (2) for each edge in scale 2 with edges in scale 1
  4. For each edge in scale 1, count the number of links (how deeply it is connected); this is the *propagation depth* of that edge.
- Figure 8b illustrates the coarse-to-fine edge linking process. Note that edges A and B have propagation depths of 1 and 2 respectively.

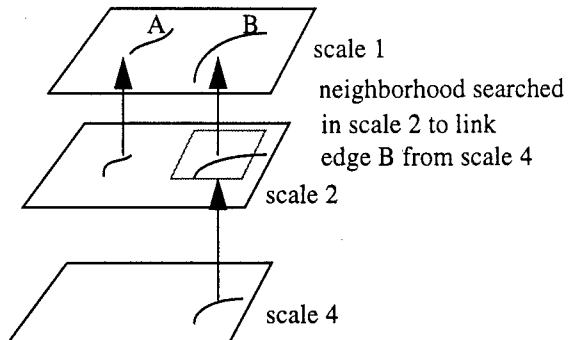


Fig 8b. Coarse-to-fine edge linking of edges A and B

#### 5.4. FEATURE VECTOR CALCULATION

We are now in a position to assign a feature vector for each edge in scale 1. The feature vector assigned to the edge will characterize its properties so that edges of cracks can be discriminated from edges of non-cracks based on classification of the feature vectors. We have selected the following attributes of an edge to be included in a feature vector:

1. Average wavelet magnitude of active pixels;
2. Propagation depth number;
3. Average wavelet magnitudes of any linked edges in scale 2 and scale 4;
4. Signs of  $\text{sum}(W_x)$  and  $\text{sum}(W_y)$  where  $W_x$  and  $W_y$  are the coefficients in the x- and y-directions of at scale 1;
5. Number of active pixels.

The wavelet magnitudes at each scale of an edge that propagates down multiple scales was included because it has been shown that under certain conditions, these values characterize the shape of an edge, e.g., a step or a ramp edge.<sup>10</sup>

#### 5.5. FEATURE CLASSIFICATION

The feature vectors are classified into one of two classes, cracks or non-cracks. We use a six input, 1 hidden layer with four elements and one output neural network trained under backpropagation with momentum to classify the feature vectors. We generated 14 feature vectors of simulated cracks and 30 feature vectors of non-cracks corresponding to rivet edges and scratches. A training set of 7 simulated cracks and 15 non-cracks were used to train the network. After 1000 training cycles, the network was approximately 72% accurate in predicting cracks with a 27% false alarm rate for the test set edges.

Figure 6a is repeated in Figure 10a. The output image of the algorithm is shown in Figure 10b.

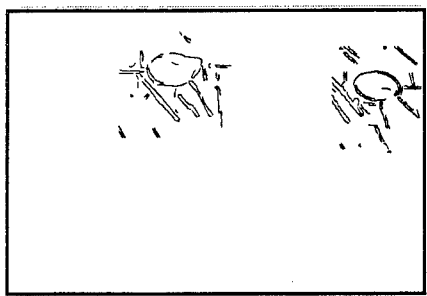


Fig 9a. Edge image at scale 1

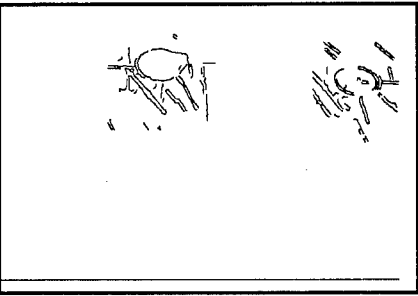


Fig 9b. Edge image at scale 2

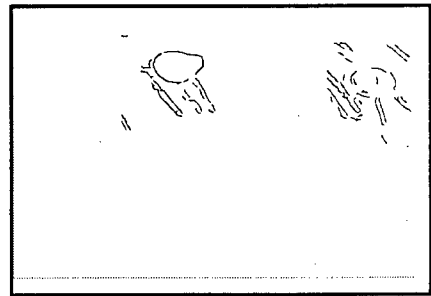


Fig 9c. Edge image at scale 4



Fig 10a. Metal surface with three synthetic cracks and other crack like features

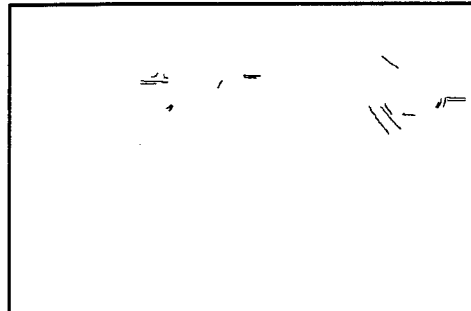


Fig 10b. Output of the crack detection algorithm.

## 6. SURFACE CORROSION DETECTION ALGORITHM

A comprehensive corrosion detection algorithm needs to detect both surface and subsurface corrosion. Surface corrosion is detected by texture visually suggestive of corrosion, whereas subsurface corrosion is detected by distortion (“pillowing”) of the surface. Thus a comprehensive algorithm requires an image and a shape profile of the inspection surface to detect both types of corrosion. In this section, we describe the algorithm we developed to detect surface corrosion. Section 7 describes our subsurface corrosion detection apparatus and algorithm.

We detect surface corrosion by a binary segmentation of the image into regions of texture suggestive of corrosion and regions of texture suggestive of freedom from corrosion. Texture can be well described by scale and orientation. This has resulted in the development of many methods based on multiresolution, multiorientation based approaches that allow scale and orientation based analysis of textures.<sup>11,12</sup> Our corrosion detection algorithm, shown as a block diagram in Figure 11, is based on a similar method.

Figure 12a displays an image of a corroded section of an aircraft surface. Figure 12b shows the output of our surface corrosion detection algorithm; bright and dark areas respectively indicate corrosion and corrosion free areas in this image. The following three sections outline the three modules of the processing pipeline indicated schematically in Figure 11.

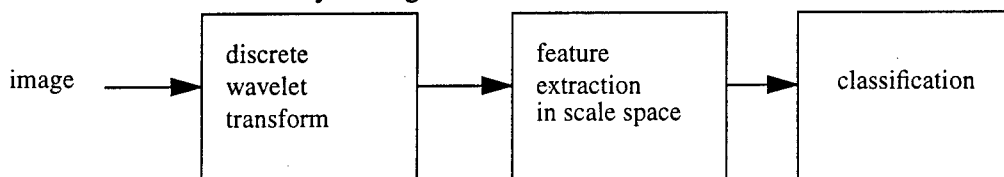


Fig 11. surface corrosion detection algorithm



Fig 12a. surface with corrosion



Fig 12b. output of corrosion detector

## 6.1. DISCRETE WAVELET TRANSFORM (DWT)

In the first module we perform a multiresolution, multiorientation decomposition of the image using the discrete wavelet transform (DWT). The DWT can be thought of as filtering of the image into sub-bands by an array of scale and orientation specific filters. Since wavelets have good spatial and frequency localization, the wavelet coefficients provide a good characterization of the texture.

We have selected Daubechies D6 orthogonal wavelet (coefficients {0.3327, 0.8069, 0.4599, -0.1350, -0.0854, 0.0352}) for the DWT. The orthogonal wavelet prevents correlation between scales in the decomposition of the image by DWT. We perform a three-level wavelet decomposition of an image which results in 10 sub-bands. Figure 13 displays the corresponding sub-bands created by the transform.

## 6.2. FEATURE EXTRACTION

In the second module, feature extraction, the image is first divided into non-overlapping blocks of size 8x8 pixels. For each block, a 10-dimensional feature vector is assigned whose components represent energy within the block in each of the wavelet transform frames  $W_{j=1:10}$  shown in Figure 13. Letting the energy of block  $B(i)$  in  $W_j$  be given by  $E_j(i)$ , we have:

$$E_j(i) = \sum_{(k, l) \in B(i)} w_j(k, l)^2$$

where  $w_j(k,l)$  is the wavelet coefficient at  $(k,l)$  in the wavelet transform frame  $W_j$ . The feature vector is normalized by the total energy of the block.

## 6.3. FEATURE CLASSIFICATION

In the third and last module we classify the features developed in the previous modules. We generated a training and test set of 2400 vectors (1200 each corrosion and corrosion free vectors), using a set of images of corrosion and corrosion free surfaces. A clustering algorithm was applied on the training sample vectors to find three prototype vectors representing clusters of the corrosion vectors and five prototype vectors representing clusters of corrosion free vectors in the training set. The algorithm uses a 1 nearest neighbor method to classify a new feature vector into corrosion or corrosion free classes based on its distance to the prototype vectors. The trained algorithm was able to detect 95% of the corrosion vectors of the test set.

Figure 14a displays an image of a corroded section of an aircraft surface. Figure 14b shows the output of the surface corrosion detection algorithm. Bright and dark areas indicate corrosion and corrosion free areas in the image.



Fig 14a. surface with corrosion

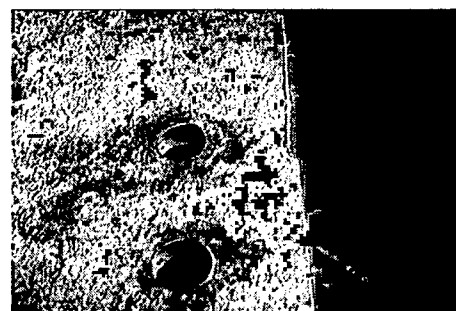


Fig 14b. output of corrosion detector

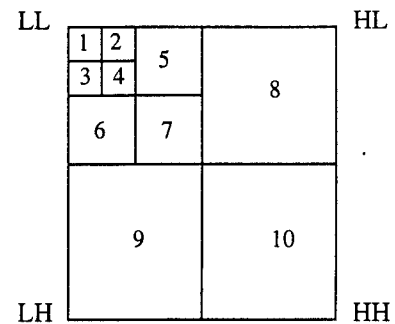


Fig 13. Three-level wavelet decomposition yielding sub-bands 1 to 10.

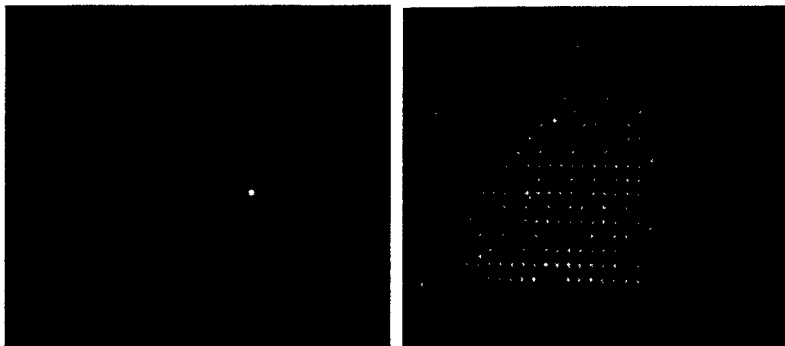


Fig 15: Left and right perspectives on the projected 17x17 laser grid. The blue dot in the right image [leftmost] corresponds to the red dot [near upper left of grid pattern] in the left image. The red dots in the right image are candidates that the matching algorithm rejected.

## 7. SUBSURFACE CORROSION DETECTION SYSTEM

Subsurface corrosion may be visible externally because of the surface “pillowing” it induces. Pillowing is a change in skin surface shape rather than surface texture; it is detectable as an increase in skin surface height toward the center of each rivet row-and-column-bounded rectangle over a region suffering from subsurface corrosion. Stereoscopic cameras are well suited to creating surface altitude maps, but the low density of high contrast features on aircraft sheet metal expanses makes the critical step of identifying corresponding points in left and right images very difficult. We circumvent this difficulty by illuminating the surface with a laser that projects a square grid of 17x17 spots; by concentrating on these spots rather than on natural textural features of the surface, the correspondance problem is easily solved.

We illustrate this system with Figure 15, which shows the dot pattern from left and right stereoscopic perspectives, one dot in the left image marked by a small red square [near the upper left of the grid, in b&w rendering], several candidates, in color, for the corresponding dot in the right image, and the dot identified as the matching one shown also in red [the leftmost small square, in b&w rendering].

Figure 16 shows the result of applying this method to a surface step (above, actually a rubber stopper) and to a slightly wrinkled piece of aircraft belly skin that is sloping downward from back to front (below).

## 8. SUMMARY DISCUSSION AND FUTURE WORK.

### 8.1. CIMP AND REMOTE VISUAL INSPECTION

We have successfully demonstrated CIMP’s remote control and imaging capability to Northwest Airlines at their Minneapolis 747 maintenance and inspection facility and to US Airways at their Pittsburgh maintenance and inspection facility. Our demonstration showed that state-of-the-art 3D stereoscopic video technology implemented by us and operated by inspectors not specifically trained in its use, delivers imagery of sufficiently high visual quality that aircraft inspectors and NDI supervisors were willing to accept it (and sometimes prefer it) as an alternative to direct visual inspection.

### 8.2. SURFACE CRACK DETECTION ALGORITHM

Based on our experience with the algorithm and insights gained through limited testing, we are convinced that the multiscale edge analysis framework on which the algorithm is based is an appropriate framework for extraction and analysis for aircraft surface cracks. We are encouraged by its performance in detecting simulated cracks though it was trained and tested using only a small sample of simulated cracks. Anticipated future development needs include: adding suitable new features to the feature vectors that describe edges, e.g., pairing adjacent rising and falling edges, linking neighboring edges with similar feature vectors, i.e., edges that presumably belong to a single object, data fusion involving multiple images of the same region under dynamic lighting conditions, and, for all of these, training and testing with a richer library of natural surface cracks.

### 8.3. SURFACE AND SUBSURFACE CORROSION DETECTION ALGORITHMS

The surface corrosion detection algorithm is successful in detecting surface corrosion as indicated by the performance on the test images. We plan on training and testing the algorithm with a wider array of corrosion test samples. The subsurface corrosion detection algorithm using a laser spot grid projector produces surface profile maps that lab experiments indicate will be useful for detecting pillow ing and other problems that are manifested as surface height variations.

## 9. CONCLUSION

Our research efforts are directed at testing the hypothesized feasibility and advantages of remote visual inspection. To test this premise, we have built CIMP, a prototype mobile robot that carries a remote imaging system and an inspection console that allows the inspector to view monoscopic or stereoscopic imagery of the remote inspection surface. In addition, the inspection console provides the inspector with a library of image enhancement and understanding algorithms that can be used to process, enhance and understand the remote imagery to aid the detection of surface defects. Through field testing, we have demonstrated successfully that our remote imaging system delivers imagery of sufficient high visual quality that aircraft inspectors are willing to accept it as an alternative to direct visual inspection. In this paper, we have described image understanding algorithms for surface crack and corrosion detection and subsurface corrosion detection, and we have reported test results that are promising. We believe that further development of these algorithms based on their adaptation to real world environments through extensive testing will significantly increase their probability of flaw detection and make them successful and productive tools for remote visual inspection.

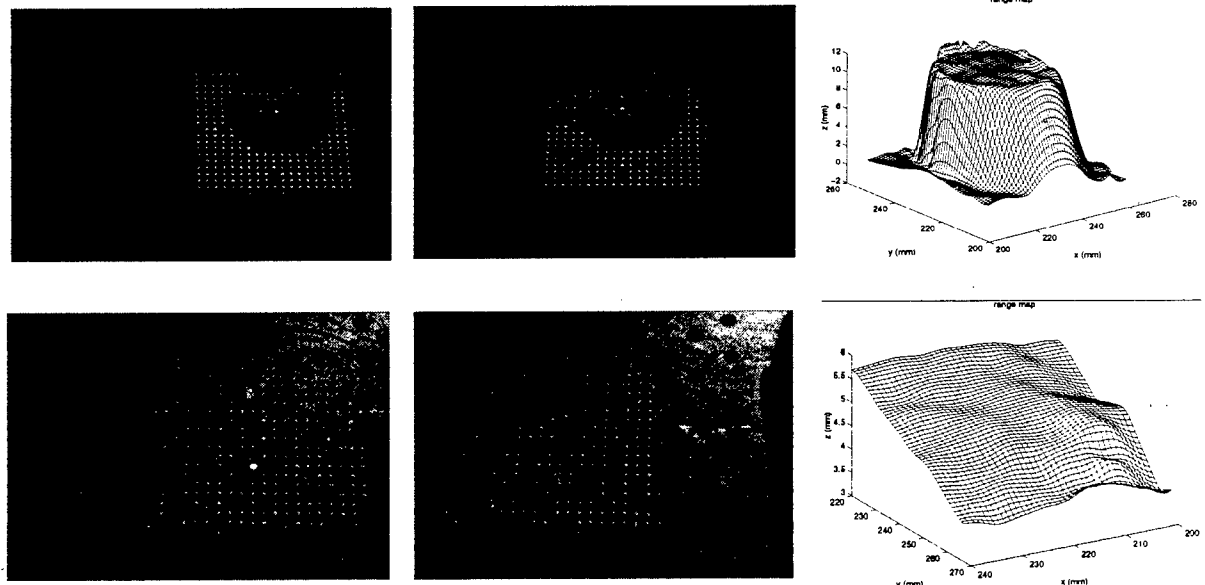


Fig 16. Method of detecting subsurface corrosion by elevation mapping of the visible surface. Top three frames are left and right perspectives of the projected laser grid illuminating a rubber stopper, and the corresponding depth map. Bottom three frames are left and right perspectives of the projected laser grid illuminating a sloping aircraft sheet metal surface, and the corresponding depth map. Elevation resolution is about 0.5 mm.

## **10. ACKNOWLEDGMENTS**

ANDI was a joint project of the Carnegie Mellon Research Institute and the Robotics Institute, with W.M Kaufman and M.W. Siegel, co-PI's, funded by the FAA Aging Aircraft Research Program. CIMP was a project of the Robotics Institute and Aircraft Diagnostic Corporation, M.W. Siegel PI, funded partially by the Ben Franklin Technology Center of Western Pennsylvania (grant RR 10032) with in-kind assistance from US Airways and valuable cooperation from Northwest Airlines. The basic research on which the stereoscopic video system implementation is based was funded by DARPA's High Definition Systems program. The authors wish to thank Gregg Podnar for the engineering design and implementation of CIMP and its geometrically correct stereoscopic camera system, and Alan Guisewite for his constant technical support.

## **11. BIBLIOGRAPHY**

1. C. Seher, "The national aging aircraft nondestructive inspection research and development plan", Proceedings of the International Workshop on Inspection and Evaluation of Aging Aircraft, May 21, 1992.
2. W. T. Shepherd, "Human factors in aircraft maintenance and inspection", Conference on aging aircraft and structural airworthiness," NASA conference Publication 3160, pp 301-304, 1991.
3. P. D. Gunatilake, M. W. Siegel, A.G. Jordan and G. W. Podnar, "Image Enhancement and Understanding for Remote Visual Inspection of Aircraft Surface", Proceedings of the SPIE Conf. of Nondestructive Evaluation of Aging Aircraft, Airports and Aerospace Hardware, Vol 2945, pp 416-427, December 1996.
4. M. W. Siegel, "Automation for Nondestructive Inspection of Aircraft ", Conference on Intelligent Robots in Field, Factory, Service and Space (CIRFFSS'94), Paul J Weitz (NASA/JSC), ed., AIAA, AIAA/NASA, pp. 367 - 377, Houston TX, March 1994.
5. M. W. Siegel, W. M. Kaufman and C. J. Alberts, "Mobile Robots for Difficult Measurements in Difficult Environments: Application to Aging Aircraft Inspection", Robotics and Autonomous Systems, Vol. 11, pp 187 - 194, July 1993.
6. S. Grinberg, G. W. Podnar, and M. W. Siegel, "Geometry of Binocular Imaging", Proceedings of the SPIE/IST Conference (San Jose), ed., SPIE/IST, SPIE/IST, February 1994.
7. V. S. Grinberg, G. W. Podnar, and M. W. Siegel, "Geometry of Binocular Imaging II: The Augmented Eye", Proceedings of the SPIE/IST Conference (San Jose), ed., SPIE/IST, SPIE/IST, February 1995.
8. P Tong, K Arin, D.Y. Jeong, R. Grief, J.C Brewer and S.N. Bobo, "Current DOT research on the effect of multiple site damage on structural integrity", NASA conference Publication 3160, pp 111-157, 1991.
9. S.N. Bobo," Visual Nondestructive Inspection Advisory Circular", 1993.
10. S. Mallat and S. Zhong, "Characterization of signals from multiscale edges", IEEE Trans Patt. Anal. and Mach. Intell., vol 12, pp 629-639, July 1990.
11. A.C. Bovik and M. Clark, "Multichannel texture analysis using localized spatial filters", IEEE Trans. Signal Processing, vol. 39, pp 2025-2043, Sept 1991.
12. M. Unser and M. Eden, "Multiresolution feature extraction and selection for texture segmentation", IEEE Trans. on Patt. Anal. and Mach. Intell., vol. 11, No. 7, pp: 717-728, 1989.

# Aging of Airframe Aluminum Alloys: From Pitting to Cracking\*

Robert P. Wei

Department of Mechanical Engineering and Mechanics  
19 Memorial Drive West  
Lehigh University  
Bethlehem, PA 18015-3085

## EXTENDED ABSTRACT

The processes of aging, or damage accumulation in airframe aluminum alloys is considered to be dominated by localized (or pitting) corrosion in the early stage, and by corrosion fatigue crack growth in the later stage (see Fig. 1). Corrosion fatigue cracking was found to nucleate at severe corrosion pits. These pits formed as a result of dissolution of the matrix that surround clusters of constituent particles in the alloys that is induced by the particle-matrix galvanic corrosion couple. Cracking away from the nucleating corrosion pits would undergo a regime of chemically-short crack growth, with anomalously higher growth rates than that to be expected from conventional long-crack data. In this presentation, a perspective overview of the current state of understanding of the aging of aluminum alloys used in commercial and military airframes is given. Experimental data on pitting, crack nucleation, and short- and long-crack growth are presented to illustrate the processes of aging. A preliminary probabilistic model for life prediction that integrates the individual processes is presented, and the linkages to NDE is discussed. It must be recognized that the results are gleaned from ongoing research at the author's laboratory. They provide an overall perspective for a multidisciplinary approach and serve as a road map for the process for integrating information on damage accumulation. No attempt is made here to cite the relevant literature on this subject.

**Keywords:** Corrosion, Localized Corrosion, Corrosion Fatigue, Aluminum Alloys, NDE, Life Prediction

### Particle Induced Pitting Corrosion

Studies of localized corrosion were focused upon pitting corrosion as a precursor to corrosion fatigue cracking in the 2024-T3 and 7075-T651 (bare) alloys, and were carried out principally at room temperature in 0.5M NaCl solutions. The results show that localized corrosion (pitting) resulted from galvanic coupling of the matrix with constituent particles in the alloys. Pitting was found to depend strongly on temperature and solution pH. The pitting rate increased with increasing temperature (corresponding to an activation energy of about  $40 \text{ kJ mol}^{-1}$ ), and was higher at more basic pH levels. The pitting process is very complex and involved 3-D interactions with the constituent particles. Corrosion sensitivity is orientation dependent; being more severe in the thickness orientations because of local segregation of these constituent particles.

Two modes of pitting corrosion were identified: namely, (i) **general** pitting over the specimen surface, and (ii) **severe** localized pitting at selected sites. General pitting occurs almost immediately upon specimen immersion,

---

\* Research supported by the Air Force Office of Scientific Research under Grant Nos. F49620-93-1-0426 and F49620-96-1-0245, and by the Federal Aviation Administration under Grant No. 92-G-0006.

and leads to the formation of small, shallow pits over the entire specimen surface. Each pit is clearly identified with a constituent particle on the specimen surface, with particle or matrix dissolution determined by the nature (anodic or cathodic) of the particle. Severe localized pitting occurred at selected sites, and was attributed to the interactions of the matrix with *a cluster or clusters* of constituent particles. The particle clusters form local galvanic cells to sustain continued matrix dissolution, and resulted in the larger and deeper pits.

Particle induced *general* pitting has been observed by scanning electron microscopy (SEM) (Fig. 2), and by transmission electron microscopy (TEM) (Fig. 3). Typical *severe* pits formed from clusters of constituent particles are shown in cross section, along with an inset of the pits at the specimen surface, in the SEM micrographs (Fig. 4). The larger of the two pits is approximately 500  $\mu\text{m}$  long and 70  $\mu\text{m}$  wide at the surface, and approximately 300  $\mu\text{m}$  deep at this section; the overall shape reflects the planar distribution of constituent particles in this alloy. A comparison of the deeper severe pit in Fig. 4 with the SEM microfractograph of a fatigue crack origin (a corrosion pit represented by the dark region at the center of the microfractograph) in Fig. 5 shows that their overall features are nearly identical. The associated surface features of the fatigue origin (not shown) are also identical to those shown in the inset in Fig. 4. The 3-dimensional nature and complex form of the severe pits are illustrated by the SEM micrographs of the replica of a typical severe pit, in plan and side view, in Fig. 6. The individual rounded features are consistent with galvanic corrosion of the matrix by the cathodically behaving constituent particles in the alloy(*cf.* Figs 2 and 3).

### Fatigue Crack Nucleation (Transition from Pitting to Crack Growth)

Corrosion fatigue crack nucleation reflects the competition between pitting and fatigue crack growth, and is characterized by the transition to fatigue crack growth from a growing pit. Two criteria for this transition have been proposed and validated. They are: (i) the cyclic stress intensity range ( $\Delta K$ ) for an equivalent crack must exceed the fatigue crack growth threshold  $\Delta K_{th}$ , and (ii) the time-based fatigue crack growth rate must exceed the pit growth rate; i.e.,

$$\Delta K \geq \Delta K_{th} \quad \text{and} \quad \left( \frac{dc}{dt} \right)_{crack} \geq \left( \frac{dc}{dt} \right)_{pit} \quad (1)$$

where  $c$  is the half-length of the equivalent crack or the corresponding pit dimension at the surface. The transition criteria may be represented graphically by a corrosion/fatigue map. The map delineates the transition  $\Delta K_{tr}$  in relation to the cyclic load frequency  $f$ , with the applied cyclic stress range as a parameter. A typical map, showing data on the pit-to-crack growth transition in a 2024-T3 alloy, is given in Fig. 7.

### Fatigue Crack Growth (Chemically Short Cracks)

Studies of the transition from pitting to corrosion fatigue crack growth (or crack nucleation) suggested that the pit size at transition is in the range of 40 to 200  $\mu\text{m}$  (or 0.04 to 0.2 mm). The extent of fatigue crack growth of interest (for example, in aircraft fuselage lap joints), on the other hand, is on the order of a few millimeters. As such, characterization and modeling of the early stage (or chemically short regime) of corrosion fatigue crack growth is important to the accurate and reliable assessment of service lives of aircraft structures.

Experiments on 2024-T3 (bare) and 7075-T651 alloy sheets in 0.5M NaCl solutions, at room temperature and 10 Hz, for crack lengths from 0.5 to 15 mm, showed chemically short-crack growth behavior. The behavior is quite complex and depends on  $\Delta K$  and dissolved oxygen concentration (see Fig. 8, for example). The effect manifested itself in increased crack growth rates at a crack length of 0.5 mm, by as much as a factor of two, at the lower  $\Delta K$  levels (see, for example, data for  $\Delta K = 5 \text{ MPa}\sqrt{\text{m}}$  in Fig. 8), and in a subsequent decrease to the long-crack rates at crack lengths that depend on  $\Delta K$ . The short-crack effect gradually disappeared at higher  $\Delta K$  levels; the particular level depended on oxygen concentration. The short-crack effect is attributed to the decrease in dissolved oxygen at the crack tip with crack prolongation. The cause for the disappearance of short-crack effect with increasing  $\Delta K$ , however, is unclear and is under active investigation.

### A Mechanistically Based Probability Approach To Life Prediction.

To demonstrate the integration of the damage processes into a mechanistically based probability framework, a dominant flaw, probability model for pitting and corrosion fatigue was formulated. This model assumed pitting corrosion to be at a constant volumetric rate, and fatigue crack growth to follow a simple power-law model. Transition from pit (hemispherical) to crack (semi-circular) was based on the use of only the first of two criteria in (1). The overall model incorporated initial defect (pit) size  $a_o$ , pitting current coefficient  $I_{P_o}$ , fatigue crack growth rate coefficient  $C_F$ , and fatigue crack growth threshold ( $\Delta K_{th}$ ) as random variables. Specifically, the time to failure was found to be:

$$t_f = \frac{2\pi n F \exp\left(\frac{\Delta H}{RT}\right)}{3MI_{P_o}} \left[ \left( \frac{\pi^{1/2} \Delta K_{th}}{2.2 \Delta \sigma} \right)^6 - a_o^3 \right] + \frac{2\pi^{3/2} \left[ \frac{2.2 \Delta \sigma}{\pi^{1/2} \Delta K_{th}} - a_f^{-1/2} \right]}{v C_F (2.2 \Delta \sigma)^3} \quad (2)$$

The first term represents the contribution from pitting corrosion, and the second term, fatigue crack growth. In (2),  $a_f$  is the final crack size,  $v$  is the cycle frequency,  $\rho$  is the density,  $M$  is the molecular weight, and  $n$  is the valence of the aluminum,  $\Delta H$  is the activation energy,  $F$  is Faraday's constant, and  $R$  is the universal gas constant. Typical results showing the influences of loading frequency are shown in Fig. 9. The potentially significant impact of corrosion may be seen from the crack initiation life. This model has been extended further to account for corrosion and fatigue from an open circular hole, and incorporates a further transition from the semi-circular crack at an open-hole to a through-thickness crack.

### Effect of Pitting Corrosion on Fatigue Life

The significance of corrosion pits on fatigue may be seen from an estimate of their effect on fatigue (or crack growth) life. In a recent re-examination of a study by Harmsworth on effect of pre-corrosion on fatigue in a 2024-T4 aluminum alloy, it was found that the observed fatigue lives could be correlated with the crack growth lives from the measured initial pit sizes. In other words, crack nucleation time, if present at all, could be reasonably neglected. The observed fatigue life, therefore, may be governed by the initiating damage (particle or pit) size and the rate of subsequent crack growth. For simplicity, fatigue crack growth is assumed to follow a power-law of the following form:

$$\frac{da}{dN} = C_F (\Delta K - \Delta K_{th})^n; \quad \Delta K = \beta \Delta \sigma \sqrt{a} \quad (3)$$

where  $C_F$  is crack growth rate coefficient;  $\Delta K_{th}$  is the fatigue threshold  $\Delta K$ ;  $\beta$  is a geometric parameter; and  $n$  is the power-law exponent. The material parameters  $C_F$  and  $\Delta K_{th}$  are both functions of the test environment, as well as temperature and other factors.

For these estimates, the initiating constituent particle, or severe corrosion pit, is again assumed to be hemispherical in shape and to be equivalent to a semi-circular crack with the same radius (with  $\beta = 2.2\pi^{1/2}$ ). Because the initiating particle and pit sizes are very small, the final crack size at fracture can be neglected, and the predicted fatigue (crack growth) life is given, from integration of (3), simply by:

$$N_F \approx \frac{2}{(n-2)C_F \beta^2 \Delta \sigma^2 (\Delta K_i - \Delta K_{th})^{(n-2)}} \left[ 1 + \frac{(n-2)\Delta K_{th}}{(n-1)(\Delta K_i - \Delta K_{th})} \right] \quad (4)$$

where  $\Delta K_i$  correspond to the initial pit radius  $a_o$ . Using  $C_F = 1.3 \times 10^{-11}$  and  $3.95 \times 10^{-11}$  (m cyc<sup>-1</sup>)(MPa<sup>1/2</sup>m)<sup>-3.55</sup>, and  $\Delta K_{th} = 0.95$  and  $0.5$  MPa<sup>1/2</sup>m for (dry) air and  $0.5M$  NaCl solution, respectively, and  $n = 3.55$  (estimated from data on the 2024-T3 alloy), the predicted fatigue lives at different stress levels (from 100 to 400 MPa) are calculated, for an initial pit radius of 10 to 200  $\mu\text{m}$ , and are shown in Fig. 10. For the estimated life in (dry) air, a particle radius of 10  $\mu\text{m}$  was used. The choice of  $\Delta K_{th}$  is somewhat arbitrary, and reflects a recognition that the levels associated with a corrosion pit may be substantially lower than that observed from long-crack experiments.

There is a striking resemblance of Fig. 10 to the conventional S-N data for corrosion fatigue; with a reduction in life and a lowering of the endurance limit. The reductions in fatigue lives are clearly identified with increases in the size of a corrosion pit. The response may be interpreted simply in terms of the effect of pre-corrosion (or pre-pitting). It may be viewed also as a reflection of fatigue at different loading frequencies; with the lower frequencies producing larger pits and shorter fatigue lives. The interpretations are consistent with the set of transition criteria that have been proposed (see (1)), and provide a framework for airworthiness and fatigue life assessments.

## Implication for NDE

Figure 10 provides a reasonable estimate of the impact of pitting (and other forms of corrosion damage) on fatigue life. Coupled with the information on pitting *per se*, it serves as a quantitative basis for assessing the challenges that confront NDE. At a stress of 300 MPa (approximating the stress at the inner bore of a rivet hole), a corrosion pit of 200  $\mu\text{m}$  in depth would result in a reduction in fatigue life by nearly two orders of magnitude from the uncorroded state (*i.e.*, from one million to less than 20,000 cycles). This pit size is to be viewed as an order of magnitude estimate of the ‘damage’ that would need to be detected with reliability by NDE. The damage (corrosion pits) is of complex geometry and would, in general, be hidden. Therein lies the challenge for NDE. It is hoped that the NDE community would broaden its interactions with the structures and materials communities to address the common challenge of ensuring the airworthiness and operational readiness of civil and military aircraft.

**Information May Be Obtained From:**

1. P. Wei and D. G. Harlow, "Corrosion and Corrosion Fatigue of Airframe Materials", U.S. Department of Transportation, Federal Aviation Administration, DOT/FAA/AR-95/76, Final Report, National Technical Information Service, Springfield, VA 22161, February 1996.
2. Robert P. Wei, "Corrosion Fatigue: Science and Engineering", in *Recent Advances in Corrosion Fatigue*, Sheffield, UK 16-17 April 1997, to appear.
3. Robert P. Wei and D. Gary Harlow, "Aging of Airframe Materials: From Pitting to Cracking", Proceedings of First Joint DoD/FAA/NASA Conference on Aging Aircraft, Ogden, Utah, July 1997, to appear.

### Crack Nucleation and Growth

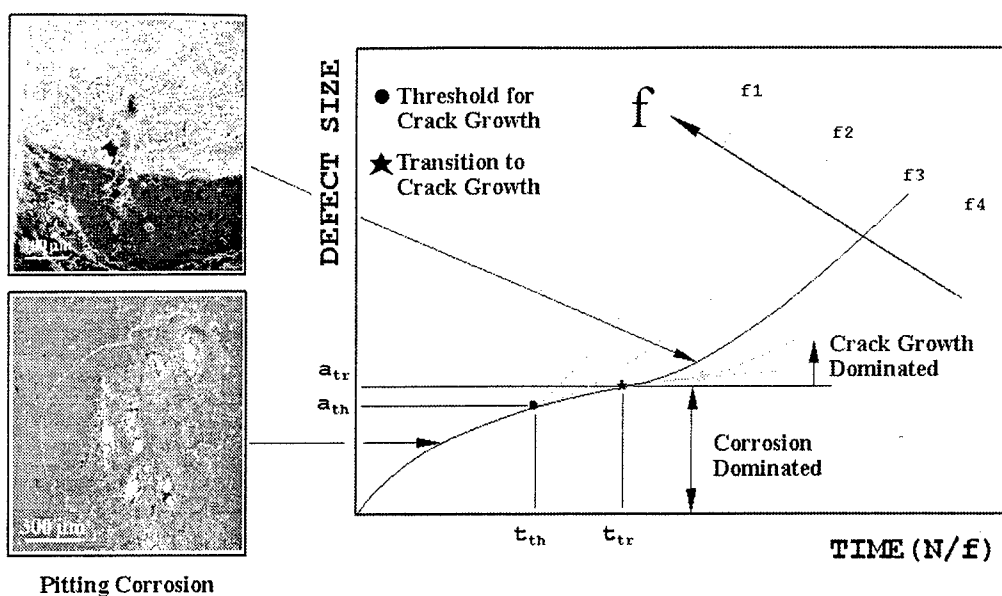


Figure 1: Schematic representation of pitting corrosion and corrosion fatigue.

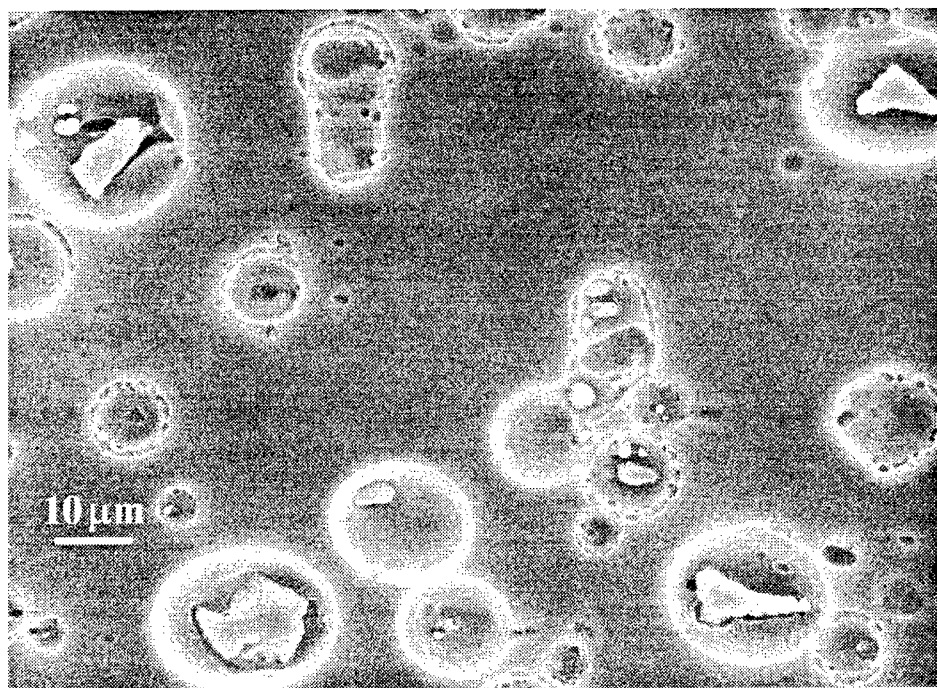


Figure 2: Scanning electron micrograph showing pitting associated with micro-constituent particles.

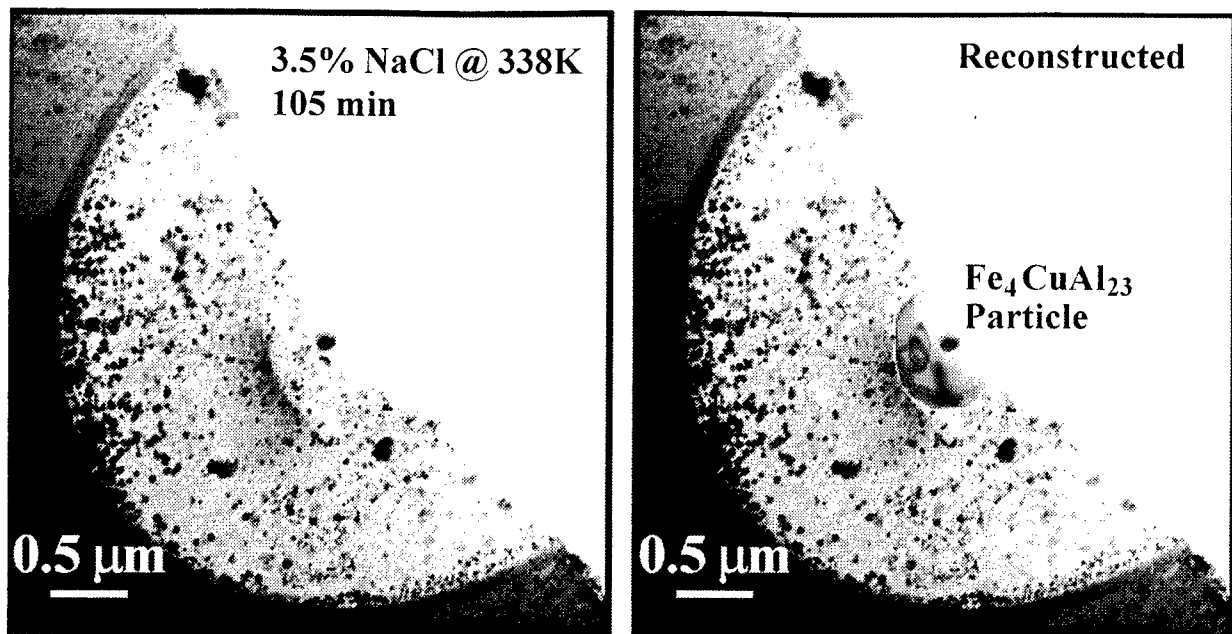


Figure 3: TEM micrograph of 7075-T651 aluminum alloy showing oxide left behind by particle-induced corrosion: (a) residual oxide, and (b) reconstructed image showing position of original particle.

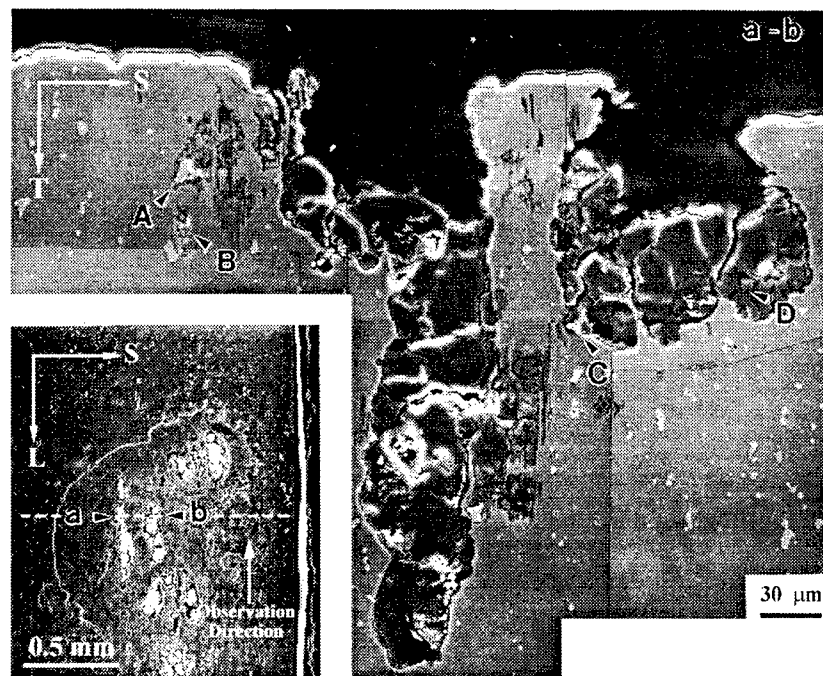


Figure 4: SEM micrograph of the cross-section of severe corrosion pits in a 2024-T3 alloy (TS) surface along with an inset, showing the corresponding surface appearance of the pits.

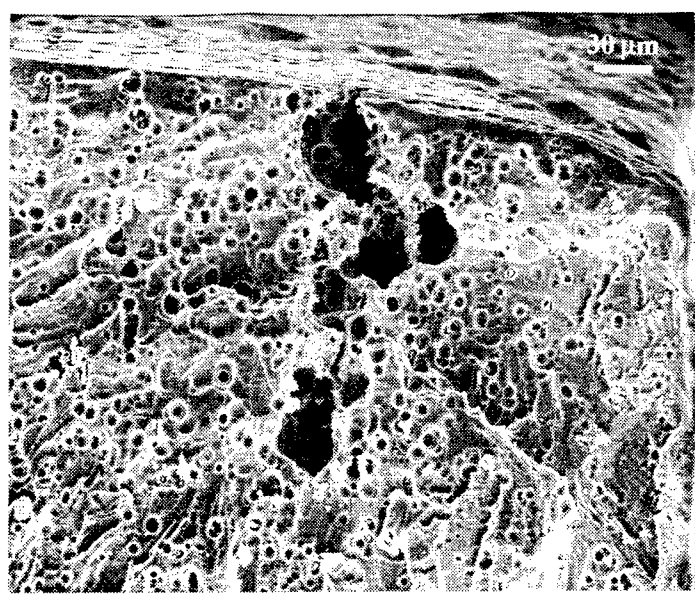


Figure 5: SEM microfractograph of fatigue fracture surface of a 2024-T3 alloy showing a severe corrosion pit as the crack nucleus.

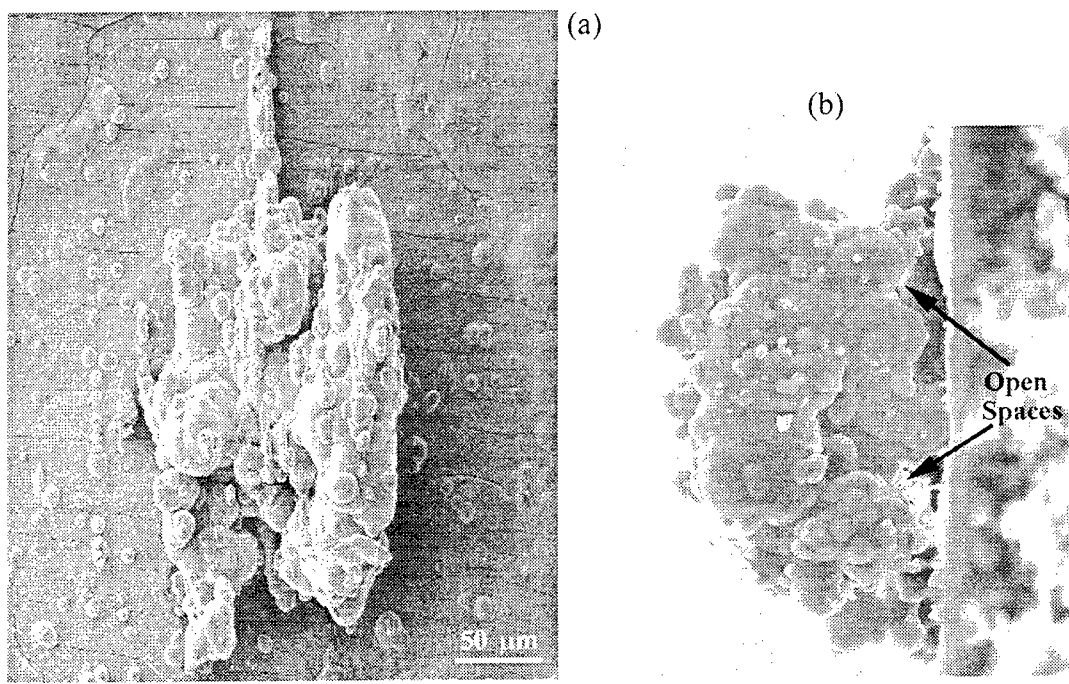


Figure 6: Replica of a typical pit: (a) plan (bottom) view, and (b) elevation (side) view; relative to the original pit.

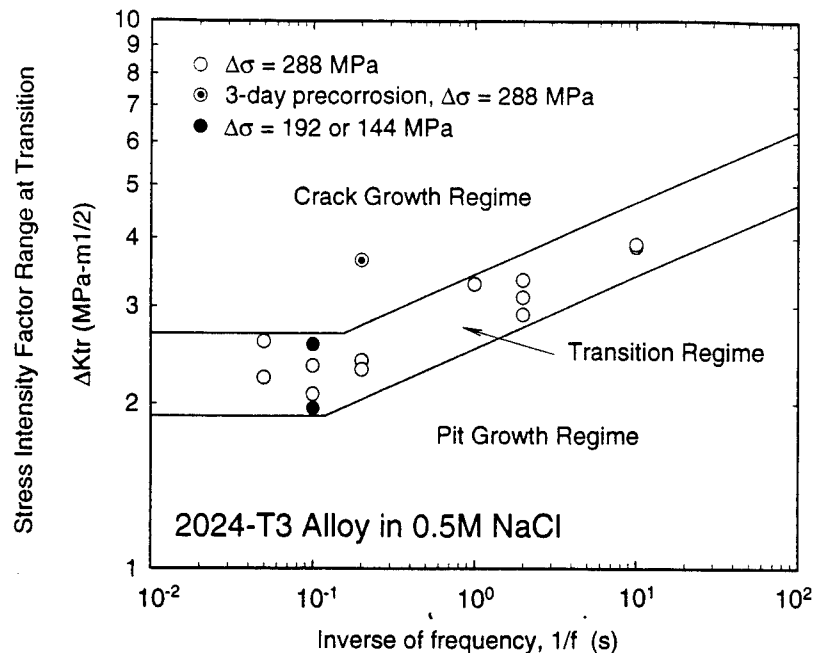


Figure 7: The relationship between the stress intensity factor range of equivalent cracks at fatigue crack nucleation and the frequency of the applied cyclic stress.

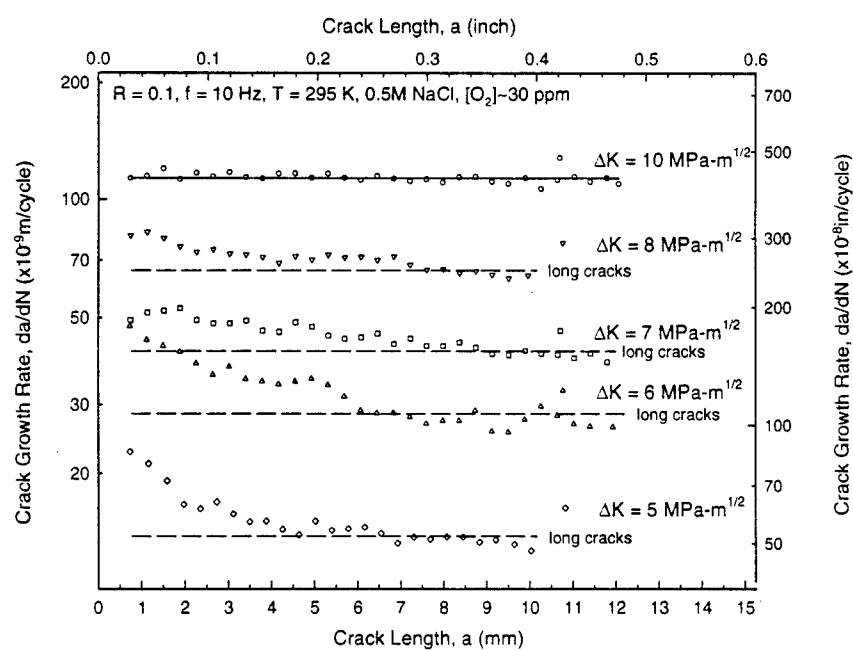


Figure 8: Effect of  $\Delta K$  level on crack growth response in an aerated 0.5M NaCl solution, with  $[O_2] = 30$  ppm, showing chemically affected short crack growth.

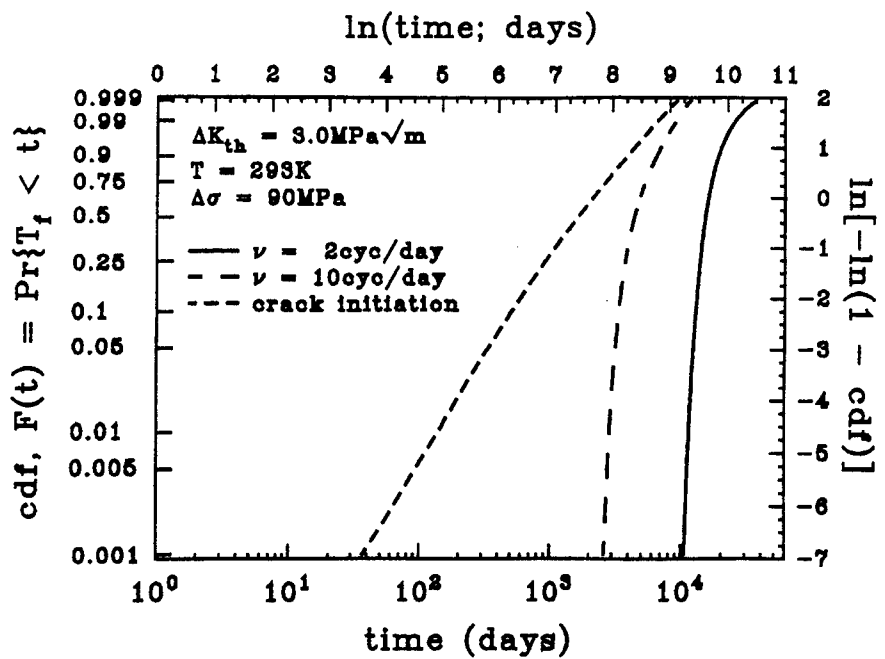


Figure 9: Relative contribution of the time to initiation and the time of crack growth on the CDF for the time to failure at 293 K and 90 MPa.

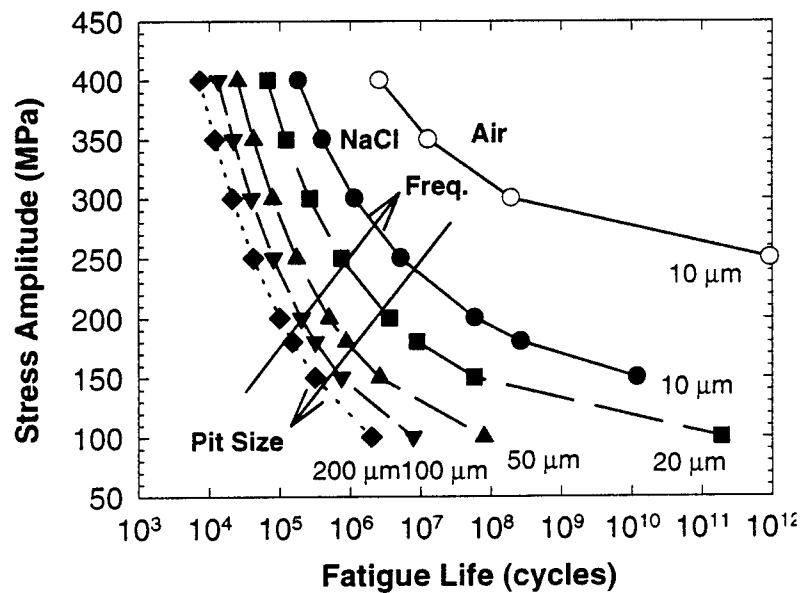


Figure 10: The influence of stress and initial pit size on fatigue life.

# Some new approaches to understanding and characterizing exfoliation corrosion in aircraft aluminum alloy sheet metal

L. E., Murr, Maria Posada, R. M. Arrowood, and D. Little

Department of Metallurgical and Materials Engineering, Materials Research Institute, and FAST Center, The University of Texas at El Paso, El Paso, Texas 79968

## ABSTRACT

In the absence of evidence for elemental excess or depletion at elongated and exfoliating grain boundaries in 2024 aluminum alloy sheet samples from KC-135 aircraft body skins, we are pursuing different analytical and experimental approaches involving the measurement and comparison of grain boundary geometry and crystallography as these relate to energetics. We have used electron backscatter diffraction in the scanning electron microscope to compare microtexture in the orthogonal sample planes along with mesotextures of special grain boundaries. These measurements are compared with transmission electron microscopy observations of grain boundary misorientations for  $[1\ 1\ 0]$  directions in identically oriented (110) and (112) neighbor grains. Fundamental issues involved in the development and propagation of exfoliation cracks within the elongated grain layers are discussed on the basis of these preliminary observations and comparisons, and a simple model is developed.

**Keywords:** exfoliation corrosion, aluminum alloy sheet, scanning and transmission electron microscopy, grain boundary energetics, misorientation distributions.

## 1. INTRODUCTION

There has been a recent interest, a renewal of sorts, in understanding corrosion phenomena in aircraft sheet metals, particularly 2xxx and 7xxx aluminum alloys. This interest stems from the fact that many aircraft, especially KC-135 military aircraft and the 707 commercial equivalent, may be expected to be operational for another 40plus years. Although in the case of the KC-135, actual flight hours are minimal, many aircraft are exhibiting a variety of corrosion problems, and exfoliation in body skins is particularly notable.

Exfoliation is a directional attack along elongated grain boundaries which has the appearance of a french pastry dough. Kelly and Robinson<sup>1</sup> have recently attributed exfoliation to a stress corrosion cracking (SCC) mechanism driven by wedging of corrosion products in the elongated grain boundary. These wedging forces are attributed to the aspect ratio of the elongated grains, and increase with increasing aspect ratio. This is a relatively new approach to exfoliation in aluminum alloy sheet, and based in part on earlier work by oxide wedging to form SCC cracks in stainless steel<sup>2,3</sup>. In fact, Habashi, et al<sup>4</sup> as well as Robinson<sup>3</sup> in earlier work, have demonstrated that exfoliation is primarily an SCC mechanism. However, Robinson<sup>3</sup> has, among others<sup>5-7</sup>, attributed the

exfoliation corrosion mechanism to electrochemical effects between grain boundary precipitates and adjacent, solutedenuded (or depleted) zones. Copper depletion has been historically linked to these electrochemical effects. However, recent work by Posada, et al<sup>8</sup> failed not only to provide any evidence for copper depletion in or near equiaxed grain boundaries in the sheet thickness for 2024 aluminum body skins from KC-135 aircraft, but there was no compelling evidence for either excesses or deficiencies of any elements. Only a slight variation in the overall precipitate composition in the matrix and generally within the grain boundaries was noted.<sup>8</sup>

The nature of exfoliation corrosion in aluminum alloy sheet such as 2024 seems to be complicated by several interconnected phenomena. First, the corrosion product must nucleate and grow in or near the grain boundary. Second, this nucleation and growth must create a large-area fracture along the grain boundary plane. Third, there appears to be some simultaneity in these events because these exfoliation failures can occur along each grain layer or multiple grain layers to create the characteristic leafing or french dough appearance. There is usually no external (resolved) stress acting to promote the exfoliation process, and a wedging action therefore seems quite plausible.

However, Campuzano-Contreras et al<sup>9</sup> have recently demonstrated that 2024 aluminum alloy corrosion products contain high concentrations of bayerite ( $\text{AlO(OH)}_3$ ) and boemite ( $\text{AlO(OH)}$ ), and it is difficult to understand how such products would be nucleated by grain boundary precipitates or other features related to interfacial electrochemical phenomena. Furthermore, it is difficult to understand the overall nature of rapid grain boundary decohesion which must contribute as a significant aspect of exfoliation.

It is the more fundamental aspects of the elongated grain boundaries in 2024 aluminum aircraft alloy sheet which are the focus of this investigation. We begin with the premise that because there is an apparent catastrophic or rapid decohesion along vast areas of grain boundary planes, there may be quantifiable aspects of grain boundary geometry or crystallography<sup>10</sup> which may render a better understanding of the overall process of exfoliation. To this end, we have begun a systematic analysis of grain boundary geometry and crystallography in exfoliated 2024 aluminum aircraft sheet<sup>11</sup> samples utilizing transmission electron microscopy (TEM)<sup>11</sup> and electron backscatter diffraction (EBSD) analysis in the scanning electron microscope (SEM)<sup>12-14</sup>.

## 2. ANALYTICAL FORMALISMS AND EXPERIMENTAL CONSIDERATIONS

### 2.1 TEM analysis of elongated grain boundaries

Figure 1 illustrates typical exfoliation features in a 2024 aluminum sheet from a KC135 aircraft body skin sample, and provides both a practical perspective and an experimental framework for the development of preliminary research to be reported herein.

We consider that rapid cracking along the elongated grain boundary planes (Fig. 1(b)) is influenced by some effective embrittlement or other weakening of the grain boundary which is normally associated with a reduced grain boundary energy<sup>11</sup>. To investigate the prospects for some propensity of low angle boundaries, we begin by considering an idealized tilt boundary utilizing the simple formalism of Read and Shockley<sup>15</sup> and Read<sup>16</sup>, as illustrated schematically in Fig. 2. This

simple formalism assumes a symmetrical dislocation array to characterize the boundary structure; i.e., edge dislocations (with Burgers vector  $\mathbf{b}$ ) spaced a distance,  $D$ , to accommodate a rotation of two crystal lattices (or grains A and B) about an orthogonal axis,  $\omega$ . In the symmetrical case, the boundary trace ( $\tau$ ) and the normal to the boundary plane ( $\mathbf{n}$ ) are orthogonal, and each bisects the total misorientation angle  $\Theta$  (Fig. 2). From the grain boundary geometry illustrated in Fig. 2

$$D = |\mathbf{b}| / 2 \sin(\Theta/2) \quad (1)$$

or for small  $\Theta$ ,  $D \approx |\mathbf{b}|/\Theta$ . The corresponding Read-Shockley energy for this idealized grain boundary is given by

$$\gamma_{RS} = \gamma_0 \Theta (A - \ln \Theta) \quad (2)$$

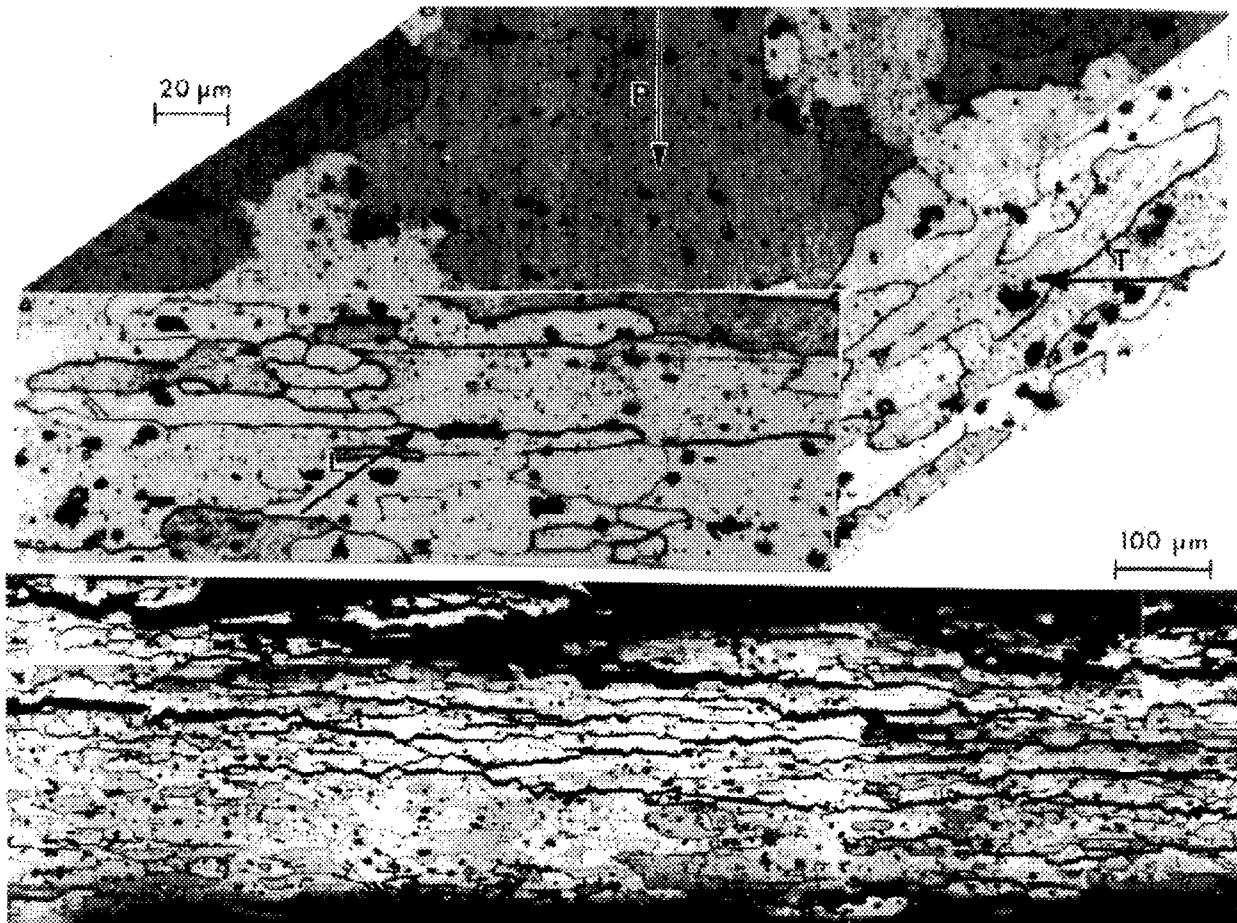


**Figure 1:** (a) Three dimensional (orthogonal plane) structure for exfoliating 2024 aluminum alloy sheet sample from a KC-135 aircraft (b). Notations are in-plane (P), longitudinal (L) and transverse (T). Exfoliating region of the sample in (a) showing leafing between elongated grain layers in the longitudinal plane.

where  $\gamma_0 = Gb/4\pi(1-\nu)$ ; and  $G$  is the shear modulus,  $\nu$  is Poisson's ratio, and  $A$  is a constant. It is often convenient and customary, based on the analysis above, to consider dislocation-structure

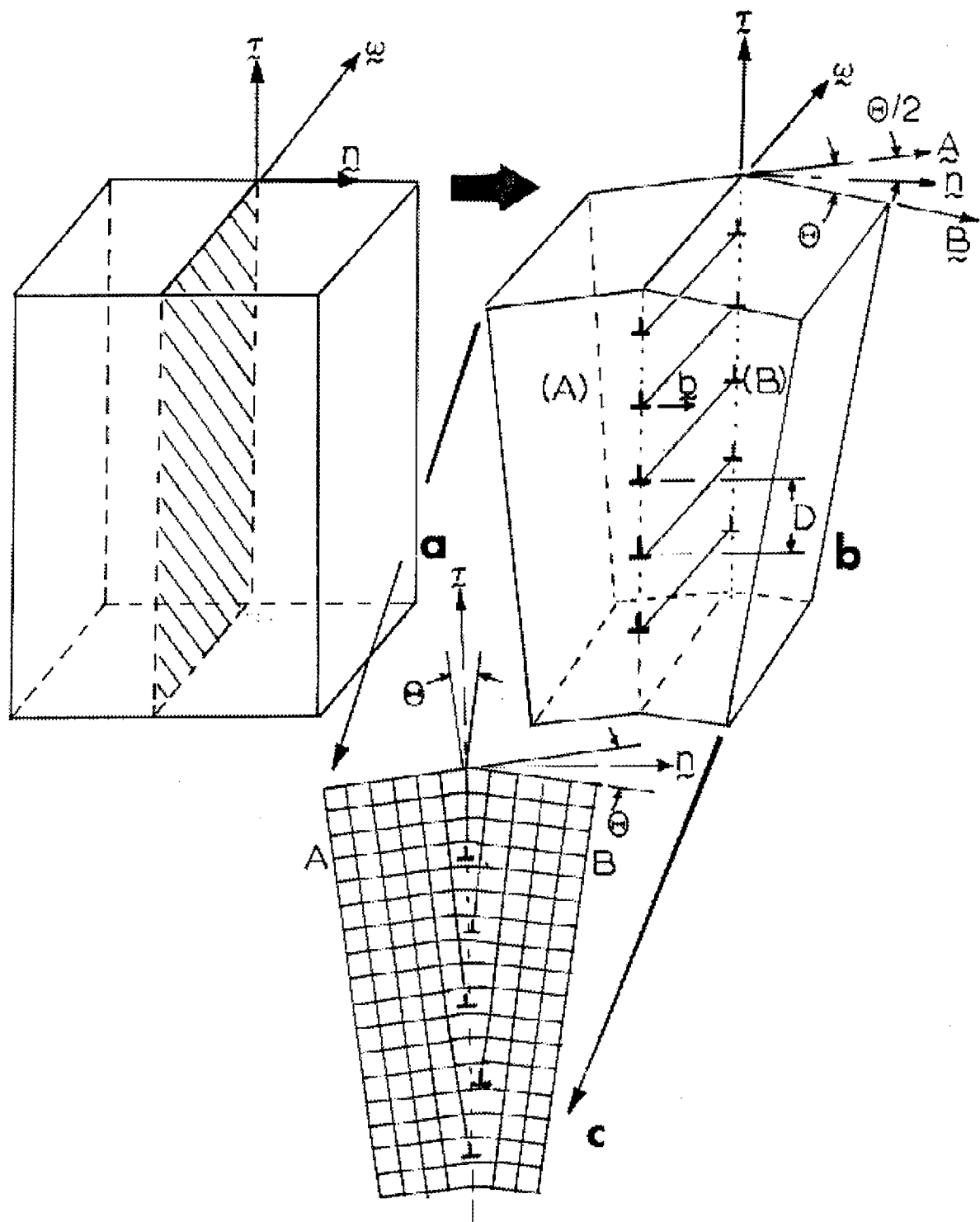


**Figure 2:** Read-Shockley<sup>15</sup> dislocation boundary development and boundary geometry and crystallography notations. (a) Single crystal lattice with the placement of a virtual grain boundary plane (shaded) normal to the reference surfaces. The boundary trace is denoted  $\tau$  and  $\mathbf{n}$  is the normal to the boundary.  $\omega$  is a rotation axis.  $\tau$ ,  $\omega$ , and  $\mathbf{n}$  are orthogonal axes. (b) Symmetric rotation of lattice A and B about  $\omega$  to produce a dislocation boundary.  $\mathbf{A}$  and  $\mathbf{B}$  are crystallographic trace directions in A and B. The total misorientation of  $\mathbf{A}$  and  $\mathbf{B}$  is denoted  $\Theta$ . (c) Shows a rendering of the lattice corresponding to a simple cubic surface orientation of A and B. Note the boundary plane (with trace  $\tau$ ) is perpendicular to the grain or crystal surfaces A and B (which are identical:  $A = B$  in this analysis).

boundaries to represent low-angle boundaries ( $\Theta < 15^\circ$ ) and high-angle boundaries to be represented by  $\Theta > 15^\circ$ . If the Read-Shockley equation (Eqn. (1)) is normalized to this condition, then we can let  $\gamma_{RS}/\gamma_m = 1$ ;  $\Theta/\Theta_m = 1$  and rewrite Eqn. (1) in the form

$$(\gamma_{RS}/\gamma_m) = (\Theta/\Theta_m)(1 - \ln(\Theta/\Theta_m)) \quad (3)$$

which can be ideally represented in the sketch shown in Fig. 3.

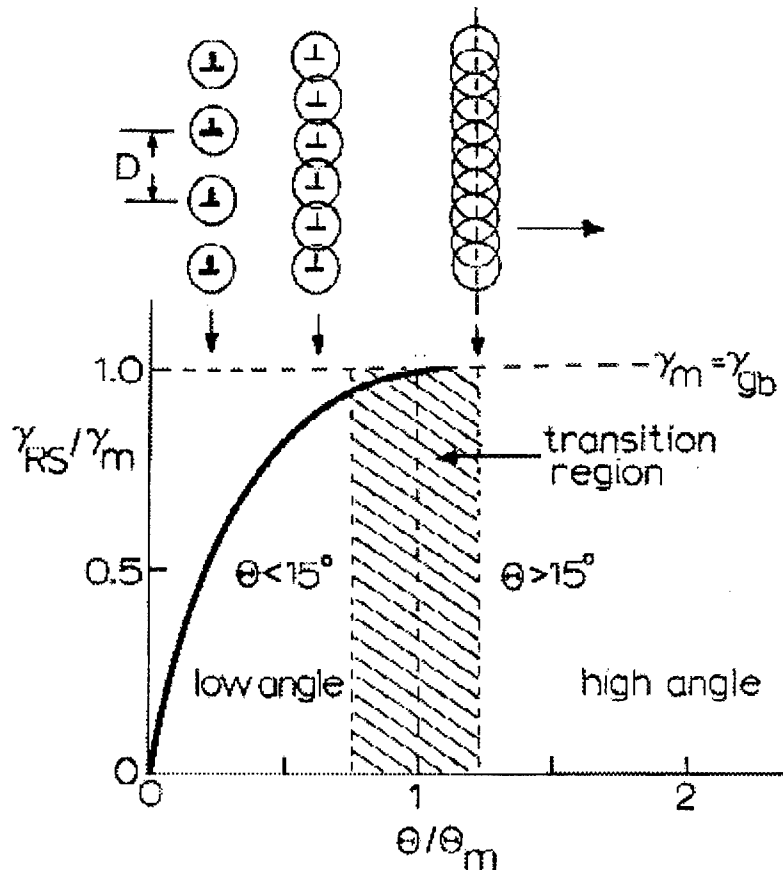


**Figure 3:** Normalized plot of grain boundary energy versus misorientation. Simple sketches of the corresponding dislocation boundary structure evolution is shown above the plot. The usual, high-angle grain boundary free energy is denoted  $\gamma_{gb}^{10}$ .

It can be observed in Fig. 3 (and by a simple interrogation of Eqn. (1)) that when  $D$  approaches the Burgers vector dimension ( $D \rightarrow b$ ), the dislocation cores will overlap. The core radius is not known absolutely, but is often approximated to be around  $5b^{10}$ , so if we assume that this overlap will become appreciable between about  $6b$  to  $3b$ , then the corresponding range of misorientation angles ( $\Theta$ ) will be  $10^\circ$  to  $19^\circ$ . This corresponds roughly to the transition region in Fig. 3. Figure 3 shows that there is a strong correlation between grain boundary energy (specific interfacial free energy<sup>10</sup>) and the misorientation angle,  $\Theta$ , in the range from 0 to about  $15^\circ$ .

To investigate the prospects for some propensity for low-angle boundaries which may contribute to exfoliation, we prepared thin, TEM sections<sup>10</sup> in the sheet thickness, parallel to the grain orientations illustrated in the section views in Fig. 1. The details of the actual thin film preparation

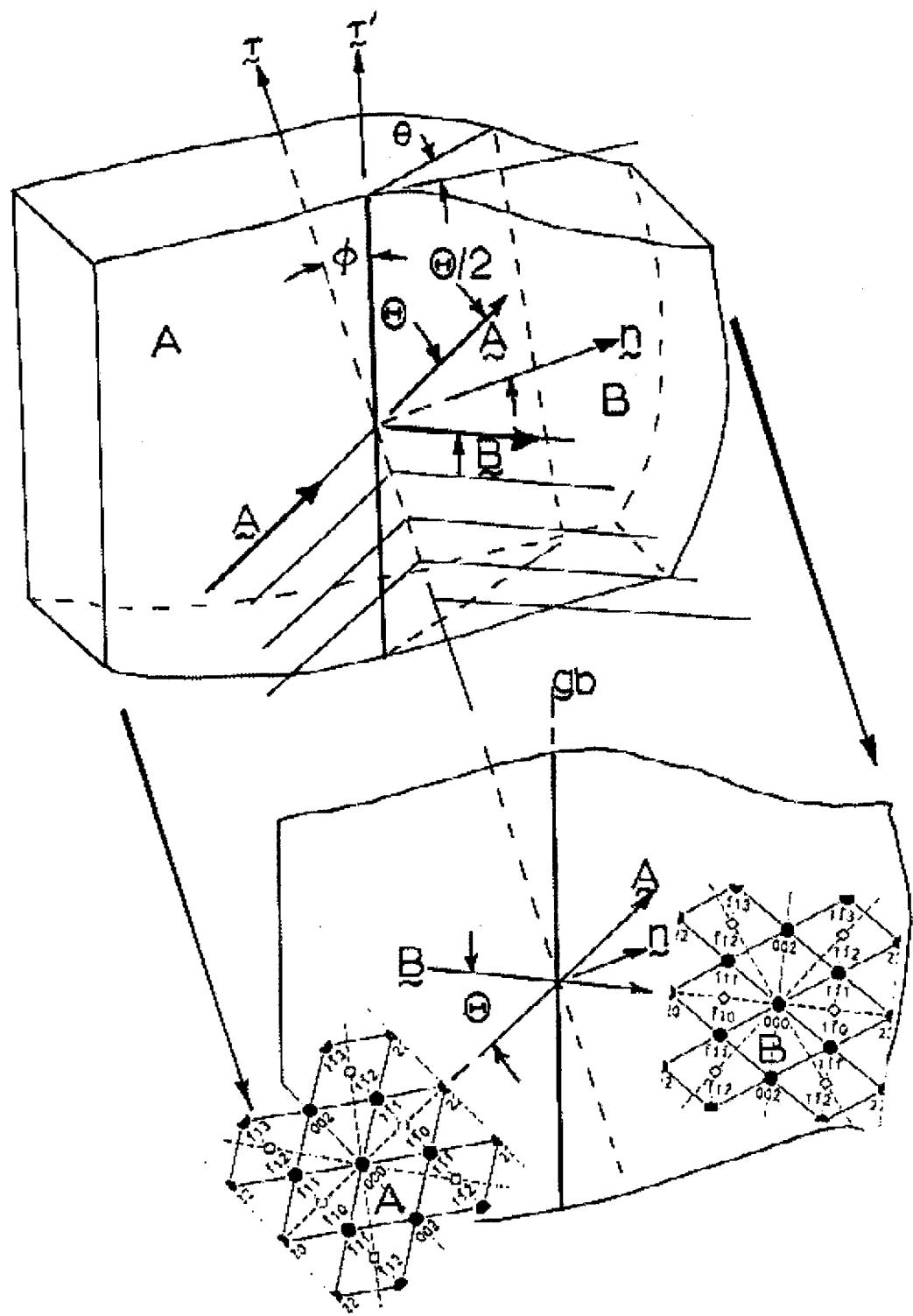


**Figure 4:** Geometrical and crystallographic conventions for grain boundary analysis in thin, electron transparent, sections in the TEM. The actual grain boundary (gb) trace is denoted  $\tau'$  in contrast to the symmetric trace,  $\tau$ . In this example,  $A = B = (110)$  and  $\mathbf{A} = \mathbf{B} = [1\bar{1}0]$  shown by the calculated fcc electron diffraction patterns inserted. Allowed (fcc) reflections are denoted by solid circles. The boundary plane inclination (with respect to the section surfaces) is denoted  $\theta$ . Other notations correspond to Fig. 3.

have been given previously<sup>17</sup>. Figure 4 shows the complete geometry and crystallography for a grain boundary in these thin TEM sections utilizing the conventions established in Fig. 2. A key experimental requirement illustrated in Fig. 4 was that the grain surface orientations for grains A and B must be the same (as determined by selected-area electron diffraction SAD)<sup>11</sup>. This uniquely defines the boundary misorientation,  $\Theta$ , which is shown as the minimum angle between trace directions  $\mathbf{A}$  and  $\mathbf{B}$ . In Fig. 4, the inserted diffraction pattern nets<sup>10</sup> are (110) and  $\mathbf{A} = \mathbf{B} = [1\bar{1}0]$ . The boundary plane is shown inclined to the surface at some angle,  $\theta$ , in Fig. 4, but in the ideal case shown in Fig. 2,  $\theta = 90^\circ$ . Indeed, since the elongated boundary plane is essentially parallel to the sheet (longitudinal) plane (Fig. 1(a)), the grain boundary planes would be expected to be nearly normal to the thin film (specimen) surface, i.e.,  $\theta \approx 90^\circ$ . Consequently, the only significant deviation from the ideal situation represented in Fig. 2 is a deviation from symmetry shown by  $\phi$  in Fig. 4. The angle  $\phi$  is commonly referred to as the asymmetry angle, and when  $\theta \approx 90^\circ$  in Fig. 4, the asymmetry modifies Eqn. (1) as follows:

$$D' = |\mathbf{b}| / 2 \sin(\Theta/2) \cos \phi \quad (4)$$

But when Eqn. (4) is interrogated for its sensitivity to  $\phi$ , we find that when  $D'/D = 0.9$ ,  $\phi \approx 26^\circ$ . For grain surface orientations such as (110) and (112), the misorientation of  $[1\bar{1}0]$  directions will vary between 0 and  $90^\circ$  while corresponding  $\phi$  values will range from 0 to  $45^\circ$ . Consequently,  $\phi$  is not very significant especially for  $\phi < 26^\circ$  (at least from an engineering perspective). Therefore, misorientation distributions should be able to provide reliable, qualitative representations of grain boundary energies or energy distributions for  $\theta$  values less than about  $26^\circ$ .

In the TEM studies to be reported in this paper, misorientations were measured for (110) and (112) grain surface orientations as shown in Fig. 5, i.e. the misorientation angle ( $\Theta$ ) was measured as the minimum angle between  $[1\bar{1}0]$  directions extended as traces in grains A and B; as shown schematically in Fig. 4. In order to check the deviations from symmetry,  $\phi$ , for misorientation ( $\Theta$ ) distributions were also measured for these two grain surface orientations.

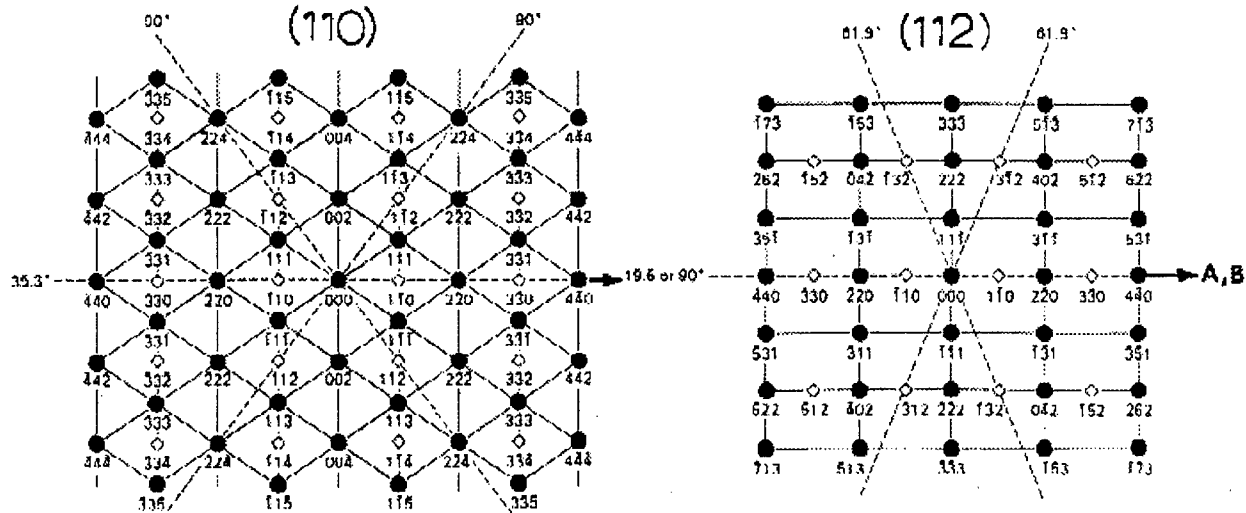


**Figure 5:** Examples of indexed fcc (110) and (112) selected-area electron diffraction (SAD) patterns. Allowed reflections are solid circles. Traces of  $\{111\}$  planes are shown dotted and their inclination with the crystallographic surface noted. The experimental trace directions  $\mathbf{A} = \mathbf{B}$  are also noted in the corresponding  $[1\bar{1}0]$  directions common to each pattern.

## 2.2 Texture comparisons, orientation distributions, and special boundary frequencies

The SEM can now be used as a convenient means to produce texture representations (pole figures) and the crystallographic directions for specific grains which constitute a grain boundary can also be utilized in determining crystallographic coincidences which would ideally describe an interface separating them. A pole figure (or inverse pole figure) is a stereographic projection or a projected section of a stereogram which illustrates the distribution of zone axes (or poles) for grains composing a section. High frequencies of specific crystallographic directions are

characteristic of textures  $\{hkl\} < h'k'l' \rangle$  where  $h,k,l$  and  $h',k',l'$  are not necessarily equal. In addition, a pole figure is only a statistical distribution of a single direction. A better description is given by a so-called orientation distribution function (ODF) which can be displayed as a three-dimensional plot with the three Euler angles as axes. There is a relationship between Euler angles and Miller indices for cubic materials. However, there is no direct association between Euler space and the specimen coordinate system. Other three-dimensional space representations can be utilized to overcome this deficiency and provide a rapid and quantitative description of the misorientation relationship between randomly oriented grains. It should be noted here that this misorientation relationship is not the specific rotation angle for identically oriented grains as described above in Figs. 3 and 4 where  $A = B$  ( $(hkl)_A = (hkl)_B$ ) and  $A$  and  $B = [hkl]_A = [hkl]_B$ . Instead this is a concept of an axis/angle rotation where in order to express the absolute orientation of a crystal (B), the reference crystal (A) is taken to be the standard cubic crystal orientation. To some extent Euler space can also relate random orientations A and B (or lattices A and B) by rotations about coordinate axes. That is, a set of cartesian  $x'$ ,  $y'$ ,  $z'$  rigid body axes initially aligned with  $\mathbf{u}_1$ ,  $\mathbf{u}_2$ ,  $\mathbf{u}_3$  can be rotated into alignment with  $\mathbf{u}'_1$ ,  $\mathbf{u}'_2$ ,  $\mathbf{u}'_3$  by three successive rotations. Figure 6(a) illustrates this concept schematically where the three Euler angles  $\alpha$ ,  $\beta$ , and  $\gamma$  define the rotation uniquely (except for multiples of  $2\pi$ ) in three-dimensional Euclidean space:

$$\mathbf{R}(\text{Euler}) = \mathbf{R}(\alpha, \beta, \gamma) =$$

(5)

$(\cos \alpha \cos \beta \cos \gamma - \sin \alpha \sin \gamma)$	$(\cos \alpha \sin \beta)$
$(-\sin \alpha \cos \beta \sin \gamma + \cos \alpha \sin \gamma)$	$(\sin \alpha \sin \beta)$
$-\sin \beta \cos \gamma$	$\cos \beta$

or

$$[\mathbf{u}'_1, \mathbf{u}'_2, \mathbf{u}'_3] = [\mathbf{u}_1, \mathbf{u}_2, \mathbf{u}_3] \mathbf{R}(\alpha, \beta, \gamma) \quad (6)$$

The concept of a Rodriguez-Frank (R-F) space<sup>11</sup> has also become a popular notation for axis/angle pair rotations of one lattice into another, especially in connection with the generation of EBSD

patterns and their analysis in the SEM<sup>11,13</sup>. Figure 6(b) illustrates this concept where

$$\mathbf{R} = \begin{pmatrix} a_{11} & a_{12} & a_{13} \\ a_{21} & a_{22} & a_{23} \\ a_{31} & a_{32} & a_{33} \end{pmatrix} \quad (7)$$

is the rotation of crystal B which brings it into the same orientation as crystal A, and  $a_{ij}$  are direction cosines between the cartesian axes. The rotation angle (or relative orientation) shown is defined by

$$\cos\theta_r = (a_{11} + a_{22} + a_{33})/2 \quad (8)$$

and the axes of crystal (lattice) B can be chosen in 24 equivalent ways (or axis/angle pairs) in which a misorientation matrix can be expressed<sup>12</sup>. The lowest rotation angle solution is quoted, and there is at least a qualitative relationship between these angles ( $\theta_r$ ) and the idealized misorientation,  $\Theta$ , described above, and illustrated for comparison in Fig. 6(c).

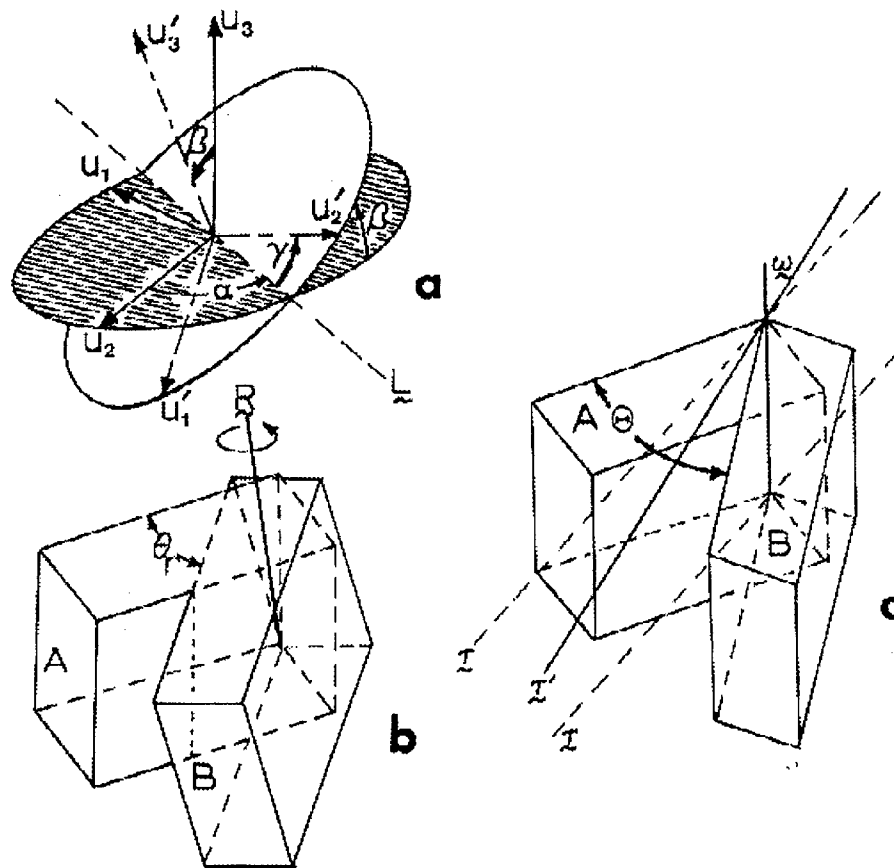


**Figure 6:** Three-dimensional representations for rigid-body (lattice) rotations and relative orientations. (a) The Euler angles  $\alpha$ ,  $\beta$ ,  $\gamma$ . The rotation through  $\beta$  is denoted by the node line,  $L$ . Note that  $\alpha$  and  $\beta$  are the spherical polar coordinates for vector  $\mathbf{u}_3$  in the  $\mathbf{u}_1$ ,  $\mathbf{u}_2$ , and  $\mathbf{u}_3$  system. (b) Rodriguez-Frank space<sup>12</sup> showing relative misorientation between two lattice A and B. A virtual grain boundary is assumed to divide these lattices. (c) Special case for simple (symmetric) rotation of identical crystal lattices A = B about  $\omega$ . Notation corresponds to Figs. 2 and 3.

EBSD patterns are obtained in the SEM using focused, backscattered electrons. These are Kikuchi (or pseudo Kikuchi) patterns similar to electron channelling patterns obtained by a rocking beam in earlier concepts<sup>11</sup>, and provide accurate orientation analysis for polished specimens with grain sizes  $> 2 \mu\text{m}$ . These patterns are used to obtain microtextures, and ODFs (or inverse pole figures) are constructed from individual grain orientation measurements.

In the context of R-F space, it is possible to plot the frequency of random boundary "misorientations" from EBSD pattern analysis and compare these with the ideal, random boundary frequency distribution which can be calculated. In addition, the axis/angle pair data which is generated can be used to plot the special boundary ( $\Sigma$ ) or coincidence site lattice (CSL)<sup>10</sup> distribution, which is often referred to as the mesotexture or grain boundary character distribution<sup>11</sup>. Although the  $\Sigma$  boundaries<sup>10</sup> have special coincidence structure, they do not necessarily have low energies in the context of low-angle boundaries shown in Fig. 3 (which are often denoted  $\Sigma 1$ ). Only the coherent twin boundary ( $\Sigma 3$ ) has a very low energy, but the corresponding  $\Theta$  is not small (it is  $70.5^\circ$  for  $A = B = (110)^{10}$ ). The ideal grain distribution and mesotexture (or  $\Sigma$  frequency distribution) for a truly random fcc material are illustrated in Fig. 7. EBSD analyses are usually compared with these frequency distributions. In the EBSD analysis, the grain boundaries or coincidence lattices are tacitly assumed to be perpendicular to the specimen plane. This is, as noted in Section 2.1, probably exactly true for the through-thickness section coincident with the exfoliated boundaries (the longitudinal plane, L, in Fig. 1(a)), but not necessarily for the other directions (or orthogonal sections (Fig. 1(a)).

Specimens for EBSD analysis were prepared by mounting the three orthogonal views (two edge and one surface plane as shown in Fig. 1(a)) in standard cold mounts, and then polished and etched as described previously<sup>17</sup>. Specimens for TEM analysis were prepared as previously described<sup>8,17</sup> and viewed in a Hitachi H-8000 analytical transmission electron microscope operated at 200 kV accelerating potential.

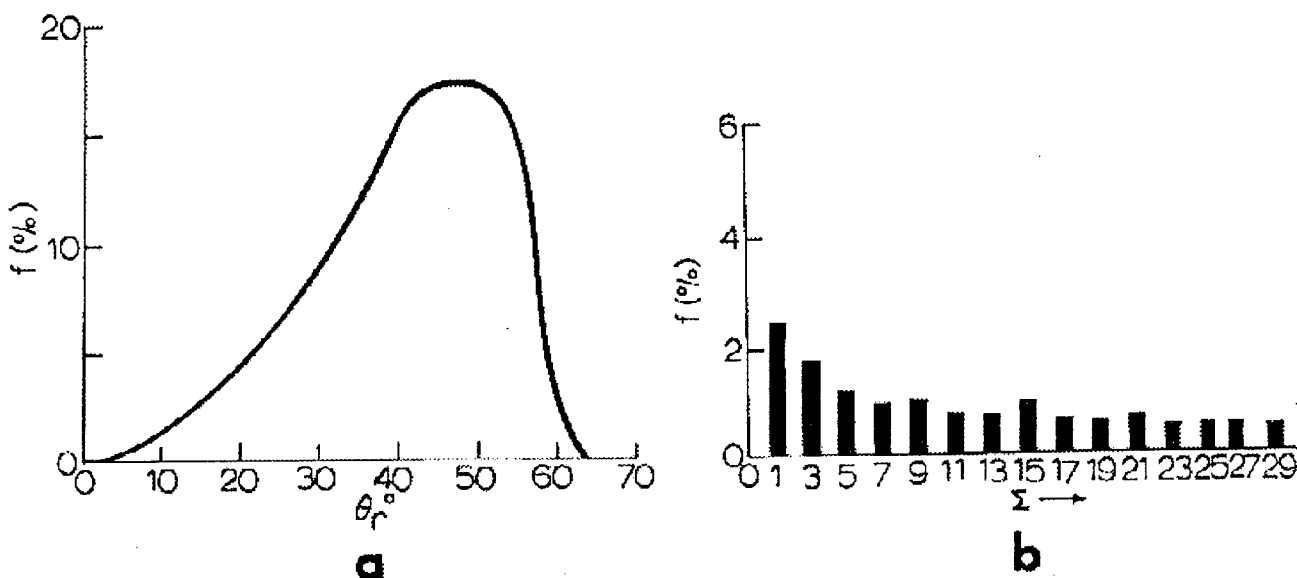


**Figure 7:** The calculated misorientation (rotation angle) distribution (a) and the CSL<sup>10</sup>/special boundary ( $\Sigma$ ) or mesotexture distribution for a randomly oriented assembly of grains (or crystal lattices) in the cubic (fcc) system. The frequency of occurrence is denoted  $f$  (in percent).

### 3. RESULTS AND DISCUSSION

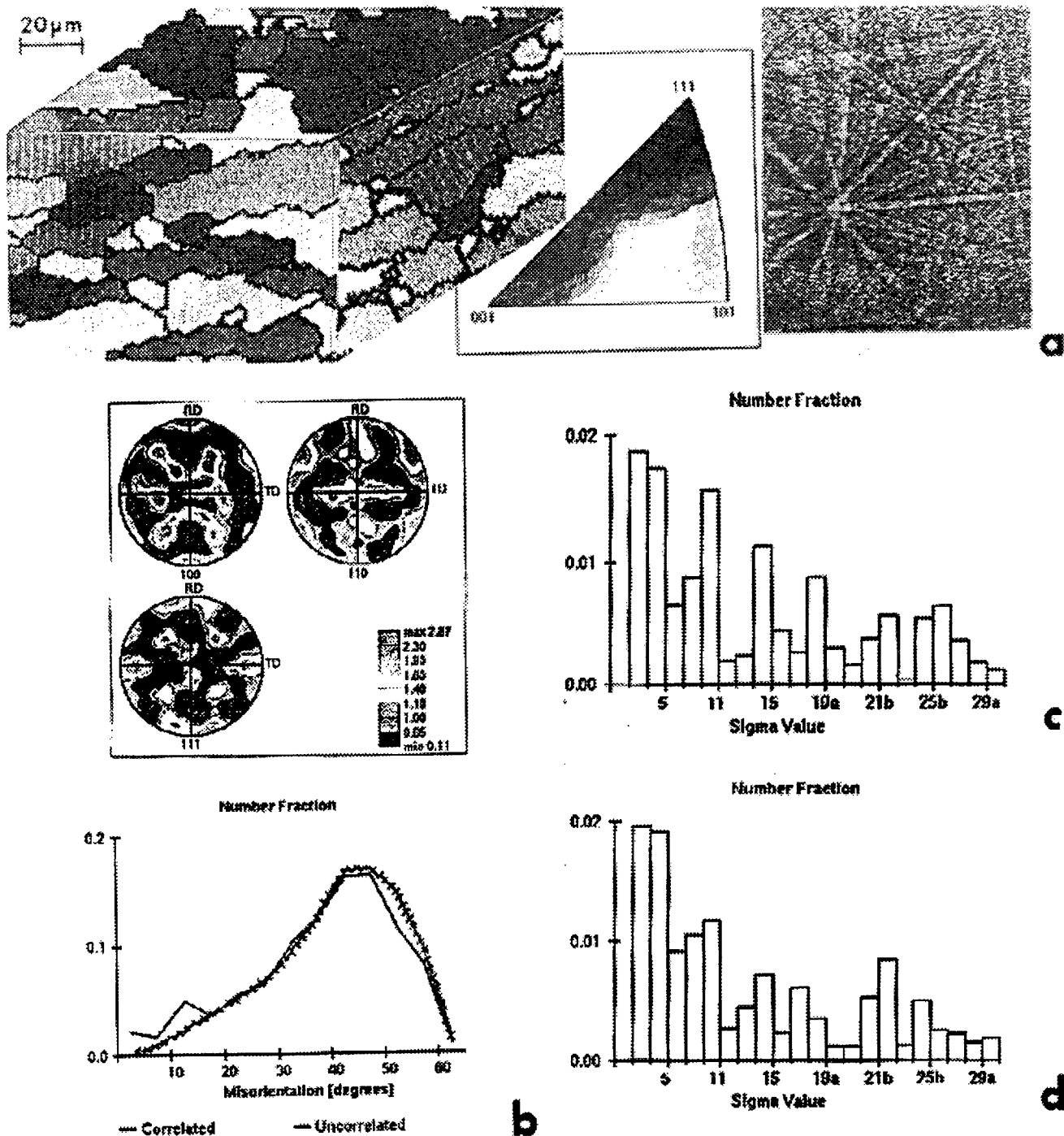
#### 3.1 EBSD studies of exfoliated 2024 aluminum aircraft specimens

Specimen sections representing each of the three orthogonal views (Fig. 1(a)) for exfoliated sheet samples in 2024 aluminum alloy from KC-135 aircraft body skin sections were examined in an SEM in the EBSD mode by TSL Laboratories, Provo, Utah. Single-grain Kikuchi patterns illustrated in Fig. 8(a) were utilized in developing ODFs and frequency distributions for each of these sections, and this data is shown for comparison in Fig. 8(b) to (d). This data, which includes essentially similar pole figures and distributions for other orientations not shown, illustrates essentially random grain orientation distributions or textures for each of the three orthogonal sections through the sheet specimens, and this seems rather surprising considering the aspect ratio variations in the grains (Fig. 8(a)) but it points up the fact that texture irregularities apparently do not contribute to exfoliation. The exfoliated grain boundaries in the elongated direction in the sheet thickness do not exhibit any obvious mesotexture either, and direct examination of the mesotexture and microtexture associated with actual exfoliated grains did not exhibit any distinctive features. This is illustrated in Fig. 9. However, there is a shift in the misorientation histogram in Fig. 9(b) in contrast to the in-plane analysis shown in Fig. 9(c).

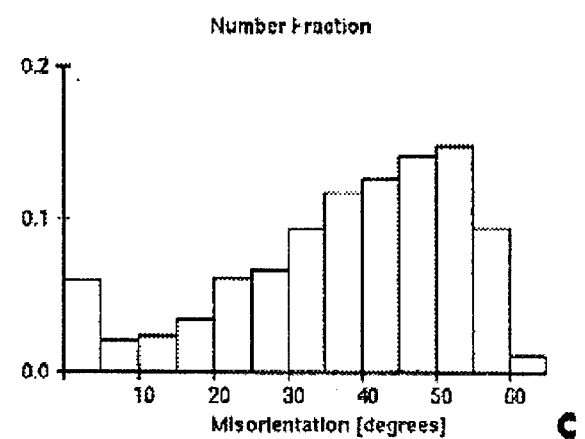
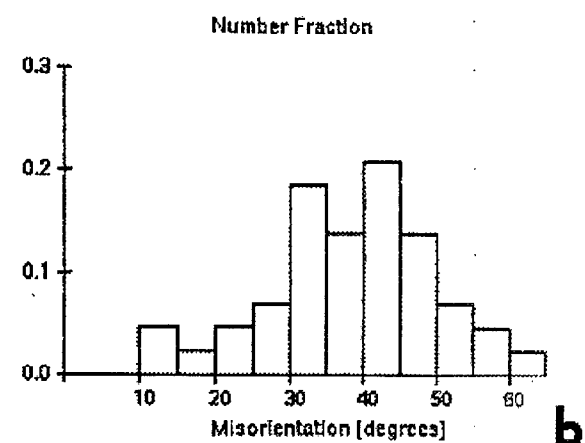
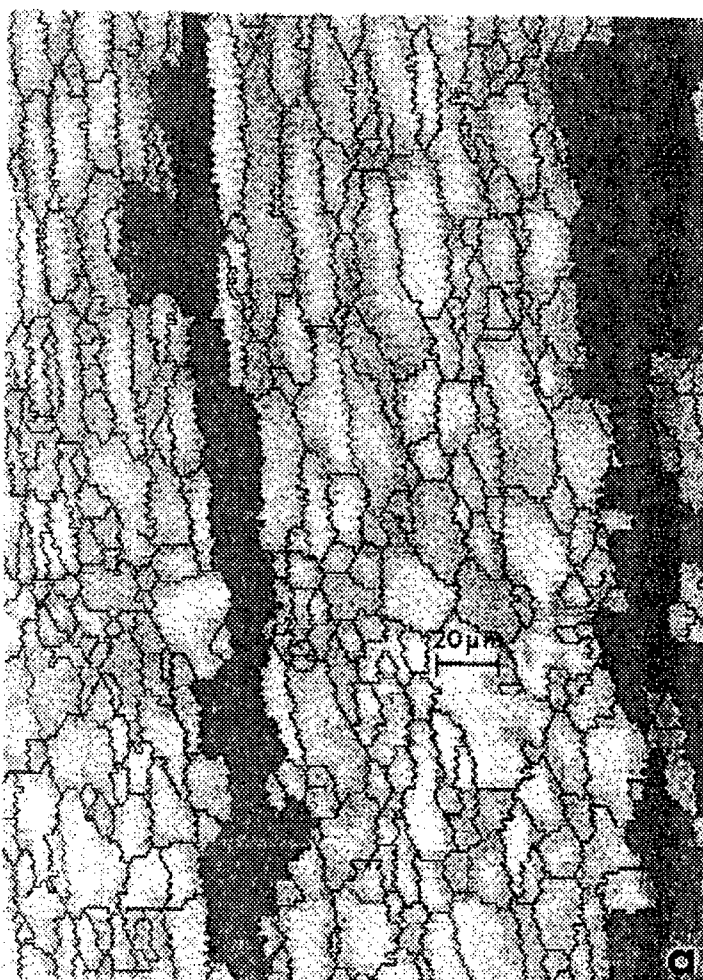
#### 3.2 TEM Studies

Figure 10(a) shows an example of the measurement of the misorientation angle ( $\Theta$ ) for a grain boundary separating two identically oriented (110) grains corresponding to the basic geometric and crystallographic features illustrated in Fig. 4. Preliminary distributions of these (110) boundary misorientations are shown in Fig. 10(b). Figure 10(c) shows for comparison a corresponding misorientation distribution histogram for (112), while Fig. 10(d) shows the combined measurements of the distribution of the grain boundary asymmetry angles,  $\phi$ . The data in Fig. 10(b) and (c) show a curious bimodal distribution of low-angle and high-angle boundaries. Since two different orientations ((110) and (112)) show the same trends, there is a compulsion to believe that this trend is a valid one in spite of the dearth of measurements which is a stark contrast to the data generated in the EBSD analysis (Fig. 8). Moreover, since there are only two measurements which exceed  $\phi \geq 26^\circ$ , these trends would tend to reflect interfacial energy regimes implicit in the histograms of Fig. 10(b) and (c).

Moreover, if this trend is meaningful, a comparison of Fig. 8(b) to (d) with Fig. 10(b) and (c) is indicative of the fundamental differences in measuring “misorientations” as illustrated in Fig. 6. Nonetheless, additional measurements at least in the plane of the sheet (Fig. 1(a)) for identical grain surface orientations ((110) and (112)) must be available for comparison before any significance can be attributed to the exfoliation process. It should be noted of course that the low-angle boundaries noted in Fig. 10(b) and (c) are correspondingly low energy boundaries and not special boundaries.



**Figure 8:** SEM-generated EBSD data for 2024 aluminum alloy aircraft sheet samples. (a) Reconstructed, orthogonal section view for comparison with Fig. 1(a) showing contiguous grain Kikuchi patterns<sup>11</sup>. The inverse pole figure insert shows a grey-scale key for the grain orientations shown. (b) Grain misorientation distribution plot for in-plane data, with pole figure insert (top). (c) Experimental  $\Sigma$ -boundary (mesotexture) frequency plot corresponding to (b). (d)  $\Sigma$  (CSL) boundary frequency distribution in longitudinal plane. The correlated curves in the distribution shown are the measured distribution while the uncorrelated curves show the distribution determined from texture measurement assuming that no spatial crystallite orientation correlation exists.



**Figure 9:** SEM-generated EBSD data specific to exfoliation cracks shown in Fig. 1(b). (a) In - thickness (longitudinal) elongated grains composing exfoliated segment. (b) Random grain misorientation distribution plot composed from EBSD data. (c) In-plane misorientation histogram for comparison with (b).

### 3.3 A model for exfoliation corrosion

In the absence of any compelling evidence for electrochemical variations (anodic sites, etc.) at the in-plane grain boundaries<sup>8</sup>, and the absence of textures or other orientation effects (including mesostructures) as illustrated in the EBSD data (Figs. 8 and 9), as well as preliminary TEM data which suggests the prospects for a peculiar, bimodal, grain boundary energy distribution (Fig. 10), a curious dilemma exists. There seems to be no obvious mechanism for nucleating and growing exfoliation cracks except for the wedging action of the corrosion products! It is not well understood how boundary precipitates, such as they are, contribute in a significant way to exfoliation, and Fig. 10(a) demonstrates that there is little morphological distinction between matrix precipitates and those observed to be associated with the elongated grain boundaries. However, there must be some simple

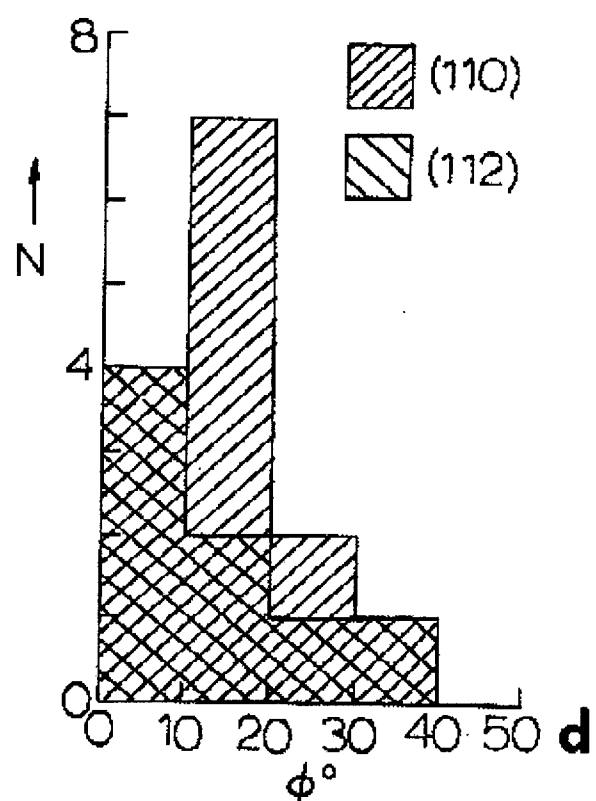
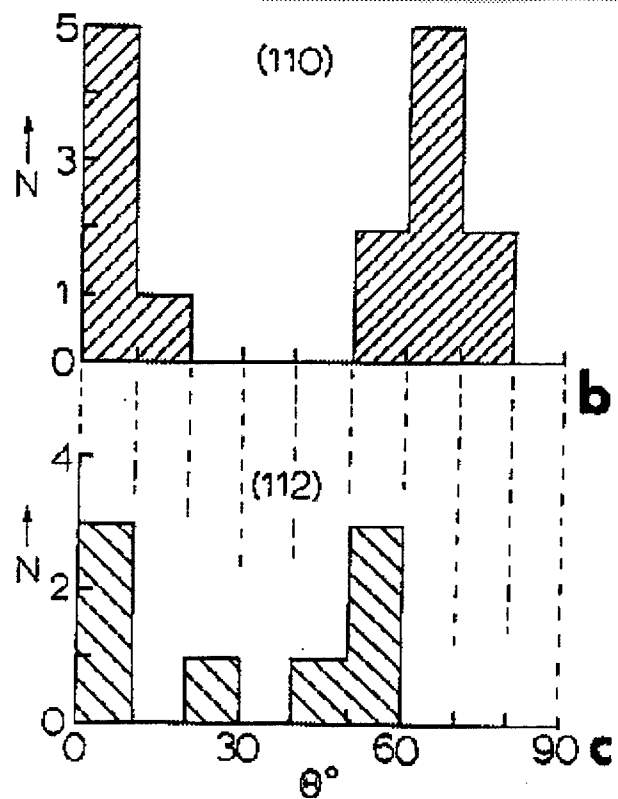
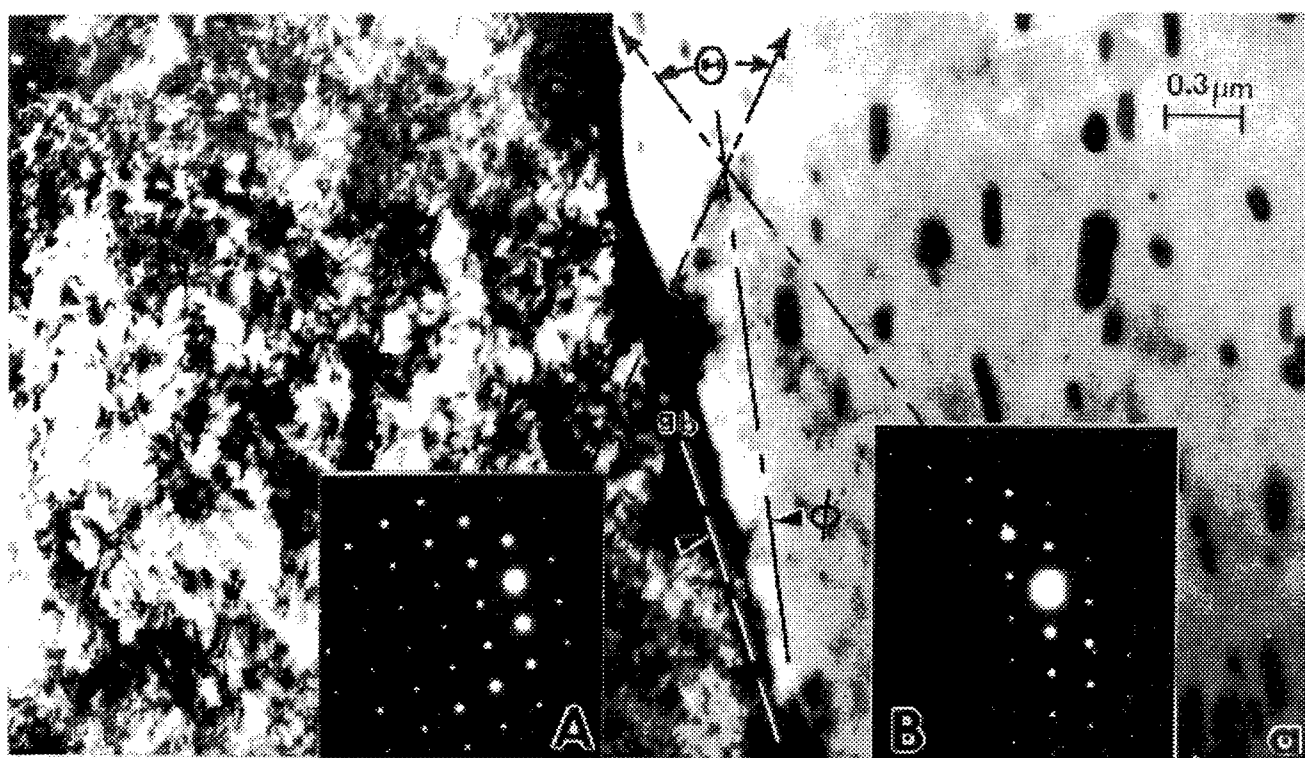


**Figure 10:** TEM measurements of misorientation ( $\Theta$ ) and asymmetry angle ( $\phi$ ) distributions in the elongated (longitudinal) sheet thickness. (a) Example of a bright-field TEM grain boundary section (in the elongated direction) and associated SAD patterns (110). (b) Misorientation distribution histogram for (110). (c) Misorientation distribution histogram for (112). (d) Asymmetry angle distribution for both (110) and (112) orientations.

thermodynamic and kinetic features connected with the migration of oxygen or water vapor (or both) to the crack tip to form  $\text{AlO(OH)}$  and  $\text{AlOH}$  wedge products<sup>9</sup>. It is possible that as the crack tip advances, new surface (on the grain boundary) could be further embrittled by oxygen or  $\text{H}_2\text{O}$  molecular dissociation on the interface, simultaneously creating a corrosion product wedge, and advancing the crack. This might be characterized by a type of dynamic embrittlement which has been described for other systems which crack uncharacteristically<sup>18</sup>. Figure 11 is an attempt to depict such a mechanism schematically, utilizing the concepts developed in Section 2. Figure 11 also illustrates a thick corrosion product on an exfoliated surface in the SEM. It will be important to attempt to look more critically into the advancing exfoliation cracks in the future in an effort to observe some of these features, and it will be necessary to verify more quantitatively the implications of Fig. 10(b) and (c). If may be, as recently demonstrated by Wei, et al<sup>19</sup>, that anodic precipitates can themselves nucleate corrosion, and this further complicates the process because there is obviously a role played by precipitates in nucleating corrosion.

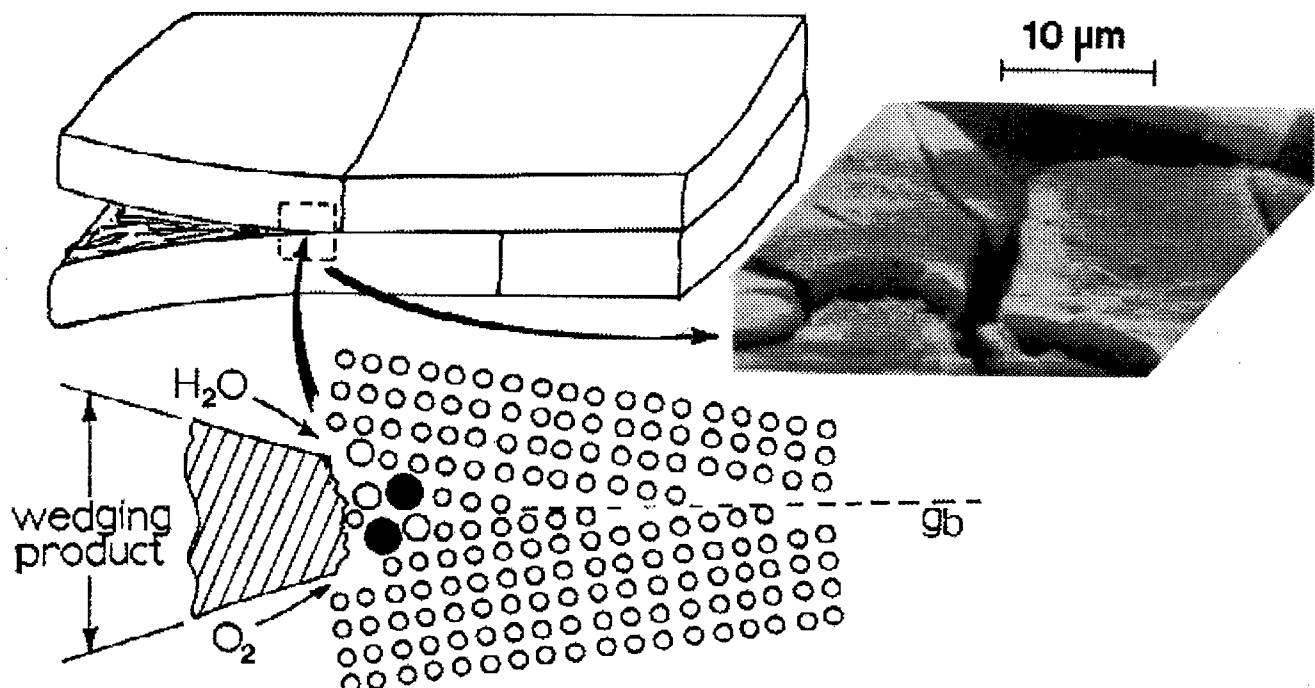


**Figure 11:** Dynamic embrittlement and corrosion product wedging model for exfoliation in 2024 aluminum alloy aircraft sheet which incorporates analytical and experimental issues presented in this paper. The SEM insert illustrates the typical appearance of corrosion product on exfoliated surfaces.

#### 4. SUMMARY AND CONCLUSIONS

We have used electron backscatter diffraction in the scanning electron microscope to examine the microtexture and mesotexture in each of the three orthogonal planes characterizing (3D) sections of 2024 aluminum alloy sheet specimens in exfoliated regions of KC-135 body skin samples. Surprisingly, these comparative measurements and plots of misorientation and  $\Sigma$  distributions for special grain boundaries failed to illustrate any significant anomalies in the elongated grain boundary direction in the sheet thickness, and in fact pole figure diagrams (and inverse pole figure diagrams)

illustrated no significant textures variations; with a random distribution of grain orientations. However, direct measurements of simple misorientations of identical (110) and (112) contiguous grains composing elongated grain boundaries utilizing transmission electron microscopy and selected-area electron diffraction techniques revealed a consistent bimodal distribution, and misorientation angles grouped in both the low-angle and high-angle regimes; corresponding to low and high-energy boundaries respectively as illustrated analytically through model development from first principles utilizing a Read-Shockley dislocation approach. In addition, we have also attempted to illustrate the utility and relationship implicit in various special representations, especially the contrast of misorientation for random grains and identical grains characterizing a simple rotation about a mutually perpendicular axis. Asymmetries associated with specific, experimental grain boundary traces were measured for (110) and (112) grain surface orientations and found not to deviate significantly from a range of angles which do not significantly influence the grain boundary misorientation (or specific interfacial free energy). While the results are rather preliminary, there may be some contributions to an effective grain boundary embrittlement promoting or facilitating exfoliation. Corrosion product formation may also affect embrittlement and create crack-tip stresses to propagate cracks. A simple model has been developed which attempts to illustrate these possible features.

Finally, we have attempted to illustrate the utility of EBSD analysis in evaluating prospects for microtexture and mesotexture variations which may contribute to corrosion problems in sheet specimens. Even though the results were not particularly helpful in delineating the mechanisms of exfoliation in 2024 aluminum alloy sheet from an KC-135 aircraft, the approach may have potential in other related aluminum alloy sheet problems.

## ACKNOWLEDGMENTS

This research was supported by AFOSR Grant F49620-95-1-0518 administered through the FAST Center for Structural Integrity of Aerospace Systems at The University of Texas at El Paso. This research was also supported through a DoD Acquisition Scholarship to Maria Posada, administered through the Northeast Consortium for Engineering Education. We are grateful to TSL (TexScan Laboratories), Inc., Provo, Utah for performing the EBSD analysis, and especially to David Field for his helpful discussions of the experimental results.

## REFERENCES

1. D. J. Kelly and M. J. Robinson, Corrosion Science, 49(10), 787-796 (1993).
2. N-A. Nielsen (Ed.) Physical Metallurgy of Stress Corrosion Fracture, p. 121, Met. Soc. Conf., Interscience, New York, 1959.
3. M. J. Robinson, Corrosion Science, 23(8), 887-894 (1983).
4. M. Habashi, E. Bonte, J. Galland, and J. J. Boda, Corrosion Science, 35(14), 169178 (1993).
5. M. Reboul and J. Bouvaist, Rev. Aluminum, Jan. 1980, p.41-55.
6. B. W. Litka and D. O. Sprowls, in Localized Corrosion - Course of Metal Failures, ASTM-STD 516, p.120 (1972).
7. W. F. Fink and L. A. Wiley, Metals Technology (METVA), 14(8) 1947.
8. Maria Posada, L. E. Murr, C-S. Niou, D. Roberson, D. Little, Roy Arrowood, and

- Debra George, Materials Characterization, in press, 1997.
9. A. L. Campuzano-Contreras, Roy Arrowood, D. Little, D. Roberson, L. E. Murr, and C-S. Niou, "Characterization of Fuselage Skin Lap Joints", Microstructural Science, Vol. 25, ASM International, Materials Park, Ohio, 1998, in press.
10. L. E. Murr, Interfacial Phenomena in Metals and Alloys, Addison-Wesley, Reading, Mass., 1975; reprinted by Tech Books, Inc. Fairfax, Virginia, 1990.
11. L. E. Murr, Electron and Ion Microscopy and Microanalysis: Principle and Applications, 2nd Edition, Marcel Dekker, Inc., New York, 1991.
12. V. Randle, Microstructure Determination and Its Application Inst. of Materials, London, 1992.
13. V. Randle, The Measurement of Grain Boundary Geometry, Inst. of Materials, London, 1993.
14. B. L. Adams, S. I. Wright, and K. Kunze, "Orientation imaging: the emergence of a new microscopy", Met. Trans. 24A, 819-831 (1992).
15. W. T. Read and W. Shockley, Phys. Rev., 78, 275-282 (1950).
16. W. T. Read, Dislocations in Crystals, McGraw-Hill, New York, 1953.
17. Maria Posada, L. E. Murr, and R. M. Arrowood, "Observations of exfoliation corrosion in aging aircraft body skins: a search for crystallographic issues", Microstructural Science, Vol. 25, ASM International, Materials Park, Ohio, 1998, in press.
18. C. McMahon, "Time - dependent interfacial decohesion," paper presented at a Commemorative Conference on Crystal Defects, Interfaces, Fracture, and Other Topics, at The University of Virginia, Charlottesville, August 14-16, 1997.
19. R. P. Wei, M. Gao, and C-M. Liao, "TEM studies of particle-induced corrosion in 2024-T3 and 7075-T6 aluminum alloys", Paper presented at 1997 TMS Annual meeting, Orlando, FL, Feb. 9-13, 1997.

## DISCUSSION

### Some New Approaches to Understanding and Characterizing Exfoliation Corrosion in Aircraft Aluminum Alloy

Speaker: Murr

Are you concluding, based on your work, that exfoliation corrosion is not influenced by grain boundary chemistry? —K. Bhansali

*This is a difficult question to answer. Based on our current work on 2024 aluminum from KC-135 aircraft, we have not found any compelling grain boundary chemistry issues (elemental excesses or deficiencies) which seem to contribute to exfoliation nucleation. In other systems, there is evidence, but the process or mechanism is often ambiguous.*

# **Electrochemical *In-Situ* Sensors for Detecting Corrosion on Aging Aircraft**

G.D. Davis,<sup>\*</sup> C.M. Dacres, M. Shook, B.S. Wenner

DACCO SCI. INC.  
10260 Old Columbia Road  
Columbia, MD 21046

## **Abstract**

An *in-situ* corrosion sensor capable of detecting and monitoring corrosion of aircraft or other structures from the earliest stages of deterioration has been developed. Two versions are available: a permanent, attached sensor and a hand-held, portable probe. The sensor utilizes electrochemical impedance spectroscopy (EIS), an established technique for investigating corrosion and coating degradation during immersion in electrolytes in the laboratory. Identical results were obtained from the sensor and conventional, remote electrode immersion measurements. The sensor extends the applicability of the EIS technique to arbitrary painted metal structures under diverse conditions, including field or service use and accelerated testing. Potential applications include corrosion monitoring of critical structures to enable condition-based maintenance and direct correlation of material deterioration during accelerated testing and use in the field.

**Keywords:** corrosion, sensor, electrochemical impedance spectroscopy, coating, paint, degradation, monitor, condition-based maintenance

## **1.0 Introduction**

The cost of corrosion is difficult to determine, but is known to be very large. Studies by the National Bureau of Standards (NBS) estimated that overall corrosion costs in the United States are 4.2% of the Gross National Product (GNP)<sup>1</sup> or \$290 billion in 1996. Military and commercial aircraft are aging and projected retirements are being extended. In 1993, 2660 Air Force planes, or 57% of the fleet, were over 20 years old.<sup>2</sup> Some military transport planes are expected to be flying until they are 80 years old. It is estimated that corrosion costs are \$4 billion annually for military aircraft systems and \$9 billion for commercial and private aircraft.<sup>3</sup>

The cost of repairs, maintenance, and replacement is a direct cost. The loss of lives and readiness are extremely important indirect costs which cannot be assessed in dollar amounts. According to Hoeppner,<sup>4</sup> corrosion-related accidents resulted in 11 fatalities for the military and 70 fatalities for the civilian air fleet over a recent 17 year period. More recently, the National Transportation Safety Board concluded that undetected corrosion was the cause of a commuter aircraft crash that killed ten people in 1995. In 1997, a 35-year old Russian passenger jet broke apart in flight with 50 deaths. Early reports indicated that extensive corrosion was responsible.

One means to prevent catastrophic failure and to increase the lifetime of hardware and structures and to get the most out of stretched maintenance budgets is to track corrosion from its *early stages* so that its progression can be monitored and predicted. Consequently, maintenance could

---

<sup>\*</sup> E-mail: gddaccosci@aol.com

be performed on a needs basis when it is relatively inexpensive before deterioration becomes critical and expensive remedial action is needed. The maintenance schedule would be a proactive one rather than one that reacts to failures.

In this paper, we report on an *in-situ* corrosion sensor capable of detecting coating deterioration and substrate corrosion underneath a paint coating.<sup>5</sup> Based on electrochemical impedance spectroscopy (EIS), the sensor is sensitive to early stages of material degradation before any visual damage is present. It allows quantification of deterioration of the actual structure of interest during both ambient service conditions and laboratory accelerated exposures. Consequently, it is applicable for

- Condition-based maintenance
- Coating development.

Two versions of the *in-situ* sensor have been developed: a permanently attached sensor and a portable hand-held sensor. The former is suitable for corrosion inspection in inaccessible areas or for automatic or semi-automatic inspection of a particular area. The hand-held sensor is suitable for spot inspection where a permanent sensor is not desired or had not been previously placed.

Electrochemical impedance spectroscopy has previously been used to detect coating degradation on steels and other metals in the laboratory.<sup>6-8</sup> Good correlation has been reported between short-term EIS measurements and long-term coating performance during immersion in different electrolytes, demonstrating the technique's predictive capabilities.<sup>9-12</sup> However, these applications involved immersion of the specimen and use of external reference and counter electrodes. Although limited success has been reported on the use of flat cells or similar apparatus for detection of corrosion in the field,<sup>13-15</sup> they require a smooth, flat surface to obtain a seal when using a liquid electrolyte (Table 1). Even the use of gels, sponges, and other solid or semisolid electrolytes can be messy and require access to the location being inspected. Such cells can only detect corrosion directly under the electrolyte.

**Table 1. Comparison of *In-Situ* Corrosion Probe with Conventional EIS**

<i>In-Situ</i> Corrosion Probe	Conventional EIS
<ul style="list-style-type: none"><li>• Suitable for field use or laboratory test chamber/immersion</li><li>• Permanent electrode is available for inaccessible regions</li><li>• Hand-held sensor is available for structures/areas without a permanent sensor</li><li>• Arbitrary structure configuration</li><li>• Easy set-up/inspection</li><li>• Inspection can detect corrosion over large area</li></ul>	<ul style="list-style-type: none"><li>• Requires immersion or clamp-on liquid cell</li><li>• Cell requires accessible, flat, horizontal area, messy electrolyte, and remote electrodes</li><li>• Set-up is time consuming and must be performed for each measurement</li><li>• Corrosion is detected only directly under cell</li><li>• Can result in artifactual degradation.</li></ul>

The *in-situ* corrosion sensor offers a quantitative measure of incipient corrosion in the field unlike other corrosion monitors (Table 2). The first field corrosion sensors simply measured the time of wetness of a surface – a useful parameter, but only one factor controlling corrosion. An early *in-situ* sensor provided some of the advantages of the current permanent sensor, but re-

quired vacuum deposition of the sensor electrode thus restricting it to small test panels or components.<sup>16-18</sup> Other sensors determine the corrosion rate of the sensor itself using coated optical fibers, mass gain/loss, or electrochemical measurements on witness electrodes that are part of the sensor package.<sup>19,20</sup> Because of differences in corrosion susceptibility of the witness electrode material(s) and the actual structure and differences in the microenvironment of the sensor and the structure, the corrosion rates measured by the witness sensors may or may not correlate with corrosion rates exhibited by the structure being inspected. Traditional nondestructive evaluation (radiography, ultrasonics, thermography) has required extensive structural degradation – loss of material, blistering delamination of paint, coatings, or of the structure itself. In some cases, these techniques are better suited for detection of strain or cracks (other serious problems) instead of corrosion. As such, they are complementary to the *in-situ* corrosion sensor. Many of these procedures either require sophisticated equipment or highly trained personnel or do not measure the corrosion of the structure of interest. In the case of x rays, significant safety issues arise with the use of ionizing radiation.

**Table 2. Comparison of *In-Situ* Corrosion Probe with Other Corrosion Detection Methods**

<i>In-Situ</i> Corrosion Probe	Other Corrosion Sensors
<ul style="list-style-type: none"> <li>• Measures corrosion of actual structure</li> <li>• Sensitive to early stages of corrosion/degradation</li> <li>• Very sensitive to moisture intrusion into bondline</li> <li>• Relatively inexpensive instrumentation</li> <li>• Monitors electrochemical process (corrosion) directly</li> </ul>	<ul style="list-style-type: none"> <li>• Time of wetness monitors</li> <li>• Corrosion of sensor itself           <ul style="list-style-type: none"> <li>• Material differences</li> <li>• Environmental differences</li> </ul> </li> <li>• Require significant loss of material</li> <li>• Require delamination or blistering</li> </ul>

The *in-situ* corrosion probe is directly applicable to detect the degree of coating degradation and the amount of substrate corrosion of real structures. Because it detects the very early stages of corrosion, it provides a warning before structure degradation occurs. Thus preventative maintenance can be scheduled in time to forestall corrosion damage. Alternatively, by detecting corrosion from the very early stages and allowing a quantifiable comparison between field or service degradation and that observed during accelerated testing, the sensor should be valuable during coating development.

## 2.0 Experimental

A variety of different paints and other coatings have been evaluated primarily on aluminum, although steel substrates have also been used. Electrochemical impedance spectroscopy measurements were made using the substrate as the working electrode and the sensor as both the counter and reference electrodes. Most of the data were acquired using a EG&G Princeton Applied Research potentiostat Model 273 with an EG&G lock-in amplifier Model 5210 with Model 398 version 1.10 software. Potentiodynamic polarization measurements (Model 352 SoftCorr II software) were also obtained to determine corrosion rates of selected samples. The remainder of the data were acquired by a Gamry Model CMS100/105/300 portable corrosion measurement system. This unit is more compact than traditional bench-top units and would be suitable for inspection in the field. The specimens were exposed to several different exposure conditions. These are given in Table 3 along with relevant instrumentation.

**Table 3. Exposure Conditions**

Exposure Conditions	Equipment
• Immersion	• EG&G Model K47 Corrosion Cell
• Humidity (95-98% RH, 50°C)	• EG&G Model K235 Flat Cell
• Salt Fog (ASTM B117)	• Blue M Model VP-100AT
• Refrigeration	• Singleton Corrosion Test Cabinet Model 20
• Laboratory Ambient	• Whirlpool EH100 Freezer
• Outdoor Weathering	• none
	• none

### 3.0 Results and Discussion

To establish the validity of the *in-situ* sensor, EIS measurements were made with the sensor and conventional three-electrode EIS on the same or identical specimens. Figure 1 shows that the impedance spectra obtained using the *in-situ* sensor and the conventional three remote electrodes in a flat cell are virtually identical. Similar comparisons have been obtained with other coatings and metals. For the hand-held sensor, measurements were taken on painted specimens with and without a scratch to simulate a defect in the coating (Figure 2). Each of three variations of the hand-held probe give results very similar to the conventional three-electrode measurements. Each measurement very clearly reflects the presence of a gross defect such as a scratch.

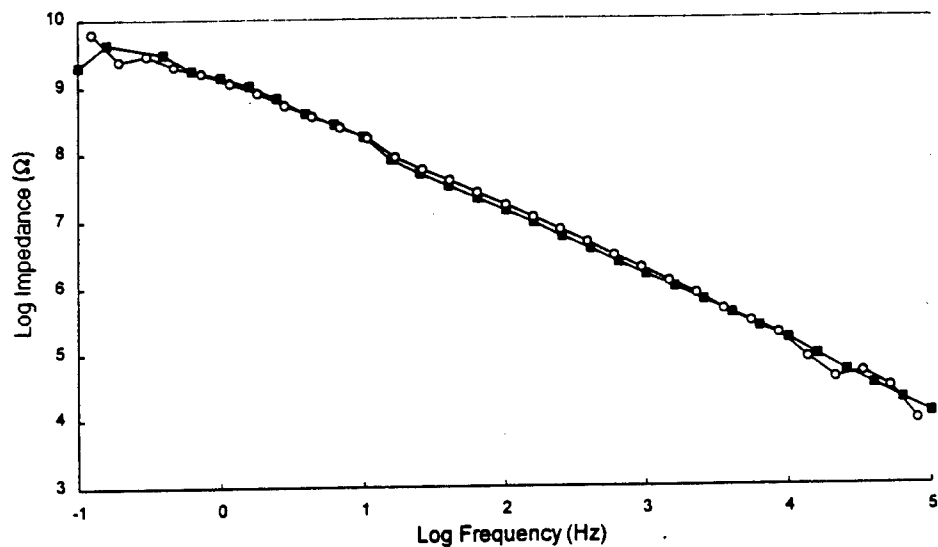


*Figure 1. Impedance spectra of painted aluminum specimen. The conventional 3-electrode measurements using a flat cell and measurements using the attached in-situ corrosion sensor are virtually identical*

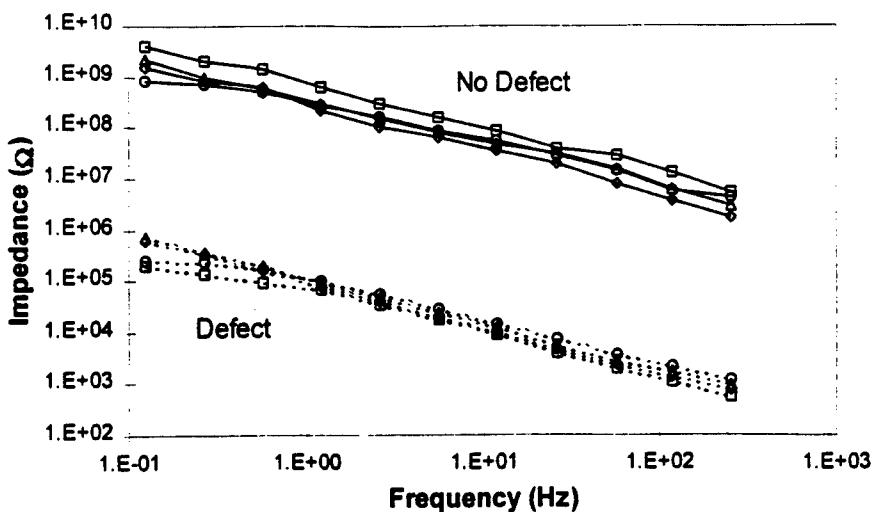


*Figure 2. Impedance spectra of epoxy-polyimide painted aluminum with and without a scratched defect. The different curves correspond to a conventional 3-electrode measurement and measurements made using 3 different hand-held probes.*

EIS and the *in-situ* sensors detect much more subtle degradation than a scratch that exposes bare metal. Figure 3 shows that initially the coated metal demonstrates capacitive behavior with very high impedance at low frequencies. As the coating degrades during immersion, its resistance decreases (as modeled in an equivalent circuit) and the impedance becomes independent of frequency at low frequencies.

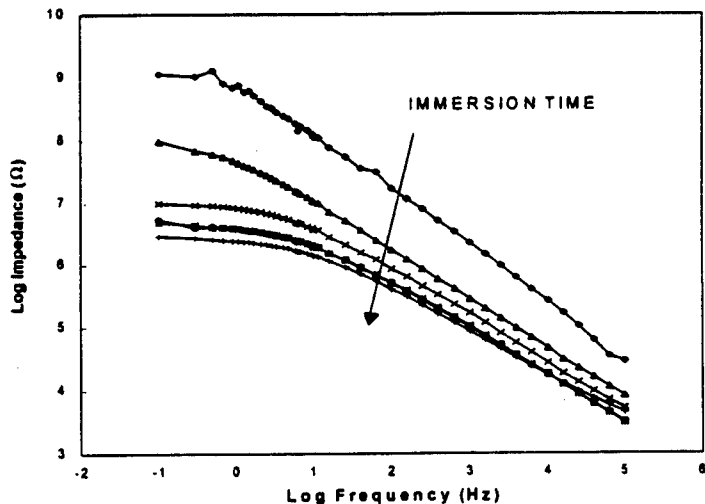


*Figure 3. Impedance spectra of painted aluminum as a function of immersion time.*

The low-frequency response can be tracked as a function of exposure. Figure 4 gives the near-DC impedance of an epoxy-coated aluminum immersed in hot water for approximately six months.<sup>21</sup> The data clearly show corrosion to occur in three stages for this system:

- Uptake of moisture by the coating
- Incubation time for corrosion
- Substrate corrosion.

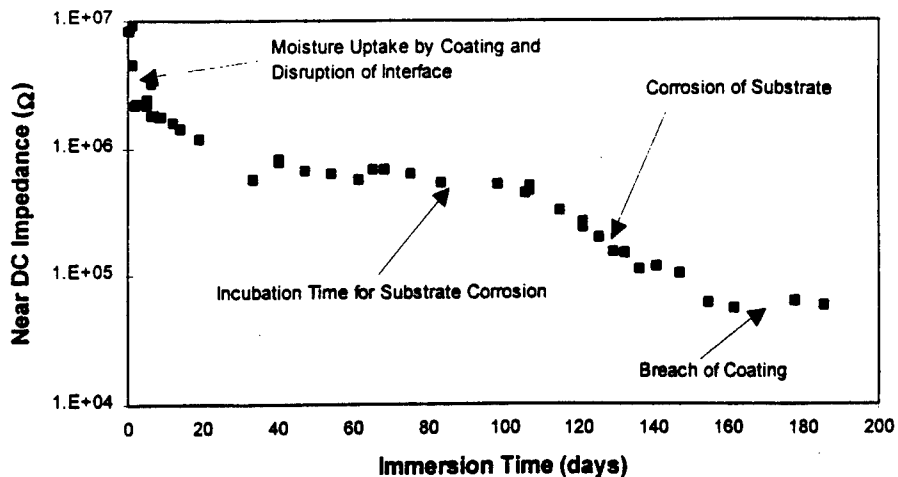


*Figure 4. Near-DC impedance of a FM-123 epoxy-coated aluminum specimen following immersion for six months at 58°C.*

In the later stage, the corrosion products erupted through the epoxy coating and allowed the electrolyte unimpeded access to the metal. The relative times and impedance decreases for the different stages will depend on the quality and chemistry of the coating, the metal underneath and any surface treatment, and the exposure conditions. For example, Figure 5 demonstrates that a waterborne coating is not as effective as an epoxy polyimide coating. The impedance of the waterborne coating drops approximately one order of magnitude more than the organic solvent coating, reflecting the greater moisture uptake. Partially as a result of the increased moisture concentration at the interface, the incubation period is shorter and active corrosion of the substrate occurs sooner.

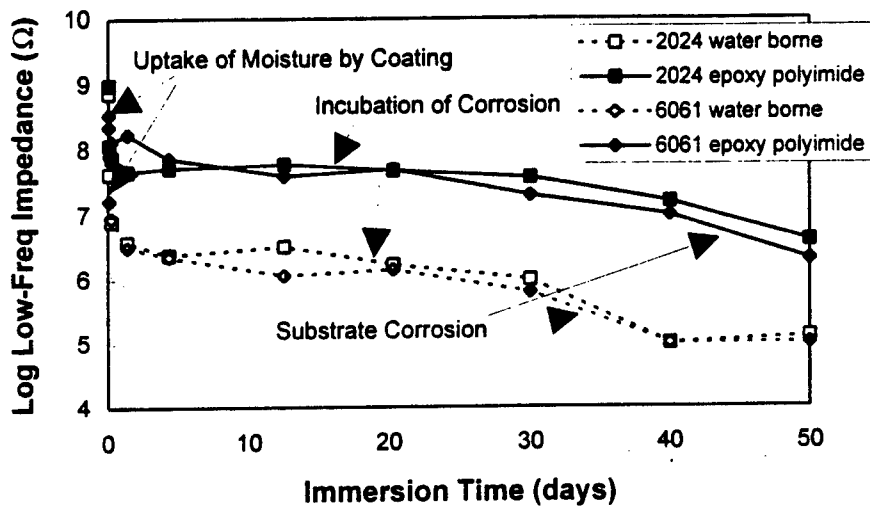


*Figure 5. Near DC (low frequency) impedance as a function of time for aluminum specimens coated with either an epoxy polyimide or a waterborne epoxy. The waterborne coating was clearly less effective than the epoxy polyimide. The coatings were immersed in water at room temperature during the experiment duration.*

One of the principal advantages of the *in-situ* corrosion sensor is its ability to monitor corrosion under a variety of conditions in addition to immersion for which conventional remote electrode EIS measurements are possible. As a result, material degradation in accelerated laboratory conditions can be directly compared to degradation occurring in the field or under different conditions. Figure 6 presents sensor results for identical aluminum panels exposed to different environments. As one would expect, no material degradation or other change was observed in specimens stored in a refrigerator or inside under ambient conditions. The specimen kept in a humidity chamber ( $50^{\circ}\text{C}$ , 98% RH) showed a steady drop in impedance until the coating reached equilibrium with absorbed moisture. The panel exposed near a busy highway in Maryland in winter/spring show little degradation during mostly dry periods, but show a response similar to that of the humidity exposed specimen during extended periods of rain. However, this decrease in impedance, representing moisture absorption, is largely reversible and once the paint dries, the impedance increases to near the original value. In this relatively short field exposure, we cannot rule out a small permanent impedance decrease that might reflect the beginning of irreversible damage. However, the majority of the changes are reversible and appear to mirror changes occurring in the humidity chamber, but at a much slower rate.

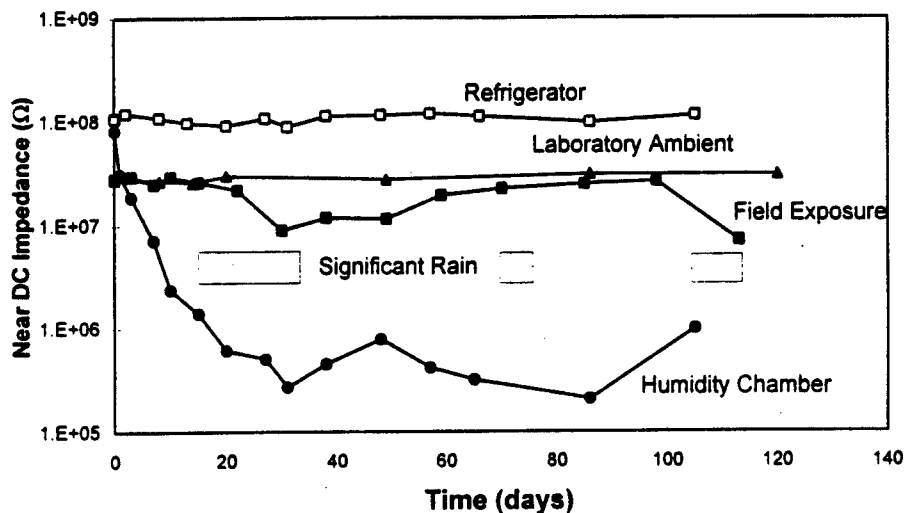
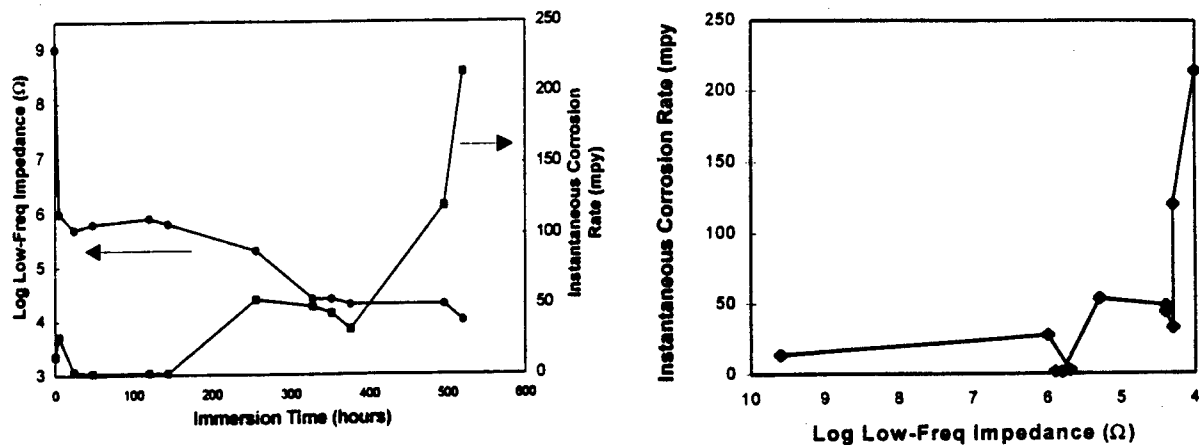


Figure 6. Near DC impedance of enamel coated aluminum panels exposed to different environments. The hand-held probe was used to obtain the data.

One issue concerning the validity of the permanent sensor measurement is the stability of the sensor itself during long-term or aggressive exposures. If the sensor electrode corroded or otherwise deteriorated during the exposure, the measurements might be indicative of the sensor and not of the structure of interest. Several different electrode materials were evaluated using different accelerated testing, including exposure to salt fog for more than 1000 hours. In this test, the electrodes showed no signs of loss of integrity or adhesion to the specimen. In fact, the experiment as ended after the glyptal coating used to protect the back and sides of the specimens began to fail. Validation of the *in-situ* sensor was achieved by the similarity of measurements taken under a variety of exposure conditions using the permanent sensor, conventional remote-electrode EIS, and the hand-held probe which is not exposed to the aggressive environments.

To correlate sensor results with corrosion rates, polarization resistance measurements were taken in conjunction with the EIS sensor measurements on scribed, painted aluminum panels immersed in water. The results are shown in Figure 7. For this material system and exposure conditions, the corrosion rate remains very low, aside from a quick oxidation of the scribed area during the very initial exposure, until the log-frequency impedance decreases to approximately  $10^5 \Omega$ . However, once the impedance approaches  $10^4 \Omega$ , the corrosion rate increases dramatically. A similar correlation was obtained using ellipsometry, the oxide film in the scribed region remained relatively thin until the third stage of the corrosion behavior. Subsequently, the thickness of the oxide coating increased as corrosion products were formed.



*Figure 7. Left: Low frequency impedance and instantaneous corrosion rate as functions of immersion time for epoxy coated aluminum. The sharp initial decrease in impedance results from the scribe which has the effect of by-passing the moisture absorption stage of Figure 4. Right: The instantaneous corrosion rate as a function of the low frequency impedance.*

The distance from which the *in-situ* sensor can detect corrosion or a coating defect depends on a number of factors, most notably the surface conductivity of the coating. As a result, it can be controlled. Under appropriate conditions, the *in-situ* sensor can distinguish between good and poor areas of the surface. However, increasing the surface conductivity of the specimen can substantially increase the detection range of a sensor. This effect is illustrated in Figure 8 and Figure 9. The current path from the sensor to the substrate will vary, depending on various conditions. If the surface resistance is very high, the dominant path will be directly across (through) the coating. In this case, detection of degradation will be localized. On the other hand, if the surface resistance is relatively low, the current can proceed along the surface until it reaches a defect or other localized region of low coating resistance. If an equivalent circuit analysis were being performed, this would be represented by an additional RC branch. As a result, the detection area of the sensor can be controlled. If a wide detection range is desired, for example, if the inspector wants to take a quick look to see if any corrosion is present, wetting the surface with a conductive fluid will allow global inspection with a minimum of sensors. On the other hand, if it is desired to localize the degradation, inspection of a dry surface will allow the area of deterioration to be pinpointed.

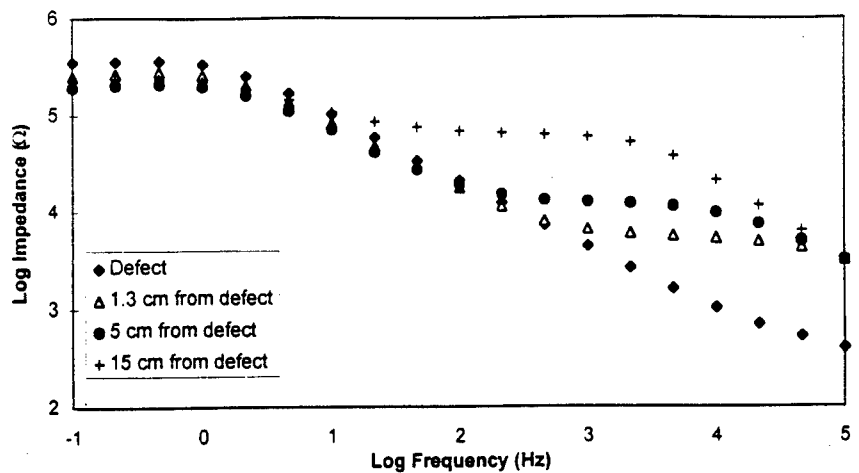


*Figure 8. Impedance spectra for a painted aluminum specimen with a scratch to simulate a coating defect. As the hand-held sensor was moved further from the defect, a plateau region at intermediate frequencies appears and corresponds to a conduction path along the surface. The surface was wetted with a conductive fluid for these tests.*

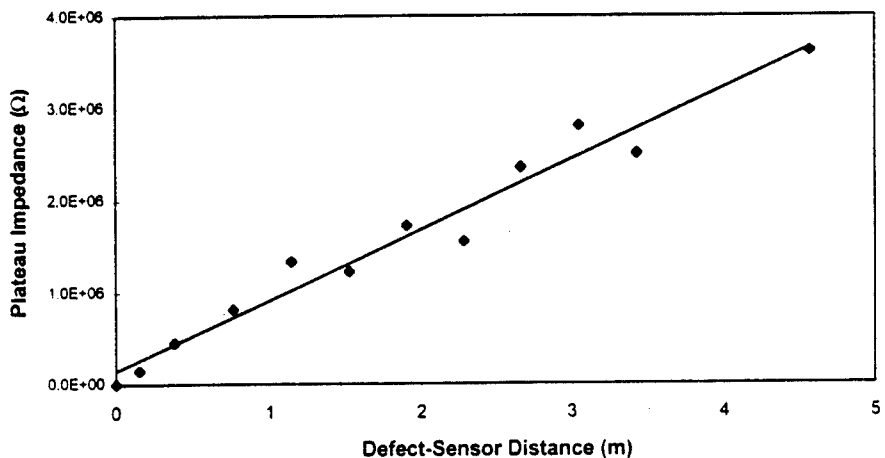


*Figure 9. Impedance of the plateau region as a function of distance of the sensor from the defect. The surface was wetted with a conductive fluid for these tests.*

A field demonstration was performed to illustrate the use of the sensor under typical depot conditions on a C-135 aircraft (Figure 10). The measurements verify that EIS measurements can be readily obtained from different areas of an airplane using the hand-held sensor in a depot. No special preparation or facilities were needed. Furthermore, the sensor could readily distinguish between good primer and deteriorated primer, which exhibited a decrease in the low-frequency dependence of at least two orders of magnitude. Measurements on other aircraft components showed a similar correlation between the EIS signal and extent of corrosion or other degradation.

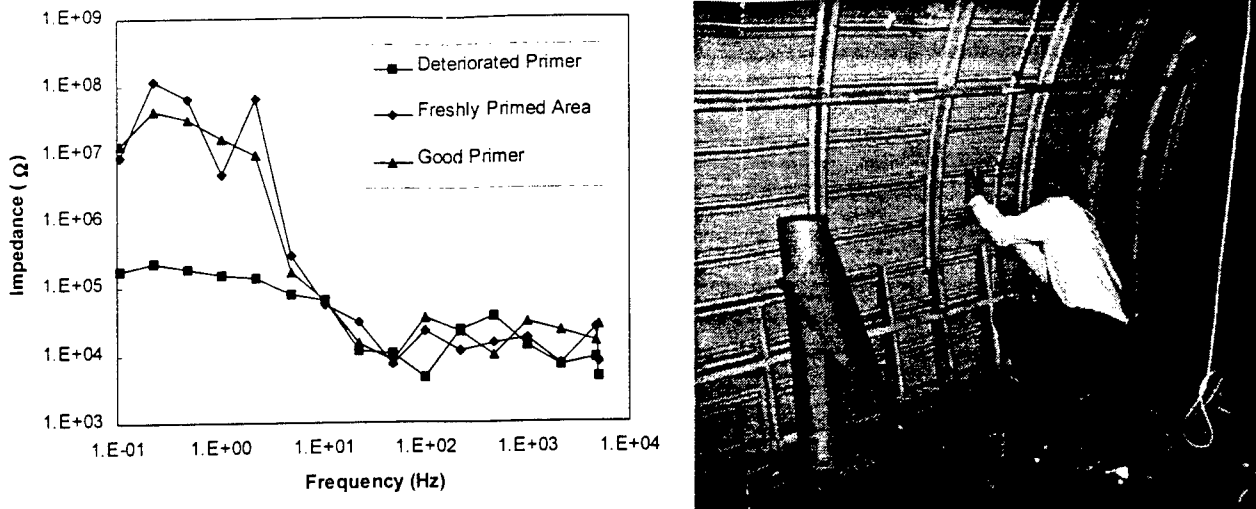


Figure 10. (Left) EIS spectra taken from three areas of a C-135 aircraft at Tinker AFB. (Right) Engineer performing measurements with hand-held sensor.

#### 4.0 Summary and Conclusions

An *in-situ* corrosion sensor has been developed that extends the applicability of electrochemical impedance spectroscopy (EIS) to monitor material degradation beyond laboratory immersion studies. Two versions of the sensor are available: a permanent electrode that is especially suited for inaccessible areas or for areas for which a corrosion history or database is desired and a portable, hand-held electrode that is especially suited for areas where a permanent sensor is not desired for aesthetics or other reasons or where only a one-time measurement is needed. Both versions provide EIS measurements identical to conventional remote electrode procedures when tested in immersion. The ability of the *in-situ* sensor to monitor material deterioration from the very initial stages in accelerated tests, such as salt fog or humidity, and during actual field service enables two applications: 1) *in-situ* corrosion monitoring of critical structures to allow condition-based maintenance and reduce the likelihood of unforeseen corrosion-induced failure and 2) enhanced coating development with the quantitative comparison of degradation occurring during accelerated testing and system service use.

#### 5.0 Acknowledgments

We would like to acknowledge the technical assistance of D. Stuart, B. Taggart, and P.L. Whisnant over the course of this investigation. We would like to express our appreciation of Courtaulds Aerospace for painting some of the specimens and of Don Nieser and Dick Kinzie for arranging field demonstrations at Tinker AFB and Robbins AFB, respectively. This effort was funded by AFSOR under SBIR contract F49620-95-C-0040.

#### 6.0 References

<sup>1</sup> J.A. Payer and G.M. Ugiansky, "Impact of the NBS - Batelle Cost of Corrosion Study in the United States," *Proc. Corrosion Symp. Int. Approaches to Reducing Corrosion Costs* (NACE, Houston, 1986).

- 2 C.I. Change, "Aging Aircraft Science and Technology Issues and Challenges and USAF Aging Aircraft Program," in *Structural Integrity in Aging Aircraft* AD-47 ed., C.I. Chang and C.T. Sun, (ASME, New York, 1995), p. 1.
- 3 "Economic Effects of Metallic Corrosion in the United States, A 1995 Update," Batelle Report to Specialty Steel Industry of North America, April 1995.
- 4 D.W. Hoeppner, L. Grimes, A. Hoeppner, J. Ledesma, T. Mills, and A. Shah, "Corrosion and Fretting as Critical Aviation Safety Issues: Case Studies, Facts, and Figures from US Aircraft Accidents and Incidents," *Proc. 18th Symp. Inter. Comm. Aeronautical Fatigue* (Melbourne, Australia, May 1995), p. 87.
- 5 G.D. Davis and C.M. Dacres, "Electrochemical Sensors for Evaluating Corrosion and Adhesion on Painted Metal Structures," patent pending.
- 6 F. Mansfeld, "Recording and Analysis of AC Impedance Data for Corrosion Studies: I. Background and Methods of Analysis," *Corrosion* 37, 301 (1981).
- 7 M. Kendig, F. Mansfeld, and S. Tsai, "Determination of the Long Term Corrosion Behavior of Coated Steel with AC Impedance Measurements," *Corros. Sci.* 23, 317 (1983).
- 8 M. Kendig and J. Scully, "Basic Aspects of the Application of Electrochemical Impedance for the Life Prediction of Organic Coatings on Metals," *Corrosion89* Paper 32, NACE (1989).
- 9 J.R. Scully, "Electrochemical Impedance of Organic-Coated Steel: Correlation of Impedance Parameters with Long-Term Coating Deterioration," *J. Electrochem. Soc.* 136, 979 (1989).
- 10 W.S. Tait, *J. Coat. Technol.* 61, 57 (1989).
- 11 J.N. Murray and H.P. Hack, "Long Term Testing of Epoxy Coated Steel in ASTM Sea Water Using EIS," *Corrosion90* Paper 140, NACE 1990.
- 12 J.A. Grandle and S.R. Taylor, "Electrochemical Impedance Spectroscopy of Coated Aluminum Beverage Containers: Part 1 – Determination of an Optimal Parameter for Large Sample Evaluation," *Corrosion* 50, 792 (1994).
- 13 A. Zdunek and X. Zhan, "A Field EIS Probe and Methodology for Measuring Bridge Coating Performance," *4th World Congress on Coating Systems for Bridge and Steel Structures*, Steel Structures Painting Council, St. Louis, MO, February 1995.
- 14 K. Homma et al., "Utilization of Electrochemical Impedance Techniques to Estimate Corrosion Damage of Steel Infrastructure," *Corrosion Forms and Control for Infrastructure*, ASTM STP 1137, Victor Chaker, ed., ASTM, Philadelphia, 1992.
- 15 P.C. Su, O.F. Devereux, and W. Madych, "Impedance Imaging for Prediction and Detection of Airframe Corrosion," *Structural Integrity in Aging Aircraft*, AD-Vol. 47, C.I. Chang, and C.T. Sun, ed., American Society of Mechanical Engineers, 1995.
- 16 T.C. Simpson, P.J. Moran, W.C. Moshier, G.D. Davis, B.A. Shaw, C.A. Arah and K.L. Zankel, "An Electrochemical Monitor for the Detection of Coating Degradation in Atmosphere," *J. Electrochem. Soc.* 136, 2761 (1989).
- 17 T.C. Simpson, P.J. Moran, H. Hampel, G.D. Davis, B.A. Shaw, C.A. Arah, T.L. Fritz, and K.L. Zankel, "Electrochemical Monitoring of Organic Coating Degradation during Atmospheric or Vapor Phase Exposure," *Corros. 46*, 331 (1990).
- 18 T.C. Simpson, H. Hampel, G.D. Davis, C.O. Arah, T.L. Fritz, P.J. Moran, B.A. Shaw, and K.L. Zankel, "Evaluation of the Effects of Acidic Deposition on Coated Steel Substrates," *Prog. Organic Coatings* 20, 199 (1992).
- 19 V.S. Agarwala, "In-Situ Corrosivity Monitoring of Military Hardware Environments," *Corrosion96* Paper 632, NACE 1996.

20 R.G. Kelly, S.H. Jones, W. Blanke, J. Aylor, and A. Batson, "Embeddable Microinstruments for Corrosion Monitoring," *Corrosion97* Paper 294, NACE 1997.

21 G.D. Davis, P.L. Whisnant, and J.D. Venables, "Subadhesive Hydration of Aluminum Adherends and its Detection by Electrochemical Impedance Spectroscopy," *J. Adhes. Sci. Technol.* **9**, 433 (1995).

## DISCUSSION

### **Electrochemical In-Situ Sensors for Detecting Corrosion on Aging Aircraft**

Speaker: Davis

It appears you do not need an electrolyte in order to carry out EIS using your probe unlike the conventional EIS. What electrolyte do you use? —K. Bhausali

*The measurements can be taken without a liquid electrolyte. The paint or other coating serves as the electrolyte between the substrate and the sensor electrode. If the surface is wet or if the specimen is immersed in a solution, that liquid acts as the electrolyte enables a longer-range detection of defects.*



# **Superconducting Quantum Interference Devices for Nondestructive Testing**

James R. Claycomb, Nilesh Tralshawala, Hsiao-Mei Cho, Mike Boyd and  
John H. Miller Jr.

Texas Center for Superconductivity and Department of Physics,  
University of Houston, Houston, TX. 77204-5932

## **ABSTRACT**

We report on the development of a Superconducting Quantum Interference Device (SQUID) based eddy current corrosion and flaw detection system utilizing High Temperature Superconducting (HTS) and  $\mu$ -metal shields. Probes incorporating various combinations of excitation coil geometries and cylindrical magnetic shields have been designed and tested. Test results are presented for SQUID-based eddy current probes as well as a design incorporating a fluxgate magnetometer with a ferromagnetic flux-focuser. We discuss how the phase of the defect signal can be used to determine the flaw's depth. We also discuss the calculated SQUID response to corrosion induced thinning for various skin depths and plate thicknesses.

**Keywords:** SQUID, high temperature superconductor, magnetic imaging, eddy current imaging, nondestructive testing, corrosion

## **1. INTRODUCTION**

Superconducting Quantum Interference Devices (SQUIDs) are the most sensitive detectors of low frequency magnetic fields in existence. A SQUID is a superconducting loop containing either one or two tunnel junctions, or weak links, known as Josephson junctions (JJs).<sup>1</sup> When a sufficient bias current is applied to a dc SQUID, consisting of two JJs in parallel, a measurable voltage arises across the JJs, and its value is a periodic function of the magnetic flux through the loop. Usually the SQUID is operated in a feedback mode, utilizing a flux locked loop, where any change of magnetic field in the SQUID loop is canceled by a feedback current. This feedback current is then monitored through an output resistor where changes in magnetic field as small as  $10 \text{ fT/Hz}^{1/2}$  can be detected, depending on the quality and type of SQUID.

The various types of SQUIDs include dc- and rf-SQUIDs that can be made from both low- and high- $T_c$  superconductors. Whereas the dc SQUID utilizes two JJs, the rf-SQUID contains only a single JJ in a superconducting loop which is coupled inductively to a tank circuit. Low- $T_c$  SQUIDs (LTSQUIDS) are generally cooled with expensive liquid helium using elaborate, and expensive, cryostats. This presents a major obstacle to their widespread use for practical applications. High- $T_c$  SQUIDs (HTSQUIDS), on the other hand, can be cooled either with inexpensive liquid nitrogen or with a single-stage closed-cycle cryocooler which requires no liquid cryogen at all. The magnetic sensors employed for the work reported here are directly-coupled dc HTSQUID magnetometers, consisting of patterned  $\text{YBa}_2\text{Cu}_3\text{O}_7$  (YBCO) thin films deposited onto  $\text{SrTiO}_3$  bicrystal substrates. The HTSQUIDS and associated electronics were obtained commercially from Conductus, Inc.<sup>2</sup> The magnetic sensors are cooled using compact cylindrical G-10 fiber epoxy dewars.

The use of SQUID magnetometers to locate defects in conducting materials was first introduced over ten years ago by H. Weinstock<sup>3</sup>. Since then several groups have demonstrated the ability of SQUIDs to locate material defects for a wide variety of electromagnetic nondestructive testing (NDT) applications<sup>4,5</sup>. The chief advantage of using SQUID magnetometers in electromagnetic NDT is that the unsurpassed sensitivity of these devices extends to very low frequencies including DC. This enables a greater eddy current depth penetration, hence the ability to detect deeply seated flaws that are out of the range of conventional eddy current inspection techniques.

Although SQUIDs are extremely sensitive magnetic field detectors, operation in a practical NDT environment is hampered by the presence of electromagnetic interference (EMI) from powerlines, radio transmitters and the Earth's magnetic field. Motion, or change of orientation, in the Earth's magnetic field can cause the SQUID electronics to reset, resulting in erratic readout where the measured voltage is no longer proportional to the applied magnetic field. Large electromagnetic noise sources can further contaminate signals of interest as well as lead to reduced sensitivity of the entire SQUID measurement system.

The superconducting eddy current probes that we have developed here are designed to be operated outside of large magnetically shielded enclosures<sup>6</sup>. This is accomplished by surrounding the SQUID with an HTS tube to screen out external EMI. Here the SQUID is located at one end of the HTS tube where distant noise sources are greatly shielded. The presence of the HTS tube, however will not significantly affect the magnetic field produced by a nearby dipole source such as that due to current flow around a material defect or a corrosion pit<sup>7</sup>.

In the following sections we discuss some of the theoretical predictions governing the detection of cracks and corrosion in non-ferrous metallic structures. We then follow with a description of the various eddy current probe designs optimized by our finite element electromagnetic modeling. Next we discuss the measurement technique and present the results of defect scans.

## 2. DEPTH ANALYSIS

In this section we illustrate how the sign of the quadrature-phase and the in-phase defect response is related to the flaw's depth. We show that for time harmonic excitations the eddy current density at 0° and 90° will change sign at certain characteristic depths in the conducting media. In general, the phase of the defect response will be roughly that of the eddy current density flowing at the depth of the flaw. In this way the flaw depth, or the layer in which the flaw resides can be determined.

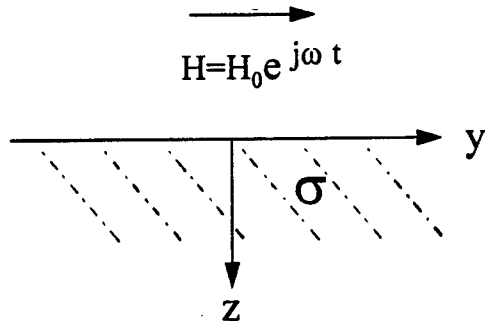


Fig. 1 Time harmonic magnetic field produced by an infinite sheet inducer tangential to a semi-infinite half-space of conductivity  $\sigma$ .

The simplest example is the eddy current density produced by an infinite sheet inducer located above and parallel to a semi-infinite half-space of conductivity  $\sigma$  (Fig.1). The sheet inducer carries a time harmonic current flowing in the x-direction. This current produces a uniform magnetic field  $H_0$  in the y direction. Inside the conducting medium the electric and magnetic fields obey the relation  $\nabla \times \vec{H} = \sigma \vec{E}$ . Taking the curl of this expression and substituting  $\nabla \times \vec{E} = -j\mu\omega \vec{H}$  results in a diffusion equation for the magnetic field inside the conducting half-space

$$\nabla^2 \vec{H} = j \frac{2}{\delta^2} \vec{H} \quad (1)$$

where  $\delta = \sqrt{2/\mu\sigma\omega}$  is the electromagnetic skin depth in the medium. Solutions to (1) are of the form  $\exp \pm \sqrt{2jz}/\delta$  with  $H_y = H_0$  and 0 at  $z=0$  and  $\infty$ , respectively. Recalling that  $\sqrt{j} = (1+j)/\sqrt{2}$ ,  $H_y$  becomes

$$H_y = H_0 e^{-(j+1)\frac{z}{\delta}}. \quad (2)$$

The eddy current density inside the conducting plane is then given by  $J_x = -\partial H_y / \partial z$  or,

$$J_x = H_0 \frac{(1+j)}{\delta} \left( \cos\left(\frac{z}{\delta}\right) - j \sin\left(\frac{z}{\delta}\right) \right) e^{-\frac{z}{\delta}}. \quad (3)$$

From this expression it is evident that

$$\text{Re}(J_x) \propto \cos\left(\frac{z}{\delta}\right) + \sin\left(\frac{z}{\delta}\right) \quad (4)$$

and that

$$\text{Im}(J_x) \propto \cos\left(\frac{z}{\delta}\right) - \sin\left(\frac{z}{\delta}\right). \quad (5)$$

From (4) it can be seen that the real part of  $J_x(z)$  changes sign at depths of  $z = (4n+3)\pi\delta/4$  and from (5) the imaginary part of the eddy current changes sign when  $z = (4n+1)\pi\delta/4$ , where  $n=0,1,2, \dots$ .

From this analysis we expect that the flaw depth can be estimated by monitoring the sign of the in-phase and quadrature-phase SQUID output. For more complex excitations involving circular, solenoidal and differential coil geometries a sign change in the real and imaginary eddy current components is still apparent, although at less precisely defined levels<sup>8</sup>. For the case of a sheet inducer above a plate of finite thickness the eddy current density is antisymmetric about the midpoint of the plate at any phase angle.<sup>9</sup>

### 3. CORROSION DETECTION

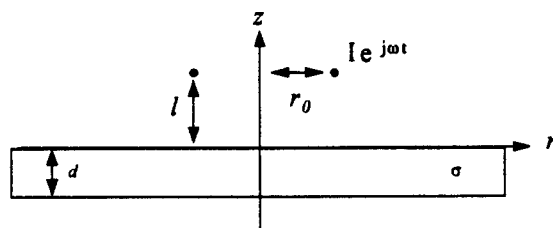


Fig.2 Circular excitation coil of radius  $r_0$  carrying a current  $I \exp(j\omega t)$  at a height  $l$  above a conducting plate of thickness  $d$ .

For the case of a circular excitation coil located above a conducting plate of finite thickness (Fig 2) we have calculated the change in magnetic field detected by a SQUID magnetometer at the center of the drive coil due to a variation of plate thickness<sup>10</sup>. In this way the SQUID's response to corrosion damage can be estimated for a given plate thickness  $d$  and amount of material loss due to corrosion  $\Delta d$ . At the center of the drive coil of radius  $r_0$  and lift-off  $l$  the magnetic field due solely to eddy currents in the conducting plate is given by

$$B_z(d, \delta) = \frac{\mu_0 I r_0}{2} \int_0^\infty J_1(\alpha r_0) e^{-2\alpha t} \frac{\alpha - \alpha_1(\delta)}{\alpha + \alpha_1(\delta)} \left( 1 + \frac{4\alpha^2 \alpha_1(\delta)}{[(\alpha - \alpha_1(\delta))^2 - (\alpha + \alpha_1(\delta))^2 \exp(\alpha_1(\delta)d)]} \right) d\alpha, \quad (6)$$

where  $J_1$  is a Bessel function of the first kind and order one,  $\delta$  is the skin depth in the plate of thickness  $d$  and  $\alpha_1(\delta) = (\alpha^2 + 2j/\delta^2)^{1/2}$ . The change in magnetic field due to corrosion induced material thinning  $\Delta d$  is then given by  $\Delta B_z = B_z(d+\Delta d, \delta) - B_z(d, \delta)$ .

In Fig. 3, the change in the z-component magnetic field ( $\phi=0^0$  and  $\phi=90^0$ ) at the center of the drive coil due to a thickness change of 1 mm is plotted as a function of skin depth for a 1 cm and a 2 cm thick plate. In both cases the maximum  $0^0$  and  $90^0$  response occurs for a value of skin depth on the order of the plate thickness, with a slightly larger  $0^0$  signature. The larger  $0^0$  response is due to more in-phase eddy current flowing at the corrosion depth.

In Fig. 4, the change in magnetic field is plotted as a function of the amount of corrosion in a 1 cm and a 2 cm plate with  $\delta$  equal to the plate thickness (near the optimum operating frequency). In this figure the magnetic response is seen to vary linearly with the amount of corrosion. The field values obtained here range here from 100 fT to 100 pT for a coil radius and lift-off of 1 cm and a 1 mA AC current. These values are well within the range of a SQUID magnetometer, but are beyond the measurement capability of conventional magnetometers.

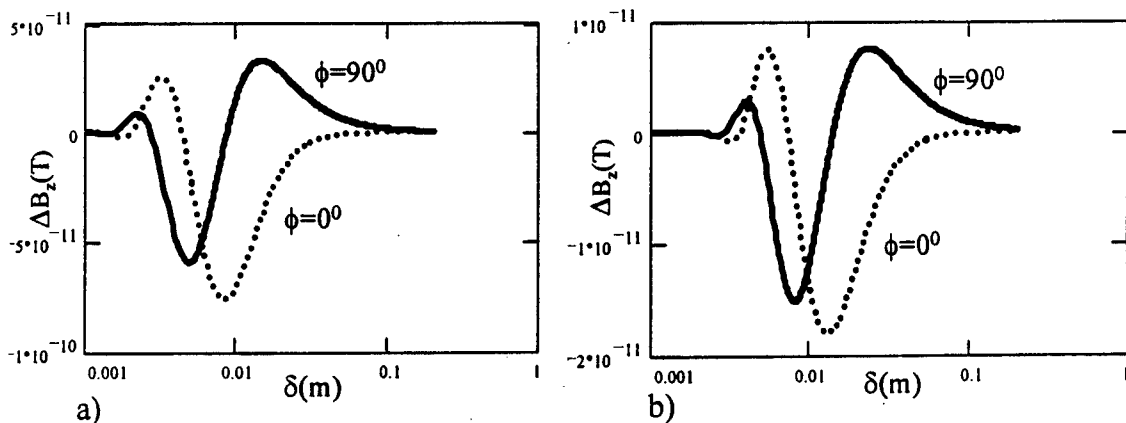


Fig. 3 Change in magnetic field ( $\phi=0^0$  and  $\phi=90^0$ ) at the center of an excitation coil as a function of skin depth due to 1 mm of corrosion in a conducting plate: a) with a thickness of 1 cm. b) with a thickness of 2 cm.

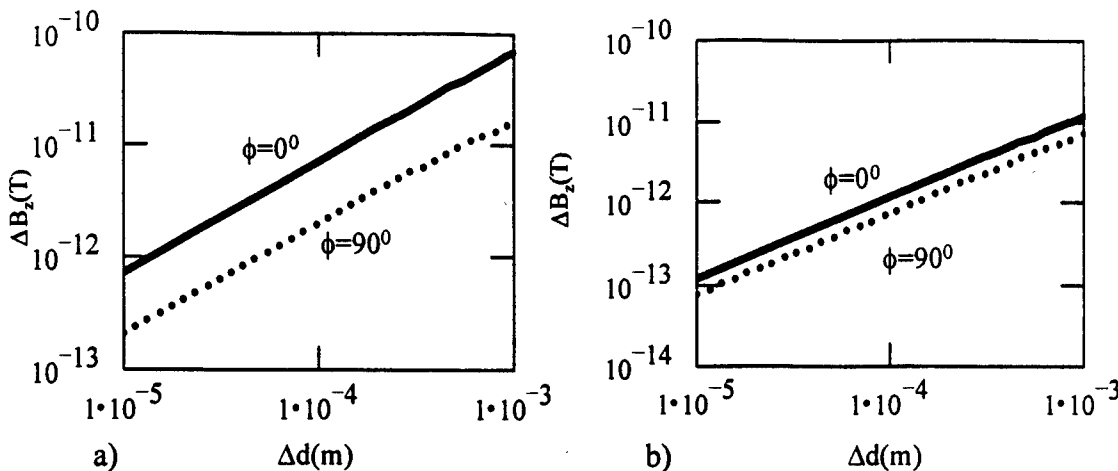


Fig. 4 Change in magnetic field ( $\phi=0^\circ$  and  $\phi=90^\circ$ ) at the center of an excitation coil as a function of the amount of corrosion in a conducting plate: a) with a thickness and a skin depth of 1 cm b) with a thickness and a skin depth of 2 cm.

#### 4. EDDY CURRENT PROBE CHARACTERISTICS

The simplest eddy current probe design consists of a circular loop or a solenoid that carries an AC current, inducing eddy currents in a conducting sample. If a SQUID sensor is positioned on the axis of the solenoid so that the SQUID pickup loop is parallel to the solenoid, then the field detected will be that due to eddy currents in the test sample as well as the primary field of the solenoid. In this configuration the primary excitation field (as well as the defect free eddy current field) will act as a source of unwanted signal, possibly overwhelming the signature of the flaw. If, on the other hand, the axis of the SQUID pickup loop is positioned on and normal to the solenoid axis, then the field detected will only be due to perturbations in the eddy current density caused by material defects (or edge effects). There still remains, however, other environmental noise factors that have to be contended with. One solution is to position two SQUID sensors back to back and electronically subtract their outputs. In this way a first order electronic gradiometer can be formed. The sensitivity of each SQUID is still effected by environmental noise, however.

In order to shield the SQUID from the primary coil as well as other sources of EMI we have used various combinations of  $\mu$ -metal and superconducting magnetic shields inserted between the drive coil and the SQUID sensor. The shielding effectiveness of ferromagnetic materials suffers at low frequencies. Its use here is primarily to focus flux into the object under test (OUT). The shielding factor of superconducting materials is essentially frequency independent and hence provides excellent shielding, even at DC<sup>6</sup>.

In order to model the electromagnetic response of various eddy current probe designs we have performed an extensive numerical study using a commercial finite element code<sup>11</sup>. This code supports a time harmonic eddy current solver. The numerical method here involves the solution of a diffusion equation for the magnetic vector potential given by  $\nabla^2 \bar{A} = j\omega\mu\sigma\bar{A}$ . This equation follows from the substitution of  $\mu \bar{H} = \nabla \times \bar{A}$  and  $\bar{E} = -j\omega\bar{A}$  into  $\nabla \times \bar{H} = \sigma \bar{E}$ . Once the vector potential is solved for, the eddy current density is then obtained from the relation  $\bar{J}_{eddy} = -j\omega\sigma\bar{A}$ .

Our modeling verifies that a tubular superconducting shield will be more effective than a  $\mu$ -metal shield in screening the field at the center of a solenoidal drive coil<sup>12</sup>. While the shielding factor is higher for a superconducting shield, the eddy current density in the part being tested becomes drastically reduced due to screening current flowing in the superconducting tube that oppose the drive coil field. The reduction of eddy current in the OUT will result in a smaller defect signal, the magnitude of which is proportional to the current density at the flaw location.

Ideally, one would like to achieve a combination of reduced field at the location of the SQUID with an enhancement in eddy current density in the conducting medium. This is accomplished with a combination of HTS and  $\mu$ -metal shielding where the  $\mu$ -metal shield is concentric with and outside of the superconducting shield. Also, placing a  $\mu$ -metal shield outside of the drive coil further serves to contain any stray flux and to focus the eddy current into a tight annulus under the probe<sup>6</sup>.

The next generation of probe design presented here incorporates a localized sheet inducer in conjunction with an HTS tube. If the axis of the SQUID pickup loop is normal to an infinite sheet inducer there will be no component of magnetic field perpendicular to the SQUID and hence no output. In the absence of defects or material edges the eddy current field will also have no component normal to the SQUID. For a sheet inducer of finite width the SQUID must be positioned directly over the half width point in order to have a null response in the absence of defects. The sheet inducer can either be placed between the SQUID and the OUT or on the opposite side of the OUT. Here the sheet inducer is positioned between the SQUID and the OUT, with the HTS tube surrounding the SQUID to screen EMI.

## 5. MEASUREMENTS

### 5.1 Fluxgate eddy current probe

The first design concept tested here consists of a fluxgate magnetometer at the center of a solenoidal drive coil (Fig. 5). A  $\mu$ -metal shield is inserted between the drive coil and the fluxgate. This shield serves to increase the flux density inside the OUT while reducing pickup from the excitation coil. An ac current is supplied to the excitation coil with a signal generator. The fluxgate signal is output to the lock-in detector referenced to the signal generator. Quadrature and in-phase components of the magnetic field are then recorded. The fluxgate operates in a bandwidth of 0-400 Hz with a field sensitivity of  $0.5 \text{ nT/Hz}^{1/2}$  and is therefore well suited for low frequency flaw detection.

The 2D quadrature-phase magnetic field plot in Fig. 6 was obtained with the configuration of Fig. 5. The excitation coil is wound on a  $\mu$ -metal form with a 1" diameter. Since the fluxgate has a diameter of 6 mm the probe radius can be reduced considerably to increase spatial resolution. The sample scanned in Fig. 6 consists of a 1" diameter hole drilled in the second layer of two 3 mm thick Al6061-T6 plates. Data were taken by manually scanning the sample under the probe and by manually recording  $0^\circ$  and  $90^\circ$  readings from the lock-in amplifier.

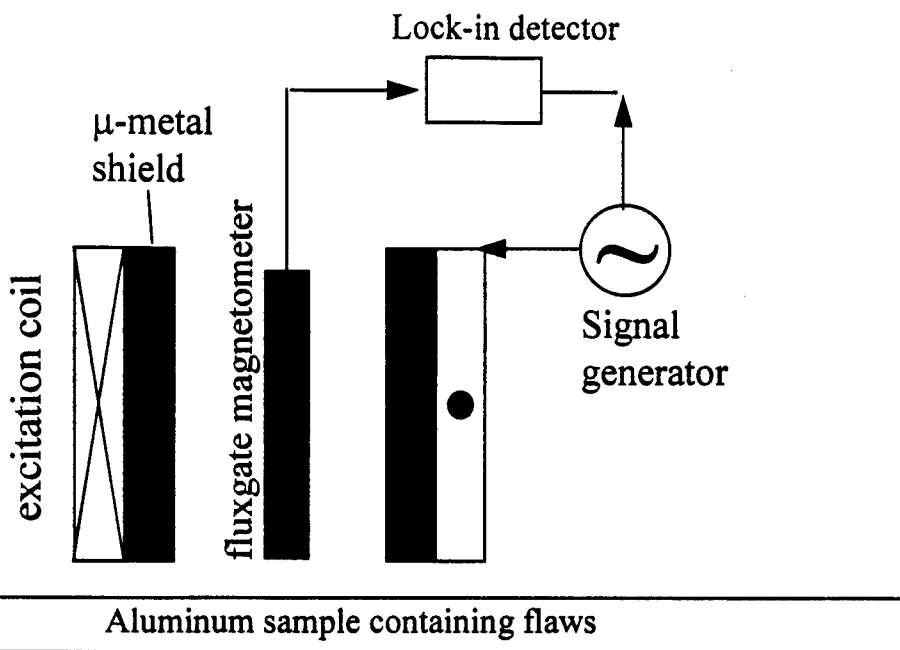


Fig. 5 Flaw detection system incorporating fluxgate magnetometer with a  $\mu$ -metal shield/flux-focuser inside the excitation coil.

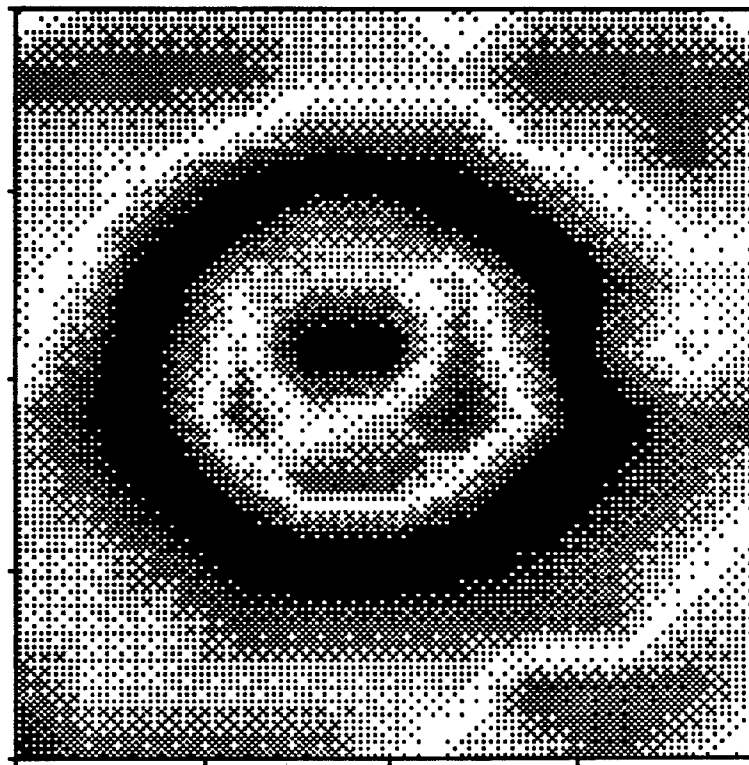


Fig. 6 Magnetic field map of a simulated corrosion pit obtained with the fluxgate flaw detection system in Fig. 5. Pit consists of a 1 cm hole drilled into the second layer of two 3 mm thick AlT6061-T6 plates.

## 5.2 SQUID-based eddy current probe with High-T<sub>c</sub> tube and $\mu$ -metal flux-focuser

The next design concept tested here incorporates a SQUID magnetometer in conjunction with a  $\mu$ -metal and an HTS tube (Fig. 7). Eddy currents are induced in the OUT by a circular excitation coil which is wound on a  $\mu$ -metal form surrounding an HTS tube. The probe is immersed in liquid nitrogen with the SQUID located at the bottom and center of the HTS tube. The output of the SQUID is fed into the lock-in detector referenced to the signal generator.

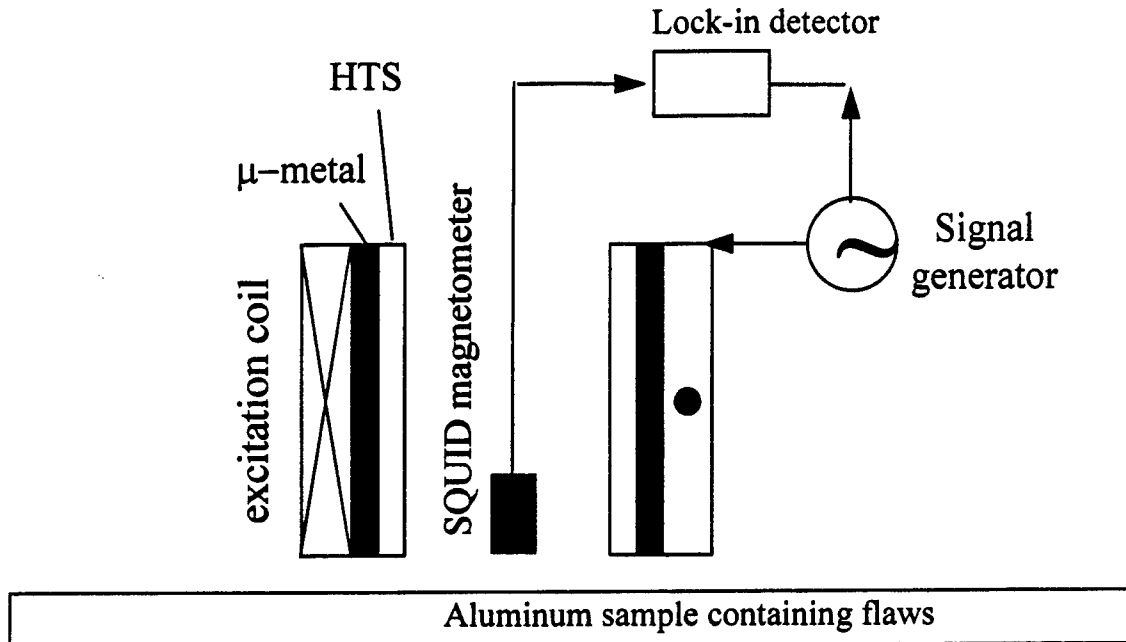


Fig. 7 SQUID-based eddy current flaw detection system incorporating an HTS tube and a  $\mu$ -metal shield surrounded by a circular excitation coil. Here the SQUID, HTS tube,  $\mu$ -metal tube and excitation coil are contained in a liquid nitrogen cryostat (not shown).

The results of 1-D scans are shown in Fig. 8 with the superconducting eddy current probe design depicted in Fig. 7. The High-T<sub>c</sub> tube has an OD of 1" and an ID of .75". The tube is wrapped in 3 layers of 5 mil thick  $\mu$ -metal foil. The sample consists of three layers of 5 mm thick aluminum plates. A flaw is simulated by joining together two smaller plates at an edge, and is used at different depths. The flaw is scanned at 13.73 Hz, 87.73 Hz and 207.3 Hz. These frequencies are chosen to avoid interference with the powerline harmonics. In Fig. 8 (a) the flaw is located at the top of the sample. The central dips in this figure corresponds to the defect signatures. Large edge effects are seen here at the sides. In Fig. 8 (b) the flaw is now located in the second layer, under 5 mm of unflawed aluminum. For the two higher frequencies the defect signature is no longer a dip but now appears as a bump. This sign change is due to the more diffuse pattern of eddy current flowing in the second layer as well as a larger fraction of eddy current near the flaw flowing at the 270° phase angle. For the defect scan in Fig 7 (c) the flaw is now located in the third layer under two layers of unflawed aluminum. At an excitation frequency of 207.3 Hz most of the eddy current is located above the flaw so that the flaw signature is very small in this case. At 13.73 Hz the eddy current is widely spread out through the sample so that only a small fraction of eddy current is perturbed by the flaw. The largest defect signature here occurs at 87.3 Hz since in this case the largest fraction of eddy current is perturbed by the flaw.

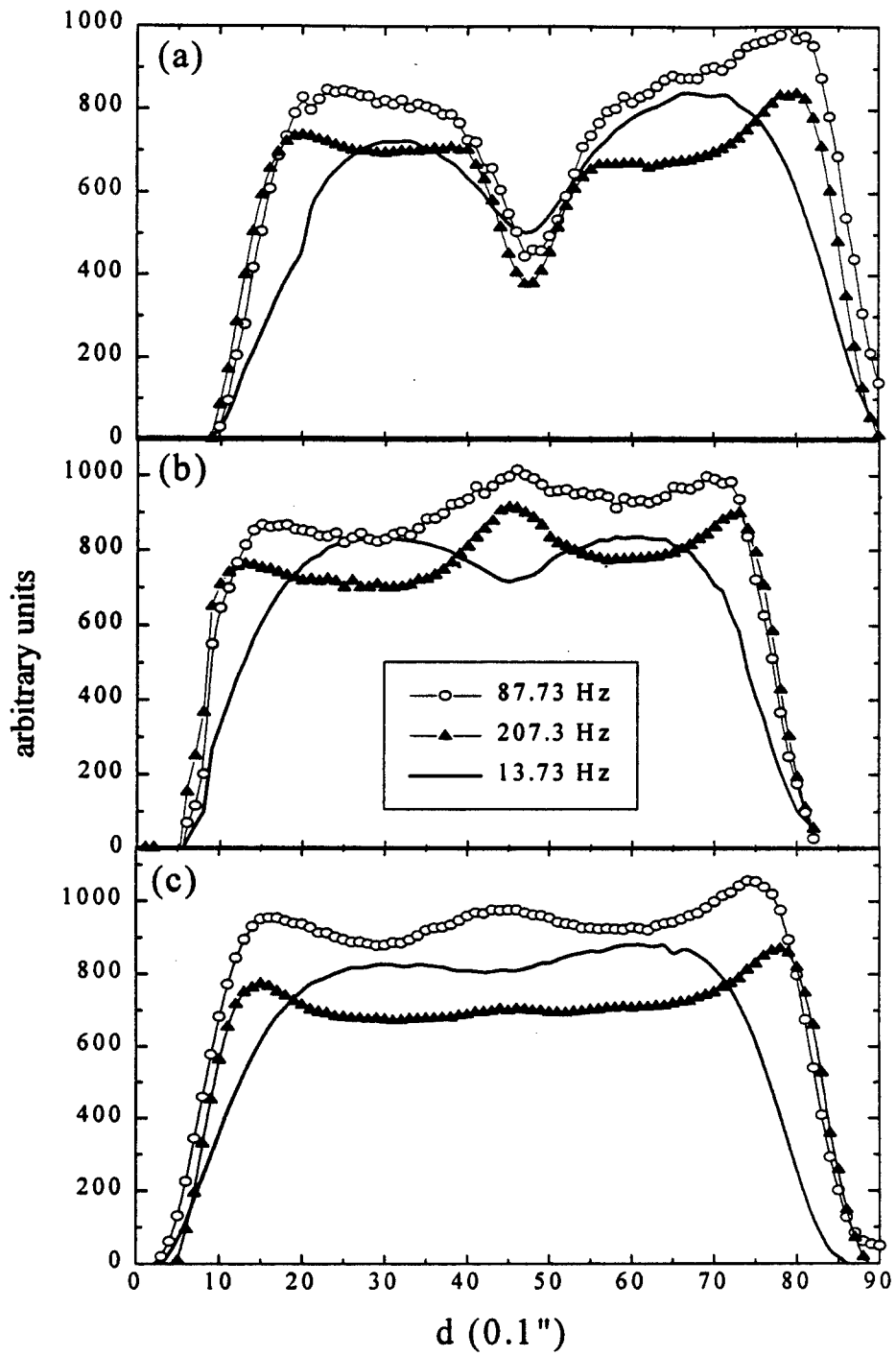


Fig. 8 Quadrature-phase SQUID output resulting from 1-D scans of layered Al6061-T6. The simulated defect resides in: a) the surface layer b) the second layer and c) the third layer of a stack of 5 mm thick plates. The flaw is formed by joining two unflawed plates at an edge. Measurements are made at 13.73 Hz, 87.3 Hz and 207.3 Hz . The defect signature is the center feature here with sharp edge effects on the sides.

### 5.3 SQUID-based eddy current probe with High-T<sub>c</sub> tube and planar sheet inducer

The third probe design tested here consists of a SQUID inside a High-T<sub>c</sub> tube centered above a localized planar sheet inducer (Fig. 9). The High-T<sub>c</sub> tube in this case serves to screen ambient EMI. The tube ID is 1.5" with an OD of 1.7". The sheet inducer is patterned on a 2.5" x 3" printed circuit board and is mounted at the bottom of the liquid nitrogen dewar. The SQUID is positioned directly over the midpoint of the sheet inducer where there is no field component in the z-direction. The SQUID will therefore have a null output at this location over an unflawed test piece. The sheet inducer is supplied with an ac current from vertical leads along the sides of the cryostat. The vertical current leads produce no field in the z-direction and hence do not contribute to the SQUID output.

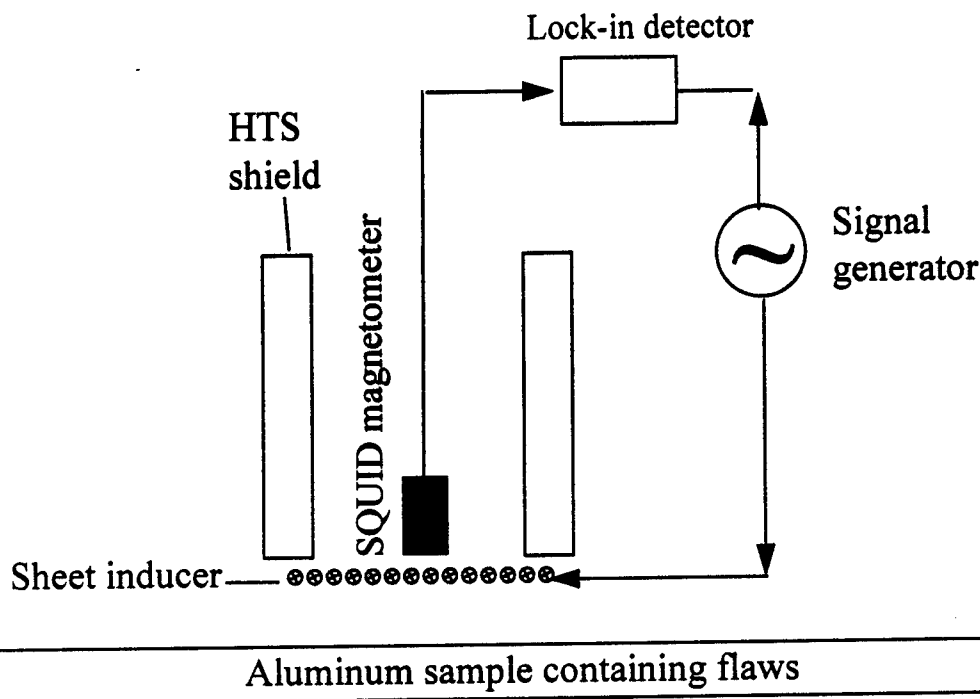


Fig. 9 SQUID-based eddy current probe design incorporating an HTS tube and a localized sheet inducer. The SQUID and HTS shield are located inside a liquid nitrogen dewar (not shown). The planar sheet inducer is attached to the bottom of the dewar.

In Fig. 10 the quadrature-phase SQUID output is plotted for 1-D scans across a 2.5 cm diameter and 2 mm deep machined flaw, simulating corrosion in the first and second layer of 5 mm thickness Al6061-T6. The defect signature at d=17 in Fig. 10 shows a sign change between the top and the second layer. The dc offset here is due a slight imbalance between the SQUID and the sheet inducer as well as the sheet inducer and the sample. Note that the sign of the edge effect is unaffected in either case.

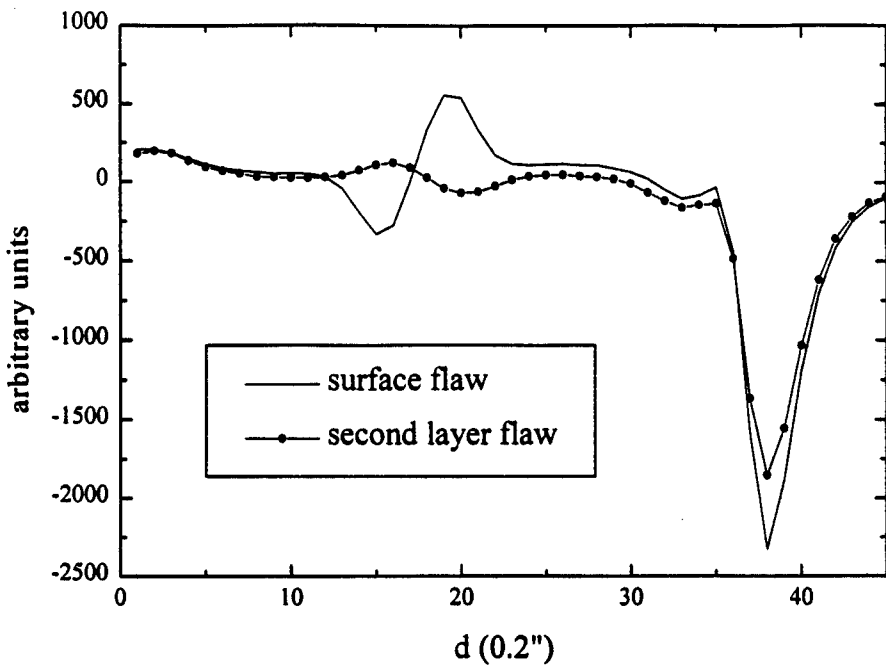


Fig.10 Quadrature-phase SQUID output resulting from 1-D scans of a simulated corrosion pit in the first and second layers of 5mm thick A16061-T6 plates. The sheet inducer carries a harmonic current at a frequency of 387 Hz. The defect signatures are located at  $d = 17$  with a phase change evident between the surface corrosion and second layer corrosion. A sharp edge effect is evident at  $d = 37$ .

## 6. CONCLUSION

We have designed and tested several eddy current probes utilizing both High- $T_c$  superconducting and normal components for corrosion and crack detection in aircraft structure. The normal eddy current probe design consists of a fluxgate magnetometer and a  $\mu$ -metal shield with a solenoidal excitation coil. The SQUID-based eddy current probe designs utilizes a combination of High- $T_c$  and  $\mu$ -metal shielding to screen ambient and drive coil EMI and to produce a larger eddy current density inside the workpiece. Finally a SQUID-based probe incorporating a High- $T_c$  shield and a planar sheet inducer has been demonstrated. All probe designs are based on a self nulling principle where the probe yields a null or minimal response in the absence of structural anomalies.

## Acknowledgements

This work was supported by NASA Grant No. NAG 9-905, by the State of Texas through the Texas Center for Superconductivity and the Texas Advanced Research Program, and by the Robert A. Welch Foundation.

## References

- [1] B.S. Josephson, "Possible new effect in superconductive tunneling," Phys. Lett., Vol.1, pp 251-253, 1962.
- [2] "iMAG" SQUID system made by Conductus Instruments and systems division, San Diego, CA 92121.
- [3] H. Weinstock and M. Nisenoff, "Defect Identification with a SQUID Magnetometer," Review of Progress in Quantitative Nondestructive Evaluation, Vol.6, pp. 669-704, 1986.
- [4] W.G. Jenks, S.S.H. Sadeghi, and J.P. Wikswo, Jr., "SQUIDs for nondestructive evaluation," J. Phys. D: Appl. Phys., Vol. 30, pp. 293-323, 1997.
- [5] G.B. Donaldson, A. Cochran and D. McA. McKirdy, "The use of SQUIDs for nondestructive evaluation," *SQUID Sensors: Fundamentals, Fabrication and Applications*, H. Weinstock (ed.), pp 599-628, Kluwer Academic Publishers, Netherlands, 1996.
- [6] N. Tralshawala, J.R. Claycomb, and J.H. Miller, Jr., "A practical SQUID instrument for nondestructive testing," Appl. Phys. Letts , Vol. 71(11), pp. 1573-1575, 1997.
- [7] N. Tralshawala, J. R. Claycomb, and J. H. Miller, Jr., "Reduction of Ambient Magnetic Field Noise for high- $T_c$  SQUID Applications," IEEE Trans. on Appl. Supercon., Vol. 7(2), pp. 2890-2893, 1997.
- [8] N. Tralshawala, J.R. Claycomb, H.M. Cho and J.H. Miller, Jr., "Development of Scanning High-Tc SQUID-based Instrument for Nondestructive Evaluation in a Magnetically Noisy Environment," To be published in *Nondestructive Characterization of Materials VIII*, R.E. Green, Jr. (ed.), Plenum, New York, 1998.
- [9] Y.P. Ma and J.P. Wikswo, Jr., "Techniques for depth-selective, low-frequency eddy current analysis for SQUID-based nondestructive testing," Journal of Nondestructive Evaluation, Vol. 14(3), pp. 149-167, 1995.
- [10] J.R. Claycomb, N. Tralshawala, and J.H. Miller, Jr., "A theoretical investigation of eddy current phenomena for low frequency eddy current testing," submitted to IEEE Transactions on Magnetics.
- [11] QuickField 3.4 User's Guide, Tera Analysis, Inc.,Granada Hills, CA 91344
- [12] J.R. Claycomb, N. Tralshawala and J.H. Miller, Jr., "Time harmonic simulations for the design of a high- $T_c$  superconducting eddy current probe for nondestructive evaluation," submitted to Rev. of Sci. Inst.
- [13] B. Wincheski, J. P. Fulton, S. Nath, M. Namkung, and J. W. Simpson, "Self-Nulling Eddy Current Probe for Surface and Subsurface Flaw Detection," Materials Evaluation, vol.52(1), pp.22-26, 1994.
- [14] N.S. Alzayed, C. Fan, D.F. Lu, K.W. Wong, M. Chester, and D.E. Knapp, "Deep nondestructive testing using a bulk high- $T_c$  rf-SQUID," IEEE Transactions on Applied Superconductivity, Vol.4(2), pp. 81-86, June 1994.
- [15] L.N.C.Morgan, C.Carr, A.Cochran,D.McA.McKirdy and G.B.Donaldson, "Electromagnetic nondestructive evaluation with simple HTS SQUIDs: measurements and modeling," IEEE Transactions on Applied Superconductivity, Vol.5(2), pp. 3127-3130, June 1995

# **Hidden Corrosion Modeled as Surface Roughness Detected Using Guided Plate Waves**

D. E. Chimenti and O. I. Lobkis  
Center for Nondestructive Evaluation and  
Aerospace Engineering & Engineering Mechanics Dept  
Iowa State University  
Ames IA 50011

## **Abstract**

Reported here are analytical and experimental results on the effect of surface roughness on ultrasonic guided waves in plates. The roughness models pillow ing corrosion in aluminum. The theoretical model is constructed by assuming the roughness degrades only the signal phase. The effect of the rough surface on the guided wave is treated by decomposing the wave modes into their constituent partial waves and considering individually the effect of the roughness on the partial wave components as they reflect from the plate surfaces. An approximate dispersion relation is derived for the traction-free rough waveguide that is formally identical to the conventional Lamb wave equation. The model calculation is also generalized to fluid-immersed plates having only a single rough surface. In addition, many experimental measurements have been performed on guided waves in plates with surface roughness, and the experimental data are critically compared to theoretical calculations. Aluminum samples, prepared by sandblasting, are measured in immersion. The model is shown to fail only when the guided wave phase velocity approaches the compressional or shear wavespeeds of the plate, where the internal partial waves strike the surfaces at grazing incidence. The simple phase-screen model cannot account for this behavior. Elsewhere in the guided wave spectrum, agreement is quite good.

**Keywords:** corrosion, guided waves, phase-screen approximation, partial wave analysis

## **INTRODUCTION**

Interaction of sound waves with rough surfaces has attracted attention owing to its significance in several fields. Scattering from wavy surfaces, seabeds, and ice in ocean acoustics has been extensively studied, as has scattering in rough dielectric waveguides, such as optical fibers. In either of these problems the fields can be assumed to be represented by a single scalar potential. The problem we consider here concerns the propagation of guided elastic waves in a planar waveguide having rough surfaces, with compressional and shear potentials that are coupled at each interface.

Most of the treatments of this problem are either mean field integral transform methods [1] or perturbation methods [2]–[4]. Those which are accurate under a broad range of conditions also typically involve complicated calculations. Those that are easier to manipulate analytically may not give such accurate results for all wave components or in all parameter limits. There is, however, a simple approximate result for scattering from a randomly rough fluid-solid interface that can be conveniently expressed as a product of the zeroeth order (smooth surface) reflection coefficient and a simple function dependent on the wavelength and the roughness parameters. We demonstrate in this paper that this approximate expression, introduced by Eckhart [5], is entirely sufficient as a basis from which to derive an initial estimate of the effect of rough surfaces in guided elastic wave propagation.

The phase-screen approximation (PSA) ignores any amplitude effects of the scattering and instead considers all the influence of the rough surface to be felt in the signal phase. Strictly speaking, the PSA is valid only in the Kirchhoff limit, when both the rms roughness height  $h$  and the fluid wavelength are much less than the roughness correlation length  $L$  ( $h, \lambda_f \ll L$ ). This expression has also been derived by Nagy and Adler [6] from the Kirchhoff integral and has been discussed by Dacol [7]. There has been essentially no work, however, on the effect of rough surfaces on elastic guided waves [4].

## THEORETICAL SUMMARY

Guided Lamb wave modes can be decomposed into propagating or evanescent compressional and shear partial waves. To derive a free rough-surface (RS) plate wave dispersion relation, we exploit the transverse resonance method [8], which naturally incorporates the partial wave reflection coefficients at the traction-free guide surfaces. In the geometry assumed throughout, the center of the infinite plate lies at the origin, the guided waves propagate in the  $x_1$  direction, and the  $x_3$  direction is normal to the plate surface. No field variable depends on  $x_2$ .

The secular equation of the homogeneous system of linear equations is,

$$1 \mp \epsilon \Gamma_{pp} e^{i\kappa_p d} \pm \delta \Gamma_{pp} e^{i\kappa_s d} - \lambda^2 e^{i(\kappa_p + \kappa_s)d} - (\epsilon\delta - \lambda^2) \Gamma_{pp}^2 e^{i(\kappa_p + \kappa_s)d} = 0 \quad (1)$$

where the  $\pm$  selects the symmetric (upper sign) or antisymmetric (lower sign) guided wave modes. The quantities  $\Gamma_{ab}$  ( $a = \{p, s\}$ ,  $b = \{p, s\}$ ) are the solid-vacuum, smooth-surface reflection coefficients for an incident  $a$ -type wave and reflected  $b$ -type wave, where  $p$  refers to compressional and  $s$  to shear waves. The relations  $\Gamma_{ss} = -\Gamma_{pp}$  and  $\Gamma_{ps}\Gamma_{sp} = (1 - \Gamma_{pp}^2)$  [8] have been used to obtain Eq. (1). The plate thickness is  $d$  and the transverse ( $x_3$ -projection) wavevector components  $\kappa_p$  (compressional) and  $\kappa_s$  (shear) are given by  $\kappa_{p,s} = (k_{p,s}^2 - \xi^2)^{1/2}$ , respectively. Here  $k_{p,s} (= \omega/V_{p,s})$  are the compressional and shear wavenumbers,  $\omega$  is the angular frequency,  $V_{p,s}$  are the two pure mode wavespeeds, and  $\xi$  is the wavenumber of the propagating guided wave.

The PSA contributions are

$$\epsilon = e^{-2h^2\kappa_p^2} \quad \delta = e^{-2h^2\kappa_s^2} \quad \lambda = e^{-h^2(\kappa_p + \kappa_s)^2/2}. \quad (2)$$

The PSA model is valid only for propagating partial waves with real  $\kappa_{p,s}$ , but in this treatment we truncate the PSA to avoid negative attenuation for evanescent partial waves. This realization implies that we should take only the real parts of  $\kappa_{p,s}$  in the expressions for  $\epsilon$ ,  $\delta$ , and  $\lambda$ . For most practical cases, however, this restriction is not important.

Equation (1) is the dispersion relation for a RS waveguide using the PSA scattering model to treat the effective attenuation of partial waves as they interact with the surface. A further simplification is possible if we assume that the shear contribution is large compared the compressional one. For materials where the Poisson ratio is greater than about 0.3 this approximation is reasonable, since the RS losses scale geometrically as  $(\kappa h)^2$ . Then, let us take  $\lambda^2 \approx \epsilon\delta$ . With one further step we can now incorporate the terms  $2h^2\kappa_p$  and  $2h^2\kappa_s$  into effective complex thicknesses  $d_p$  and  $d_s$ , whose imaginary parts introduce the lossy rough-surface contribution. Using the explicit form of  $\Gamma_{pp}$ , from [8] for example, Eq. (1) may be expressed as

$$(k_s^2 - 2\xi^2)^2 \left\{ \frac{\cot(\kappa_p d_p/2)}{\tan(\kappa_p d_p/2)} \right\} + 4\xi^2 \kappa_p \kappa_s \left\{ \frac{\cot(\kappa_s d_s/2)}{\tan(\kappa_s d_s/2)} \right\} = 0. \quad (3)$$

Equations (3) are formally identical to the conventional smooth-surface symmetrical (upper terms) and antisymmetrical (lower terms) Lamb wave dispersion relations, but with complex thickness parameters given by

$$\begin{aligned} d_p &= d + 2i\kappa_p h^2 \\ d_s &= d + 2i\kappa_s h^2. \end{aligned} \quad (4)$$

If the rms roughness parameter  $h$  vanishes, we recover the ordinary Lamb wave equations.

By way of example, the simple dispersion relation in Eq. (3) allows us to estimate quickly the damping of a 100-kHz  $S_0$  Lamb wave mode propagating in 0.5-inch thick steel plate having a rms roughness of 200  $\mu\text{m}$ . We obtain a value of 5.4 dB/100-m, and a value of 82 dB/100-m for the same conditions, but at 150 kHz. Using Eq. (3) this estimate required no more complication than that of solving the conventional Lamb wave equation. The rapid increase in RS loss in this calculation illustrates the significant partial wave reconfiguration between these two frequencies. The large increase in transverse partial wave motion at 150 kHz accounts for the majority of the change in damping.

A comparison of the solutions of the two equations Eqs. (1) and (3) is shown in Fig. 1 for the  $A_4$  mode. The real part of the solution is plotted as phase velocity in the lefthand frame for Eq. (1) (solid) and Eq. (3) (dashed); the imaginary solution is plotted as normalized guided wavenumber  $\xi/k_s$  in the righthand frame, each as a function of frequency  $f$ . If the sample had a smooth surface the imaginary solution would vanish in the absence of other material losses.

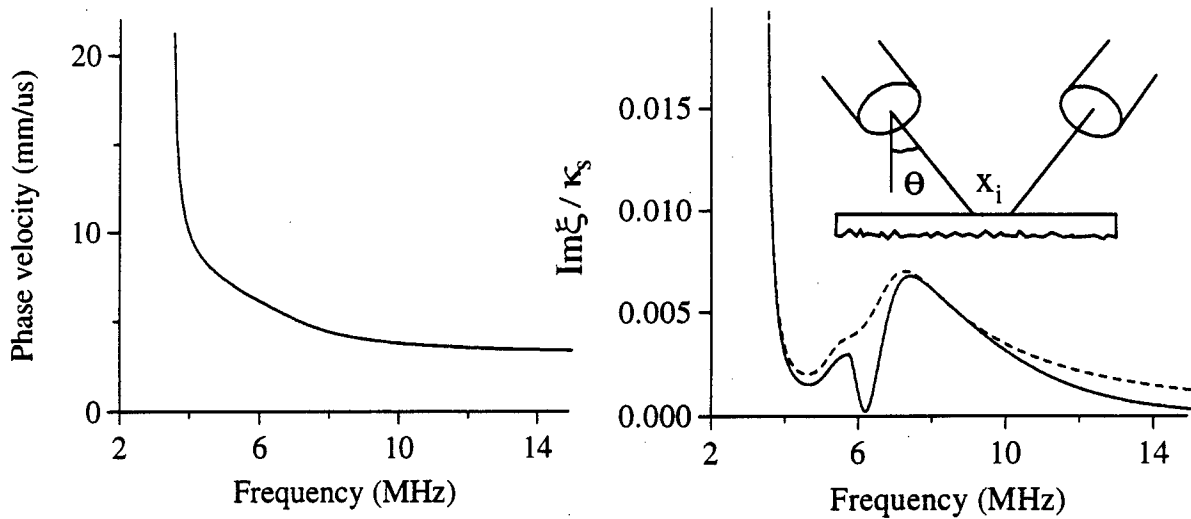


Figure 1: Real and imaginary parts of  $A_4$  antisymmetric mode in a 2.3-mm Al plate with Eq. (1) (solid curve) and Eq. (3) (dashed curve). Lefthand frame shows phase velocity, almost the same as the conventional Lamb wave; righthand frame shows normalized rough-surface damping loss  $\Im(\xi)/k$ , for the two approximations. Inset shows experimental geometry. Incident angle is  $\theta$ , and  $x_i$  is separation of transducer central rays.

In Fig. 1 the real RS solution changes almost not at all from the smooth-surface result. In the lower frame the large increase in imaginary wavenumber at the mode cutoff near 4 MHz is explained by noting that near cutoff, both the partial wavevectors propagate nearly normal to the plate surface, implying many reflections per wavelength and leading to a large increase in surface-induced losses. The minimum in the solid curve near 6 MHz occurs close to the compressional critical angle  $\beta_p$ . Near this branch point conversion of compressional to shear wave energy is at a minimum, and therefore the lower attenuation of the compressional wave dominates at this point. After the critical angle the  $p$  wave eventually ceases to be a factor, and the  $s$ -wave damping increases as  $f^2$ . At even higher frequency, the  $s$  partial wavevector makes progressively larger angles with the plate normal as it approaches its critical value  $k_s$ , and the partial wave interaction with the rough surface is predicted to decrease. The dashed approximation of Eq. (3) is somewhat less accurate as either critical angle is approached.

The rough plate reflection coefficient (RC) is constructed from the halfspace RS reflection coefficients, using an expression derived for the plate RC that combines halfspace scattering coefficients [9],

$$R = R_h + [T_p(\tau_{pf}(1 - \tau_{ss}) + \tau_{sf}\tau_{ps}) + T_s(\tau_{sf}(1 - \tau_{pp}) + \tau_{pf}\tau_{sp})]/[(1 - \tau_{pp})(1 - \tau_{ss}) - \tau_{ps}\tau_{sp}], \quad (5)$$

where  $R_h$  and  $T_p$  and  $T_s$  are the joined halfspace reflection and compressional and shear transmission coefficients for a fluid-solid interface. The term in Eq. (5)  $\tau_{\alpha\beta}$  refers to the

following RC products,

$$\tau_{\alpha\beta} = R_{\alpha p}^{II} R_{p\alpha}^I + R_{\alpha s}^{II} R_{s\beta}^I \quad (6)$$

with  $\alpha = \{p, s\}$  and  $\beta = \{f, p, s\}$  ( $f$ : fluid), as before;  $R_{\alpha\beta}^{I,II}$  are smooth-surface reflection and transmission coefficients on solid-fluid interfaces I and II, where the rough/smooth surface terms  $R$  and  $T$  are given in [10].

## EXPERIMENTAL TECHNIQUE

Broadband piezoelectric piston transducers are excited with tone burst rf signals  $50-\mu\text{s}$  in length, with or without power amplification. The acoustic wave generated in this way interacts with the plate and is reradiated into the fluid, where it is detected by a second, nominally identical device. This detected signal is amplified and either envelope-detected by an rf receiver or captured on a digital oscilloscope for analysis. The time-domain signal is Fourier transformed numerically in order to isolate a particular frequency component from the narrow, but finite bandwidth burst. A schematic diagram of the immersion experimental setup is shown in the inset of Fig. 1.

Samples for this study have been fabricated by a chaotic bombardment of small abrasive particles, such as sandblasting. All samples are fabricated from 2024 aluminum (physical properties:  $V_p = 6.37 \text{ km/s}$ ,  $V_s = 3.13 \text{ km/s}$ ,  $\rho = 2720 \text{ kg/m}^3$ ). These samples have been selected from a series of 9-mm thick plates used in a previous study and have been independently characterized. Acoustic scattering studies indicate a correlation length of between  $500 \mu\text{m}$  and  $1000 \mu\text{m}$ , which is typical of rough surfaces made in this manner. The only significant aspect of  $L$  is that it is much larger than the rms roughness  $h$ . Further experimental details can be found elsewhere [10].

## RESULTS AND DISCUSSION

To interpret the data one additional element must be added to the theoretical results above, a transducer voltage calculation [11]. In order to isolate the effects of roughness and provide the basis of a reliable inspection method, it is essential to eliminate all geometric influences on the signal, such as those arising from diffraction and transducer placement. The voltage calculation allows us to do this, and all subsequent immersion results have been calculated by incorporating the RS reflection coefficient into the voltage integral expression, or into its asymptotic analytical form.

We present a series of plots for which the roughness is on the *lower* plate surface only to emphasize the effect of the roughness on the guided wave. The model works best well away from critical angles where partial waves make grazing incidence on the plate surfaces. In the following plots we therefore investigate the performance of the model under three different conditions: well below the compressional critical angle  $\beta_p$ , near  $\beta_p$ , and well above  $\beta_p$ . In Fig. 2 with an incident angle of  $20^\circ$  and a transducer separation of  $x_i = 0$  (see inset

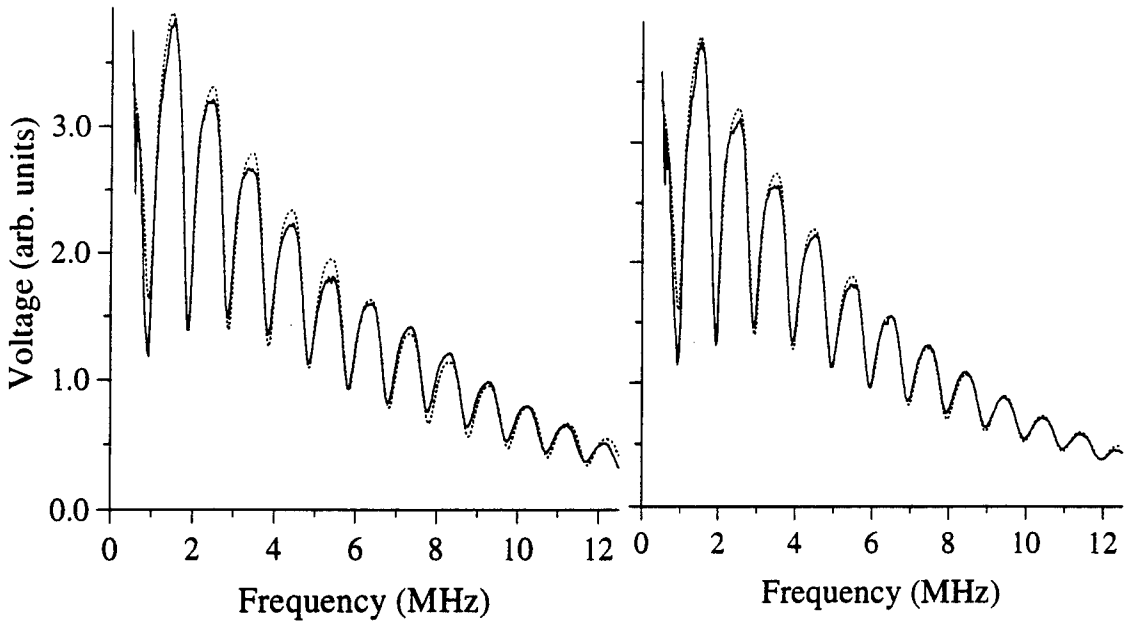


Figure 2: Experimental (solid) and theoretical (dashed) frequency dependence of receiver voltage for smooth (lefthand frame) and lower rough (righthand frame) plate surfaces with  $h = 26 \mu\text{m}$ ,  $x_i = 0 \text{ mm}$ , and incidence at  $20^\circ$ .

of Fig. 1), we are beyond the compressional critical angle, and only shear partial waves are propagating in the plate. For this circumstance, we expect our model to function quite well. With zero transducer separation, on the other hand, there should be little RS contribution to the attenuation, in fact at any incident angle.

In this and each of the following cases, the lefthand frame shows the measurement (solid curve) and theoretical prediction (dashed curve) for a smooth plate ( $0 \mu\text{m}$  rms roughness) as a function of frequency from 2 to 12.5 MHz. The righthand frame shows the corresponding rough-surface ( $26\text{-}\mu\text{m}$  rms roughness) data for the same experimental conditions. The regular oscillations in the signal mark the excitation of guided wave modes of varying order and symmetry in the plate. There is little difference between the two frames in Fig. 2, owing to the small effective signal path on the rough surface. Simple plate reflection measurements cannot probe subtle hidden-surface roughness with high sensitivity. The prediction is in good agreement with the data, both with and without roughness, confirming the accuracy of the receiver voltage model as expressed in [11]. To obtain a closer fit to the data, the theory curves have all been calculated for a rms roughness of  $28 \mu\text{m}$ . This disparity is explained below.

In Fig. 3 the transducer separation  $x_i = 20 \text{ mm}$  is now sufficient to remove almost all directly reflected rays (except at the very lowest frequencies) from the received signal. Here, the peaks mark the guided wave excitations, and the effect of the roughness is pronounced. At low frequency there is almost no difference between the two frames, growing to about 8 dB difference at 8 MHz, and almost complete signal loss above 12 MHz. This strong frequency

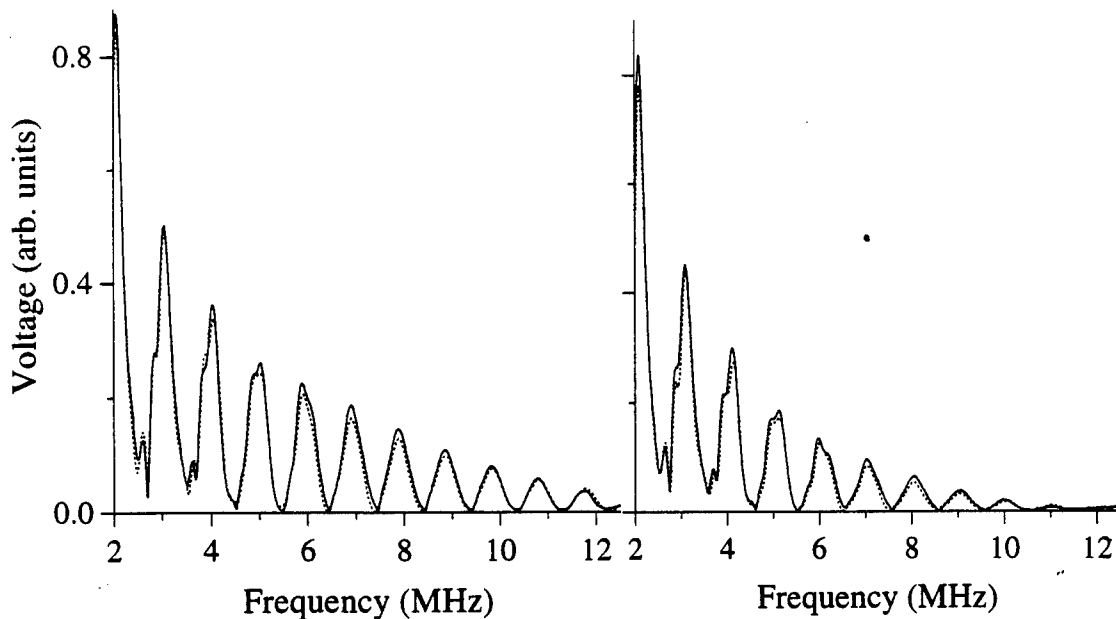


Figure 3: Experimental (solid) and theoretical (dashed) frequency dependence of receiver voltage for smooth (lefthand frame) and lower rough (righthand frame) plate surfaces with  $h = 26 \mu\text{m}$ ,  $x_i = 20 \text{ mm}$ , and incidence at  $20^\circ$ .

behavior is to be expected, since the losses are climbing as  $\exp(f^2)$ . Again, the agreement between prediction and measurement is quite good in both frames.

At incidence near the compressional and shear critical angles, grazing incidence behavior of the partial waves renders the model less accurate. Data in Fig. 4 taken at  $15^\circ$  for a transducer separation of  $x_i = 20 \text{ mm}$  show this effect. The smooth surface data in the lefthand frame are well modeled in the calculation, but the experimental curve lies well below the prediction for the RS plate in the righthand frame. By 8 MHz the predicted peak is about three times as large as the measurement. The model assumptions are not valid when the partial waves strike the plate surfaces at nearly  $90^\circ$  from the normal. Furthermore, since the transit path across the plate for grazing partial waves is long, the predicted RS loss vanishes at this point, leading to the substantial underestimate of the damping seen in Fig. 4.

In these calculations there are no adjustable parameters, only the geometrical variables and the rms roughness height  $h$ . However, since our samples have been sectioned from a larger piece of material, we have found that the best comparison with the data is achieved by assuming a slightly different rms roughness ( $h = 28 \mu\text{m}$ ) for the coarser of the two specimens. We have made no further attempt to perfect the comparisons, and predictions reported here for the sandblasted plates have been calculated with the  $13\text{-}\mu\text{m}$  or  $28\text{-}\mu\text{m}$  estimates.

In Fig. 5 are shown the collected data and predictions for the  $A_3$  guided wave mode in the  $26\text{-}\mu\text{m}$  plate as a function of angle. The experimental points are obtained from the

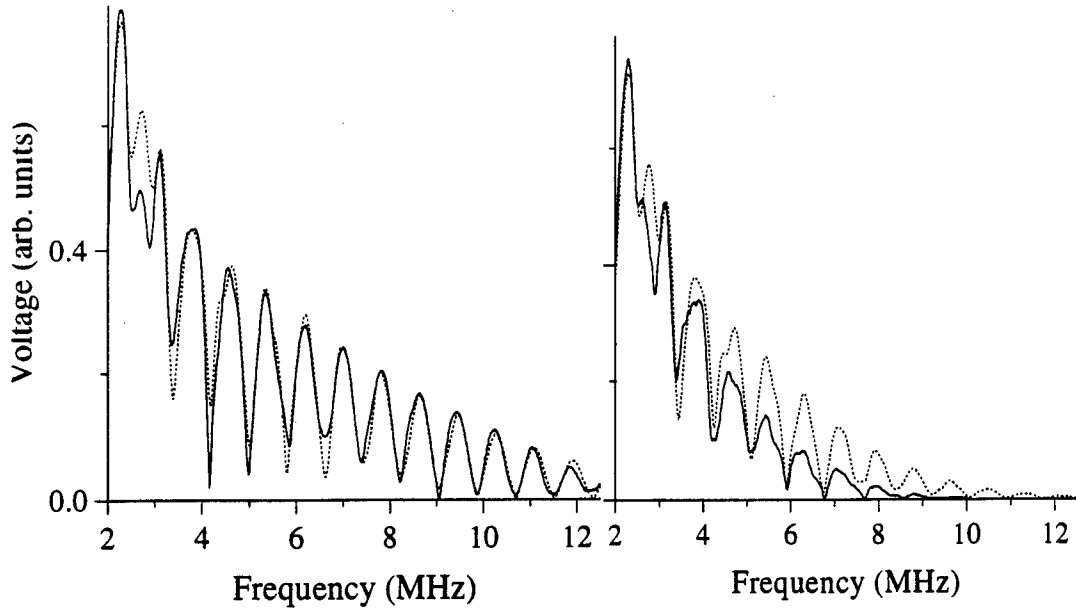


Figure 4: Experimental (solid) and theoretical (dashed) frequency dependence of receiver voltage for smooth (lefthand frame) and lower rough (righthand frame) plate surfaces with  $h = 26 \mu\text{m}$ ,  $x_i = 20 \text{ mm}$ , but incidence at  $15^\circ$ , near compressional critical angle.

spectra (such as Figs. 2 to 4) by estimating the voltage amplitude ratio for the smooth and rough surface at the frequency of the  $A_3$  mode occurrence. A typical experimental uncertainty, consisting of run-to-run variation at different sample positions, is illustrated by the error bar. The electronic noise is very small and not a factor. Any disparity between prediction and measurement is likely caused by systematic error. The solid curve in Fig. 5 is the prediction for the same conditions.

## ACKNOWLEDGMENTS

This work was supported by the Aerospace Sciences Directorate, Air Force Office of Scientific Research under Grant F49620-95-1-0294. We thank P. B. Nagy of the University of Cincinnati for the loan of characterized rough-surface samples.

## References

- [1] A. G. Voronovich, *Wave Scattering from Rough Surfaces*, (Springer-Verlag, Berlin, 1994).
- [2] D. K. Dacol and D. H. Berman, "Sound scattering from a randomly rough fluid-solid interface", *J. Acoust. Soc. Am.* **84**, 292-302 (1988).

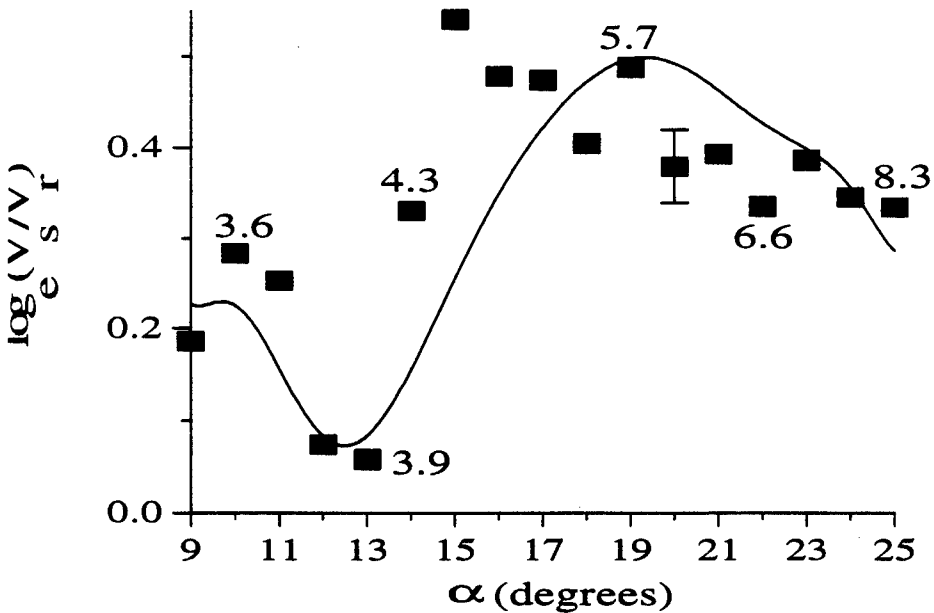


Figure 5: Collected experimental (discrete points) and theoretical (solid curve) voltage ratio  $V_e$  for the smooth surface over  $V_r$  for lower rough surface versus incident angle  $\theta$ . Plot shows the  $A_3$  Lamb mode with  $h = 26 \mu\text{m}$  and  $x_i = 20 \text{ mm}$ . The numbers attached to data points show frequency in MHz at which the  $A_3$  mode occurs at that angle.

- [3] W. A. Kuperman and H. Schmidt, "Self-consistent perturbation approach to rough surface scattering in stratified elastic media", J. Acoust. Soc. Am. **86**, 1511–22 (1989).
- [4] J. D. Sheard and M. Spivak, "Wave scattering in a rough elastic layer adjoining a fluid halfspace", J. Acoust. Soc. Am. **97**, 72–83 (1995).
- [5] C. Eckhart, "The scattering of sound from the sea surface", J. Acoust. Soc. Am. **25**, 566–70 (1953).
- [6] P. B. Nagy and L. Adler, "Surface roughness induced attenuation of reflected and transmitted ultrasonic waves", J. Acoust. Soc. Am. **82**, 193–7, (1987).
- [7] D. K. Dacol, "The Kirchhoff approximation for acoustic scattering from a rough fluid-elastic solid interface", J. Acoust. Soc. Am. **88**, 978–83 (1990).
- [8] B. A. Auld, *Acoustic Waves and Fields in Solids*, 2nd ed, (Krieger, Malabar, FL, 1990).
- [9] M. Deschamps and C.-W. Cao, "Reflection /refraction of a solid layer by Debye's series expansion", Ultrasonics **29**, 288–96 (1991).
- [10] O. I. Lobkis and D. E. Chimenti, "Elastic Guided Waves in Plates with Surface Roughness. I. Model Calculation", J. Acoust. Soc. Am. **102**, 143–49 (1997); "Elastic Guided Waves in Plates with Surface Roughness. II. Experiments", *ibid.* **102**, 150–59 (1997).

- [11] O. I. Lobkis, A. Safaeinili, and D. E. Chimenti, "Precision ultrasonic reflection studies in fluid-coupled plates", J. Acoust. Soc. Am. **99**, 2727–36 (1996).

## DISCUSSION

### Hidden Corrosion Detection Using Guided Plate Waves Modeled as Surface Roughness

Speaker: Chimenti

Does this methodology apply to the case of discrete defects such as pitting corrosion? —R. P. Wei

*The waveguide surfaces are modeled in our calculation as randomly rough with a Gaussian distribution of surface height, a small average roughness, and a large correlation length. Therefore, the calculation applies to surfaces that have a small amount of roughness everywhere. Pitting corrosion, insofar as it is a discrete defect or collection of defects, differs from this assumption in several critical ways. Another model, aimed more at discrete scattering, would be called for in this case.*

I am wondering if other mechanisms might compete with the effect of surface roughness, because energy is converted from coherent to an incoherent form and real quantities become complex. I am thinking of the effect of damping. If such other effects are important would it be possible to calibrate such effects out?

—J. D. Achenbach

*Yes, there are other competing mechanisms of wave energy loss. These are radiation damping (leaky waves), material damping, and diffraction. It has been our objective in this work to establish an understanding of the phenomenology of wave guide losses from surface roughness. Therefore, we chose to make measurements in water-coupled geometry, but in aluminum. The wave leakage does indeed have many of the same dependencies as the surface roughness loss and understandably so, since both mechanisms depend on out-of-plane displacements at the plate surfaces. Material damping, on the other hand, plays a relatively minor role by comparison, especially in aluminum. Beam diffraction is modeled theoretically, but we are aided by the fact that all experiments are performed with the same transducers in the same geometry. Other effects, however, such as a plate thickness differences (1-2 %), are even more influential, and these must be normalized out of the results to enable critical comparisons among samples with different roughness.*

*The major competing factor in our study, however, is the leaky wave. In an industrial realization of the technology, wave coupling would be achieved by other means, and this element would not be present.*



# The Application of Neural Networks to Defect Sizing

M. Takadoya and T. Ogi

Advanced Science Department  
Mitsubishi Research Institute  
Tokyo 100, Japan

and

J. D. Achenbach

Center for Quality Engineering and Failure Prevention  
Northwestern University  
Evanston, IL 60208

## ABSTRACT

In the first part of the paper a neural network with an analog output is presented to estimate the crack-depth from ultrasonic signals backscattered from an inclined surface-breaking crack in an aluminum plate. The network has only one response unit and this unit directly reports the crack depth as an analog value from the measured signals. A completely synthetic data set, spot-checked by comparison with experimental results, is utilized for the training of the network. The synthetic data set is obtained by solving the boundary integral equations governing the crack scattering problem by the boundary element method. In the second part the same problem is addressed by using a fuzzy reasoning method based on principal component analysis. This method is able to characterize the waveforms and interpolate the data stored in the knowledge base, and absorb the error between the numerical analysis and the experimental results by adjusting the shapes of the membership functions. The method was applied to the crack depth evaluation for perpendicular cracks and inclined cracks. The synthetic data and the experimental data were used to estimate crack lengths with high accuracy.

Keywords: ultrasonics, estimation, crack depth, neural network, fuzzy reasoning

## INTRODUCTION

For many purposes of nondestructive inspection the knowledge that a crack larger than a certain length does not exist in a structure, because it has not been detected with, say, an ultrasonic test that operates with a known probability of detection, provides sufficient information from the point of view of structural safety. As more and more sensitive sensors are being used, and as cracks longer than minimally detectable ones may be permissible, the interest has shifted beyond detection, which would not be a source of difficulty, to quantitative characterization with regard to orientation and size. This paper is concerned with sizing of surface breaking cracks by the use of artificial neural networks.

Over the last decade one of the most significant advances in nondestructive evaluation has been the evolution of NDE from a conglomeration of empirical techniques to a well defined field of interdisciplinary science and engineering. In the course of this development it has become well recognized that a fundamental approach to NDE must be based on quantitative models of the measurement processes of the various inspection techniques. A model's principal purpose is to predict, from first principles, the measurement system's response to specific anomalies in a given material or structure, (e.g. cracks, voids, distributed damage, corrosion, deviations in material properties from specifications, and others). Thus, a measurement model includes the configuration of

probe and component being inspected as well as a description of the generation, propagation and reception of the interrogating energy. In the ultrasonic case, this description requires computations of the transducer radiation pattern, refraction of the beam at the part's surface, the beam profile and the propagation characteristics in the host material including effects of material anisotropy, attenuation, diffraction losses, etc. Detailed modeling of the field-flaw interactions which generate the measurement system's response function are also included, as well as information of material and other conditions that produce noise and add an uncertainty to the measurement results. A well constructed measurement model should be able to predict specific instrumental responses to anomalies in complex materials and structures as well as to "standard" flaws placed in various calibration blocks.

A number of measurement models have been formulated in the past several years for different inspection techniques. For practical applications, the challenge lies in making approximations that permit the computations to be tractable while retaining sufficient accuracy so that the engineering applications are not compromised.

The availability of a measurement model has many benefits. Numerical results based on a reliable model are very helpful in the design and optimization of efficient testing configurations. A good model is also indispensable in the interpretation of experimental data and the recognition of characteristic signal features. The relative ease of parametrical studies based on a measurement model facilitates an assessment of the probability of detection of anomalies. A measurement model is a virtual requirement for the development of an inverse technique based on quantitative data. Last, but not least, a measurement model whose accuracy has been tested by comparison with experimental data provides a practical way of generating a training set for a neural network or a knowledge base for an expert system. Measurement models for ultrasonic techniques have been discussed in some detail elsewhere<sup>1</sup>.

In this paper we will concentrate on an essential component of a measurement model for quantitative ultrasonics, namely, the modeling of the interaction of ultrasound with a defect.

For certain problems of flaw detection and sizing, it is to be expected that the volume of the data will be large and that it will be difficult to discriminate between signals generated by flaws and harmless sources. As a consequence a human operator will not be effective in extracting relevant information for decision making purposes from an overwhelming flow of data. Artificial neural networks can play a major role in the recognition of sets of data that are related to damage or failure phenomena in the component of structure that is being monitored.

Artificial neural networks must, however, be applied in an intelligent manner. A brute force application of a neural network will require a very large set of training data (usually not available) and a large computer, and then might still not give very satisfactory results.

The approach that is advocated here combines a thorough understanding of the physics behind the signals that are to be detected with a measurement model of the signal generation, signal detection and signal processing. The role of a neural network in the proposed system is shown in Fig. 1.

This paper is concerned with the use of an artificial neural network to determine the depth of a surface-breaking crack from backscattering data. It is based on the papers by Takadoya, et al.<sup>2,3</sup> and Ogi, et al.<sup>4</sup>.

## SIMULATED DATA

In the neural network strategy of this paper, a numerical analysis based on two-dimensional elastic wave theory is carried out to create the training data set for the network. The boundary element method (BEM) has been used extensively to solve two-dimensional wave scattering problems. Only scattering by surface-breaking cracks is considered in this study.

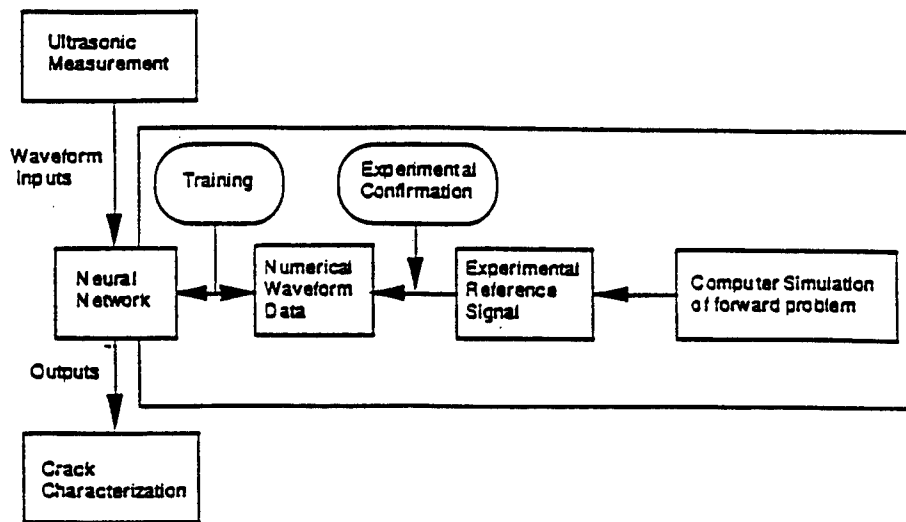


Figure 1. Identification system based on neural networks.

First the crack opening displacement (COD) is calculated using the BEM, and then the far-field displacements are determined by substituting the COD results into an integral representation. Although time-domain techniques are available, these methods are usually complicated and the computational procedures are very time consuming. Therefore, in this paper, scattered wave results are first calculated for an harmonic incident wave and the results for a pulse-like incident wave are obtained with the help of the Fast Fourier transform. The numerical results for the far-field displacements in both the time- and frequency-domains have been used for neural network training and testing.

In the present applications, a surface-breaking crack in a half-space is considered. Since the detailed treatment of this problem can be found in a paper by Zhang and Achenbach<sup>5</sup>, details of the analysis will not be given.

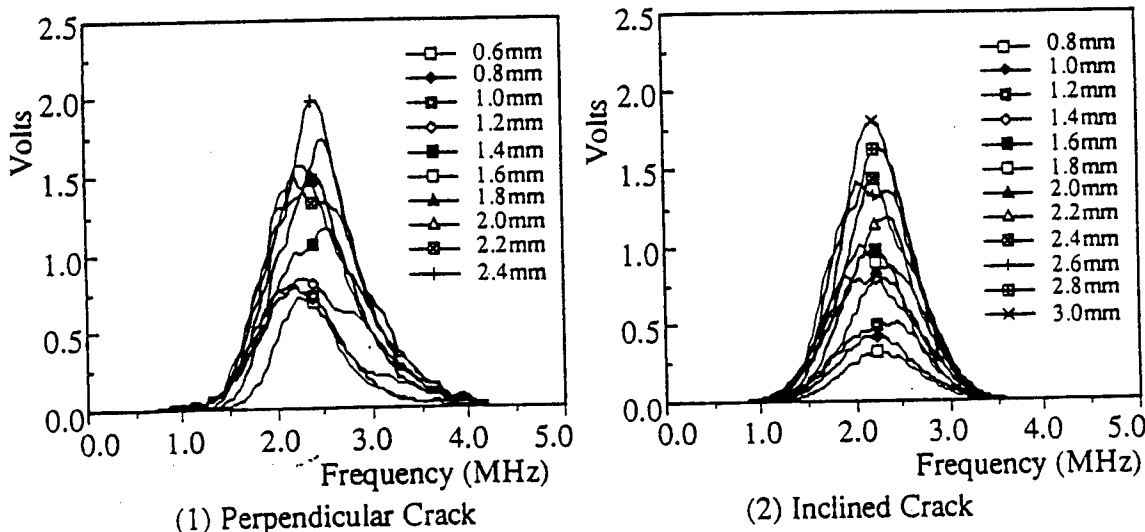


Figure 2. Waveform data for the perpendicular and the inclined cracks.

The integral representation for the scattered field may be expressed in terms of integrals over the boundaries of the half-space  $\Gamma_s$  and the crack surface  $\Gamma_c$ :

$$u_\gamma^{sc}(\mathbf{x}_p) = \int_{\Gamma_s} \sigma_{\alpha\beta\gamma}^G(\mathbf{x}; \mathbf{x}_p) u_\alpha^{sc} n_\beta d\mathbf{s}(\mathbf{x}) + \int_{\Gamma_c} \sigma_{\alpha\beta\gamma}^G(\mathbf{x}; \mathbf{x}_p) \Delta u_\alpha n_\beta d\mathbf{s}(\mathbf{x}), \quad \mathbf{x}_p \notin \Gamma (\Gamma_s + \Gamma_c) \quad (1)$$

This representation is used to obtain boundary integral equations for the crack-opening displacement  $\Delta u_\alpha$  in the frequency domain. In Eq. (1),  $\sigma_{\alpha\beta\gamma}^G$  is the full-space Green's stress tensor, and  $u_\gamma^{sc}$  is the scattered displacement field. Once the solution for  $\Delta u_\alpha$  on  $\Gamma_c$  has been obtained by solving the boundary integral equations, with an appropriate treatment of the singularities in the equation and the use of crack tip elements, the scattered far-field is expressed in terms of a half-space integral representation as

$$u_\gamma^{sc}(\mathbf{x}_p) = \int_{\Gamma_s} \bar{\sigma}_{\alpha\beta\gamma}^G(\mathbf{x}; \mathbf{x}_p) \Delta u_\alpha n_\beta d\mathbf{s}(\mathbf{x}), \quad \mathbf{x}_p \notin \Gamma_c \quad (2)$$

where  $\bar{\sigma}_{\alpha\beta\gamma}^G$  now is the far field approximation to the Green's stress tensor of the half-space. In this representation, the scattered field is related only to the crack opening displacement and not to the displacement on the free boundary of the half-space.

In the sequel we define  $H_{\text{crack}}^{\text{BEM}}(\omega)$  as the displacement component normal to the top face of the plate

$$H_{\text{crack}}^{\text{BEM}}(\omega) = u_3^{sc}(\mathbf{x}_p, \omega) \quad (3)$$

Theoretical results for a perpendicular and an inclined crack are shown in Fig. 2.

## EXPERIMENTAL CONFIGURATION

An experimental configuration of a surface-breaking crack of depth  $a$  in a steel plate of thickness  $h$  has been used. The plate is immersed in a water bath as shown in Fig. 3. Ultrasound is generated by an immersed

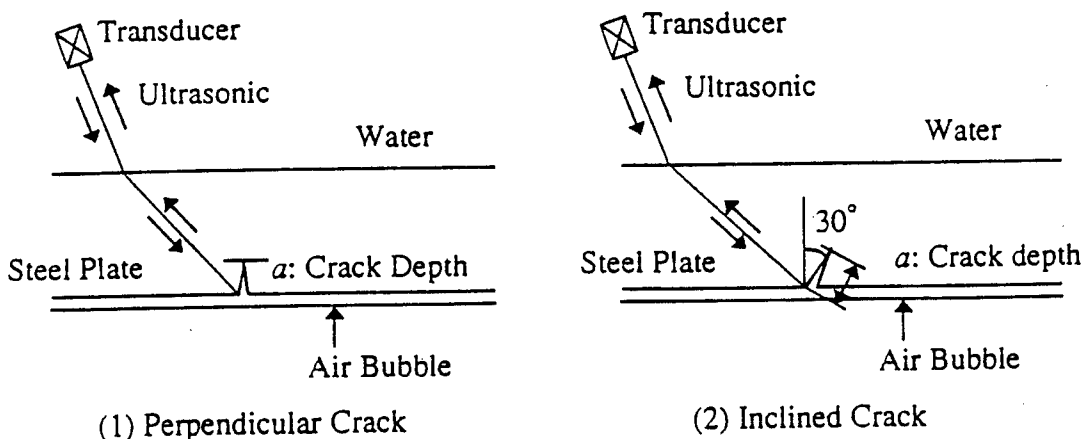


Figure 3. Crack types and experimental conditions.

piezoelectric transducer. The angle of incidence with the normal to the insonified top face of the plate exceeds the critical angle, and the incident ultrasonic beam is therefore primarily converted into a beam of transversely polarized ultrasound in the plate. Measured back-scattered signals for some crack depths have been used to check the synthetic training data while experimental data for other crack depths have been used as input to verify the performance of the neural network.

In the frequency domain the experimentally obtained transducer output of the back-scattered signal may be expressed as

$$Y_{\text{exp}}(\omega) = T_0 H_w H_b H_{ws} H_{\text{crack}}^{\text{exp}} H_{sw} H_w T_r. \quad (4)$$

The response functions in this expression represent the effects of

$T_0(\omega)$ : transducer output,  $H_w(\omega)$ : water path,

$H_b(\omega)$ : beam spreading,  $H_{ws}(\omega)$ : water  $\rightarrow$  solid interface,

$H_{sw}(\omega)$ : solid  $\rightarrow$  water interface,  $T_r(\omega)$ : transducer reception,

and

$H_{\text{crack}}^{\text{exp}}(\omega)$ : interaction with crack in solid.

For the corresponding theoretical results, the expression is exactly the same except for the response of the crack:

$$Y_{\text{theory}}(\omega) = T_0 H_w H_b H_{ws} H_{\text{crack}}^{\text{BEM}} H_{sw} H_w T_r. \quad (5)$$

In Eq. (5),  $H_{\text{crack}}^{\text{BEM}}(\omega)$  represents the interaction of the incident wave with the crack as calculated by the boundary element method (BEM).

To cancel the response functions except the term of  $H_{\text{crack}}^{\text{BEM}}(\omega)$  in Eq. (5), the signal for a corner reflection is introduced as the reference signal. For the same transducer angle, the same water paths, and the same specimen but with a rectangular corner, this reference corner signal can be written as

$$X_{\text{ref}}(\omega) = T_0 H_w H_b H_{ws} H_{\text{cor}}(\omega) H_{sw} H_w T_r, \quad (6)$$

where  $H_{\text{cor}}(\omega)$  represents the corner reflections in the solid. No mode conversion occurs for the angle of incidence of 45°. The formal deconvolution of the experimental signal of Eq. (4) by the reference signal of Eq. (6) yields

$$\frac{Y_{\text{exp}}(\omega)}{X_{\text{ref}}(\omega)} = \frac{H_{\text{crack}}^{\text{exp}}(\omega)}{H_{\text{cor}}(\omega)}. \quad (7)$$

As the term  $H_{\text{cor}}(\omega)$  be calculated analytically, Eq. (7) may be directly compared with the theoretically calculated interaction,  $H_{\text{crack}}^{\text{BEM}}$ . To get better agreement, theoretical data have been modified by the use of a correction factor, determined by comparison of theoretical and experimental results.

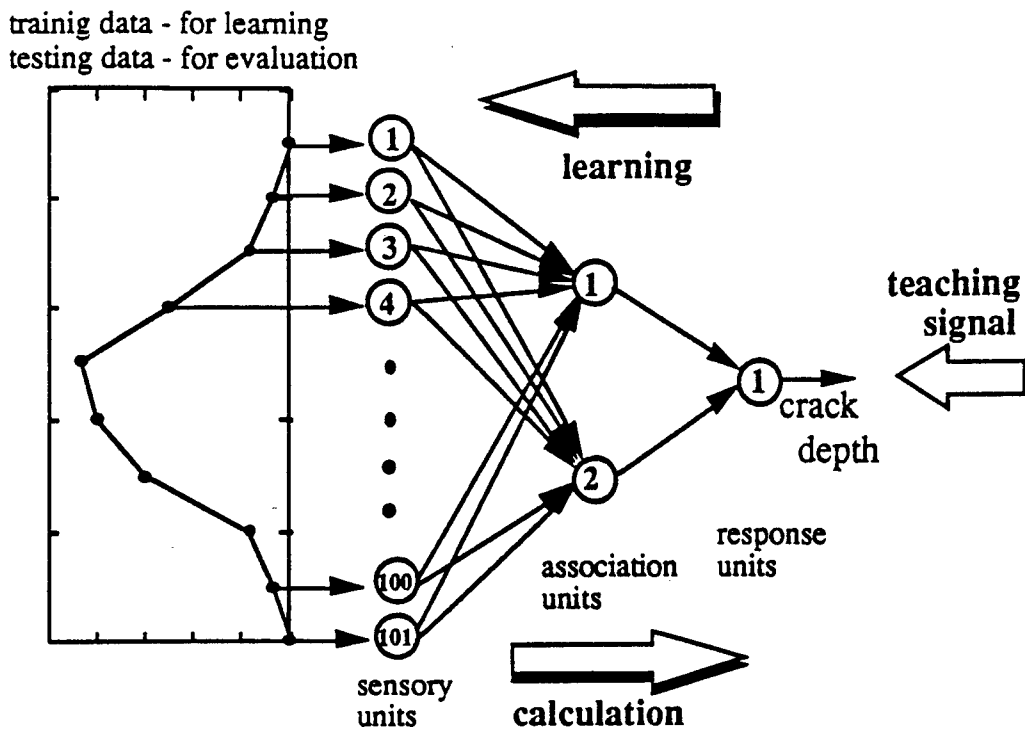


Figure 4. Neural network structure, learning and evaluation procedures.

### NEURAL NETWORK

A schematic architecture of an analog output type neural network is shown in Fig. 4. The network is a standard three-layered feedforward network, which has 101-units in the input layer, 2-units in the hidden layer and one unit in the output layer. The unit in the output layer directly reports the crack depth as an analog value. The number of units in the hidden layer was determined after some trial studies. The transfer function is the dominant characteristic of a unit, because the relationship between inputs and outputs at any instant is specified by this function. The sum of the weighted inputs becomes the input to the transfer function which then specifies the output from the unit. Here the sigmoid function is utilized as a transfer function. As for the learning algorithm, an error-backpropagation is used.

Table 1. Convergence check of the neural network.

Input : waveforms for crack depth of (mm)	0.80	1.00	1.20	1.40	1.60	1.80	2.00	2.20	2.40	2.60	2.80	3.00
Output : crack depth from response unit (mm)	0.82	0.98	1.20	1.41	1.61	1.83	1.92	2.20	2.39	2.59	2.83	3.00

For a crack inclined under an angle of 30°, the training data were prepared by digitizing the waveforms of the synthetic data. Then, these data were normalized by the maximum value of the waveforms, which was obtained from a crack of 3.00mm depth. The actual crack depths were normalized to (0,1) and utilized as teaching signals. Table 1 summarizes the convergence check of the network when the same waveform used for training was entered again into the trained network. The training required fourteen thousand iterations.

Table 2. Network performance for inputs of synthetic data.

<b>Input : waveforms for crack depth of (mm)</b>	0.90	1.10	1.30	1.50	1.70	1.90	2.10	2.30	2.50	2.70	2.90
<b>Output : crack depth from response unit (mm)</b>	0.90	1.09	1.31	1.49	1.75	1.88	2.02	2.34	2.46	2.70	2.95

Table 2 summarizes the network performance for synthetic data different from the data used for training. A total of eleven waveforms for crack depths ranging from 0.9mm to 2.90mm with equal increments of 0.2mm crack depth were used as input data. For example, for the input of a synthetic waveform for a crack depth of 2.9mm, the network reports a crack depth of 2.95mm. Since the mean average error is 1.38%, it can be stated that the network is able to estimate synthetic data not used in the training process almost precisely.

Table 3. Network performance for inputs of experimental data.

<b>Input : waveforms for crack depth of (mm)</b>	1.190	1.558	2.318	2.778
<b>Output : crack depth from response unit (mm)</b>	1.08	1.56	2.37	2.58

Our primary interest is focused on verifying the performance of the network for experimentally measured signals. Table 3 lists the network performance for inputs of measured signals. For the inputs of measured waveforms for cracks of 1.190mm, 1.558mm, 2.318mm and 2.778mm, the network estimates the crack depths as 1.08mm, 1.56mm, 2.37mm, and 2.58mm, respectively. The maximum error of 9.2% occurs in the estimation of the smallest crack depth. For the other three cases, the accuracy of the estimation is quite good. The estimation errors are respectively 0.13%, 2.24% and 7.12% for cracks of 1.558mm, 2.318mm and 2.778 mm depth. The analog output type network provides very satisfactory estimates of the depth of the inclined cracks.

## FUZZY REASONING

Figure 5 shows the block diagram of a fuzzy reasoning method based on principal component analysis. In this method, waveform data calculated by numerical analysis are not used directly to build a knowledge base, but are pre-processed using principal component analysis. The knowledge base is constructed of fuzzy rules using principal components. The measured data are also pre-processed using principal component analysis and are transmitted to the inference engine. The output value of the inference engine is determined using the mechanism of fuzzy reasoning. In this process, principal component analysis functions effectively to characterize waveform data. The fuzzy reasoning works to interpolate the data and to absorb the error between numerical analysis and experimental results.

Waveform data for various kinds of defects were calculated by numerical analysis to construct the knowledge base. However, waveforms are expressed by a large amount of data. It is difficult to build the rule base directly from the waveform data. Therefore, the waveform data were pre-processed using principal

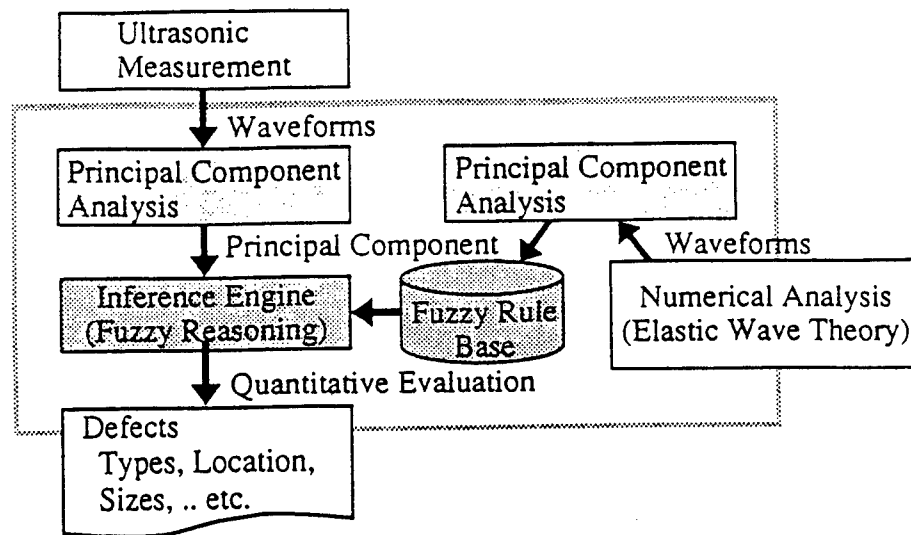


Figure 5. A block diagram of the fuzzy reasoning method based on principal component analysis.

component analysis. Principal component analysis is an analytical technique by which the number of variables can be decreased with little information loss. The generated principal components are expressed by linear equations using the original variables. For example, when the original variables are  $x_1, x_2, \dots, x_m$ , the principal components  $z_1, z_2, \dots, z_n$  are expressed as follows:

$$\begin{aligned}
 z_1 &= a_{11}x_1 + a_{12}x_2 + \dots + a_{1m}x_m \\
 z_2 &= a_{21}x_1 + a_{22}x_2 + \dots + a_{2m}x_m \\
 &\dots \\
 z_n &= a_{n1}x_1 + a_{n2}x_2 + \dots + a_{nm}x_m
 \end{aligned} \tag{8}$$

The original variables  $x_1, x_2, \dots, x_m$  are sampled from the waveform data, and the number of variables is decreased from  $m$  to  $n$ . A cumulative contribution rate in the principal component analysis was set to 0.99. The generated principal components are expected to characterize the waveforms.

The knowledge base was constructed of fuzzy rules using the principal components of the numerical analysis data. For example, if the value of the first principal component  $z_1$  is 6.5 when the crack depth is 1.6mm, the fuzzy rule is expressed as follows:

IF the first principal component is about 6.5,  
THEN the crack depth is about 1.6mm.

With this rule, a flexible degree of reasoning is achieved, since the value of "about 6.5" and "about 1.6mm" are expressed by the fuzzy sets.

The fuzzy sets are defined by the membership functions. Figure 6 shows the typical shapes of the membership functions used in the fuzzy rules. The membership functions indicate the degree to which the variables satisfy the propositions of the fuzzy sets and are expressed by isosceles triangles in this rule. Figure 6 shows that when the crack depths are 1.4mm, 1.6mm and 1.8mm, the values of the principal component are 5.2, 6.5 and 7.4 respectively. The interval of the calculated crack depths is  $t$ , and the intervals of the principal component values are  $d_1$  and  $d_2$ . As for the "IF" part, the base of the isosceles triangle takes the longer length of

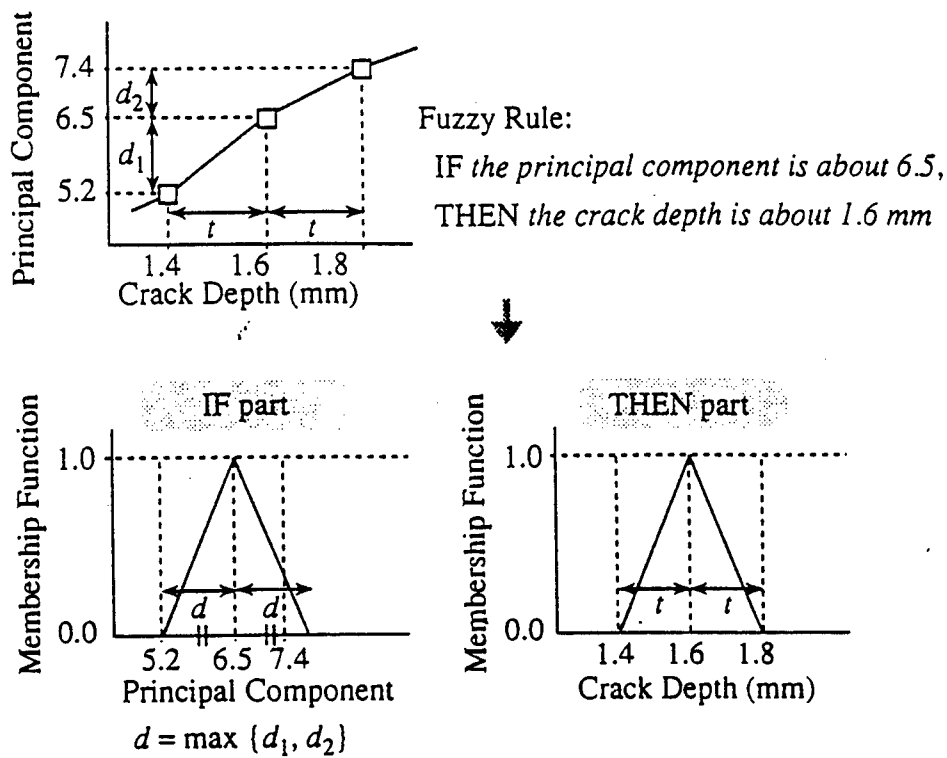


Figure 6. Typical shapes of the membership functions used in the fuzzy rules.

the neighboring intervals  $d_1$  and  $d_2$ . As for the "THEN" part, the length of the base is the interval of the crack depth. Since the fuzzy sets have vague values, the fuzzy rules function when the input data are close to the fuzzy values in the "IF" parts. Therefore, these rules interpolate the wave data stored in the knowledge base.

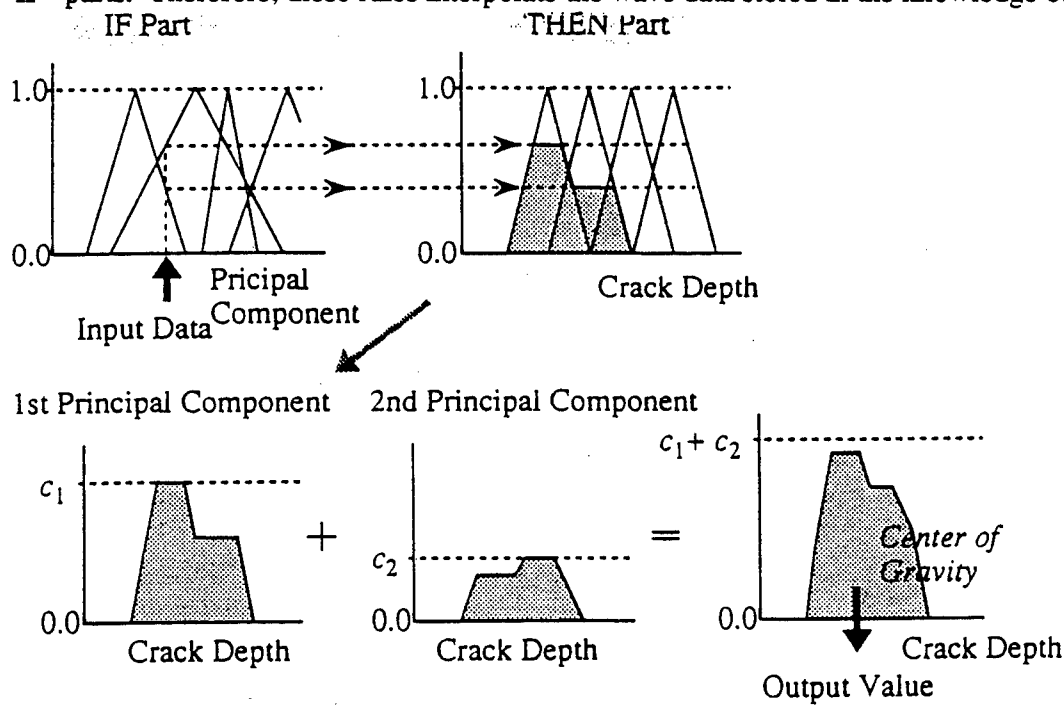


Figure 7. Mechanism of the fuzzy reasoning method based on principal component analysis.

Fuzzy reasoning is performed using these fuzzy rules. Figure 7 shows the mechanism of the fuzzy reasoning method. When the value of the principal component is inputted into the "IF" part, the degree that the condition in the "IF" part is satisfied is determined. According to the degree, the value of the "THEN" part is determined. In the ordinary fuzzy reasoning method, the output from each rule is simply added and the total output value is determined by the center of gravity. However, in the fuzzy reasoning method based on principal component analysis, the output from each rule is scaled to the value of the contribution rate of the principal component before determining the total output value. In Figure 7, the output values from these rules are scaled to  $c_1$  and  $c_2$ , respectively and added to determine the total output value, since the contribution rates of the first principal component and the second principal component are  $c_1$  and  $c_2$ . Therefore, each rule has a weight according to the contribution rate of the principal component.

The fuzzy reasoning method based on principal component analysis was applied to the evaluation of a surface-breaking crack in a steel plate. Two cases of the crack types were considered. In the first case, the crack was perpendicular to the surface of the plate. In the second case, the crack was inclined 30 degrees with the vertical. Figure 4 shows the crack types and the experimental conditions. The steel plate was immersed in water. The depth  $a$  of the surface-breaking crack was quantitatively evaluated from the information in the back scattered ultrasonic signal. In each case, both the numerical analysis data and the experimental data were evaluated.

The numerical analysis data were evaluated to verify the ability to interpolate the data stored in the knowledge base. To construct a knowledge base, waveform data generated by the interaction with cracks of various depths were calculated using the boundary element method. In the case of a perpendicular crack, the numerical analysis data for crack depths from 0.6mm to 2.4mm with increments of 0.2mm were calculated and used to construct the knowledge base. The numerical data from 0.8mm to 3.0mm crack depths with increments of 0.2mm were used for the inclined crack. Figure 2 shows the calculated waveform data in the frequency domain for each crack type. 100 data points were sampled from the waveform data and pre-processed using the principal component analysis. As a result, the number of variables was decreased from 100 to 6. The fuzzy rule base was constructed using the principal components.

Table 4. Results of the evaluation for the numerical analysis data.

(1) Perpendicular Crack Depth

Crack Depth	0.70	0.90	1.10	1.30	1.50	1.70	1.90	2.10	2.30
Evaluation	0.77	0.83	1.12	1.30	1.51	1.70	1.89	2.11	2.28

Average Error = 0.022 (mm)

(2) Inclined Crack Depth

Crack Depth	0.90	1.10	1.30	1.50	1.70	1.90	2.10	2.30	2.50	2.70	2.90
Evaluation	0.92	1.10	1.30	1.50	1.69	1.90	2.10	2.30	2.50	2.70	2.89

Average Error = 0.004 (mm)

The numerical data which were not used for the construction of the knowledge base were then evaluated. For the case of a perpendicular crack, waveform data for crack depths from 0.7mm to 2.3mm with increments of 0.2mm were evaluated. For the case of the inclined crack, the waveform data from 0.9mm to 2.9mm with increments of 0.2mm were evaluated. Table 4 shows the results of the evaluation. The average error was 0.022mm for the perpendicular crack and 0.004mm for the inclined crack. When a neural network was used, the average errors were 0.038mm and 0.028mm, respectively. It is clear that the fuzzy reasoning method based on principal component analysis interpolates the waveform data stored in the knowledge base and evaluates the crack depth with high accuracy.

Next, the method was applied to the evaluation of the experimental data. The knowledge base constructed with the numerical data was used to evaluate the experimentally measured data. Four sets of experimental data were evaluated for each case. The perpendicular cracks had the following depths: 0.67mm, 1.05mm, 1.49mm, and 2.19mm and the inclined cracks had depths of 1.19mm, 1.56mm, 2.32mm, and 2.78mm. In general, there is an inevitable error between the experimental data and the numerical data which depends on the modeling in the numerical analysis and the variance of the experimental conditions.

In this study, the variations of the evaluation errors caused by the change of the shapes of the membership functions were examined. The modulus of the membership function which indicates the expansion rate of the base length of the membership function in the "IF" part was changed as discussed elsewhere<sup>4</sup>. The average error of the perpendicular crack was minimum when the modulus of the membership function was 1.7, and the average error of the inclined crack was minimum when the modulus of the membership function was 2.3. These results demonstrate that this method is able to absorb the error between the numerical analysis and the experimental results by adjusting the shapes of the membership functions.

Table 5 shows the results of the evaluation when the modulus of membership function was adjusted so that the average error was minimal. For the perpendicular crack, the average error was 0.075mm, and for the inclined crack, it was 0.084mm. When the neural network was used, these errors were 0.078mm and 0.091mm respectively. Thus the fuzzy reasoning method was able to evaluate the experimental data accurately.

Table 5. Results of the evaluation for the experimental data.

(1) Perpendicular Crack Depth

Crack Depth	0.67	1.05	1.49	2.19
Evaluation	0.78	1.12	1.46	2.10

Average Error = 0.075 (mm)

(2) Inclined Crack Depth

Crack Depth	1.19	1.56	2.32	2.78
Evaluation	1.11	1.71	2.36	2.84

Average Error = 0.084 (mm)

## CONCLUSION

Depth estimation of inclined surface-breaking cracks in an aluminum plate has been investigated by using a neural network with and without fuzzy reasoning, ultrasonic measurements and a theoretical analysis based on elastodynamic theory. The trained networks estimate the depth of perpendicular and inclined cracks from measured data within an acceptable error range.

## ACKNOWLEDGMENT

The work of J. D. Achenbach was supported by the Office of Naval Research under Grant N00014-89J-1362/P14. The efforts of M. Takadoya and T. Ogi were supported by the Science and Technology Agency of Japan.

## REFERENCES

1. J. D. Achenbach, "Measurement Models for Quantitative Ultrasonics," J. Sound and Vibration, 159, pp.385-401, 1992.
2. M. Takadoya, M. Notake, M. Kitahara, J. D. Achenbach, Q. C. Guo and M. L. Peterson, "Crack-Depth Determination by a Neural Network with a Synthetic Training Data Set," in *Review of Progress in QNDE*, eds. D. O. Thompson and D. E. Chimenti, Vol. 12A, pp. 803-810, Plenum, New York, 1993.
3. M. Takadoya, Y. Yabe, J. D. Achenbach, Q. C. Guo and M. L. Peterson and M. Kitahara, "Depth Estimation of Inclined Surface-Breaking Cracks by a Neural Network," in *Review of Progress in QNDE*, eds. D. O. Thompson and D. E. Chimenti, Vol. 13A, pp. 887-894, Plenum, New York, 1994.
4. T. Ogi, T. Mandai, Y. Yabe, M. Kitahara and J. D Achenbach, "Quantitative Evaluation of Defects by Fuzzy Reasoning," in *Review of Progress in QNDE*, eds. D. O. Thompson and D. E. Chimenti, Vol. 15A, pp. 781-788, Plenum, New York, 1996.
5. Ch. Zhang and J. D. Achenbach, "Scattering of Body Waves by an Inclined Surface Breaking Crack," Ultrasonics, Vol. 26, pp. 132-138, 1988.

## DISCUSSION

### The Application of Neural Networks to Defect Sizing

Speaker: Achenbach

How did you get input for crack depth? —Glenn Light

*The cracks were two-dimensional, i.e., the crack depths could be determined from the positions of the crack tips on the sides of the specimens. This was particularly easy for the inclined cracks, which were EDM notches. For the perpendicular cracks the depths were also estimated from the observation of crack tip diffraction.*

Do principal components of the Fuzzy Logic correspond to physical parameters? —Glen Light

*The principal components used in this work do not specifically correspond to physical quantities or parameters. I would expect that the best results would be obtained for principal components that have physical significance.*

Did you try different shapes of membership functions? If you allow different shapes, you get one more parameter to change, and you may be able to get an even better fit. —Vladik Kreinovich

*No, we did not. We only used the triangular shapes. It is conceivable that other shapes have advantages, but the triangles have the virtue of simplicity.*

How were these cracks induced? Through EDM Notch as crack initiative or are the EDM notches the cracks themselves? —Krishnan Balasubramaniam

*The inclined cracks were EDM notches. The normal cracks were fatigue cracks that were started from notches.*

How large was the training set for your ANN and how many inputs did you use? —Carlos Ferregut

*We used 108 inputs per data set, and we used about 20 data sets, i.e., simulated data for 20 cracks.*



# INNOVATIVE APPROACHES TO THE ANALYSIS OF NDE DATA

S. S. Udpal and L. Udpal

Materials Characterization Research Group  
Dept. of Electrical and Computer Engineering  
Iowa State University, Ames, IA

## ABSTRACT

This paper presents an integrated approach to the analysis of natural gas pipeline inspection data. The analysis is performed in three stages. The first stage uses a multi-layer perceptron to identify signals representing benign pipeline components that do not warrant any analysis. The remaining signals are then compensated for the effects of probe velocity and variations in pipewall permeability. The third stage involves the analysis of the compensated signal to generate a three dimensional profile of the defect. The results are displayed in a virtual reality environment that allows the user to navigate both within and outside the pipe. The strengths of a variety of neural networks are exploited in the application.

<b>KEYWORDS:</b>	Neural Network	Radial Basis functions
	Wavelet Basis Functions	Nondestructive Evaluation
	Gas Pipeline Inspection	Signal Compensation
	Defect Classification	Defect Characterization

## 1. INTRODUCTION

Natural gas is one of the most important sources of energy in the United States. Its continued and uninterrupted supply is vital for the economic security of the country. Natural gas is produced at remote well sites and transported to consumer locations through a vast network of pipelines<sup>[1]</sup>. A typical transmission gas pipeline, for example, is a 24" diameter, 0.034" thick cast steel pipe that is usually buried several feet below in the ground. These pipes are inspected periodically to detect wall thinning and metal loss on the outer surface that is often caused by corrosion. The inspection is carried out using a device called a pig that is propelled forward inside the pipe by the gas pressure.

Although several different inspection methodologies (ultrasonics, EMATS, etc.) have been proposed, the most popular technique involves the use of the magnetostatic method. Figure 1 shows a highly simplified sketch of a pig that relies on the magnetostatic approach<sup>[2]</sup>. The pig employs pairs of very high-energy magnets as part of a magnetic circuit that includes backing plates, a steel brush and the pipewall. The steel brush rubs against the pipewall, thereby providing a magnetic path even when the pig is in motion inside the pipe. The high field strength of the magnets ensures that the pipewall is magnetically saturated. The presence of a defect such as a corrosion pit on the outer surface of the pipe causes the magnetic flux to "leak" out of the pipe as shown in Figure 2. Sensors can be arranged to measure either the axial, radial or circumferential components of the magnetic flux leakage (MFL) signal.

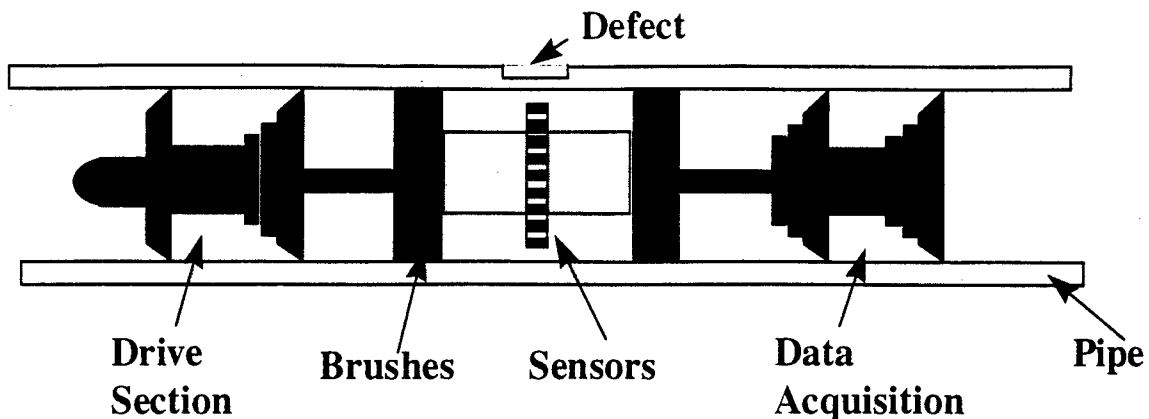


Figure 1. A schematic of the gas transmission pipeline inspection tool.

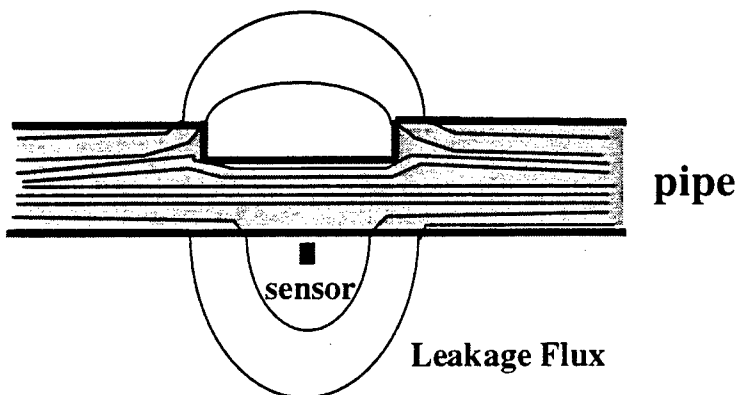


Figure 2. Magnetic leakage flux path due to a defect in the pipewall.

The pig employs a number of magnetic field sensors, such as Hall elements, that are arranged circumferentially in close proximity to the pipe wall. Figure 3 shows the components of the leakage signal generated by an exterior defect. It is a common industry practice to measure only the axial component of the leakage flux signal.

The pig is instrumented to record the signals generated by all the magnetic field sensors along with other pertinent information, such as odometer readings, temperature, tool canting angle, etc., in a compressed digital format. Over 12 gigabytes of compressed data are typically generated for every 100 miles of pipeline that is inspected. The main objective of the inspection process is to detect, locate, and characterize all flaws in the pipeline by interpreting the recorded data. The current practice is to interpret this voluminous amount of data manually.

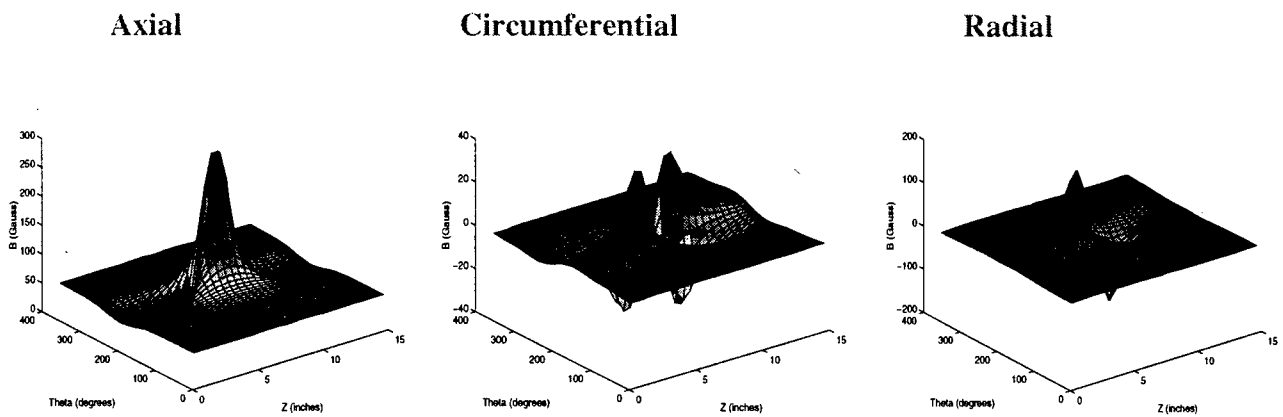


Figure 3. Flux leakage signal components generated by an exterior defect.

The gas industry is keenly interested in automating the interpretation process. Key advantages of the automation process include improvement in the accuracy, speed and consistency of interpretation. This paper presents an integrated approach to the task of managing, interpreting and visualizing data.

## 2. ANALYSIS STRATEGY

The key steps involved in the analysis are shown in Figure 4. The first step involves the classification of signals as representing benign or defect indications. The pipeline system consists of several components including tees, valves, and sleeves, as well as other artifacts, such as welds. Each of these produce a distinctive MFL signal. The first step involves recognition of such signals as benign and withdrawing such signals from the data stream and avoid any further analysis. The second step involves compensating the effects of operational variables, such as pig velocity, pipewall permeability and pipewall thickness. The MFL signal shape and amplitude vary as a function of various operational parameters such as pig velocity, pipewall permeability, residual stress, etc. These effects have to be first adequately compensated for.

After the signal is compensated, a multiresolution wavelet based reconstruction algorithm is used to predict the three dimensional profile of the defect. The final result is displayed in a virtual reality environment where the user has the flexibility to "navigate" within the pipe. The virtual reality environment allows the user to enter and exit the pipe and observe three-dimensional views of the defect and other benign artifacts from any arbitrary perspective. The visualization package displays prestored images of benign artifacts, such as tees and valves, upon receiving an appropriate trigger from the classifier in the first stage. Each of the subsystems is described in greater detail below.

## 3. NEURAL NET CLASSIFIER

A multilayer perceptron type neural network is used to distinguish benign artifact signals (tees, valves, sleeves, welds, etc.) from defect signals. The approach is conventional in that literature abounds with reports of similar strategies being used in applications ranging from speech signal processing to x-ray radiography.

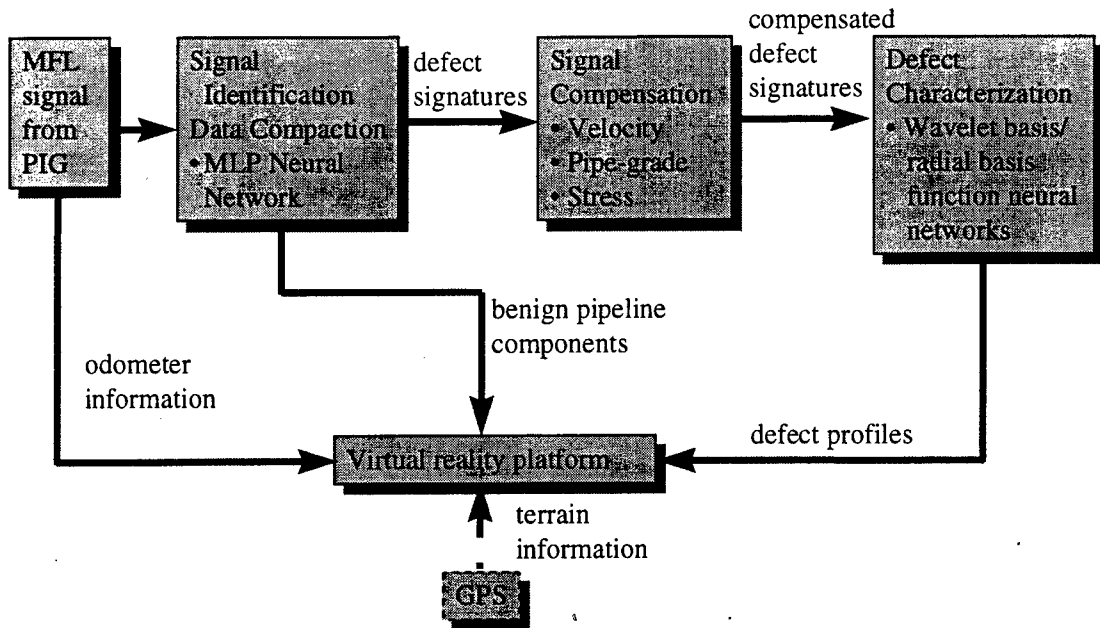


Figure 4. Steps in the overall signal analysis procedure.

A schematic of the classification procedure is shown in Figure 5. The signal is filtered and segmented using a procedure that is largely heuristic. The first twenty eigenvalues, together with two geometry related features, extracted from the segmented images constitute the input to a two hidden layer perceptron. The MLP is trained, using the well-known back-propagation learning rule<sup>[3]</sup> such that a specific node goes "high" when a signal representing a certain artifact appears at the input terminals

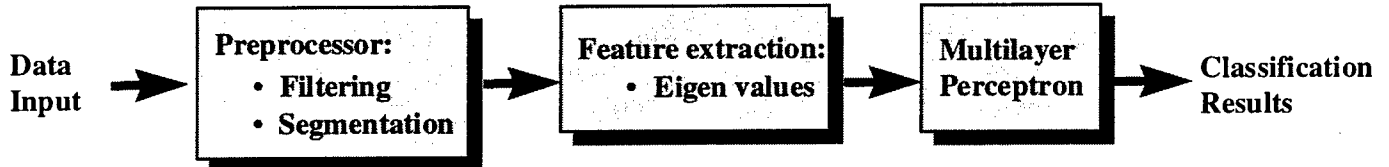


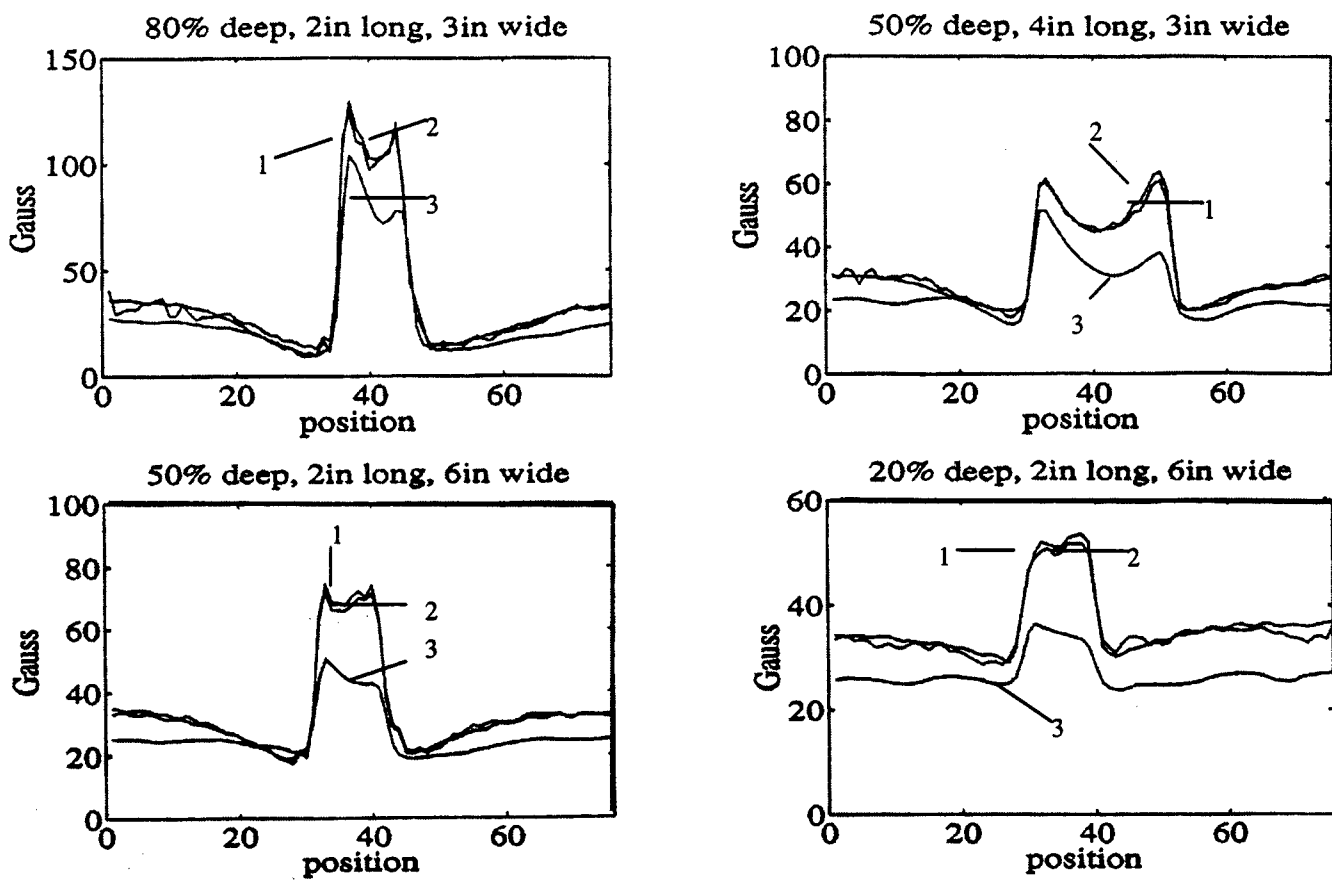
Figure 5. Schematic of the signal classification procedure.

#### 4. SIGNAL COMPENSATION

As indicated earlier, the MFL signals are affected by a number of factors, including inspection tool velocity, pipeline permeability, pipewall thickness and remnant magnetization. Other factors, such as stresses in the pipe, affect the pipewall permeability which, in turn, have an impact on the MFL signal. The effect of these factors have to be compensated for prior to characterization. The signal is typically compensated for the effects of tool velocity and permeability. This is accomplished in two stages.

##### 4.1 Velocity Compensation

In the first, the signal is compensated for velocity effects using a statistical Wiener filter<sup>[4]</sup>. Figure 6 shows examples of MFL signals obtained at low (desired signals) and high (distorted signals) pig velocities. Signals compensated using the Wiener filter are also shown.



1 = Compensated, 2 = Desired, 3 = Distorted

Figure 6. Results of velocity compensation procedure.

#### 4.2 Permeability Compensation

The permeability compensation schemes fuses information contained in two different MFL signal measurements to achieve permeability invariance. Consider signals generated by an independent, heterogeneous pair of sensors measuring the same physical process. In the present context, the two sensors could, for example, be measuring the axial and radial components of the MFL signal. Both signals are sensitive to a number of test variables, such as the defect length ( $\ell$ ), defect depth (d) and the permeability of the pipewall. Let  $X_A$  and  $X_B$  denote the two signals and let  $t$  denote the pipewall permeability. An appropriate feature, such as its peak value or moment, is extracted from the signals  $X_A(d, \ell, t)$  and  $X_B(d, \ell, t)$ . Let the two features be denoted as  $x_A(d, \ell, t)$  and  $x_B(d, \ell, t)$ . We wish to identify a function  $f$  of the two features that is independent of the parameter  $t$ ; i.e.,

$$f\{x_A(d, \ell, t), x_B(d, \ell, t)\} = g(d, \ell) \quad (1)$$

A sufficient condition for obtaining invariance to the parameter  $t$  is

$$g(d, \ell) \Leftrightarrow g_1(x_A(d, \ell, t)) = g_2(x_B(d, \ell, t)) \quad (2)$$

where  $\diamond$  denotes a homomorphic operator. Then

$$f(x_A, x_B) = g(d, \ell) = g_2(x_B) \diamond g_1^{-1}(x_A) \quad (3)$$

The choice of the functions  $g_1$  and  $g_2$  is dictated by several factors. The function  $g$  may, for example, be chosen to be a linear function of defect depth.  $g_2$  could be chosen on the basis of the dynamic range of the signal. As an example, if the dynamic range of the signal is large, the choice of a logarithmic function may be appropriate. The function  $g_1$  serves the role of a universal approximator. A suitable functional form is chosen for  $g_1$  and the coefficients are estimated to satisfy equation (3). The equation can be satisfied by sampling the function space.

$$\begin{aligned} H(d_i, \ell_j) \diamond g_1\{x_A(d_i, \ell_j, t_k)\} &= g_2\{x_B(d_i, \ell_j, t_k)\} \\ i = 1, 2, \dots, m, j = 1, 2, \dots, n \text{ and } k = 1, 2, \dots, p. \end{aligned} \quad (4)$$

For the application on hand, we chose the axial ( $X_A$ ) and radial ( $X_B$ ) components of the MFL signal. The peak-to-peak value of the signals were chosen as features ( $x_A$  and  $x_B$ ),  $g_2$  is assumed to be an identity function (i.e.,  $g_2(x) = x$ ) and the homomorphic operator is multiplicative. Thus,

$$g(d, \ell, w) = \frac{P_z(d, \ell, w, t)}{g_1\{P_r(d, \ell, w, t), P_z(d, \ell, w, t), D_r, D_c\}} \quad (5)$$

where  $d$ ,  $\ell$ , and  $w$  represent the depth, length and width of the defect,

$P_r$  and  $P_z$  denote the peak-to-peak value of the radial and axial components of the MFL signal

$D_r$  is the distance between the positive and negative peak of the radial component of the MFL signal, and

$D_c$  is the support of the axial component of the signal along the circumferential direction.

$D_r$  and  $D_c$  are closely linked to the defect length and width, respectively.

The function  $g_1$  can be synthesized using neural networks that are suitable for functional interpolation. Radial basis function (RBF) networks<sup>[5]</sup> and Wavenets<sup>[6]</sup> are excellent choices. RBF networks synthesize functions using a linear combination of activation or radial basis functions  $\phi(\cdot)$ ; i.e.,

$$g_1(X) = \sum_{i=1}^n \lambda_i \phi(\|x - c_i\|) \quad (6)$$

where  $n$  is the number of RBFs used in the expansion,

$c_i$  is the center of the  $i^{\text{th}}$  RBF,

$\lambda_i$  are the expansion coefficients, and

$\|\cdot\|$  represents the  $\ell_2$  norm.

If a Gaussian RBF is used, equation (6) becomes

$$g_1(X) = \sum_{i=1}^n \lambda_i \exp\left(\frac{\|X - c_i\|}{2\sigma_i^2}\right) \quad (7)$$

where  $\sigma$  denotes the degree of locality. Although optimal values of parameters  $\lambda_i$ ,  $c_i$ ,  $\sigma$  and  $n$  can be estimated by minimizing an appropriate cost function, we use a simpler method that relies on picking a reasonable number for  $n$  and using the K-Means clustering algorithm<sup>[7]</sup> to provide estimates of  $c_i$  and  $\sigma_i$ . Equation 7 can be written in matrix form as

$$G = A\Lambda \quad (8)$$

from which the coefficients  $\lambda$  can be estimated from

$$\Lambda = A^+ G \quad (9)$$

where  $A^+$  represents the pseudo-inverse of  $A$ . If the number of examples available for training the network is small,  $c_i$  could correspond to the training data points. The MFL signal is scaled using the computed value of the invariant function to obtain the permeability invariant flux density signal.

Figure 7 shows some typical examples of results obtained using this approach. The MFL signals are derived from 3% long defects that are 20%, 50% and 80% deep, respectively, in three different pipe grades (which imply three different magnetization characteristics). The permeability compensated signals shown alongside indicate that the approach works very well.

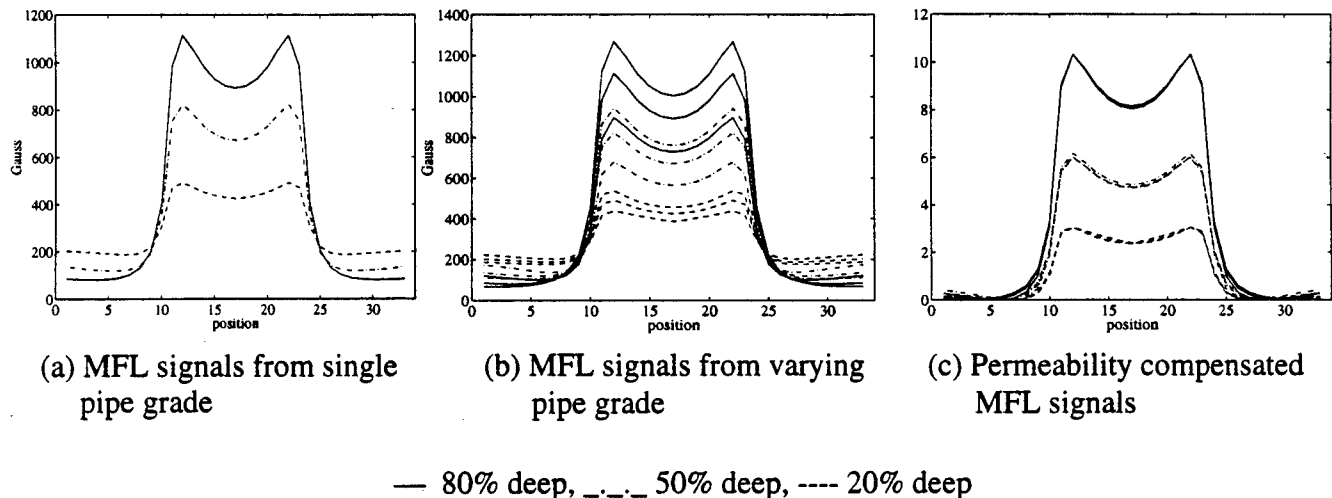


Figure 7. Results of permeability compensation procedure

## 5. DEFECT CHARACTERIZATION

The final step in the analysis procedure involves mapping of the compensated signal, using a Wavenet<sup>[6]</sup>, to obtain the three dimensional profile of the defect. The Wavenet or the wavelet basis network is based

on the concept of multiresolution representation of the function using wavelet transforms. A more detailed description of the concept can be found in a number of references<sup>[8]</sup>. Briefly, the approach involves expansion of a function  $f(x)$  starting from the coarsest resolution and progressively adding additional terms representing higher resolution versions of the function

$$\begin{aligned}
 f_L(x) &= \sum_{j=1}^{N_L} S_j^L \phi_j^L(x) \\
 f_{L-1}(x) &= f_L(x) + \sum_{j=1}^{N_{L-1}} d_j^{L-1} \Psi_j^{L-1}(x) \\
 &\vdots \\
 f(x) &= f_0(x) = \sum_{j=1}^{N_1} S_j^L \phi_j^L(x) + \sum_{k=1}^L \sum_{j=1}^{N_k} d_j^k \Psi_j^k(x)
 \end{aligned} \tag{10}$$

The architecture of the network is shown in Figure 8. The scaling function  $\phi$  is a Gaussian, while the wavelet function  $\Psi$  is a Mexican hat function. At the coarsest level, the centers are estimated using the K-Means clustering algorithm. From the second resolution onwards, a dyadic scheme is used to determine the centers. The procedure used for training the network is summarized in Figure 9. The input signal is a  $(42 \times 61)$  matrix representing the compensated magnetic flux leakage signal. The output is a  $(61 \times 61)$  matrix with entries representing the depth of the flaw. The number of scaling function nodes is 3. A major advantage of the approach is that the user has control over the level of prediction accuracy by changing the number of resolutions. The improvement in accuracy is obtained at the expense of greater computational effort.

Figure 10 shows cutouts of typical defect profiles obtained by the network at progressively increasing levels of resolution. A line scan of the true and predicted profiles are shown for comparison.

## 6. VISUALIZATION

The defect profile data is exported to a visualization package that displays the data in a virtual reality environment. The package allows the user to navigate inside the pipe where a wire frame display for the leakage field signal can be seen. Perturbations in the wireframe display provide a visual cue for the user that a defect or a benign pipeline component, such as a valve or a sleeve, is present. The user can navigate outside the pipe and visualize the defect from any arbitrary perspective. Prestored three-dimensional views of pipeline components are invoked whenever the signal classification algorithm generates a signal indicating the presence of the component. Figure 11 shows a three dimensional view of a corrosion pit on the outer surface of the pipe. The visualization package allows rapid assimilation of data and minimizes information overload.

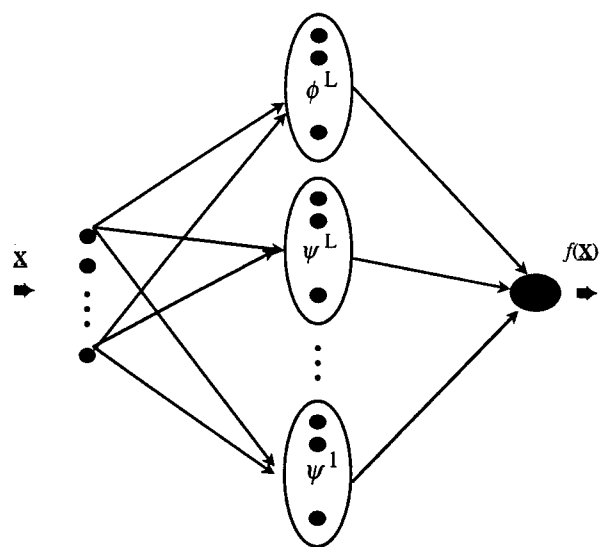


Figure 8. Architecture of the wavenet.

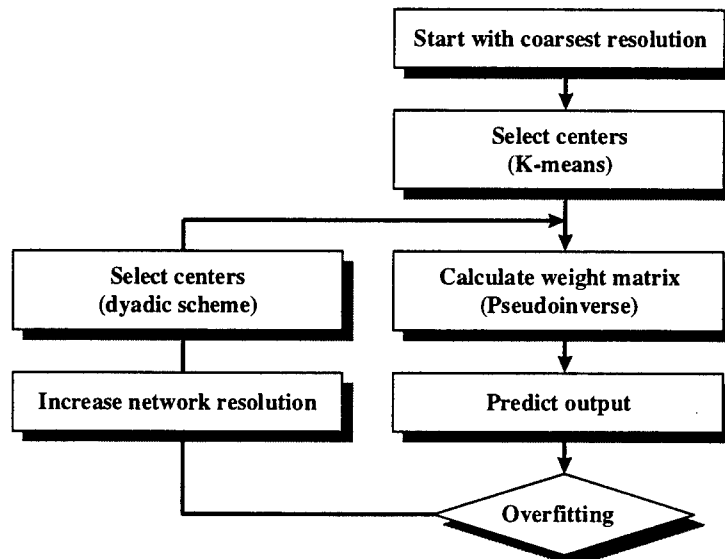


Figure 9. Procedure for training the wavenet.

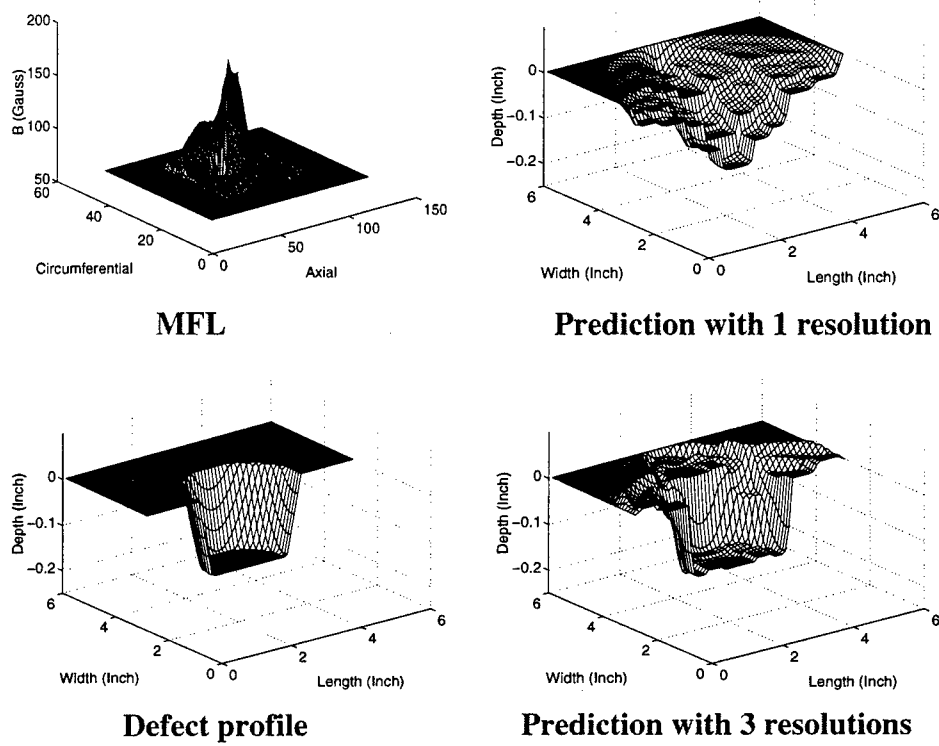


Figure 10. Defect reconstruction at different resolutions.

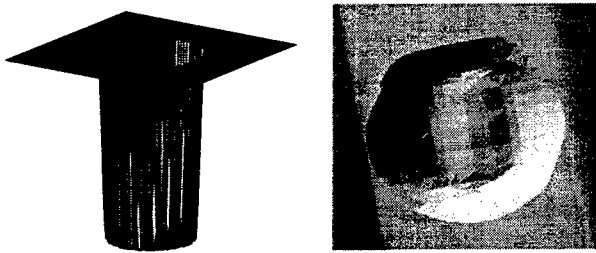


Figure 11. Three-dimensional view of a corrosion pit.

## 7. CONCLUSIONS

This paper presents an integrated approach for the systematic and rapid analysis of pipeline NDE data. The method uses three different types of neural network capturing, exploiting in the process, each of their strengths. Some of the algorithms can be easily adapted to solve NDE problems of interest to the U.S. Air

force. An example is the extension of the compensation algorithm for rendering eddy current signals invariant to the effects of lift-off variations during the inspection of aircraft components.

## 8. REFERENCES

- [1] Udpa, L., Mandayam, S., Udpa, S., Sun, Y., and Lord, W., "Developments in Gas Transmission Inspection Technology", *Materials Evaluation*, Vol. 54, No. 4, pp. 467-472, 1996
- [2] Lord, W. and Oswald, D. J., "Leakage Methods of Field Detection," *International Journal of Nondestructive Testing*, Vol. 4, pp. 249-274, Gordon and Breach, Great Britain, 1972.
- [3] Lippmann, R. P., "An Introduction to Computing with Neural Nets," *IEEE ASSP Magazine*, pp. 4-22, April 1987.
- [4] Gonzalez, R. C., and Wintz, P., *Digital Image Processing*, Addison-Wesley, Reading, MA, 1987.
- [5] Broomhead, D. S. and Lowe, D., "Multivariate Functional Interpolation and Adaptive Networks," *Complex Systems*, Vol. 2, pp. 321-355, 1988.
- [6] Bakshi, R. B. and Stephanopoulos, G., "Wave-Net: A Multiresolution, Hierarchical Neural Network with Localized Learning," *AICHE Journal*, Vol. 39, pp 57-81, 1993.
- [7] Tou, T. J. and Gonzalez, R. C., *Pattern Recognition Principles*, Addison-Wesley, Reading, MA 1974.
- [8] Mallat, S. G., "A Theory for Multiresolution Signal decomposition: The Wavelet Representation," *IEEE Transaction on Pattern Analysis and machine Intelligence*, Vol. 11 (7), pp. 674-693, 1989.



# NEURAL NETWORKS FOR DAMAGE IDENTIFICATION

Thomas L. Paez and Scott E. Klenke

Experimental Structural Dynamics Department  
Sandia National Laboratories  
Albuquerque, New Mexico 87185-0557

## ABSTRACT.

Efforts to optimize the design of mechanical systems for preestablished use environments and to extend the durations of use cycles establish a need for in-service health monitoring. Numerous studies have proposed measures of structural response for the identification of structural damage, but few have suggested systematic techniques to guide the decision as to whether or not damage has occurred based on real data. Such techniques are necessary because in field applications the environments in which systems operate and the measurements that characterize system behavior are random.

This paper investigates the use of artificial neural networks (ANNs) to identify damage in mechanical systems. Two probabilistic neural networks (PNNs) are developed and used to judge whether or not damage has occurred in a specific mechanical system, based on experimental measurements. The first PNN is a classical type that casts Bayesian decision analysis into an ANN framework; it uses exemplars measured from the undamaged and damaged system to establish whether system response measurements of unknown origin come from the former class (undamaged) or the latter class (damaged). The second PNN establishes the character of the undamaged system in terms of a kernel density estimator of measures of system response; when presented with system response measures of unknown origin, it makes a probabilistic judgment whether or not the data come from the undamaged population. The physical system used to carry out the experiments is an aerospace system component, and the environment used to excite the system is a stationary random vibration. The results of damage identification experiments are presented along with conclusions rating the effectiveness of the approaches.

## NOMENCLATURE.

ANN	: Artificial Neural Network
PNN	: Probabilistic Neural Network
PPC	: Probabilistic Pattern Classifier
VETO	: Virtual Environment for Test Optimization
$X, Y$	: vector of random variables with dimension n
$F_X(\cdot)$	: cumulative distribution function estimator
$H_X, H_Y$	: a priori probabilities of $X$ and $Y$
$L_X, L_Y$	: loss factors associated to sources $Y$ and $X$
$N$	: number of measured data realizations
$S$	: covariance matrix
$T$	: a transform operator
$f_X(\cdot), f_Y(\cdot)$	: probability density functions
$n$	: dimensionality of a source of data
$u$	: uniformly distributed random variable
$w$	: uncorrelated standard normal random variable
$z$	: datum of unknown source
$\Phi(\cdot)$	: cumulative distribution function of a standard normal random variable
$\sigma$	: smoothing parameter

## 1. INTRODUCTION

Structural engineering design usually dictates that systems be fabricated to optimum weight and cost specifications, and yet safely sustain the loads applied to them for a preestablished duration. This can be accomplished because great strides are being made in analysis, design and testing practice, but it is complicated by the fact that the loads applied to any real structure are unknown and the material properties and geometry of a structure are random. In view of this, responses of critical structures must be monitored, and the information used to infer structural functionality and safety.

Many frameworks can be used to assess the relative health of a structure, and this paper presents two of them. They are the classical PNN of Specht (1990), and a PPC that we have developed. The former is an ANN implementation of the Bayes' decision analysis procedure. The latter is a formal statistical procedure that permits us to judge the source of data of unknown origin.

The PNN requires data sets from two or more sources. When presented with a datum of unknown origin, it judges which set of known data is the likeliest source of the unknown datum. The PNN implements Bayes' decision rule representing the probability density functions (pdf's) of the known data sets with kernel density estimators. These were first developed in the form in which they are used today by Parzen (1962), and their form was later generalized to the multivariate case by Cacoullos (1966). A text that summarizes kernel density estimators is that of Silverman (1986). The PNN is briefly described in Section 2.

When one or more measures of structural behavior representing both damaged and undamaged system states are available, they can be used to establish the parameters of a PNN. When corresponding measures of structural behavior are taken from a structure not known to be damaged or undamaged, they can be presented to the PNN for its judgment regarding the state of the system.

The PPC requires a data set from one source. When presented with a datum of unknown origin, it judges whether the datum is a member, an outlier, or a nonmember of the set whose source is known. This tool also uses the pdf representation of Parzen and Cacoullos, but given that representation it defines a transform (see Rosenblatt, 1952) into the space of uncorrelated standard normal random variables. Data of unknown origin are transformed into this space, and a test of hypothesis is performed to judge the source of the data. The PPC is developed in Section 3.

When one or more measures of structural behavior representing undamaged system states are available, they can be used to establish the parameters of a PPC. When corresponding measures of structural behavior are taken from a structure not known to be damaged or undamaged, they can be presented to the PPC for its judgment regarding membership of the data in the set of undamaged data. The data will be judged members, outliers, or nonmembers of the undamaged data set. Details of the approaches used perform the statistical damage diagnoses described above are given in Section 4.

The real test of a damage diagnosis tool is its effectiveness in practical application. The two health monitoring tools considered in this study are applied to the monitoring of damage in a physical system. The system is a stereolithography model of an aerospace component. The system was tested using random vibration and its response measured and used to characterize the undamaged system. Next, a small amount of damage was introduced into the system, and it was tested and characterized again. This step was repeated four more times; each time incremental damage was introduced into the system before retesting. Finally, the PNN and PPC were used to determine whether the incremental damage could be recognized. The results were successful, and are presented in detail in Section 5.

## 2. CLASSICAL PROBABILISTIC NEURAL NETWORK

The classical PNN uses the Bayesian decision analysis cast into an ANN framework to judge the origin of datum  $z$  given that data from two random variable sources,  $X$  and  $Y$ , are known. The known data are denoted  $x_j, y_j, j = 1, \dots, N$ . The sources  $X$  and  $Y$  are assumed to be vector random variables with dimension  $n$ , and their corresponding realizations are also assumed to be vectors. For the two-source case, the origin of  $z$  is determined based on the following Bayesian decision rule

$$\begin{aligned} z \in X & \text{ if } H_X L_X f_X(z) > H_Y L_Y f_Y(z) \\ z \in Y & \text{ if } H_X L_X f_X(z) < H_Y L_Y f_Y(z). \end{aligned} \quad (1)$$

Where  $f_X(z)$  and  $f_Y(z)$  are the probability density functions (pdf's) for the sources  $X$  and  $Y$ , respectively;  $H_X$  and  $H_Y$  are the a priori probabilities of sources  $X$  and  $Y$ ; and  $L_X$  and  $L_Y$  are the losses resulting from incorrect decisions that the sources are  $Y$  and  $X$ , respectively. Often the a priori probabilities can be determined for the source data, however, the loss factors require some subjective evaluation based on the application from which the source data have come. The key to using Eq. (1) is the ability to estimate the probability density functions  $f_X(z)$  and  $f_Y(z)$  based on experimental data. These joint pdf's can be approximated using the kernel density estimator (see Parzen (1962), Cacoullos (1966) and Silverman (1986)). The kernel density estimator (kde) is a data based estimator and one form is

$$\hat{f}_X(z) = \frac{1}{N(2\pi)^{1/2} \|S\|^{1/2}} * \sum_{j=1}^N \exp\left(-\frac{1}{2}(z - x_j)^T S^{-1}(z - x_j)\right) \quad (2)$$

Of course, the kernel in this expression, is a multivariate normal pdf. The kernel density estimator is a superposition of  $N$  multivariate normal densities centered at each measured realization of  $X$ . This summation is normalized so that its hyperspace volume equals one.  $S$  is the covariance matrix for the kernel. This matrix can conveniently be approximated by the special form

$$S = \sigma^2 I \quad (3)$$

where  $I$  is the identity matrix and  $\sigma$  is the smoothing parameter of the kde. A small smoothing parameter can cause the estimated density function to show distinct modes at the locations of the training data, while a large value of  $\sigma$  provides greater smoothing or interpolation between points in the density estimation. The following smoothing factor was used in the kde's of this study.

$$\sigma = 0.9 * (4/(n+2))^{1/(n+4)} * \sqrt{\left\{ \sum_j std(x_j) \right\}^2} * N^{-1/(n+4)} \quad (4)$$

where  $std(x_i)$  refers to the standard deviation of the  $i$ th random variable vector source  $X$ , and the other parameters were previously described.

### 3. PROBABILISTIC PATTERN CLASSIFIER

The PPC) similar to the PNN in that it seeks to distinguish the source of a datum of unknown origin. However, the PPC differs from the PNN in that the PPC seeks to answer the question: Is the datum of unknown origin a member of the data set of interest, or is it an outlier, or is it a nonmember? It answers this question by: (1) characterizing the data set of interest using the kernel density estimator of Eq. (2), (2) using this expression to develop a Rosenblatt transformation to the space of uncorrelated standard normal random variables, then (3) transforming the datum of unknown origin to the standard normal space where we perform a test of hypothesis to judge its membership in the reference set.

We commence the development by assuming that a random variable  $X$  is characterized by a collection of data denoted  $x_j, j = 1, \dots, n$ . The source and the data it produces may be vector quantities. The kernel density estimator for the data is given by Eq. (2). We seek a transformation from the space of  $X$  to the space of uncorrelated standard normal random variables. Such a transformation can be developed using the Rosenblatt transformation (see Rosenblatt, 1952).

The Rosenblatt transformation is a unique and invertible mapping that permits the conversion of vector realizations of random variables with arbitrary joint probability distribution to vector realizations of independent, uniformly distributed random variables on the interval  $[0,1]$ . To develop the transformation, note that there is a cumulative distribution function (cdf) estimator that corresponds to the kde in Eq. (2). It is easy to obtain because of the form of the covariance matrix in Eq. (3), and is given by

$$F_X(\mathbf{x}) = \int_{-\infty}^{\xi_1} d\alpha_1 \dots \int_{-\infty}^{\xi_n} d\alpha_n f_X(\boldsymbol{\alpha}) = \frac{1}{N} \sum_{j=1}^N \prod_{k=1}^n \Phi\left(\frac{\xi_k - x_{kj}}{\sigma}\right) \quad (5)$$

where  $\mathbf{x}$  is the variate vector and  $\xi_k$  is its  $k$ th element,  $x_{kj}$  is the  $k$ th vector element in the  $j$ th data point  $\mathbf{x}_j$ ,  $F(\cdot)$  is the cdf of a standard normal random variable and the other quantities in the expression are defined following Eq. (2). This is the joint cdf of all the random variables,  $X_k, k = 1, \dots, n$ , in the vector  $X$ . From this function all the lower order joint cdf's (including marginal cdf's) and conditional cdf's can be developed. The Rosenblatt transformation takes the form

$$\begin{aligned} u_1 &= F_{X_1}(\xi_1) \\ u_2 &= F_{X_2|X_1}(\xi_2 | \xi_1) \\ &\dots \\ u_n &= F_{X_n|X_{n-1}, \dots, X_1}(\xi_n | \xi_{n-1}, \dots, \xi_1) \end{aligned} \quad (6)$$

where the  $u_j, j = 1, \dots, n$ , are realizations of independent, uniformly distributed random variables on  $[0,1]$ , the  $\xi_j, j = 1, \dots, n$ , are elements of the vector  $\mathbf{x}$ , and the functions on the right hand side are one marginal (the first equation) and several conditional cdf's obtained from Eq. (5). The following shorthand notation can be adopted for Eqs. (6).

$$\mathbf{u} = \mathbf{T}(\mathbf{x}) \quad (7)$$

where  $u$  is the vector of elements  $u_j, j = 1, \dots, n$ , and  $x$  is the vector of elements  $\xi_j, j = 1, \dots, n$ .

Because the cdf defined in Eq. (5) is monotone increasing (The standard normal cdf,  $\Phi(\cdot)$  is a monotone increasing function.), the transformation of Eqs. (6) and (7) is invertible, therefore,

$$x = T^{-1}(u) \quad (8)$$

Because we can define the forward and inverse transformations in Eqs. (6) through (8) for a vector of random variables  $X$  with arbitrary distribution, we can also define the transformation for a vector of random variables  $W$  that are uncorrelated with standard normal distribution (i.e., each element of  $W$  is normally distributed with mean zero and unit variance.). The forward and inverse transformations may be denoted

$$u = T_{sn}(w) \quad w = T_{sn}^{-1}(u) \quad (9)$$

where the subscript "sn" refers to the fact that these are transformations to and from the standard normal space.

The existence of the transformation in Eq. (7) and the second transformation in Eq. (9) implies that a transformation from a realization of a vector random variable with arbitrary joint probability distribution to a realization of a vector of uncorrelated standard normal random variables can be defined. In terms of the notation in Eqs. (7) and (9), it is

$$w = T_{sn}^{-1}(T(x)) \quad (10)$$

This transformation, developed using the detailed forms of Eqs. (5) and (6), forms the basis of the PPC. The transformation reflects the character of the data source  $X$  via its measured realizations  $x_j, j = 1, \dots, N$ , because the cdf's in Eq. (6) come from Eq. (5), and Eq. (5) involves the  $x_j, j = 1, \dots, N$ .

The PPC operates on the following basis. We consider a datum  $z$  of unknown origin, and make the hypothesis that it comes from the random source  $X$ . We transform  $z$  to the space of realizations of uncorrelated standard normal random variables using Eq. (10). The operation yields

$$w_z = T_{sn}^{-1}(T(z)) \quad (11)$$

Note that the distance from the origin of a random vector in uncorrelated standard normal space is related to the chi squared distribution. Specifically, the square of the distance from the origin of a random vector with dimension  $n$ , whose components are standard normal random variables, is chi squared distributed with  $n$  degrees of freedom. In view of this, the hypothesis specified above is rejected at the  $\alpha \times 100\%$  level of significance if the norm of  $w_z$  (i.e.,  $\|w_z\|$ ) falls outside the interval  $[0, \sqrt{\chi^2_{n,1-\alpha}}]$ , where

$$F_{\chi_n^2}(\chi^2_{n,1-\alpha}) = 1 - \alpha \quad (12)$$

and  $F_{\chi_n^2}(\cdot)$  is the cdf of a chi squared distributed random variable with  $n$  degrees of freedom. Otherwise, the hypothesis is accepted at the discretion of the analyst. (The need for discretion arises here because measure of performance may simply not have been one that leads to rejection of the hypothesis; i.e., other measures of structural response may have led to rejection.)

In summary, we transform the datum  $z$  using Eq. (11), compute the norm of  $w_z$ , then observe whether  $\|w_z\|$  falls within  $[0, \sqrt{\chi_{n,1-\alpha}^2}]$ . If it does, then we may conclude that  $z$  is a realization of the random variable  $X$ ; otherwise, we conclude that it is not. It is anticipated that, on average,  $(1-\alpha) \times 100\%$  of the realizations  $z$  that come from the random source  $X$  will fall in the interval. When we perform a test under practical conditions, we will often set the significance level in the range 0.1% through 5%. In a heuristic sense, we can conclude that when  $\|w_z\|$  is outside the interval  $[0, \sqrt{\chi_{n,1-\alpha}^2}]$ , but not too much greater than  $\sqrt{\chi_{n,1-\alpha}^2}$ , then  $z$  may simply be an outlier of the random variable  $X$ . When  $\|w_z\|$  is much greater than  $\sqrt{\chi_{n,1-\alpha}^2}$ , then we conclude that  $z$  did not arise from the random source  $X$ .

#### 4. APPLICATION OF PROBABILISTIC NEURAL NETWORKS TO STRUCTURAL HEALTH MONITORING

The current research effort has focused on the development of two PNN software codes (the classical PNN and the PPC) to address the health of mechanical structures based on experimental data. These ANN approaches use measures of system response (and sometimes input) data to characterize the dynamic behavior of a component. The PNN uses measures of both damaged and undamaged system behavior to characterize a structure; the PPC uses only the latter. Once these models have been developed with measured response data, they can be used to enhance the decision making process related to the health of the structure. On-line measurements of both inputs and responses of an operating system, such as equipment on a production or manufacturing line, can be used to train the ANN. Once trained, the ANN can be used to monitor system health, either in real-time, or via post processing of data. There is no limitation on the types of structural response measures that can be used in the ANN training process to help assure that change in structural response or structural damage is clearly detected.

There are several key elements that are required to develop a useful PNN. First, the selection of a kde plays an important role in the ANN development process. The kde is an estimator of the pdf required in the decision analysis. Second, the selection of appropriate measures of structural response are needed that help to clearly reveal structural damage. These elements are a critical part of the development of a PNN that can be used to establish a measure of system health.

There are limitations to using these ANNs. Care needs to be taken when calculating multivariate density estimates. The size of the exemplar or training set needed in kernel density estimation increases dramatically as the order or dimensionality of the density estimation increases (Silverman, 1986). Thus, the requirement for large amounts of experimental data in estimating the probability densities might cause some limitations of these ANN techniques. Also, these two techniques are currently limited to assessing whether damage has occurred in a structure and they do not provide a method for determining the location or extent of the damage in the structure. In addition, the type of smoothing chosen in the kernel density estimation could limit not only the accuracy but also the computational speed of the estimation. Finally, when the sample set is large, the choice of kernel estimator may be very important in reducing the computation time of the probability density estimation (Silverman, 1986).

## 5. NUMERICAL EXAMPLE

An aerospace housing component was selected as test case hardware for generating experimental data where the health of the system could be monitored under different structural conditions. A test design tool called the Virtual Environment for Test Optimization (VETO) was used to design an optimal experiment for this housing component. The frequency band of interest was selected to include the first five vibration modes of the structure. A solids model of the aerospace housing component was used to generate a rapid prototype component through a stereolithography process. The testing was performed on this stereolithography component. Figure 1 shows a test setup photo.

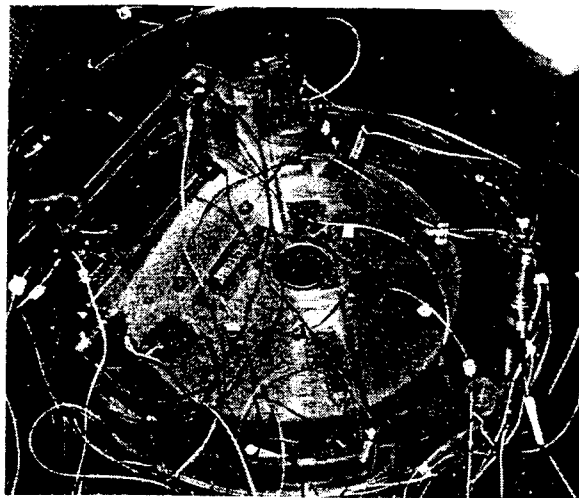


Figure 1. Experimental test setup.

The excitation used in the experiment was a stationary random vibration; acceleration response was measured at 55 locations. Using the visualization software within the VETO environment, two separate locations on the housing structure were selected for the introduction of damage. The basis for the selection of these locations was made by animating the vibration modes of interest while observing maximum strain energy density on the structure. Five separate damage cuts - each of one-quarter inch depth - were introduced at two locations with high strain energy density.

The selection of independent response measures for training the PNN was an important factor in developing a useful tool to measure the health of the housing component. The goal in choosing these measures was to minimize the dimension of the ANN while preserving or amplifying the response differences as damage was introduced into the structure. Responses measured at five locations were used in the analyses. It was determined that measures of static flexibility at the five measurement locations on the housing component would be used to train the PNNs to detect structural damage. Selecting static flexibility as the measure of structural response to use in the ANN applications required some analysis to be completed on the experimental data. Large sample sets of data were collected from input as well as for each of these response locations on the structure. Thirty-nine frequency response function (frf) realizations were calculated using smaller blocks of this large sample set of data. An approximation of the static flexibility was calculated given each of these frf realizations. The method for estimating the static flexibilities was to average the low frequency frf behavior to asymptotically approximate these measures. The difficulty in determining these estimates was in selecting an appropriate frequency range to make the calculations. A typical frf measure is shown in Figure 2.

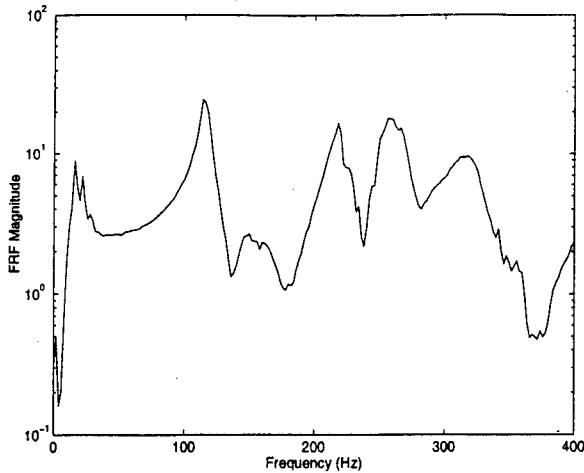


Figure 2. Typical frequency response function.

The first case study utilized these measures of static flexibility at the five selected locations on the housing structure as input to the classical PNN. Operation of the classical PNN requires data from at least two known sources; one set of static flexibilities from the undamaged case and one or more sets of static flexibilities from the group of damaged cases. When the classical PNN was presented with data from an unknown source (this unknown data was taken from the sample set of undamaged or damaged flexibilities and was subsequently not used as PNN training data), the PNN would judge the origin of that data based on the Bayesian decision criterion shown in Eq. (1). The a priori probabilities given the two known sources of data were 0.5 and the loss factors were set to 1. The results from the classical PNN study were perfect with the code predicting the correct origin of an unknown source 78 out of a possible 78 times in all damage cases. Because of the obvious difficulties in graphically presenting the results of a five-dimensional density, two of the five locations on the housing structure were arbitrarily selected for displaying results from the classical PNN. Figure 3 shows the two-dimensional scatter plot of the static flexibilities plotted against one another for the undamaged (o) and five successive damaged cases (+). The differences between the undamaged and damaged cases for these two static flexibility measures are quite apparent enabling the PNN to easily detect the origin of an unknown source. The classical PNN was able to distinguish the damaged from the undamaged data in all cases, including the most lightly damage case.

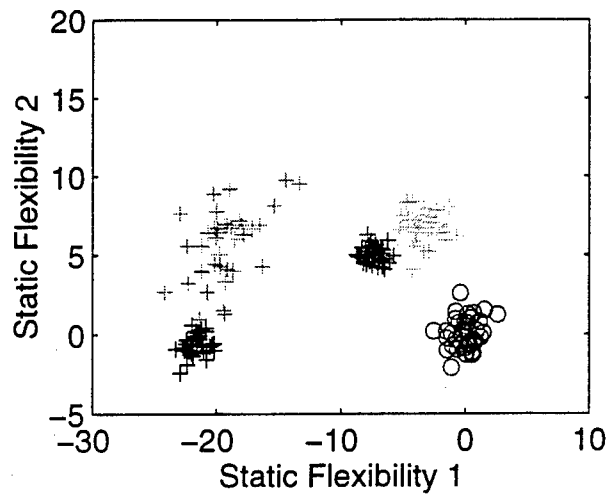


Figure 3. Scatter plot of static flexibilities.

The second case study utilized the same measures of static flexibility as input to the PPC. In this case, the PPC requires data from only a single source, such as the undamaged set of flexibilities, and seeks to judge whether or not the data from an unknown origin comes from that source. The Rosenblatt transformation was used to map the static flexibility data

from the space of the kernel density estimator into the space of uncorrelated, standard normal random variables. This transformation was also used to transform the data from an unknown source, static flexibility data from the damage cases, into the standard normal space. A distance from the origin was used as criterion to judge whether the data from the unknown source (data from successive damage cases) came from the known undamaged source. An acceptance region, distances from the origin considered as part of the undamaged source, was established based on the use of the chi square distribution. A chi square random variable with five degrees of freedom has a 99.9% probability of a distance from the origin less than 4.53. The results for the five damage cases input into the PPC are shown in Figure 4 as well as the maximum distance from the origin in standard normal space at which a 5-dimensional datum could be considered a realization of a 5- vector of uncorrelated standard normal random variables (4.53). (This is the straight line at  $\beta=4.53$ .) This figure shows the trend that as damage increases in the structure the distance measure in standard normal space also increases. The data near beta = 12 correspond to the first damage case. The data near beta = 50, 90 (smoother curve), and 110, correspond to the second, third, and fourth level damage cases, respectively. The data near beta = 90 (more erratic curve) correspond to the fifth level damage case. At this time it is not clear to us why the fifth level damage case yields lower beta values than the fourth level damage case.

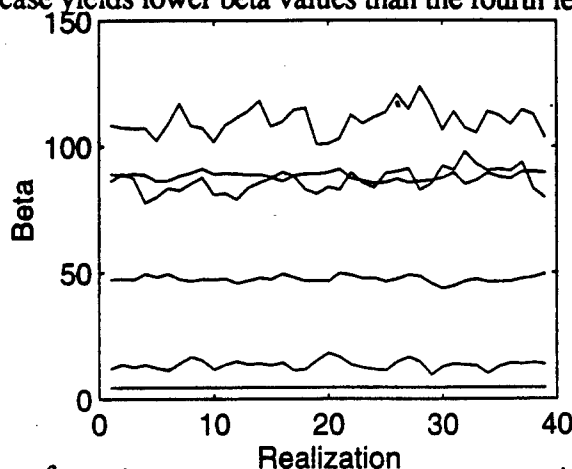


Figure 4. Plot of distance from the origin of data in standard normal space.

## 6. CONCLUSIONS

The results obtained using both the classical PNN and the PPC were quite successful. The damage in the aerospace housing component was identified, even in the most lightly damaged case, using both techniques. These ANNs clearly offer a robust method for assisting in the identification of damage in structures.

There are, however, a number of limitations in using these ANN techniques. The first is the limitation of these methods to provide or determine the location and extent of the structural damage. Further research in these ANNs will explore the combining of these techniques with data condensation methods to assist identifying the location and ultimately the extent of the structural damage. Some additional research will focus on the sensitivity of these ANNs to boundary conditions. Studies will be done to assess the effects that changing test configurations might have on the ANN results.

## 7. REFERENCES

Cacoullos, T., (1966) Estimation of a Multivariate Density. *Annals of the Institute of Statistical Mathematics* (Tokyo), Vol. 18(2), pp. 179-189.

Parzen, E., (1962) On Estimation of a Probability Density Function and Mode. *The Annals of Mathematical Statistics*, Vol. 33, pp. 1065-1076.

Rosenblatt, M., (1952) Remarks on a Multivariate Transformation, *The Annals of Mathematical Statistics*, Vol. 23, pp. 470-472.

Silverman, B.W., (1986) Density Estimation for Statistics and Data Analysis. Chapman and Hall, New York.

Specht, D.F., (1990) Probabilistic Neural Networks. *Neural Networks*, Vol. 3, pp. 109-118.

## DISCUSSION

### Neural Networks for Damage Identification

Speaker: Paez

Can the a priori probabilities can be updated if you have information that your network made a correct or wrong prediction. Can this be done in an adaptive way? —Carlos Ferregut

*The a priori probabilities can and should be modified adaptively if information regarding the outcome of successive experiments is available. Such adaptation is usually easy to implement because the a priori probabilities can be specified as parameters in a call to a decision analysis function subroutine.*

Do the a priori probabilities total one? —Mel Siegel

*Yes, the a priori probabilities total one. They can be thought of as conditioning probabilities in the Bayes' decision analysis implementation of the network.*

What are the loss factors? (Subjective?) —Mel Siegel

*The loss factor  $L_x$  is the loss associated with the decision that the source is Y when, in fact, the source is X. The loss factor  $L_y$  is defined similarly. The loss factors may need to be specified subjectively. However, there are situations where the loss associated with an incorrect decision can be specified through analysis, economic or otherwise.*



# **Recent advances in NDE technologies for aircraft inspection**

William P. Winfree

MS 231

Nondestructive Evaluation Sciences Branch, Materials Division  
NASA Langley Research Center  
Hampton, VA, 23681-0001

## **ABSTRACT**

A review of progress is presented of several techniques under development at NASA Langley Research Center for detection and quantification of flaws in aircraft structures. The techniques focus on the detection of cracks, corrosion and disbonds in thin laminated structures. The techniques range from thermal procedures which give a rapid indication of the regions of concern to eddy current instrumentation for detecting small cracks and multilayer corrosion. Results are presented on specimens with both manufactured defects for calibration of the techniques, specimens removed from aircraft and measurements in the field on aircraft.

**Keywords:** NDE, Crack detection, Corrosion detection, Eddy Current, Ultrasonics, Thermography, Radiography

## **1. INTRODUCTION**

The NASA Airframe Structural Integrity Program was initiated in October, 1990 with the objective of developing methodologies to support the safe and reliable operation of commercial aircraft. The program has three principal focuses; Structural Mechanics, Fracture Mechanics and Quantitative Nondestructive Evaluation (NDE). The Quantitative Nondestructive Evaluation Program has concentrated on the development of inspection techniques to detect small cracks, disbonds and corrosion in the fuselage with emphasis on the lap joints and tear straps.

Four methodologies have been developed to detect and characterize defects in the airframes. They are based on eddy current, ultrasonic, thermal and x-ray excitations of the structure. The eddy current technique is based on a new probe design which has an output that is easily interpreted and reduced sensitivity to lift off error. It detects small cracks in up to the top three layers of a laminated structure and characterizes aluminum thinning in first and second layers. The ultrasonic technique is a pulse echo based technique which detects disbonds and accurately quantifies aluminum thinning in the first layer of the structure. It has been integrated into a small portable scanner to enable rapid imaging of the corrosion area. The thermal technique is a large area technique capable of detecting disbonds and locating regions with aluminum thinning of 10% or more. Finally, the x-ray technique is based on a novel x-ray concept call "reverse geometry x-ray" which enables the detection of interior defects in the structure.

The techniques are complementary. The thermal system quickly surveys the structure to locate suspect regions. The ultrasonic technique verifies the presence of disbonds and accurately quantifies the corrosion in the outer layer. The eddy current technique detects small cracks and accurately quantifies aluminum thinning in the first and second layer and, with the complementary ultrasonic data,

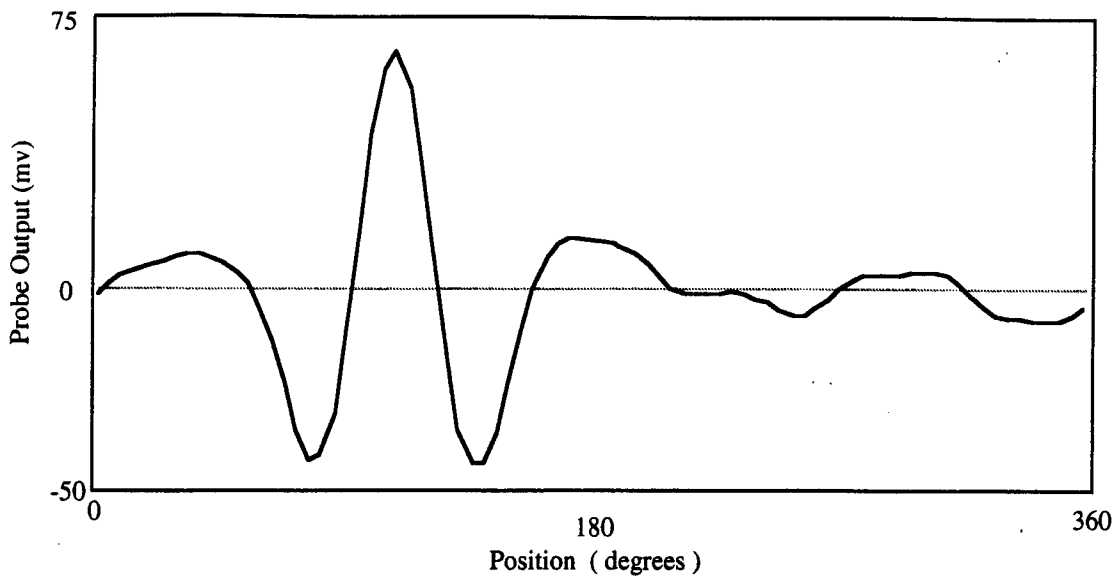


Figure 1. Output of self nulling probe during rotation around rivet with 37 mil crack.

determines the extent of aluminum thinning in the second layer as compared to the first layer. Finally, x-ray radiation enables the detection of cracks and corrosion in thick or multilayered structures.

## 2.EDDY CURRENT SELF-NULLING PROBE

Eddy current techniques are among the most common used for detection of cracks and corrosion in commercial aircraft structures. A new probe was recently developed at NASA Langley Research Center for performing eddy current inspections<sup>1</sup>. The probe has two concentric coils which are separated radially and at one end by an electromagnetic shield. At one end there is no shielding and electromagnetic coupling between the two coils when the probe is held in the air. If a high frequency alternating voltage is applied to the outer coil, there is an easily detected induced voltage in the inner coil. When the open end of the probe is placed against a thick layer of highly conductive material, the electro-magnetic coupling is significantly reduced and the induced voltage in the inner coil is reduced to approximately zero. Therefore the probe is often referred to as a self-nulling probe.

When a constant voltage is applied to the outer coil, the amplitude of the induced voltage in the inner coil is a monotonically increasing function of the coupling between the two coils. The extent of coupling depends on the structure's ability to sustain an eddy current and therefore is affected by the presence of cracks, thinning of the highly conductive sheet and other structural defects. The existence of conditions is detectable by variations in the amplitude of the voltage of the inner coil. An advantage of the probe is the simplicity of this measurement compared to traditional eddy current measurements requiring a measurement of the impedance of the coil.

The most mature application of the probe has been the detection of cracks under rivets heads. The presences of a crack significantly reduces the generation of eddy current in a thin aluminum sheet. Therefore as the probe passes over a crack, there is a significant increase in the induced voltage in the inner coil. The probability of detecting a crack is greatly increase by rotating the probe around the rivet. Regions where no crack exists are used as a reference against which to compare regions with cracks. The output voltage for the probe as it rotates around a rivet with a crack is shown in figure 1. The rotation of the probe is centered on the rivet. As the probe passes over the crack a 90°, there is a

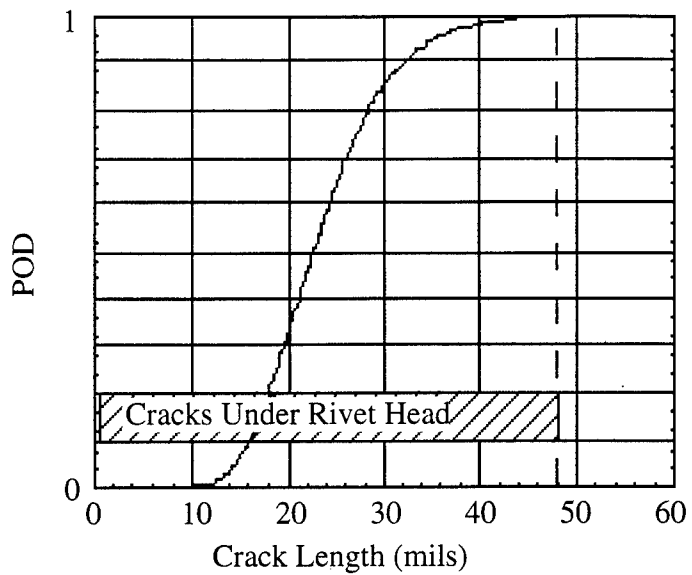


Figure 2. Probability of detecting a crack of a given length using the rotating self-nulling probe. POD study performed on samples at FAA Aging Aircraft NDI Validation Center.

significant increase in the output voltage of the probe. The crack is a 37 mil fatigue crack as measured from the shank of the rivet and therefore is totally hidden under the head of the rivet. As can be seen from the figure, there is a significant signal from the crack. The rotating probe is configured in an instrument enabling its testing at the FAA Aging Aircraft NDI Validation Center<sup>2,3</sup> in Albuquerque, New Mexico. From this testing a POD curve, shown in figure 2, was generated. This POD curve indicates the probability of detecting a 32 mil crack is 90%, which enables the detection of small cracks under the rivet head.

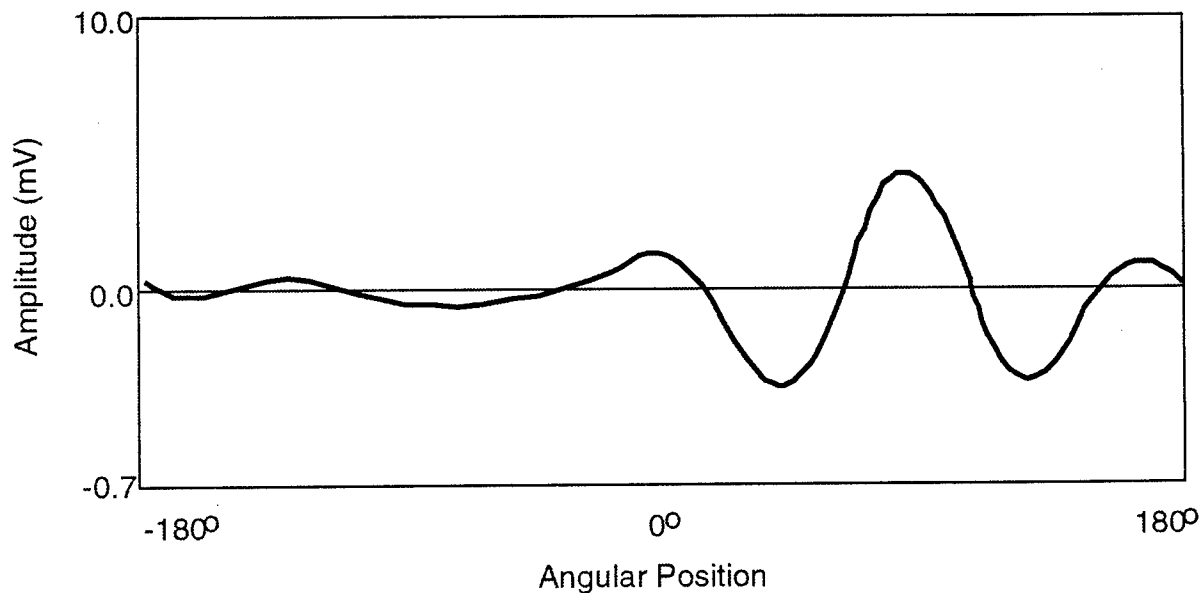


Figure 3. Output of self nulling probe during rotation around rivet with 60 mil crack second layer crack.

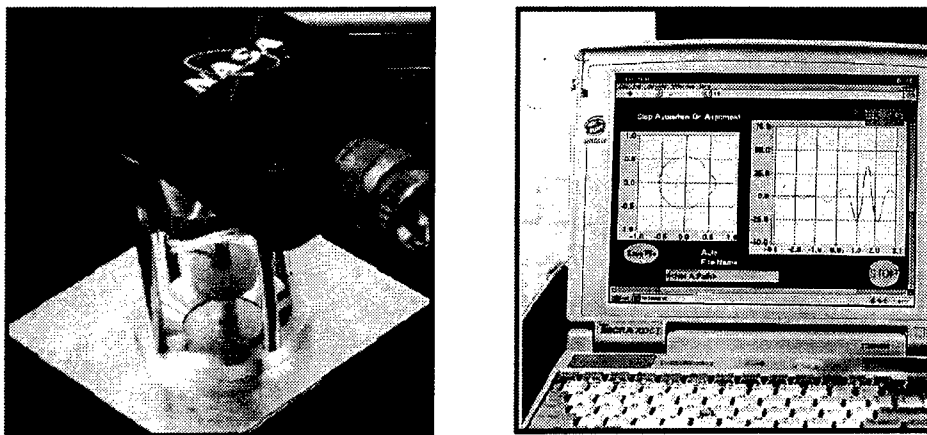


Figure 4. Head with rotating self-nulling probe and computer controller.

When the operating frequency of the probe is decrease, the generated eddy currents penetrate deeper into the conducting layer. This enables the detection of cracks that are in the second and third layer of a multilayered structure. When the drive frequency is reduced to 3.5 kHz, second layer cracks are detectable. The output of the probe as it rotates around a rivet with a 60 mil EDM notch in the second layer is shown in figure 3. The response from the crack at 90° is significantly greater than the response for rivets with no cracks. Insufficient data currently exist for establishing an accurate POD curve for this measurement.

Detection of cracks in the third layer is also possible with this system. The present configuration has been tested at the FAA NDI Validation Center on panels with third layer cracks. In this testing the 90% POD crack length was found to be 200 mils. Currently probe designs are being considered to reduce the active region of the probe to improve its sensitivity to cracks in the third layer.

The rotating probe has been developed into an instrument which can be easily carried into the field for inspection of aircraft. The head on which the probe is mounted (shown in figure 4) is easily held in one hand against the surface of the aircraft. A lap top computer controller provides real time feedback to the operator on the centering error of the rotation relative to the position of the rivet. When the centering error is less than a preset value, the computer controller captures the output of the probe for a single rotation and plots the output on the computer screen. A threshold is set to determine if a crack is present. This instrument is being commercialized to enable its implementation in the field.

### **3. PORTABLE ULTRASONIC BOND AND CORROSION INSPECTION SYSTEM**

Ultrasonic techniques are often applied to the detection of disbonds and thickness gauging in layer structures. In relatively thick layers where the echoes from the front and back surfaces of the layers are clearly resolvable this is simple. However in thin aluminum sheets, such as found in aircraft fuselages, the echoes are difficult to resolve in time. For this case, the ultrasonic response of the layer is more difficult to interpret. Quick interpretation of ultrasonic response can be performed with an artificial neural network<sup>4</sup>. The input into the neural network is a processed ultrasonic response of the lap joint or tear strap. The neural network quickly classifies the region as being bonded or disbonded. Classification accuracy is close to 100%, even in the presence of varying paint thicknesses.

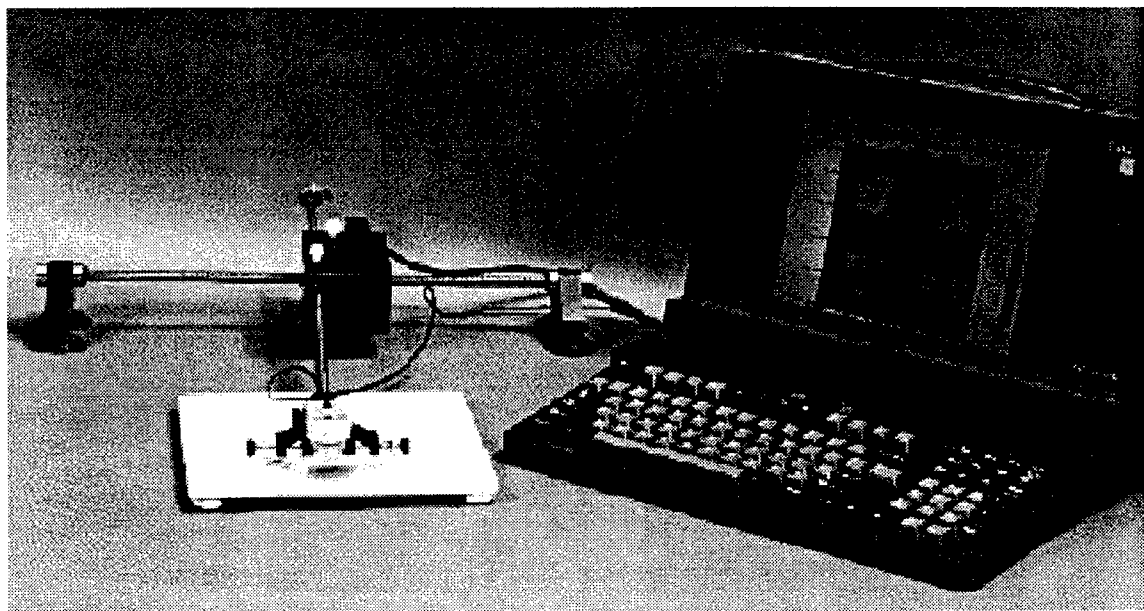


Figure 6. Portable ultrasonic scanner with computer controller.

Regions which have been classified as disbonded may also have corrosion present. From the same ultrasonic response, top layer thinning can be quantified by analyzing the response in the frequency domain. Measurements were performed on a series of samples of known thicknesses. A comparison of mechanical measurements and ultrasonic measurements of the thickness are shown in Figure 5. As can be seen from the figure the agreement between the two is excellent. From these measurements, it was determined the technique is capable of measuring the thickness of the upper layer to within 3%.

Real time imaging of defects of an aircraft is performed by integrating these techniques into a portable scanner shown in figure 6. Implemented on the portable scanner is a ART2 (adaptive resonance theory)

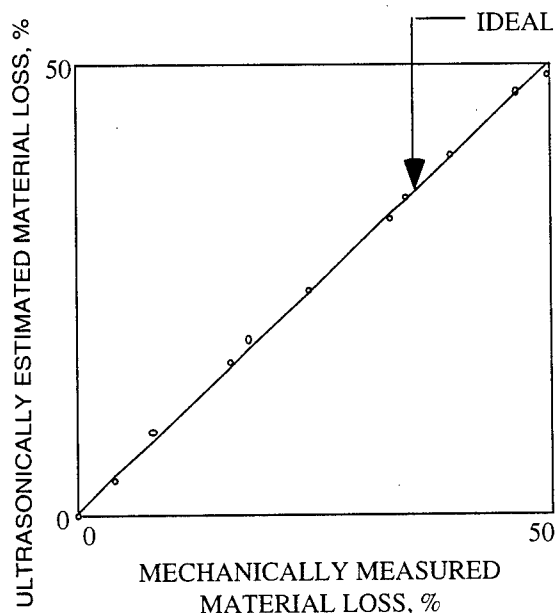


Figure 5. Comparison of ultrasonic estimation of material thinning and mechanical measurement.

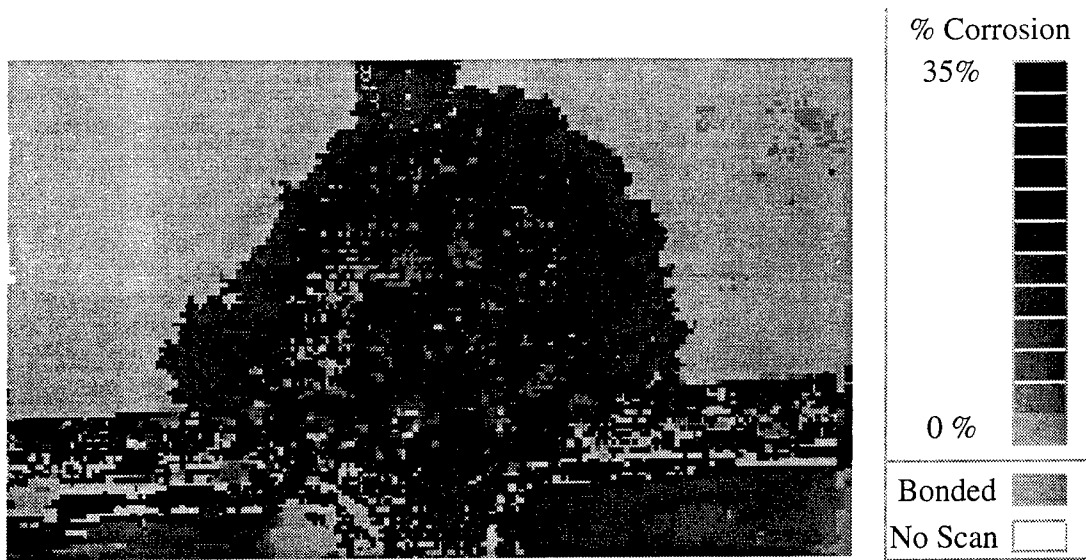


Figure 7a. Ultrasonic image of corrosion in Boeing 737 at the FAA Aging Aircraft NDI Validation Center.

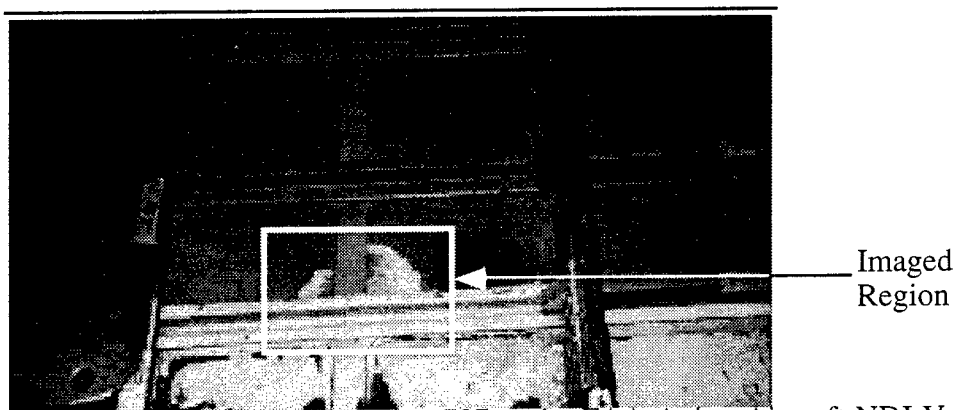


Figure 7b. Photograph of corroded section of Boeing 737 at the FAA Aging Aircraft NDI Validation Center.

neural network. An ART neural network identifies only the disbonded responses for the layered structure. This reduces the time and number of responses required to train the network. A portable scanner has been programmed to allow for training of the network on the aircraft if necessary. Disbonded responses can be obtained by performing measurements near, but not on the bonded region to be inspected. This increases the versatility of the system and enables rapid setup on most aircraft. The ultrasonic response of the structure is first reduced by a neural network to determine if the structure is bonded or disbonded. If the lap joint is disbonded, the resonance frequency of the top layer is determined from a Fourier transform of the response.

The thickness of the layer calculated from the resonance frequency is displayed on a color monitor as a color coded pixel. The process is real time, all the processing being performed in a time insignificant to the time required to move the transducer to a new position. The result is a real time image of the extent of disbonding and corrosion in the lap joint. A typical image is shown in Figure 7. This shows the results of measurements on a section of the Boeing 737 at the FAA NDI Validation Center. The corroded region is clearly seen in the image. The shape of the corroded area is also clearly seen in photographs of the interior of the aircraft. The advantage of the ultrasonic technique is an image of the

corrosion can be obtained from the exterior of the aircraft, without removing insulation or other materials which would inhibit viewing the corrosion directly. Additionally the image gives a accurate representation of the residual thickness of the material.

#### 4.THERMOGRAPHIC INSPECTION SYSTEM

A large area technique capable of detecting disbonds and corrosion is the relatively new technique of thermography. Thermographic imaging has a significant advantage over other techniques in that it does not require physical contact or coupling between the inspection system and the aircraft. Infrared thermography is performed with an infrared imager capable of scanning large areas in a fraction of a second. The complete inspection of a square meter is possible in 3 to 4 minutes. Recent technological advancements have further enhanced thermographic inspections, significantly increasing the reliability of the technique. In particular, the development of small inexpensive image processors and computers have permitted precise timing of the application of heat, an increased signal to noise ratio for thermographic images and post processing of the thermographic images. The reduction in size of computers and image processors has lead to portable thermographic inspection systems such as shown in figure 8. The system is comprised of a infrared camera, two quartz lamps and a lap top computer with special image processing boards. The computer controls the heating and the acquisition of data. The image processing boards perform real time analysis of the data, yielding images immediately following the heating cycle.

To perform measurements on aluminum, a thin layer of high emissivity material must be present on the surface. Paint is typically an excellent coating, with a high emissivity independent of its color in the 8-12  $\mu\text{m}$  region. Therefore aircraft which are painted typically require no special treatment before inspection. An unpainted aircraft can be coated with commercially available water washable coatings to increase the surface emissivity.

A thermographic inspection involves heating the surface of a structure and measuring surface

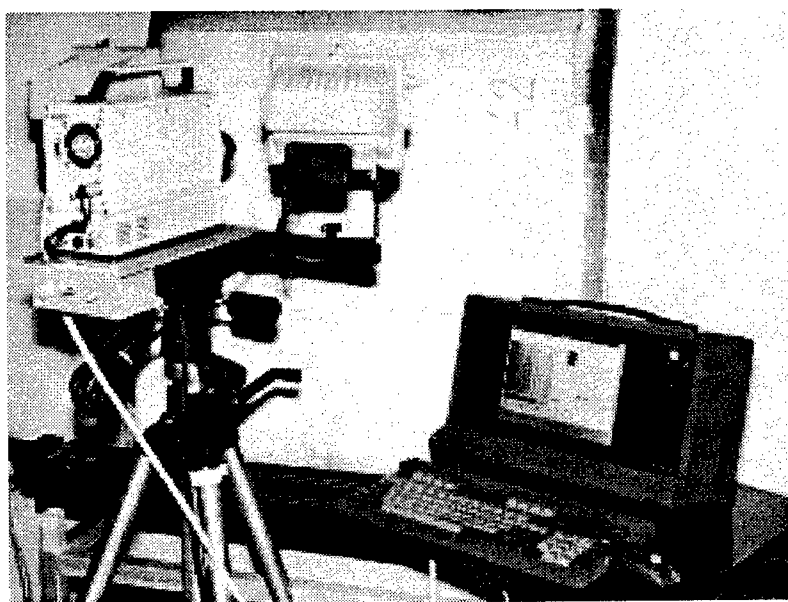


Figure 8. Portable thermographic inspection system

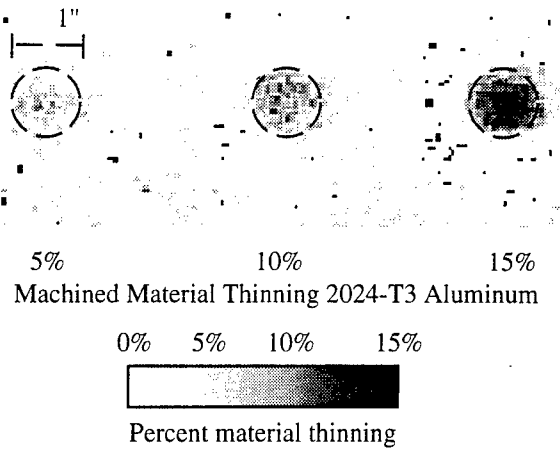


Figure 9. Thermographic characterization of extent of thinning in 40 mil aluminum sheet.

temperatures as a function of time. For aircraft lap joint inspections, flash lamps or quartz lamps are used to apply heat to the exterior surface of the aircraft and the temperature of the exterior surface temperature is measured with an infrared camera. In a relatively short period of time, heating the surface creates temperature differentials which indicate the presence of disbonds or corrosion. These temperature differentials can be used to identify regions of disbonding or corrosion.

For a single layer of aluminum, it is possible to determine the amount of material thinning from the thermographic images<sup>5</sup>. Images of material thinning in a single layer of aluminum with 5%, 10% and 15% material thinning is shown in Figure 9. As can be seen from this image there is good agreement between the material loss as estimated from this technique and mechanical measurements. This relationship is only accurate while there is not significant lateral heat flow in the layer. For longer times, lateral heat flow reduces the contrast between corroded and noncorroded regions.

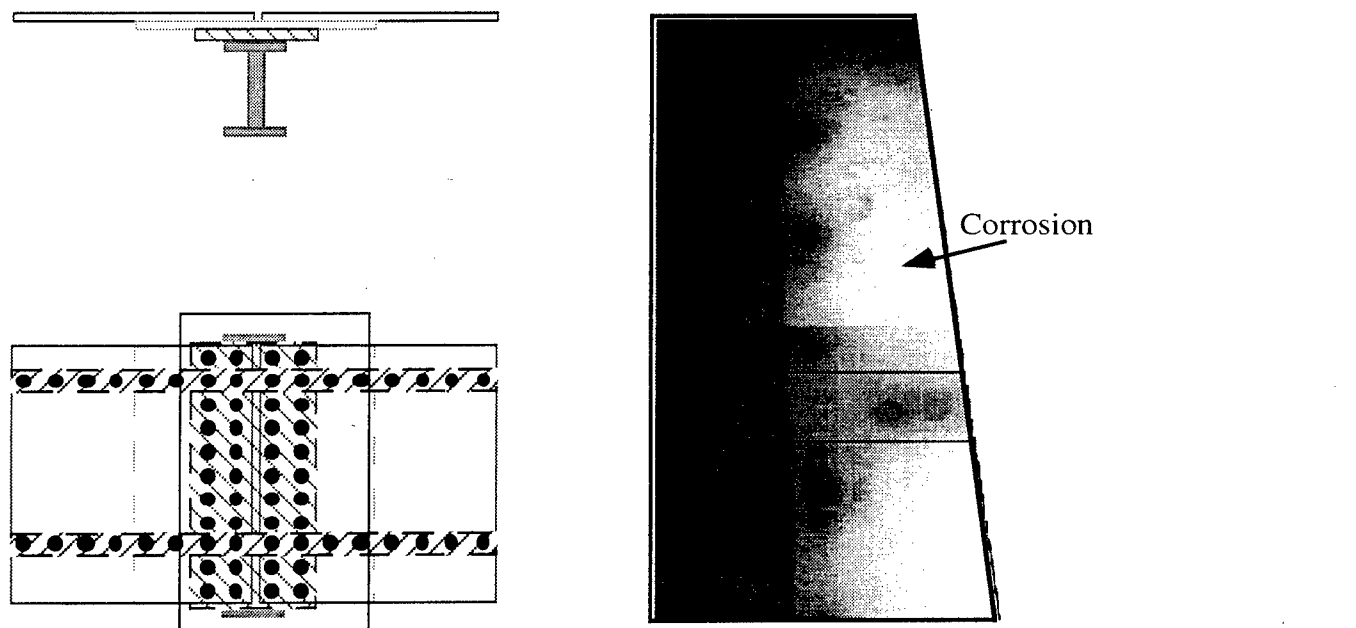


Figure 10. Thermographic image of corrosion in butt joint.

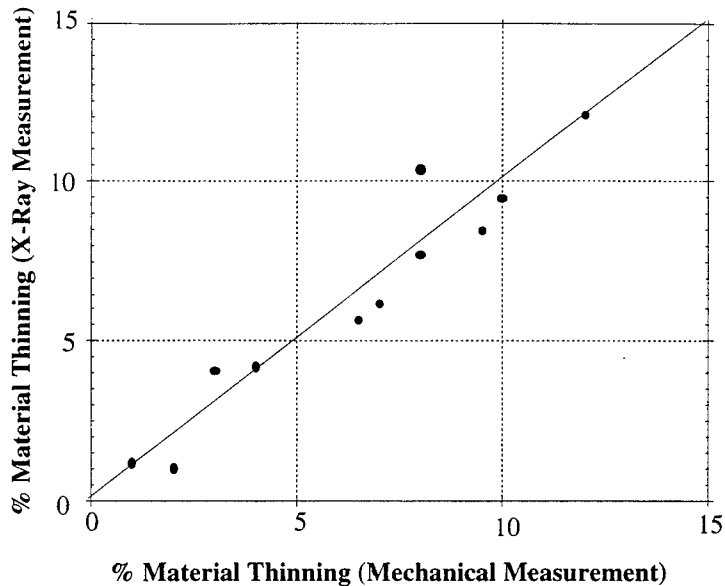


Figure 11. Quantification of extent of material thinning in bonded structure fabricated to simulate structure with corrosion.

Quantitative measurements in multilayered structures<sup>6</sup> is difficult, requiring separation of the thermal response of the aluminum layers from layers of corrosion products, adhesive materials and air gaps. This is possible if the initial time dependence of the temperature is following flash heating is sampled at 1 KH, but this measurement is difficult with infrared imagers. However the infrared technique is still an excellent technique for detection corroded regions. Results have indicated corroded regions with material loss of 10% or more are easily detected with this technique. A thermographic inspection of a butt joint specimen with corrosion is shown in Figure 10. As can be seen from the figure there is extensive corrosion on the right side of the joint.

## 5.REVERSE GEOMETRY X-RAY

Radiographic inspection is different from other techniques in its ability to perform full volume inspections. Its major disadvantage is safe application limits access to the aircraft during the inspection. However, for some inspections, x-rays are capable of detecting flaw which are inaccessible with other techniques. A recent development in x-ray radiography call “Reverse Geometry X-ray®” (“Reverse Geometry X-ray” is a registered trade mark of Digidray Corporation, San Ramon, CA) offers significant advantages over conventional radiographic techniques.

The principal difference between “Reverse Geometry X-ray®” imaging and conventional radiography is the source. For conventional radiography, the source is a point source from which x-rays are emitted. The structure to be inspected is placed a sufficient distance from the source to illuminate the region of interest. For “Reverse Geometry X-ray®” the source is a scanned source which is placed near the structure. In contrast to conventional radiography where an area detector is typically used, the radiation intensity for “Reverse Geometry X-ray®” is measured with a point detector. By synchronization of the detector output with the position of the x-ray source, an x-ray image of the structure being inspected is generated.

There are several advantages in scanning the source. One is that the detector can be designed to reduce

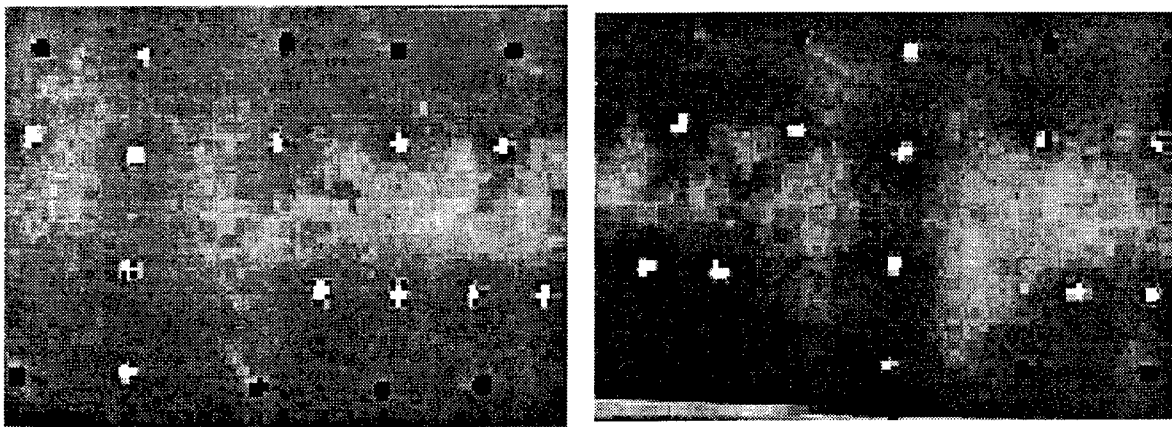


Figure 12. Typical reverse geometry x-ray images of corrosion.

the amount of received scattered radiation, which causes blurring in the image. Another is that point detectors can be made which are much smaller than conventional x-ray sources. The detector can be remotely positioned inside a structure to improve the interpretability of the images. Finally, more than one point detector can be used at a time to yield structural depth information.

One of the possible applications for this system is the detection and quantification of corrosion. The change in x-ray intensity after the x-rays have passed through a structure is a function of the amount of material along the path taken by the x-rays. Since this functional dependence is well known, it is possible to determine from the change in intensity, the amount of material loss along the path. The results of measurements<sup>7</sup> performed on a series of specimens fabricated to simulate corrosion are shown in figure 11. As can be seen from the figure there is generally good agreement between mechanical measurements and measurements from the "Reverse Geometry X-ray®" system. While the overall agreement is within 2% of the mechanically measured value, several points have a large deviation from the mechanical measurements. This may be a result of corrosion products being packed into the corroded area. If the corroded area is packed with corrosion products, the attenuation of the x-rays, as they passed through the corrosion products, will result in an apparent increase in the thickness of the layer. Other efforts have shown it is possible to eliminate this error by performing measurement at several different x-ray energies. Typical images of corroded aircraft components are shown in figure 12.

## 6.SUMMARY

New techniques have been developed for the detection and quantification of corrosion. The four techniques presented here are eddy current, ultrasonic, thermographic and x-ray technologies. Each of the techniques complement the others by filling an inspection requirement. The thermographic technique performs rapid surveys of the structure to locate corroded regions. The ultrasonic technique accurately determines the thickness of the top layer. The eddy current is able to quantify the material loss in one than more layer. Finally the x-ray technique is able to detect corrosion in built up structures.

## 7.REFERENCES

1. Wincheski,B., Fulton,J., Nath,S. and Namkung,M. "New Eddy Current Probe for Thickness Gauging of Conductive Materials", in "Review of Progress in Quantitative Nondestructive Evaluation", 13B, 1994, pp1939-1946.
2. Spencer,F, and Schurman,D., "Reliability Assessment at Airline Inspection Facilities, Vol III:

Results of an Eddy Current Inspection Reliability Experiment”, DOT/FAA/CT-92/12, III, 1995

3. Wincheski,B., Todhunter, R. and Simpson, J. “A New Instrument for the Detection of Fatigue Cracks Under Airframe Rivets”, in “Review of Progress in Quantitative Nondestructive Evaluation”, 16B, 1997, pp2113-2120.
4. Prabhu,D.R.,Abedin,M.N. and Johnston,P.H., in “Review of Progress in Quantitative Nondestructive Evaluation”, 13B, 1994, pp1919-1926.
5. Syed, H.I, Winfree,W.P., Cramer,K.E. and Howell,P.A., “Thermographic Detection of Corrosion in Aircraft Skin” in “Review of Progress in Quantitative Nondestructive Evaluation”, 12B, 1993, pp2035-2041.
6. Emeric,P.R. and Winfree,W.P., “Thermal Characterization of Multilayer Structures from Transient Thermal Response” in “Review of Progress in Quantitative Nondestructive Evaluation”, 14A,1995, 475-482
7. Birt,E.A., Parker,F.R. and Winfree, W.P., “Quantification of Corrosion Damage in Aircraft Skin Using a Novel X-ray Radiography System”, in “Review of Progress in Quantitative Nondestructive Evaluation”, 13B, 1994, pp1963-1970.



# Model-based fault detection using Lamb waves

C.Wolters  
S.A.Billings

S.G.Pierce

K. Worden  
G.R.Tomlinson

Department of Automatic Control  
and Systems Engineering  
University of Sheffield  
Mappin Street  
Sheffield S1 3JD  
United Kingdom

Optoelectronics Division  
Department of Electronic  
and Electrical Engineering  
University of Strathclyde  
204 George Street  
Glasgow G1 1XW  
United Kingdom

Dynamics Research Group  
Department of Mechanical  
Engineering  
University of Sheffield  
Mappin Street  
Sheffield S1 3JD  
United Kingdom

## ABSTRACT

A model-based approach to fault detection is adopted, based on Lamb wave data. Input and output data are collected, where the output wave has been scattered by a defect, and a NARMAX time-series model is estimated. In order to account for the potential non-uniqueness of the NARMAX model, the Higher-order Frequency Response Functions (HFRFs), which are invariants of the system, are computed. In this preliminary study, it is shown that the gain of the third HFRF is correlated with the defect size and therefore has potential as a feature for signalling and sizing damage.

Keywords: Model-based NDE, Lamb waves, NARMAX models, Higher-order Frequency Response Functions

## 1. INTRODUCTION

Ultrasonic Inspection of structures using Lamb waves has been discussed by a number of authors<sup>1-6</sup>, who reported on its use to detect various material failures in composites, including delaminations, fibre fracture and matrix cracking. The technique has advantages over the conventional C scan, the main one being its ability to scan the structure along a line, as opposed to the C scan which makes a point by point scan of the structure. The potential reduction in inspection time is significant. A possible disadvantage is its comparatively lower resolution.

The works cited above achieved their objectives by using signals of considerable purity and measuring simple features from the time-histories of the wave intensity. Reflections and transmissions from defects were identified and damage was localised using time-of-flight information. A rather different approach was adopted in the studies<sup>7,8</sup>, where the emphasis was on more complex signal processing. In these recent works, novelty detectors were constructed which signalled damage in composites on the basis of raw time-histories of the wave intensity, the defects were also located with accuracy. This also served to automate the process of fault detection. The novelty detectors were based on wavelet analysis<sup>7</sup> and a neural network<sup>8</sup> and the basic principle was of pattern recognition; a scalar *novelty index* was required to report patterns which deviated significantly from the norm. The approaches

were *data-based* in the sense that the diagnosis was made on raw or processed measurement data. An alternative approach to damage detection is *model-based*, where the data is used to construct a model at each inspection and damage is inferred by deviations in the model structure. The object of this paper is to investigate if Lamb wave observations can be used to construct a model-based diagnostic.

In order to establish an input-output process model, it is necessary to have input and output data, this is achieved here by sampling the Lamb wave intensity before and after scattering by a defect. The process model used is a polynomial NARMAX<sup>9,10</sup> model which can be used to represent almost arbitrary nonlinear systems. Although NARMAX models can represent the input-output process with great accuracy, it is known that they are not unique. This means that the model parameters can not be used as features for damage detection as the coefficients may change between inspection for an entirely innocent reason. The way around this problem is to construct invariant features from the models, and in this case the Higher-order Frequency Response Functions (HFRFs)<sup>11</sup> are used.

The layout of the paper is as follows: section two serves to introduce the NARMAX models and section three describes the HFRFs. Section four describes the basic properties of Lamb waves and describes the experimental procedures followed for this study. Section five gives the results for Lamb wave scattering from a number of simple defects in an Aluminium plate. The paper then concludes.

## 2. NARMAX MODELS

The NARX model<sup>9</sup> (Nonlinear Auto-Regressive with eXogenous inputs) of a system is based on a discrete-time representation, which maps sampled input data  $\mathbf{x}_i$  into sampled output data  $y_i$ . The functional form of the model is simply,

$$y_i = F(y_{i-1}, \dots, y_{i-n_y}; \mathbf{x}_{i-1}, \dots, \mathbf{x}_{i-n_x}) \quad (1)$$

and this reveals the source of the name; the present output  $y_i$  is regressed on the last  $n_y$  values of the output and on the last  $n_x$  values of the exogenous input  $\mathbf{x}_i$ . The function  $F$  can be arbitrary, but a useful choice is to make  $F$  a multinomial in the variables. An example of a NARX model of cubic polynomial order is,

$$y_i = a_1 y_{i-1} + a_2 y_{i-2} + b_1 \mathbf{x}_{i-1} + c y_{i-1}^3 \quad (2)$$

where  $a_1, a_2$  and  $b_1$  are the parameters of the model which are chosen by making the model respond as closely to the real system as possible on a given measured input sequence. The usual technique for fitting parameters is by least-squares optimisation and there are a number of ways of implementing this numerically, the method used here is based on the orthogonal estimator<sup>12</sup>.

In the restricted case of a linear system, the relevant model is the ARX model,

$$y_i = \sum_{j=1}^{n_y} a_j y_{i-j} + \sum_{j=1}^{n_x} b_j \mathbf{x}_{i-j} \quad (3)$$

It has been proved<sup>9,10</sup> under very mild assumptions, that any input-output process has a representation by a model of the form (1). And if the system nonlinearities are polynomial in nature, this model will represent the system well for all levels of excitation. If non-polynomial terms are needed in the expansion for  $F$ , they can be added without difficulty.

The preceding analysis unrealistically assumes that the measured data is free of noise. In reality noise arises from the truncation error associated with finite-accuracy instrumentation and arithmetic etc. If the measured signal  $y(t)$  is composed of a 'clean' process part  $y_c(t)$  and a noise component  $\zeta(t)$ , the relationship between input and output is changed. For example, the equation relating measured input and output for the system (2) becomes,

$$y_i = a_1 y_{i-1} + a_2 y_{i-2} + b_1 x_{i-1} + c y_{i-1}^3 \\ + \zeta_i - a_1 \zeta_{i-1} - a_2 \zeta_{i-2} + c y_{i-1}^2 \zeta_{i-1} + c y_{i-1} \zeta_{i-1}^2 + \zeta_{i-1}^3 \quad (4)$$

and even simple additive noise on the output introduces cross-product terms if the system is nonlinear. Although these terms all correspond to unmeasurable states they must be included in the model. If they are ignored the parameter estimates will generally contain systematic errors called *bias*. The system model (1) is therefore extended by the addition of a *noise model* so,

$$y_i = F(y_{i-1}, \dots, y_{i-n_y}; x_{i-1}, \dots, x_{i-n_x}; \zeta_{i-1}, \dots, \zeta_{i-n_\zeta}) + \zeta_i \quad (5)$$

This type of model is referred to as NARMAX (Nonlinear Auto-Regressive Moving-Average with eXogenous inputs). Actually, in forming a NARMAX model, it is assumed that the system noise is the result of passing a zero-mean white noise sequence  $\{e_i\}$  through a (possibly nonlinear) digital filter, such a noise-model is called a Moving-Average model, the final form of the NARMAX model is therefore,

$$y_i = F(y_{i-1}, \dots, y_{i-n_y}; x_{i-1}, \dots, x_{i-n_x}; e_{i-1}, \dots, e_{i-n_e}) + e_i \quad (6)$$

This then, is the model structure adopted for this study, the problem of deciding which terms should be in the model is essentially solved using a forward selection algorithm and the coefficients are established using orthogonal least-squares<sup>12</sup>.

Having obtained a model, it is important to validate it, there are several metrics for evaluating the goodness-of-fit of a model. Three commonly used metrics are described below in increasing order of stringency. In the following,  $y_i$  denotes a measured output while  $\hat{y}_i$  denotes an output value predicted by the model. The first metric is the *One-Step-Ahead (OSA) prediction* error.

Given the NARMAX representation of a system (6), the one-step-ahead prediction of  $y_i$  is made using measured values for all past inputs and outputs. Estimates of the residuals are obtained from the expression  $\hat{e}_i = y_i - \hat{y}_i$  i.e.

$$\hat{y}_{OSA,i} = F(y_{i-1}, \dots, y_{i-n_y}; x_{i-1}, \dots, x_{i-n_x}; \hat{e}_{i-1}, \dots, \hat{e}_{i-n_e}) \quad (7)$$

The one-step-ahead series can then be compared to the measured outputs. Good agreement is clearly a necessary condition for model validity.

The second metric is Model-Predicted-Output (MPO) error. In this case, the inputs are the only measured quantities used to generate the model output, i.e.

$$\hat{y}_{MPO,i} = F(\hat{y}_{MPO,i-1}, \dots, \hat{y}_{MPO,i-n_y}; x_{i-1}, \dots, x_{i-n_x}; 0, \dots, 0) \quad (8)$$

The zeroes are present because the prediction errors will not generally be available when one is using the model to predict output. This test is usually stronger than the previous one; in fact the

one-step-ahead predictions can be excellent in some cases when the model predicted output shows complete disagreement with the measured data.

The final metrics are the *correlation tests*<sup>13</sup> and these are the most stringent of the validity checks. The correlation function  $\phi_{uv}(k)$  for two sequences of data  $u_i$  and  $v_i$  is defined by

$$\phi_{uv} = E(u_i v_{i+k}) \approx \frac{1}{N-k} \sum_{i=1}^{N-k} u_i v_{i+k} \quad (9)$$

For a linear system it is known<sup>13</sup> that necessary conditions for model validity are

$$\phi_{ee}(k) = \delta_{0k} \quad (10)$$

$$\phi_{xe}(k) = 0 \quad \forall k \quad (11)$$

and the interpretation of these tests is well-known.

In the case of a nonlinear system it is sometimes possible to satisfy the requirements above even if the model is invalid. It has been shown<sup>13</sup> that an exhaustive test of the fitness of a nonlinear model requires the evaluation of three additional correlation functions. The extra conditions are

$$\phi_{e(ex)}(k) = 0 \quad \forall k \geq 0 \quad (12)$$

$$\phi_{x^2 e}(k) = 0 \quad \forall k \quad (13)$$

$$\phi_{x^2 e^2}(k) = 0 \quad \forall k \quad (14)$$

The dash which accompanies  $x^2$  above indicates that the mean has been removed. Normalised estimates of all the correlation functions above are obtained using

$$\hat{\phi}_{uv}(k) = \frac{\frac{1}{N-k} \sum_{i=1}^{N-k} u_i v_{i+k}}{\{E(u_i^2)E(v_i^2)\}^{\frac{1}{2}}} \quad k \geq 0 \quad (15)$$

with a similar expression for  $k < 0$ . The normalised expression is used because it allows a simple expression for the 95% confidence interval for a zero result, namely  $\pm 1.96/\sqrt{(N)}$ .

Finally, as stated above, the NARMAX model is not necessarily unique for a given system and invariant features are needed for fault detection. Given a NARMAX model, such invariants, the Higher-order FRFs can be constructed straightforwardly, and are described in the next section.

### 3. HIGHER-ORDER FREQUENCY RESPONSE FUNCTIONS

It is well-known that any linear system or input-output process  $x(t) \rightarrow y(t)$  can be realised as a mapping

$$y(t) = \int_{-\infty}^{+\infty} d\tau h(\tau)x(t - \tau) \quad (16)$$

where  $h(\tau)$  uniquely characterises the system. Also well-known, is the dual frequency-domain representation,

$$Y(\omega) = H(\omega)X(\omega) \quad (17)$$

where  $Y(\omega)$  (resp.  $X(\omega)$ ) is the Fourier transform of  $y(t)$  (resp.  $x(t)$ ).  $H(\omega)$  is the linear system Frequency Response Function (FRF). These equations are manifestly linear and cannot hold for nonlinear systems. However, an appropriate generalisation of (16) exists<sup>14</sup>, and it takes the form of an infinite series,

$$y(t) = y_1(t) + y_2(t) + y_3(t) + \dots + y_n(t) + \dots \quad (18)$$

where

$$y_n(t) = \int_{-\infty}^{+\infty} \dots \int_{-\infty}^{+\infty} d\tau_1 \dots d\tau_n h_n(\tau_1, \dots, \tau_n) x(t - \tau_1) \dots x(t - \tau_n) \quad (19)$$

The functions  $h_n$  are referred to as the *Volterra kernels*.

As in the linear case, there exists a dual frequency-domain representation for nonlinear systems based on the *higher-order FRFs* (HFRFs) or *Volterra kernel transforms*,  $H_n(\omega_1, \dots, \omega_n)$ ,  $n = 1, \dots, \infty$  which are defined as the multi-dimensional Fourier transforms of the kernels.

$$H_n(\omega_1, \dots, \omega_n) = \int_{-\infty}^{+\infty} \dots \int_{-\infty}^{+\infty} d\tau_1 \dots d\tau_n h_n(\tau_1, \dots, \tau_n) e^{-i(\omega_1 \tau_1 + \dots + \omega_n \tau_n)}. \quad (20)$$

Given a model of a system whether it is continuous-time or discrete-time there are a number of methods for determining the kernels for a given system; possibly the most well-known is the method of harmonic probing<sup>14</sup>. An effective and efficient recursive variant of the algorithm has been obtained<sup>15</sup> and is the form used in this study.

The advantage of characterising nonlinear systems with the HFRFs is that they represent uniquely the transfer characteristics where the NARMAX model (or even a differential equation model for that matter) does not. The model coefficients and terms can change. As the object of this paper is damage detection, it is inadvisable to use features which can change from one normal condition to another, as such innocent changes in the model may be interpreted as damage.

#### 4. THE LAMB WAVE EXPERIMENTS

The basic facts of Lamb wave propagation are fairly straightforwardly explained<sup>16</sup>. They are simply thin-plate elastic waves. Amongst their other properties, they are dispersive and can propagate in a number of modes, and these facts can complicate the practical use of the waves. The propagation is typically characterised by the product of the wave frequency and the sample thickness, or *frequency-thickness product* (FT), and can be summarised effectively by the dispersion curves which show the phase velocity for a given Lamb wave mode at a given FT. For low values of FT (typically,  $FT < 1$  MHz.mm in Aluminium), only two modes can propagate, the fundamental symmetric ( $S_0$ ) and the fundamental antisymmetric ( $A_0$ ). As the frequency-thickness product increases, so does the number of allowed modes. Clearly Lamb wave testing is considerably simplified if a known single mode is launched over a non-dispersive region of the FT product, and the symmetric mode  $S_0$  is used throughout this study.

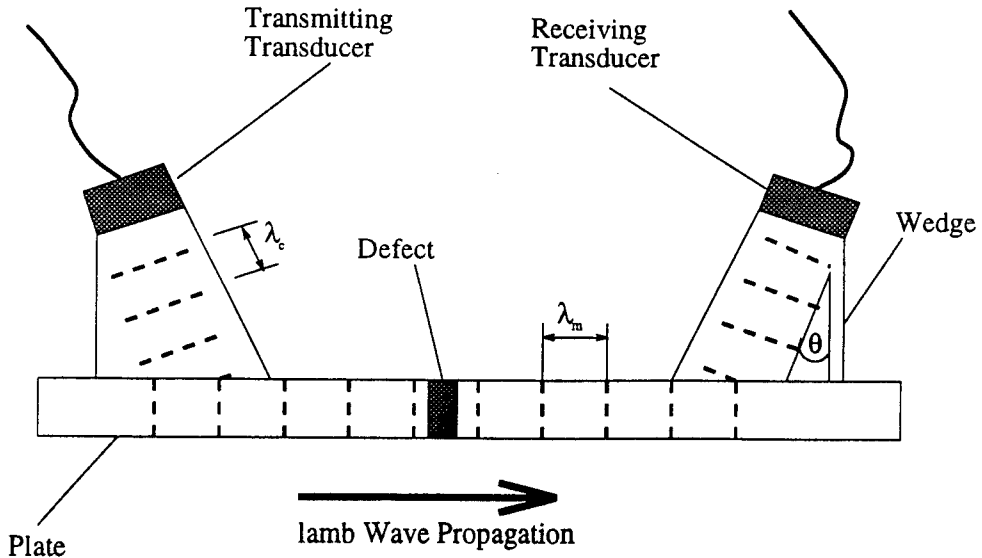


Figure 1. Basic Lamb Wave Experiment.

Selection of a given mode at a given FT is by adjusting the coupling angle of the launch transducer to the propagating medium. Consider Figure 1 which shows the basic experimental setup used for this study. Perspex wedges are typically used to couple the transducer to the plate. If the wavelength in the coupling medium (resp. plate material) is  $\lambda_c$  (resp.  $\lambda_m$ , it follows simply from the geometry in Figure 1 that,

$$\sin \theta = \frac{\lambda_c}{\lambda_m} \quad (21)$$

Assuming the standard relation  $c = f\lambda$  between wave velocity and wavelength ( $f$  is frequency), it follows that,

$$\theta = \sin^{-1} \frac{c_c}{c_m} \quad (22)$$

where  $c_c$  is the longitudinal wave velocity in the coupling medium and  $c_c$  is the phase velocity of the required mode in the plate, and the latter is obtained from standard dispersion curves for the material<sup>16</sup>. Each mode has a distinct phase velocity, so by choosing  $\theta$  accordingly it is possible to launch a pure mode. For a perspex wedge coupled to a 1mm thick Aluminium plate as used here, the appropriate angle to launch a  $S_0$  wave is about 31°. To provide effective acoustic coupling at the various interfaces in the experiment, silicon gel was used.

In this study, lamb waves were generated by a Hewlett-Packard (HP) arbitrary function generator 33120 A amplified by a ENI class A RF amplifier, model 2100L. The transducers were Panametrics A402-SB, resonant at 1 MHz. Perspex variable angle wedges were used. The output data was recorded using a HP TDS 420 oscilloscope in combination with a personal computer running the HP acquisition software BENCHLINK. The reason for choosing the arbitrary function generator rather than a simple pulser-receiver is that system identification or model identification is best performed using a wideband input signal and it was possible to produce a pseudo-random Lamb wave spanning the frequency range 0.0 MHz to 1.0 MHz using the equipment described. The bandwidth of the signal is limited by two factors. In the first case, the transducers are resonant at 1 MHz and their response falls at frequencies removed from this value. Secondly, in order to launch

a non-dispersive broadband signal in a single mode, there should be a flat region of the dispersion curve over the frequency range. The input signal was obtained by generating a sequence of 15000 normally distributed numbers and then filtering with a seventh-order Butterworth filter. The low pass was designed with a cut-off frequency of 1.5 MHz with a gain attenuation of -40 dB at 2 MHz.

The input signal for the identification, was the input to the arbitrary function generator and the output was taken from the output transducer. Note that the output signal is essentially convolved with the impulse response transducer so the identification necessarily shows a component due to the transducer. This does not present a problem for damage detection purposes as long as the same transducer is always used in the inspection process. 30000 points of the input and output data were sampled at 10 MHz.

All together, four plates were tested. The first was fault-free. The second had a 2mm hole drilled in the centre. The third had a  $10 \times 0.4$  mm slot in the centre, aligned parallel with the Lamb wavefront and the final plate had a  $40 \times 0.4$  slot.

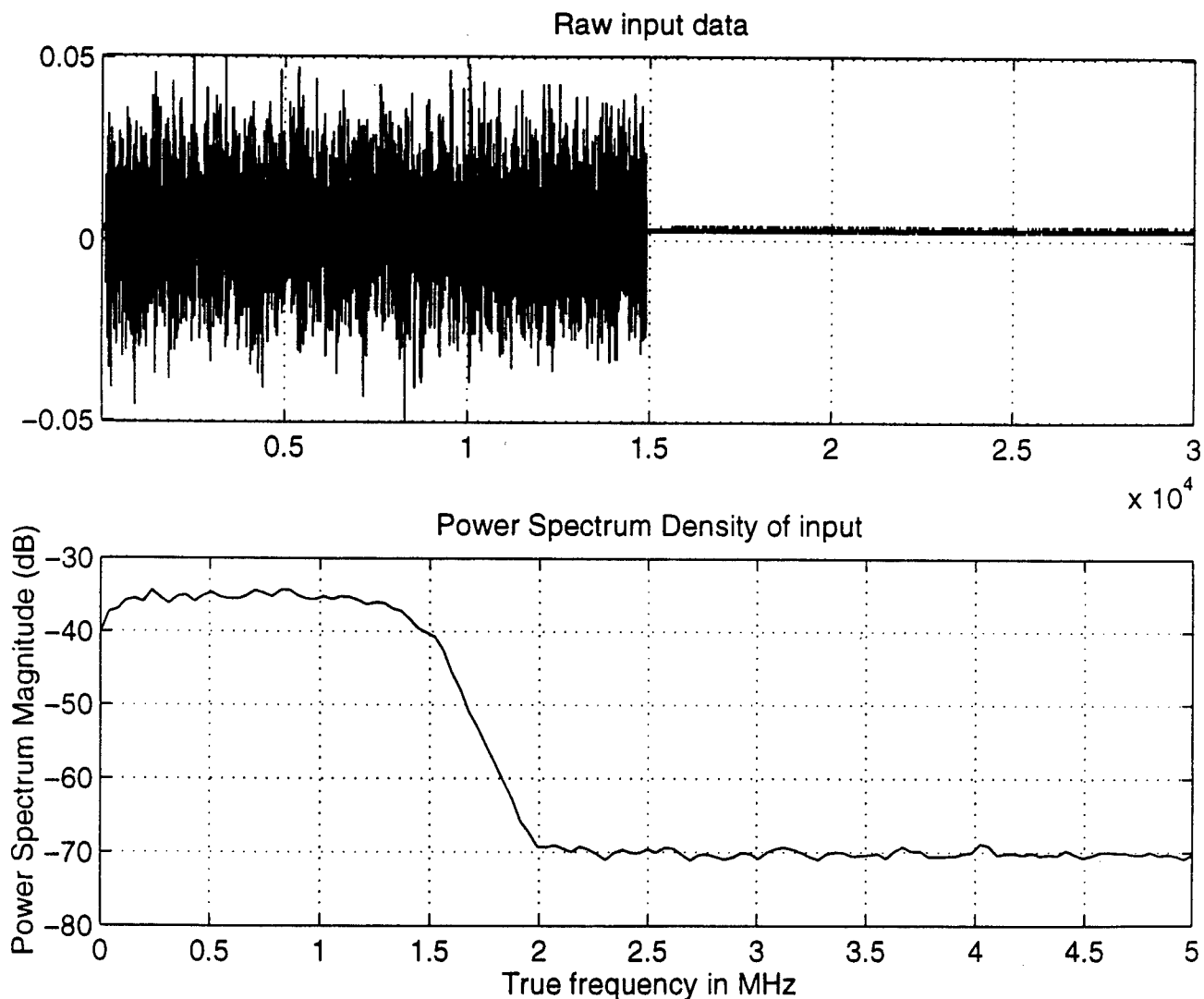


Figure 2. Time-history and power spectrum of system input: faultless plate.

## 5. RESULTS

The first set of results discussed is for the fault-free plate. The input and corresponding output time-histories for the experiment are shown with their power spectra in Figures 2 and 3 respectively. The parts of the data with low intensity are essentially included in order to estimate accurately the delay between input and output, note that the signal does not decay away immediately as there are multiple reflections of the wave within the plate etc. which contribute to the decaying field.

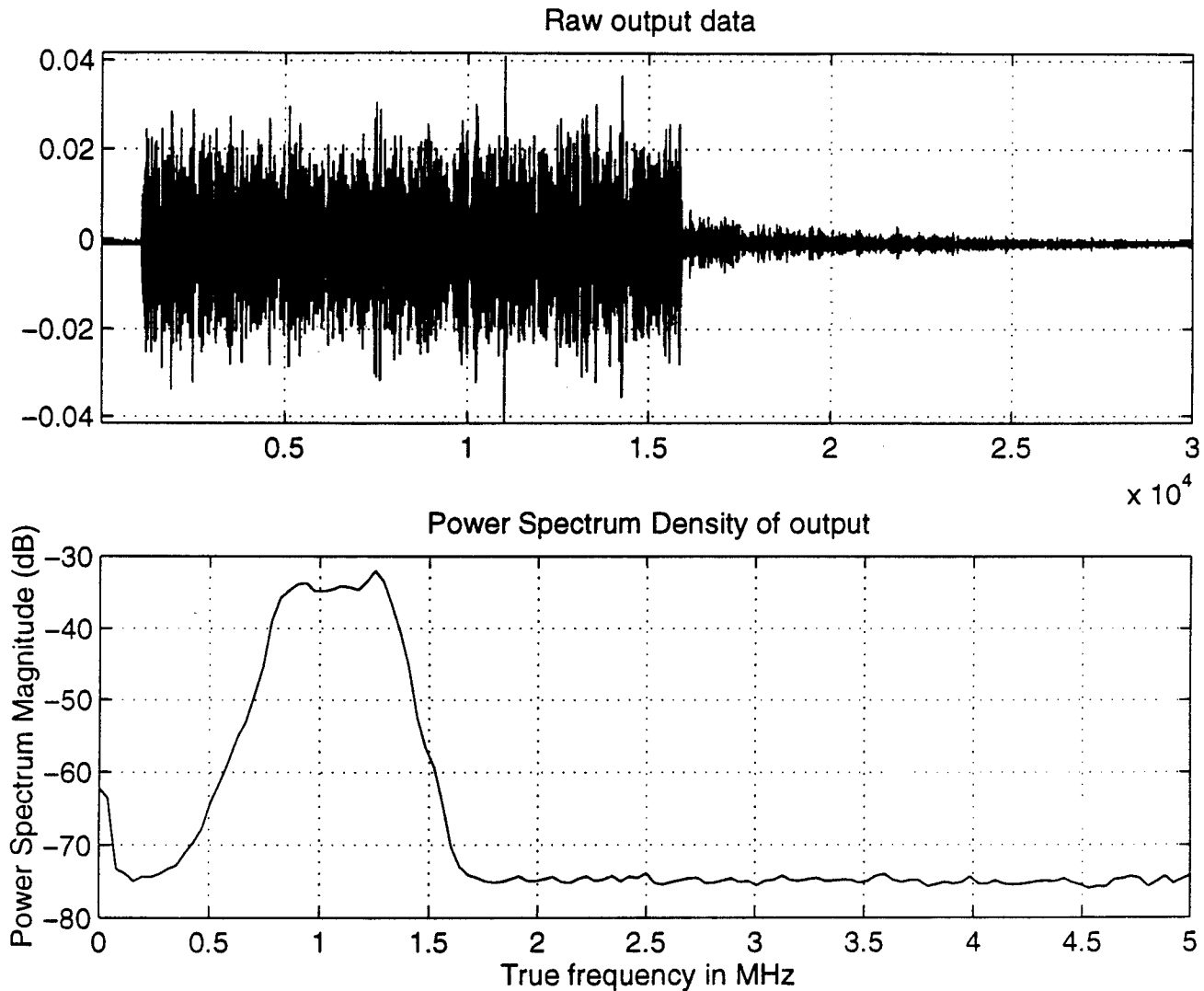


Figure 3. Time-history and power spectrum of system output: faultless plate.

Before fitting the NARMAX model, a little pre-processing was required. Figures 2 and 3 show that the delay for the signal transmission between input and output measurement points was about 1000 samples or 100 microseconds. Using the velocities of sound in Aluminium and perspex a delay of 96 microseconds was estimated. Subsequent signal processing revealed a value of 95.8 microseconds which shows excellent agreement. In order to generate a causal NARMAX model, the output data was shifted by the time-delay plus 20 samples. The data was also normalised in an attempt to

eliminate effects due to variations in the coupling between transducer and plate. Only 1000 points of pre-processed input and output data were used to fit the model as shown in Figure 4.

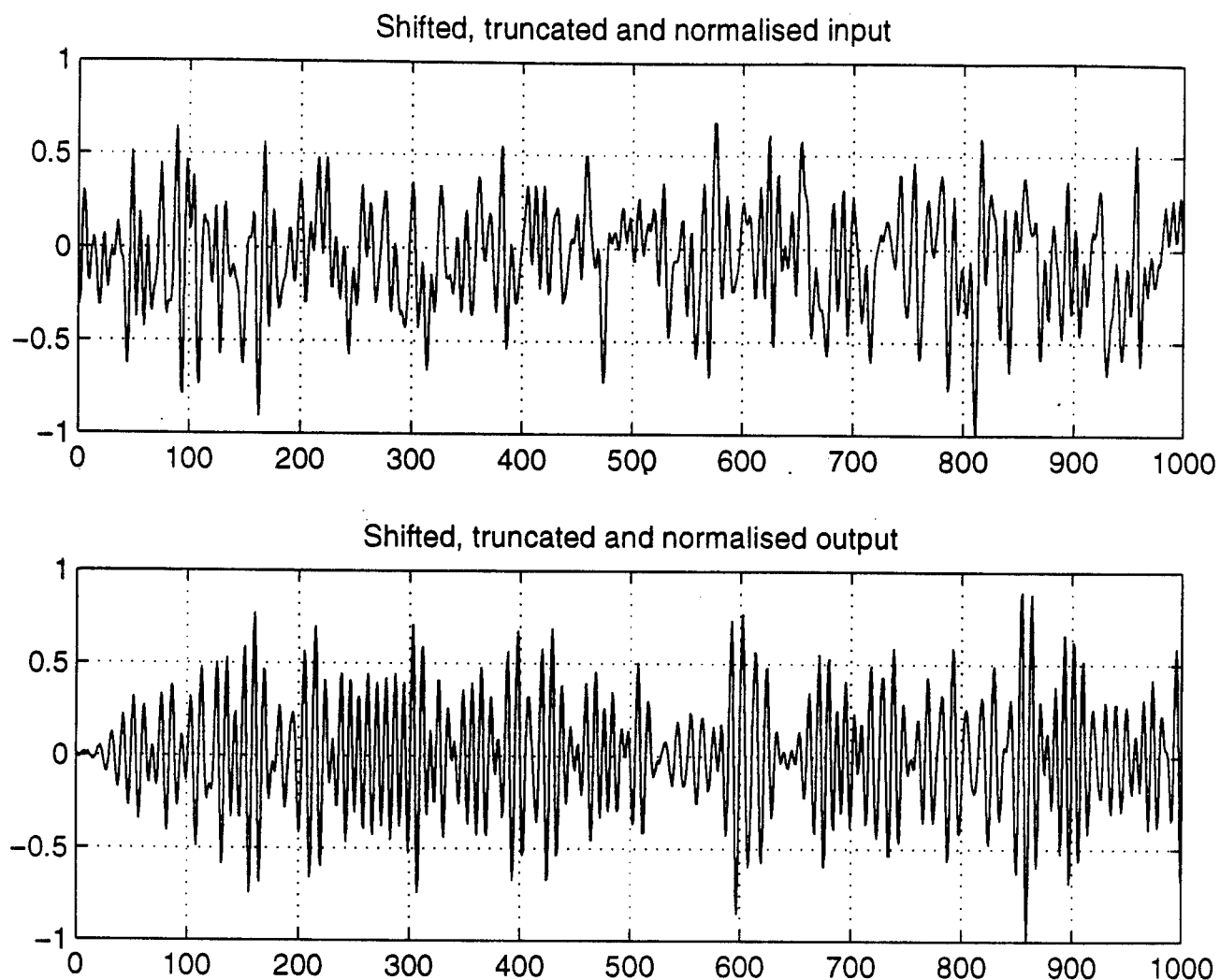


Figure 4. Pre-processed data for model fitting: faultless case.

Both linear and nonlinear NARMAX models were fitted to the data. The linear model proved to be completely acceptable as the correlation tests in Figure 5 show clearly, all the curves fall within the 95% confidence bounds for a zero result. The OSA and MPO predictions were both excellent, it is considered sufficient to give here only the most stringent validity check.

The linear model needed 50 process (non-noise) terms and lags up to the 99<sup>th</sup> were needed in both input and output. Because the model is linear, the system has no higher-order FRFs. If the identified models for the faulted plates are nonlinear, the HFRFs will exist and may serve as features for fault detection.

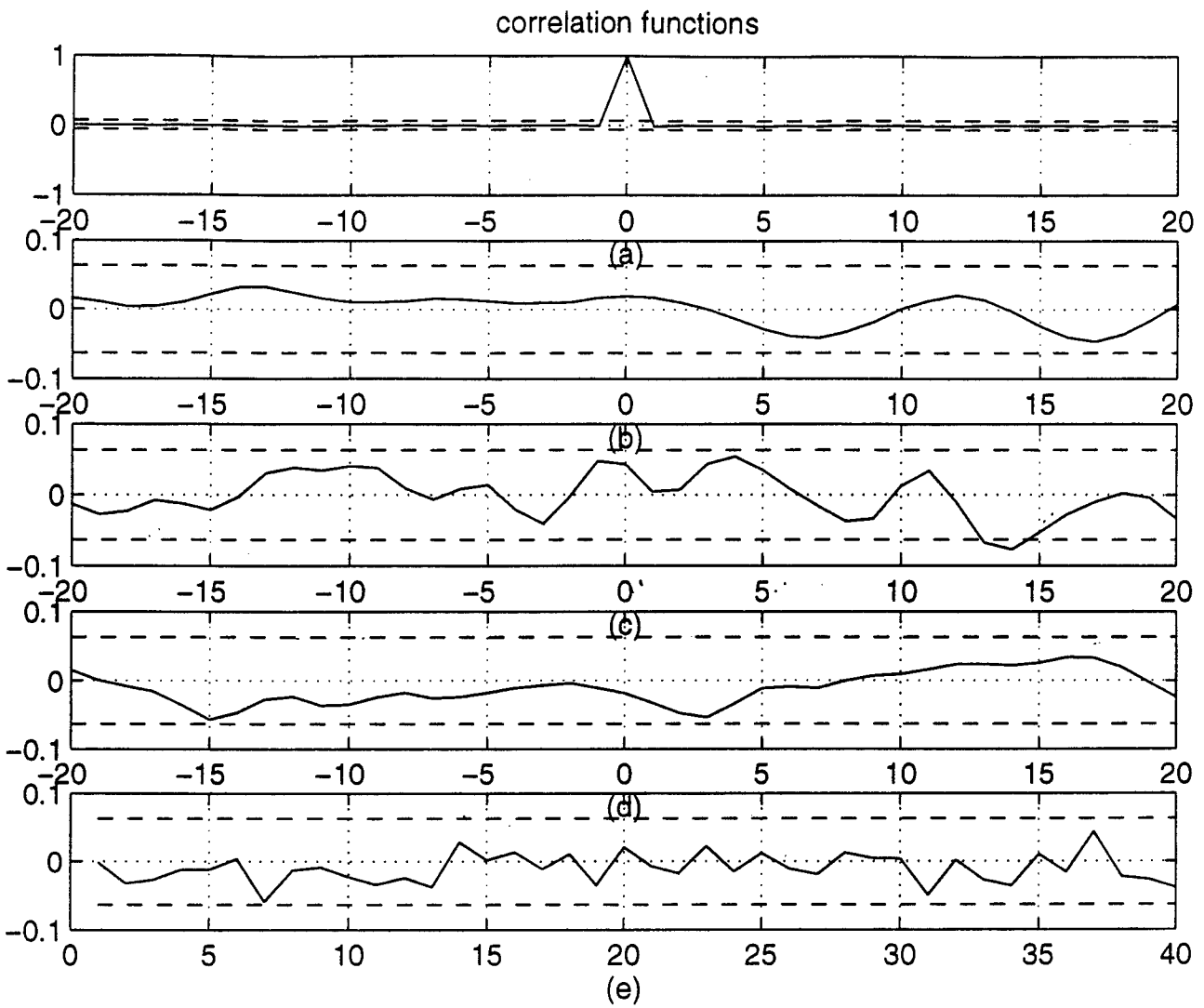


Figure 5. Correlation tests for linear model: faultless case.

The second plate investigated was the plate with 2mm hole. The same input sequence was used as before. Again linear and nonlinear NARMAX models were attempted. In this case however, it was necessary to go to a nonlinear model of cubic order in order to obtain acceptable correlation tests and model predictions. 69 model terms were needed: the 32 most significant terms were all linear, the remainder of the model contained nonlinear terms. Lags of up to 96 were needed in the output, up to 93 in the input. Note that different linear model terms appeared than in the fault-free case.

In this case, the model is nonlinear with some cubic model terms. This means that the HFRFs exist and can potentially be used to signal damage. The HFRFs are obtained by harmonic probing of the model. The majority of the nonlinear terms were cubic, so the study from this point will consider the third-order HFRF, although second order terms were present in the model and did generate a second-order HFRF. Figure 6 shows the third-order FRF. Note that the HFRF depends on three frequency variables and is also complex. In order to visualise the function, the restriction to the frequency plane  $f_1 = f_3$  was made and only the magnitude of the complex quantity was shown i.e. Figure 6 depicts  $|H_2(f_1, f_2, f_1)|$ . The topography of the FRF shows two sets of distinct

ridges emerging from background noise. The ridge structures are a manifestation of third-order nonlinear coupling in the model, the important point is that any variations in the model structure due to non-uniqueness will still generate the same ridge structure as this simply reflects the physical interactions between frequencies as a result of nonlinearity. Note that the peak gain is around 0 dB.

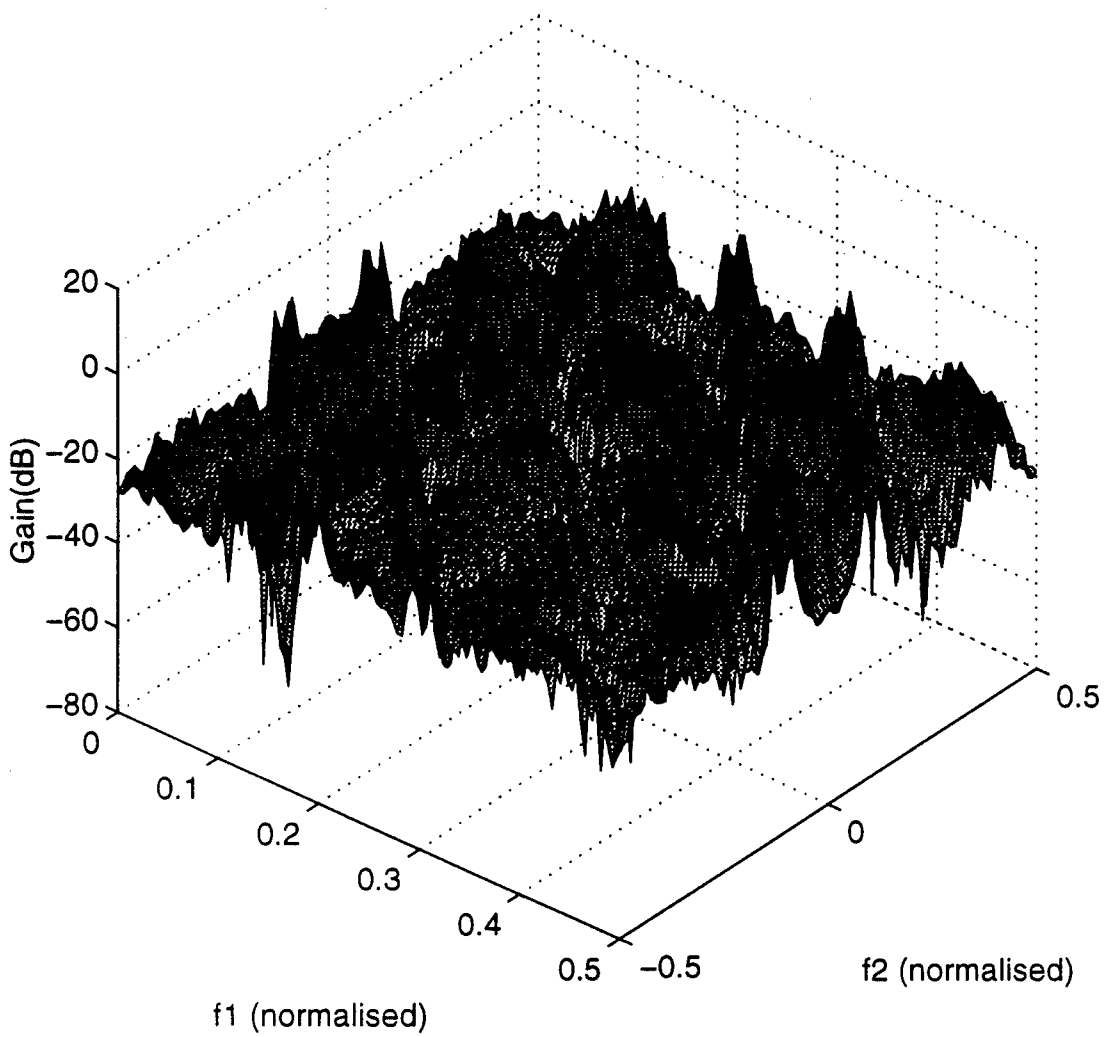


Figure 6. Magnitude of  $H_3$  for the plate with 2mm hole.

The third case investigated was a plate with a  $10 \times 0.4$  mm slot generated by spark erosion. The fault was seeded with a 2 mm hole. As before, linear and cubic nonlinear models were fitted. Although neither model gave perfect correlation tests, the nonlinear model showed better results and the MPO error was lower. The reason for slight deviations in the correlation tests can sometimes be attributed to a failure to model quartic and higher terms. As the number of candidate model terms grows combinatorially with the number of lags and nonlinear order it was considered prohibitive to consider a quartic model. 97 input lags and 94 output lags were the maxima and the total process

model contained 81 terms. It should be pointed out that all the models fitted in this study included nonlinear noise models. However, the noise models are simply there to ensure that the process models are unbiased and they take no part in the computation of the HFRFs.

Figure 7 shows the cubic FRF for the plate with 10 mm slot. The characteristic ridges are present but more prominent than before. On this occasion, the peak gain has been raised to approximately 20 dB. A marked increase on the 2mm hole plate.

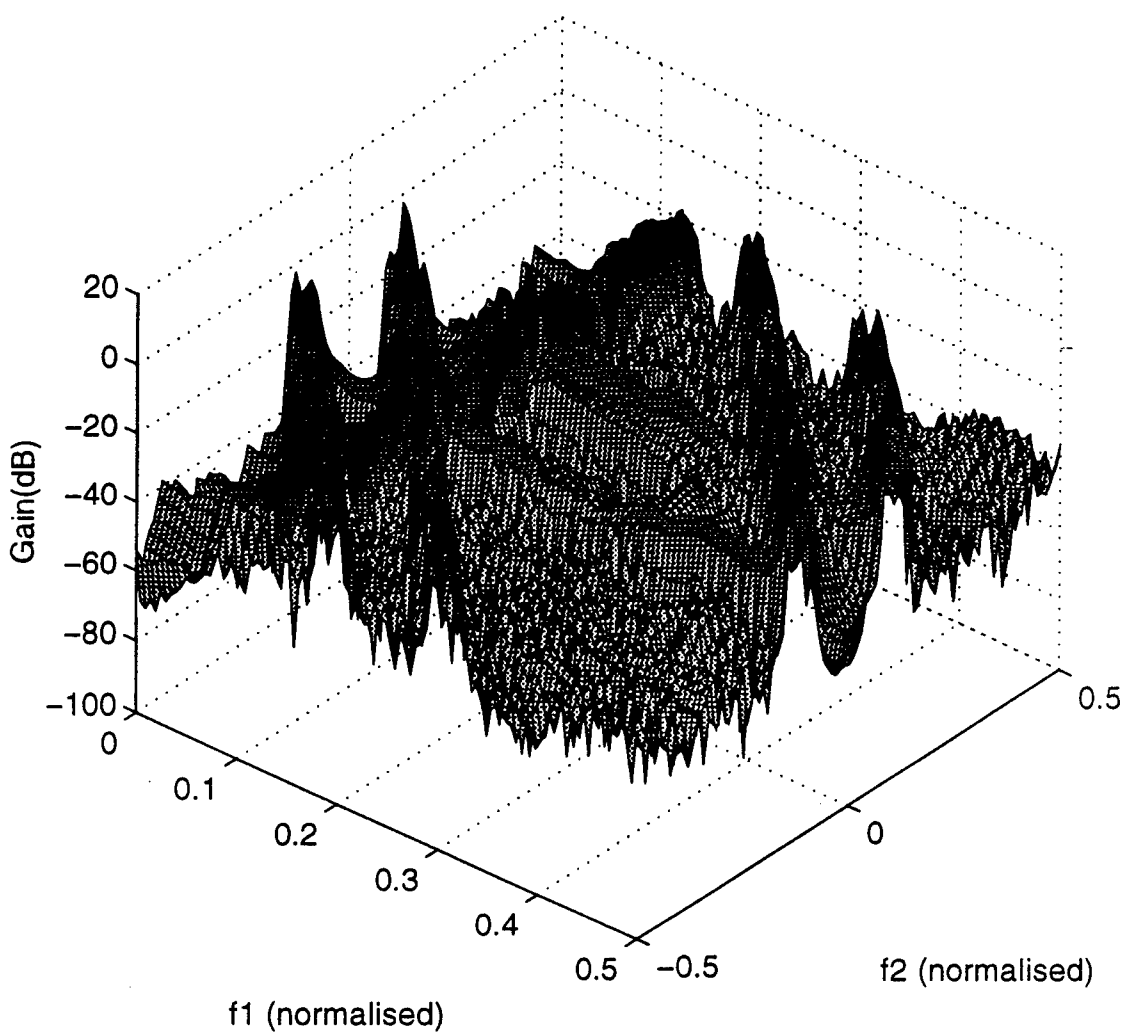


Figure 7. Magnitude of  $H_3$  for the plate with 10mm slot.

The final plate considered, had a  $40 \times 0.4$  mm slot, generated as before. Both linear and cubic models were fitted, the cubic model gave a lower MPO error and arguably better correlation test results. The cubic model contained 47 terms including the 91<sup>st</sup> lag in output and 87<sup>th</sup> lag in input. As before, the dominant terms were linear and the majority of nonlinear terms were cubic. The third-order HFRF was computed and is given in Figure 8. Again, the characteristic ridges are

prominent. The gain has increased markedly from the 10mm slot plate, rising to approximately 40 dB.

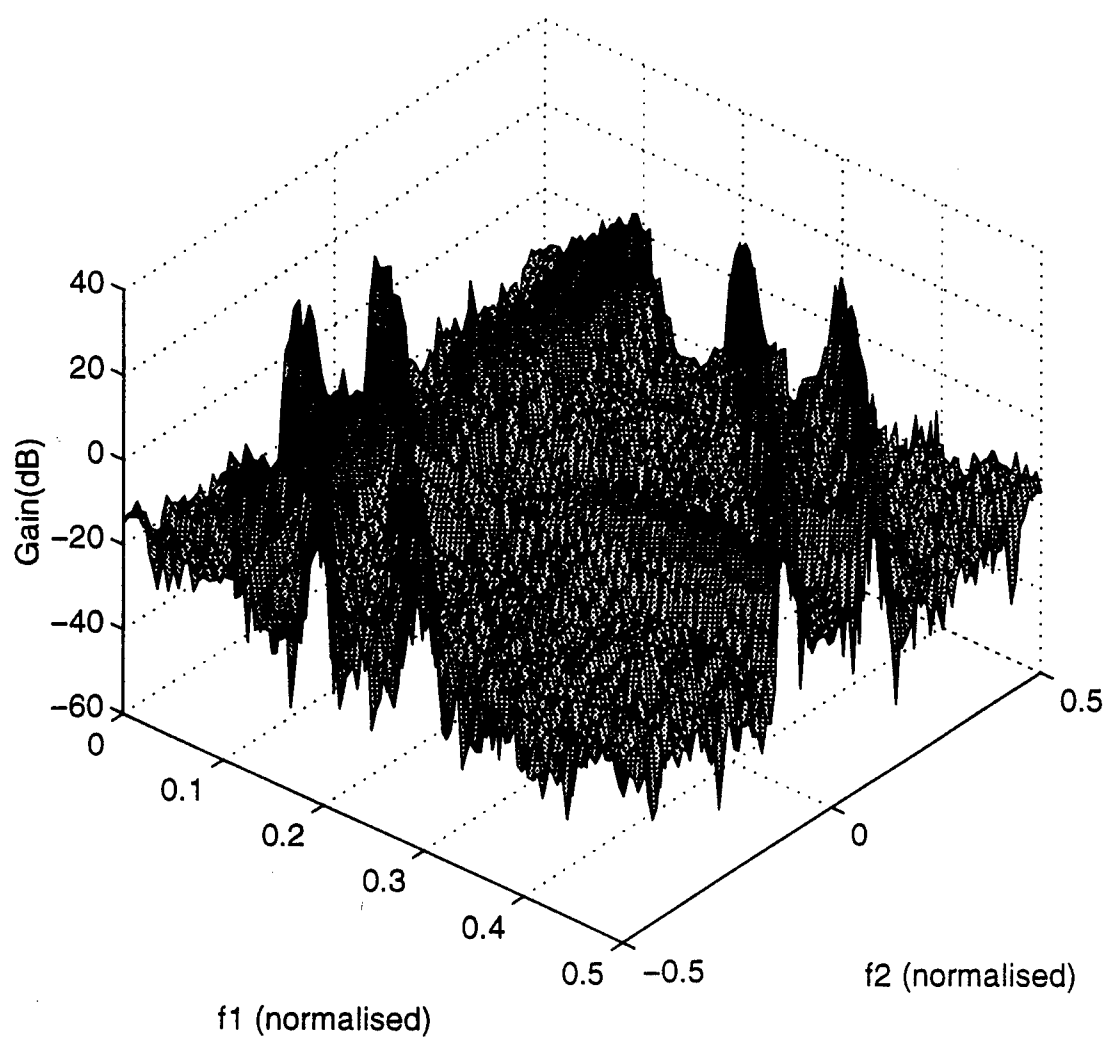


Figure 8. Magnitude of  $H_3$  for the plate with 40mm slot.

## DISCUSSION AND CONCLUSIONS

It appears that a model-based approach to Lamb wave inspection of plates is possible. In the situations considered here, the model is a input-output model where the input is a signal injected into the Lamb wave transducer and the output is a Lamb wave intensity measured after the wave has been transmitted over a possible defect. Because the NARMAX models considered here are not unique they have transformed into Higher-order Frequency Response Functions (HFRFs). It has been demonstrated that the existence of a  $H_3$  HFRF appears to be an indicator of damage and that the magnitude of the quantity is correlated with the defect size.

There are a number of points which should be discussed before this methodology could be proposed for practical inspection. In the first case, the fitting of NARMAX models and HFRFs is rather time-consuming and faster algorithms and processors would be needed in order to make the method practical for on-line inspection. The second important point relates to the confidence which the HFRF allows in the assertion that damage has taken place. The signals and noise are stochastic and different observations will lead to slightly different HFRFs. One must be confident that an observed variation in the features is truly due to damage and not just a statistical variation in normal condition. In connection with this, a method for generating confidence bounds for HFRFs has recently been obtained<sup>17</sup>. The final point for consideration relates to the existence of the Volterra series and consequently the existence of the HFRFs. Conditions are known for existence<sup>18</sup> and are satisfied by the model structures given here. Another problem relates to the *convergence* of the Volterra series, and if convergence is assured, where the acceptable cut-off for truncation is. These matters are not yet settled and should be before the interpretation of the HFRFs can be carried out with total confidence.

## REFERENCES

1. Alleyne (D.N.) & Cawley (P.), "The interaction of Lamb waves with defects", *IEEE Trans UFFC*, **39**(3), pp.381-397, 1992.
2. Alleyne (D.N.) & Cawley (P.), "Optimisation of Lamb wave inspection techniques", *NDT&E International*, **25**(1), pp.11-22, 1992.
3. Guo (N.) & Cawley (P.), "Lamb wave reflection for the quick non-destructive evaluation of large composite laminates", *Materials Evaluation*, **52**(3), pp.404-411, 1994.
4. Jansen (D.P.), Hutchins (D.A.) & Mottram (J.T.), "Lamb wave tomography of advanced composite laminates containing damage", *Ultrasonics*, **32**(2), pp.83-89, 1994.
5. Pierce (S.G.), Philp (W.R.), Culshaw (B.), Gachagan (A.), McNab (A.), Hayward (G.) & Lecuyer (F.), "Surface-bonded optical fibre sensors for the inspection of CFRP plates using ultrasonic Lamb waves", *Smart Materials and Structures*, **5** pp.776-787, 1996.
6. Cawley (P.) & Alleyne (D.N.) "The use of Lamb waves for the long range inspection of large structures", *Ultrasonics*, **34**, pp.287-290, 1996.
7. Staszewski (W.J.), Pierce (S.G.), Worden (K.), Philp (W.R.), Tomlinson (G.R.) & Culshaw (B.), "Wavelet signal processing for enhanced lamb wave defect detection in composite plates using optical fibre detection", *Optical Engineering*, **36**, pp.1877-1888, 1997.
8. Worden (K.), Pierce (S.G.), Staszewski (W.J.), Philp (W.), Tomlinson (G.R.) & Culshaw (B.), "Detection of faults in Carbon fibre reinforced plates using Lamb wave based novelty detection", *Proceedings 3<sup>rd</sup> International Conference on Modern Practice in Stress and Vibration*, (ed.) M.Gilchrist, Balkema, pp.45-50, 1997.
9. Leontaritis (I.J.) & Billings (S.A.), "Input-output parametric models for nonlinear systems. Part I: deterministic nonlinear systems", *International Journal of Control*, **41**, pp.303-328, 1985.

10. Leontaritis (I.J.) & Billings (S.A.), "Input-output parametric models for nonlinear systems. Part II: stochastic nonlinear systems", *International Journal of Control*, **41**, pp.329-344, 1985.
11. Billings (S.A.) & Tsang (K.M.), "Spectral analysis for nonlinear systems, part II: interpretation of nonlinear frequency response functions", *Mechanical Systems and Signal Processing*, **3**, pp.341-359, 1989.
12. Korenborg (M.), Billings (S.A.) & Liu (Y.P.), "An orthogonal parameter estimation algorithm for nonlinear stochastic systems", *International Journal of Control*, **51**, pp.193-210, 1988.
13. Billings (S.A.) & Voon (W.S.F.), "Structure detection and model validity tests in the identification of nonlinear systems", *IEE Proceedings*, **130**, pp.193-199, 1983.
14. Bedrossan (E.) & Rice (S.O.), "The output properties of Volterra systems driven by harmonic and Gaussian inputs", *Proceedings IEEE*, **59**, pp.1688-1707, 1971.
15. Peyton Jones (J.C.) & Billings (S.A.), "Recursive algorithm for computing the frequency response of a class of non-linear difference equation models", *International Journal of Control*, **50**, pp.1925-1940, 1989.
16. Viktorov (I.A.), *Rayleigh and Lamb Waves*, Plenum Press, New York, 1970.
17. Worden (K.), "Confidence bounds for higher-order frequency response functions from time-series models", *Submitted to Mechanical Systems and Signal Processing*, 1997.
18. Palm (G.) & Poggio (T.), "The Volterra representation and the Wiener expansion: validity and pitfalls", *SIAM Journal on Applied Mathematics*, **33**(2), 1977.

## DISCUSSION

### Model-based fault detection using Lamb waves

Speaker: Worden

In order to correlate physical damage (to the structure) to the nonlinearity in your algorithm, it will be necessary to fully understand the nature of the interaction of lamb waves with defects. It would also be difficult to detect very small fatigue cracks using very low frequency lamb waves- the effects will be below noise level in real data. Contrary to your claim regarding past research on lamb waves, there has been extensive work on it in the U. S. (Mal and Guo, Bar-Cohen, Chimenti, etc.). —Ajit Mal

*As I indicated in the presentation, an understanding of the interaction of Lamb waves with defects is essential if the results of this preliminary study are to be carried forward. I agree with Professor Mal, that there are difficulties associated with the detection of small defects using low frequency Lamb waves. The method presented is not, in principle, restricted to low frequency. However, the presence of many modes at higher frequencies will almost certainly mean that more complex input-output models are needed, so testing at higher frequencies may well be impractical, we intend to investigate. Finally, as I recall, I made no claims at all regarding the past Lamb wave research. The six papers cited in the current paper happen to be those that I had at hand; there was no intention to present a comprehensive survey. If that had been my intention there would have been many references in the US work.*

I would be interested in knowing how you are defining "damage"? How is it related to your "linear to non-linear" detection requirement? —D. O. Thompson

*"Damage" in the context of this paper is a change in the initial virgin state of the structure from linear to nonlinear. This is because the diagnostic detects non-linearity. This clearly does not encompass all damage states of interest; exactly which states it does apply to is a subject for further research. To refer back to the first question, it is necessary to have an understanding of the interaction between Lamb waves and defects.*

Do you think your phenomenon is somehow related to a description of an emerging crack as a phase transition of second type, with scaling parameter changing? Research in this direction was done, e.g., by Professor Chudnosky at the University of Illinois at Chicago Circle. —Vladik Kreinovich

*I am not familiar with the work you have cited and so I cannot comment. If the theory can shed light on the results described in the current paper, I would be very interested in it.*

# Preliminary evaluation of NDE technologies for the detection and characterization of high-cycle fatigue damage

Glenn M. Light

Southwest Research Institute  
P.O. Box 28510  
San Antonio, Texas 78228-0510

## ABSTRACT

The U.S. Air Force (AF) has experienced a series of high-cycle-fatigue (HCF)-related engine failures in fighters. To significantly reduce the number of HCF failures in the future, the AF has decided to develop a damage-tolerant structure design methodology. A key technical challenge faced by this design methodology is development of NDE methods to detect microcracks and monitor their growth. SwRI developed a plan for (1) identifying NDE methods which have potential for detecting HCF damage, (2) fabricating test specimens, and (3) evaluating the identified NDE techniques on the test specimens.

NDE methods identified as having potential for HCF included acoustic microscopy, acoustic reverberation, positron annihilation, surface acoustic waves, surface-skimming waves, eddy current, and the krypton emission technique (KET<sup>TM</sup>). Test samples were generated with real cracks ranging from 0.0004 to 0.001 inch (10 to 20  $\mu\text{m}$ ) and EDM notches ranging from 0.002 to 0.016 inch (50 to 400  $\mu\text{m}$ ). The primary goal of the project was to attempt to determine limits of defect detectability for surface-oriented defects. Results obtained showed all methods tested could detect EDM notches 50 microns in length and greater—eddy current could detect 20-micron defects, and the KET<sup>TM</sup> could detect real cracks in the range of 50 microns.

**Keywords:** high-cycle fatigue, NDE, ultrasonics, eddy current, KET<sup>TM</sup>, surface wave, positron annihilation

## 1. INTRODUCTION

The U.S. Air Force (AF) has experienced a series of high-cycle-fatigue (HCF)-related engine failures in fighter jets. In some cases, the fan blades experienced foreign object damage, which can start a crack. In other cases, the crack may have initiated at a subsurface defect that was either not detected or believed to be benign. To significantly reduce the number of HCF failures in the future, the AF has decided to develop a damage-tolerant structure design methodology over the next 7 years.

For damage-tolerant life extension, it is important to identify microstructural changes which can adversely affect structural integrity. A key technical challenge in the overall HCF program of fracture mechanics model development and testing is the development of NDE methods for detection of microcracks and the monitoring of their growth. The AF had an internal program funded to evaluate surface wave ultrasonics, electrical potential drop, and eddy current for detecting and monitoring HCF damage. No reports have been published at the present time.

The goals of this project were to (1) identify existing NDE methods for potential to detect and monitor HCF damage, (2) fabricate test samples, and (3) evaluate identified methods on simulated HCF defects. Also, as part of the program, test specimens with simulated HCF defects, ranging from 50 to 400  $\mu\text{m}$ , were to be generated.

## 2. TECHNICAL DISCUSSION

### 2.1 Identification of NDE methods

Most NDE methods in their present stage of development have limited ability to provide reliable early detection of HCF damage because their main purpose has been to detect and characterize macrocracks, which are much larger

than the grain size of the material (typically 25 µm and larger). However, it is also clear that a number of methods have the potential to be improved and enhanced upon to a point where they could be used to detect HCF damage (expected to be on the order of 10 to 20 µm and greater). For this project, three selection criteria were established to identify these potential NDE methods: (1) potentially sensitive to small defects, either internal to the volume or on the surface; (2) reasonable cost associated with making each measurement; and (3) potentially fieldable in terms of equipment cost and size.

A number of methods were identified for review. Table 1 lists these methods and their applicability to (1) determine volumetric microstructural changes or (2) detect small cracking and monitor crack propagation. These methods are briefly discussed in the following sections.

**Table 1. List of potential NDE methods and associated application for detecting and monitoring HCF damage**

Method	Assessment or Monitoring of	
	Microstructural Changes	Crack Initiation and Propagation
Scanning Acoustic Microscope	Yes	Yes
Surface Acoustic Waves	Maybe	Yes
Surface-Skimming Acoustic Waves	Maybe	Yes
Reverberation Decay	Yes	No
Eddy Current	Maybe	Yes
Replication	No	Yes
Scanning Electron Microscope	No	Yes
Positron Annihilation*	Yes	No
Krypton Emission Technique*	No	Yes

\*Added after project awarded

### **2.1.1 Scanning acoustic microscopy (SAM) method**

The SAM method has excellent potential for detecting cracks as small as 10 µm deep using transducer frequencies as high as 1GHz. Data obtained by Pan et al.<sup>2</sup> showed that defects on or near the surface and as small as 20 µm in length could be imaged.

However, two operational requirements associated with using SAM made it impractical for HCF damage evaluation in the field. First, the part under inspection must be polished to a 1-µm surface finish. The parts that will ultimately need inspection have no better than a 16-µm finish. Second, an accurate mechanical scanning capability is needed to collect usable acoustic images. This requires the SAM mechanical system to be large, which does not lend itself to potential field application.

### **2.1.2 Surface acoustic wave (SAW) method**

The SAW method relies on Rayleigh waves produced by an unfocused contact probe mounted on an acrylic wedge (Figure 1). The surface wave is propagated over the material surface, with the depth of penetration generally on the order of one wavelength. Because of this property, surface waves are mostly used for surface-connected cracks and other types of flaws located close to the examination surface of the material. As a surface wave interacts with a surface defect, it radiates some of its energy back into the medium in contact with the surface.

### **2.1.3 Surface-skimming acoustic wave (SSAW) method**

Conventional straight-beam (0-degree or down-looking) ultrasonic transducers have difficulties in seeing just below the examination surface of the material. These near-surface dead-zone limitations of existing ultrasonic

inspection technology motivated SwRI, in 1990, to develop the two multibeam transducers shown in Figures 2 and 3. The 4-MHz transmitted surface-skimming bulk longitudinal ( $L_b$ ) and shear ( $S_b$ ) waves used in this method were produced by the back elements (probes B) of the SLIC-30 and SLIC-45\*, respectively.

The original designs of the SLIC-30/45 transducers were modified for evaluation of HCF by: (1) increasing the angle of the transmitted beams ( $L_b$  in Figure 2 and  $S_b$  in Figure 3) from about 60 to about 80 degrees; (2) eliminating the acoustic barrier in the acrylic transducer wedge normally used to prevent direct feedthrough (crosstalk) between the transmitting back probe and the receiving front probe, and (3) adjusting the X position of probe B relative to probe A until the exit point of probe B (point b) coincided with the entry point of probe A (point a). A modified SLIC-45 (designated as SLIC-48) proved much more sensitive to the presence of the test defects of interest than a modified SLIC-30.

#### 2.1.4 Reverberation decay method

The reverberation decay method uses bulk (in contrast to surface or surface-skimming) ultrasonic waves and is directed at observing the scattering of the transmitted wave by random phase and grain boundaries in the material.

#### 2.1.5 Eddy current (ET) method

The ET method uses a coil energized with alternating current to generate eddy currents in the material under inspection. When the ET direction is changed by interaction with a defect (difference in electrical conductivity), a corresponding change in the magnetic field produced by the eddy currents is generated and is detected by either an impedance change in the exciting coil or by voltage induced in a separate sensing coil on the material. It is believed that microstructural defects caused by HCF damage would produce changes in the conductivity of the material and thus cause changes in the ET signal. Also, discrete cracks will produce an ET response. Typically, the ET method is most effective for detecting surface defects.

#### 2.1.6 Positron annihilation method

The positron annihilation method is based upon the detection of annihilation gamma-ray energy, which is caused by the combination of electrons in the material with the positrons entering the material under inspection (as shown in Figure 4). The incident electrons are from a beta-ray source, and they strike valence electrons in the material producing two gamma-rays of equal and opposite momentum given by

$$e^+ + e^- \rightarrow h\nu . \quad (1)$$

The energy of each gamma ray is equal to the rest-mass energy of an electron, which is 0.511 ev. As the positrons go through the material, the probability that they will combine with electrons in the material is greatest as the velocity of the positrons approaches zero. The positrons are most likely to combine with the outer-shell electrons rather than the K or L shell because the positrons would be strongly repelled by the electric field of the nucleus as it approaches the K and L shells. When the positrons enter the material, the maximum depth of penetration depends on the source and atomic number density of the material. That is, the higher the energy of the positron, the greater the penetration, and the greater the atomic number density, the lower the penetration. For example, for Ti 6-4 ( $r = 4.54 \text{ g/cm}^3$ ) to have a range of 1 mm, the positron must have an energy of approximately 0.2 MeV.

Materials having fatigue damage appear to have more vacancies, thus, more free electrons that can interact with the incident electrons to produce positron annihilation. This leads to a decrease in positron annihilation intensity.<sup>3-5</sup>

#### 2.1.7 Krypton emission technique (KET<sup>TM</sup>)

The KET<sup>TM</sup> is a method for detecting small surface defects that have openings in the range of 0.01 to 10  $\mu\text{m}$  and lengths ranging from 4  $\mu\text{m}$  to 1mm. It is a penetrant NDE method using a krypton gas, which is 5 percent radio-

\*SLIC = Shear and Longitudinal waves used simultaneously for material Inspection and defect Characterization

active  $^{36}\text{K}^{85}$ .  $^{36}\text{K}^{85}$  is a beta-ray emitter with a 10.8-year half life and a beta-ray energy spectrum with an average value of 0.23 MeV and a maximum energy value of 0.67 MeV. The KET™ process is conducted as follows. First, the part to be inspected is subjected to a vacuum to remove air from the open surfaces. Then the part is exposed to krypton gas, and any defects absorb and trap the gas. The krypton gas is then bled out of the system and again exposed to air. A liquid film (developed by Kodak) is sprayed onto the part in darkroom conditions. The trapped beta particles expose the film and produce dark regions where the defects exist. These dark regions allow the defects to be detected. This method is useful over the range of surface defect openings from 0.4 to 1300  $\mu\text{m}$ , and it can also be used to detect surface fretting, as well as wall thinning in hollow turbine blades.

## 2.2 Fabrication of test specimens

One of the most important factors in evaluating the capability of various NDE methods to detect HCF damage is to have test specimens with known levels of damage. Since HCF damage is difficult to detect, parts with actual field-service-induced HCF damage are difficult to obtain. Therefore, part of this effort was dedicated to developing simulated HCF damage. HCF is generally defined as low-amplitude stress applied over approximately  $10^8$  or more cycles. These large cycle numbers make it costly and time consuming to try to simulate this type of damage using conventional stress-cycling machines. For example, it would take over 3 years to obtain  $10^8$  cycles at a rate of 10 Hz and complete the test specimen. Therefore, using conventional fatigue testing machines did not seem appropriate for this effort.

A strategy for fabricating the test specimens with small defects was adopted. This strategy was to place starter voids (approximately 10 by 40  $\mu\text{m}$ ) in flat Ti 6-4 specimens utilizing an ion milling process used at SONY in San Antonio. These starter voids would then be subjected to three-point bending fatigue until cracks were generated. Again, the goal was to generate cracks in the range of 50 to 400  $\mu\text{m}$  in length. Using this approach, two test specimens (Nos. 518 and 519) were developed for evaluating the various NDE methods. However, only cracks in the range of 20  $\mu\text{m}$  in length were obtained. Attempts at obtaining larger cracks led to failure of the specimen.

Since the goal of the project was to evaluate NDE methods on defects in the range of 50 to 400  $\mu\text{m}$  in length and it appeared to be difficult to obtain real cracks in this range, it was decided to fabricate a Ti 6-4 plate specimen with nine paper-thin EDM notches. On one side, which had a smooth, highly polished surface (16-rms finish), four notches were machined. On the other side, which had a rough surface (125-rms finish), five were machined. These two sets of EDM notches are described in Table 2.

## 2.3 Results of NDE method evaluation and discussion

### 2.3.1 Surface acoustic wave (SAW) method results

Specimens Nos. 518 and 519 were inspected by surface waves using both 25-MHz immersion and 10-MHz contact methods. None of the cracks in these specimens were detected by either method.

The wavelength of the surface waves over Ti 6-4 was approximately 120  $\mu\text{m}$ . Hence, sizes of the cracks on the surface of specimen No. 518 were much smaller than the wavelength of the sound waves. Therefore, it is believed that higher frequency transducers are needed to detect such small cracks. But high-frequency sound energy is more attenuative in Ti 6-4 metals due to the large grain size, so there is a tradeoff between better resolution and deeper penetration.

The Ti 6-4 specimen with notches was inspected using the immersion mode (transducer incident angle set at 30 degrees). In the immersion test, all notches were scanned, and B-scan images (depicting throughwall dimension of the defect) of all notches were obtained. All four notches on the smooth side could be detected. However, the signal of the smallest notch (notch A) was weak. The B-scans obtained from the rough side show the multiple echoes from the surface roughness features. Nevertheless, the five notches were detectable. The notches on the smooth and rough sides were inspected in the contact mode using the 10-MHz transducer mounted on the wedge (with an angle of 53 degrees). Table 3 shows the peak- to-peak amplitude of responses from the notches. All but the smallest notches on both sides of the Ti 6-4 test specimen could be detected by using the contact inspection.

Table 2. Dimensions of 0.005-inch-wide EDM notches placed on smooth and rough sides of Ti 6-4 test specimen

Notch ID	Desired Notch Length [inch ( $\mu\text{m}$ )]	Actual Notch Length [inch ( $\mu\text{m}$ )]	Desired Notch Depth [inch ( $\mu\text{m}$ )]	Actual Notch Depth [inch ( $\mu\text{m}$ )]
Side with 16-rms Smooth Surface				
A	0.002 (50)	0.0034 (85)	0.001 (25)	0.0018 (45)
B	0.004 (100)	0.0064 (160)	0.002 (50)	0.0004 (10)
C	0.008 (200)	0.0086 (215)	0.004 (100)	0.0044 (110)
D	0.016 (400)	0.0175 (438)	0.008 (200)	0.0078 (195)
Side with 125-rms Rough Surface				
A*	0.002 (50)	0.0036 (90)	0.001 (25)	0.0018 (50)
B*	0.004 (100)	0.0054 (135)	0.002 (50)	0.0032 (80)
C*	0.004 (100)	0.0058 (145)	0.002 (50)	0.006 (150)
D*	0.008 (200)	0.0107 (268)	0.004 (100)	0.0054 (135)
E*	0.016 (400)	0.0176 (440)	0.008 (200)	0.008 (200)
The 9 notches listed in this table were used to evaluate the NDE methods listed in Table 1.				

Table 3. Peak-to-peak amplitude of responses from the test specimen notches

Surface	Notch ID				
	A	B	C	D	E
Peak-to-peak voltage from smooth side (16-rms surface)	Not able to detect	0.06 v	0.20 v	0.45 v	No Defect
Peak-to-peak voltage from rough side (125-rms surface)	A*	B*	C*	D*	E*
	Not able to detect	0.09 v	0.15 v	0.20 v	0.35 v

### 2.3.2 Surface-skimming acoustic wave (SSAW) method results

The results obtained with the SSAW method using the SLIC-48 are presented and discussed below.

#### (1) Defect detection tests

**Smooth-surface notches**—The four surface notches (A through D in Table 2) on the smooth side of the Ti 6-4 test specimen were used to evaluate the SSAW method's ability to detect and characterize (as to orientation and size) small surface fatigue cracks. The detection trials were not conducted under blind test conditions (i.e., the ultrasonic examiner was informed about defect location, orientation, and size). Pulse amplitude (A), time of flight (screen position), and RF phase were the recorded signal parameters.

Figure 5 shows the background interference [noise only (a)] RF waveform along with those obtained for the four smooth-surface notches from the right side[(b) through (e)]. Occasionally, noise excursions up to 6 percent of FSH occurred in the time window (i.e., between the 5th and 6th screen division mark). All notches were readily detected with SNR values greater than 6 dB.

**Rough-surface notches**—The five surface notches (labeled A\* through E\* in Table 2) on the rough side of the test specimen were also measured to determine the effect, if any, of surface roughness on the SSAW method's ability to detect small surface fatigue cracks.

Figure 6(a) shows the rough-surface-reverberation-induced (noise only) RF waveform. Noise excursions in the time window measured up to 10 percent of FSH, as compared to 6 percent on the smooth surface. Also shown in Figure 6 are the RF waveforms obtained for the five rough-surface notches from the left side. As expected, these notches were less readily detected than the notches breaking the smooth surface of the test specimen. The SNR value for notch A\*, for example, was only 4 dB.

**A small fatigue crack**—The limit of crack detectability by the SLIC-48 module was reached when the waveform received from the cracked center area of test specimen No. 519 of the Ti 6-4 specimen could not be distinguished from the “noise only” waveform received from a known crack-free area 6 mm away from the center.

## (2) Defect orientation tests

The dependence of signal amplitude on the orientation angle, defined as the angle between the short (width) axis of the surface notch and the transducer scanning (X) axis, was investigated by moving the transducer 360 degrees around a 250- $\mu\text{m}$ -long x 50- $\mu\text{m}$ -wide (5-to-1 aspect ratio) reference notch. No effect of signal amplitude relative to transducer orientation was obtained; therefore, it was concluded that due to the nearly vertical nature of the received waves, the signal amplitude depends on defect surface area (length x width) and not on defect depth.

## (3) Defect sizing tests

Since the notch lengths were much smaller than the length of the 4-MHz transmitted surface-skimming waves, the usefulness of only the amplitude comparison method for defect sizing was investigated. No correlation was found between signal amplitude and notch depth. This finding is consistent with the noted independence of signal amplitude from the orientation of the nine measured surface notches.

### 2.3.3 Eddy current method results

The ET experiments were performed at 6 and 20 MHz. These frequencies were chosen to obtain high current density near the examination surface (because of the skin effect) to maximize the response from small surface defects. (The skin depth in Ti 6-4 is approximately 260 and 150  $\mu\text{m}$  for 6 and 20 MHz, respectively.) Six megahertz was chosen because it is the highest frequency available in most commercially available ET instruments and, thus, could be readily adapted for field use. Because the SwRI laboratory equipment is capable of higher frequencies, 20 MHz was also chosen to determine if the defect response could be further improved with shallower skin depth.

The probe configuration used differential sensing coils surrounded by a single excitation coil. This probe design was chosen for its high spatial resolution and low sensitivity to liftoff variations. The 6-MHz probe had a ferrite core in each sensor and was surrounded by a ferrite shield to increase the spatial resolution and sensitivity. The 20-MHz probe had no cores or shield because the electrical losses in the ferrite material are too large at the high frequency and, therefore, the effectiveness of the ferrite would be minimal. The probes were the smallest commercially available to increase spatial resolution.

The experimental setup consisted of a Stanford Research Systems model DS345 function generator, which drove the excitation coil in the ET probe, and a Stanford Research Systems model SR844 lock-in amplifier to detect the signal from the differential sensor coils. It was anticipated that at 20 MHz, noise could be introduced by capacitance changes associated with movement of the cable, so the Ti 6-4 notched specimen and specimen No. 519 were scanned by keeping the probe stationary and moving the specimens. The probe was held against the examination surface using spring pressure. Scan motion was accomplished by a precision computer-controlled laboratory scanner, and the signal output from the lock-in amplifier was digitized and stored as a function of scan position.

It was believed that the 20-MHz probe would provide higher sensitivity to small defects because the depth of penetration (skin depth) of the eddy currents was smaller at higher frequencies and, thus, a defect of a given depth interrupts a greater proportion of the current. The experimental results showed, however, that at 20 MHz, the response to probe liftoff (gap between the probe and specimen) and tilt variations were quite severe. Even though the probe was held by double cantilever springs, which provide up and down motion while minimizing tilt, the tilt and liftoff response during scanning and indexing of the specimen caused large responses. These responses tended to mask signals from small defects. It was not clear whether this response was caused by changes in electromagnetic coupling between the probe and specimen (which is the typical mechanism at lower frequencies) or by capacitive coupling (which would be more prevalent at higher frequencies). Although it may be possible to add conductive shielding to the probe to minimize capacitive coupling effects, this was beyond the scope of this effort.

At 6 MHz, the liftoff/tilt response was significantly reduced compared to 20 MHz, and signals from the defects were much more distinct. All of the notches were detected. There are also other indications in the image that are not associated with the surface notches. Examination of the specimen surface under the microscope showed that these indications are caused by small surface scratches.

ET data from the notches on the rough side of the notched test specimen showed that all notches were detected; however, the background signals were strong.

Fatigue crack specimen No. 519 was also scanned, and the results are shown in Figure 7. This specimen contained a 20- $\mu\text{m}$  ion-milled starter void and a 20- $\mu\text{m}$  crack growing from one edge of the void. This specimen also had a polished surface with a smoother finish than the 16-rms finish on the smooth side of the test specimen. A defect indication is obtained; however, this indication is a combination of the responses from both the starter void and the crack. Although it is not possible to separate the two responses, the stronger signal obtained on the right side of the indication may be caused by the presence of the crack, which is located on the side of the void.

### 2.3.4 Krypton emission technique (KET<sup>TM</sup>) results

The fatigue test specimens (Nos. 501, 518, and 519) were evaluated using KET<sup>TM</sup>. A large number of cracks were detected on specimens Nos. 518 and 519. These cracks were as small as 50  $\mu\text{m}$  in length. Using KET<sup>TM</sup>, these defects were detectable. The smaller defects (10 and 20  $\mu\text{m}$  in length) in these specimens were not detectable in any specimens using KET<sup>TM</sup>. It is unclear why these defects were not detected. Perhaps the cracks were either too tight or too shallow to absorb sufficient krypton gas to ultimately expose the photographic emulsion.

## 3. SUMMARY OF RESULTS AND CONCLUSIONS

- (1) All NDE methods identified as having the potential to detect HCF damage (except KET<sup>TM</sup>) in this project were tested on EDM surface notches ranging from 50 to 800  $\mu\text{m}$ . The actual detection capability for three methods is shown in Table 4. KET<sup>TM</sup> also showed the capability to detect fatigue cracks greater than 50  $\mu\text{m}$  long.
- (2) SwRI was not successful in developing test specimens with actual HCF damage.
- (3) SwRI was successful in developing test specimens with actual LCF cracks ranging from 10 to 20 microns.

This project has established limits of detectability for the various NDE methods tested under laboratory conditions.

## 4. REFERENCES

1. Nicholson, Ted. Presentation at a Road Map Review Meeting, Dayton, Ohio, July 15–17, 1997.
2. Pan, J. Z., E. R. De Los Rios, and K. J. Miller. "Detecting Small Fatigue Cracks by Acoustic Microscopy." *Fatigue Fract. Engng. Mater. Struct.* Vol. 16, No. 12, pp. 1329–1337 (1993).
3. Stewart, A. T. "Positron Annihilation in Metals." *Proceedings of the Positron Annihilation Conference*, edited by A. T. Stewart and L. O. Roellig (Academic Press, New York), pp. 17–50 (1967).
4. Liu, Liang B., David Gidley, and Albert F. Yee. "Effect of Cyclic Stress on Structural Changes in Polycarbonate as Probed by Positron Annihilation Lifetime Spectroscopy." *Journal of Polymer Science: Part B: Polymer Physics*, Vol. 30, pp. 231–238 (1992).
5. Hill, A. J., I. M. Katz, and P. L. Jones. "Isothermal Volume Relaxation in Aged Polycarbonate Measured by Positron Annihilation Lifetime Spectroscopy." *Polymer Engineering and Science*, Vol. 30, No. 13, pp. 762–768 (1990).

Table 4. Summary of NDE methods identified and experimentally determined defect detection sensitivity

Defect Size ( $\mu$ s)	NDE Method			
	Surface Acoustic Wave	Surface Skimming Wave	Eddy Current	KET™
10	ND	ND	ND	ND
20	ND	ND	Maybe	ND
85	D	D	D	NT
90	D	D	D	NT
135	D	D	D	NT
145	D	D	D	NT
160	D	D	D	NT
215	D	D	D	NT
268	D	D	D	NT
438	D	D	D	NT
440	D	D	D	NT

Note: Defect length is provided and a 2 to 1 length versus depth aspect ratio is assumed.

ND = Not Detected

D = Detected

NT = Not Tested

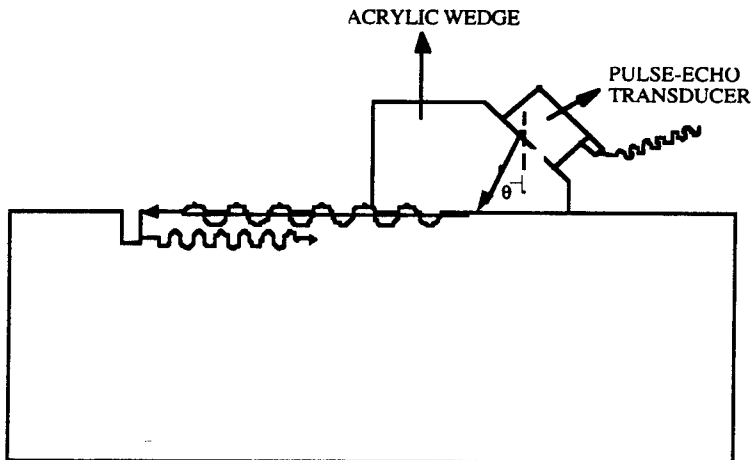
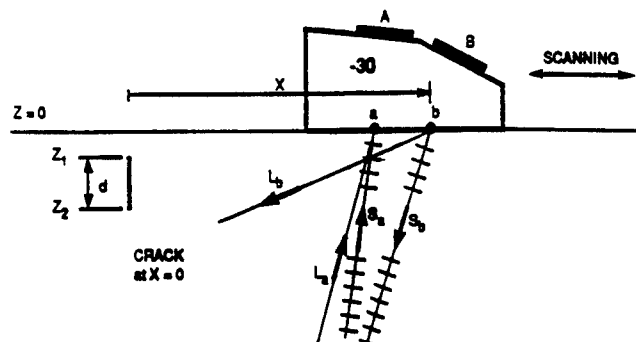
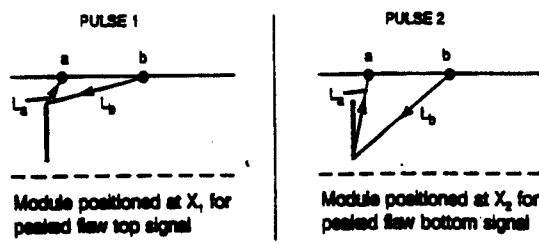


Figure 1. Illustration of the surface acoustic wave method.

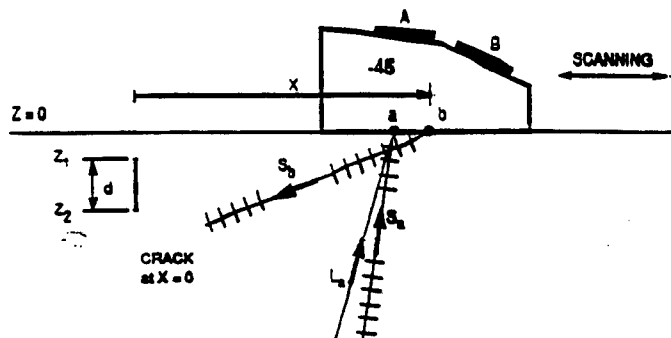


(a) Transmitted ( $L_b$ ,  $S_b$ ) and received ( $L_a$ ,  $S_a$ ) beams

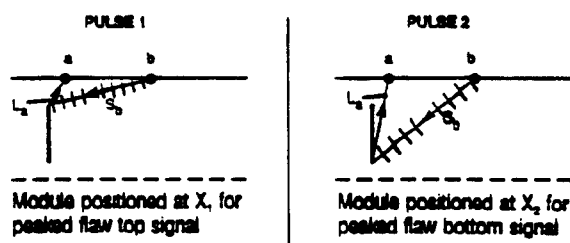


(b) Ray paths for the L-wave pulses

Figure 2. Interaction of the transmitted 60-degree longitudinal wave ( $L_b$ ) of the SLIC-30 transducer with a subsurface crack resulting in two L-wave pulses (pulses 1 and 2, shown) and two S-wave pulses (not shown).



(a) Transmitted ( $S_b$ ) and received ( $L_a$ ,  $S_a$ ) beams



(b) Ray paths for the L-wave pulses

Figure 3. Interaction of the transmitted shear wave ( $S_b$ ) of the SLIC-45 transducer with a subsurface crack resulting in two L-wave pulses (shown) and two S-wave pulses (not shown).

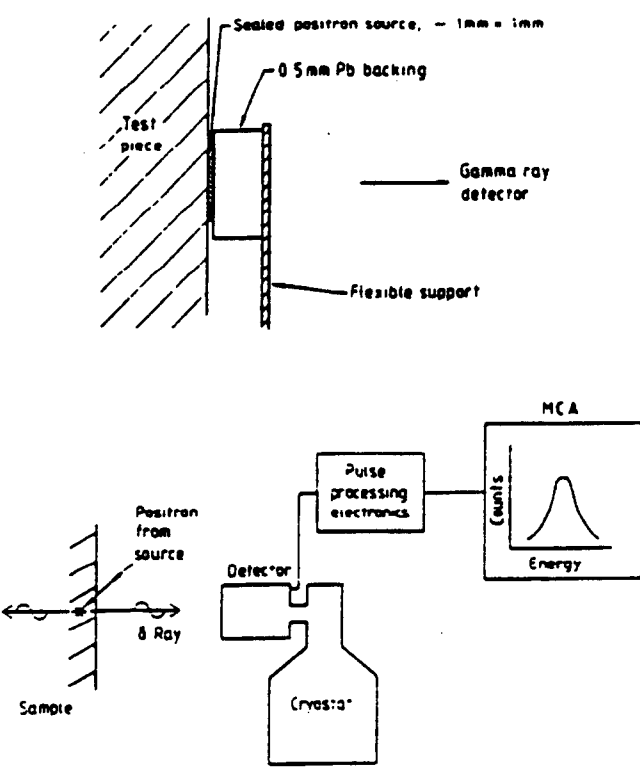
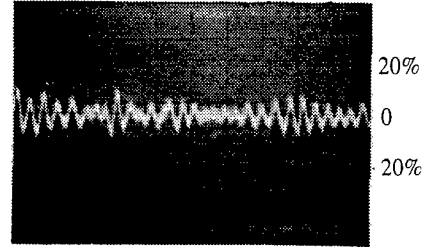
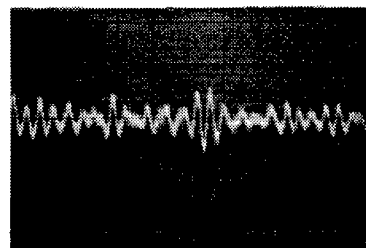


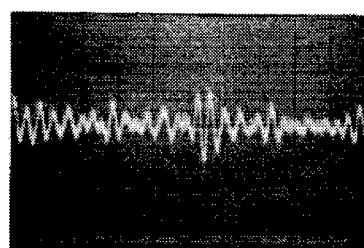
Figure 4. Illustration of the positron annihilation method. The top view shows the positron source on the test piece, the lower left view shows the concept of positrons entering the specimen and ejecting a gamma ray, and the lower right view shows detection and signal output. (Courtesy of AEA Technology.)



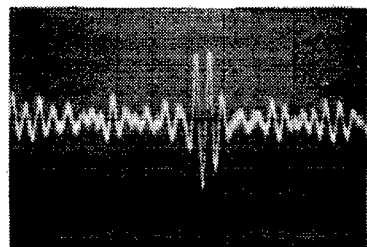
(a) Noise Only



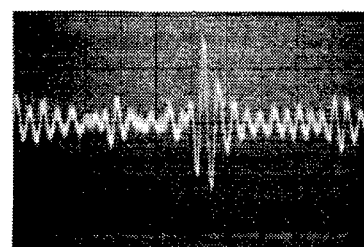
(b) Notch A   A=11%



(c) Notch B   A=14%



(d) Notch C   A=24%



(e) Notch D   A=30%

Figure 5. RF waveforms obtained against the background noise (a) for the four smooth-surface test specimen notches from the X direction.

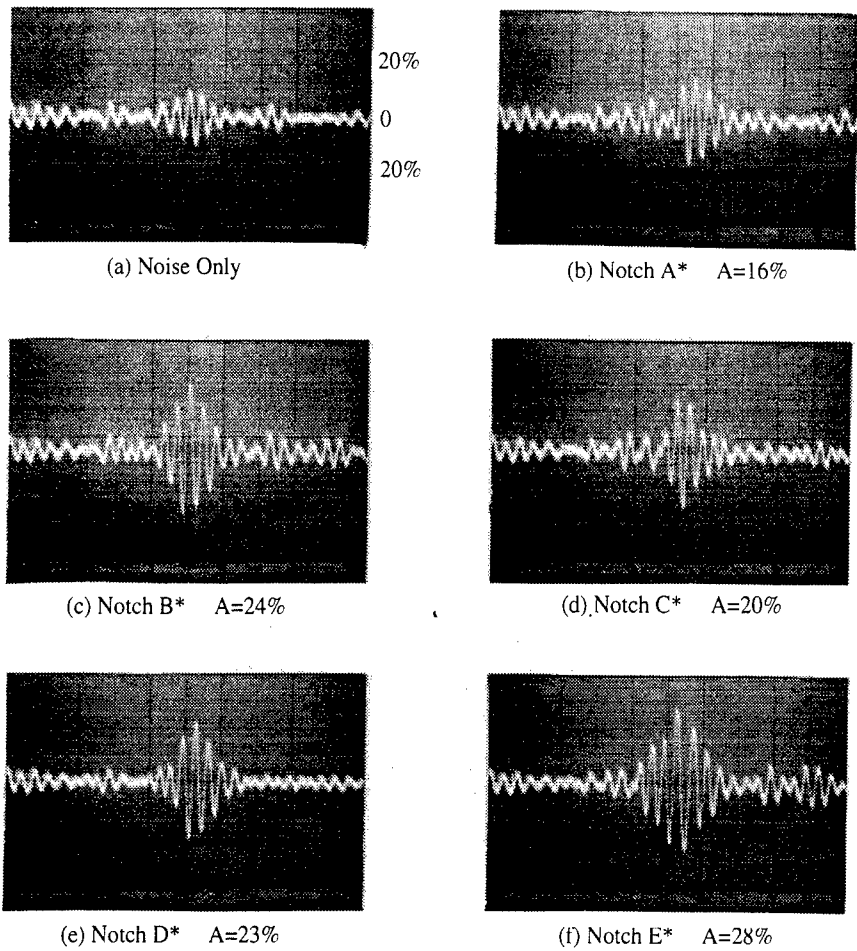


Figure 6. RF waveforms obtained against the background noise (a) for the five rough-surface test specimen notches from the X direction.

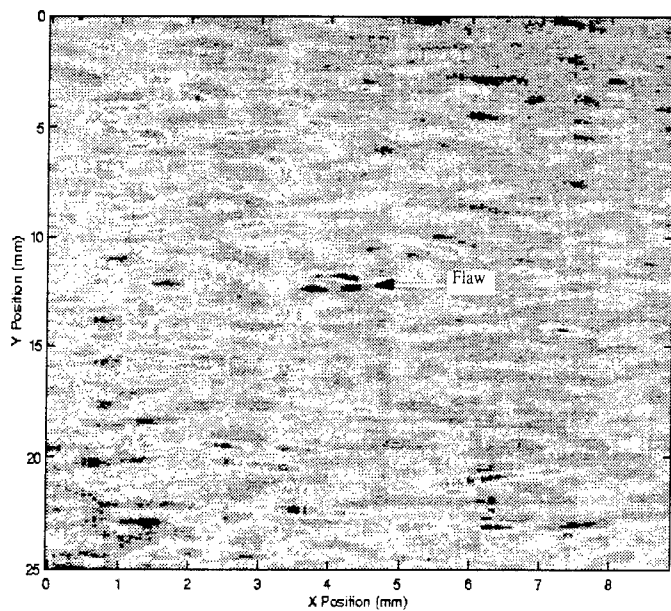


Figure 7. Color image of eddy current signals from raster scan of 20- $\mu$ s crack on specimen No. 519

## **Real-Time Characterization of Isotropic Plates Using Lamb Waves**

E. Rodriguez, H. Pardo, S. Nazarian, and J.H. Pierluissi

Center for Structural Integrity of Aerospace Systems

The University of Texas at El Paso

El Paso, TX 79968

ph: 915-747-8710

fax: 915-747-5921

e-mail: eurodrig@utep.edu

### **Abstract**

A fast and accurate technique to determine, in real-time, the elasticity constants of the material in isotropic thin plates using ultrasonic plate (Lamb) waves is described in this paper. It allows for the calculation and measurement of the dispersion curves of a plate wave propagating in the lowest symmetric mode. Time signals captured with two piezoelectric transducers in contact with the plate are first transformed to the frequency domain. Then the cross phase spectra is calculated to obtain the phase shift, which in turns yields the phase velocity. The experimental set up automatically and in real-time acquires and processes the data, finds the operating frequency range, and displays the results as dispersion curves. Ultimately, Young's and shear moduli are calculated from the measured dispersion curves by means of an inverting algorithm. The accuracy of phase velocity measurements in aluminum plates was found to be, on the average, within  $\pm 1\%$  when compared to the theoretical dispersion curves, and the inversion process yielded elasticity constants that were very close to the nominal values.

### **INTRODUCTION**

The nondestructive characterization of thin plates with ultrasonic plate waves requires that their associated dispersion curve (phase velocity versus frequency) be accurately measured. Measurement of the phase velocities can be made either in the time or in the frequency domain. However, the time domain measurements provide limited accuracy due to the ambiguous identification of the equiphase points in a traveling wave. A frequency domain technique is developed in this paper to measure the phase velocity of plate waves propagating in the lowest symmetric mode. This technique may be automated and provides a continuous dispersion curve in a short range of frequencies in real-time. The lowest symmetric mode was selected because it is more sensitive to changes in the stiffness constants and may be uniquely established at low frequencies. Theoretically, plate waves can be transmitted at any wavelength (or frequency and phase velocity). However, in practice it is very difficult to generate a unique mode with small diameter transducers, and at certain frequencies an undesirable multimode wave is usually excited. The adaptability of plate waves to propagate with a wide range of wavelengths is particularly advantageous when testing composite plates. Since this kind of material presents high attenuation coefficients at high frequencies it is possible to use low frequency waves to characterize it.

The spectral analysis approach is not new, since several researchers have developed applications based on this technique. Nazarian and Desai (1993) automatically obtained the dispersion curves of soil sites and pavement systems from surface waves measurements. Sachse and Pao (1978) described a method for measuring the dispersion curves of longitudinal bulk waves in solids using spectral analysis. Their method measured the phase and group velocities using the spectral analysis of a 35 nsec pulse sent through a specimen, together with the received pulse on the opposite side. Another technique used by Rogers (1995), yields the elasticity constants of isotropic plates by directly measuring the phase shifts of continuous plate waves with the  $\pi$ -phase method. His measurements of phase velocity had an accuracy of 0.5%; the elasticity constants calculated by a nonlinear least squares algorithm had an uncertainty of less than 2%.

Other methods for the characterization of composite plates by ultrasonic oblique isonification and immersion coupling in pitch-catch, through-transmission or reflectivity arrangements have been used successfully by several researchers. Among others, Chimenti and Nayfeh (1988) characterized the effective homogeneous anisotropic elastic behavior of a unidirectional composite laminate in the long wavelength limit. They developed a theoretical model that agrees well with the measurements of the phase velocity of leaky Lamb waves in a water-coupled experimental apparatus. Dayal and Kinra (1989) derived a model for a unidirectional composite plate and measured phase velocity and attenuation of the leaky Lamb waves from readings of maximum amplitudes of a leaky wave as function of the angle of incidence of the exciting pulse. Rohklin and Wang (1989) reconstructed the elasticity constants from bulk wave velocity measurements in several specific directions of anisotropic materials. They placed a small specimen in a special goniometer immersed in water, produced ultrasonic bulk waves with an ultrasonic pulser, and measured the reflection time, which gave the bulk wave phase velocity. The work of Bar-Cohen and Mal (1993) includes ray theory to explain the important features of the reflected signals from a unidirectional composite immersed in water. They found that water loading has significant influence on the dispersion curves of leaky Lamb waves; and that while certain stiffness constants significantly influence dispersion curves, others have negligible impact.

The present work was motivated by the need for measuring, nondestructively, the elastic constants of isotropic and anisotropic plates in real-time, using an apparatus suitable for field work. By using contact transducers to capture the waves on the same side of the plate, the technique presented is much simpler than the leaky Lamb waves technique. Additionally, the inversion algorithm developed to get the elasticity constants from plate waves phase velocity is effective and accurate. The integrated measuring system is easy to operate, faster than the traditional time-of-flight-bulk-velocity methods and as accurate as the Pulse-Echo-Overlap or  $\pi$ -Phase methods (Papadakis 1990).

## I. Theory

An elementary monochromatic wave moving in the positive x direction in a non-attenuating medium is represented as

$$u(x,t) = \exp[j(\omega t - kx)] \quad (1)$$

where  $k$  is the wave number and  $\omega$  is the angular frequency and  $t$  is time. In a dispersive medium,  $k$  is a function of frequency. The relationship between wave number and

frequency is called a dispersion relation. The main objective in the field is to experimentally determine the dispersion relation  $k(\omega)$  so that the dispersion curve can be calculated from the phase velocity  $v(\omega)$

$$v(\omega) = \frac{\omega}{k(\omega)} \quad (2)$$

The Fourier transform of a delayed time signal is given by (Bracewell, 1965)

$$U(\omega) = U_o(\omega) \exp(j\omega\tau) \quad (3)$$

where  $U_o(\omega)$  is the Fourier transform of the undelayed signal, and  $\tau$  is the time delay. Applying this theorem to a wave passing by two transducers separated a distance  $D$ , allows for time delay to be obtained from the phase velocity as

$$\tau = \frac{D}{v(\omega)} \quad (4)$$

Since phase velocity is related to the wave number through Equation 2, then

$$\tau = \frac{k(\omega)D}{\omega} \quad (5)$$

Substituting Equation (5) into Equation (3), the Fourier transform of the wave at the second transducer is then

$$U(\omega) = U_o(\omega) \exp[jk(\omega)D] \quad (6)$$

Representing  $U_o(\omega)$  in polar form

$$U_o(\omega) = |U_o(\omega)| \exp(j\phi_o) \quad (7)$$

Substituting Equation (7) into Equation (6) gives

$$U(\omega) = |U_o(\omega)| \exp\{j[\phi_o + k(\omega)D]\} \quad (8)$$

From this result the phase spectrum of the wave at the second transducer may be stated as

$$\phi(\omega) = \phi_o + k(\omega)D \quad (9)$$

If  $\phi(\omega)$  is available from measurements, the phase velocity may be obtained by substituting Equation (9) into Equation (2) as

$$v(\omega) = \frac{\omega}{k(\omega)} = \frac{\omega D}{\phi(\omega) - \phi_o} \quad (10)$$

The phase information from the cross power spectrum between the time signals of two receivers a distance  $D$  apart yields a relationship that can be readily used to calculate the dispersion curve described in Equation (10).

An inversion algorithm may then be used to obtain the elasticity constants from the experimental dispersion curve. For isotropic plates, only two elastic constants are required to characterize the material. The inversion procedure used in this work is based on the minimization of the sum of the squared errors between the measured phase velocity and the theoretical phase velocity at each frequency. The theoretical phase velocity is a function of the frequency, density, and elasticity constants  $C_{11}$  and  $C_{12}$  (for isotropic materials) through

$$v_i(f_i, v_i, C_{11}, C_{12}, \rho, h) = \text{root}\left(\frac{\tanh(\alpha d)}{\tanh(\beta d)} - \frac{(2k^2 - k_T^2)^2}{4k^2 \alpha \beta}\right)$$

with  $k = \omega/v_i$ ,  $\alpha^2 = k^2 - \omega^2/v_L^2$ ,  $\beta^2 = k^2 - \omega^2/v_T^2$ ,  $v_L^2 = C_{11}/\rho$ ,  $k_T^2 = \omega/v_T^2$ , and  $v_T^2 = C_{12}/\rho$ . Parameter  $v_i$  is the initial guess to find the root and is usually taken as the measured phase velocity at the given frequency  $f_i$ . Parameter  $d$  is equal to half the plate thickness,  $v_L$  is the longitudinal wave velocity,  $v_T$  is the shear wave velocity.

The elasticity constants are estimated by locating the minimum of the sum of the squared differences between the measured and calculated dispersion functions,

$$\text{Min} \left[ \sum_{i=1}^n (v_i^{(T)} - v_i^{(M)})^2 \right]$$

The superscripts T and M refer to theoretical and measured velocities, respectively. An inversion algorithm has been developed based on the general inverse theory (Nazarian, Yuan, 1993) that rapidly converges to the desired elastic constants. For isotropic materials, the shear and longitudinal wave velocities are the parameters determined by the algorithm.

## II. Experimental Setup

A schematic diagram of the experimental setup is shown in Figure 1. The essential equipment required to measure the phase velocity of Lamb waves includes digitizing oscilloscope with a GPIB port; a function generator with a GPIB port; two wideband amplifiers; two small diameter, wideband piezoelectric transducers adaptable to a Plexiglas variable-angle wedge; a fixture to keep the receiving and transmitting transducers aligned; and two Plexiglas angled-adapters to hold the receiving transducers; and a tube of high vacuum grease to be used as ultrasonic couplant.

The operation of the experimental apparatus was controlled by a "Virtual Instrument" (a National Instruments term to designate the simulation of a real instrument using their LabView software), running in a personal computer. The first activity of the virtual instrument is to program the arbitrary function generator through the GPIB bus, so that a five cycles sine burst modulated with a Hamming window was generated every 100 ms. This excitation function has a narrow band spectrum at a selected center frequency. When transmitted with a proper angle of incidence, a Lamb wave propagating in the fundamental symmetrical mode,  $S_0$ , is excited in the plate. For instance, in an aluminum plate 1.5 mm thick a 500KHz transducer can excite  $S_0$  plate waves in a range of frequencies from 300 to 800 KHz. The Lamb waves, detected by two contact transducers separated a distance  $D1$  from the source and a distance  $D2$  between them, were amplified 40 dB, and averaged and digitized by the oscilloscope. The digitized records are transferred to the computer through the GPIB bus. Additional parameters, such as distance between receivers, apriori shear wave velocity, acceptable signal level threshold, and bandwidth level, are introduced into the software. This information is needed so that a theoretical dispersion curve can be developed, and visually compared with the measured one obtained from Equations (2) through (10). The mean square error between the theoretical and measured phase velocity values is also displayed. If this error is large, the virtual instrument controls can be adjusted iteratively until the error is reached below a certain level.

## Experimental Analysis

A block diagram of the complete process is shown in Figure 2. In the first step, a fast Fourier transform algorithm is employed to calculate the cross power spectrum between the time signals of the two receivers. As shown in Figure 3, the cross power spectrum amplitude level is normally high enough only in a short range of frequencies. Outside of this band, the amplitude is too small to yield reasonable results.

Figure 4 shows the measured and theoretical phase-spectra of a 500 KHz plate wave. The range of frequencies which are above a preset threshold amplitude on either side of the input central frequency is used for this purpose. The elastic parameters of the plate are measured by simultaneously displaying the measured and the theoretical phase spectra, and visually adjusting the parameters of the theoretical spectrum until the two graphs are superimposed over the useful range of frequencies. The unwrapped theoretical and the measured phase spectra are shown in Figure 5.

Figure 6 shows the measured dispersion curves for a 1.5 mm thick aluminum plate together with the theoretical dispersion curve for the fundamental symmetrical mode. A 500 KHz transducer at an angle of  $31^\circ$  was used to generate plate waves of several frequencies. The measured dispersion curve was assembled from several segments obtained by incrementing the center frequencies of the exciting pulse between 300 and 900 KHz. The measured phase velocities are within 1% of the theoretical values. Above certain frequencies more than one mode is simultaneously excited. In this case it may be necessary to adjust the number of samples in the oscilloscope time window to minimize the impact of the unwanted modes. This is done from the virtual instrument by decrementing an indicator and observing the time signal while the program is running. Generally the useful time response consists of the same number of sinusoidal cycles as in the exciting pulse, (five cycles in this experiment). This modification also limits the frequency content of the receiver signals, since the waves are dispersive and the first arriving waves are the lowest frequencies.

## IV. CONCLUSIONS

In this paper the theoretical and practical considerations involved in the automatic measurement of phase velocity of Lamb waves by the contact method are discussed. The analytical and experimental aspects of using cross-phase spectrum of two time response signals produced by a plate wave to construct a dispersion curve are presented. The time signals are easily detected at two different points in the path of the wave by two piezoelectric transducers in contact with the plate, and the phase velocity is measured in real-time with an experimental apparatus. A "Virtual Instrument" has been developed to perform automatically all the steps required to measure phase velocity as a function of the frequency, from which the dispersion curve of an isotropic plate is obtained. Using the dispersion curve as input to an inversion algorithm, the elasticity constants of isotropic plates are calculated. This algorithm uses a linearized model and singular value decomposition for fast convergence.

## References

- Bar-Cohen, Y., Mal, A.K., Shih-Shiu Lih, "NDE of Composite Materials Using Ultrasonic Oblique Isonification", Material Evaluation, vol. 51, No.11, 1993.
- Bracewell, R. The Fourier Transform and Its Applications, Mc Graw-Hill , 1965.
- Chimenti, D.E., Nayfeh, A.H., "Propagation of Guided Waves in Fluid-Coupled Plates of Fiber-Reinforced Composite", Journal of Acoustical Society of America, Vol. 83, No.5, 1988.
- Dayal, V., Kinra,V.K., "Leaky Lamb Waves in an Anisotropic Plate. I: An Exact Solution and Experiments", Journal of the Acoustic Society of America, Vol. 85, No. 6, 1989.
- Nazarian, S., Desai, M.R., "Automated Surface Wave Method: Field Testing", Journal of Geotechnical Engineering, Vol. 119, No. 7, July, 1993.
- Rogers, W.P., "Elastic Property Measurement Using Rayleigh-Lamb Waves", Research in Nondestructive Evaluation, Vol. 6, 1995.
- Papadakis, E.P., "The Measurements of Ultrasonic Velocity", Physical Acoustics, vol. XIX, ed. by W.P. Mason and R.N. Thurston, Academic Press, New York, pp. 81-106, (1990)
- Rokhlin, S.I., D.E. Chimenti, "Reconstruction of Elastic Constants from Ultrasonic Reflectivity Data in a Fluid Coupled Composite Plate", Review of Progress in Quantitative Nondestructive Evaluation, Vol. 9, Plenum Press, 1990.
- Rokhlin, S.I., Wang, W., "Ultrasonic Evaluation of In-Plane and Out-of Plane Elastic Properties of Composite Materials", Review of Progress in Qualitative Non-Destructive Evaluation, Vol. 8B,pp.1489-1496, 1989.
- Sachse W., Pao, Y.H., "On the Determination of Phase and Group Velocities of Dispersive Waves in Solids", Journal of Applied Physics, Vol. 49, No. 8, August 1978.
- Yuan, D., Nazarian, S. , "Automated Surface Wave Testing: Inversion Technique", Journal of Geotechnical Engineering", American Society of Civil Engineering, Vol. 119, No. 7, pp.1112-1126. 1993.

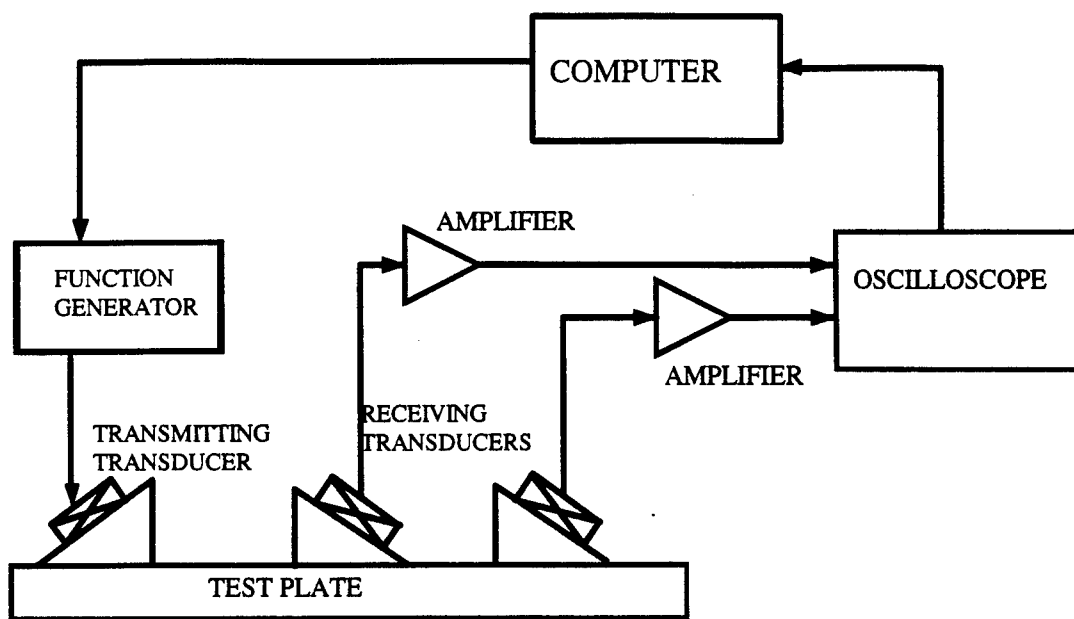


Figure 1. Block diagram of the experimental setup

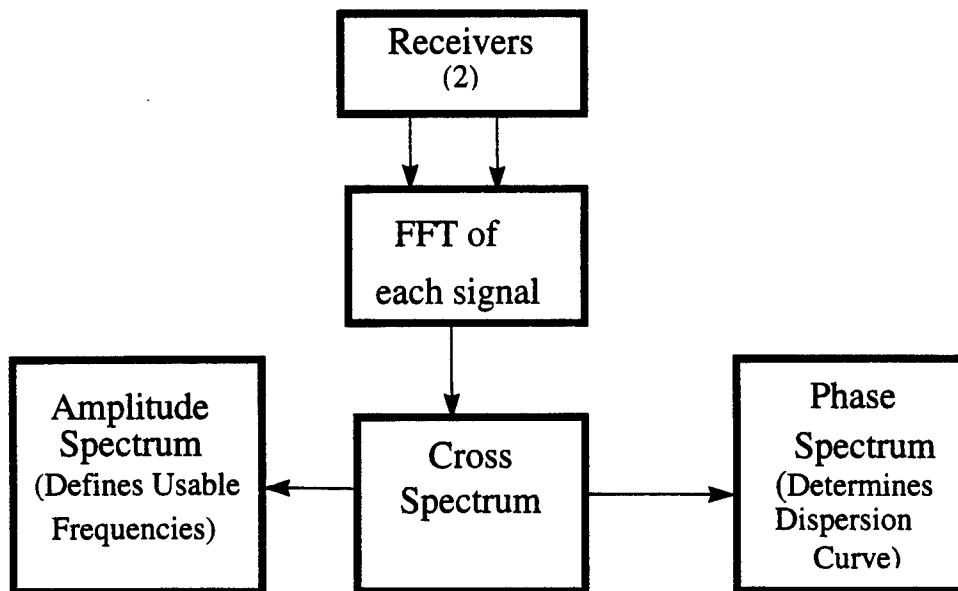


Figure 2. Block Diagram of the Process to Measure Dispersion Curves

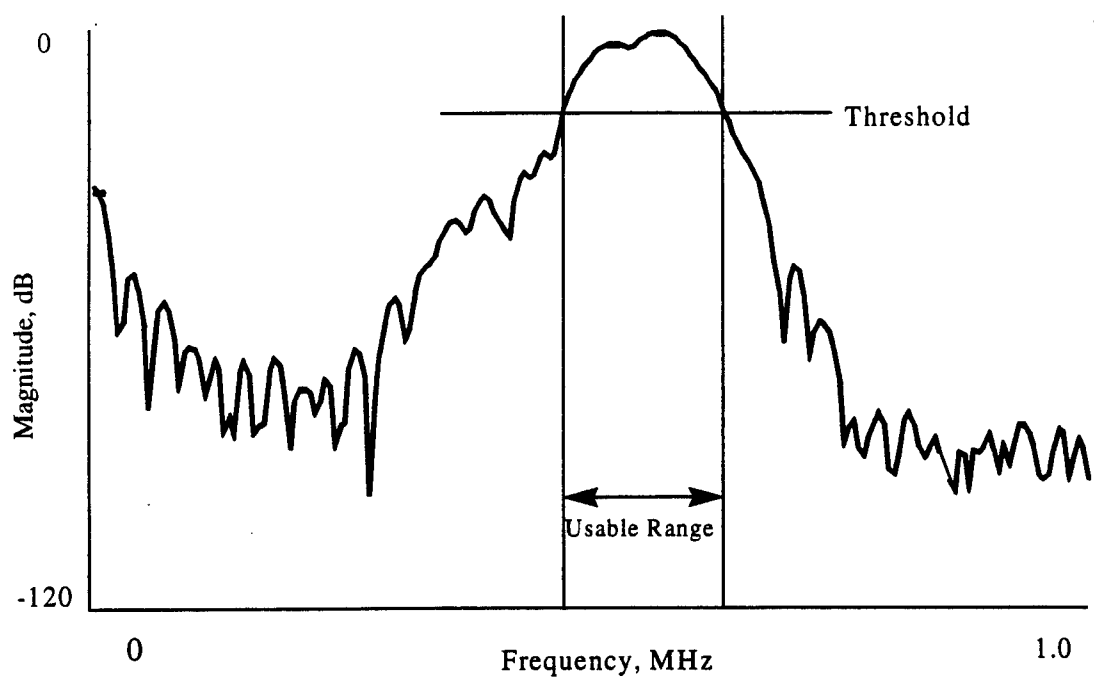
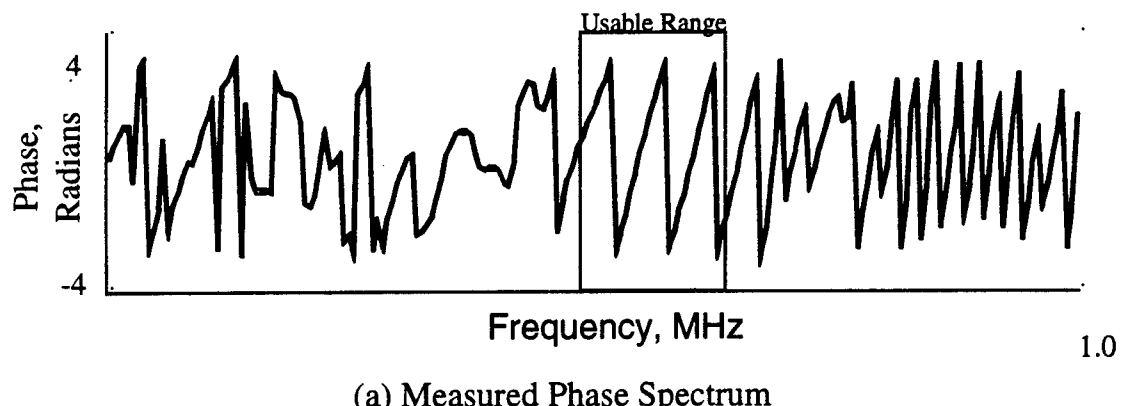
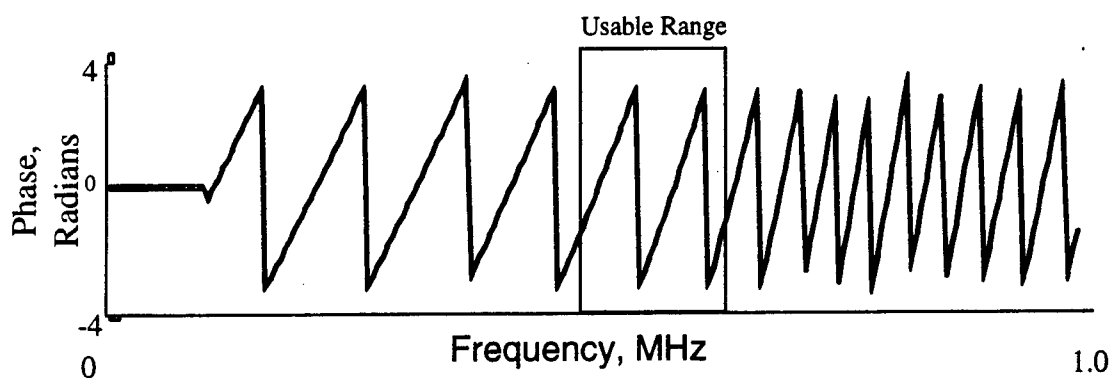


Figure 3. Amplitude Cross-spectrum of Plate Wave.



(a) Measured Phase Spectrum



(b)Calculated Phase Spectrum

Figure 4. Theoretical and Measured Phase Spectra

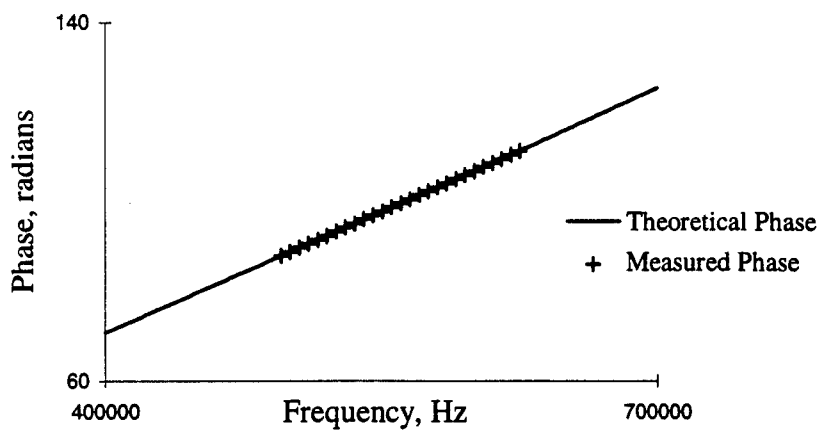


Figure 5. Theoretical and Measured Unwrapped Phase Spectrum

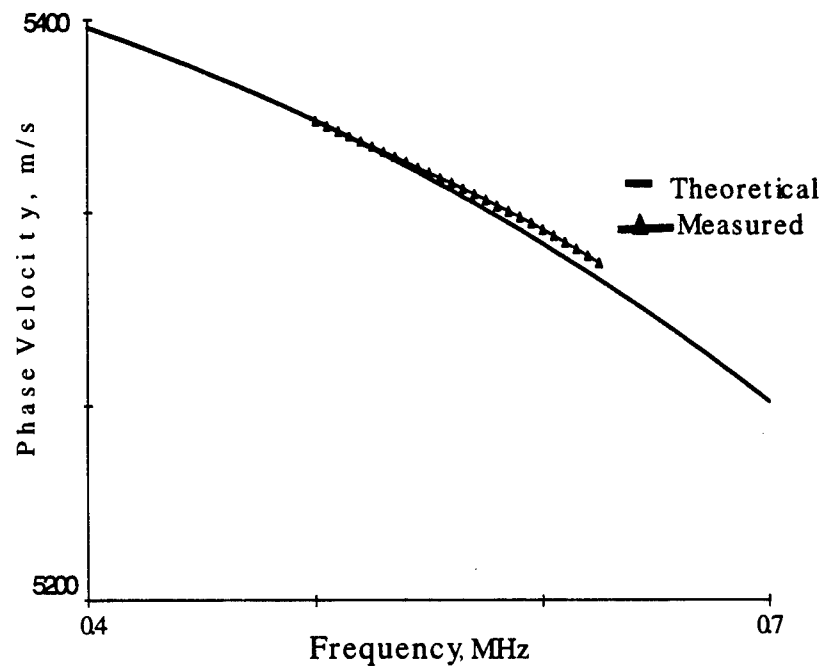


Figure 6. Measured and Theoretical Dispersion Curves

## **DISCUSSION**

### **Real-time Characterization of Isotropic Plates Using Lamb Waves**

Speaker: Rodriguez

Have you used this approach for double wall radiography? —Glenn Light

Why do you need angled (wedge) transducers to pick up the lamb wave signals? Only the waves are generated by the variable angle transducer, they could be picked up by transducers placed directly on the surface of the plate. —Ajit Mal

# **Emerging technologies for NDE of aging aircraft structures**

Robert E. Green, Jr.

Center for Nondestructive Evaluation  
The Johns Hopkins University  
Baltimore, MD 21218

## **ABSTRACT**

Several emerging technologies affording new opportunities for the nondestructive evaluation of aging aircraft structures. Among these technologies are ultrasonic attenuation detection of fatigue and corrosion damage; non-contact ultrasound including laser-laser, laser-EMAT, laser-air, and air-air; laser based acoustic emission source identification; full-field double-pulse holographic imaging; nonlinear assessment of adhesive bond quality; x-ray diffraction topographic imaging of the quality of nickel based alloy single crystal turbine blades.

**Keywords:** ultrasound, lasers, air-coupling, EMATs, acoustic emission, holography, fatigue, corrosion, adhesive bonds, x-ray diffraction, turbine blades

## **1. FATIGUE AND CORROSION DAMAGE MONITOR**

The first ultrasonic technique used to study the development of fatigue damage during fatigue cycling was ultrasonic attenuation. Although, for over 40 years, this technique has been proven to be the optimum one to detect early fatigue damage, it has not proven useful for field use because of the problem of acoustically coupling the transducer to the structure in a reproducible fashion that does not influence the measured attenuation values. Experiments conducted in the early seventies to monitor the development of fatigue damage during cycling of an aircraft aluminum alloy show that ultrasonic attenuation can detect fatigue damage much earlier than conventional ultrasound reflection from a crack (Figure 1). Although detection of corrosion damage has increased in priority with the necessity of flying many aircraft well past their original design life, none of the techniques currently under development involve ultrasonic attenuation measurements. Moreover, since any corrosion on the surface of aluminum alloys will result in an increase in ultrasonic attenuation, this technique also has a very high probability of detecting even small amounts of hidden corrosion.

## **2. NON-CONTACT ULTRASOUND**

Although piezoelectric ceramics have been predominantly used as transducer materials, a major problem with their use is that they are bonded to the test material with a coupling medium such as water or grease. Often more harmful, is the necessity of immersing the structures to be tested in tanks of water or using water squirters. For velocity measurements, which are necessary for material thickness measurements and to locate the depth of defects, the couplant can cause transit time errors. It can also lead to serious errors in attenuation measurements which is the reason that so few reliable measurements of attenuation are reported in the literature.

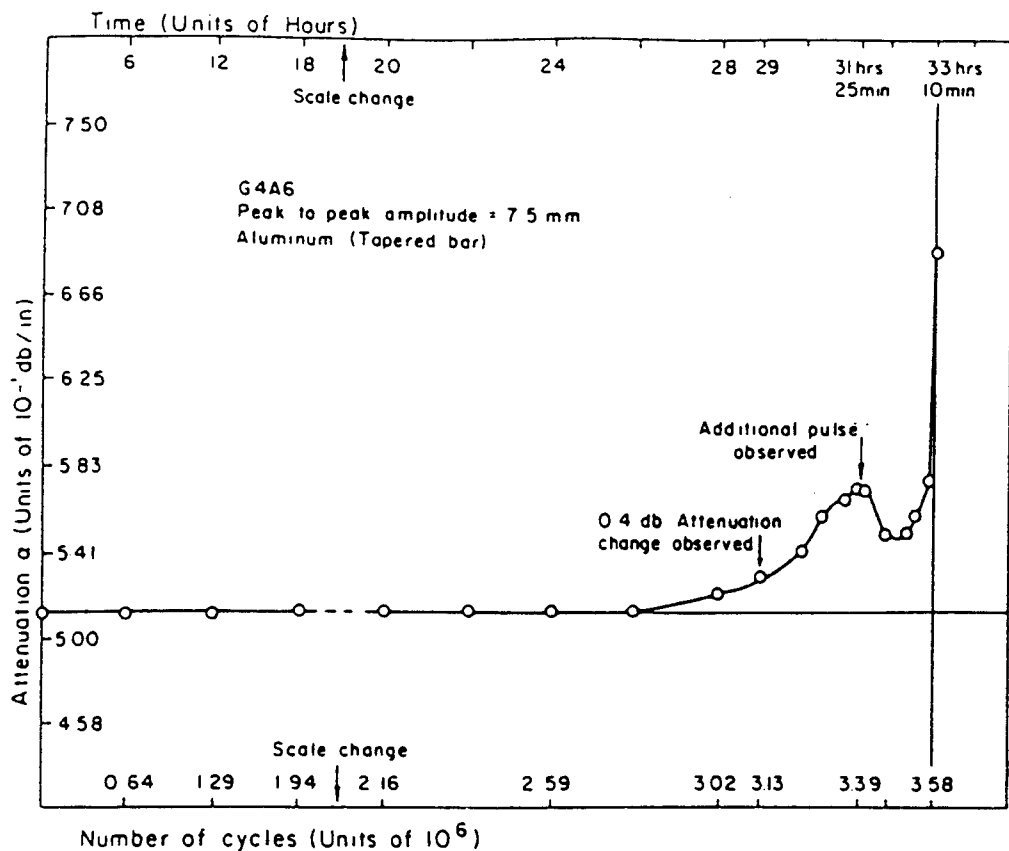
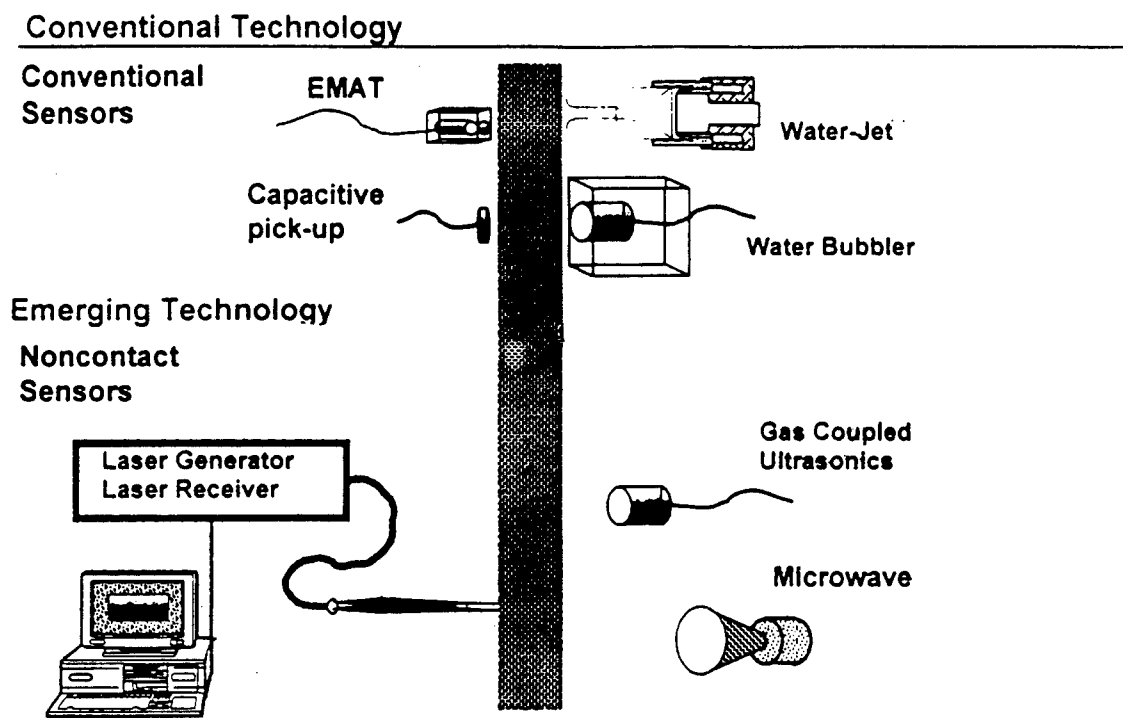


Figure 1. Ultrasonic attenuation yields early warning of fatigue failure in aircraft aluminum alloy

Several non-contact techniques are presently available in various stages of development, namely capacitive pick-ups, electromagnetic acoustic transducers (EMATs), laser beam optical generators and detectors, and air(gas)coupled ultrasonic systems (Figure 2). However, capacitive pick-ups cannot be used as ultrasonic generators and, even when used as detectors, the air gap required between the pick-up and test structure surface is extremely small, which in essence causes the device to be very nearly a contact one. EMATs have been successfully used for material defect characterization in metals. One major problem with EMATs is that the efficiency of ultrasound generation and detection rapidly decreases with lift-off distance between the EMATs face and the surface of the test object. They can obviously only be used for examination of electrically conducting materials. They are much better detectors than generators of ultrasound. Laser ultrasonics affords the opportunity to make truly non-contact ultrasonic measurements in both electrically conducting and non-conducting materials, at elevated temperatures, in hostile environments, and in geometrically difficult to reach locations. However, although laser ultrasonics has been under development since 1963, it has not met with overwhelming success. This is because expensive high power lasers are required for ultrasound generation and often to obtain an ultrasonic wave of sufficient amplitude to be practically useful, the surface of the test specimen must be ablated. Although often lower power lasers can be used for interferometric detection, unless

the surface of the specimen is a good optical reflector, such detection systems will not work. This necessitates either painting the surface with an autoreflective paint or applying a similar strippable coating. In other cases, a more powerful laser must be used for detection than for generation. Air(gas)coupled ultrasonic systems have been under development for some time and research is underway to optimize them for practical non-contact ultrasonic applications. These systems are relatively similar to conventional contact ones and, therefore, when optimized may play an important role in modern nondestructive testing.



**Figure 2.** Conventional and emerging ultrasonic techniques

## 2.1 Laser ultrasonics

A completely new design laser generation system capable of generating discrete narrow band frequency ultrasound rather than the broad frequency band ultrasound generated by conventional laser pulses has been optimized (Figure 3). This multi-element laser system is composed of ten Q-switched Nd:YAG cavities with a common power supply and timing electronics. The timing circuit allows the lasers to be fired with any desired delay. Turning mirrors are used to direct the light pulses through a cylindrical lens to the surface of the test specimen. The arrangement allows each laser's pulse to be focused to a single point or on a line at a fixed distance on the metal's surface. The ten laser system permits operation in two modes: phased array or narrow band generation of ultrasound. In the phased array mode, the individual laser beams from each of the 10 lasers are directed to a sequence of spots or lines on a surface and fired in an appropriately timed sequence in order that sound generated by one laser is reinforced by the subsequent firing of the next consecutive laser and so on until all 10 lasers are fired. This results in great enhancement of the signal-to-noise. In order to generate

amplitudes as large as obtained with the 10 laser array system, it would be necessary to increase the power intensity of a single laser to a level which would damage the surface of most materials, particularly composites. The second mode of operation is one in which narrow band (tone burst) ultrasound is generated. Narrow band generation takes place when all of the laser elements are focused to the same point on the material surface but fired periodically in sequence so that a rapid burst of energy arrives at that point. This laser array generation system has been applied for experiments involving laser generation/laser detection of ultrasound.

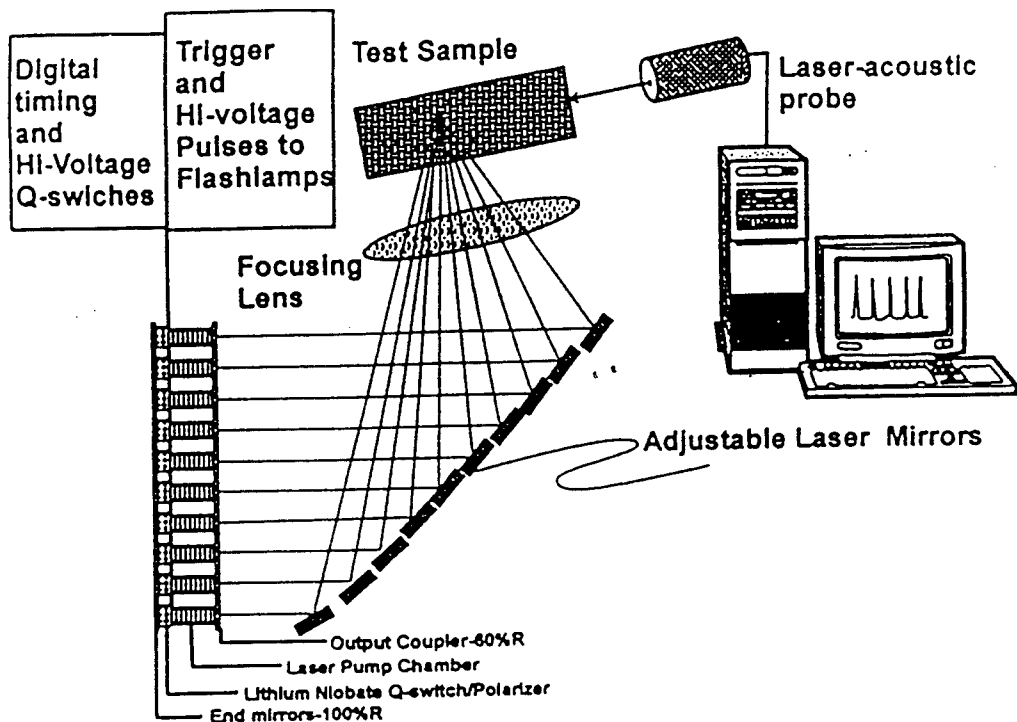


**Figure 3.** Advanced non-contact narrow band laser ultrasound system

## 2.2 Air(gas)coupled ultrasonics

An air-coupled ultrasonic system was developed for C-scan imaging of defects in wooden panel paintings for the Smithsonian Institution. The major components of this system is a state-of-the-art ultrasonic unit, special transducers, and a high-resolution scanning bridge. The transmitting transducer, mounted onto the moving element of the scanning bridge, is driven by a computer-controlled high power tone burst gated amplifier. Even though this unit permits generation of frequencies from below 100 kHz to 20 MHz, the C-scan system is usually operated at 500 kHz due to the currently available air-probe transducers. Depending on the focus of these transducers and or specimen thickness, the standoff distance can range from less than 1/8 inch to more than 2 inches. In addition to transmission C-scan imaging of cracks in wooden panel painting supports, the system has been used to scan wooden two-by-fours, graphite/epoxy prepregs, and graphite/epoxy panels (Figure 4). Current effort is directed at measurement of adhesive bond quality between aluminum plates.



**Figure 4.** Air-coupled c-scan image of graphite/epoxy panel containing more intentionally introduced porosity on right side than on left

### 3. LASER BASED ACOUSTIC EMISSION SOURCE DETECTION AND IDENTIFICATION

The primary importance of acoustic emission monitoring lies in the fact that proper detection and analysis of acoustic emission signals can permit remote identification of source mechanisms and the associated structural alteration of materials and structures. Although the phenomenon of acoustic emission has been the subject of scientific investigations and technological applications for more than 40 years, it has not optimally fulfilled its promise as a practical nondestructive testing technique since the precise characteristics of the acoustic emission stress waves emitted from specific defects remain unknown.

In order to positively identify the source of an acoustic emission signal and be able to make a definitive statement as to whether the material alteration causing the acoustic emission signal is harmful to the integrity of the engineering structure, it is necessary to be able to determine the unmodified waveform and frequency spectrum of the signal itself. Moreover, once this determination is made, one must be able to compare the characteristics of the acoustic emission signal in question with a previously characterized set of acoustic emission signals recorded from known material defects. An optical interferometer is the only detector that is actually non-contact and permits detection of surface displacements caused by acoustic emission events without any modification of the detected waveform or frequency spectrum. No acoustical impedance matching couplant is required. Optical probes have inherent broad flat frequency responses. They can probe internally in transparent materials. They can be used to make measurements on hot and extremely cold materials and in other hostile environments. Since the focused laser beam diameters are very small, they can probe very close to a microscopic size material defect. An experimental system which used micro-tensile test specimens with very small gauge sections and laser interferometric detection, permitted successful identification of the source of acoustic emission signals (Figure 5). Using this technique with steel it was found that the specimens failed by void nucleation, growth, and coalescence. Examination of the fracture surface of each specimen in a scanning electron microscope revealed that each void contained a rather large intermetallic particle, some of which had cracked in a brittle manner (Figure 6). Scanning the entire fracture surface of the steel gauge section and counting the number of broken intermetallic particles resulted in a near one-to-one correspondence between fractured intermetallic particles and the number of acoustic emission bursts.

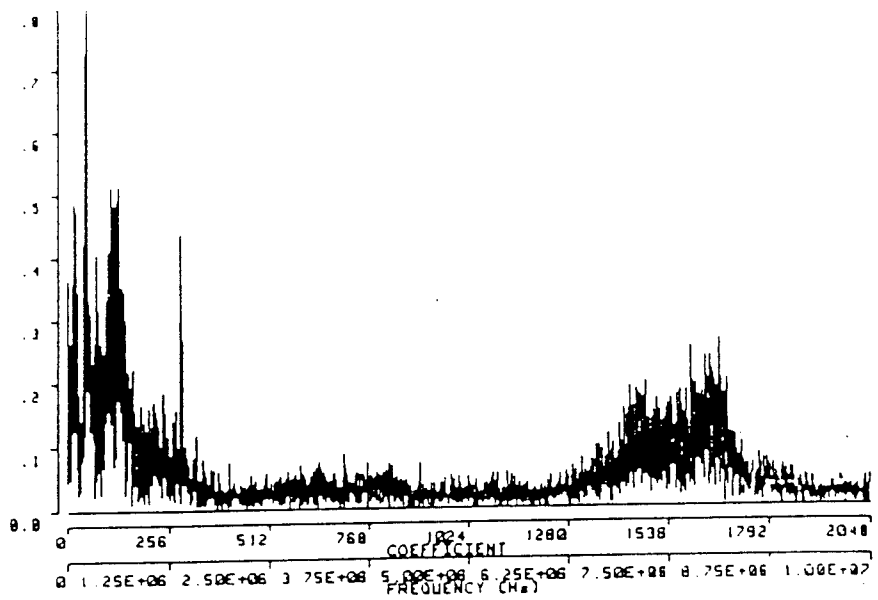


**Figure 5.** Laser detected acoustic emission frequency spectrum indicating both low and high frequency sources



**Figure 6.** Electron microscope image of fractured ceramic particle causing observed high frequency acoustic emission

#### 4. DOUBLE PULSE FULL-FIELD HOLOGRAPHIC IMAGING

Heterodyne holographic interferometry also permits full-field imaging of surface displacements on solid materials due to ultrasonic wave propagation. An example of the implementation of this technique is as follows.

A full-field laser source is used to record a holographic image of the entire front surface of a graphite-epoxy composite panel. Subsequently, a second point source laser pulse, possessing sufficient energy to cause ultrasonic wave generation in the panel by thermoelastic heating, is incident at the center of the surface of the plate. After sufficient time for the resulting thermoelastically generated ultrasonic wave to travel to outward from the source, a third full-field laser pulse is used to re-expose the holographic plate. The resulting interference pattern showed the surface displacements of the panel caused by the ultrasonic wavefront traveling outward from the source with the influence of the anisotropic character of the panel clearly evident (Figure 7). Moreover, the interference pattern exhibited a retardation of the wavefront on one side caused by a delamination in that region of the panel.



**Figure 7.** Double pulse full-field holographic image of anisotropy and defect in composite plate

## 5. ADHESIVE BOND QUALITY

The only NDE techniques which are possibly capable of quantifying the physical strength of an adhesive bond are ultrasonic ones since ultrasonic waves can propagate along the adhesive bondline and therefore measure the properties of the bondline in an optimum fashion. Most literature sources state that the normal incidence longitudinal pulse-echo reflection technique is good for detecting debonds, but is not good for evaluation of bond strength, since the bondline constitutes a small fraction of the ultrasonic wave path length. However, it has been reported that comparison of the amplitude of longitudinal pulse-echo waves reflected from the top and bottom surfaces of the bond is an indicator of bond strength. Actually this is an ultrasonic attenuation technique. The use of normal incidence shear (transverse) pulse-echo waves should be much better for this application, particularly with regard to attenuation measurements, but no such measurements have been reported in the literature for bond line strength investigations.

It has been reported that ultrasonic spectrum analysis permits evaluation of the efficiency of the adhesive as a whole and correlates satisfactorily with the bond strength. This is true for both pulse-echo reflection and through transmission techniques. Since the presence of a debond causes a change in the resonant frequency when using an ultrasonic or sonic resonance technique, these techniques are good for detecting debonds, but not good for accessing bond strength. Several investigators have reported the successful use of acousto-ultrasonics to evaluate bond strength. The apparent success of this technique for bond line applications relies on the generated pulse following a path into the metal, passing through the adhesive bond, and reemerging again from the metal to be detected by the receiving transducer. In an optimum situation, the stress waves would undergo multiple reflections at the boundary surfaces of the bond and therefore interact with a significant fraction of the bondline volume that lies in their path.

A large number of investigators have used some type of guided wave (interface waves, Lamb waves) to monitor bond strength. In fact this appears to be the most highly regarded technique. The advantage of this technique, in common with the acousto-ultrasonic technique, is that the interrogating waves propagate along the bond line rather than perpendicular to it producing shear strains in the bond-line region, and thus provide information about the quality of the bond itself.

A unique weak bond screening technique, which is not precisely nondestructive, is based on utilization of high power ultrasound. The high power ultrasound is generated by a piezoelectric driven exponential horn operating in the 10-40 kHz range of frequencies. By coupling the horn to the surface of an adhesively bonded structure and adjusting the power level so as to disrupt weak bonds and create a discontinuity, but not to affect bonds with normal strength, subsequent inspection by conventional ultrasonic methods can reveal the locations where the weak bonds were converted into disbonds.

## 5.1 Nonlinear ultrasonics

Recently research has been initiated to use nonlinear ultrasonic methods to measure adhesive bond quality. Nonlinear ultrasonic waves differ from linear ultrasonic waves, which are commonly used for nondestructive evaluation, in several important aspects. An initially sinusoidal longitudinal wave of a given frequency distorts as it propagates, and energy is transferred from the fundamental to the harmonics that appear. Monitoring the amount of harmonic generation developed in materials subjected to mechanical or thermal loading or other environmental alterations can be used to access the state of resulting damage. Figure 8 shows the results of nonlinear ultrasonic testing of adhesive bond between two aluminum plates.

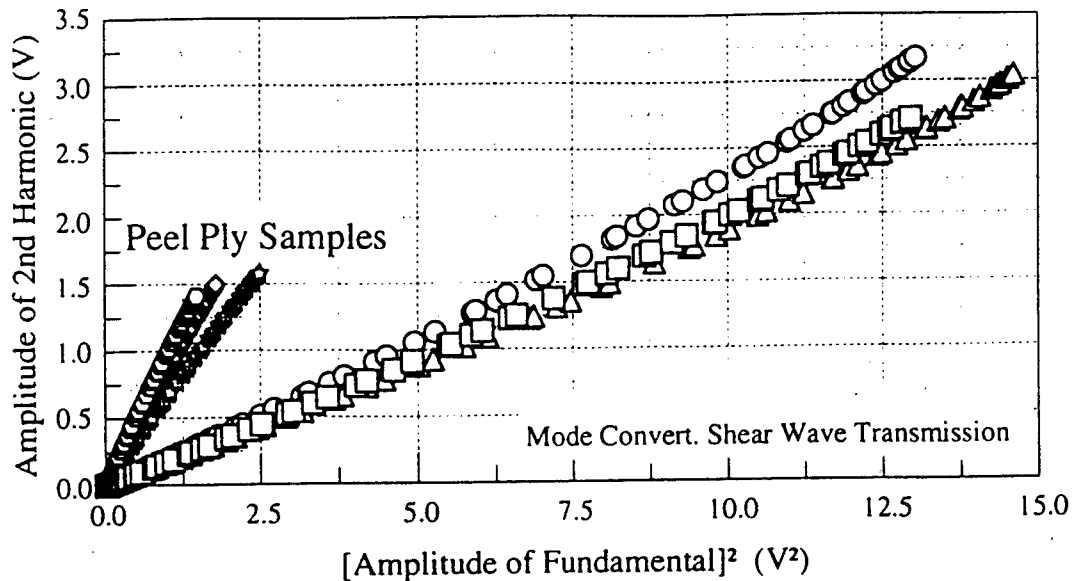


**Figure 8.** Results of nonlinear ultrasonic testing of adhesive bond between two aluminum plates

## 6. QUALITY OF SINGLE CRYSTAL TURBINE BLADES

The efficiency of modern aircraft gas turbine engines increases with increasing combustion temperature, while the performance increases with increasing inlet temperatures. The physical requirements which limit the choice of turbine blade materials for high temperature operation are low density, thermal stability, thermal fatigue resistance, toughness, resistance to high-temperature oxidation, and resistance to creep. Creep caused by dislocation motion is resisted by addition of alloying elements in solid solution and formation of stable hard precipitates, both of which serve as dislocation pinning points. Diffusional creep is resisted by increasing the grain size, directional solidification to produce long grains with boundaries parallel to the applied stress, and most optimally by eliminating the grain boundaries completely, i.e. using single crystal blades. Among the problems encountered with single crystal turbine blades is the ability to determine the overall crystalline perfection of the final blades.

### 6.1 X-ray diffraction topography

Conventionally, the Laue back-reflection x-ray diffraction technique is used to determine the orientation of one small localized point on the turbine blade. Examination of the entire blade using this point probe method requires an inordinately long time. An asymmetric crystal topographic (ACT) x-ray diffraction technique permits imaging of a large portion of the single crystal blade at one time, while incorporation of an x-ray sensitive electro-optical detector permits this to be done in real-time. In the ACT technique each individual topographic image is essentially a large Laue "spot" generated by diffraction from a particular set of "parallel" lattice planes covering a large area of the crystal. The x-ray beam incident on the specimen illuminates a large area and, because of the special beam expanding monochromizing silicon crystal, experiences minimal divergence.

Figure 9 shows a schematic diagram of the ACT experimental arrangement used for inspection of the single crystal nickel based alloy turbine blade. Figure 10 is an ACT image of a large portion of the turbine blade which shows that the single crystal portion imaged contains a substructure indicating the presence of fairly large substructure probably caused by dendritic segregation during solidification of the blade. It should be noted that the size of the individual portions of the substructure is approximately the same size as the area of the blade that would be covered by an incident x-ray beam when using the conventional pinhole collimating system. This illustrates most vividly the failing of pinhole collimating systems for inspection of turbine blades.

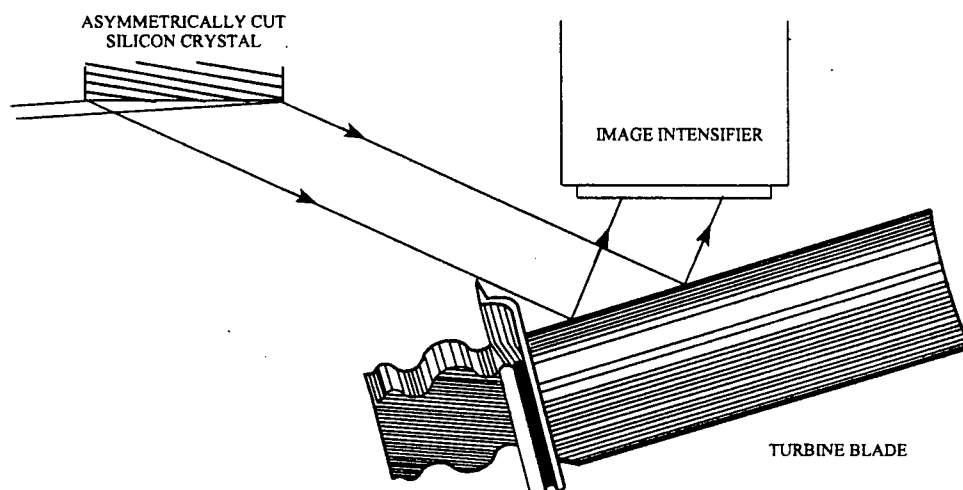


**Figure 9.** Experimental x-ray topographic system for determination of perfection of nickel alloy single crystal turbine blade



**Figure 10.** X-ray topographic image showing dendritic segregation caused misorientations along length of nickel alloy single crystal turbine blade

## 7. CONCLUSIONS

It has become increasingly evident that emerging technologies such as described in this article should be used for nondestructive evaluation of aging aircraft. Other techniques including in-situ sensors can be combined with radio telemetry systems for continuous remote monitoring of aging aircraft structures. Application of these advanced sensors and artificial intelligence algorithms will play an extremely important role in the future.

## 8. ACKNOWLEDGMENTS

This research was supported in part by the Defense Advanced Research Projects Agency, Wright Laboratory Nondestructive Evaluation Branch, Air Force Office of Scientific Research, NASA Langley Research Center, Westinghouse Power Systems Division, and Howmet Corporation.

## 9. REFERENCES

1. R.E. Green, Jr., "Nondestructive Methods for the Early Detection of Fatigue Damage in Aircraft Components," *Proceedings of AGARD/NATO Lecture Series No. 103, Nondestructive Inspection Methods for Propulsion Systems and Components*, AGARD-LS-103, pp. 6-1 to 6-31, 1979.
2. R.B. Mignogna, J.C. Duke, Jr., and R.E. Green, Jr., "Early Detection of Fatigue Cracks in Aircraft Aluminum Alloy Sheets," *Materials Evaluation*, Vol. 38, pp. 37-42, 1980.
3. R.E. Green, Jr., "Nondestructive Evaluation of Materials," *Annual Review of Materials Science*, Vol. 20, pp. 197-217, 1990.
4. J.W. Wagner, "Optical Detection of Ultrasound," *Physical Acoustics*, Volume 19, pp. 201-266 Academic Press, New York, 1990.
5. C.B. Scruby and L.E. Drain, *Laser Ultrasonics: Techniques and Applications*, Adam Hilger, Bristol, UK, 1990.
6. A. Murray, E.S. Boltz, M. Renken, C.M. Fortunko, M.F. Mecklenburg and R.E. Green, Jr., *Nondestructive Characterization of Materials VI*, pp. 103-110 Plenum Press, New York, 1994.
7. W.A. Grandia and C.M. Fortunko, "NDE Applications of Air-Coupled Ultrasonic Transducers," *IEEE International Ultrasonics Symposium Proceedings*, Vol. 1, pp. 697-709, November 1995, Seattle Washington, USA (in press).
8. C.H. Palmer and R.E. Green, Jr., "Optical Detection of Acoustic Emission Waves," *Applied Optics*, Vol. 16, pp. 2333-2334, 1977.

9. C.H. Palmer and R.E. Green, Jr., "Optical Probing of Acoustic Emission Waves," *Nondestructive Evaluation of Materials*, Chapter 15, pp. 347-378, Plenum Publishing Corp., New York, 1979.
10. Bruchey, W.J., "Optical Probing of Acoustic Emission During Deformation of Micro-Tensile Specimens," *Ph.D Thesis*, The Johns Hopkins University, 1980.
11. J.W. Wagner, L.C. Phillips, E.P. Mueller, and R.E. Green, Jr., "Using Optical Correlation to Measure Leak Rates in Sealed Packages," *Applied Optics*, Vol. 21, pp. 3702-3705, 1982.
12. R.E. Green, Jr., "Direct Display of X-ray Topographic Images," *Applications of X-ray Analysis*, Vol. 20, pp. 221-235, Plenum, Press, NY, 1977.
13. J.M. Winter, Jr., and R.E. Green, Jr., "Characterization of Industrially Important Materials Using X-ray Diffraction Imaging Methods," *Nondestructive Characterization of Materials*, pp. 771-779 Springer Verlag, New York, 1989.
14. K.A. Green and Green, R.E., Jr., "Application of X-ray Topography for Nondestructive Inspection of Industrial Materials," *Review of Progress in Quantitative NDE*, Volume 13A, pp. 571-578, Plenum Press, NY, 1994.
15. K.G. Lipetzky, R.E. Green, Jr., and P.J. Zombo, "Development of X-ray Diffraction Methods to Examine Single Crystal Turbine Blades," Proceedings of 8th International Symposium on Nondestructive Characterization of Materials, Boulder, Colorado (June, 1997) to be Published by Plenum Press, NY.

# Inversion of Ultrasonic Data using Genetic Algorithms for Application in Composite Material Characterization.

Krishnan Balasubramaniam  
Department of Aerospace Engineering and Mechanics  
Mail Stop 9549  
Mississippi State University, MS 39762, USA  
Tele : 601-325-7296  
Fax : 601-325-7730  
KB1@ra.msstate.edu

## ABSTRACT

In this paper, efforts on the inversion of the ultrasonic oblique incidence data to obtain the stiffness constants, fiber orientation and ply lay-up of orthotropic symmetry material systems such as fiber reinforced composites will be discussed. Inverse genetic algorithms were used in this effort and the performance of the genetic algorithms will be evaluated. Several ultrasonic regimes/domains for data acquisitions were tested using the genetic algorithm. The acoustical data domains used was the plate wave dispersion curves. The list of parameters studied included the genetic algorithm parameters such as number of generations, population and bits.

## INTRODUCTION

Fiber reinforced composites are rapidly replacing traditional engineering materials in a variety of fields. A decade or two ago, their popularity was primarily restricted to the aerospace industry which was attracted to their higher stiffness to weight ratios despite prohibitive manufacturing costs. However, due to the development of better cost-effective manufacturing techniques in recent years, their scope of application has widened to include among others, the automobile and construction industries.

Consequently, characterization of the material properties of composites has become more and more important in terms of accuracy and economics. Ultrasonic non-destructive evaluation, (NDE) which has already been established as a vital tool for characterizing traditional (especially isotropic) materials, has as a result, gained an increasing amount of importance as a potentially rapid, accurate, less labor intensive and economical testing technique. Various theoretical models and experimental techniques have been and continue to be adapted or developed to investigate these materials.

Despite considerable success, there still are challenging problems to be tackled in this regard. The anisotropic characteristic of composites renders experimentation and modeling of acoustic wave behavior more complex and involved. Plus, the multi-oriented layered composite structures commonly used, heighten this complexity. Furthermore, in quite a few cases, it is necessary to solve highly non-linear inverse problems in order to completely characterize material properties, especially stiffness. These problems definitely tend to dampen the advantages of NDE, and thus, require increased research efforts.

Coming to multi-oriented layered composite laminates, ply lay-up (stacking sequence) identification is an essential exercise. Lay-up identification falls under the realm of non-linear inverse problems. Few attempts in this direction are quoted in literature. Of note are the works of Komsky and co-workers (*Komsky, et al. 1994, 1992*), where shear wave transmission signals have been used in conjunction with theoretical models or neural networks.

In this paper, the feasibility of first identifying the stiffness constants of a unidirectional single layer composite is first illustrated using dispersion curve analysis. Then, the lay-up identification in layered composites with well-characterized material properties, is examined via a sensitivity analysis based on the dispersion curve behavior of fluid-loaded laminates.

## GENETIC ALGORITHMS

Genetic Algorithms (GAs) are randomized search methods that are based on stochastically generated population models. As opposed to other random search techniques, rather than being a computationally expensive brute-force approach, GAs are an intelligent way of rapidly sampling the search space and arriving very close to optimal global solutions - both unique and non-unique ones.

Further, in contrast to conventional methods where the search space is treated as a real vector space of  $\mathbb{R}^N$  ( $N$  being the number of parameters to be identified); GAs usually operate on finite length alphabet strings (chromosomes) which are coded to represent points in the equivalent vector space. Binary coding is the simplest and most frequently used, although other types of coding (real-valued and Gray coding) are not uncommon.

A genetic algorithm (GA) begins with a randomly generated population of points in a prescribed finite search space - as defined by the physically acceptable bounds imposed on the identification parameters which are nothing but constraints on the problem. These can be regarded as probable solutions to the given problem. Each point is coded as a chromosome composed of concatenated sub-strings that represent the real-valued parameters of the problem. Each chromosome is then divided into its sub-strings and these are decoded into their corresponding parameters. Next, the chromosome's raw fitness value (a measure of the distance of this probable solution from the global optima) is evaluated from the fitness function, which is nothing but the function that must be optimized. Note that, in the context of GAs, fitness is defined according to whether the problem is a minimization or maximization one. Pertaining to the reconstruction problem, the fitness function is in a minimization form. As the fitness function has to be minimized, population members with lower errors have higher fitness.

Subsequent to the random creation and fitness evaluation of the first and initial generation of probables, the raw fitnesses are scaled and three basic stochastic operations -selection, crossover, and mutation - are performed in that order on this first choice of candidate solutions to begin the evolution process.

Fitness scaling is essential for maintaining population diversity and preventing premature convergence. Of the numerous scaling techniques proposed, rank scaling where the fitness rank is the scaling parameter, and sigma scaling are worth mentioning.

Selection is a procedure that decides which member of the current population should survive and be allowed to reproduce and form a mating pool, so as to create the next generation. This operator is biased towards members with above average fitness. Hence, such individuals reproduce more often than poorly fit ones (similar to the Darwinian principle of survival of the fittest).

Crossover consists of randomly choosing two individuals from the newly formed mating pool and exchanging random portions of their strings (chromosomes), in order to form two new chromosomes (children). The crossover operation is however performed with a specified probability  $P_C$  which is normally kept at a very high value. Crossover operations vary from single-point (the simplest) through multi-point to uniform crossover - the difference being the number of points at which the parent chromosomes are cut. Crossover is responsible for the propagation of parental characteristics to the children.

Mutation involves intentionally changing the value (allele) of an alphabet (gene) in a particular position (gene locus) of the chromosome string, with a specified probability  $P_M$  that is usually kept very low to prevent unwanted disruption of the population. For the case of binary coding, the mutation operator just flips every one to a zero and vice-versa. The purpose of mutation is to create unexceptionably fit members compared to current ones and thus allow the search to gain momentum. This innovative operation rescues the GA from pitfalls of stagnation and incorporates increasing robustness and globalism in the search.

After applying the above operators on the current population, a new population is created and the fitnesses of its members are once again evaluated by dividing and decoding the chromosomes. The new population is then compared with the previous one, and decisions on which members of the new population will survive to replace part of the old population are made, based on a certain set of updating (protection) rules. Protection schemes are

necessary to conserve the history of previous generations and guiding the search. It should be noted that the protection scheme chosen for this study was borrowed from *Stoffa* and *Sen* (1991). In this scheme, every individual in the current generation is compared to one randomly picked from the previous generation without replacement. The older member replaces the current one with a specified update probability ( $P_{UPDATE}$ ) only if it is fitter; otherwise the current one survives.

Finally, the updated population is used to create the next generation by going back to the process of fitness scaling, followed by the three stochastic operations once again. The new generation is then compared with the previous one to form yet another updated population. This whole process is continued iteratively till a stopping criterion on either the maximum raw fitness of a generation or on the number of generations themselves is attained.

For a more detailed account on GAs, the texts by *Goldberg* (1989) and *Mitchell* (1996) are suggested.

## SENSITIVITY ANALYSIS

Dispersion curves define the optimum condition for the generation of plate wave modes in a structure. This is dependent upon the geometrical thickness of the plate, the stiffness constants, and the density along with the boundary conditions. The dispersion curve is obtained from the theoretical model using the well known phenomena that if the acoustic impedance of the plate and the loading fluid (in this case water was used as the fluid), the minima in the reflection factor spectrum (when reflection factor is plotted as a function of frequency\*plate-thickness( $fd$ ) product or as a function of angle of incidence) will correspond to the conditions which are suited for the generation of plate wave modes. There are several types of dispersion curve plots. The one we have employed here provides relationship between the phase velocity and the frequency\*plate-thickness( $fd$ ) product. Here, the phase velocity is related to the incidence angle of the longitudinal wave ( $\theta$ ) through the well known Snell's Law.

Dispersion curves in the  $\phi = 0^\circ, 90^\circ$  incident planes for four different stacking sequences - three having different levels of stagger and one inverted - were computed and examined. The elastic constants used and the lay-ups considered are listed in Table 1. The Transfer Matrix Method with numerical truncation incorporated, was used as the model for describing the reflection factor behavior. Not all portions of the dispersion curves could be found. This was because some very narrow minima in the reflection factors were skipped by the computer code.

## SINGLE LAYER STIFFNESS CONSTANTS INVERSION

Ideally, each point on the dispersion curves satisfies the dispersion equations. However, due to their nonlinear nature, the dispersion curves have to be obtained numerically by searching for points in the  $fd$ - $c$  plane at which the absolute values of the dispersion functions tend to approach zero. Such a process is indeed cumbersome and time consuming. Consequently, it would not be practical from a computational time point of view to pose the inverse problem in a least squares minimization form which minimizes the error between the measured and the guessed dispersion curves. *Rokhlin* and *Clementi* (1990) have used such an approach on the nonlinear equation for the reflection factors. An alternative way of posing the inverse problem is to make use of the conditions which determine the dispersion curves - referred to as the determinant minimization method, in this paper. *Karim et al.* (1990) have followed this approach. However, the least squares minimization method appears to be more stable to noise than the alternative approach because not all portions of the dispersion curves are sensitive to the elastic constants (*Rogers*, 1995).

Nevertheless, going by the greater importance of computational time, the determinant minimization approach is employed in this paper. The inverse problem - depending on the medium surrounding the plate (ie. dry or wet case) - can thus be stated as follows:

*MINIMIZE*

$$Det(C) = \sum_{i=1}^{i=n} |S(c_i, fd_i, \rho, \phi, C)| + \sum_{j=1}^{j=m} |A(c_j, fd_j, \rho, \phi, C)|$$

*OR*

$$Det(\mathbf{C}) = \sum_{k=1}^{k=p} |R(c_k, fd_k, \rho, \rho_f, \phi, \mathbf{C})|$$

SUBJECT TO UPPER AND LOWER BOUNDS ON THE ELASTIC CONSTANTS :

$$C_{min} < C < C_{max}$$

where

$(fd_i, c_i)$  and  $(fd_j, c_j)$  are the experimentally determined points in the  $fd$ - $c$  plane of the symmetric and anti-symmetric modes respectively;  
 $n$  and  $m$  are the total number of input inversion data of the symmetric and anti-symmetric modes respectively;

or

$(fd_k, c_k)$  are dispersion curve data corresponding to the reflection factor minimas obtained from immersion experiments;

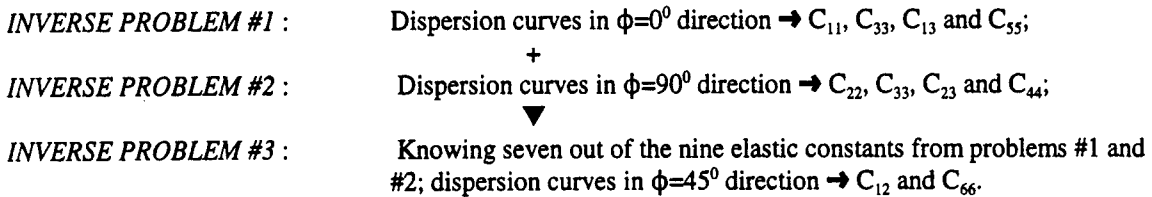
$p$  is the total number of input inversion data;

and

$Det$  is the GA fitness function, whose minima represent optimized conditions for the solution sought.

It should be noted that for wave propagation along an axis of orthotropic symmetry ( $\phi=0^\circ$  or  $\phi=90^\circ$ ), the particle motions decouple into a shear horizontally polarized (SH) wave and flexural waves (sagittal plane motion). It is the sagittal plane motion which defines the symmetric and antisymmetric modes for Lamb waves. Consequently, along the fiber direction ( $\phi=0^\circ$ ), only four elastic constants ( $C_{11}$ ,  $C_{33}$ ,  $C_{13}$  and  $C_{55}$ ) influence the dispersion curves, while across the fiber direction, only  $C_{22}$ ,  $C_{33}$ ,  $C_{23}$  and  $C_{44}$  are involved. For off-symmetry propagation directions, the composite material is of monoclinic symmetry, and hence, the particle motions are coupled, resulting in the dependence of the dispersion curves on all nine of the elastic constants.

Thus, it appears that in order to reconstruct all nine of the elastic constants, dispersion curves in any off-symmetry direction is enough. However, due to sensitivity problems and difficulties in experimentally measuring phase velocities in such directions, this approach is avoided here. It is important to pose inverse problems that exploit sensitivities of the parameters to the maximum possible extent. It is apparent that dispersion curves for directions along and across fibers, will be most sensitive to the elastic constants (all except  $C_{12}$  and  $C_{66}$ ). Hence, a more suitable approach is to solve three inverse problems to back out all nine of the elastic constants, as follows :



## SINGLE LAYER STIFFNESS CONSTANT INVERSION RESULTS

Noise-free GA inversion on an overdetermined data set using the three-step procedure outlined before, was examined for the known Graphite-Epoxy material systems #1. The bounds for all reconstructions were set at  $\pm 50\%$  of the original values. The input, overdetermined noise-free data set consisted of a few representative computer generated points ( $fd, c$ ) on the respective dispersion curve regions for the material considered. The  $c$ -ranges of the input data were chosen based on the sensitivity analysis performed earlier on material #1 such that the maximum sensitivities possible were exploited - ie. the difference in weights of all the data used for inversion were reduced. Due to experimental limitations on high frequency regions, the  $fd$ -ranges for all inversion data were chosen to be

small. Hence, even though some portions of the dispersion curves (for example, at first critical angles) might be difficult to experimentally obtain, the noise-free data sets chosen for inversion were close to a representative experimentally measured set. To test the repeatability of the GA inversion, all the noise-free inversions were performed ten times consecutively. The results are given in Table 2. From the very low errors in the means and low standard deviations for all three materials, it can be concluded that the GA inversion for noise-free data is accurate and repeatable.

### MULTI-LAYER PLY LAY UP INVERSE STATEMENT

For a longitudinal wave obliquely incident on a fluid-loaded multi-oriented layered anisotropic plate, the reflection factor derived using the Thomson-Haskell Transfer Matrix Method (Nayfeh, 1995) is given by :

$$R(\theta, fd, \phi, C) = \frac{[(M_{21} + QM_{22}) - Q(M_{11} + QM_{12})]}{[(M_{21} - QM_{22}) - Q(M_{11} - QM_{12})]}$$

where

- $\theta$  is the incidence angle of the longitudinal wave;
- $fd$  is the frequency\*laminate thickness parameter;
- $M_{IJ}$  for  $I,J = 1,2$  are certain  $3 \times 3$  subdeterminants of the global transfer matrix [A]
- $Q$  is a parameter depending on the fluid characteristics.
- $\phi$  is the lay-up vector  $[\phi_1, \phi_2, \phi_3, \dots, \phi_n]^T$  consisting of the layer azimuthal orientations  $\phi_k$  beginning from the top face of a  $n$ -layered structure;
- $C = [C_{11} : C_{22} : C_{33} : C_{12} : C_{13} : C_{23} : C_{44} : C_{55} : C_{66}]^T$  is the elastic constants tensor expressed as a vector using the contracted indicial notation.

Applying the total transmission criteria, the dispersion curve relation in the  $fd-c$  plane, corresponding to minimas in the reflection factor, is given by :

$$|R(c, fd, \phi, C)| = 0$$

where

$c$  is the phase velocity

Employing the determinant minimization approach, for a well stiffness-characterized material system, the inverse problem for lay-up reconstruction can be stated as :

**MINIMIZE**

$$Det(\phi) = \sum_{k=1}^{k=p} |R(c_k, fd_k, \phi, C)|$$

**SUBJECT TO LOWER AND UPPER BOUNDS ON THE LAYER ORIENTATIONS**

$$\phi_{min} < \phi < \phi_{max}$$

where

$(fd_k, c_k)$  are the leaky dispersion curve data to be inverted;

$p$   
 $Det$  is the total number of input inversion data;  
is the genetic fitness function, whose minima represent optimized conditions for the solution sought.

Furthermore, increase in stagger level gives rise to substantial  $fd$  - shifts and changes in length of branching along the  $c$  - axis. However, it should be noted the  $S_0$  mode has a somewhat decreasing level of sensitivity as the stagger level increases; with only certain portions (where mode turning occurs) being sensitive.

Figure 1 compares the dispersion curves for case 1 in the  $\phi = 0^\circ$  and  $90^\circ$  directions, respectively. This is equivalent to comparing two lay-ups of same stagger level but one being an inverted lay-up of the other - like cases 1 and 4. Once again, substantial sensitivity to such stacking sequence changes is visible.

From the above observations, it can be inferred that leaky plate wave dispersion curves are indeed sensitive to the ply stacking sequence.

## LAY UP IDENTIFICATION RESULTS

Genetic ply lay-up inversion on model-accurate (noise-free) data was attempted on the stacking sequences of cases 1 and 2. A four ply symmetric laminate ( ie.  $[\phi_1 / \phi_2 / \phi_3 / \phi_4]_S$ ) was assumed with azimuthal angle bounds of  $-90^\circ \leq \phi_k \leq +90^\circ$ , a  $c$ -range of  $1.5 \leq c \leq 7.0$  km./sec. and a  $fd$ -range of  $0.0 \leq fd \leq 5.0$  Mhz.mm. All data in the  $fd$ - $c$  plane were picked from dispersion curves computed at 0.25 km./sec.  $c$ -intervals. The genetic parameters and operators employed are listed in Table 3. It should be noted that the genetic parameters were not finely tuned for this problem. This was because of the huge amount of computational time required for the inversion as a result of the slow execution of the forward code.

Repeatability tests were conducted by performing ten consecutive inversions for each case. The results for case 1 is summarized in Table 4, respectively, where the reconstruction results for all runs are given. It can be observed from these tables that the inversion is reliable within a degree on average, and seemingly multiple solutions exist, but these are equivalent considering that  $\phi = -90^\circ$  and  $\phi = +90^\circ$  are both transverse to the fibers. Nevertheless, multiple solutions do exist in the search space as seen by the GA or the inversion tool, in general.

Considering the success in identifying the lay-up of the cross-ply laminates chosen, it can be concluded that genetic ply lay-up inversion does indeed show promise. However, a few problems need to be surmounted. The speed of inversion is drastically low and needs to be increased. Parallel computing could be a solution. Further, the influence of experimental error coupled with actual experimental data inversion needs to be examined. It should be noted that as always accurate experimentation is required. Finally, the effectiveness of the inversion to more general lay-ups (eg. angle plies) having greater number of assumed layers needs to be studied.

## SUMMARY AND RECOMMENDATIONS

Dispersion curves for cross-ply laminate stacking sequences having inverted and staggered lay-ups were computed using a mathematical model based on the Thomson-Haskell Method for simulating the ultrasonic oblique incidence reflection factor response from multi-layered fiber-reinforced composite plates. In the above forward analysis (ie. using apriori knowledge on the ply-Lay-up the ultrasonic data was computed), it was observed that changes in stacking sequence of the ply-Lay-up significantly influences the behavior of these curves. There is a strong uniqueness associated with the ply-Lay-up on these dispersion curves. Consequently, it can be concluded that ply lay-up identification using leaky guided waves is potentially feasible provided accurate experimentation can be conducted.

In order to demonstrate the inversion of the ultrasonic data to obtain the unknown parameter which is the ply-lay up, a genetic algorithm (GA) based optimization technique was used. It is also important that the stiffness constants and the visco-elastic constants values at the frequency range of interest (1-10 MHZ) along with the density and thickness must all be known apriori. The authors have shown that using a unidirectional laminate, it is possible to obtain all of 9 independent elastic stiffness constants using a Genetic Algorithm (GA) based inversion process (*Balasubramaniam and*

Rao, 1997). It was also demonstrated that Genetic Algorithms can be used as the optimization tool for this inversion process for determining ply-Lay-up. Genetic Algorithms are robust search techniques which can locate whereabouts of global extrema in complex, multimodal search spaces. In contrast, the conventional gradient-based optimization techniques are local in nature and often require close initial guesses to avoid entrapment at false local minima. Moreover, Genetic Algorithms are better equipped than gradient searches, to handle search spaces which are not smooth and have several local minima..

## REFERENCES

- Balasubramaniam, K., and Rao, N.S., 1997, "On a truncation procedure for the improved performance of the Thomson -Haskell Transfer Matrix approach," Submitted to letters-to-editor, *Journal of Acoustical Society of America*.
- Balasubramaniam, K., and Rao, N.S., 1997, "Inversion of Composite Material Elastic Constants from Ultrasonic Bulk Wave Phase Velocity Data using Genetic Algorithms," to be published in *Composites, Part B : Engineering*.
- Castaings, M., and Hosten, B., 1994, "Delta operator technique to improve the Thomson-Haskell-method stability for propagation in multilayered anisotropic absorbing plates," *Journal of the Acoustical Society of America*, Vol. 95, No. 4, pp. 1931-1941.
- Chimenti, D.E., and Nayfeh, A.H., 1990, "Ultrasonic reflection and guided wave propagation in biaxially laminated composite plates," *Journal of the Acoustical Society of America*, Vol. 87, No. 4, pp. 1409-1415.
- Deschamps, M., and Hosten, B., 1992, "The effects of viscoelasticity on the reflection and transmission of ultrasonic waves by an orthotropic plate," *Journal of the Acoustical Society of America*, Vol. 91, No. 4, pp. 2007-2015.
- Hosten, B., and Castaings, M., 1993, "Transfer matrix of multilayered absorbing and anisotropic media. Measurements and simulations of ultrasonic wave propagation through composite materials," *Journal of the Acoustical Society of America*, Vol. 94, No. 3, pp. 1488-1495.
- Komsky, I.N., Daniel, I.M., and Lee, Y.C., 1992, "Ultrasonic Determination of Layer Orientation in Multilayer Multidirectional Composite Laminates," *Review of Progress in Quantitative Nondestructive Evaluation*, (Ed. D.O. Thompson and D.E. Chimenti), Plenum Press, New York, Vol. 11, pp. 1615-1622.
- Komsky, I.N., Zgonc, K., and Daniel, I.M., 1994, "Ultrasonic Determination of Layer Orientation in Composite Laminates using Adaptive Signal Classifiers," *Review of Progress in Quantitative Nondestructive Evaluation*, (Ed. D.O. Thompson and D.E. Chimenti), Plenum Press, New York, Vol. 13, pp. 787-794.
- Levesque, D., and Piche, L., 1992, "A robust transfer matrix formulation for the ultrasonic response of multilayered absorbing media," *Journal of the Acoustical Society of America*, Vol. 92, No. 1, pp. 452-467.
- Nayfeh, A.H., and Chimenti, D.E., 1991, "Elastic wave propagation in fluid-loaded multiaxial anisotropic media," *Journal of the Acoustical Society of America*, Vol. 89, No. 2, pp. 542-549.
- Nayfeh, A.H., 1995, "Wave Propagation in Layered Anisotropic Media with Applications to Composites," *North-Holland Series in Applied Mathematics and Mechanics*, (Ed. J.D. Achenbach et al), Elsevier Science B.V., Amsterdam, The Netherlands, Vol. 39.

Table 1 : Ply lay-up and the elastic constants used in the simulation.

GRAPHITE/EPOXY ( $\rho = 1.61 \text{ g/cm}^3$ )									
ELASTIC CONSTANT $C_{ij}$ (GPa)	$C_{11}$	$C_{22}$	$C_{33}$	$C_{12}$	$C_{13}$	$C_{23}$	$C_{44}$	$C_{55}$	$C_{66}$
	144	13.6	12	5.47	5	7	3.7	6	6.5
CASE		PLY LAY-UP				TYPE			
1		$[0^\circ_4 / 90^\circ_4]_S$				Low Stagger			
2		$[0^\circ_2 / 90^\circ_2 / 90^\circ_2 / 0^\circ_2]_S$				Medium Stagger			
3		$[0^\circ / 90^\circ]_S$				High Stagger			
4		$[90^\circ_4 / 0^\circ_4]_S$				Low Stagger, but CASE 1 Inverted			

Table 2 : Inversion results for Graphite Epoxy material system#1 considered in this paper.

RECONSTRUCTION RESULTS FROM GRAPHITE/EPOXY (MATL. #1) DISPERSION CURVES (units in GPa; $\rho = 1.61 \text{ g/cm}^3$ )							
$\phi=0^\circ$ (ALONG FIBERS)							
$C_u$	ORIGIN AL DATA	0% NOISE		1% fd, 2% c NOISE		2% fd, 4% c NOISE	
		MEAN (% ABS. ERROR)	STD. DEV.	MEAN (% ABS. ERROR)	STD. DEV.	MEAN (% ABS. ERROR)	STD. DEV.
$C_{11}$	144.00	144.00 (0.00)	0.00	147.06 (2.13)	4.00	153.02 (6.26)	7.27
$C_{33}$	12.00	12.00 (0.00)	0.00	11.99 (0.11)	0.13	12.32 (2.67)	0.33
$C_{13}$	5.00	5.00 (0.00)	0.00	5.03 (0.53)	0.52	6.63 (32.54)	0.89
$C_{55}$	6.00	6.00 (0.00)	0.00	6.04 (0.74)	0.21	5.89 (1.84)	0.56
$\phi=90^\circ$ (TRANSVERSE TO FIBERS)							
$C_u$	ORIGIN AL DATA	0% NOISE		1% fd, 2% c NOISE		2% fd, 4% c NOISE	
		MEAN (% ABS. ERROR)	STD. DEV.	MEAN (% ABS. ERROR)	STD. DEV.	MEAN (% ABS. ERROR)	STD. DEV.
$C_{22}$	13.60	13.60 (0.02)	0.00	14.43 (6.10)	1.04	17.69 (30.09)	2.34
$C_{33}$	12.00	12.00 (0.00)	0.00	11.95 (0.40)	0.20	11.88 (1.04)	0.29
$C_{23}$	7.00	7.00 (0.03)	0.00	7.43 (6.10)	0.71	9.07 (29.58)	1.09
$C_{44}$	3.70	3.70 (0.00)	0.00	3.70 (0.08)	0.03	3.56 (3.89)	0.10
$\phi=45^\circ$							
$C_u$	ORIGIN AL DATA	0% NOISE		1% fd, 2% c NOISE		2% fd, 4% c NOISE	
		MEAN (% ABS. ERROR)	STD. DEV.	MEAN (% ABS. ERROR)	STD. DEV.	MEAN (% ABS. ERROR)	STD. DEV.
$C_{12}$	5.47	5.47 (0.05)	0.00	3.63 (33.66)	1.21	2.74 (49.96)	0.00
$C_{66}$	6.50	6.50 (0.00)	0.00	6.49 (0.16)	0.39	6.43 (1.14)	0.54

Table 3 : Genetic parameters and operators used for all inversions.

OPERATION	TYPE OF OPERATION	PARAMETERS
CHROMOSOME CODING	BINARY STRING	PARAMETER STRING LENGTH = 8
POPULATION	CONSTANT, OVERLAPPING	POPULATION SIZE = 20
FITNESS SCALING	SIGMA SCALING	-
SELECTION	STOCHASTIC REMAINDER SELECTION WITHOUT REPLACEMENT	-
CROSSOVER	UNIFORM CROSSOVER	$P_C = 0.8$
MUTATION	BITWISE MUTATION	$P_M = 0.05$
PROTECTION	UPDATING	$P_{UPDATE} = 1.00$
STOPPING CRITERIA	NUMBER OF GENERATIONS	MAXIMUM GENERATIONS = 100

Table 4 : Genetic inversion of ply lay up for case 1 in Table 2.

PLY ANGLE	$\phi_1$	$\phi_2$	$\phi_3$	$\phi_4$
ORIGINAL	0	0	$\pm 90.00^\circ$	$\pm 90.00^\circ$
INVERSION #1	-0.35	+0.35 <sup>o</sup>	+90.00 <sup>o</sup>	-89.29
INVERSION #2	-0.35	+0.35 <sup>o</sup>	+90.00 <sup>o</sup>	+90.00 <sup>o</sup>
INVERSION #3	-0.35	-0.35	+90.00 <sup>o</sup>	+89.29 <sup>o</sup>
INVERSION #4	-0.35	-0.35	-90	-90
INVERSION #5	-0.35	-0.35	+89.29 <sup>o</sup>	-90
INVERSION #6	+0.35 <sup>o</sup>	-0.35	-90	-90
INVERSION #7	-0.35	-0.35	-90	+89.29 <sup>o</sup>
INVERSION #8	+0.35 <sup>o</sup>	+0.35 <sup>o</sup>	-89.29	+90.00 <sup>o</sup>
INVERSION #9	-0.35	-0.35	-90	+89.29 <sup>o</sup>
INVERSION #10	+0.35 <sup>o</sup>	-0.35	-90	-90

### Dispersion Curves in the PHI = 0 Deg. Direction

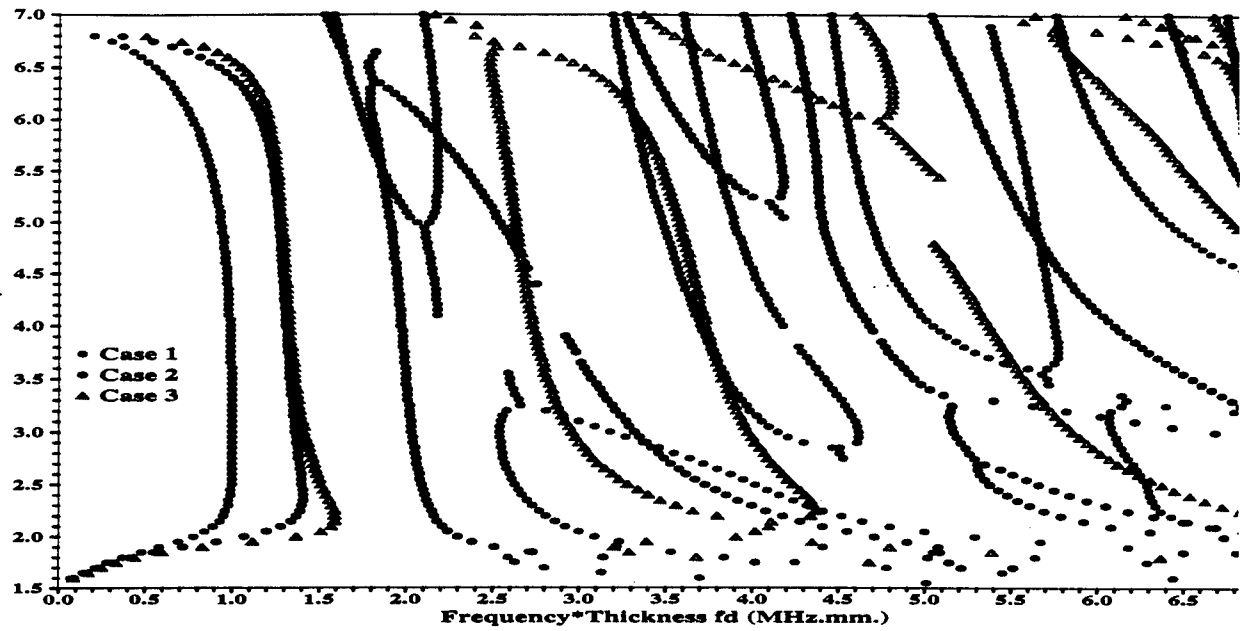


Figure 1 : Dispersion curves in the  $\phi = 0^0$ , incident for the cases 1, 2, and 3 showing sensitivity to ply-lay-up.





## Keyword Index

- acoustic emission, 267  
adhesive bonds, 267  
aerospace structures, 59, 93  
aging aircraft, 59, 141, 267  
aging aircraft inspection, 1, 93  
air-coupling, 267  
aircraft, 83  
aluminum alloy sheet, 123  
aluminum alloys, 113  
ANDI, 47, 101  
AutoCrawler, 47  
automated, 47  
autonomous inspection, 47  
CIMP, 47, 101  
coating, 141  
combination of theories, 23  
composite, 1, 73, 167  
condition-based maintenance, 141  
corrosion detection, 217  
corrosion fatigue, 113  
corrosion, 1, 83, 113, 141, 155, 267  
crack depth, 179  
crack detection, 217  
crawlers, 93  
damage detection, 37  
degradation, 141  
eddy current imaging, 155  
eddy current, 217, 245  
electrochemical impedance spectroscopy, 141  
EMAT's, 267  
enhanced, 101  
epoxy, 73  
estimation, 179  
exfoliation corrosion, 123  
fatigue, 245, 267  
flexibility, 23  
fracture, 267  
futuristic aircraft, 59  
fuzzy reasoning, 179  
geometry, 59  
grain boundary energetics, 123  
graphite, 73  
guided waves, 167  
health monitoring, 37  
high temperature superconductor, 155  
high-cycle fatigue, 245  
Higher-order Frequency Response Functions, 229  
holography, 267  
Imaging, 1  
infrared imaging, 83  
inspection, 47, 101  
intelligent inspection, 93  
KET<sup>TM</sup>, 245  
lamb waves, 229, 257, 245  
lasers, 229  
lattice, 267  
life prediction, 113  
localized corrosion, 113  
MACS, 47, 93  
magnetic imaging, 155  
manufacturing, 1  
MAUS, 93  
misorientation distributions, 123  
model-based NDE, 229  
monitor, 141  
multiresolution, 101  
NARMAX models, 229  
NDE, 1, 93, 113, 217, 245  
NDI, 47  
neural network, 59, 179, 193  
nondestructive, 73  
nondestructive damage detection, 23  
non-destructive evaluation, 59, 193  
nondestructive testing, 155  
on-line, 1  
paint, 141  
partial wave analysis, 167  
performance evaluation, 23  
phase-screen approximation, 167  
positron annihilation, 245  
radiography, 217  
real-time, 1  
remote operation, 93  
remote, 101  
robot, 47  
robotic, 101  
ROSTAM, 47  
rotor blades, 37  
scanning and transmission electron microscopy, 123  
sensor, 141  
shearography, 73  
SQUID, 155  
stereoscopic, 101  
strain energy, 23  
surface wave, 245  
symmetry groups, 59  
synergistic diagnostics, 11  
thermal wave, 83  
thermography, 217  
turbine blades, 267  
ultrasonics, 179, 217, 245  
ultrasound, 267  
visual, 47, 101  
wavelet transform, 37  
weighted general mean, 23  
x-ray diffraction, 267

## Author Index

<i>Achenbach, J.D.</i> .....	179	<i>Maji, A.K.</i> .....	73
<i>Arrowood, R.M.</i> .....	123	<i>Miller Jr, J.H.</i> .....	155
<i>Balasubramaniam, K.</i> .....	279	<i>Murr, L.E.</i> .....	123
<i>Bar-Cohen, Y.</i> .....	93	<i>Nazarian, S.</i> .....	257
<i>Billings, S.A.</i> .....	229	<i>Ogi, T.</i> .....	179
<i>Boyd, M.</i> .....	155	<i>Osegueda, R.</i> .....	59
<i>Chimenti, D. E.</i> .....	167	<i>Paez, T.L.</i> .....	205
<i>Cho, H.M.</i> .....	155	<i>Pardo, H.</i> .....	257
<i>Choi, S.</i> .....	23	<i>Pierce, S.G.</i> .....	229
<i>Claycomb J.R.</i> .....	155	<i>Pierluissi, J.H.</i> .....	257
<i>Dacres, C.M.</i> .....	141	<i>Posada, M.</i> .....	123
<i>Davis, G.D.</i> .....	141	<i>Rodriguez, E.</i> .....	257
<i>Deng, X.</i> .....	37	<i>Rogers, C.A.</i> .....	37
<i>Favro, L.D.</i> .....	83	<i>Sachse, W.</i> .....	11
<i>Ferregut, C.</i> .....	59	<i>Shook, M.B.</i> .....	141
<i>George, M.J.</i> .....	59	<i>Siegel, M.</i> .....	47,101
<i>Giurgiutiu, V.</i> .....	37	<i>Stubbs, N.</i> .....	23
<i>Govekar, E.</i> .....	11	<i>Sutton, M.A.</i> .....	37
<i>Grabec, I.</i> .....	11	<i>Takadoya, M.</i> .....	179
<i>Green Jr, R.E.</i> .....	267	<i>Thomas, R.L.</i> .....	83
<i>Gunatilake, P.</i> .....	101	<i>Tomlinson, G.R.</i> .....	229
<i>Gutierrez, J.M.</i> .....	59	<i>Tralshawala, N.</i> .....	155
<i>Han, X.</i> .....	83	<i>Udpa, L.</i> .....	193
<i>Harrison, G.</i> .....	1	<i>Udpa, S. S.</i> .....	193
<i>Klenke, S.E.</i> .....	205	<i>Wang, Q.</i> .....	37
<i>Kreinovich, V.</i> .....	59	<i>Wei, R.P.</i> .....	113
<i>Lasser, M.E.</i> .....	1	<i>Wenner, B.S.</i> .....	141
<i>Light, G.M.</i> .....	245	<i>Winfree, W.P.</i> .....	217
<i>Little, D.</i> .....	123	<i>Wolters, C.</i> .....	229
<i>Lobkis, O.I.</i> .....	167	<i>Worden, K.</i> .....	229
<i>Lu, X.</i> .....	11		